50 YEARS OF STATISTICAL PHYSICS IN MEXICO: DEVELOPMENT, STATE OF THE ART AND PERSPECTIVES

EDITED BY: Ramon Castañeda-Priego, Enrique Hernandez-Lemus, Susana Figueroa-Gerstenmaier and Atahualpa Kraemer

PUBLISHED IN: Frontiers in Physics

frontiers Research Topics

ISSN 1664-8714
ISBN 978-2-88971-295-3
DOI 10.3389/978-2-88971-295-3

About Frontiers

Frontiers is more than just an open-access publisher of scholarly articles: it is a pioneering approach to the world of academia, radically improving the way scholarly research is managed. The grand vision of Frontiers is a world where all people have an equal opportunity to seek, share and generate knowledge. Frontiers provides immediate and permanent online open access to all its publications, but this alone is not enough to realize our grand goals.

Frontiers Journal Series

The Frontiers Journal Series is a multi-tier and interdisciplinary set of open-access, online journals, promising a paradigm shift from the current review, selection and dissemination processes in academic publishing. All Frontiers journals are driven by researchers for researchers; therefore, they constitute a service to the scholarly community. At the same time, the Frontiers Journal Series operates on a revolutionary invention, the tiered publishing system, initially addressing specific communities of scholars, and gradually climbing up to broader public understanding, thus serving the interests of the lay society, too.

Dedication to Quality

Each Frontiers article is a landmark of the highest quality, thanks to genuinely collaborative interactions between authors and review editors, who include some of the world's best academicians. Research must be certified by peers before entering a stream of knowledge that may eventually reach the public - and shape society; therefore, Frontiers only applies the most rigorous and unbiased reviews.
Frontiers revolutionizes research publishing by freely delivering the most outstanding research, evaluated with no bias from both the academic and social point of view. By applying the most advanced information technologies, Frontiers is catapulting scholarly publishing into a new generation.

What are Frontiers Research Topics?

Frontiers Research Topics are very popular trademarks of the Frontiers Journals Series: they are collections of at least ten articles, all centered on a particular subject. With their unique mix of varied contributions from Original Research to Review Articles, Frontiers Research Topics unify the most influential researchers, the latest key findings and historical advances in a hot research area! Find out more on how to host your own Frontiers Research Topic or contribute to one as an author by contacting the Frontiers Editorial Office: frontiersin.org/about/contact

50 YEARS OF STATISTICAL PHYSICS IN MEXICO: DEVELOPMENT, STATE OF THE ART AND PERSPECTIVES

Topic Editors:
Ramon Castañeda-Priego, University of Guanajuato, Mexico
Enrique Hernandez-Lemus, Instituto Nacional de Medicina Genómica (INMEGEN), Mexico
Susana Figueroa-Gerstenmaier, University of Guanajuato, Mexico
Atahualpa Kraemer, National Autonomous University of Mexico, Mexico

Citation: Castañeda-Priego, R., Hernandez-Lemus, E., Figueroa-Gerstenmaier, S., Kraemer, A., eds. (2021). 50 years of Statistical Physics in Mexico: Development, State of the Art and Perspectives. Lausanne: Frontiers Media SA.
doi: 10.3389/978-2-88971-295-3

Table of Contents

frontiers in Physics

EDITORIAL
published: 09 July 2021
doi: 10.3389/fphy.2021.727582

Editorial: 50 years of Statistical Physics in Mexico: Development, State of the Art and Perspectives

Ramón Castañeda-Priego[1]*, *Susana Figueroa-Gerstenmaier*[1]*, *Enrique Hernández-Lemus*[2,3]* and *Atahualpa S. Kraemer*[4]*

[1]Sciences and Engineering Division, University of Guanajuato, Guanajuato, Mexico, [2]Computational Genomics Division, National Institute of Genomic Medicine, Mexico City, Mexico, [3]Center for Complexity Sciences, Universidad Nacional Autónoma de México, Mexico City, Mexico, [4]Department of Physics, School of Sciences, Universidad Nacional Autónoma de México, Mexico City, Mexico

Keywords: Statistical Physics, complex systems, soft matter, interdisciplinary physics, mathematical physics

Editorial on the Research Topic

50 years of Statistical Physics in Mexico: Development, State of the Art and Perspectives

OPEN ACCESS

Edited and reviewed by:
Alex Hansen,
Norwegian University of Science and Technology, Norway

***Correspondence:**
Ramón Castañeda-Priego
ramoncp@fisica.ugto.mx
Susana Figueroa-Gerstenmaier
sfigueroa@ugto.mx
Enrique Hernández-Lemus
ehernandez@inmegen.gob.mx
Atahualpa S. Kraemer
ata.kraemer@ciencias.unam.mx

Specialty section:
This article was submitted to Interdisciplinary Physics, a section of the journal Frontiers in Physics

Received: *18 June 2021*
Accepted: *28 June 2021*
Published: *09 July 2021*

Citation:
Castañeda-Priego R, Figueroa-Gerstenmaier S, Hernández-Lemus E and Kraemer AS (2021) Editorial: 50 years of Statistical Physics in Mexico: Development, State of the Art and Perspectives. Front. Phys. 9:727582. doi: 10.3389/fphy.2021.727582

In the autumn of 1971, the small group of physicists then working at the Instituto Mexicano del Petróleo (IMP), in Mexico City, was expecting the visit of several distinguished scientists from abroad, who had been invited for talks and seminars on various topics of Statistical Physics. The Mexican physicists at IMP realized that it was an excellent opportunity to organize a meeting on the subject; it could be held the coming January, when most of the would-be speakers were available. Nevertheless, no formal organizing committee was appointed. Leopoldo García Colín, then director of the Applied Research Division at IMP, oversaw the whole operation, made the formal invitations and secured the financial support from IMP. The meeting itself was organized by Fernando del Río, who was assisted by his then Ph.D. student, Luis Mier y Terán, and by Sigurd Larsen, who was on sabbatical stay at the Institute.

Besides a few Mexican speakers who joined the visitors from abroad, the participants in that meeting were mostly graduate students who were working on the subject. By a combination of sheer luck and common sense, the meeting was planned to be held at Oaxtepec, a lush site about 70 km south of Mexico City that boasts a spring-like weather all year round. The meeting had no title nor name, and nobody foresaw that it would become a yearly event, nor thought to take a group photograph. Among the foreign speakers on that (first) meeting were Melville Green, Sigurd Larsen, Joel Lebowitz, Anneke Sengers, Jan V Sengers, and Robert Zwanzig. The meeting had a wide success. The talks were of the highest quality, and the ample time available and pleasant surroundings was profited by the young Mexican students, who interacted closely with the speakers. This success spurred the decision to organize a yearly event every winter. Since then, 49 meetings have been held, the last one in January 2020. This year should have seen the 50th, but it was suspended due to the Covid pandemic. The Winter Meeting on Statistical Physics (WMSP) constitute the series of physics gatherings of longest standing in Mexico, and have been a valuable asset in promoting the growth and consolidation of the discipline. In these 50 years, Statistical Physics in Mexico has grown from a single site of research and a handful of practitioners to almost twenty centers around the country and hundreds of scientists.

The present collection aims to commemorate the long standing tradition of the WMSP. It begins with a review of molecular-based equations of state. Regardless of how they are derived (experimental data or simulation results) when obtained from statistical mechanics; these equations are labeled molecular-based. In this work, a general scheme for the derivation of truly perturbed equations is presented. Two approaches are identified, Bottom-up and Top-down, and

individual steps are discussed in detail along with several rules, reflecting the fundamentals of fluid physics. To exemplify these approaches, the author shows some well-established theoretical approximations, such as the Statistical Association Fluid Theory, to study the equation of state for water.

During the last decades, thermodynamic properties of model fluids have been studied using theoretical tools of Statistical Physics. As an example of the contribution of the Mexican community on the development of accurate approximations to account for the phase behavior of molecular fluids, López de Haro and Rodríguez Rivas solved the equation of state of a parabolic-well fluid combining both a second-order thermodynamic perturbation theory and molecular simulations.

Next, an investigation about the intermediate phase in glasses via a lattice gas model with a modified Hamiltonian considering different energies for cycles of connected atoms (glass with contaminants that form rigid and flexible structures) is presented. Authors study density transitions as a function of chemical potential and a parameter representing the quantity of contaminants. Finally, using hysteresis loops over these quantities they calculate the heat flow of the system, showing that the model present an intermediate phase, minimizing the non-reversing heat flow.

Statistical Physics often use the tools of Quantum Mechanics, but the converse is also true. In a macroscopic system in equilibrium, the probability for a system to occupy a given state is proportional to $\exp(-E/k_BT)$ (Boltzmann factor) where E is the energy of that state and k_BT the kinetic energy. This result can be obtained by maximizing entropy while constraining the energy. On the other hand, the amplitude for a quantum system undergoing a given path is proportional to $\exp(-S/i\hbar)$ (Feynman factor) where S is the action of that path. The similarity between both factors raises the question about the quantum analog of entropy. This quantity is called "quantropy." Here, an extension of quantropy is presented in an integrated version.

Brownian particles have drawn the attention of physicists since the beginning of the last century. Recently, it has been seen that the diffusion of this type of particle is affected when the system is near a jammed state or in the presence of external potentials. This change in dynamical behavior where the particles slow down or accelerate occurs in certain time regimes. In this article, authors report experimentally and numerically different time regimes of a single, colloidal particle diffusing under the influence of a periodic optical potential. They show that the time at which a regime change occurs depends only on the height of the periodic potential.

Soft condensed matter is well represented in this volume. For instance, Vázquez-Vergara et al. investigated the relaxation dynamics of resonances in viscoelastic microfluidics. Aside from their theoretical importance as models for non-equilibrium phenomena in non-Newtonian hydrodynamics, pulsatile flows of viscoelastics have important applications in nano-fabrication and lab-on-a-chip devices. Experimental analysis of a viscoelastic zero-mean flow slug subjected to periodic pulses allow the authors to propose and validate a model for the constitutive equations. Delicate experimental measurements of the hydro-mechanical properties of DMPC/Cholesterol mixed monolayers were performed by Bañuelos-Frías et al. via Langmuir force determination and Brewster angle microscopy. Measurements were made under physiological concentration and pH conditions, leading to further advances in the understanding of why double chain lipids are better than single chain lipids to made up the cell membrane.

Structured soft condensed matter presents challenges to statistical mechanical modeling. Among these challenges, self-assembly of liquid crystals in constrained fields is relevant due to theoretical and practical reasons. The study of the nonlinear dynamical equations for coupled conserved and non-conserved fields describing nanoparticle concentration and liquid crystal order parameters under such conditions was also discussed here. The team lead by Guzmán, tackled this question by writing down these equations and solving them for bidimensional domains to determine approximate relaxation dynamics for the order parameter of the liquid crystal. Assembling dynamics are also at the center of the manuscript by Valadez-Pérez et al. Reversible aggregation of purely short-ranged attractive colloidal particles led to cluster formation with fractal-like morphology. Authors found that the fractal dimension of competing interaction fluids does depend on the second virial coefficient, as in the purely attractive case. And that the addition of repulsive forces in the potential between colloids changes the clustering morphology.

Propagation of topological defects in self-assembly liquid crystals is of particular interest in the production of metamaterials. Three-dimensional topological properties of liquid crystals had much of the attention through the two-dimensional variants are of interest from a theoretical and technological point of view. Calderon-Alcaráz et al. present molecular dynamics simulations to study strongly confined two-dimensional liquid crystals. The impact of constrained geometries on the phase diagram and the appearance of prominent topological defects are analyzed in detail.

Pattern formation and aggregation were also studied in relation to chocolate surfaces. Delgado et al. applied topography atomic force microscopy and cone-plate rheometry to experimentally characterize temperature-dependent pattern formation dynamics of melted chocolate with and without additives (sugar and lecithin), as well as 2D computer simulations of the polymorphic phase molecules under the *NVT* ensemble using a Mie-segmented coarse-grained potential. Experimental and simulation results showed agreement with the Avrami model for aggregation based on phase change kinetics. These observations led to predict sizes for chocolate grains which compare accurately with real sizes.

When colloids are confined to non-flat and closed geometries, they experience curvature effects that can induce new phenomena in the static and dynamical properties not seen typically in flat and open spaces. In the particular case of interacting colloids diffusing on a spherical surface, Ledesma-Durán et al. provide evidence that the different dynamical transitions observed at the level of the mean-square displacement can be explained in terms of the existence of an entropic potential that limits the number of accessible states to the colloids. Furthermore, colloids are a class of soft materials that also serve to understand fundamental questions in Statistical Physics. One of the latter concerns with the validity of some thermodynamic processes at the molecular level. In his contribution, Gómez-Solano reviews and describes

both the operation and performance of a colloidal heat engine under finite-time Stirling cycles.

Single-file diffusion refers to transport of particles in narrow channels such that mutual passage is excluded. This degree of confinement induces a kind of anomalous diffusion as a result of the correlation between particle displacements. To further understand the diffusive behavior in quasi-one-dimensional channels, Huerta et al. report on molecular dynamic results of the collective dynamics in a system made up of hard disks. The results show that the transverse excitations obey very specific dispersion law associated to optical transverse modes, not typically seen in both 1*D* and 2*D* cases.

Since the birth of Statistical Physics, it has contributed to the development and growth of other branches of science, such as Mathematics, Chemistry and Ecology, just to mention a few examples. This fundamental aspect has brought the possibility of applying the tools and methods of the Statistical Physics in multidisciplinary problems. In his contribution, Hernández-Lemus nicely summarizes the main elements and aspects of the modern theory of random fields and discusses in detail some of its recent applications not only in Physics, but also in Biology and Data Science; applications that will serve to better understand problems of interdisciplinary character. Among the other applications of Statistical Physics is the study of how DNA compact within cells, or a biopolymer can be encapsulated. Linear chains of molecules are called semiflexible polymers, these include DNA, biopolymers, or common polymers like polyester. Castro-Villareal and Ramirez develop the theory to study semiflexible polymers in the 3-dimensional domain, applying their results via Monte Carlo simulations to the case of a an open domain, an sphere and a cube, where they observe a shape transition in the polymer for the closed domains, one state where the mean square distance from end-to-end exhibits an oscillating behavior, and the other exhibits a monotonic behavior.

Hopefully, the content of this issue will allow the reader to witness the qualitative growth, geographical expansion and maturity reached by Mexican researchers in Statistical Physics, plus the very welcome contribution from abroad. We can be confident that these Winter Meetings will continue to be held for many years ahead, for this discipline is foundational to an increasing number of fields, and young students and mature researchers alike will certainly continue profiting and enjoying the interaction with their peers from around the world.

AUTHOR CONTRIBUTIONS

All authors listed have made a substantial, direct, and intellectual contribution to the work and approved it for publication.

ACKNOWLEDGMENTS

Authors are grateful to the community that has supported the Winter Meeting on Statistical Physics during the last 50 years. Authors also appreciate the nice historical contribution from Prof. Fernando del Río and his enthusiastic and permanent support that has been pivotal for our community to become a highly competitive household on Statistical Physics.

Conflict of Interest: The authors declare that the research was conducted in the absence of any commercial or financial relationships that could be construed as a potential conflict of interest.

frontiers in Physics

REVIEW
published: 29 September 2020
doi: 10.3389/fphy.2020.00287

On Molecular-Based Equations of State: Perturbation Theories, Simple Models, and SAFT Modeling

Ivo Nezbeda [1,2]*

[1] I. N. Institute of Chemical Process Fundamentals, Academy of Sciences of the Czech Republic, Prague, Czechia, [2] Faculty of Science, Purkinje University, Ústí nad Labem, Czechia

With the exception of purely empirical equations of state, the remaining equations can bear the tag "molecular based." Depending on their derivation, their molecular basis varies from those having only some traits of ideas/results of molecular considerations to equations obtained truly by application of statistical mechanics. Starting from formulations of statistical mechanics of liquids, a general scheme for derivation of truly perturbed equations is formulated. Two approaches, Bottom-Up and Top-Down, are identified, and the individual steps are discussed in detail along with several rules that reflect the essentials of the physics of fluids, which should be observed. Approximations and simplifications used in the implementation of the scheme are then analyzed in light of these rules, and a classification of equations of state is introduced. To exemplify these approaches in detail, theoretical and SAFT routes toward an equation of state are considered for water along with a potential way of merging these two approaches to obtain a reliable equation with a potential to *predict* the behavior of real fluids and not only to correlate them.

Keywords: perturbation theory, simple reference fluids, classification of equations of state, primitive models, thermodynamic perturbation theory, SAFT equations

OPEN ACCESS

Edited by:
Susana Figueroa-Gerstenmaier, University of Guanajuato, Mexico

Reviewed by:
Ana Laura Benavides, University of Guanajuato, Mexico
Víctor Manuel Trejos Montoya, Autonomous University of the State of Hidalgo, Mexico

***Correspondence:**
Ivo Nezbeda
ivonez@icpf.cas.cz

Specialty section:
This article was submitted to Interdisciplinary Physics, a section of the journal Frontiers in Physics

Received: *10 April 2020*
Accepted: *25 June 2020*
Published: *29 September 2020*

Citation:
Nezbeda I (2020) On Molecular-Based Equations of State: Perturbation Theories, Simple Models, and SAFT Modeling. Front. Phys. 8:287. doi: 10.3389/fphy.2020.00287

1. INTRODUCTION

In addition to experimental measurements, the thermodynamic properties of pure fluids and their mixtures can be obtained by methods of statistical mechanics, both by theoretical calculations and molecular simulations. Particularly important properties are those of pressure-volume-temperature (PVT) relations, which are usually presented in the form of equations of state (EoS). They can be obtained using different methods, and several points of view can be adopted to sort them out and classify them. Undoubtedly, it is possible to distinguish two basic types of equations: empirical and molecular based. The former are typically obtained by fitting the known experimental (but also molecular simulation) data of the considered real/model system to what is usually an arbitrary many-parameter function, and they should thus be more appropriately called correlation functions. Some examples we may mention include the IAPWS equation for water [1] or the equation for the Lennard-Jones (LJ) fluid of Johnson et al. [2]. The latter equations are based, to various degrees, on ideas and results of statistical mechanics.

The term "molecular based" itself, covering all non-empirical equations, is rather vague, and equations falling into this category need to be further differentiated. Any statistical mechanical treatment requires as input one indispensable ingredient: an intermolecular interaction model whose choice depends on the goal of such computations. In studies aiming at the elucidation of molecular mechanisms governing the behavior of fluids, idealized simple models (referred to

further in the paper as primitive models) are used, whereas if the goal is a prediction of behavior of real fluids, the model is rather a complex function (referred to as a force field) defying any exact treatment. In addition to their simplicity, an advantage of the simple models is a possibility to obtain the final results in a close analytic form, and these results may then be conveniently used also in treatment of complex fluids. Examples are solutions of the Percus-Yevick equation for the fluid of hard spheres (HS) [3, 4], sticky hard spheres [5], square-well fluid [6, 7], the mean spherical approximation result for dipolar hard spheres (DHS) [8], Dahl-Andersen solution for the double square-well model [9], or results of the thermodynamic perturbation theory (TPT) for various primitive models of associating fluids [10–15].

Dealing with real fluids, the only method making it possible to derive an EoS in an analytic form is a perturbation expansion. There is one exception, however: theoretical results for various Yukawa models. The Yukawa model is rather flexible, and, because it is able to describe, with reasonable accuracy, properties of simple fluids, it has attracted a lot of attention, and vast amounts of literature dealing with the Yukawa model is available. Analytic results for the model have been obtained by solving the Ornstein-Zernike equation using different variants of the mean spherical approximation, see, e.g., [16–18], or a variational perturbation theory [19].

The perturbation expansions, and hence the resulting EoS, differ in the way how the reference system is defined and the correction terms treated. There are two different statistical-mechanical approaches: Bottom-Up (BU), beginning at the specific and moving to the general, and Top-Down (TD), going from the general to the specific. The TD approach starts from a complex realistic (preferably the best available) interaction model, analyzes the effect of different interactions on the properties of the considered fluid and discards its less important parts, and it comes gradually via well-defined approximations to a coarse grained model and, ultimately, to a theoretically tractable (simple/primitive) model for the fluid in hand. Such a model is/may thus be commonly used as a reference in a perturbation theory. The BU approach is, in a certain sense, a macroscopic (phenomenological) approach and corresponds to a common classification of liquids according to their increasing complexity (see the next chapter). It starts from a simple intuitive/speculative model whose use is justified by either previously or *a posteriori* obtained results of molecular theories and simulations. It is (implicitly) assumed that the model captures the basic features of the studied class of considered fluids and additional terms accounting for other interactions are then added. The parameters appearing in the expressions are evaluated by fitting to data of the considered fluid, either simulation or experimental ones, and may not thus be directly linked to the actual molecular characteristics.

Each of the above approaches has its advantages and disadvantages. The BU approach makes it possible to treat very complex systems (using a simplified intuitive modeling) that otherwise defy any rigorous treatment. On the other hand, it is virtually impossible, because of its intuitive basis, to systematically improve its performance with respect to the underlying molecular mechanisms, and further progress toward better results has to go via empirical corrections only. Furthermore, for the development of the parameters of the proposed EoS a large number of experimental data is required, and the use of the EoS outside the range of the data is problematic. In general, BU equations enjoy great flexibility, and if their performance is not acceptable, it can be improved by adding additional terms, making their parameters state dependent, etc. In the TD approach, everything is clearly defined from the very beginning and performance of the developed EoS can be gradually improved by accounting for the known neglected effects. An advantage of this approach is that it also provides a guidance for developing non-intuitive simple models that, in turn, may serve as a theory-based reference in the BU approach. Its disadvantage is that, when strictly adhering to theory, it may be limited to fluids made up of relatively small and medium-sized molecules. Furthermore, it is tied to a parent interaction model and cannot thus perform better than the model itself. Nonetheless, it is worth emphasizing that, although conceptually completely different, both methods, TD and BU, may formally end up with the same result. A typical example is the vdW EoS, which was derived originally by an intuition and belief in the existence of molecules as volume excluding entities (hard bodies; BU approach) but which can also be derived rigorously by starting from a realistic intermolecular potential (TD approach) and applying then a perturbation expansion about a suitable short-ranged repulsive reference model (see section 2.3).

The two potential ways to develop a molecular-based EoS outlined above are not usually distinguished, which may also hinder further (faster) progress toward better equations, often making the results more complex. Typically, instead of going to the basics, (empirical) corrections of corrections of corrections are introduced. As a typical example, we may again mention the vdW EoS and dozens of its empirical modifications. When derived by statistical mechanical tools, it is clear that the first term represents an EoS of the fluid of hard spheres (excluded volume) and the other term a mean field approximation. Using a perturbation theory, both these terms are well-defined and can be systematically improved reflecting the corresponding theoretical development (e.g., better EoS of hard spheres). On the other hand, using the original form of the equation, improvements are made only by empirical adjustment of the parameters of the equation (e.g., hundreds of cubic equations with their temperature or/and density dependence of parameters).

An overwhelming majority of molecular-based EoS are of the vdW-type, i.e., they were developed using the BU approach. Within this group of equations belong also SAFT (Statistical Association Fluid Theory) equations [20–23] (although this is not usually acknowledged), which have gained great popularity in the last two decades and which are the most versatile engineering equations in use today. Although called "SAFT equations," it should be emphasized that (as stated by pioneers of the SAFT approach) "…SAFT is not a rigid equation of state but a *method* that allows for the incorporation of the effect of association" [22]. This concept, referred to further as a van der Waals-type, was introduced in the end of 1980s as an alternative to what was exclusively used at that time: "perturbed hard body" EoS.

Emerging in the early 1980s, instead of a hard body term for the short-range reference, it employs simple (primitive) models that capture the effect of association [24–26]. SAFT equations have been quite successful in modeling/correlating thermodynamic properties of fluids (over 100 phase equilibria data of pure fluids [27] and 60 binary fluid mixtures [28] were correlated), and SAFT is arguably considered the state-of-the-art engineering method for this goal.

The success of SAFT equations stems directly from theoretical and simulation results on the effect of the range of interactions. However, because its construction is only intuitive and without a reference to any actual interaction model, the potential of the theoretical findings has not been yet fully explored, and developments and improvements of SAFT equations have followed an empirical path as documented, for example, by a large number of different versions of SAFT and by dozens of different equations for one and the same compound. The goal of this paper it to review in detail the general theoretical basis of the derivation of molecular-based equations, produce an analysis of the individual steps and approximations, and identify/suggest potential ways for their improvement. This program is then exemplified for water for which more than 40 different SAFT EoS have been developed [29] and which is likely the most intensively investigated compound and a challenge for both theorists and applied scientists to fully understand and describe its complex behavior. The paper is organized as follows. In the next section, we review the necessary theoretical background for the derivation of EoS and present both intuitive and force-field-associated simple (primitive) models as well as basic results of the thermodynamic perturbation theory. Their general discussion with respect to the TD and BU approaches and application to water makes up section 3, which is followed by an outline of a potential development toward more accurate equations of state with firm molecular footing.

2. THEORETICAL BACKGROUND

2.1. Brief Historical Survey

Any theoretical consideration at the atomistic level must start from an intermolecular interaction model. Nowadays, using results of quantum chemical computations, molecules are pictured as bodies made up of individual atoms, groups of atoms, or, in general, simply of a set of certain interaction sites that are a fountainhead of interactions. Assuming then pair-wise additivity, the potential functions are written in a uniform way as a sum of interactions between these sites:

$$u(\mathbf{q}_1,\mathbf{q}_2) \equiv u(R_{12},\Omega_1,\Omega_2) = \sum_{i\in\{1\}}\sum_{j\in\{2\}} u_{\mathrm{ss},ij}(|\mathbf{r}_1^{(i)}-\mathbf{r}_2^{(j)}|) \equiv \sum_{i\in\{1\}}\sum_{j\in\{2\}} u_{\mathrm{ss},ij}(r_{ij}) \,, \tag{1}$$

where $\mathbf{q}_i$ are generalized coordinates of molecule i, R_{12} is the separation between the reference sites within the molecules (not necessarily their centers of mass), Ω stands for orientation, and $u_{\mathrm{ss},ij}$ is a spherically symmetric (!) simple interaction acting between site i on molecule 1 and site j on molecule 2 with $\mathbf{r}_k^{(i)}$ being their position vector. The individual site-site interactions are non-electrostatic (referred to also as vdW or dispersive interactions) and Coulombic between charges localized within the molecules. It is also usually assumed that, for the sake of simplicity, for relatively small molecules the geometrical arrangement of the sites is fixed within the molecules (rigid monomer).

The composite site-site interactions in Equation (1) produce an electrostatic field that may be approximated by an interaction between molecular electric multipoles. It has thus been common to write, alternatively, the interaction potentials as

$$u(\mathbf{q}_1,\mathbf{q}_2) \equiv u_{\mathrm{non-el}}(\mathbf{q}_1,\mathbf{q}_2) + \sum_{\{\mathrm{multipoles}\}} u_{\mathrm{multipole-multipole}}(\mathbf{q}_1,\mathbf{q}_2) \tag{2}$$

where $u_{\mathrm{non-el}}$ stands for non-electrostatic interactions and $u_{\mathrm{multipole-multipole}}$ for the interaction between the permanent multipoles of the molecules. The multipole-multipole interaction is usually considered up to the quadrupole-quadrupole level. However, since this approximation of the (truncated) interaction is not able to capture complex interactions in associating fluids (i.e., the fluids exhibiting hydrogen bonding; HB; H-bonding), at the BU level, an artificial term accounting for H-bonding is formally added:

$$u(\mathbf{q}_1,\mathbf{q}_2) \equiv u_{\mathrm{non-el}}(\mathbf{q}_1,\mathbf{q}_2) + \sum_{\{\mathrm{multipoles}\}} u_{\mathrm{multipole-multipole}}(\mathbf{q}_1,\mathbf{q}_2) + u_{\mathrm{assoc}}(\mathbf{q}_1,\mathbf{q}_2) \,, \tag{3}$$

It must, however, be emphasized that the inclusion of the last term does not represent any real physical force but captures a net effect of existing electrostatic interactions. Nonetheless, in certain circumstances, its use may be justified. Finally, following the original van der Waals way of thinking and results of early molecular simulations it is further convenient to consider separately repulsive and attractive parts of the vdW interaction, i.e.,

$$u(\mathbf{q}_1,\mathbf{q}_2) = u_{\mathrm{rep}}(\mathbf{q}_1,\mathbf{q}_2) + u_{\mathrm{att}}(\mathbf{q}_1,\mathbf{q}_2) + u_{\mathrm{elstat}}(\mathbf{q}_1,\mathbf{q}_2) + u_{\mathrm{assoc}}(\mathbf{q}_1,\mathbf{q}_2) \tag{4}$$

The form of Equation (4) forms the basis for a classification of fluids based on the increasing complexity of the constituent molecules and their properties [30]. It also offers itself intuitively for development of molecular-based EoSs, starting with the simplest class of real fluids, the so called normal fluids for which $u_{\mathrm{elstat}} \approx 0$ and $u_{\mathrm{assoc}} \approx 0$, and proceeding then toward fluids with increasing complexity.

An interpretation of early simulation results, namely that the strong short-range *repulsive* interactions have a predominant effect on the properties of fluids (this unfortunate interpretation will be discussed further in the text), suggested that the fluid of HS is a suitable reference (vdW way of thinking). Further extension of the HS model to general hard non-spherical bodies of an arbitrary shape (for a review see [31]) subsequently provided an EoS that served then as a suitable reference system model

for describing the properties of simple non-polar fluids, e.g., lower hydrocarbons.

To move beyond normal fluids, the next class of fluids in the complexity hierarchy are polar fluids. First attempts followed the (mis)interpretation of simulation results of the structure of fluids being determined, in general, by the strong purely repulsive interactions and treated the long-range multipole-multipole interactions as a perturbation. However, despite all the effort invested, the obtained results using this approach did not fullfil the expectations (see, for example, [32]) for simple physical reasons that will become clear in the following section. It became evident that a more complex yet simple model, preferable from the same class of fluids, is needed as a reference system. The simplest and most logically suitable reference model for polar fluids appears to be that of dipolar HS. The analytic result (required in the perturbation theory) for its properties was obtained by Wertheim [8] using the mean-spherical approximation, and this result made it possible to consider the reference dipolar HS model for developing a theory for polar fluids. However, this route did not work satisfactorily either [32]. It is therefore not surprising that a similar approach applied to the third class of fluids in complexity, associating ones, failed as well. As an example, Muller and Gubbins [33] used the interaction model in the form of an extended Stockmayer potential,

$$u = u_{\mathrm{LJ}} + u_{\mathrm{DD}} + u_{\mathrm{HB}} = u_{\mathrm{ref}} + u_{\mathrm{HB}} \ , \tag{5}$$

where u_{LJ} is the Lennard-Jones (LJ) potential, u_{DD} stands for the dipole-dipole interaction, and the additional H-bonding term, u_{HB}, was treated as a perturbation. Comparison with simulations gave rather disappointing result [33, 34].

To summarize, it turned out that building an EoS on the basis of an available EoS of a preceding simpler fluid is a blind alley and that another approach should be applied. A breakthrough in this field is associated with (i) the development of simple suitable models, (ii) development of theory for such models, and (iii) simulation results that pursued a different classification of fluids [35], see section 2.4.

Several simple models that aimed at capturing the main features of H-bonding (strong and strongly directional short-range attractive interaction) appeared, approximately, at the same time: the model of Bol [24], double-square well model of Dahl and Andersen [25], and the model of Smith and Nezbeda (SN) [26]. The gist of both the Bol's and SN models was that their formulation allowed formation of not only dimers [36] but also chains and rings. After focusing first on water and methanol [37, 38], this idea was later extended to capture properties of other associating and polar fluids [39, 40] and also to model colloids (colloids with patchy sites [41, 42]). As it will be shown in section 2.4, it is fully justified to use these models, either directly or indirectly, as a suitable reference system for developing an EoS following both the TD and BU approach. This application is facilitated by availability of analytic EoS's obtained from the TPT. An example of this approach is the family of SAFT equations.

2.2. Perturbation Expansion and Equation of State

The assumption inherent to all applications of perturbation methods is a possibility to split the considered function (property) into two: reference and perturbation parts. In the case of the classical many particle systems, such a function is the pair interaction potential,

$$u(\mathbf{q}_1, \mathbf{q}_2) = u_{\mathrm{ref}}(\mathbf{q}_1, \mathbf{q}_2) + u_{\mathrm{pert}}(\mathbf{q}_1, \mathbf{q}_2) \tag{6}$$

Since the expansion is then carried out in powers of u_{pert}, from the formal mathematical point of view, it is required that the perturbation term be much smaller in comparison to the reference term. However, as it will become clear later, this is not the case of the considered physical systems and a different constraint is imposed on split (6). Any general perturbation expansion of fluid systems (system of many interacting particles) involves an expansion of the exponential $\exp[-\beta U]$ [43–45],

$$\exp[-\beta U] = \exp[-\beta U_{\mathrm{ref}}](1 - \beta U_{\mathrm{pert}} + \frac{\beta}{2} U_{\mathrm{pert}}^2 + \dots) \tag{7}$$

where U is the system's internal energy, $U = \sum_{i<j} u(\mathbf{q}_i, \mathbf{q}_j)$. The Helmholtz free energy is usually considered as the pivot function to be expanded from which then any thermodynamic property may be evaluated using the standard thermodynamic relations. Alternatively, since the pair correlation function, $g = g(\mathbf{q}_1, \mathbf{q}_2)$ [46], provides the complete information on the properties of fluids [43, 44], it is also possible to compute thermodynamic properties from the expansion of the pair correlation function [6],

$$g = g_{\mathrm{ref}} + \beta\epsilon g^{(1)} + \dots \tag{8}$$

where ϵ scales energy. It is easy to show that results of the first-order expansion of the Helmholtz free energy are equivalent to the result obtained from the zero-order expansion of the correlation function.

For the purpose of the discussion of the relation between the perturbation expansion and various EoSs and to make all subsequent steps in the perturbation expansion (further introduced approximations) clear, it is more convenient to use the expansion of the correlation function. We thus start directly with the expression for pressure (compressibility factor, z) in terms of the interaction potential and the pair correlation function [43, 44]:

$$z \equiv \frac{PV}{Nk_{\mathrm{B}}T} = 1 - \frac{\beta\rho}{6V} \int_{(V)} \frac{\mathrm{d}u(\mathbf{q}_1, \mathbf{q}_2)}{\mathrm{d}R_{12}} g(\mathbf{q}_1, \mathbf{q}_2) \mathrm{d}\mathbf{q}_1 \mathrm{d}\mathbf{q}_2 \tag{9}$$

Here, P is the pressure, T is the temperature, ρ is the number density, $\rho = N/V$, and $g(\mathbf{q}_1, \mathbf{q}_2)$ is the pair correlation function of the fluid at hand.

The above separation of the potential, Equation (6), implies that the corresponding thermodynamic functions also split into two terms, i.e.,

$$z = 1 - \frac{\beta\rho}{6V} \int_{(V)} \left[\frac{\mathrm{d}u_{\mathrm{ref}}(\mathbf{q}_1, \mathbf{q}_2)}{\mathrm{d}R_{12}} + \frac{\mathrm{d}u_{\mathrm{pert}}(\mathbf{q}_1, \mathbf{q}_2)}{\mathrm{d}R_{12}} \right] g(\mathbf{q}_1, \mathbf{q}_2) \mathrm{d}\mathbf{q}_1 \mathrm{d}\mathbf{q}_2 \tag{10}$$

Now, using the zero order approximation for g, i.e., $g \approx g_{\mathrm{ref}}$, we get

$$z \cong 1 - \frac{\beta\rho}{6V}\int_{(V)}\left[\frac{\mathrm{d}u_{\mathrm{ref}}(\mathbf{q}_1,\mathbf{q}_2)}{\mathrm{d}R_{12}} + \frac{\mathrm{d}u_{\mathrm{pert}}(\mathbf{q}_1,\mathbf{q}_2)}{\mathrm{d}R_{12}}\right] g_{\mathrm{ref}}(\mathbf{q}_1,\mathbf{q}_2)\mathrm{d}\mathbf{q}_1\mathrm{d}\mathbf{q}_2 \quad (11)$$

$$= z_{\mathrm{ref}} - \frac{\beta\rho}{6V}\int_{(V)}\frac{\mathrm{d}u_{\mathrm{pert}}(\mathbf{q}_1,\mathbf{q}_2)}{\mathrm{d}R_{12}} g_{\mathrm{ref}}(\mathbf{q}_1,\mathbf{q}_2)\mathrm{d}\mathbf{q}_1\mathrm{d}\mathbf{q}_2 \quad (12)$$

$$= z_{\mathrm{ref}} + z_{\mathrm{pert}}\{u_{\mathrm{ref}}\} \quad (13)$$

where the curly braces indicate that z_{pert} is a *functional* of the reference interaction potential, i.e., z_{pert} is evaluated with respect to the chosen reference system. Equation (13) is the fundamental equation which makes it possible to differentiate between different approaches used to "derive" molecular-based EoS.

Interpretation of Equation (13) is evident: provided that the *structure* of the reference and original systems is nearly identical (in other words, if the perturbation interaction has only a marginal effect on the structure of the entire system), then it is possible to estimate the properties of the studied system by means of those of the reference fluid with some added corrections.

As a next step we must therefore find a way to determine the properties of the reference fluid (which, however, may not be a simpler problem either), and this may involve another approximation (expansion). For simplicity, we are going to exemplify this step by considering the simple LJ fluid

$$u_{\mathrm{LJ}}(r) = 4\epsilon\left[(\frac{\sigma}{r})^{12} - (\frac{\sigma}{r})^{6}\right] \quad (14)$$

Considering the Barker-Henderson theory [43, 44], the split of u_{LJ} reads as

$$u_{\mathrm{LJ}}(r) = 4\epsilon H(\sigma - r)\left[(\frac{\sigma}{r})^{12} - (\frac{\sigma}{r})^{6}\right] + 4\epsilon H(r-\sigma)\left[(\frac{\sigma}{r})^{12} - (\frac{\sigma}{r})^{6}\right] \quad (15)$$

$$= u_{\mathrm{ref}}(r) + u_{\mathrm{pert}}(r) \equiv u_{\mathrm{ref,rep}} + u_{\mathrm{pert}}(r) \quad (16)$$

with the soft repulsive fluid as a reference whose properties must be now determined. Unfortunately, no accurate analytic results for this fluid are available, and we thus have to resort to another approximation, and it is only at this point where the HS fluid enters the game. Results of molecular simulations tell us that *the structure of the soft repulsive reference can be very well-approximated by that of a fluid of hard spheres*. The pair correlation function of the HS fluid is known and may thus be conveniently used to evaluate the perturbation integrals with the thermodynamic properties of the repulsive reference being mapped onto those of a certain HS fluid of an unknown diameter σ_{HS}:

$$z = z_{\mathrm{ref,rep}} - \frac{\beta\rho}{6V}\int_{(V)}\frac{\mathrm{d}u_{\mathrm{pert}}(\mathbf{q}_1,\mathbf{q}_2)}{\mathrm{d}R_{12}} g_{\mathrm{ref,rep}}(\mathbf{q}_1,\mathbf{q}_2)\mathrm{d}\mathbf{q}_1\mathrm{d}\mathbf{q}_2 \quad (17)$$

$$\cong z_{\mathrm{HS}} - \frac{\beta\rho}{6V}\int_{(V)}\frac{\mathrm{d}u_{\mathrm{pert}}(\mathbf{q}_1,\mathbf{q}_2)}{\mathrm{d}R_{12}} g_{\mathrm{HS}}(\mathbf{q}_1,\mathbf{q}_2)\mathrm{d}\mathbf{q}_1\mathrm{d}\mathbf{q}_2 \quad (18)$$

It is necessary now to bear in mind that while Equation (13) results from the perturbation expansion used to determine the properties of the original simple fluid, Equation (18) results from a further approximation applied to the reference system to determine its properties. In other words, *Equation (18) cannot be interpreted as a perturbation expansion about the hard sphere reference fluid to deal with realistic simple fluids although it may look so!*

To summarize, the perturbation expansion for realistic models is a two-step process, first to find a suitable reference model that guarantees convergence of the expansion and then to devise a method for the description of its properties.

2.3. Equations of State Classification

In the light of the results of the preceding subsection we may now clearly categorize molecular-based equations of state.

2.3.1. Theoretical (Perturbed) Equations

The derivation starts with an *explicit* expression of the interaction model. Using then the equations derived in the preceding subsection, the resulting EoS possesses the form

$$z = z_{\mathrm{ref}} + \Delta z \quad (19)$$

where Δz is evaluated with respect to the chosen reference system and represents a perturbed correction over the reference system. To accomplish all the calculations, the pair correlation function of the reference system is required, which imposes, to a considerable extent, severe limits on this approach. A typical example of such theoretical equations are the results of the TPT applied to various primitive models [39, 40]. Considering realistic models, truly theoretical EoS's obtained by a perturbation expansion are also available, e.g., for the square-well fluid [6, 7] or Yukawa fluid [16, 47, 48]. For further discussion, see section 3.1.

2.3.2. van-der-Waals-Type Equations

This is a mixed molecular-macroscopic BU approach and overwhelming majority of available equations belong to this category. Without considering an explicit form of the interaction potential u, it is assumed that a potential can be split into several terms (in principle of the equal weight)

$$u = u_0 + u_1 + u_2 + \ldots \quad (20)$$

and that, accordingly, the Helmholtz free energy can be written as a sum of the corresponding terms,

$$A = A_0 + A_1 + A_2 + \ldots \quad (21)$$

and hence also the EoS,

$$z = z_0 + z_1 + z_2 + \ldots \quad (22)$$

This approach then starts from Equation (21) with the goal to find/choose appropriate expressions for the individual terms A_i corresponding to u_i in (20). The key difference between Equations (19) and (22) is that the individual terms in (22) are

mutually independent, and there are thus no constraints impose on them. Although the leading term A_0 is usually predominant, the remaining terms, Δz, are just certain corrections and should be properly called "correction terms." These EoSs are sometimes used also for an interpretation of molecular mechanisms governing the behavior of the fluid systems of interest, but such an interpretation is not justified because there is no guarantee that real fluids do follow such mechanisms, and some of their conclusions may thus be misleading.

A typical example of this approach is the original vdW equation, and it is worth comparing now the above two ways toward an EoS to elucidate the difference although both approaches will end up with the same equation. Let us consider a simple realistic fluid, e.g., the Lennard-Jonesium. Applying the Barker-Henderson method for the description of the soft repulsive reference system, the theoretical route yields [43]

$$z_{\rm th} = z_{HS}(\sigma(T)) + \int_{\sigma}^{+\infty} g_{\rm HS}(r) u_{\rm pert}(r) r^2 {\rm d}r \qquad (23)$$

where σ is the well-defined reference HS diameter obtained from the original $u_{\rm LJ}$ potential. Using now a crude approximation of a uniform distribution of molecules outside the effective hard spheres, we get

$$z_{\rm th} = z_{HS}(\sigma(T)) + {\rm const} \times \beta\rho \qquad (24)$$

We get the same equation following the vdW way of thinking. Molecules are objects excluding certain volume (hard spheres) and they are further subject to an attractive interaction due to the presence of other molecules in the system. By waving hands (using certain intuitive physical arguments), he set $\Delta z = {\rm const} \times \beta\rho$, which is the same result as in Equation (24). However, whereas the perturbation term in Equation (24) is clearly defined and can be improved by using better approximations for $g_{\rm ref}$, in the vdW approach, there are no clues how to improve it, and any arbitrary correction can be made.

2.3.3. Semi-theoretical Equations

There are two main obstacles in the theoretical approach:

- A lack of availability of results for the pair correlation function of the reference fluid that would make the evaluation of the perturbation integral possible
- A reliance on the chosen force field (interaction model)

The latter problem can be bypassed by lifting the link of the equation to the chosen force field and considering its interaction parameters as adjustable ones and evaluating them by fitting real experimental data. The former problem is more severe. The reference model must account for the structure of the molecules comprising the considered fluid and cannot thus be fully general and applicable for other liquids. It is, however, worth reminding that neither these models are unique, and, for one and the same compound, the structure of its molecule may vary from model to model. For example, for water alone, there are several geometrical arrangements of the interaction sites upon which the corresponding force fields have been developed. It is therefore necessary again to lift some of the theoretical constraints and the direct link to a specific force field. To describe the structure is a problem for itself. In this respect, the equations derived in this way may converge to equations obtained by the BU approach.

2.4. Choice of the Reference System

The choice of the reference system is a crucial step in any perturbation expansion. The choice is dictated by both physical and mathematical considerations. From the physical point of view, one would like to ensure the reference be as close as possible to the original system. However, in such a case, handling the reference may be as difficult as handling the original system. On the other hand, mathematical considerations tend to as simple as possible reference to make it mathematically tractable.

Perturbation theories of fluids came to existence only after it had been shown that the structure of the HS fluid is practically identical to that of the LJ fluid, which estimates the properties of noble gases quite well. The interpretation of this result claimed (and this misinterpretation is one that can still be seen today [49]) that the structure of liquids is determined primarily by strong short-ranged *repulsive* interactions, but, as already discussed in section 1, this approach however failed when applied, for instance, to polar fluids.

Besides the classification of fluids according to the increasing complexity of their molecules, another view was offered by Andersen [35]. He classified fluids according to the range of intermolecular interactions. The underlying idea of this classification is that it is not the type of interaction (repulsive, attractive, etc.) but its *range* that matters. Consequently, the interpretation of the early simulation results was correct but only due to sheer coincidence: in the case of normal (non-associating and non-polar) fluids, the short range part of the interaction coincides with its repulsive part, but this is not the case for strongly polar and associating fluids. A systematic investigation of the effect of the range of interactions on the properties of fluids was undertaken by Nezbeda and coworkers using a trial potential that maintains the total interaction at close separations intact and switches off the long-range Coulombic interactions at separations beyond a certain threshold [50],

$$\begin{aligned} u^{\rm T}(\mathbf{q}_1, \mathbf{q}_2) &= u(\mathbf{q}_1, \mathbf{q}_2) && \text{for } R_{12} \le R_0 \\ &= u_{\rm non-el}(\mathbf{q}_1, \mathbf{q}_2) && \text{for } R_{12} > R_{\rm range} \,. \end{aligned} \qquad (25)$$

where it is only a purely technical matter how to actually construct such a $u^{\rm T}$ within the narrow transition range $R_0 < R_{12} < R_{\rm range}$. First studies focused on water [51–53], and, later on, other associating and polar fluids were also considered [54–56]. Considering a series of values of the cutoff parameter, $R_{\rm range}$, the effect of its changes on both the spatial and orientational structure on these fluids was examined. All the results indicated that the influence of the switching range is nearly lost when the short-range model $u^{\rm T}$ covers, approximately, the first coordination shell. It means that the structure of the systems defined by u and $u^{\rm T}$ is very similar (nearly identical). In other words, *the long-range part of the Coulombic interactions has only a marginal effect on the structure of pure fluids* [50, 57]. In addition to the structural properties, the bulk thermodynamic

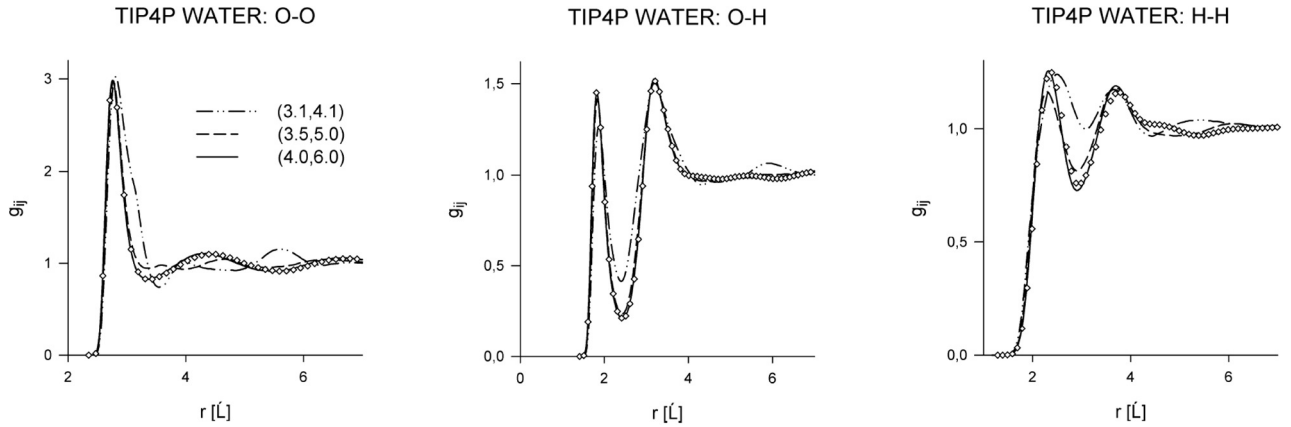

FIGURE 1 | Site-site correlation functions of TIP4P water at ambient conditions in dependence on the switching range, see Equation (25). Curves correspond to different switching ranges, and the circles are simulation results for the full potential.

behavior and vapor-liquid and selected kinetic properties were also examined. Selected results are shown in **Figures 1**–**3** and in **Table 1**.

It has therefore been necessary to correct the original interpretation of early simulation results, which has been misleading. *The properties of fluids are determined primarily by the short-ranged interactions*, which may, however, be not only repulsive (which is the case of simple fluids) but also attractive. In addition to its utilization for equations of state development, this result forms also, for example, the basis for the local molecular field theory of Rodgers et al. [58] who explore a possibility to use a spherical cutoff of the long-range Coulombic interactions. It is also worth mentioning in passing that this conclusion may apply also even to electrolyte solutions as witnessed, for example, by the success of the use of simple short-range models to estimate their properties; see, for example [59–62].

The above findings thus (i) fully justify the use of simple short-range models at all thermodynamic conditions to estimate properties of fluids and (ii) thus explain why equations of state based on simple short-range models (BU approach) may yield reasonably good results. Such models, if properly constructed, should provide an accurate estimate of the structure of both polar and associating fluids but not necessarily of all their thermodynamic properties. In **Figure 3**, we compare the orthobaric pressure of the full models and their short-range versions for several fluids, and in **Table 1** the same comparison is presented for the internal energy and pressure. Whereas the internal energy is also captured quite accurately by the short-range model, this is not the case of pressure, particularly at the dense liquid phase. It means that the contribution of the neglected long-range Coulombic interactions should be the main correction to pressure of the short-range models.

2.5. Primitive Models

We are going to use the term "primitive model" (PM) to refer to simple *short-range* models (toy models) that capture *qualitatively* the key physical properties of a given class of fluids but that cannot (should not) be used to estimate *quantitatively* their thermodynamic properties. For non-polar fluids, the simplest models serving this purpose are purely repulsive hard spheres, various hard bodies, or flexible chains of hard spheres.

To reproduce the structure of polar or associating fluids, the Coulomb interaction at short intermolecular separations has to be incorporated as well. It is assumed that molecules contain charges corresponding to lone electrons and hydrogen atoms (protons). Coulombic-type sites of two kinds (to mimic plus and minus charges and their interaction) are therefore embedded to the hard core of molecules (see **Figures 5** and **6**). A general primitive model thus assumes the form

$$u_{\rm PM}(1,2) = u_{\rm rep,core}(1,2) + \sum_{i\in\{1\},j\in\{2\}} u_{\rm rep}(r_{ij}) + \sum_{i\in\{1\},j\in\{2\}} u_{\rm attr}(r_{ij}) \tag{26}$$

where the summation in the second term runs over the pairs of the like sites and in the third term runs over the pairs of the unlike sites. This is a general definition of the primitive model that captures the physical reality, namely that, simultaneously with the attractive interaction between the unlike charges, there is also an inextricable repulsive interaction of the same strength between the like charges. Only these two types of interactions together give rise to H-bonding in real fluids. This corresponds to the TD approach in which the models are not constructed arbitrarily but descend from a realistic parent model. For general rules for the construction of such models see [63, 64]. Two remarks seem here appropriate. First, although the actual choice for the repulsive and attractive site-site interactions seem obvious, a hard sphere interaction for the repulsion and a square-well interaction for the attractive interaction, there are at least two possibilities of defining the attraction between the unlike sites, see **Figure 4**: (i) Bol [24] defines the attractive interaction between sites i and j with respect to the vector R_{12} connecting the reference sites

$$\begin{aligned} u_{\rm HB}^{\rm (Bol)}(R_{12},\mathbf{r}_i^{(1)},\mathbf{r}_j^{(2)}) &= -\epsilon_{\rm SW} \qquad \text{for } R_{12} < r_c; \quad \theta_1,\theta_2 < \theta_c \\ &= 0 \qquad\quad \text{otherwise}, \end{aligned} \tag{27}$$

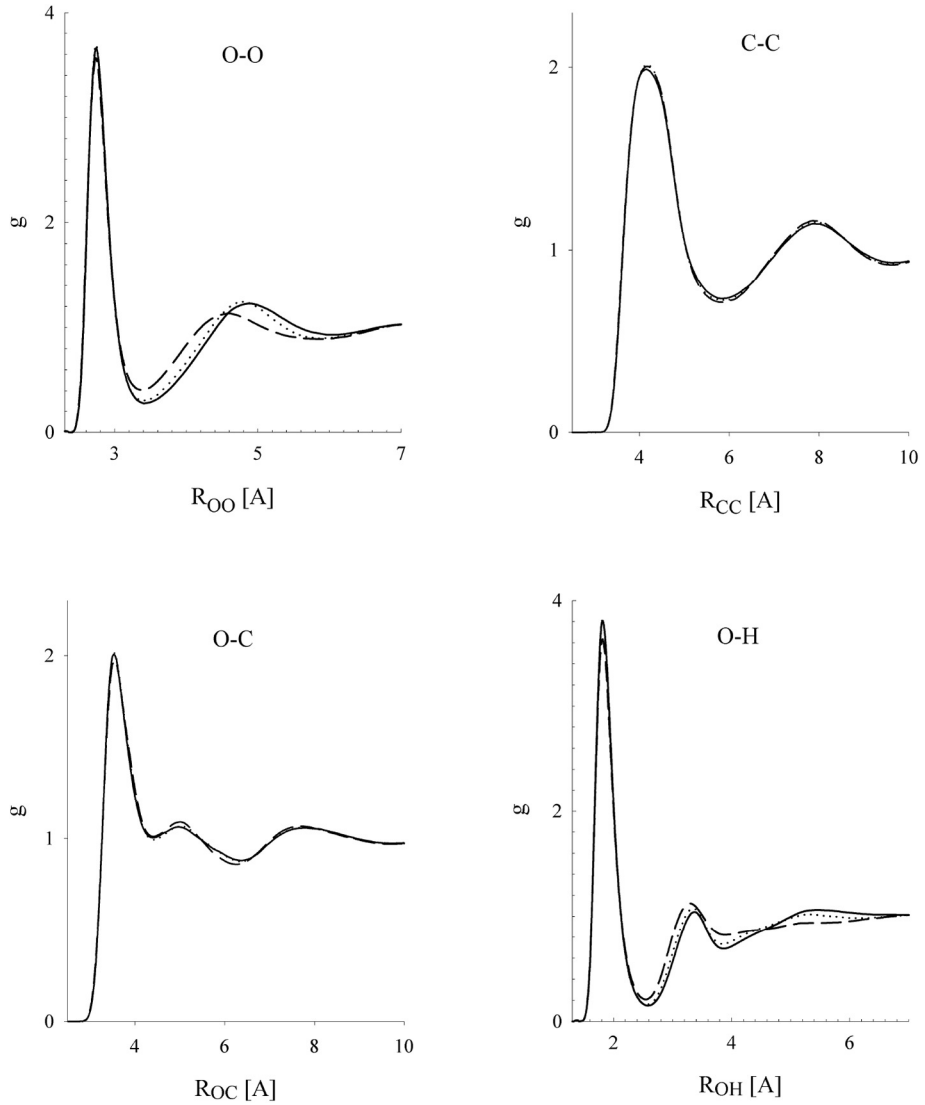

FIGURE 2 | Site-site correlation functions of methanol at density $\rho = 761.9$ kg/m^3 and temperature $T = 298$ K in dependence on the switching range: dashed line (4,6) [Å]; dotted line (4.7,6.7) [Å]; full line (5.7,7.7) [Å]. Reprinted with permission from *J. Phys. Chem. B* (2002) 106:7537.

(ii) whereas Smith and Nezbeda [26] defined this interaction directly by the separation between the interaction sites

$$u_{\rm HB}^{\rm (SN)}(r_{12}) \equiv u_{\rm SW}(|\mathbf{r}_1 - \mathbf{r}_2|; \lambda) = -\epsilon_{\rm SW} \quad \text{for } r_{12} \equiv |\mathbf{r}_1 - \mathbf{r}_2| < \lambda\sigma$$
$$= 0 \quad \text{for } r_{12} > 0 \quad . \qquad (28)$$

A consequence of these different definitions is that the orientational part of the configurational space over which an H-bond can be established is constant in Bol's formulation, whereas it is tapered with increasing separation between the reference sites in the SN formulation. Second, the inclusion of the repulsive interaction between the like sites means that when all the attractive interactions are switched off, we do not get a common hard body but the so called pseudohard hard body (PHB) [65], the body that captures the actual excluded volume [66, 67], an important concept in molecular physics of fluids; albeit purely repulsive, it can also yield, to a milder extent, preferred orientations similar to H-bonding [68]. The PHB is not a simple hard body, however; it possesses a flavor of non-additivity, and there is currently no theory for the PHB fluids available.

In general, there are no a priori constraints imposed on model's parameters. Such constraints may be imposed, for example, in connection with the application of a specific theory. For example, to make the application of the TPT possible, it is required that the conditions

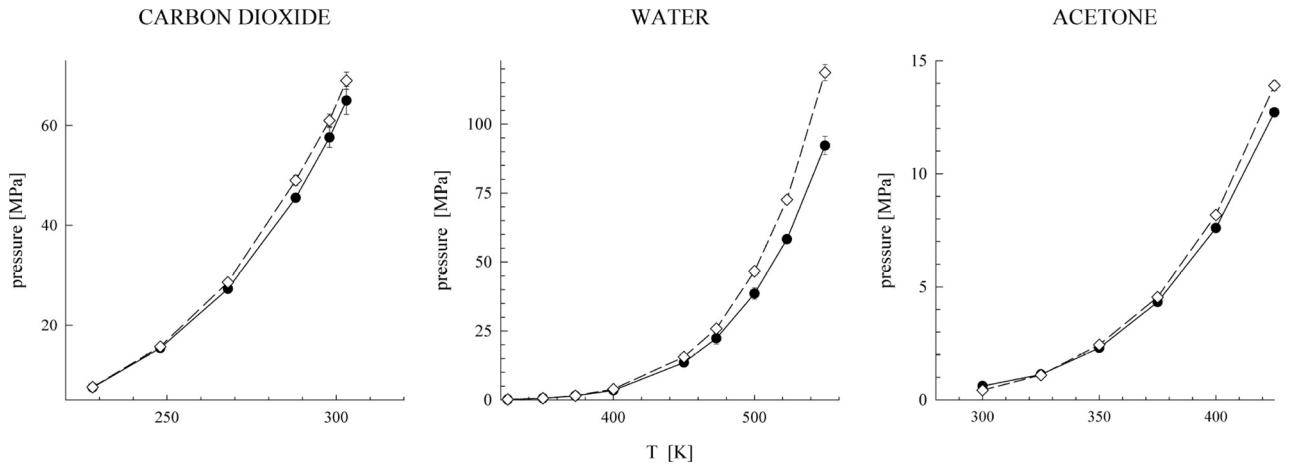

FIGURE 3 | Orthobaric pressures of the full (filled symbols) and short-range versions (open symbols).

TABLE 1 | Comparison of the internal energy and pressure of the parent and their associated short-range models.

	Parent		Short-range	
ρ	U	P	U	P
[kg/m^3]	[kJ/mol]	[MPa]	[kJ/mol]	[MPa]
Water; $T = 298$ K				
1,000	−41.42 (23)	29.20 (4,016)	−41.98 (28)	−36.23 (3,747)
1,120	−42.02 (28)	358.9 (510)	−42.69 (28)	286.8 (439)
Water; $T = 353$ K				
1,000	−38.57 (28)	112.3 (425)	−38.91 (29)	64.44 (3,757)
1,120	−39.56 (21)	462.9 (431)	−39.98 (23)	421.9 (411)
Acetonitrile; $T = 298$ K				
800	−34.48 (8)	283.4 (4)	−31.53 (3)	107.1 (19)
Hydrogen fluoride; $T = 350$ K				
1,200	−25.94 (04)	2,634 (103)	−26.26 (06)	2,379 (119)

Numbers in parentheses denote the error of last digits.

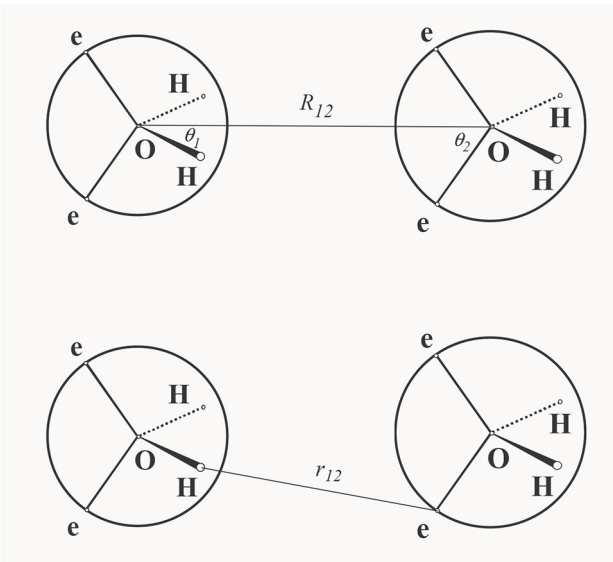

FIGURE 4 | Schematic representation of the H-bonding: Bol's notation **(upper)** and Smith-Nezbeda's notation **(lower)**.

of the so-called steric incompatibilities be satisfied, see section 2.5.

The above procedures of constructing the primitive models make it possible to examine their structure and, consequently, verify their suitability for the reference fluid. Although the structure is an important physical property, its main use is in theoretical considerations only; in applications with primary focus on the thermodynamic properties, the structure plays only a marginal role. This is the case of the BU approach which focusses on the final net effect of the Coulombic interactions, i.e., on the establishing of H-bonds only, but not on the interactions themselves. It means that in the BU methodology, the second term in (26) is omitted.

Another way for constructing primitive models has thus been followed. Chapman and coworkers, while developing SAFT, utilized the idea of hard bodies with embedded interaction sites and constructed a caricature of molecules also as bodies made up of segments with certain interaction sites [21]. However, bearing in mind the TPT to be used for the evaluation of the thermodynamic behavior of the models, no site location was specified because the TPT of the first order is independent of the site's location. Furthermore, to make the models as simple as possible, and thus (i) easily tractable by theory and (ii) readily applicable to a variety of different fluids, smaller molecules are simply pictured as hard spheres, and larger non-spherical molecules are pictured as chains of hard spheres, see **Figure 7**. These models (i.e., SAFT models) consequently do not have any relation to real molecules and any realistic intermolecular

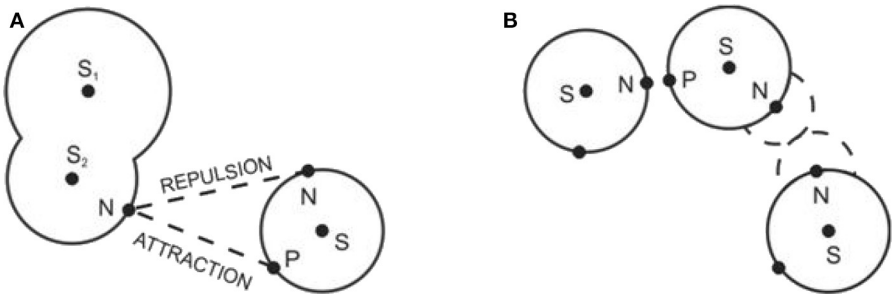

FIGURE 5 | Schematic representation of the site-site interaction in the primitive model **(A)** and the associated pseudohard body **(B)**. Symbols N and P denote the negatively and positively charged sites, resp. Reprinted with permission from *Pure Appl. Chem.* (2013) 85:201.

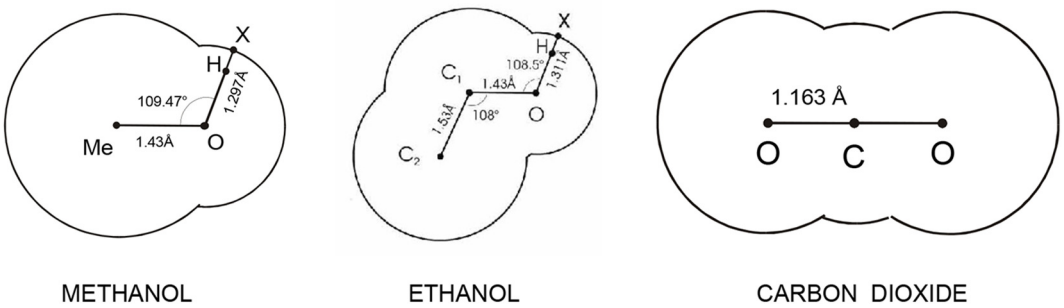

FIGURE 6 | Primitive models descending from realistic force fields.

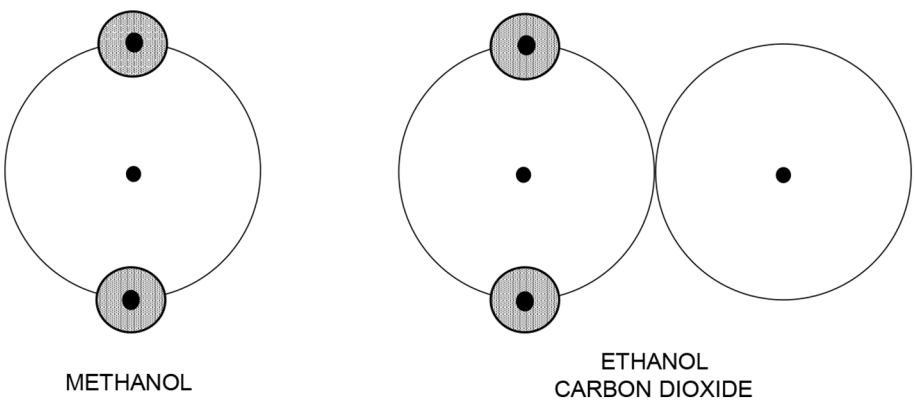

FIGURE 7 | Intuitive primitive models used in SAFT modeling. Shaded circles denote Coulombic interaction sites.

interaction model, and their actual form is therefore rather arbitrary with all its parameters treated as adjustable.

2.6. Thermodynamic Perturbation Theory

The TPT was developed by Wertheim in a series of papers [69–72] to deal with systems exhibiting association or polymerization, i.e., the systems with strongly orientation-dependent and short-ranged attractive interactions with the general interaction in the form of Equation (26). He presented a concise scheme that produces also integral equations (solved analytically, for example, for the one-site SN model [10]). It is not a general theory in the sense that (i) it requires a special form of the interaction function and (ii) explicit results are not universal functions but have to be developed specifically for the model at hand (e.g., number of the interaction sites per molecule). There are two important constraints imposed on the interaction model for the TPT to be applicable, the so-called steric incompatibilities: (1) one interaction site can be engaged in establishing one bond only, and (2) only one bond can be established between two molecules. Provided that these two constraints are not

satisfied, the results rapidly start to deteriorate (when compared to simulation data), and when the constraints are ignored, any application of the TPT is only a formal use of certain formulas with unpredictable results. Here we provide only the basic relations of the theory referring the reader to original papers and to a detailed pedagogical review by Zmpitas and Gross [73] for details. For the demonstration of the model dependence and discussion, we present here explicit results for the four-site model, which is a typical model of water (ST2-type models with tetrahedral geometry [74]); explicit expressions of the EoS for different compounds/models can be found in [13] (Equations 22–24 therein).

The TPT theory assumes the interaction function in the form of Equation (26) and starts from its decomposition into a repulsive reference part and a highly directional perturbation part:

$$u = u_{\mathrm{Wref}} + u_{\mathrm{Wpert}} \tag{29}$$

where $u_{\mathrm{Wref}} = u_{\mathrm{hardcore}}$, i.e., the fluid with all attractive interactions switched off, and subscripts "W..." are used to distinguish these potentials from those used in a general perturbation expansion. The quantity addressed by the theory is the excess Helmholtz free energy, A_{Wref}, which is expanded about a reference, and, using the diagrammatic technique, it tries to evaluate the contribution due to the association given by u_{Wpert} by rearranging the graphs and neglecting certain classes thereof.

The key function of the TPT are integrals I, which involve the Mayer function of the HB bond interaction and (in the first-order theory) the reference (hard body) fluid pair correlation function:

$$I = \int g_{\mathrm{Wref}}(\mathbf{q}_1, \mathbf{q}_2) f_{\mathrm{HB}}(\mathbf{q}_1, \mathbf{q}_2) \mathrm{d}\mathbf{R}_{12} \mathrm{d}\Omega_1 \mathrm{d}\Omega_2 \tag{30}$$

where f_{HB} is the H-bonding Mayer function, $f_{\mathrm{HB}} = \exp(-\beta u_{\mathrm{HB}}) - 1$. For a four-site model with two (P)-sites and two (N)-site embedded to a hard sphere, the final result for the residual free energy in the first order expansion is given by [75]

$$\beta A = A_{\mathrm{Wref}} + \frac{2c}{1+c} - 4\ln(1+c) \tag{31}$$

where c is obtained as the solution of a simple equation involving the integral I as a parameter,

$$c = \frac{1}{2}[\sqrt{(1+8I\rho)} - 1] \tag{32}$$

As mentioned in the preceding subsection, simple models may have also odd number of Coulombic sites. In this case, one site has to establish two bonds that may cause problems with the application of the TPT—the condition of steric incompatibility is not satisfied. Using the TPT as is in the first order for such models is definitely not correct, but this problem may be bypassed, at least partially, by considering the theory in the second order.

TPT is an approximate theory, and its accuracy is therefore an important issue. Surprisingly, only little attention has been paid to it. Nezbeda et al. [75] examined TPT for a four-site primitive model of water within the context of other theories for primitive models and reported rather disappointing results. A more thorough examination was carried out by Slovak and Nezbeda [76] considering both the site-site and angular interaction formalism. Physical properties examined were the internal energy, pressure (equation of state), and the heat capacity, C_P. A general conclusion they drew from the comparison of the theory with the simulation results was that the theory is only fairly accurate at liquid densities and low temperatures and becomes reasonably accurate only at higher temperatures and low densities. They attributed the found discrepancy to only an approximate resummation of graphs at the level of the first order expansion when only one pair of H-bonded molecules is considered in the reference hard body fluid. Better results may be/are obtained from higher order theories. Application of the TPT to water represents a very stringent test. Although no similar examination for simpler models (fluids) has been carried out, it may be assumed that the theory will perform better for other fluids.

Vlček et al. [15] implemented the TPT of the second order and carried out molecular simulations again. Besides a model of water, they also considered a primitive model of methanol that has only one pair of the Coulombic sites. In this latter case, the TPT was in perfect agreement with simulations over the entire range of thermodynamic conditions. The model of water was in perfect agreement with simulations at higher temperatures and at low and intermediate densities; yet the agreement was at least semi-quantitative at very low temperature and high density.

3. TOWARD AN EQUATION OF STATE

3.1. Perturbed Theoretical Equation of State

As mentioned in section 2.2, to implement the perturbation expansion, a reference fluid has to be determined first, and, according to Equation (13), its correlation function is then required for the correction terms to be evaluated. This step is accomplished by approximating the reference fluid by an appropriate primitive model. In the case of simple fluids, this does not bring about any problem because such a primitive model is the fluid of hard spheres. For other fluids, the primitive model contains both a hard core and an orientation dependent attractive interaction. There are theoretical tools available how to estimate its thermodynamic properties, but this is not the case of correlation functions. Immediately available is the correlation function for the SN model [11], but for other PM models we have to resort to an additional approximation. Integral equations are, with the exception of the Yukawa fluid, out of the question because they yield only numerical results. There thus seems to be only one general tool that may offer an analytic result for $g(\mathbf{q}_1, \mathbf{q}_2)$: the RAM (Reference-Average-Mayer function) perturbation theory [77]. Accuracy of this theory was examined by its application to a PM of water [75] with the results found of medium accuracy only. Since it is required that the result be in an analytic form, this would further require additional

approximations. Accounting for the fact that the TPT itself may not be sufficiently accurate, it is then questionable whether such an effort is worth trying at all because it is very likely that only a low-quality result can be expected. Nonetheless, the RAM theory can be used for other purposes, see, for example, section 3.3.

It can thus be concluded that there is no theoretical method able to provide a reliable and good description of the *structure* of the PMs in an analytic form. As it thus stands, it seems that the truly pure theoretical TD approach to develop an analytic EoS has reached its limits.

3.2. van der Waals-Type Approach: SAFT

A typical example of modern vdW-type EoS is the family of SAFT equations. SAFT methodology views molecules as objects built from spherical segments (atoms, molecules, or functional groups) that interact through isotropic interaction forces. It does not consider any explicit intermolecular interaction model but *implicitly* assumes that there are three major contributions to the total intermolecular interaction energy [22]: (1) the repulsion-attraction contribution between the individual segments (monomers), (2) a contribution due to the formation of chains, and (3) a contribution due to formation of association complex between different segments. The Helmholtz free energy is then written as a sum of three mutually independent contributions, each of them corresponding to the above type of interaction. In terms of the corresponding compressibility factor, it reads as [22]

$$z_{\mathrm{SAFT}} = z_{\mathrm{segment}} + z_{\mathrm{chain}} + z_{\mathrm{assoc}} \tag{33}$$

Decomposition (33) does not have any a priori justification and was based only on intuitive physical considerations in the same way as the original vdW equation. Only later studies on the effect of the range of interactions discussed in section 2.4 have provided a support for it. Specifically, it is the explicit inclusion of the association term because it is the short-range Coulombic interaction, which plays the predominant role. In this respect, Equation (33) should be more appropriately, at least formally, written in another order with z_{assoc} as the leading term.

The monomer-monomer interaction is the subject of choice. The most common choice used to be the LJ potential for which several analytic equations of state are available [2, 78, 79]. The hard-core Yukawa can also be a potential choice for the same reason [47, 48]. It is also used for the description of screed Coulombic interactions while the Sutherland potential is useful for systems with multipolar interactions. The exponents of the LJ potential, $(m, n) = (12, 6)$, were originally chosen for convenience without deeper physical justification. Lafitte et al. [80] let the (m,n) exponents be free adjustable parameters (Mie potential) gaining greater flexibility (two more parameters for fitting) for the description of the softness/hardness of repulsions and also for the range of the attractive interaction. The specific choice of the monomer-monomer interaction also affects the evaluation of the corresponding contribution to the EoS and a lot of effort has also been invested into its development. This activity brings researchers back to the period when perturbation theories of simple fluids were in their focus.

An open question remains whether to directly incorporate also the long-range Coulombic interactions into Equation (33). In their paper [33], Muller and Gubbins conclude that these interactions are more important than it was previously thought and this would also fully agree with the results shown in **Table 1**. An extension of Equation (33) by including explicitly the dipole-dipole contribution was considered by Karakatsani et al. [81] to deal with strongly dipolar fluids and recently also by Ahem et al. [82]. An extension along the same path was made by Liu et al. [83] who, in addition to incorporating the dipole-dipole interaction, employed the hard-core Yukawa for the monomer-monomer interaction instead of the LJ. On the other hand, Clark et al. [84] argue that this contribution is not necessary and can be captured in an average fashion by short-range primitive models. Although this may be acceptable from the point of final numerical results, this attitude contradicts the primary finding of section 2.4 and takes SAFT farther away from physical reality.

The incorporation of the dipole-dipole interaction contribution to Equation (33) deserves a further discussion. The intermolecular interactions have their origin in the electrostatic interactions whose contribution can be expressed as a sum of multipole-multipole interaction contributions:

$$u = u_0 + u_{\mathrm{DD}} + \cdots + u_{\mathrm{oct-oct}} + \sum u_{\mathrm{higher\ multipoles}} \tag{34}$$

This interaction gives rise to the H-bonding phenomenon at short intermolecular separations. It means that it is thus possible to rewrite Equation (34) into the form

$$\begin{aligned} u &= u_{\mathrm{HB}} && \text{for } R_{12} \le R_{\mathrm{cut}} \\ &= u_0 + u_{\mathrm{DD}} + \cdots + u_{\mathrm{oct-oct}} \\ &\quad + \sum u_{\mathrm{higher\ multipoles}} && \text{for } R_{12} > R_{\mathrm{cut}} \end{aligned} \tag{35}$$

where R_{cut} is a certain cutoff. It becomes now clear that the simultaneous inclusion of the dipole-dipole contribution and the H-bonding contribution means that the dipole-dipole contribution from short intermolecular distances is counted twice: its contribution from the short separations is already accounted for by the H-bonding term. This should be evidently avoided but the question to what extent this double counting affects the results needs to be examined.

To obtain an EoS in an analytic form, the key integrals of type I, Equation (30), have to be evaluated. The integrals contain the correlation function of the reference fluid which, with exception of the fluid of HS, is not available. Since the integration range should be quite narrow, which is required by the conditions of steric incompatibilities, an obvious approximation is to use the rectangular rule for the evaluation of the integral and approximate g_{HS} by its contact value, g^*_{HS}. Nezbeda and Iglesias-Silva [85] approximated g close to contact by a straight line defined by the contact value of g_{HS} and its first derivative, whereas Jackson et al. [86] used the approximation $r^2 g^*_{\mathrm{HS}} \approx$ const. Nonetheless, comparison of simulation results with those based on these approximations showed that the results were nearly identical and that inaccuracies in I had only marginal effect [76]. This finding may thus make evaluation of I easier in cases when

the reference fluid is not that of HS because the use of rather crude approximations may be justified.

As is obvious from the above discussion, there is nearly an unlimited number of possibilities to modify or extend SAFT equations. This is in fact the property inherent to any EoS developed using the BU approach and reflects the fact that SAFT is a methodology and not a rigid EoS [22]. It is not the goal of this paper to review SAFT equations, and let us mention therefore at least their main types. Besides the original SAFT with hard sphere monomers, SAFT-HS, two other main versions are SAFT-VR (variable range) [87, 88] and PC-SAFT (perturbed chain) [49]. Furthermore, there is also a group contribution version, SAFT-γ [89], SAFT-RPM [90–92] dealing with electrolytes, and SAFT-VR-D [81, 93] for dipolar and dipolar and associating fluids. The most recent development includes SAFT-μ [80, 94] whose monomer units interact via a Mie-type potential with adjustable exponents. Furthermore, here is a number of modifications and applications of all these versions and we refer the reader to available review articles for further reading [22, 23, 95, 96].

3.3. Equations of State for Water

3.3.1. SAFT Equations

Number of SAFT equations developed for water is enormous. In their recent review from 2016 on SAFT for water, Vega and Llovell [29] list altogether 47 SAFT equations belonging to 9 different versions of SAFT. Yet, many other equations (typically of the same type of equation but with different sets of parameters) are missing. The molecular size and energy parameters of the listed versions vary within the range 1.91–3.59[Å] for σ and 839–2,932[K] for ϵ/k_B pointing again to the fact that these parameters may hardly have anything common with physical reality and are pure numbers. As an interesting example we may mention conclusions of the very recent paper by Ahmed et al. [82]. They report excellent results for the VLE of water and other compounds with one interesting feature: to obtain these results, the size of the monomer unit has to swell with increasing temperature, which contradicts both common sense and the observed (and obtained by theory) behavior; with increasing temperature, the molecules attain kinetic energy and get closer to each other which means that, effectively, their excluded volume shrinks.

The primary question concerns which model of the water molecule to use and all three possibilities, models with two, three, and four Coulombic sites were considered. It is also argued that the number of sites may not be fixed and should be conveniently changed, particularly in aqueous solutions according to solutes. Two-site geometries have therefore also been used. For arguments and discussion of these choices see [29].

There are many papers which include, among other compounds also water but not many papers with the focus on water. An exception are two papers by Jackson et al. [84] and Dufal et al. [94]. The above problem was subject to a thorough research of Clark et al. [84] not from the point of the relation of the water model to reality but which model suits best SAFT. They considered all three possibilities, two, three, and four Coulombic site models. Since the four-site model turned out to yield superior results they furthermore considered four different sets of parameters for this model. They concluded that the model with four Coulombic sites with the W2 set of parameters is the most appropriate in describing the H-bonding in water, yielding the largest ratio of the H-bonding and dispersion energies, and also more realistic degree of association. This could, however, be anticipated, as the four-site arrangement does not give to molecules too many chances to adopt other arrangement but tetrahedral. Despite all the effort invested and careful analysis and discussion in that paper, the recommended parameters are just numbers because the model ignores completely all long-range Coulombic interactions, which is compensated by adjusted values of the parameters.

The other paper [94] discusses in detail an application of the TPT to the model $u = u_{\text{Mie}} + u_{\text{assoc}}$ and it deserves a comment. Although, in general, SAFT assumes some form of the interaction model, we are not aware of any paper where the structure corresponding to the model is examined. The excellent agreement of thermodynamic data may hide deficiencies in the structure which would debase the equation. For example, as a step beyond the hard core with interaction sites, a more "realistic" model, the LJ particle decorated with H-bonding sites was proposed [97]. Nezbeda and Slovak simulated this model [98] with the following result: (i) when the H-bonding energy parameter found in [97] was used, the resulting structure was typically argon-type; (ii) to obtain a water-type structure, it was necessary to increase the energy parameter to a very high value, and the model then behaved like HS with bonding sites. It may be expected that a similar result will be obtained also with the $u_{\text{Mie}} + u_{\text{assoc}}$ model. It would be therefore interesting to examine which structure it will actually produce.

Water is known to exhibit a number of anomalies that seem to be ignored in most applications of SAFT. This is quite surprising because the anomalies are fingerprints of water and their (at least qualitative) reproduction is therefore very important if the equation is to describe the behavior of real water. However, behavior of pure water outside the region of phase equilibria is only rarely addressed. An exception is paper [94] in which some response functions are reported, albeit only at high pressures.

To summarize, there is no doubt that SAFT equations are able to do great job concerning the correlation of experimental data but their contribution to better understanding of the behavior of water has so far been minimal.

3.3.2. Semitheoretical Equations

In their first application of PMs to water, Nezbeda and Pavliček [99] constructed the full EoS similarly as in SAFT fashion with the ST2 geometry of the PM, considering also the dipole-dipole term. The EoS was thus in the form

$$z = z_{\text{PM}} + z_{\text{disp}} + z_{\text{DD}} \tag{36}$$

The dispersion term was considered in its simplest form as the mean field contribution, and the DD term, to avoid double counting of electrostatic contributions at close separation, was assumed as a dipolar hard sphere of a diameter larger than the H-bonding radius. Parameters of the EoS were evaluated, as usual, by fitting the VLE data, and the results were found satisfactory.

A more sophisticated equation along this line was developed by Nezbeda and Weingerl [100] using a four-site parent model and the first-order TPT. The EoS had the same form as above and the parameters were evaluated so as to obtain the best representation of the vapor pressure and coexistence liquid densities from the triple point up to 643.15 K. The equation remains reliable also for various thermodynamic properties outside the coexistence region. It reproduces the anomaly in the isothermal compressibility locating its minimum at $T = 38°C$ (vs. the experimental value $T = 46°C$) at $P = 1$ bar. Its overall performance is of the same quality as that of the SAFT-YDD (Yukawa-dipole-dipole) [83] one.

An attempt to derive an equation following the theoretical route was made by Jirsak and Nezbeda [101]. Within the spirit of perturbation theory, we considered modeling water not as a whole but only by its short-range part, and its description by a PM was considered. The parent model was the best non-polarizable model of water, TIP4P/2005 [74]. The short range reference was obtained by deducting its long range Coulombic interaction and the associated PM was then obtained by making use of the RAM [77] and Barker-Henderson theories [6]. The PM thus contained only one parameter, the H-bonding energy ϵ/k_B, the parameter which does not exist in the parent model. To keep contact with it (and hence also with real water), they set the value of ϵ/k_B to 4440K to obtain, approximately, the experimental temperature of the density maximum and applied the 2nd order TPT developed in [15]. Having in mind that it is the theory of the short-range reference and not of complete water, the *qualitative* behavior of the response functions, the thermal expansion coefficient, α, the coefficient of isothermal compressibility, κ, and the residual isopiestic heat capacity were examined with the following result. At low pressures, α is a monotonous function that becomes negative with decreasing temperature, which means that the density exhibits a maximum. At elevated pressures, the maximum of ρ moves to lower temperatures in agreement with experimental observations. Another interesting feature of α is crossing of all isobars in a small region around 360 K and $\alpha \approx 0.4 \times 10^{-3}$. This behavior corresponds surprisingly well to that observed on real water: α of real water exhibits the same phenomenon around 325 K with $\alpha \approx 0.45 \times 10^{-3}$. All these findings correspond to rather a very complex behavior of α as a function of pressure along isotherms. The temperature dependence of the coefficient of isothermal compressibility exhibits a minimum that becomes less pronounced with increasing pressure in agreement with the experiment, and there is also a decrease of κ with increasing pressure. The residual isopiestic heat capacity is found to be only weakly temperature dependent, exhibiting, in agreement with reality, a very shallow minimum. The pressure effect on ΔC_P is very small.

To summarize, the fact that the proposed theoretical approach reproduces the known anomalies of water semi-quantitatively without any reference to or incorporation of H-bonding should be considered as a great success of theory. Accounting further for the fact that all the results are available in an analytic form this would be the perfect reference system for developing a perturbation-theory-based EoS.

4. SUMMARY AND CONCLUSIONS

The ultimate goal of the statistical mechanics of matter is to provide methods of explaining and predicting the experimentally measurable quantities of a given substance in terms of the properties of its constituent particles. From the purely theoretical point of view this is feasible because all gears, theories, and simulation methods are readily available. The problem is their implementation. In chemical engineering applications, it is demanded that the obtained equations be in an analytic form while most of the exact statistical mechanical results are in a numerical form only. It is therefore necessary to restore to approximations, but this has to be done with caution. Results of statistical mechanics possess the great power of predictability, whereas too crude approximations may debase them to mere correlation schemes; some recommendations are summarized below.

The theoretical perturbed equations and SAFT equations represent two extreme methods for developing EoS. As already discussed in section 3.1, the theoretical approach is too strictly bound to a parent realistic model which itself has always some deficiency. Furthermore, it also imposes certain limits on theoretical tools, e.g., the simple model used in the process is subject to certain rules. Finally, it may hardly handle fluids made up of large flexible molecules. On the other hand, SAFT is not linked to any real fluid, and its connection with molecular theory is at the same level as it would be the vdW equation in which the original hard sphere term was replaced by the correct EoS of the fluid of HS: a very rough model of molecules is treated by the very sophisticated TPT. Although attempts to improve its performance have been made, these attempts are driven by intuition and analogies only and also keep the resulting EoS only more complex. No doubt that the SAFT equations have been very successful in correlating experimental data, but their potential to predict the properties of fluids in the regions where no data are available—a factor of great importance and necessity—is very questionable.

As it appears, the best way to obtain an accurate and reliable EoS with a potential of predictability may be a combination of both above approaches, i.e., a semi-theoretical approach. It is evident that the crucial point along this way is the choice of a reference fluid that should capture most of the behavior of the studied system (or, more accurately, of the short-range reference fluid) and remove the burden imposed on the correction terms. At this point, the theoretical route may fullfil its role: to supply a primitive model mimicking more or less faithfully real molecules, their interaction, and the structure of the fluid. If this is satisfied, the correction terms will play much less important role and will not need too sophisticated elaboration.

A very important problem is the evaluation of the parameters of equations. It is important to bear in mind that the primitive model should reproduce as faithfully as possible the properties of the *reference* fluid and not of the considered fluid. It means that the parameters of the primitive model and of the correction terms have to be evaluated separately, which will make this route different from the current SAFT and previous semitheoretical approaches. Concerning the evaluation of the parameters of the

correction terms, this is discussed in [84]. A typical choice used in the majority of papers on SAFT are vapor-liquid equilibrium (VLE) data. Clark et al. discuss this problem and are aware of the fact that the pairwise additive force fields are not able, in principle, to describe simultaneously the behavior of liquid and gas [102] of strongly associating fluids and that only the orthobaric pressures and liquid saturated densities should be used in fitting.

Another important problem concerns the inclusion of the dipole-dipole interaction. The best and simplest, and also most commonly used, is the Padé approximant of Rushbrook et al. [103]. However, its incorporation is not straightforward, which is not always recognized. It is not possible to formally add this term as is to the EoS. As mentioned in section 3.2, the dipole-dipole interaction at short separations is part of the electrostatic interactions that result in H-bonding and is thus already included in the models with the explicit H-bonding terms. If this is not taken care of, the electrostatic interaction at short separations will be counted twice. To assess the importance/effect of this inconsistency remains to be done.

An associated problem is the choice of properties to use to assess the developed EoS. In the overwhelming majority cases, how accurately the equation can correlate the equilibrium data is reported as a rule despite the fact that such data were, at least partially, used for the evaluation of the parameters. It is not necessary to bother with the structure because this should be the problem of the primitive model to be developed. We think that the useful and fair way to assess accuracy/correctness of the EoS is to go away from the phase equilibrium region and to present the response functions, i.e., the second derivatives of the Helmholtz free energy. Not only water but also other associating fluids exhibit an interesting behavior of these functions. This comparison could cast light on the quality of the derived equation.

The last remark concerns the future development. In this review, we have focused on pure fluids, which is of importance for theory, but in applications, we have to deal primarily with mixtures. Mixtures were in the focus of research in the early stages of the development of theories of fluids, but we are not aware of any systematic theoretical research activities at the present time. Moreover, whereas for pure fluids force fields are being continuously developed and improved, practically no results are available for the intermolecular interaction between the molecules of species A and B. In other words, the effect of the presence of molecule B on the pair interaction A–A is not known, and empirical combining rules must be employed. This deficiency could be, at least partially, bypassed by employing polarizable force fields but then the theoretical path is out of question. Consequently, a SAFT-type approach remains at present the only available tool to deal with mixtures (and other complex problems such as for example, interfacial phenomena). With regards to theory, it can be assumed that the effect of the range of interactions found for pure liquids will hold true also for mixtures. A natural choice for the reference system will then be a mixture of primitive models, though with the only exception [104] that results for the thermodynamic properties of such mixtures are missing. It is generally accepted that excluded volume effects are responsible for a number of observed properties of mixtures, and the primitive models (or their pseudohard cores) may capture them. It is also known that mixtures/solutions, e. g., aqueous solutions of alcohols, exhibit anomalies in their structural properties and primitive models may be able to capture them. All these theoretical results may lead to a more sophisticated reference system, which is the key to developing accurate and reliable equations of state.

AUTHOR CONTRIBUTIONS

The author confirms being the sole contributor of this work and has approved it for publication.

FUNDING

Support for this work was provided by the Czech Science Foundation (Grant No. 20-06825S).

REFERENCES

1. Wagner W, Pruss, A. The IAPWS formulation 1995 for the thermodynamic properties of ordinary water substance for general and scientific use. *J Phys Chem Ref Data.* (2002) **31**:387–535. doi: 10.1063/1.1461829
2. Johnson JK, Zollweg JA, Gubbins KE. The Lennard-Jones equation of state revisited. *Mol Phys.* (1993) **78**:591–618.
3. Wertheim MS. Analytic solution of Percus-Yevick equation. *J Math Phys.* (1964) **5**:643–51.
4. Nezbeda I. Analytic solution of Percus-Yevick equation for fluid of hard spheres. *Czech J Phys B.* (1974) 24:55–62.
5. Jelinek J, Nezbeda I. Analytic solution of the Percus-Yevick equation for sticky hard sphere potential. *Phys A.* (1976) 84:175–87.
6. Barker JA, Henderson D. What is "liquid"? Understanding the states of matter. *Rev Mod Phys.* (1976) **48**:587–671.
7. Nezbeda I. Percus-Yevick theory for the system of hard spheres with a square-well attraction. *Czech J Phys.* (1977) **27**:247–54.
8. Wertheim MS. Exact solution of mean spherical model for fluids of hard spheres with permanent electric dipole moments. *J Chem Phys.* (1971) **55**:4291–8.
9. Dahl LW, Andersen HC. A theory of the anomalous thermodynamic properties of liquid water. *J Chem Phys.* (1983) **78**:1980–93.
10. Wertheim MS. Integral-equation for the Smith-Nezbeda model of associated fluids. *J Chem Phys.* (1988) **88**:1145–55.
11. Kalyuzhnyi YV, Nezbeda I. Analytic solution of the Wertheim's OZ equation for the Smith-Nezbeda model of associated liquids. *Mol Phys.* (1991) **73**:703–13.
12. Kolafa J, Nezbeda, I. Implementation of the Dahl-Andersen-Wertheim theory for realistic water-water potentials. *Mol Phys.* (1989) **66**:87–95.
13. Kolafa J, Nezbeda I. Primitive models of associated liquids: equation of state, liquid-gas phase transition and percolation threshold. *Mol Phys.* (1991) **72**:777–85.
14. Slovak J, Nezbeda I. Extended 5-site primitive models of water: theory and computer simulations. *Mol Phys.* (1997) **91**:1125–36.

15. Vlcek L, Slovak J, Nezbeda I. Thermodynamic perturbation theory of the second-order: implementation for models with double-bonded sites. *Mol Phys.* (2003) **101**:2921–7. doi: 10.1080/00268970310001606795
16. Tang Y, Tong Z, Lu B. Analytic equation of state based on the Ornstein-Zernike equation. *Fluid Phase Equil.* (1997) **134**:21–42.
17. Reiner A, Hoye JS. Self-consistent Ornstein-Zernike approximation for the Yukawa fluid with improved direct correlation function. *J Chem Phys.* (2008) **128**:114507. doi: 10.1063/1.2894474
18. Heinen M, Holmquist P, Banchio AJ, Nagele G. Pair structure of the hard-sphere Yukawa fluid: an improved analytic method versus simulations, Rogers-Young scheme, and experiment. *J Chem Phys.* (2011) **134**:044532. doi: 10.1063/1.3524309
19. Sun JX. Analytical equations of state for multi-Yukawa fluids based on the Ross variational perturbation theory and the Percus-Yevick radial distribution function of hard spheres. *Mol Phys.* (2007) **105**:3139–44. doi: 10.1080/00268970701769938
20. Chapman WG, Gubbins KE, Jackson G, Radosz M. SAFT - equation-of-state solution model for associating fluids. *Fluid Phase Equil.* (1989) **52**:31–8.
21. Chapman WG, Gubbins KE, Jackson G, Radosz M. New reference equation of state for associating liquids. *Ind Eng Chem Res.* (1990) **29**:1709–21.
22. Muller EA, Gubbins KE. Molecular-based equations of state for associating fluids: a review of SAFT and related approaches. *Ind Eng Chem Res.* (2001) **40**:2193–211. doi: 10.1021/ie000773w
23. McCabe C, Galindo A. SAFT associating fluids and fluid mixtures. in eds Goodwin ARH, Sengers JV, Peters CJR, editors. *Applied Thermodynamics of Fluids.* The Royal Society of Chemistry (2010). p. 215–79.
24. BoL W. Monte-Carlo simulations of fluid systems of waterlike molecules *Mol Phys.* (1982) 45:605–16.
25. Dahl LW, Andersen HC. cluster expansions for hydrogen-bonded fluids. 3. Water *J Chem Phys.* (1983) **78**:1962–79.
26. Smith WR, Nezbeda I. A simple model for associated fluids. *J Chem Phys.* (1984) **81**:3694–99.
27. Huang SH, Radosz M. Equation of state for small, large, polydisperse, and associating molecules. *Ind Eng Chem Res.* (1990) **29**:2284–94.
28. Huang SH, Radosz, M. Equation of state for small, large, polydisperse, and associating molecules - extension to fluid mixtures. *Ind Eng Chem Res.* (1991) **30**:1994–2005.
29. Vega LF, Llovall, F. Review and new insights into the application of molecular-based equations of state to water and aqueous solutions. *Fluid Phase Equil.* (2016) **416**:150–73. doi: 10.1016/j.fluid.2016.01.024
30. Rowlinson JS, Swinton FL. *Liquids and Liquid Mixtures*. London: Butterworths (1982).
31. Boublik T, Nezbeda I. P-V-T behaviour of hard body fluids. Theory and experiment. *Coll Czech Chem Commun.* (1986) **51**:2301–432.
32. Gray CG, Gubbins KE, Joslin CG. *Theory of Molecular Fluids.* Vol. 2. Oxford: Oxford Univ. Press (2011).
33. Muller EA, Gubbins K. An equation of state for water from a simplified intermolecular potential. *Ind Chem Eng Res.* (1995) **34**:3662–73.
34. Nezbeda I. On molecular-based equations of state: rigor versus speculations. *Fluid Phase Equil.* (2001) **182**:3–15. doi: 10.1016/S0378-3812(01)00375-2
35. Andersen HC. Structure of liquids. *Ann Rev Phys Chem.* (1975) **26**:145–66.
36. Chapman WG, Gubbins KE, Joslin CG, Gray CG. Theory and simulation of associating liquid-mixtures. *Fluid Phase Equil.* (1986) **29**:337–46.
37. Kolafa J, Nezbeda I. Monte Carlo simulations on primitive models of water and methanol. *Mol Phys.* (1987) **61**:161–75.
38. Nezbeda I. Simple short-ranged models of water and their application. A review. *J Mol Liq.* (1997) **73–4**:317–36.
39. Vlcek L., Nezbeda I. Thermodynamics of simple models of associating fluids: primitive models of ammonia, methanol, ethanol, and water. *Mol Phys.* (2004) **102**:771–81. doi: 10.1080/00268970410001705343
40. Vlcek L, Nezbeda I. From realistic to simple models of fluids. III. Primitive models of carbon dioxide, hydrogen sulphide, and acetone, and their properties. *Mol Phys.* (2005) **103**:1905–15. doi: 10.1080/00268970500083630
41. Sciortino F. Primitive models of patchy colloidal particles. A review. *Coll Czech Chem Commun.* (2010) **75**:349–58. doi: 10.1135/cccc2009109
42. Bianchi E, Blaak R, Likos CN. Patchy colloids: state of the art and perspectives *Phys Chem Chem Phys.* (2011) **13**:6397–410. doi: 10.1039/c0cp02296a
43. Boublik T, Nezbeda I, Hlavaty K. *Statistical Thermodynamics of Simple Liquids and Their Mixtures*. Amsterdam: Elsevier (1980).
44. Gray CG, Gubbins KE. *Theory of Molecular fluids.* Vol. 1. Oxford: Oxford Univ. Press (1984).
45. Hansen JP, McDonald IR. *Theory of Simple Liquids*. Amsterdam: Elsevier (2006).
46. Nezbeda I, Smith WR. The use of a site-centered coordinate system in the statistical mechanics of site interaction molecular fluids. *Chem Phys Lett.* (1981) **81**:79–82.
47. Duh DM, Mier-Y-Teran L. An analytical equation of state for the hard-core Yukawa fluid. *Mol Phys.* (1997) **90**:373–80.
48. Montes J, Robles M, Lopez de Haro M. Equation of state and critical point behavior of hard-core double-Yukawa fluids *J Chem Phys.* (2016) **144**:084503. doi: 10.1063/1.4942199
49. Gross J, Sadowski G. Perturbed-chain SAFT: an equation of state based on a perturbation theory for chain molecules. *Ind Eng Chem Res.* (2001) **40**:1244–60. doi: 10.1021/ie0003887
50. Nezbeda I. Towards a unified view of fluids. *Mol Phys.* (2005) **103**:59–76. doi: 10.1080/00268970420002747 75
51. Nezbeda, I. Structure of water: short-ranged versus long-ranged forces. *Czech J Phys B.* (1998) **48**:117–22.
52. Nezbeda I, Kolafa J. Effect of short- and long-range forces on the structure of water: temperature and density dependence. *Mol Phys.* (1999) **97**:1105–16.
53. Kolafa J, Nezbeda I. Effect of short- and long-range forces on the structure of water. II. Orientational ordering and the dielectric constant. *Mol Phys.* (2000) **98**:1505–20. doi: 10.1080/00268970009483356
54. Kolafa J, Nezbeda I, Lisal M. Effect of short- and long-range forces on the properties of fluids. III. Dipolar and quadrupolar fluids. *Mol Phys.* (2001) **99**:1751–64. doi: 10.1080/00268970110072386
55. Kettler M, Nezbeda I, Chialvo AA, Cummings PT. Effect of the range of interactions on the properties of fluids. Phase equilibria in pure carbon dioxide, acetone, methanol, and water. *J Phys Chem B.* (2002) **106**:7537–46. doi: 10.1021/jp020139r
56. Chialvo AA, Kettler M, Nezbeda I. Effect of the range of interactions on the properties of fluids. Part II. Structure and phase behavior of acetonitrile, hydrogen fluoride, and formic acid. *J Phys Chem B.* (2005) **109**:9736–50. doi: 10.1021/jp050922u
57. Zhou S, Solana JR. Progress in the perturbation approach in fluid and fluid-related theories. *Chem Res.* (2009) **109**:2829–58. doi: 10.1021/cr900094p
58. Rodgers JM, Hu Z, Weeks JD. On the efficient and accurate shirt-range simulations of uniform polar molecular fluids. *Mol Phys.* (2011) **109**:1195–211. doi: 10.1080/00268976.2011.554332
59. Nezbeda I. Can we understand (and model) aqueous solutions without any electrostatic interactions? *Mol Phys.* (2001) **99**:1631–9. doi: 10.1080/00268970110064781
60. Nezbeda I. Modeling of aqueous electrolytes at a molecular level: Simple short-range models and structure breaking and structure enhancement phenomena. *J Mol Liquids* (2003) **103-4C**:309–17. doi: 10.1016/S0167-7322(02)00149-6
61. DeMille RC, Molinero V. Coarse-grained ions without charges: Reproducing the solvation structure of NaCl in water using short-ranged potentials. *J Chem Phys.* (2009) **131**:034107. doi: 10.1063/1.3170982
62. Drunsel F, Gross J. Theory of model electrolyte solutions: Assessing the short- and long-ranged contributions by molecular simulations. *Fluid Phase Equil.* (2016) **430**:195–206. doi: 10.1016/j.fluid.2016.09.026
63. Nezbeda I, Vlcek L. Thermophysical properties of fluids: From realistic to simple models and their applications. *Int J Thermophys.* (2004) **25**:1037–49. doi: 10.1023/B:IJOT.0000038498.47700.3f
64. Vlcek L, Nezbeda I. From realistic to simple models of associating fluids. II. Primitive models of ammonia, ethanol, and models of water revisited. *Mol Phys.* (2004) **102**:485–97. doi: 10.1080/00268970410001668417
65. Nezbeda I. Fluids of pseudo-hard bodies. *Mol Phys.* (1997) **90**:661–4.
66. Nezbeda I, Rouha M. Extended excluded volume: its origin and consequences. *Pure Appl Chem.* (2013) **85**:201–10. doi: 10.1351/PAC-CON-12-04-04
67. Rouha M, Nezbeda I. Excess properties of aqueous solutions: Hard spheres versus pseudo-hard bodies. *Mol Phys.* (2011) **109**:613–7. doi: 10.1080/00268976.2010.542779

68. Nezbeda I, Skvor J. Excluded volume versus hydrogen bonding: complementary or incompatible concepts? *Mol Phys.* (2012) **110**:2987–92. doi: 10.1080/00268976.2012.689875
69. Wertheim MS. Fluids with highly directional attractive forces: I. Statistical thermodynamics. *J Stat Phys.* (1984) **35**:19–34.
70. Wertheim MS. Fluids with highly directional attractive forces: II. Thermodynamic perturbation theory and integral equations. *J Stat Phys.* (1984) **35**:35–47.
71. Wertheim MS. Fluids with highly directional attractive forces: III. Multiple attraction sites. *J Stat Phys.* (1986) **42**:459–76.
72. Wertheim MS. Fluids with highly directional attractive forces: IV. Equilibrium polymerization. *J Stat Phys.* (1986) **42**:477–92.
73. Zmpitas W, Gross J. Detailed pedagogical review and analysis of Wertheim's thermodynamic perturbation theory. *Fluid Phase Equil.* (2016) **428**:121–52. doi: 10.1016/j.fluid.2016.07.033
74. Vega C, Abascal JLF. Simulating water with rigid non-polarizable models: a general perspective. *Phys Chem Chem Phys.* (2011) **13**:19663–88. doi: 10.1039/c1cp22168j
75. Nezbeda I, Kolafa J, Kalyuzhnyi YV. Primitive model of water. II. Theoretical results for the structure and thermodynamic properties. *Mol Phys.* (1989) **68**:143–60.
76. Slovak J, Nezbeda I. On accuracy of Wertheim's thermodynamic perturbation theory for primitive models of water. *Mol Phys.* (2003) **101**:789–98. doi: 10.1080/0026897031000075633
77. Smith WR, Nezbeda I, Melnyk TW, Fitts DD. Reference system selection and the average Mayer-function perturbation theory for molecular fluids. *Faraday Discuss Chem Soc.* (1978) **66**:130–7.
78. Kolafa J, Nezbeda I. The Lennard-Jones fluid: an accurate analytic and theoretically-based equation of state. *Fluid Phase Equil.* (1994) **100**:1–34.
79. Thol M, Rutkai G, Koster A, Lustig R, Span R, Vrabec J. Equation of state for the Lennard-Jones fluid. *J Phys Chem Ref Data.* (2016) **45**:023101. doi: 10.1063/1.4945000
80. Lafitte T, Apostolakou A, Avenda C, Galindo A, Adjiman CS, Muller EA, et al. Accurate statistical associating fluid theory for chain molecules formed from Mie segments. *J Chem Phys.* (2013) **139**:154504. doi: 10.1063/1.4819786
81. Karakatsani EK, Spyriouni T, Economou IG. Extended Statistical Associating FLuid Theory (SAFT) equations of state for dipolar fluids. *AIChE J.* (2005) **51**:2328–42. doi: 10.1002/aic.10473
82. Ahmed S, Ferrando N, de Hemptinne JC, Simonin JP, Bernard O, Baudouin O. A new PC-SAFT model for pure water, water-hydrocarbons, and water-oxygenates systems and subsequent modeling of VLE, VLLE, and LLE. *J Chem Eng Data.* (2016) **61**:4178–90. doi: 10.1021/acs.jced.6b00565
83. Liu ZP, Li YG, Chan KY. Equation of state for nonpolar, polar, chain, and associating fluids based on the dipolar Yukawa potential. *Ind Eng Chem Res.* (2001) 40:973–79. doi: 10.1021/ie000627q
84. Clark GNI, Haslam AJ, Galindo A, Jackson G. Developing optimal Wertheim-type models of water for use in Statistical Association Fluid Theory (SAFT) and related approaches. *Mol Phys.* (2006) **104**:3561–81. doi: 10.1080/00268970601081475
85. Nezbeda I, Iglesias-Silva GA. Primitive model of water. III. Analytic theoretical results with anomalies for the thermodynamic properties. *Mol Phys.* (1990) **69**:767–74.
86. Jackson G, Chapman WG, Gubbins KE. *Mol Phys.* (1988) **65**:1–31.
87. Gil-Villegas A, Galindo A, Whitehead PJ, Mills SJ, Jackson G, Burgess AN. Statistical associating fluid theory for chain molecules with attractive potentials of variable range. *J Chem Phys.* (1997) 106:4168–86.
88. Patel BH, Docherty H, Varga S, Galindo A, Maitland GC. Generalized equation of state for square-well potentials of variable range? *Mol Phys.* (2005) **103**:129–39. doi: 10.1080/00268970412331303990
89. Lymperiadis A, Adjiman CS, Galindo A, Jackson G. A group contribution method for associating chain molecules based on the statistical associating fluid theory (SAFT-gamma). *J Chem Phys.* (2007) **127**:234903. doi: 10.1063/1.2813894
90. Tan SP, Ji X, Adidharma H, Radosz M. Statistical associating fluid theory coupled with restrictive primitive model extended to bivalent ions. SAFT2: 1. Single salt plus water solutions. *J Phys Chem B.* (2006) **110**:16694. doi: 10.1021/jp0625107
91. Tan SP, Ji X, Adidharma H, Radosz M. Statistical associating fluid theory coupled with restrictive primitive model extended to bivalent ions. SAFT2: 2. Brine/seawater properties predicted. *J Phys Chem B.* (2006) **110**:16700. doi: 10.1021/jp062511z
92. Eriksena DK, Lazarou G, Galindo A, Jackson G, Adjiman CS, Haslam AJ. Development of intermolecular potential models for electrolyte solutions using an electrolyte SAFT-VR Mie equation of state. *Mol Phys.* (2016) **114**:2724–9. doi: 10.1080/00268976.2016.1236221
93. dos Ramos MC, Goff KD, Zhao H, McCabe C. Modeling the phase behavior of H2S+n-alkane binary mixtures using the SAFT-VR+D approach. *J Phys Chem B.* (2008) **112**:9417–27. doi: 10.1021/jp800397n
94. Dufal S, Lafitte T, Haslam A, Galindo A, Clark GNI, Vega C, et al. The A in SAFT: developing the contribution of association to the Helmholtz free energy within a Wertheim TPT1 treatment of generic Mie fluids. *Mol Phys.* (2015) **113**:948–84. doi: 10.1080/00268976.2015.1029027
95. Economou IG. Statistical associating fluid theory: a successful model for the calculation of thermodynamic and phase equilibrium properties of complex fluid mixtures. *Ind Eng Chem Res.* (2002) **41**:953–62. doi: 10.1021/ie0102201
96. Tan SP, Adidharma H, Radosz M. Recent advances and applications of statistical associating fluid theory. *Ind Eng Chem Res.* (2008) **47**:8063–82. doi: 10.1021/ie8008764
97. Chapman WG. Prediction of the thermodynamic properties of associating Lennard-Jones fluids - theory and simulation. *J Chem Phys.* (1990) 93:4299–304.
98. Nezbeda I, Slovak J. Can Lennard-Jones particles with four bonding sites realistically model water? *Chem Phys Lett.* (1996) **260**:336–40.
99. Pavlicek J, Nezbeda I. Application of primitive models of association: a simple theoretical equation of state of water. *Fluid Phase Equil.* (1996) **116**:530–6.
100. Nezbeda I, Weingerl U. A molecular-based theory for the thermodynamic properties of water. *Mol Phys.* (2001) **99**:1595–606. doi: 10.1080/00268970110064790
101. Jirsak J, Nezbeda I. Towards a statistical mechanical theory of water: analytical theory for a short-ranged reference system. *J Chem Phys.* (2007) **127**:12450. doi: 10.1063/1.2771547
102. Rouha M, Nezbeda I, Hruby J, Moucka F. Higher virial coefficients of water. *J Mol Liq.* (2018) **270**:81–6. doi: 10.1016/j.molliq.2017.11.105
103. Rushbrook GS, Stell G, Hoye JS. Theory of polar liquids I. Dipolar hard spheres *Mol Phys.* (1973) **26**:1199–215.
104. Rouha M, Nezbeda I. Thermodynamics of pseudo-hard body mixtures. *Mol Phys.* (2008) **106**:2481–5. doi: 10.1080/00268970802570342

Conflict of Interest: The author declares that the research was conducted in the absence of any commercial or financial relationships that could be construed as a potential conflict of interest.

frontiers in Physics

ORIGINAL RESEARCH
published: 05 February 2021
doi: 10.3389/fphy.2020.619320

Microscopic Model of Intermediate Phase in Flexible to Rigid Transition

Aldo Sayeg Pasos-Trejo and Atahualpa S. Kraemer**

Departamento de Física, Facultad de Ciencias, Universidad Nacional Autónoma de México, Ciudad Universitaria, México, Mexico

We introduce a lattice gas model with a modified Hamiltonian considering different energy for cycles of connected atoms. The system can be interpreted as a chalcogenide glass with pollutants forming floppy and rigid structures. We consider an energetic penalization for redundant bonds in the network. This penalization allows us to incorporate the topology constraints of rigidity in the network to study the thermodynamics of the system. We observe, depending on the parameter used for the penalization, that the system exhibits a typical first-order phase transition, or a stepped transition between the low and high density while varying the chemical potential. We also observe a hysteresis loop in the density and energy of the system. We use the area of these loops to calculate the irreversible enthalpy. There are two regimes, one where the enthalpy decreases linearly and the other with almost constant enthalpy. As the enthalpy is almost constant and very low, we interpreted this as the intermediate phase of the chalcogenide glasses.

Keywords: chalcogenide glasses, covalent network, rigidity, intermediate phase, phase transition, lattice gas

OPEN ACCESS

Edited by:
Giancarlo Ruocco,
Italian Institute of Technology (IIT), Italy

Reviewed by:
Matthieu Micoulaut,
Sorbonne Universités, France
Lucia Comez,
National Research Council (CNR), Italy
James Charles Phillips,
Rutgers, The State University of New Jersey, United States

****Correspondence:***
Aldo Sayeg Pasos-Trejo
sayeg@ciencias.unam.mx
Atahualpa S. Kraemer
ata.kraemer@ciencias.unam.mx

Specialty section:
This article was submitted to Soft Matter Physics, a section of the journal Frontiers in Physics

Received: *20 October 2020*
Accepted: *30 November 2020*
Published: *05 February 2021*

Citation:
Pasos-Trejo AS and Kraemer AS (2021) Microscopic Model of Intermediate Phase in Flexible to Rigid Transition. Front. Phys. 8:619320. doi: 10.3389/fphy.2020.619320

1 INTRODUCTION

Lattice gas models are among the simplest thermodynamic models that exhibit a phase transition with an exact solution in 2D. The nearest neighbor interaction and limitation of occupation in volume allows emulating a real gas in potentials such as Lennard-Jones [1]. This model has proven to be useful in different contexts, such as condensation of DNA [2], or the absorption in controlled-pore Glasses [3]. There is also a direct relationship with the Ising model, which was first used to study ferromagnetic materials [4], and then many other materials as spin-crossover materials [5], or spin glasses [6] among others. On the other hand, chalcogenide glasses seem to be some of the most promising materials for future technology, with important applications [7–9], ranging from solid state batteries [10, 11] to optics and photonics infrared devices [12, 13]. Topology and rigidity of the network are characterizing properties of these glasses [14, 15].

Experimental modulated differential scanning calorimetry (MDSC) and computational molecular dynamics (MD) studies near the glass transition over chalcogenide materials have found anomalies in the behavior of the macroscopic variables of these materials, giving rise to what is known as the intermediate phase [16–18]. Although theoretical explanations regarding the significance and existence of this phase exist, as far as we know, no microscopic model which recovers the thermodynamic macroscopic properties of the system has been constructed to this date. The purpose of the paper is to provide a simplified microscopic model that reproduces the behavior of thermodynamic variables in the intermediate phase.

2 INTERMEDIATE PHASE AND RIGIDITY IN CHALCOGENIDE GLASSES

The anomalies mentioned previously, along with most of the bulk properties of chalcogenide glasses, have been related to a microscopic property of their covalent network called rigidity [19]. It can be defined as the property of atoms being able to move without deforming current bond angles and lengths. More precisely, a whole mathematical formalism can be developed to study rigidity [20].

Independently of the mathematical theory of rigid networks, simplified models have been extensively used to study the rigidity of glasses, with particular focus on reproducing the transition between rigid and floppy modes [21]. The most relevant of them is the percolation rigidity model, based on constraint counting, which can be exactly solved using mean-field approximations [22].

Besides the obvious complexity arising from the absence of long-range order in amorphous solids, the challenge in building a model that recovers macroscopic properties relies on the difficulty of representing the vibrational entropy accumulated near the boson peak and the inherent degeneracy of most of the configurations [23].

Such difficulty is directly related to the problem of effectively quantifying the rigidity of the network so it can be incorporated into the microscopic model. Mean-field theories are incapable of describing the microscopic scale accurately. In the particular case of two-dimensional networks, the pebble game algorithm [24] is capable of decomposing a network onto its rigid components with sufficient speed, but it does not give a method of relating rigidity to thermodynamic variables.

The algorithm relies on Laman's theorem [25] which characterizes exactly the rigidity of a network embedded in a two-dimensional Euclidean space. The referred theorem hasn't been successfully extended to other dimensions due to the difficulty of the exactly characterizing the rigid components of a network embedded in an arbitrary geometry. For dimensions greater than two, approximations are commonly used [26]. As we are only interested in quantifying the rigidity as a function of thermodynamic variables in a more accurate way than the mean-field theories, we could aim to use a non-precise but a simplified model of the network by using a modified lattice gas model. This model should take into account the results obtained by the pebble game algorithm when simulating the transition to a rigid system.

2.1 Description and Behavior of Chalcogenide Glasses

Chalcogenide glasses are amorphous solids built upon members of the 16 group of the periodic table (S, Se, Te) by doping them with members of another group, most commonly group 15 (As,Sb). To a molecular level they can be completely described by a continuous random network (CRN) [27]: a molecular network where each edge represents a covalent bond. Although van der Waal forces between pairs of free electrons are normally present in the system, those interactions are weak enough to be left out of the CRN model.

Raman Spectroscopy allows us to obtain the resonant frequencies of the vibrational modes of the network, which is related to the different molecular structures (components) of the network. This information allows to calculate the entropy by using the formula $S = \sum x_i log\,(x_i)$ where x_i is the relative fraction of each component [28]. This approach has been particularly useful in numerical studies [23].

The relationship between the topology of the network and its rigidity to the macroscopic properties of the system via the changes in its density of states was first proposed by Phillips [14, 15] and further confirmed from mean-field constraint counting approaches to rigidity by Thorpe [19, 29]. Experiments have also shown that when examining glasses of the same compound but different stoichiometries, which is equivalent to changing the mean coordination number of the network, macroscopic properties change as a function of the stoichiometries and present a transition when passing for coordination numbers similar to the theoretically predicted by mean-field theory [30, 31]. In addition, when performing experimental MDSC calorimetry studies of chalcogenide glasses, we can measure the heatflow during endothermic and exothermic processes of the system. With these measurements, the irreversible enthalpy when passing through the glass transition can be obtained. When analyzing such data as a function of the stoichiometry of the glass, a reversibility window is found, in which the irreversible enthalpy vanishes [16]. Such a window can not be directly associated with a rigid or floppy phase of the CRN; it forms a new phase called *intermediate phase* [16].

The importance and existence of the intermediate phase are confirmed by the exotic behavior of other macroscopic properties of the glasses in such a window [32], such as ionic conduction [33] and infrared reflectance [34]. The intermediate phase has also been observed by measuring the configurational entropy of the system [23, 28, 35, 36]. Studies on other chalcogenide glasses and oxide glasses also exhibit an intermediate phase with similar anomalies in the macroscopic variables [17], and it can also be observed in molecular dynamics simulations [18].

Such experiments have also measured quantities that are directly related to the average coordination number and the number of floppy modes (see for example [17] and references inside), which can be used to quantify the constraint density [16]. Those quantities have been also developed in analytical and numerical treatment of this materials [14, 17].

Despite the experiments and simulations carried out the intermediate phase is still controversial especially due to contradicting experimental studies in which a structural origin of the phase isn't found [37–41].

2.2 Microscopic Models

Besides the experimental controversy, some efforts have been made in order to construct a microscopic (structural) model that reproduces the exotic behavior of the macroscopic variables of the system. Outside of the intermediate phase context, several microscopic models have been developed [27, 42], more recently putting effort into describing the glass transition and the Arrhenius-like behavior [43, 44].

One of the first models [45], uses a random bond network that allowed to control the number of rings of bonds, which are problematic in the rigidity percolation theory. The authors used a computer simulation that allowed constructing the network beginning in a floppy mode and growing it by adding bonds that restrict movement in a non-redundant way (i.e., the bonds reduce the degrees of freedom of the system). After all of the independent bonds have been placed, the bond allocation continues and its performed at random. With this model, the authors were able to observe a transition from a floppy state to a rigid, non stressed (i.e., without redundant bonds) and from there to a stressed network. The key element in the model is in the procedure of the building that allows for self-organization in the network.

This model was further developed by Chubynsky et al. Ref. 46 in order to work with networks in thermodynamic equilibrium, as the network construction process of the original model could lead to highly atypical networks for the system. This model changes the original only in a small way: it grows the network from a floppy state by adding independent bonds, but every time it adds a bond it deletes and creates a bond that doesn't change the stress (i.e., the redundancy of another bond) of the network.

Another model Ref. 47 also uses the self-organization of the network, in this case by explicitly describing the Hamiltonian as the number floppy modes. The network is restricted to a Bethe-like lattice (of finite size). The system is then studied using Monte Carlo simulations, switching configurations by rewiring two randomly selected nodes. The intermediate phase is found in terms of changes in the probability of a stressed cluster that exists and percolates through the entire lattice.

It must be acknowledged that the three mentioned models depend on the Pebble Game algorithm in order to describe the independent bonds of the network. Other models have been studied before those mentioned [48]. They do not depend directly on the exact description of the rigid components of the network, but instead approximate those components via loops or cycles of the covalent graph. They are also known as *tree-like percolation* models. Most of these models do not produce a uniform ensemble with equal probability for all tree-like structures, although they can be treated as if they were in thermodynamic equilibrium. Tree-like percolation models also include self-organization by avoiding the building of loops.

Models that directly attack the thermodynamic properties from the hamiltonian either analytically [49] or numerically via stochastic descriptions [23] have also been developed. Another important aspect of the models in this subsection is the fact that most of them are designed only to describe the system in moments where we can accurately characterize the vibrational entropy of the atoms. Such an assumption implies that the temperature T of our systems is much smaller than the Debye temperature T_D.

3 MODEL

Similar to tree-like percolation models, we can argue that in two-dimensions the redundant constraints put by adding a bond to an atom with zero degrees of freedom is equivalent to whether the connectedness of the graph will depend on such bond. In a lattice gas model, an independent bond will be a bridge edge of the graph, and rigid components become equivalent to components isomorphic to cycles. To obtain the macroscopic variables from the microscopic model, we need its hamiltonian. We will base our model in the lattice gas model, which has the following hamiltonian:

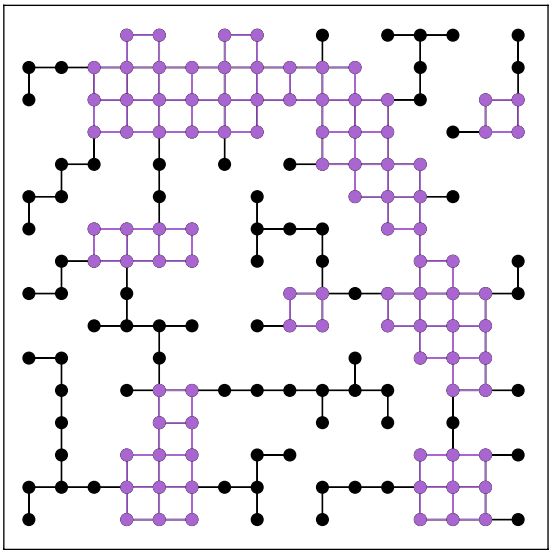

FIGURE 1 | Search of rigid clusters for a 16×16 square lattice system with closed boundary conditions.

$$H = -\mu \sum_i n_i - J \sum_{\langle i,j \rangle} n_i n_j \tag{1}$$

where μ is the chemical potential, n_i is 1 or 0 depending if the site i is or not occupied, and J is the energy of the bound between two nearest neighbors represented by $\langle i, j \rangle$.

This hamiltonian will be modified to take into account the energy cost of stress (redundant constrains). In our model these redundant constrains are the bonds forming cycles. Then, adding a cost energy of the bonds belonging to a cycle to **Eq. 1**, we obtain:

$$H = -\mu \sum_i n_i - J \sum_{\langle i,j \rangle} n_i n_j + C \sum_{\langle i,j \rangle \in L} n_i n_j = H_{\text{chem}} + H_{\text{int}} + H_{\text{rig}} \tag{2}$$

here L is the set of all the nearest neighbors that form clusters without bridge edges. This is equal to the set of all the edges between vertices in cycles. $C > 0$ represents a penalization for forming rigid clusters that delay the normal phase transition of the system between a low-density and a high-density state. This allows our system to find new non-rigid configurations and stay near them for large simulation times. **Figure 1** shows occupied sites as circles, while the bridge edges are in black, and cycles are plotted in purple.

Our model differs from the original tree-like percolation [50] due to the fact that, although it is also an Ising-like model, in the tree-like model the connectedness problem arises as an

interpretation of the system, meanwhile that in our model we are explicitly modifying the hamiltonian with a new term.

In the limit $T \to 0$ we can approximate how the system in a square lattice will behave in order to orient the range of parameters of the Hamiltonian for which we will see certain transitions.

For $C \sim \mu \sim J$, if we have N atoms with a fraction l of them forming rigid clusters, we can suppose than adding a new atom adds three rigid bonds and change two normal bonds to rigid bonds on average (see **Figure 2**), which becomes equally likely when

$$H_{\text{chem}}(N) + H_{\text{int}}(N) + H_{\text{rig}}(lN) < H_{\text{chem}}(N) - \mu + H_{\text{int}}(N) - 3J + H_{\text{rig}}(lN) + 5C, \tag{3}$$

which gives a critical value μ_{c1} for the chemical potential when the inequality becomes an equality:

$$\mu_{c1} = 5C - 3J \tag{4}$$

and suggests a change between medium and high density. Physically, this medium density corresponds to the case where adding particles in rigid, non stressed components is favored. This can be related to the constrain density n_c of the network, so that $\mu > \mu_{c1}$ will correspond to high constrain density n_c (fully connected system).

For $\mu, J \gg C$ or $C \approx 0$ we have the same behavior than a normal lattice gas, and the critical value for μ is expected at $\mu_{c2} = -2J$ with a jump between low and high density.

For sufficiently high values of $C \gg \mu, J$ energy minimization will be achieved by having as less cycles as possible. For N atoms in the system not belonging to a cycle, it will be equally probable to add or remove atoms if:

$$H_{\text{chem}}(N+1) + H_{\text{int}}(N+1) = H_{\text{chem}}(N) + H_{\text{int}}(N) \tag{5}$$

which happens for $\mu_{c3} = -J$ and predicts a transition between high and low density states. $\mu < \mu_{c3}$ will correspond to a floppy system with low constrain density $n_c \sim 0$. For $\mu_{c1} \gtrsim \mu_{c3}$, which is obtained for $C_c \gtrsim 2J/5$ we can expect only a double transition in the system.

Summarizing, μ_{c1} the critical value for the transition from a medium to high density (rigid to stressed), μ_{c2} is the typical critical value from zero density to one in the lattice gas model, and μ_{c3} correspond to the value where appear a transition from zero to non zero (floppy to rigid) density.

4 SIMULATIONS

We studied the model performing Markov Chain Monte Carlo simulations, based on the Metropolis-Hastings algorithm. The stability and convergence of chains were analyzed to determine the number of Monte Carlo Sweeps (algorithm steps per lattice site) needed to achieve convergence. For $\tau = 100$ Monte Carlo Sweeps all the systems are thermalized. This is also confirmed after seeing a drastic reduction of the standard deviation of samples between the whole system and the last $\tau/2$ states.

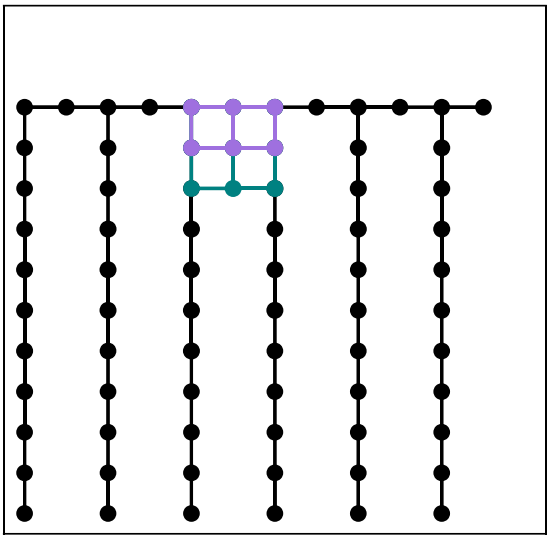

FIGURE 2 | New bonds (green) created by adding a new atom next to a rigid cluster (purple) in a square lattice.

We simulated for 41×31 equally spaced values of (μ, C) in the $[-3.5, 0.0] \times [0.5, 1.2]$ interval and fixed $J = 2$, $K_B T = 0.5$ over four independent square lattices with periodic boundary conditions of side $L = 32$ and 40. Macroscopic variables were calculated as the average of the thermalized values as shown in **Figure 3**.

The simulation was coded in the Julia Language [51], and can be found online in a public repository at: https://github.com/sayeg84/latticeModels

5 DISCUSSION

5.1 Macroscopic Variables

In a canonical ensemble, the probability to be in a particular state is proportional to $\exp(-H/KT) = \exp(-\beta H)$. This give us a relation between temperature and the parameters of the hamiltonian. Developing this expression we obtain $\exp(-\beta H) = \exp(\beta\mu \sum n_i)\exp(-\beta(H_{\text{int}} + H_{\text{rig}}))$. Given so, varying the parameter μ is roughly equivalent to varying $\beta = 1/KT$, by this we mean both variables can be used to induce the transitions in a similar way, but the corresponding critical exponents are different [52]. Varying the other two parameters is not equivalent to varying β, since these are not multiplied not by the sum of n_i, but by the sum of the product (for many configurations, the product $\beta C \sum n_i n_j = 0$). However, these parameters can be useful to extend the model to study the effects of pressure or to perform simulations varying T instead of μ.

Changing pressure on the system is equivalent to deforming the lattice (change the volume V) which translates into a change of the potential energy because $J = J(V)$ and $C = C(V)$. The probability to be in a particular state in the *NPT* isothermal-isobaric ensemble is proportional to $\exp -\beta(H + PV - N\log(V)/\beta)$ [53]. This probability looks like the probability for

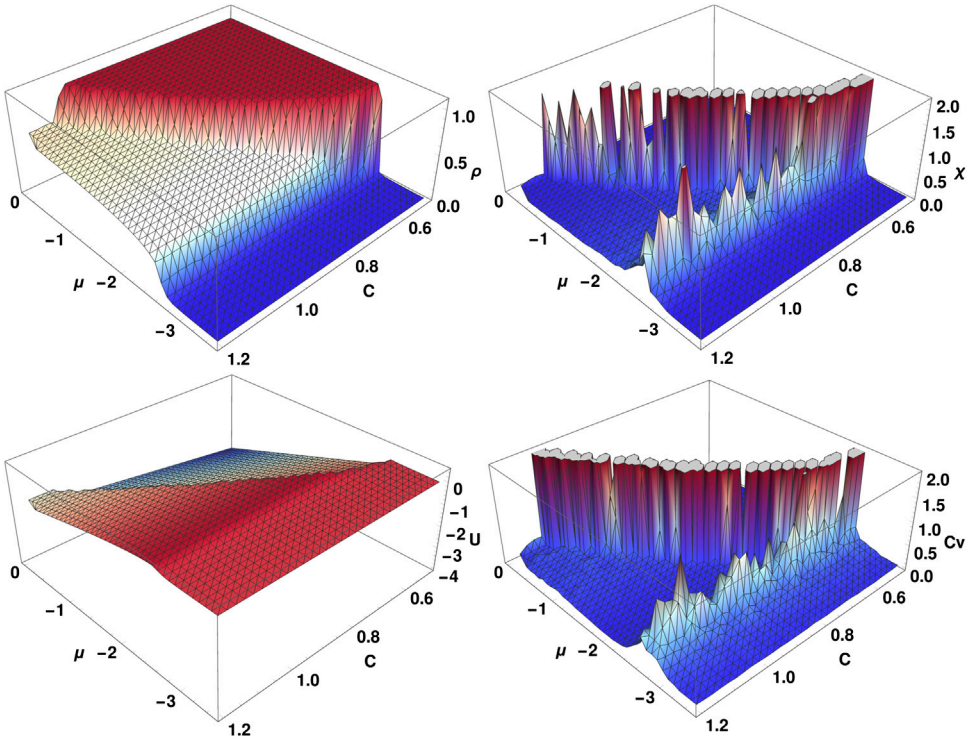

FIGURE 3 | Macroscopic variables for a square lattice model: density ρ (top left), internal energy U (top right), density susceptibility χ (bottom left) and heat capacity at constant volume C_V (bottom right), for $L = 40$ as a function of chemical potential μ and the parameter C.

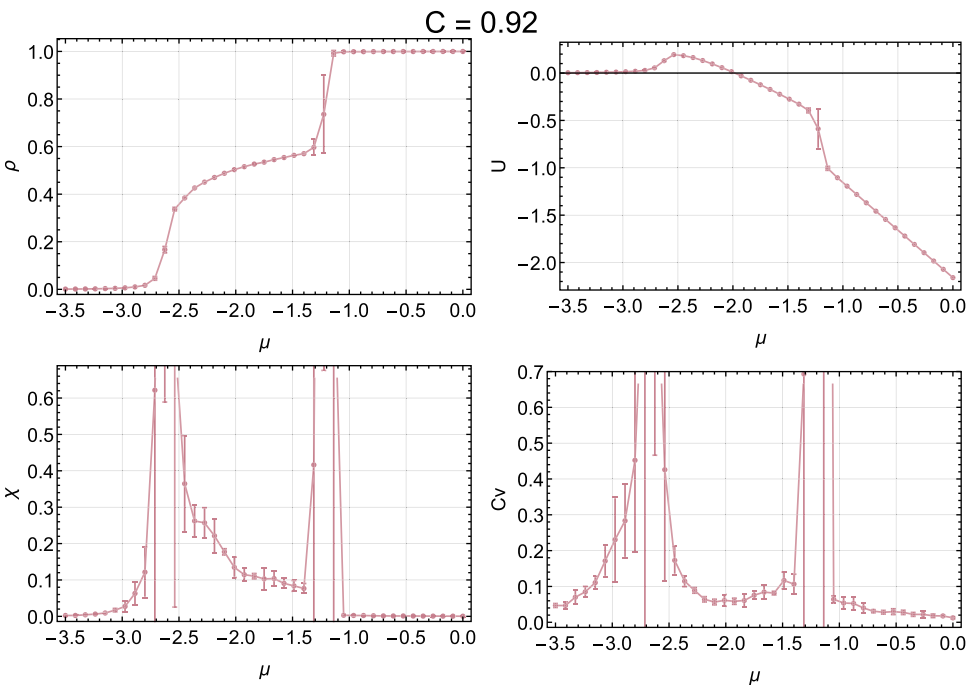

FIGURE 4 | Macroscopic variables for a square lattice: density ρ (top left), internal energy U (top right), density susceptibility χ (bottom left) and heat capacity at constant volume C_V (bottom right) for constant $C = 0.92$ for $L = 40$ as function of μ. Dark line in U separates positive and negative energies.

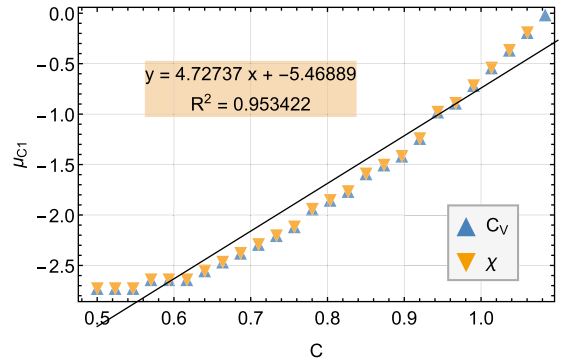

FIGURE 5 | μ_{c1} as function of C taken from both C_V and χ. Values of μ_{c1} concide for both variables at all the values of C. The linear fit was performed jointly for both data.

the NVT-ensemble, except that instead of H, now we have $H' = H + PV - N\log(V)/\beta$. For the Monte-Carlo simulation, this means that we need to add the possibility to change the volume of the system instead of changing a node in the lattice. The only missing part is a model for J and C. A good model for J is $J(V) = A_0 V^2$, where A_0 is the harmonic contribution to the elastic interaction energy between two neighbors [54]. However, we still don't have a good model for $C(V)$. This ensemble is also probably more suitable to variate the temperature than the NVT-ensemble, since the experiments are performed at constant pressure, and if the volume is fixed, when the temperature increases the probability to change a node tends to 1, which means that the density tends to 1/2, so the whole transition is not reached, the reason why we used μ instead. We would now like to give an interpretation of C.

Average coordination number $\langle r \rangle$ and rigidity are correlated and are considered as the defining parameters for the study of the intermediate phase. Redundant bonds have an energy cost that we related with C in **Eq. 2**. In this case, the total energy cost is the product of all the redundant bonds times C. We can variate then the energy cost by varying the number of redundant bonds (so, by varying $\langle r \rangle$) or by varying C. So, we can interpret the variation of C as the variation of the percentage of pollutants if the reached configuration is the same. Then, small values of C correspond to flexible configuration and high values of C to rigid or stressed configurations.

The susceptibility χ and the specific heat C_v show two large jumps near values $\mu_{c3} = \approx -2.5$ and $\mu_{c1} > \mu_{c3}$. We observe that $\mu > \mu_{c1}$ shows a high density state, while $\mu_{c1} > \mu > \mu_{c3}$ gives a medium density state and $\mu_{c3} > \mu$ returns to low density.

Because a medium-density state could be unexpected for a model of this kind, we checked that its existence is independent of system size by performing simulations for smaller sizes. It occurs for every size and even becomes more stable as N grows. We define μ_{c1} as the value of μ where there is a transition from medium to high density. In **Figure 3** we can see that this also corresponds to the value of μ that maximizes the derivatives of the variables, that in this case result in the density susceptibility χ and the specific heat C_v. To better visualize these plots, in **Figure 4** we show a cut of each macroscopic variable when C = 0.92. We define $\mu_{c1}(C_v) = \text{argmax}(C_v(\mu))$ and $\mu_{c1}(\chi) = \text{argmax}(\chi(\mu))$. In **Figure 5** is displayed the relationship between $\mu_{c1}(C_v)$, $\mu_{c1}(\chi)$ and C.

The linear fit of the data displays parameters close to the theoretical analysis done previously (**section 3**, and equation refeq: mu1) with a high correlation coefficient even if the analysis was very rough. An analysis of hexagonal and triangular 2D lattices revels that the macroscopic variables exhibit the same behavior for those values of μ but for a different interval of C. This is expected from a theoretical point of view due to the critical point dependence of the average rigid bonds added when going from the spanning tree configuration to a rigid configuration.

5.2 Hysteresis

The simulations presented in the previous subsection were all performed by initializing the system with a random low-density configuration and making the simulations over it in a μ-increasing direction. When performing the same procedure but for μ-decreasing and beginning with a high-density configuration, the macroscopic thermodynamic variables show a different path. This difference in the path is called hysteresis.

Hysteresis is usually related to loss of internal energy and the work that the system produces [55, 56]. The area of the hysteresis loop in the density of the lattice gas is directly proportional to the work ΔW, while the area of the hysteresis loop in the internal energy corresponds to the loss of energy ΔU in the process. Using the first law of thermodynamics, we can obtain the heat $\Delta Q = \Delta W + \Delta U$, which we associate with the irreversible enthalpy. The area enclosed by the loop can be positive or negative depending on how the loop is walk by varying μ. To correctly define the sign, we will say that the area is positive if the loop is walked counterclockwise, and negative otherwise.

The hysteresis loops and their areas, corresponding to the work produce by the system ΔW and the change of the internal energy ΔU are shown in **Figure 6**. **Figure 7** shows the heat $\Delta Q = \Delta W + \Delta U$ as a function of C. The integrals used to calculate the area of the loops were calculated using a trapezoidal rule.

Comparing **Figures 3**, **6** we can see that the difference in internal energy ΔU is negative when there is a middle step in the transition when varying μ. The interval where this occurs is from $C \in [0.6, 1.14]$, and the minimum is reached for $C \sim 1.0$. For ΔW, the function decreases in the interval $C \in [0.5, 0.65]$, for $C \in [0.65, 85]$, a local minimum is reached, then the function becomes increasing until a maximum around $C \sim 1.1$ is found, and then it decreases again until $C \sim 1.14$, where $\Delta W \sim 0$.

As a result $\Delta Q = \Delta W + \Delta U$ is a linearly decreasing function in the interval $C \in [0.5, 0.78]$, while in the interval $C \in [0.78, 1.14]$, $\Delta Q \sim c$ remains constant, with $c \sim 0.1$. We associate this interval $C \in [0.78, 1.14]$ (shaded area) with the intermediate phase reported in chalcogenide glasses when a pollutant is added. This region was also obtained as the region where there is a step on the plot of ρ, passing through $\rho = 0.5$. However for values $C > 1.14$, we did not observed an increase of ΔQ as reported in literature [17], instead we observed $\Delta U \sim \Delta W \sim \Delta Q \sim 0$. We associate this with the limitations of the model, where a transition is not fully achieved when C is too high.

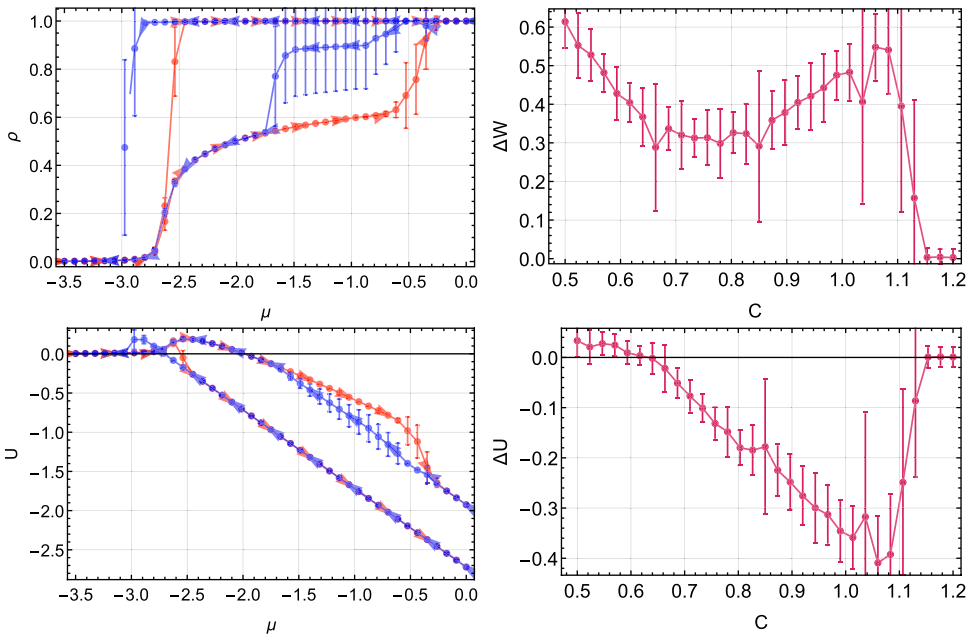

FIGURE 6 | Hysteresis in the thermodynamic variables for different values of C. Light colors are for $C = 0.64$ and darker colors are for $C = 1.0367$. The integral of the curve is shown in the right side.

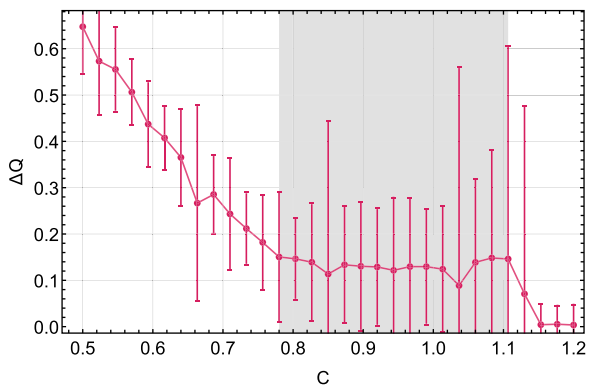

FIGURE 7 | $\Delta Q = \Delta W + \Delta U$ as a function of C for the values obtained in **Figure 6**, the shaded area corresponds to the region where there is a step on the plot of ρ, passing through $\rho = 0.5$.

Recalling the association of the parameter C with $\langle r \rangle$ we see that our results have qualitatively a similar behavior to the experimental studies in literature [17]. Comparing with the other numerical results of microscopic models, our results display phase separation in terms of the macroscopical variables related to the hamiltonian. Even if a more concise comparison with experimental results is not able with our work, the model is sufficiently generic to be expanded in order to achieve more precise simulations that could reproduce experimental results.

6 CONCLUSION

We present a simple model that exhibits a change in enthalpy behavior when varying the rigidity of the system, a behavior similar to that reported in chalcogenide glasses when increasing the amount of added pollutants. The fact that the model is simple results in efficient simulations, that allows us to make large enough systems and study how they change by varying different parameters. In addition, this model allows us to obtain density, internal energy, density susceptibility, and specific heat.

For certain parameters, the model exhibits a step transition in the density, while for others the transition is with no medium values of density. From the values of C_v and χ we observe that the first transition is not clear while the second seems to be a first-order transition. We interpreted the two possible states as "solid" and "fluid".

We were able to analytically approximate the parameter range where the transitions would appear. Our numerical results are in close agreement with such rudimentary approximations. Furthermore, our model is the first to connect the microscopic properties with the macroscopic thermodynamic variables.

Studying the hysteresis loops we were able to observe a change in behavior of the enthalpy, which is related to the change in density observed when the chemical potential (or temperature) varies when the transition becomes stepped width a medium density.

Despite success in qualitatively describing the first transition (flexible-rigid) to the intermediate phase, we were not able to reproduce the transition to stressed systems. We speculate that to see such a transition we would need to vary the temperature instead of the chemical potential.

DATA AVAILABILITY STATEMENT

The raw data supporting the conclusions of this article will be made available by the authors, without undue reservation.

AUTHOR CONTRIBUTIONS

AP performed the simulations and both authors contributed to designing the simulations, discussing the results, and writing and revising the manuscript prior to submission.

FUNDING

This work was partially funded by Universidad Nacional Autónoma de México via PAPIIT project IA106618.

ACKNOWLEDGMENTS

The authors appreciate the computing platform provided by the Laboratorio de Cómputo de Alto Rendimiento, under coordination of Departamento de Matemáticas of Facultad de Ciencias, UNAM. We also thank David P. Sanders and Adrian Huerta for fruitful discussions regarding the direction of this paper.

REFERENCES

1. Lavis DA, Bell GM. *Statistical mechanics of lattice systems*. Chichester: Springer Berlin Heidelberg (1999).
2. Vtyurina NN, Dulin D, Docter MW, Meyer AS, Dekker NH, Abbondanzieri EA. Hysteresis in dna compaction by dps is described by an ising model. *Proc Natl Acad Sci U.S.A.* (2016) 113:4982–7. doi:10.1073/pnas.1521241113
3. Gelb LD, Salazar R. Adsorption in controlled-pore glasses: comparison of molecular simulations with a mean-field lattice gas model. *Adsorption* (2005) 11:283–8. doi:10.1007/s10450-005-5938-z
4. Ising E. Beitrag zur theorie des ferromagnetismus. *Z Phys* (1925) 31:253–8. doi:10.1007/bf02980577
5. Muraoka A, Boukheddaden K, Linares J, Varret F. Two-dimensional ising-like model with specific edge effects for spin-crossover nanoparticles: a monte carlo study. *Phys Rev B* (2011) 84:054119. doi:10.1103/PhysRevB.84.054119
6. Saccone M, Scholl A, Velten S, Dhuey S, Hofhuis K, Wuth C, et al. Towards artificial ising spin glasses: thermal ordering in randomized arrays of ising-type nanomagnets. *Phys Rev B* (2019) 99:224403. doi:10.1103/PhysRevB.99.224403
7. Zakery A, Elliott S. Optical properties and applications of chalcogenide glasses: a review. *J Non-Cryst Solids* (2003) 330:1–12. doi:10.1016/j.jnoncrysol.2003.08.064
8. Seddon A. Chalcogenide glasses: a review of their preparation, properties and applications. *J Non-Cryst Solids* (1995) 184:44–50. doi:10.1016/0022-3093(94)00686-5
9. Eggleton BJ, Luther-Davies B, Richardson K. Chalcogenide photonics. *Nat Photon* (2011) 5:141–8. doi:10.1038/nphoton.2011.309
10. Tatsumisago M, Hayashi A. Chalcogenide glasses as electrolytes for batteries In: *Chalcogenide glasses*. Elsevier (2014). p 632–54.
11. Asobe M. Nonlinear optical properties of chalcogenide glass fibers and their application to all-optical switching. *Opt Fiber Technol* (1997) 3:142–8. doi:10.1006/ofte.1997.0214
12. Shaw LB, Cole B, Thielen PA, Sanghera JS, Aggarwal ID. Mid-wave ir and long-wave ir laser potential of rare-earth doped chalcogenide glass fiber. *IEEE J Quant Electron* (2001) 37:1127–37. doi:10.1109/3.945317
13. Boolchand P, Bresser W. Mobile silver ions and glass formation in solid electrolytes. *Nature* (2001) 410:1070–1073. doi:10.1038/35074049
14. Phillips J. Topology of covalent non-crystalline solids i: short-range order in chalcogenide alloys. *J Non-Cryst Solids* (1979) 34:153–81. doi:10.1016/0022-3093(79)90033-4
15. Phillips J. Topology of covalent non-crystalline solids ii: medium-range order in chalcogenide alloys and a si(ge). *J Non-Cryst Solids* (1981) 43:37–77. doi:10.1016/0022-3093(81)90172-1
16. Boolchand P, Georgiev D, Goodman B. Discovery of the intermediate phase in chalcogenide glasses. *J Optoelectron Adv Mater* (2001) 3:703–20.
17. Micoulaut M. Relaxation and physical aging in network glasses: a review. *Rep Prog Phys* (2016) 79:066504. doi:10.1088/0034-4885/79/6/066504
18. Bauchy M, Micoulaut M. Densified network glasses and liquids with thermodynamically reversible and structurally adaptive behaviour. *Nat Commun* (2015) 6:6398. doi:10.1038/ncomms7398
19. Thorpe M. Continuous deformations in random networks. *J Non-Cryst Solids* (1983) 57:355–70. doi:10.1016/0022-3093(83)90424-6
20. Demaine ED, O'Rourke J. *Geometric folding algorithms: linkages, origami, polyhedra*. Cambridge University Press (2007).
21. Thorpe M. Rigidity percolation in glassy structures. *J Non-Cryst Solids* (1985) 76:109–16. doi:10.1016/0022-3093(85)90056-0
22. Thorpe M, Jacobs D, Chubynsky N, Rader A. Generic rigidity of network glasses In: *Fundamental materials research*. Kluwer Academic Publishers (2002). p 239–77.
23. Yan L. Entropy favors heterogeneous structures of networks near the rigidity threshold. *Nat Commun* (2018) 9, 1359. doi:10.1038/s41467-018-03859-9
24. Jacobs DJ, Hendrickson B. An algorithm for two-dimensional rigidity percolation: the pebble game. *J Comput Phys* (1997) 137:346–65. doi:10.1006/jcph.1997.5809
25. Laman G. On graphs and rigidity of plane skeletal structures. *J Eng Math* (1970) 4:331–40. doi:10.1007/BF01534980
26. Chubynsky MV, Thorpe MF. Algorithms for three-dimensional rigidity analysis and a first-order percolation transition. *Phys Rev E* (2007) 76:041135. doi:10.1103/PhysRevE.76.041135
27. Zallen R. *The physics of amorphous solids*. 1st ed. Blacksburg: John Wiley & Sons (1998).
28. Gjersing EL, Sen S, Aitken BG. Structure, connectivity, and configurational entropy of GexSe100-x glasses: results from 77se MAS NMR spectroscopy. *J Phys Chem C* (2010) 114:8601–8. doi:10.1021/jp1014143
29. Feng S, Thorpe MF, Garboczi E. Effective-medium theory of percolation on central-force elastic networks. *Phys Rev B* (1985) 31:276–80. doi:10.1103/PhysRevB.31.276
30. Tanaka K. Structural phase transitions in chalcogenide glasses. *Phys Rev B* (1989) 39:1270–9. doi:10.1103/PhysRevB.39.1270
31. Narayanan RA, Asokan S, Kumar A. Evidence concerning the effect of topology on electrical switching in chalcogenide network glasses. *Phys Rev B* (1996) 54:4413–5. doi:10.1103/PhysRevB.54.4413
32. Chen P, Holbrook C, Boolchand P, Georgiev DG, Jackson KA, Micoulaut M. Intermediate phase, network demixing, boson and floppy modes, and compositional trends in glass transition temperatures of binaryAsxS1-xsystem. *Phys Rev B* (2008) 78:224208. doi:10.1103/physrevb.78.224208
33. Micoulaut M, Malki M, Novita DI, Boolchand P. Fast-ion conduction and flexibility and rigidity of solid electrolyte glasses. *Phys Rev B* (2009) 80:184205. doi:10.1103/PhysRevB.80.184205
34. Rompicharla K, Novita DI, Chen P, Boolchand P, Micoulaut M, Huff W. Abrupt boundaries of intermediate phases and space filling in oxide glasses. *J Phys Condens Matter* (2008) 20:202101. doi:10.1088/0953-8984/20/20/202101
35. Chakravarty S, Chbeir R, Chen P, Micoulaut M, Boolchand P. Correlating melt dynamics and configurational entropy change with topological phases of AsxS100–x glasses and the crucial role of melt/glass homogenization. *Front Mater* (2019) 6, 166. doi:10.3389/fmats.2019.00166
36. Chen P, Holbrook C, Boolchand P, Georgiev DG, Jackson KA, Micoulaut M. Intermediate phase, network demixing, boson and floppy modes, and compositional trends in glass transition temperatures of binary as_xs_{1-x} system. *Phys Rev B* (2008) 78:224208. doi:10.1103/PhysRevB.78.224208

37. Shatnawi MTM, Farrow CL, Chen P, Boolchand P, Sartbaeva A, Thorpe MF, et al. Search for a structural response to the intermediate phase in ge_xse_{1-x} glasses. *Phys Rev B* (2008) 77:094134. doi:10.1103/PhysRevB.77.094134
38. Micoulaut M. Concepts and applications of rigidity in non-crystalline solids: a review on new developments and directions. *Adv Phys X* (2016b) 1:147–75. doi:10.1080/23746149.2016.1161498
39. Zeidler A, Salmon PS, Whittaker DAJ, Pizzey KJ, Hannon AC. Topological ordering and viscosity in the glass-forming ge–se system: the search for a structural or dynamical signature of the intermediate phase. *Front Mater* (2017) 4:32. doi:10.3389/fmats.2017.00032
40. Chen G, Inam F, Drabold DA. Structural origin of the intermediate phase in ge–se glasses. *Appl Phys Lett* (2010) 97:131901. doi:10.1063/1.3495775
41. Rowlands RF, Zeidler A, Fischer HE, Salmon PS. Structure of the intermediate phase glasses gese3 and gese4: the deployment of neutron diffraction with isotope substitution. *Front Mater* (2019) 6:133. doi:10.3389/fmats.2019.00133
42. Elliott S. *Physics of amorphous materials*. Incorporated. Essex: John Wiley & Sons (1986).
43. Hall RW, Wolynes PG. Microscopic theory of network glasses. *Phys Rev Lett* (2003) 90:085505. doi:10.1103/physrevlett.90.085505
44. Garrahan JP, Chandler D. Coarse-grained microscopic model of glass formers. *Proc Natl Acad Sci U.S.A.* (2003) 100:9710–4. doi:10.1073/pnas.1233719100
45. Thorpe M, Jacobs D, Chubynsky M, Phillips J. Self-organization in network glasses. *J Non-Cryst Solids* (2000) 266–269:859–66. doi:10.1016/S0022-3093(99)00856-X
46. Chubynsky MV, Brière MA, Mousseau N. Self-organization with equilibration: a model for the intermediate phase in rigidity percolation. *Phys Rev* (2006) 74:016116. doi:10.1103/physreve.74.016116
47. Barré J, Bishop AR, Lookman T, Saxena A. Adaptability and "intermediate phase" in randomly connected networks. *Phys Rev Lett* (2005) 94:208701. doi:10.1103/physrevlett.94.208701
48. Straley JP. Treelike percolation. *Phys Rev* (1990) 41:1030–3. doi:10.1103/physreva.41.1030
49. Naumis GG. Energy landscape and rigidity. *Phys Rev* (2005) 71:026114. doi:10.1103/physreve.71.026114
50. Stephen M. Percolation problems and the potts model. *Phys Lett* (1976) 56:149–50. doi:10.1016/0375-9601(76)90625-3
51. Bezanson J, Edelman A, Karpinski S, Shah VB. Julia: a fresh approach to numerical computing. *SIAM Rev* (2017) 59:65–98. doi:10.1137/141000671
52. Cardy J. *Scaling and renormalization in statistical physics*. Vol. 5. Cambridge: Cambridge University Press (1996).
53. Landau DP, Binder K. *A guide to Monte Carlo simulations in statistical physics*. Cambridge: Cambridge University Press (2014).
54. Boukheddaden K. Monte carlo investigations on surface elastic energy of spin-crossover solids: direct access to image pressure and the eshelby constant. *Phys Rev B* (2013) 88:134105. doi:10.1103/physrevb.88.134105
55. Love AEH. *A treatise on the mathematical theory of elasticity*. Cambridge: Cambridge University Press (2013).
56. Chikazumi S, Graham CD. *Physics of ferromagnetism 2e*. 94. Oxford: Oxford University Press on Demand (2009).

Conflict of Interest: The authors declare that the research was conducted in the absence of any commercial or financial relationships that could be construed as a potential conflict of interest.

frontiers in Physics

ORIGINAL RESEARCH
published: 26 February 2021
doi: 10.3389/fphy.2020.627017

Thermodynamic Properties of the Parabolic-Well Fluid

Mariano López de Haro[1]* *and Álvaro Rodríguez-Rivas*[2]

[1]*Instituto de Energías Renovables, Universidad Nacional Autónoma de México, Temixco, Mexico,* [2]*Departamento de Matemática Aplicada II, Escuela Politécnica Superior, Universidad de Sevilla, Seville, Spain*

The thermodynamic properties of the parabolic-well fluid are considered. The intermolecular interaction potential of this model, which belongs to the class of the so-called van Hove potentials, shares with the square-well and the triangular well potentials the inclusion of a hard-core and an attractive well of relatively short range. The analytic second virial coefficient for this fluid is computed explicitly and an equation of state is derived with the aid of the second-order thermodynamic perturbation theory in the macroscopic compressibility approximation and taking the hard-sphere fluid as the reference system. For this latter, the fully analytical expression of the radial distribution function, consistent with the Carnahan-Starling equation of state as derived within the rational function approximation method, is employed. The results for the reduced pressure of the parabolic-well fluid as a function of the packing fraction and two values of the range of the parabolic-well potential at different temperatures are compared with Monte Carlo and Event-driven molecular dynamics simulation data. Estimates of the values of the critical temperature are also provided.

Keywords: van hove potential, parabolic-well fluid, thermodynamic perturbation theory, equation of state, Monte Carlo simulation, Event-driven molecular dynamics simulation

OPEN ACCESS

Edited by:
Ramon Castañeda-Priego, University of Guanajuato, Mexico

Reviewed by:
Francisco Gámez, University of Granada, Spain
Ángel Mulero Díaz, University of Extremadura, Spain

***Correspondence:**
Mariano López de Haro
malopez@unam.mx

Specialty section:
This article was submitted to Soft Matter Physics, a section of the journal Frontiers in Physics

Received: *07 November 2020*
Accepted: *29 December 2020*
Published: *26 February 2021*

Citation:
López de Haro M and Rodríguez-Rivas Á (2021) Thermodynamic Properties of the Parabolic-Well Fluid. Front. Phys. 8:627017. doi: 10.3389/fphy.2020.627017

1 INTRODUCTION

The issue of *Frontiers in Physics* this paper belongs to is devoted to commemorating the celebration of fifty consecutive annual Winter Meetings in Statistical Physics in Mexico. Therefore, we have chosen to write on a subject that has been present in these meetings from the beginning; namely, the thermodynamic properties of fluids that we are persuaded can still offer some interesting results.

We begin by recalling that, in an attempt to prove the validity of the thermodynamic limit of classical statistical mechanics, van Hove [1] introduced in 1949 a potential $\phi(r)$ consisting of a hard core of radius r_0 and a finite-range attractive tail. The actual form of this so-called *van Hove potential* is

$$\phi(r) = \begin{cases} \infty, & 0 \le r \le r_0, \\ < 0, & r_0 < r \le b \\ > -\varepsilon_0, & r_0 < r \le b, \\ 0, & r > b, \end{cases} \tag{1}$$

where r is the distance, b corresponds to the range, and $-\varepsilon_0$ corresponds to the lower bound of the attractive tail, whose form is rather arbitrary. It should be pointed out that two popular models of intermolecular potentials used in liquid state physics, namely, the triangle-well potential and the

square-well potential, fulfill the condition of being van Hove potentials and their thermodynamic properties have been thoroughly studied (see, for instance, Refs. [2–11] for the former model and Refs. [12–24] for the latter and references therein). Surprisingly, as far as we know, the parabolic-well potential, which is also a van Hove potential, has not been used for that purpose. The main aim of this paper is to contribute to partly remedying this situation.

We consider a parabolic-well fluid whose molecules interact with a potential of the form

$$u(x) = \begin{cases} \infty, & 0 \le x \le 1, \\ \varepsilon\left[\left(\dfrac{x-1}{\lambda-1}\right)^2 - 1\right], & 1 < x \le \lambda, \\ 0, & x > \lambda, \end{cases} \tag{2}$$

where $x = r/\sigma$ is the reduced distance (r being the distance), σ is the diameter of the hard core, $\varepsilon > 0$ is the well depth, and $\lambda > 1$ is the potential range. As it occurs with other relatively simple models, the main asset of this model potential is probably that, despite being an idealized representation, it nevertheless contains the main features of true molecular interactions in fluids, namely, a repulsive hard-core and an attractive interaction that continuously goes to zero as the intermolecular distance increases. In this regard, it is interesting to recall what Widom [25] pointed out in the case of the square-well fluid: "Where I speak of the necessity to treat accurately the effects of the attractive or repulsive forces, I do not mean that it is important to know the corresponding part of $\phi(r)$ with quantitative accuracy. Indeed, even if the $\phi(r)$ of Figure 1 were idealized as a square-well potential, as in Figure 3, but the statistical mechanical consequences of such a potential were then determined without further approximation, there would undoubtedly result in an essentially correct description of all the macroscopic properties of matter throughout a vast region of the p and T plane, including the neighborhoods of the triple and critical points. Thus, what matters is not the quantitative accuracy of the assumed $\phi(r)$, but rather the qualitative accuracy of the resulting spatial correlations of molecular positions; the triple and critical points are distinguished by having the relevant qualitative features of this correlation, and the nature of its propagation through the fluid, determined primarily by the short-range repulsive forces between molecules, or by the longer ranged attractive forces, respectively." Something similar may be said about the parabolic-well potential. In fact, an interesting asset of this model is that its thermodynamic properties are readily amenable for treatment within the second-order thermodynamic perturbation theory of Barker and Henderson [26]. Within this approach, in order to derive the Helmholtz free energy of the parabolic-well fluid, two ingredients are required: on the one hand, one needs the Helmholtz free energy of the reference hard-sphere fluid of diameter σ. On the other hand, one also requires an expression for the radial distribution function $g_{HS}(x)$ of the hard-sphere fluid. In this work, we will profit from the availability of a method [27], the so-called rational function approximation (RFA) method, to (analytically) obtain an approximate $g_{HS}(x)$ which is thermodynamically consistent with the equation of state of the hard-sphere fluid and make use of this fact to derive the equation of state of the parabolic-well fluid.

The paper is organized as follows. In the next section, we recall the main aspects of the RFA method for the computation of $g_{HS}(x)$ and provide the explicit expression for this quantity in the first coordination shell. This is followed in **Section 3** with the *completely analytic* derivation of the equation of state of the parabolic-well fluid within the second-order Barker-Henderson thermodynamic perturbation theory in the macroscopic

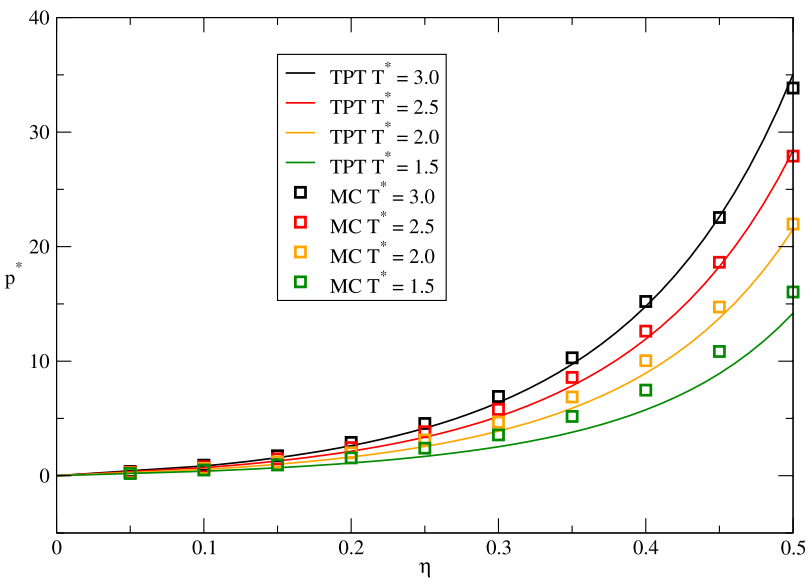

FIGURE 1 | Various isotherms of the parabolic-well fluid for $\lambda = 1.25$. The label TPT indicates that the results have been obtained using thermodynamic perturbation theory while the label MC refers to Monte Carlo simulation results.

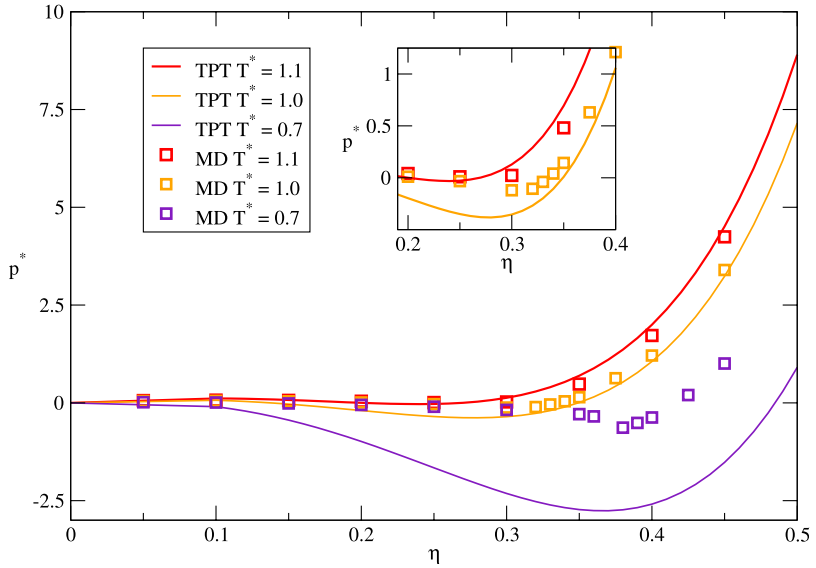

FIGURE 2 | Various subcritical isotherms of the parabolic-well fluid for $\lambda = 1.75$. The label TPT indicates that the results have been obtained using thermodynamic perturbation theory while the label MD refers to Event-driven Molecular Dynamics simulation results. The inset shows an enlargement of the intermediate packing fraction region for the isotherms with $T^* = 1.0$ and $T^* = 1.1$.

compressibility approximation and taking the hard-sphere fluid as the reference system. **Section 4** contains some illustrative results for the reduced pressure of the parabolic-well fluid and a comparison with our own Monte Carlo and Event-driven Molecular Dynamics simulation data. We close the paper in the final section with further discussion and some concluding remarks.

2 THE RFA METHOD FOR THE COMPUTATION OF THE RADIAL DISTRIBUTION FUNCTION OF THE HARD-SPHERE FLUID

In this section, we provide the analytic result for the radial distribution function (rdf) of the hard-sphere fluid $g_{HS}(x)$, as derived with the RFA method [27], and its explicit expression in the range $1 < x \leq 2$. We begin by recalling two important relationships between the thermodynamic and structural properties of the hard-sphere fluid derived from statistical mechanics. On the one hand, the compressibility factor $Z_{HS} = \frac{p}{\rho k_B T}$ (where p is the pressure, ρ the number density, k_B the Boltzmann constant, and T the absolute temperature) of the hard-sphere fluid is related to the contact value of the rdf $g_{HS}(1^+)$ through

$$Z_{HS} = 1 + 4\eta g_{HS}(1^+), \tag{3}$$

where $\eta = \pi\rho\sigma^3/6$ is the packing fraction. On the other hand, the hard-sphere isothermal susceptibility $\chi_{HS} \equiv \left[\frac{d(\eta Z_{HS}(\eta))}{d\eta}\right]^{-1}$ is related to the rdf through

$$\chi_{HS} = 1 + 24\eta \int_0^\infty dx\, x^2 \left[g_{HS}(x) - 1\right]. \tag{4}$$

In the RFA method [27], the Laplace transform of $x\, g_{HS}(x)$ is taken to be given by

$$G(t) = \mathcal{L}\{x\, g_{HS}(x)\} = \frac{t}{12\eta} \frac{1}{1 - e^t \Phi(t)}, \tag{5}$$

where

$$\Phi(t) = \left(1 + S_1 t + S_2 t^2 + S_3 t^3 + S_4 t^4\right) / \left(1 + L_1 t + L_2 t^2\right),$$

and the six coefficients S_1, S_2, S_3, S_4, L_1, and L_2 (which depend on the packing fraction) may be evaluated in an algebraic form by imposing the following requirements: (i) χ_{HS} must be finite and hence the first two integral moments of the total correlation function $h(x) \equiv g(x) - 1$, i.e., $\int_0^\infty dx\, x^n h(r)$ with $n = 1, 2$, must be well defined; (ii) the approximation must be thermodynamically consistent with a prescribed equation of state; i.e., the thermodynamic relationship $\chi_{HS} = \left[\frac{d\eta Z_{HS}(\eta)}{d\eta}\right]^{-1}$ must be satisfied. Using the first requirement, one finds that L_1, S_1, S_2, and S_3 are linear functions of L_2 and S_4. Imposing the requirement (ii) leads to explicit expressions for L_2 and S_4 in terms of χ_{HS} and Z_{HS} [27]. Finally, the expressions for all the coefficients are as follows:

$$L_1 = \frac{1}{2} \frac{\eta + 12\eta L_2 + 2 - 24\eta S_4}{2\eta + 1}, \tag{6}$$

$$S_1 = \frac{3}{2}\eta \frac{-1 + 4L_2 - 8S_4}{2\eta + 1}, \tag{7}$$

$$S_2 = -\frac{1}{2} \frac{-\eta + 8\eta L_2 + 1 - 2L_2 - 24\eta S_4}{2\eta + 1}, \tag{8}$$

$$S_3 = \frac{1}{12}\frac{2\eta - \eta^2 + 12\eta^2 L_2 - 12\eta L_2 - 1 - 72\eta^2 S_4}{(2\eta+1)\eta}, \tag{9}$$

$$L_2 = -3(Z_{HS}-1)S_4, \tag{10}$$

$$S_4 = \frac{1-\eta}{36\eta(Z_{HS}-1/3)}\left[1-\left[1+\frac{Z_{HS}-1/3}{Z_{HS}-Z_{PY}}\left(\frac{\chi_{HS}}{\chi_{PY}}-1\right)\right]\right]^{1/2}. \tag{11}$$

Here, $Z_{PY} = \frac{1+2\eta+3\eta^2}{(1-\eta)^2}$ and $\chi_{PY} = \frac{(1-\eta)^4}{(1+2\eta)^2}$ are the compressibility factor and isothermal susceptibility arising in the Percus-Yevick theory. To close the problem, one has to give an expression for Z_{HS}, so all the procedure is a function of this choice. For a given Z_{HS}, the radial distribution function is given by

$$g_{HS}(x) = \begin{cases} 0, & 0 \le x < 1, \\ \dfrac{1}{12\eta x}\displaystyle\sum_{n=1}^{\infty}\varphi_n(x-n)\theta(x-n), & x \ge 1 \end{cases} \tag{12}$$

with $\theta(x-n)$ being the Heaviside step function and

$$\varphi_n(x) = \mathcal{L}^{-1}\{-t[\Phi(t)]^{-n}\}. \tag{13}$$

Explicitly, using the residues theorem,

$$\varphi_n(x) = -\sum_{n=1}^{4} e^{t_i x}\sum_{m=1}^{n}\frac{A_{mn}(t_i)}{(n-m)!}x^{n-m}, \tag{14}$$

where

$$A_{mn}(t_i) = \lim_{t\to t_i}\frac{1}{(m-1)!}\left(\frac{d}{dt}\right)^{m-1}(t-t_i)t[\Phi(t)]^{-n}, \tag{15}$$

with t_i being the four roots of $1 + S_1 t + S_2 t^2 + S_3 t^3 + S_4 t^4 = 0$; namely,

$$t_1 = -\frac{S_3}{4S_4} + y_p - y_n, \tag{16}$$

$$t_2 = -\frac{S_3}{4S_4} + y_p + y_n, \tag{17}$$

$$t_3 = -\frac{S_3}{4S_4} - y_p - y_m, \tag{18}$$

$$t_4 = -\frac{S_3}{4S_4} - y_p + y_m, \tag{19}$$

where

$$y_p = -\frac{1}{2}\sqrt{\frac{S_3^2}{4S_4^2} - \frac{2S_2}{3S_4} + y_r + \frac{y_s}{3S_4}}, \tag{21}$$

$$y_r = -\frac{S_2^2 - 3S_1S_3 + 12S_4}{3S4y_s}, \tag{22}$$

$$y_n = \frac{1}{2}\sqrt{\frac{S_3^2}{4S_4^2} - \frac{4S_2}{3S_4} - y_r - \frac{y_s}{3S_4} - \frac{S_3^3}{8y_pS_4^3} + \frac{S_2S_3}{2y_pS_4^2} - \frac{S_1}{y_pS_4}}, \tag{23}$$

$$y_m = \frac{1}{2}\sqrt{\frac{S_3^2}{4S_4^2} - \frac{4S_2}{3S_4} - y_r - \frac{y_s}{3S_4} + \frac{S_3^3}{8y_pS_4^3} - \frac{S_2S_3}{2y_pS_4^2} + \frac{S_1}{y_pS_4}}, \tag{24}$$

$$y_s = -\frac{1}{2^{1/3}}\left[y_t + \sqrt{-4\left(S_2^2 - 3S_1S_3 + 12S_4\right)^3 + y_t^2}\right]^{1/3}, \tag{25}$$

$$y_t = 2S_2^3 + 9S_1S_2S_3 + 27S_3^2 + 27S_1^2S_4 - 72S_2S_4. \tag{26}$$

As we will indicate below, once $Z_{HS}(\eta)$ has been chosen, **Eqs. 5–26** are all that is needed to evaluate the first- and second-order perturbation terms for the free energy of the parabolic-well fluid within the Barker-Henderson thermodynamic perturbation theory taking the hard-sphere fluid as the reference system. To close this section and for later use, we now write the explicit expression for the radial distribution function up to the first coordination shell which reads

$$g_{HS}(x) = \begin{cases} 0, & 0 \le x < 1, \\ \displaystyle\sum_{i=1}^{4}\frac{a_i}{x}e^{t_i(x-1)}, & 1 \le x \le 2 \end{cases} \tag{27}$$

where

$$a_i = \frac{-t_i\left(1 + L_1 t_i + L_2 t_i^2\right)}{12\eta\left(S_1 + 2S_2 t_i + 3S_3 t_i^2 + 4S_4 t_i^3\right)} \quad (i = 1, 2, 3, 4). \tag{28}$$

3 THERMODYNAMIC PERTURBATION THEORY AND THE EQUATION OF STATE OF THE PARABOLIC-WELL FLUID

Perturbation approaches for the computation of thermodynamic properties of fluids are well established theoretical tools [28, 29]. In the Barker-Henderson perturbation theory [26], one splits the potential into a hard-sphere part and a perturbation part; namely, $u(r) = u_{HS}(r) + u_1(r)$, where

$$u_{HS}(x) = \begin{cases} \infty, & 0 \le x \le 1, \\ 0, & x > 1 \end{cases} \tag{29}$$

and

$$u_1(x) = \begin{cases} 0, & 0 \le x \le 1, \\ \varepsilon\left[\left(\dfrac{x-1}{\lambda-1}\right)^2 - 1\right], & 1 < x \le \lambda, \\ 0, & x > \lambda \end{cases} \tag{30}$$

Once this separation has been made, the Helmholtz free energy per particle of the parabolic-well fluid is expressed as a power series in the inverse of the reduced temperature $T^* = k_B T/\varepsilon$, which up to second order reads

$$\frac{f}{Nk_BT} = \frac{f_{HS}}{Nk_BT} + \frac{1}{T^*}\frac{f_1}{Nk_BT} + \frac{1}{T^{*2}}\frac{f_2}{Nk_BT} \tag{31}$$

Here, N is the number of particles and f_{HS} stands for the Helmholtz free energy of the reference hard-sphere fluid while f_1 and f_2 (this latter in the so-called macroscopic compressibility approximation) are given, respectively, by

$$\frac{f_1}{Nk_BT} = \frac{12\eta}{\varepsilon}\int_1^{\lambda} g_{HS}(x)u_1(x)x^2dx \tag{32}$$

and

$$\frac{f_2}{Nk_BT} = \frac{6\eta\chi_{HS}}{\varepsilon^2}\int_1^\lambda g_{HS}(x)u_1^2(x)x^2dx. \quad (33)$$

Note that we have made use of the fact that $g_{HS}(x)$ vanishes for $0 \le x < 1$ and of the expression for $u_1(x)$ given in **Eq. 30**, respectively, to set the lower and upper limits of the integrals in **Eqs. 32**, **33**. In turn, the equation of state of the parabolic-well fluid in this approximation is given by

$$Z \equiv \frac{p}{\rho k_BT} = Z_{HS} + \frac{1}{T^*}\eta\frac{\partial}{\partial\eta}\left(\frac{f_1}{Nk_BT}\right) + \frac{1}{T^{*2}}\eta\frac{\partial}{\partial\eta}\left(\frac{f_2}{Nk_BT}\right). \quad (34)$$

And, the chemical potential may be readily obtained as

$$\frac{\mu}{k_BT} = \frac{f}{Nk_BT} + Z, \quad (35)$$

where $\frac{f}{Nk_BT}$ is given in **Eq. 31**, together with **Eqs. 32**, **33**, and Z is given in **Eq. 34**. So, provided we choose Z_{HS}, which of course also determines χ_{HS} and f_{HS}, and take g_{HS} to be the one computed with the RFA approach and such compressibility factor, the completely analytic formulation of the second-order Barker-Henderson thermodynamic perturbation theory in the macroscopic compressibility approximation for the parabolic-well fluid taking the hard-sphere fluid as the reference system has been derived. In our subsequent calculations, we will be restricted to relatively narrow wells ($1 < \lambda \le 2$) so that **Eq. 27** for $g_{HS}(r)$ will be used. Furthermore, Z_{HS} and χ_{HS} will be chosen to be those corresponding to the Carnahan-Starling (CS) equation of state [30]; namely,

$$Z_{HS}(\eta) \equiv Z_{CS}(\eta) = \frac{1+\eta+\eta^2-\eta^3}{(1-\eta)^3} \quad (36)$$

and

$$\chi_{HS}(\eta) \equiv \chi_{CS}(\eta) = \frac{(1-\eta)^4}{1+4\eta+4\eta^2-4\eta^3+\eta^4}. \quad (37)$$

Further, from the CS equation of state, it also follows that

$$\frac{f_{HS}(\eta)}{Nk_BT} = \frac{f_{CS}(\eta)}{Nk_BT} = -1 + \ln\frac{6\eta}{\pi} + \frac{(4-3\eta)\eta}{(1-\eta)^2}. \quad (38)$$

The availability of the completely analytic (albeit approximate) forms of the Helmholtz free energy and the equation of state of the system (which are themselves not very illuminating and therefore will not be explicitly written down [31]) allows us in principle to compute, for a given value of λ, the compressibility factor using **Eq. 34**, the vapor-liquid coexistence curve from the equality of pressures, and chemical potentials of the two phases and also to obtain the critical point in the usual way.

Preliminary results for the isotherms will be presented in the following section, together with a comparison with our simulation data. But before presenting such results, we will take advantage of the simple form of the intermolecular potential of this fluid to compute its second virial coefficient. This is given by

TABLE 1 | Reduced Boyle temperatures $T_B^* \equiv k_BT_B/\varepsilon$ (up to three significant figures) of triangle-well, parabolic-well, and square-well fluids for various values of the range λ.

λ	T_B^*(Triangle-well fluid)	T_B^*(parabolic-well fluid)	T_B^* (square-well fluid)
5/4	0.72	0.94	1.39
3/2	1.32	1.78	2.85
7/4	2.08	2.87	4.84
2	3.03	4.25	7.49

TABLE 2 | Estimates of the reduced critical temperatures $T_c^* \equiv k_BT_c/\varepsilon$ (up to three significant figures) of triangle-well, parabolic-well, and square-well fluids for various values of the range λ, as obtained from the second virial coefficient and the use of the Vliegenthart and Lekkerkerker criterion.

λ	T_c^*(triangle-well fluid)	T_c^*(parabolic-well fluid)	T_c^* (square-well fluid)
5/4	0.43	0.55	0.78
3/2	0.69	0.90	1.39
7/4	1.00	1.35	2.21
2	1.38	1.90	3.27

$$B_2(T) \equiv -2\pi\sigma^3\int_0^\infty x^2\left(e^{\frac{u(x)}{k_BT}} - 1\right)dx \quad (39)$$
$$= -\frac{\pi}{6}\sigma^3\left[\frac{6k_BT}{\varepsilon}\left(1 - 2e^{\frac{\varepsilon}{k_BT}} + \lambda\right)(\lambda-1)^2 - 4\lambda^3\right.$$
$$\left. + 3\frac{\sqrt{\pi k_BT}e^{\frac{\varepsilon}{k_BT}}}{\varepsilon^{3/2}}\left(2\varepsilon + k_BT(\lambda-1)^2\right)(\lambda-1)Erf\left(\sqrt{\frac{\varepsilon}{k_BT}}\right)\right].$$

Equation 39, which to the best of our knowledge has not been reported before, allows us to obtain the Boyle temperature T_B of the parabolic-well fluid as a function of λ by equating $B_2(T_B)$ to zero and solving numerically for T_B. In **Table 1**, we show some particular values and, for comparison, we also include the values corresponding to triangle-well and square-well fluids with the same range λ.

To close this section, we will also take advantage of the knowledge of the second virial coefficient, to obtain estimates of the critical temperature according to the Vliegenthart and Lekkerkerker criterion [32], namely, from equating this coefficient with $-6v_m$, where $v_m = \frac{\pi}{6}\sigma^3$ is the volume of the spherical core. The results for given values of the range are given in **Table 2**, where we have also included such estimates for the cases of the triangle-well and square-well fluids with the same range λ.

Note that, for all three model fluids, the values of both the reduced Boyle temperatures and the estimates of the reduced critical temperatures increase as the range λ is increased. Also note that the geometrical form of the well influences such values as reflected in the fact that, for the same value of the range, the ones corresponding to the triangle-well fluid are smaller than those of the parabolic-well fluid which, in turn, are smaller than those of the square-well fluid.

4 ILLUSTRATIVE RESULTS

Now we return to our main aim. In order to assess the value of the thermodynamic perturbation theory approach presented in the previous section, we have carried out NVT Monte Carlo (MC) simulations to compute the pressure of parabolic-well fluids for various values of the range $\lambda \leq 2$ and supercritical temperatures for later comparison with our theoretical results. The details of such simulations are as follows. The number of particles in our simulations is $N = 1372$ and we have considered a cubic box, of length L and with periodic boundary conditions. Reduced units are used, so that lengths are expressed in units of σ ($L = l\sigma$, with l a pure number), the reduced temperature is T^*, the packing fraction is $\eta = \frac{\pi}{6}\frac{N}{V}\sigma^3$ (where $V = L^3$ is the volume), and the reduced pressure is $p^* = p\sigma^3\varepsilon^{-1}$.

For the sake of illustration, we report here the results of the simulations for $\lambda = 1.25$ and 1.75, along various isotherms. For each isotherm, eight different packing fraction values $\eta = 0.05$ to 0.5 with $\Delta\eta = 0.05$ were simulated in order to compute the reduced pressure p^*. Each run was carried out using $1.5 \cdot 10^6$ Monte Carlo steps (MCS) discarding the first 10^6 MCS for equilibration, and the properties were measured every 20 MCS and averaged every 1000 MCS; furthermore, for each packing fraction, the values of p^* were averaged over 20 parallel simulations to obtain better statistics.

Finally, the pressure was calculated using the expression

$$p^* = \frac{6}{\pi}\eta T^*\left[1 + 4\eta g_{PW}(1^+) - \frac{4\eta}{T^*}\int_1^\lambda g_{PW}(x)\frac{du_1^*(x)}{dx}x^3 dx\right]. \quad (40)$$

Here, $u_1^*(x) = u_1(x)/\varepsilon$, $g_{PW}(x)$ is the radial distribution function of the parabolic-well fluid (computed in the usual way [33] with the subscript PW standing for parabolic well), and the second term on the right-hand side of **Eq. 40**, obtained following a similar procedure to the one used by Rotenberg [12] in the case of the square-well fluid, accounts for the hard-core contribution to the parabolic-well potential.

In **Figures 1**-**3**, we show the comparison between the results of the isotherms obtained with the thermodynamic perturbation theory and from simulation. Note the good agreement between theoretical and simulation results for all the values of T^* above the critical temperature that we considered.

On the other hand, the subcritical isotherms were obtained by means of Molecular Dynamics (MD) Event-driven simulations. We have performed event-driven simulations of $N = 108000$ elastic smooth spheres carried out with the DynamO software package [34]. The spheres interact by a stepped parabolic-well type potential [35–37], a discretized version consisting of a sequence of 15 steps of widths 0.05σ, steps more than reasonable in most instances [37]. We have used σ, $\tau = \sqrt{m\sigma^2/\varepsilon}$, m, and T^* as units of length, time, mass, and temperature, respectively. The MD event-driven simulations were performed for one value of the range of the potential, namely, $\lambda = 1.75$, along the isotherms $T^* = 1.1$, 1.0 and 0.7. In the first stage, we have performed NVT simulations with an Andersen thermostat during 2×10^8 collisions, and after the equilibration, the second stage of NVE simulations with a duration of 8×10^8 collisions was performed [38]. The full pressure tensor for the system was determined by means of the expression

$$P = P_{kinetic} + P_{interaction} \quad (41)$$

where the kinetic pressure is given by

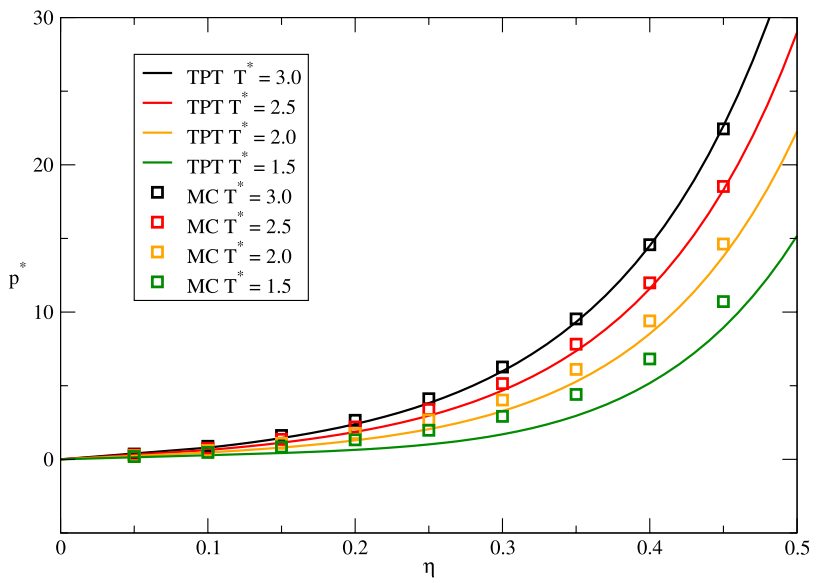

FIGURE 3 | Various isotherms of the parabolic-well fluid for $\lambda = 1.75$. The label TPT indicates that the results have been obtained using thermodynamic perturbation theory while the label MC refers to Monte Carlo simulation results.

$$P_{kinetic} = \frac{1}{2V}\sum_{i}^{N} v_i v_i \,, \tag{42}$$

with $v_i v_i$ being a dyadic product which yields a matrix result and the masses of the particles are set as $m_i = 1$. The contribution to the pressure due to interactions is given by

$$P_{interaction} = \frac{1}{Vt_{sim}}\sum_{ij}^{event} \Delta p_i r_{ij} \,, \tag{43}$$

where the summation is over each two-particle i, j event interaction, t_{sim} is the total simulation time, Δp_i is the momentum impulse on particle i, and $r_{ij} = r_i - r_j$ is the separation vector between the interacting particles. Finally, the hydrostatic pressure, which in this instance coincides with the reduced pressure, was computed from the trace of the tensor

$$p^* = tr\,(P)/3 = \left(P_{xx} + P_{yy} + P_{zz}\right)/3 \,. \tag{44}$$

In **Figure 2**, we show the comparison of the subcritical isotherms obtained with the thermodynamic perturbation theory and from simulation for a range $\lambda = 1.75$. The typical van der Waals loop is clearly seen for the theoretical isotherm with $T^* = 0.7$ (which grossly underestimates the simulation data) and is still present in the isotherms with $T^* = 1$ and $T^* = 1.1$, respectively. On the other hand, we have checked both through Monte Carlo and Event-driven MD simulations and also through the outcome of the thermodynamic perturbation theory that the isotherm with $T^* = 1.35$ (not shown), which according to the Vliegenthart and Lekkerkerker criterion should be the critical one, is a supercritical isotherm. In fact, the simulation data indicate that the real critical isotherm for this value of the range lies above but close to the one corresponding to the theoretical curve for $T^* = 1.1$.

While it is clear from **Figures 1–3** that the qualitative trends observed in all the simulation results are correctly accounted for by the theory, a better perspective of its performance may be gained by looking at the quantitative differences. Therefore, in **Table 3**, we display the actual numerical values for a couple of isotherms. In both cases, it is clear that the good qualitative agreement seen in **Figures 1**, **2**, respectively, is not accompanied by quantitative agreement. In fact, the first theoretical isotherm ($\lambda = 1.25$ and $T^* = 1.5$), which is a supercritical isotherm, yields an underestimation of the reduced pressure when compared to the simulation values. On the other hand, for the second isotherm ($\lambda = 1.75$ and $T^* = 1.1$), which is subcritical, the general overall trend is that the theoretical curve overestimates the value of the reduced pressure. As one would expect, in the case of the supercritical isotherms, the quantitative agreement is improved as the reduced temperature is increased.

TABLE 3 | Theoretical and simulation results for the reduced pressure at various packing fractions in two isotherms of the parabolic-well fluid. The labels MC, MD, and TPT stand for Monte Carlo, Event-driven MD, and thermodynamic perturbation theory, respectively.

$\lambda = 1.25$, $T^* = 1.5$		
η	Simulation (MC)	TPT
0.1	0.4984	0.3912
0.15	0.9408	0.6931
0.2	1.5577	1.1066
0.25	2.4038	1.6873
0.3	3.5641	2.5289
0.35	5.1764	3.7918
0.4	7.4700	5.7559
0.45	10.8447	8.9191
0.5	16.0428	14.1890
$\lambda = 1.75$, $T^* = 1.1$		
η	Simulation (MD)	TPT
0.1	0.0694	0.1129
0.15	0.0642	0.0738
0.2	0.0413	0.0007
0.25	0.0094	–0.0280
0.3	0.0227	0.1287
0.35	0.4810	0.6941
0.4	1.7221	1.9983
0.45	4.2439	4.5110

5 CONCLUDING REMARKS

In this paper, we have addressed the study of the thermodynamic properties of a fluid whose molecules interact through a parabolic-well potential. For this model, we obtained the exact second virial coefficient which in turn allowed us to compute the Boyle temperature and to estimate the critical temperature for arbitrary values of the potential range λ. The parabolic-well potential is in the same family as the triangle-well potential and the square-well potential, being in some sense intermediate between the other two. A reflection of this is the behavior of both the Boyle temperatures and the estimates of the critical temperatures in which, for a fixed range, the values corresponding to the parabolic-well potential lie between the ones corresponding to the other two. Whether this points out to a deeper relationship between the geometrical shape of the well and the location of the critical point in van Hove fluids is not clear to us at this stage but might be worth considering in the future.

In order to obtain further analytic results, we considered a thermodynamic perturbation theory approach for this fluid within the Barker-Henderson second-order macroscopic compressibility approximation and taking the hard-sphere fluid as the reference fluid. Restricting ourselves to values of the range in the interval $1 < \lambda \leq 2$ and evaluating the radial distribution function of the hard-sphere fluid according to the RFA method with the CS equation of state, we were able to derive (albeit approximate) fully analytic expressions for the Helmholtz free energy, the equation of state, and the chemical potential of the parabolic-well fluid. With such expressions, we were able to compute theoretically various isotherms for a given potential range. These were subsequently compared to our own Monte Carlo NVT and Event-driven MD simulation results. It must be emphasized that these simulation data are to our knowledge the only ones available in the literature for this system.

It should be clear that the calculations that we have presented in the previous section are still preliminary but we want to stress that further work on this subject is currently being carried out. Nevertheless, at this stage, a few additional comments are in order. We begin by pointing out that the qualitative agreement between the results for the isotherms above the critical one obtained from thermodynamic perturbation theory and those stemming out of NVT Monte Carlo simulations, as well as the improvement of the quantitative agreement as the reduced temperature is increased, although clearly rewarding, are not very surprising in view of the fact that our theoretical approximation relies on the convergence of the perturbation expansion for high temperatures. Also rewarding is the fact that the results of the Event-driven MD simulation for the isotherm $T^* = 1.0$ in the case in which the range is $\lambda = 1.75$, which is a subcritical isotherm, are also well accounted for by the curve obtained using thermodynamic perturbation theory. The same happens with the isotherm with $T^* = 1.1$. On the other hand, the gross underestimation of the theoretical curve for the subcritical isotherm with $T^* = 0.7$ and the same value of the range indicates that the convergence of the perturbation series is very poor for this reduced temperature. In any case, it is fair to say that the present theoretical approach provides a good starting point for the study of the thermodynamic properties of parabolic-well fluids. Future work with the same approach contemplates the computation of the critical point and the liquid-vapor coexistence curve of such fluids. Finally, since we are persuaded that the parabolic-well fluid may still offer some other insights on the thermodynamic behavior of fluids, we hope that the results of the present paper may also motivate others to conduct more studies using this model.

DATA AVAILABILITY STATEMENT

The raw data supporting the conclusions of this article will be made available by the authors, without undue reservation.

AUTHOR CONTRIBUTIONS

MLH worked out the theoretical development of the thermodynamic properties and ÁRR performed the NVT Monte Carlo and Event-driven molecular dynamics simulations. Both authors worked on the written version of the paper.

FUNDING

This study was funded by Universidad Nacional Autónoma de México (salary of Mariano López de Haro) and Junta de Andalucía (support funds for the group of investigation of ÁRR).

ACKNOWLEDGMENTS

ARR acknowledges the financial support of Junta de Andalucía, through Project "Ayuda al grupo PAIDI FQM205."

REFERENCES

1. van Hove L. Quelques propriétés générales de L'intégrale de configuration D'un système de particules avec interaction. *Physica* (1949) 15:951–61. doi:10.1016/0031-8914(49)90059-2
2. Largo J, Solana JR. A simplified perturbation theory for equilibrium properties of triangular-well fluids. *Phys Stat Mech Appl* (2000) 284:68–78. doi:10.1016/s0378-4371(00)00232-6
3. Betancourt-Cárdenas FF, Galicia-Luna LA, Sandler SI. Thermodynamic properties for the triangular-well fluid. *Mol Phys* (2007) 105:2987–98. doi:10.1080/00268970701725013
4. Betancourt-Cárdenas FF, Galicia-Luna LA, Benavides AL, Ramírez JA, Schöll-Paschinger E. Thermodynamics of a long-range triangle-well fluid. *Mol Phys* (2008) 106:113–26. doi:10.1080/00268970701832397
5. Zhou S. Thermodynamics and phase behavior of a triangle-well model and density-dependent variety. *J Chem Phys* (2009) 130:014502–12. doi:10.1063/1.3049399
6. Koyuncu M. Equation of state of a long-range triangular-well fluid. *Mol Phys* (2011) 109:565–73. doi:10.1080/00268976.2010.538738
7. Guérin H. Improved analytical thermodynamic properties of the triangular-well fluid from perturbation theory. *J Mol Liq* (2012) 170:37–40. doi:10.1016/j.molliq.2012.03.014
8. Rivera LD, Robles M, López de Haro M. Equation of state and liquid–vapour equilibrium in a triangle-well fluid. *Mol Phys* (2012) 110:1327–33. doi:10.1080/00268976.2012.655338
9. Bárcenas M, Odriozola G, Orea P. Coexistence and interfacial properties of triangle-well fluids. *Mol Phys* (2014) 112:2114–21. doi:10.1080/00268976.2014.887801
10. Trejos VM, Martínez A, Valadez-Pérez NE. Statistical fluid theory for systems of variable range interacting via triangular-well pair potential. *J Mol Liq* (2018) 265:337–46. doi:10.1016/j.molliq.2018.05.116
11. Benavides AL, Cervantes LA, Torres-Arenas J. Analytical equations of state for triangle-well and triangle-shoulder potentials. *J Mol Liq* (2018) 271:670–6. doi:10.1016/j.molliq.2018.08.110
12. Rotenberg A. Monte Carlo equation of state for hard spheres in an attractive square well. *J Chem Phys* (1965) 43:1198–201. doi:10.1063/1.1696904
13. Barker JA, Henderson D. Perturbation theory and equation of state for fluids: the square-well potential. *J Chem Phys* (1967) 47:2856–61. doi:10.1063/1.1712308
14. Luks KD, Kozak JJ. *Adv Chem Phys* (1978) 37:139–201.
15. Carley DD. Thermodynamic properties of a square-well fluid in the liquid and vapor regions. *J Chem Phys* (1983) 78:5776–81. doi:10.1063/1.445462
16. del Río F, Lira L. Properties of the square-well fluid of variable width. *Mol Phys* (1987) 61:275–92. doi:10.1080/00268978700101141
17. del Río F, Lira L. Properties of the square-well fluid of variable width. II. The mean field term. *J Chem Phys* (1987) 87:7179–83. doi:10.1063/1.453361
18 Benavides AL, del Río F. Properties of the square-well fluid of variable width. *Mol Phys* (1989) 68:983–1000. doi:10.1080/00268978900102691
19. López-Rendón R, Reyes Y, Orea P. Thermodynamic properties of short-range square well fluid. *J Chem Phys* (2006) 125:084508–5. doi:10.1063/1.2338307
20. Rivera-Torres S, del Río F, Espíndola-Heredia R, Kolafa J, Malijevský A. Molecular dynamics simulation of the free-energy expansion of the square-well fluid of short ranges. *J Mol Liq* (2013) 185:44–9. doi:10.1016/j.molliq.2012.12.005
21. Elliot JR, Schultz AJ, Kofke DA. Combined temperature and density series for fluid-phase properties. I. Square-well spheres. *J Chem Phys* (2015) 147:1141101–12. doi:10.1063/1.4930268
22. Padilla L, Benavides AL. The constant force continuous molecular dynamics for potentials with multiple discontinuities. *J Chem Phys* (2017) 147: 034502–6. doi:10.1063/1.4993436

23. Sastre F, Moreno-Hilario E, Sotelo-Serna MG, Gil-Villegas A. Microcanonical-ensemble computer simulation of the high-temperature expansion coefficients of the Helmholtz free energy of a square-well fluid. *Mol Phys* (2018) 116: 351–60. doi:10.1080/00268976.2017.1392051
24. Río Fd., Guzmán O, Martínez FO. Global square-well free-energy model via singular value decomposition. *Mol Phys* (2018) 116:2070–82. doi:10.1080/00268976.2018.1461943
25. Widom B. Intermolecular Forces and the Nature of the Liquid State: liquids reflect in their bulk properties the attractions and repulsions of their constituent molecules. *Science* (1967) 157:375–82. doi:10.1126/science.157.3787.375
26. Barker JA, Henderson D. What is "liquid"? Understanding the states of matter. *Rev Mod Phys* (1976) 48:587–671. doi:10.1103/revmodphys.48.587
27. López de Haro M, Yuste SB, Santos A. Alternative approaches to the equilibrium properties of hard-sphere liquids. In: A Mulero, editor. *Theory and simulation of hard-sphere fluids and related systems, lecture notes in physics 753*. Berlin, Germany: Springer (2008). p. 183–245.
28. Zhou S, Solana JR. Progress in the perturbation approach in fluid and fluid-related theories. *Chem Rev* (2009) 109:2829–58. doi:10.1021/cr900094p
29. Solana JR. *Perturbation theories for the thermodynamic properties of fluids and solids*. Boca Raton, Florida: CRC Press (2013).
30. Carnahan NF, Starling KE. Equation of state for nonattracting rigid spheres. *J Chem Phys* (1969) 51:635–6. doi:10.1063/1.1672048
31. These expressions are available, however, in a Mathematica code that we have employed and which we are willing to supply if requested.
32. Vliegenthart GA, Lekkerkerker HNW. Predicting the gas-liquid critical point from the second virial coefficient. *J Chem Phys* (2000) 112:5364–9. doi:10.1063/1.481106
33. Frenkel D, Smit B. *Understanding molecular simulation: from algorithms and applications*. San Francisco, CA: Academic press (2002).
34. Bannerman MN, Sargant R, Lue L. DynamO: a free ${\cal O}$(N) general event-driven molecular dynamics simulator. *J Comput Chem* (2011) 32: 3329–38. doi:10.1002/jcc.21915
35. Chapela GA, Scriven LE, Davis HT. Molecular dynamics for discontinuous potential. IV. Lennard-Jonesium. *J Chem Phys* (1989) 91:4307–13. doi:10.1063/1.456811
36. Thomson C, Lue L, Bannerman MN. Mapping continuous potentials to discrete forms. *J Chem Phys* (2014) 140:034105–13. doi:10.1063/1.4861669
37. López de Haro M, Rodríguez-Rivas A, Yuste SB, Santos A. Structural properties of the jagla fluid. *Phys Rev E* (2018) 98:012138–48. doi:10.1103/physreve.98.012138
38. Bannerman MN, Lue L, Woodcock LV. *J Chem Phys* (2010) 132:084607–12. doi:10.1063/1.3328823

Conflict of Interest: The authors declare that the research was conducted in the absence of any commercial or financial relationships that could be construed as a potential conflict of interest.

frontiers in Physics

ORIGINAL RESEARCH
published: 02 March 2021
doi: 10.3389/fphy.2020.622872

A Bidimensional Gay-Berne Calamitic Fluid: Structure and Phase Behavior in Bulk and Strongly Confined Systems

A. Calderón-Alcaraz[1], *J. Munguía-Valadez*[1], *S. I. Hernández*[2], *A. Ramírez-Hernández*[3], *E. J. Sambriski*[4] *and J. A. Moreno-Razo*[1]*

[1]Departamento de Física, Universidad Autónoma Metropolitana-Iztapalapa, Mexico City, Mexico, [2]Unidad Multidisciplinaria de Docencia e Investigación-Juriquilla, Facultad de Ciencias, Universidad Nacional Autónoma de México, Juriquilla, Querétaro, Mexico, [3]Department of Biomedical Engineering and Chemical Engineering, and Department of Physics and Astronomy, The University of Texas at San Antonio, San Antonio, TX, United States, [4]Department of Chemistry, Delaware Valley University, Doylestown, PA, United States

A bidimensional (2D) thermotropic liquid crystal (LC) is investigated with Molecular Dynamics (MD) simulations. The Gay-Berne mesogen with parameterization GB(3, 5, 2, 1) is used to model a calamitic system. Spatial orientation of the LC samples is probed with the nematic order parameter: a sharp isotropic-smectic (I-Sm) transition is observed at lower pressures. At higher pressures, the I-Sm transition involves an intermediate nematic phase. Topology of the orthobaric phase diagram for the 2D case differs from the 3D case in two important respects: 1) the nematic region appears at lower temperatures and slightly lower densities, and 2) the critical point occurs at lower temperature and slightly higher density. The 2D calamitic model is used to probe the structural behavior of LC samples under strong confinement when either planar or homeotropic anchoring prevails. Samples subjected to circular, square, and triangular boundaries are gradually cooled to study how orientational order emerges. Depending on anchoring mode and confining geometry, characteristic topological defects emerge. Textures in these systems are similar to those observed in experiments and simulations of lyotropic LCs.

Keywords: confinement, topological, disclination, transition, nematic, simulation

OPEN ACCESS

Edited by:
Atahualpa Kraemer, National Autonomous University of Mexico, Mexico

Reviewed by:
Patrick Huber, Hamburg University of Technology, Germany
Ramon Castañeda-Priego, University of Guanajuato, Mexico

***Correspondence:**
J. A. Moreno-Razo
jamr.uam@gmail.com

Specialty section:
This article was submitted to Interdisciplinary Physics, a section of the journal Frontiers in Physics

Received: *29 October 2020*
Accepted: *29 December 2020*
Published: *02 March 2021*

Citation:
Calderón-Alcaraz A, Munguía-Valadez J, Hernández SI, Ramírez-Hernández A, Sambriski EJ and Moreno-Razo J A (2021) A Bidimensional Gay-Berne Calamitic Fluid: Structure and Phase Behavior in Bulk and Strongly Confined Systems. Front. Phys. 8:622872. doi: 10.3389/fphy.2020.622872

1 INTRODUCTION

Bulk materials exhibit properties imbued by their underlying chemical makeup: the packing of and interactions between atoms and/or molecules impart characteristic traits. On the other hand, *metamaterials* are synthetically produced and depend more on the relative positioning of building blocks within the structure. Such a trait allows metamaterials to achieve novel properties not exhibited by bulk materials (prominently of an electromagnetic and/or an optical nature). This has facilitated the expansion and miniaturization of existent technologies [1, 2].

Building blocks capable of molecular recognition are essential in the bottom-up production of metamaterials [3–7]. Specifically, complementary moieties can display the ability to "latch" in solution, onto a substrate, or in a combination of scenarios to produce desirable architectures. The threshold concentration of building blocks and formation steps are some issues to consider when optimizing their fabrication [8]. Structural properties in a metamaterial will remain stable provided the interaction strength between units withstands thermal fluctuations in the medium. Bottom-up approaches exploit this feature to circumvent the use of mechanical intervention. Production is

scaled by merely increasing the amounts of reactants and relying on system kinetics for product formation. Packing specificity can be modulated by carrying out the assembly under spatial confinement [9–15]. Many fabrication protocols have been optimized by mimicking the strategies latent in biomolecular systems [4, 16, 17].

The solvent is a key component in the production of metamaterials, which must effectively disperse building blocks and stabilize noncovalent interactions holding structures together. Self-assembly reliant on the chemical complementarity embedded in building blocks relegates the solvent to a passive role, serving in large measure as a dispersing agent. A paradigm shift is to screen solvents for an active role in the generation of metamaterials [18–22]. In this scenario, the solvent provides additional bottom-up control that extends the gamut of attainable targets [23–26].

The solvent "paradigm shift" is exemplified in the elastic forces mediated within a liquid crystal (LC) fluid. The intrinsic anisotropy of LCs facilitates spatially ordered mesophases. Solvent order at certain state points can be disturbed in the presence of colloidal inclusions, resulting in topological defects that exert static and dynamic control. Because of their ability to spatially "communicate," topological defects can couple (obeying topological charge rules) to yield specific colloidal arrangements, including dimers [27–38], wires (i.e., chains) [21, 28, 35, 39–44], and arrays [21, 31–34, 36–38, 43, 45, 46]. Solvents recruited as active agents contributing to the self-assembly of metamaterials enhance a variety of structural possibilities.

Much research has been devoted to three-dimensional (3D) self-assembly [25], though a two-dimensional (2D) variant continues to be of interest from an exploratory perspective [47–55] as well as in applied technologies [1, 56]. Optimal function is achieved *via* slab geometry in many devices, including optoelectronic/photonic materials [57–61], sensors [60, 62–68], display technologies [69–71], smart glass [72, 73], spatial light modulators [74–77], and tunable filters [78–81]. However, dimensionality plays an essential role in the type and extent of structural order that a condensed phase can maintain [52, 82–88]. When coupling the elastic forces of topological defects in LC media, colloidal ordering induced *via* a substrate can differ significantly from that observed *via* topological mediation in the bulk [21, 24, 25, 35, 36]. Slab assembly becomes relevant in 3D colloidal arrangements because it yields intermediates: metamaterials are finalized upon "stacking" slabs in layer-by-layer synthesis to achieve a target 3D structure [89–91].

In this work, we focus on two aspects of a thermotropic calamitic LC fluid relevant to colloidal self-assembly: 1) the changes in topology of the solvent phase diagram due to a reduction in dimensionality from 3D to 2D, and 2) the mesophase behavior of the solvent under strong confinement in slab geometry. The Gay-Berne (GB) model [92] is used here because it captures salient mesogenic features and has a relatively low computational overhead. Prior work with the GB mesogen has focused on different mesophases in bulk 3D systems [93–98]. Additionally, surface-induced ordering (i.e., anchoring) *via* boundary walls has been studied in thin films [99], droplets [100], and toroidal cavities [101]. Several GB parameterizations have reproduced nematic and smectic phases [102–104]. More recently, a discotic parameterization has been used to explore nematic and columnar phases [105–109], providing insight on structural and dynamic measurements at the molecular level [110–112]. The recognition of specific design principles has stimulated the attainment of novel targets [27].

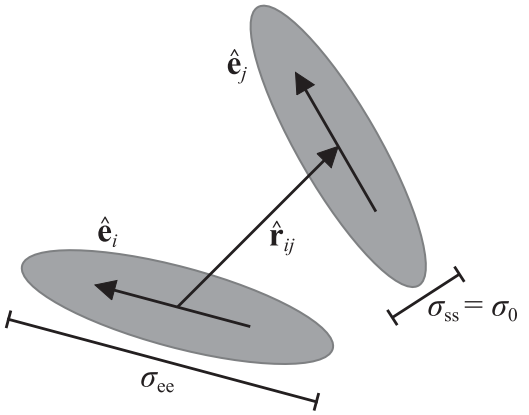

FIGURE 1 | Schematic defining the degrees of freedom and parameters associated with the GB(3, 5, 2, 1) mesogens. Molecular axes are defined by unit vectors $\hat{\mathbf{e}}_i$ and $\hat{\mathbf{e}}_j$. The center-to-center unit vector $\hat{\mathbf{r}}_{ij}$ tempers the interaction potential relative to mesogen-mesogen orientation, affecting both length [**Eq. 2**] and energy [**Eq. 5**] scales. The interaction potential is scaled by a model length σ_0 defined with respect to the side-side length σ_{ss}. The end-end length σ_{ee} is used to define the molecular aspect ratio; for the parameterization used in this work, $\sigma_{ee}/\sigma_{ss} = 3$.

Despite serving as a point of reference for 3D phenomena, the phase behavior of a strictly 2D thermotropic GB LC system has been limited [113, 114]. On the experimental front, optical microscopy commonly provides information on quasi-2D samples, and in most cases, data merely reflect 2D projections of an underlying 3D system [56, 115]. Renewed interest in the organization of rigid biopolymers as effective 2D systems (in bulk and under confinement) has led to new and interesting textures observed under strong confinement [116–122]. Simple simulation models reproduced the phenomenology observed in 2D [123–126]. Because those efforts focused on lyotropic liquid crystals, we extend the field by considering a thermotropic fluid. Specifically, we explore how shape of the confining area and type of anchoring induced by boundary walls affect mesophase behavior.

2 MODEL AND METHODS

The GB model is a generalization of the Lennard-Jones potential defining the interaction between anisotropic molecules. Each molecule i is represented as an ellipsoid having a center-of-mass position $\mathbf{r}_i$ and a unit vector $\hat{\mathbf{e}}_i$ along the principal (major) axis denoting its orientation (**Figure 1**).

The intermolecular interaction between the ith and jth mesogens is written as

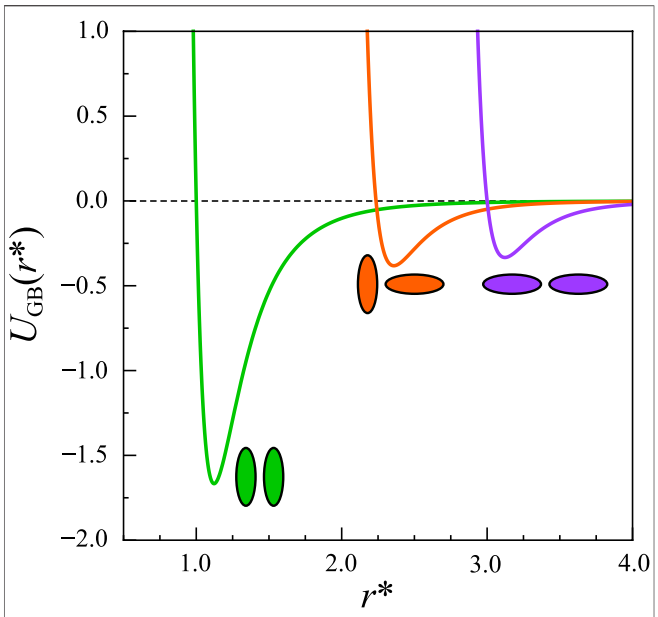

FIGURE 2 | Intermlecular potential for the GB(3, 5, 2, 1) mesogen as a function of intermesogen distance. Representative mesogen arrangements are highlighted to emphasize how $U_{GB}(r)$ is tempered according to relative mesogen-mesogen orientation.

$$U_{GB}\left(\mathbf{r}_{ij}, \hat{\mathbf{e}}_i, \hat{\mathbf{e}}_j\right) = 4\,\varepsilon\left(\hat{\mathbf{r}}_{ij}, \hat{\mathbf{e}}_i, \hat{\mathbf{e}}_j\right)\left[\,\Xi_{ij}^{-12} - \Xi_{ij}^{-6}\,\right], \tag{1}$$

where $\mathbf{r}_{ij} = \mathbf{r}_i - \mathbf{r}_j$ and the scaled distance is given by

$$\Xi_{ij} = \frac{1}{\sigma_0}\left[\,\mathbf{r}_{ij} - \sigma\left(\hat{\mathbf{r}}_{ij}, \hat{\mathbf{e}}_i, \hat{\mathbf{e}}_j\right) + \sigma_0\,\right], \tag{2}$$

where σ_0 the width of the mesogen (i.e., the minor axis) and $\mathbf{r}_{ij} = \left|\mathbf{r}_{ij}\right|$ is the magnitude of the intermolecular (center-to-center) separation vector. The relative orientation of mesogens within the medium must be taken into account to regulate the strength of the intermesogen interaction. This requires a fully specified function of a general variable ω,

$$\Gamma(\omega) = 1 - \omega\left[\frac{c_i^2 + c_j^2 - 2\,\omega\,c_i\,c_j\,c_{ij}}{1 - \omega^2\,c_{ij}^2}\right], \tag{3}$$

where $c_i = \hat{\mathbf{e}}_i \cdot \hat{\mathbf{r}}_{ij}$, $c_j = \hat{\mathbf{e}}_j \cdot \hat{\mathbf{r}}_{ij}$, $c_{ij} = \hat{\mathbf{e}}_i \cdot \hat{\mathbf{e}}_j$, and $\hat{\mathbf{r}}_{ij} = \mathbf{r}_{ij}/\left|\mathbf{r}_{ij}\right|$ is the unit (center-to-center) separation vector. The orientation-dependent length scale (range) parameter $\sigma\left(\hat{\mathbf{r}}_{ij}, \hat{\mathbf{e}}_i, \hat{\mathbf{e}}_j\right)$ is computed as

$$\sigma\left(\hat{\mathbf{r}}_{ij}, \hat{\mathbf{e}}_i, \hat{\mathbf{e}}_j\right) = \sigma_0\left[\Gamma(\chi)\right]^{-1/2} \tag{4}$$

Here, $\chi = (\kappa^2 - 1)/(\kappa^2 + 1)$, where $\kappa = \sigma_{ee}/\sigma_0 = \sigma_{ee}/\sigma_{ss}$ is the length-to-width (aspect) ratio of the mesogen (**Figure 1**). The strength anisotropy function $\varepsilon\left(\hat{\mathbf{r}}_{ij}, \hat{\mathbf{e}}_i, \hat{\mathbf{e}}_j\right)$ is defined by the product

$$\varepsilon\left(\hat{\mathbf{r}}_{ij}, \hat{\mathbf{e}}_i, \hat{\mathbf{e}}_j\right) = \varepsilon_0\left[\varepsilon_1\left(\hat{\mathbf{e}}_i, \hat{\mathbf{e}}_j\right)\right]^{\nu}\left[\varepsilon_2\left(\hat{\mathbf{r}}_{ij}, \hat{\mathbf{e}}_i, \hat{\mathbf{e}}_j\right)\right]^{\mu}, \tag{5}$$

where the exponents ν and μ are adjustable parameters. The energy anisotropy functions are defined as

$$\varepsilon_1\left(\hat{\mathbf{e}}_i, \hat{\mathbf{e}}_j\right) = \left[1 - \chi^2\left(\hat{\mathbf{e}}_i \cdot \hat{\mathbf{e}}_j\right)^2\right]^{-1/2} \tag{6}$$

and

$$\varepsilon_2\left(\hat{\mathbf{r}}_{ij}, \hat{\mathbf{e}}_i, \hat{\mathbf{e}}_j\right) = \Gamma(\chi'). \tag{7}$$

The parameter χ' depends on the ratio of the potential well depths corresponding to side-side (ss) and end-end (ee) configurations, $\kappa' = \varepsilon_{ss}/\varepsilon_{ee}$. More specifically, $\chi' = [(\kappa')^{1/\mu} - 1]/[(\kappa')^{1/\mu} + 1]$.

The GB model uses four parameters conventionally represented as GB$(\kappa, \kappa', \mu, \nu)$. Previous work has shown that specific parameter sets reproduce thermodynamic and structural properties of experimental systems [105, 107, 127]. A complete phase diagram of the 3D GB model is available for GB(3, 5, 2, 1) [104, 128–132], which corresponds to a calamitic mesogen. Moreover, this parameterization has been used to investigate intermolecular interactions in nematic samples [133–135]. Simulations have been previously reported for GB discotic mesogens focused on tracing changes in phase behavior under confinement [99, 130, 136–140] and in droplets [141]. The reader interested in additional parameterizations is referred to previous work [127, 129, 135, 142–146].

The GB(3, 5, 2, 1) parameterization is used in this work to elucidate the role that dimensionality plays on mesophase behavior. Shown in **Figure 2** are representative interaction energy curves as a function of intermesogen distance for different relative orientations. For the GB(3, 5, 2, 1) mesogen, the side-side arrangement is preferred over other configurations, a feature that promotes the nematic phase at reasonably accessible temperatures. The GB(3, 5, 2, 1) parameterization was chosen because it has been extensively used as a model for prolate LCs, such as the alkylbiphenyl mesogen family.

Confined systems were modeled with walls constructed from an array of spherical (i.e., circular in 2D) particles. The mesogen-wall interaction is obtained by taking the limit of **Eqs. 1** and **2** when one of the interacting mesogens becomes a sphere (i.e., a wall particle) [147–149]. In that limit, the range parameter and strength anisotropy functions are given by

$$\sigma_w\left(\hat{\mathbf{r}}_{ij}, \hat{\mathbf{e}}_j\right) = \sigma_0\left[1 - \chi\left(\hat{\mathbf{r}}_{ij} \cdot \hat{\mathbf{e}}_j\right)^2\right]^{-1/2} \tag{8}$$

and

$$\varepsilon_w\left(\hat{\mathbf{r}}_{ij}, \hat{\mathbf{e}}_j\right) = \varepsilon_0\left[1 - \chi'_w\left(\hat{\mathbf{r}}_{ij} \cdot \hat{\mathbf{e}}_j\right)^2\right] \tag{9}$$

where

$$\chi'_w = 1 - \left(\varepsilon_h/\varepsilon_p\right)^{1/\mu}. \tag{10}$$

For **Eqs. 8–10**, the *i*th molecule denotes a wall-type particle, the *j*th molecule refers to a mesogen, ε_h corresponds to the energy scale for *homeotropic* anchoring (when $\hat{\mathbf{e}}_j$ is locally perpendicular to the confining wall), and ε_p represents the energy scale for

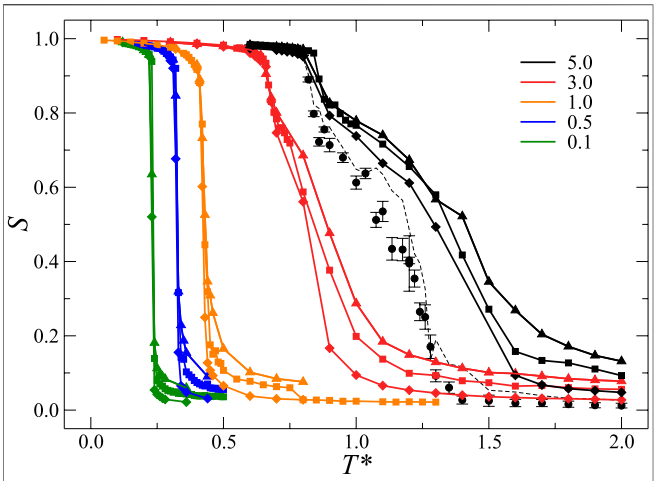

FIGURE 3 | Order parameter S as a function of temperature T^* at different pressures $P^* \in$ [5.0 (black), 3.0 (red), 1.0 (orange), 0.5 (blue), 0.1 (green)] in the bulk 2D system. The response in the order parameter S is compared among different ensemble sizes: $N \in$ [500 (triangles), 1,000 (squares), 4,000 (diamonds)]. Finite-size effects become pronounced as pressure increases (and correspondingly at higher temperature). For $P^* = 5.0$, results are also included for $N \in$ [10,000 (dashed line), 50,000 (circles with error bars)]. Finite-size effects appear to dissipate when N is of $\mathcal{O}(10^4)$.

planar anchoring (when $\hat{\mathbf{e}}_j$ is locally parallel to the confining wall). Anchoring conditions can thus be controlled by adjusting these two parameters.

We focus on a strictly 2D thermotropic liquid crystal in this work: "flat" ellipsoidal mesogens evolve in a plane. All results reported herein were generated by performing MD simulations in the canonical (*NAT*, where A is constant area for 2D, analogous to *NVT* where V is constant volume in 3D) and isothermal-isobaric (*NPT*) ensembles. Translational and rotational equations of motion were integrated using the velocity-Verlet algorithm [150]. For bulk samples, in either the *NAT* or *NPT* ensembles, the time step used was $\delta t = 0.001$. For systems in confined regions, the time step used was $\delta t = 0.002$. The coupling parameters for simulations were as follows: $Q_{\text{thermostat}} = 10$, $Q_{\text{barostat}} = 1,000$. In the case of bulk samples, the simulation cell was defined with lateral dimensions L_x and L_y: periodic boundary conditions were applied in all directions. All simulations were initialized at relatively high temperature (i.e., $T^* = k_B T/\varepsilon_0 = 1.0$). Low-temperature states ($T^* = k_B T/\varepsilon_0 = 0.1$) were attained by cooling the system gradually. Velocities were assigned from a Maxwell-Boltzmann distribution and the moments of inertia were set to $I = (\sigma_0^2/20)(\kappa^2 + 1)$ [151]. All particles were set to unit mass ($m = 1$) and intermolecular potentials were truncated at a cutoff length scale $r_c = (\kappa + 1)\sigma_0$ for expediency. Interparticle potentials were shifted to enforce a smoothly vanishing force at r_c. Simulations were run for at least 5×10^6 time steps for equilibration and another 5×10^6 time steps for production.

Global orientational order is characterized by the orientational traceless tensor $\mathbf{Q}$ [152], specialized for the 2D case [153] as

$$\mathbf{Q} = \frac{1}{N}\sum_{i=1}^{N}(2\hat{\mathbf{e}}_i \otimes \hat{\mathbf{e}}_i - \mathbf{I}), \tag{11}$$

where $\otimes$ denotes the tensor product and $\mathbf{I}$ is the identity matrix. Diagonalization of $\mathbf{Q}$ leads to two eigenvalues (λ_+ and λ_-). The nematic (Maier-Saupe) order parameter S is defined in terms of the highest eigenvalue λ_+, so that $S = \lambda_+$. The parameter S is equal to zero for isotropic configurations and increases as orientational order increases.

3 RESULTS AND DISCUSSION

3.1 Orientational Order and Liquid Structure

In this section, we present data for a series of samples of increasing size (mesogen number) to elucidate the orientational order of the LC liquid as a function of temperature. We focus here on characterizing differences due specifically to sample size, considering $N \in \{500, 1000, 4000\}$. Profiles for the Maier-Saupe order parameter are presented in **Figure 3**.

The nematic order parameter S displays a state with low orientational order ($S \approx 0$) when the temperature exceeds a threshold depending on the pressure P^* of the system. The onset of orientational order shows a jump in S, such that $S \approx 1$ when the temperature is sufficiently low: this high value of S indicates the formation of the smectic phase. An isotropic-smectic transition (I-Sm) takes place without an intermediate nematic state when the pressure is sufficiently low (i.e., for $P^* < 2$). As the pressure increases, the I-Sm transition occurs by passing through a range of nematic state points, corresponding approximately to $0.25 < S < 0.75$. A finite-size effect in S becomes pronounced at higher pressure (i.e., $P^* \gtrsim 2$): the transition appears less sharp as the ensemble size N decreases.

To investigate how finite-size effects are pronounced at higher pressures, simulations were performed for $P^* = 5.0$. At this pressure, finite-size effects are accentuated. We performed simulations for $N \in \{10000, 50000\}$. As can be gleaned from **Figure 3**, results for the larger two systems are close to one another. Hence, finite-size effects seemingly dissipate when the ensemble size is at least of $\mathcal{O}(10^4)$.

To gain insight into the local structure, we analyzed MD snapshots for $N = 50,000$ when $P^* = 5.0$ *via* a temperature sweep shown in **Figure 4**. An eightfold magnification of a portion of the ensemble is shown to aid discerning local mesophase order: the entire ensemble for each temperature is provided in the **Supplementary Material**. At high temperatures, translational entropy overwhelms the cohesive energy of the LC medium and a disordered phase is the most stable state accessible to the system. At intermediate temperatures, the ensemble displays small clusters of mesogens with correlated orientation. Clustering grows in spatial extent with decreasing temperature. At even lower temperatures, the cohesive energy overtakes the decreasing translational entropy: a liquid phase with smectic order ensues at these temperatures. The smectic mesophase is stabilized

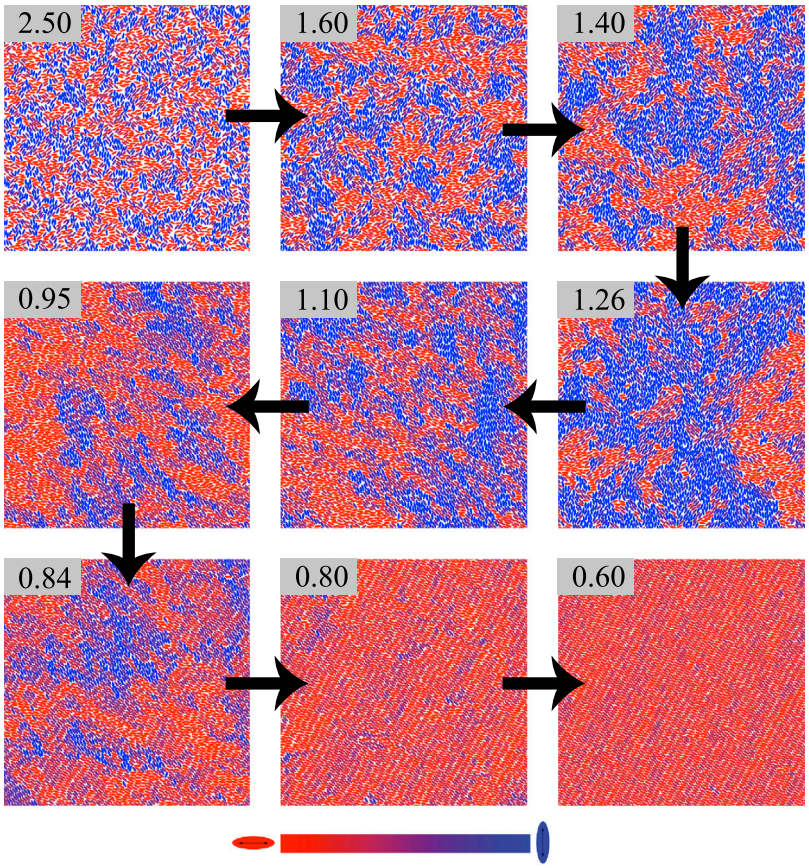

FIGURE 4 | Snapshots of the bulk 2D system when P^*= 5.0 and N = 50, 000. Shown is an eightfold-magnified region of the ensemble to discern the local order of mesogens. Configurations are arranged as a temperature sweep (arrows) with each configuration showing its temperature T^*. Mesogens are colored according to orientation, as indicated by the color bar (bottom).

(i.e., structural order increases in spatial extent) upon further cooling.

3.2 Phase Diagram Topology and Mesophases

A major contribution in this study is the orthobaric [i.e., (ρ^*, T^*)] phase diagram for the 2D system shown in **Figure 5**. The 3D case for the same GB mesogen is overlaid with gray and red shadows: such a comparison enables us to appreciate how dimensionality affects topology. The phase diagram for the 3D case was previously reported [128, 129]. The 2D phase diagram reported here was obtained from MD simulations performed in the isothermal-isobaric (NPT) ensemble. The pressure P^* was controlled with a Nosé-Hoover barostat; samples consisted of $N = 1,000$ mesogens. Phase regions were outlined by acquiring data for $P^* \in \{0.1, 0.5, 1.0, 2.0, 3.0, 5.0\}$. For each pressure, the system was initialized at a high temperature and gradually cooled in steps of $\Delta T^* = 0.02$ for at least 5×10^6 time steps.

When compared to the 3D case, the 2D system displays an evident shift in its phase boundaries. This behavior is justified by the fact that thermal fluctuations are stronger when the dimensionality of the system is reduced [154–156]. The 2D system shows that the nematic phase emerges over a wider (nearly double) range in temperature at slightly lower densities. Additionally, the isotropic phase occupies a larger area of stability in the (ρ^*, T^*)-plane, extending to lower temperatures and higher densities in 2D. The critical point appears at a lower temperature $(T_c^* = 0.202 \pm 0.007)$ and slightly higher density $(\rho_c^* = 0.159 \pm 0.002)$ when compared to the 3D system. Our result for the 2D critical point compares very well with previous work [157, 158].

It is instructional to consider how finite-size effects influence the topology of the phase diagram. For this purpose, three isobars are included: $P^* \in \{0.1, 3.0, 5.0\}$. For the (ρ^*, T^*) region shown, only slight deviations from the boundaries in the top-right corner would be expected. Boundaries shown on the phase diagram serve as a guide to the eye based on the available data extracted from the isothermal-isobaric simulations. The slim regions conveyed by solid lines are best estimates that outline the limits of phase stability and do not represent true coexistence lines.

We note that isothermal-isobaric simulations can probe metastable regions that elude canonical simulations without

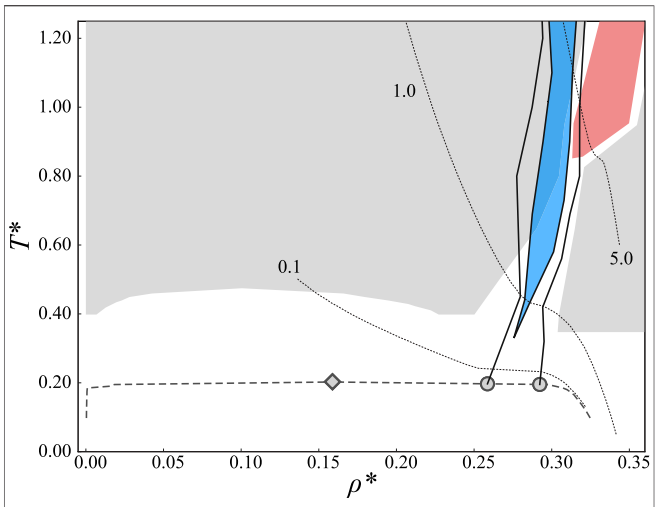

FIGURE 5 | The orthobaric phase diagram for the GB(3, 5, 2, 1) mesogen in 2D (lines) and 3D (gray shadow). The 2D critical point (diamond) appears when $\rho_c^* = 0.159 \pm 0.002$ and $T_c^* = 0.202 \pm 0.007$. The nematic phase region is highlighted in both cases: 2D (blue shadow) and 3D (red shadow). For 2D, the nematic region is stable over a wider T^*-range for a slightly narrower ρ^*-range. Three specific isobars (dotted lines, labeled with P^*) are shown for comparison. Only the top-right region of the phase diagram is most sensitive to finite-size effects as shown in the response of the order parameter S in **Figure 3**.

yielding coexistence (i.e., phase separation). The complete mapping of such phase boundaries would require free energy calculations, such as Gibbs ensembles [159–161], Gibbs-Duhem integration [162], histogram reweighting [163], or the Frenkel-Ladd method [164], among others. The coexistence of mesophases, however, was verified by independent canonical simulations. A sample cooling routine highlighting the coexistence of different mesophases is shown in **Figure 6**. The snapshots trim out sparsely populated regions of the full simulation cell observed at lower temperatures.

3.3 Confinement: Point Defects and Domain Walls

The extent to which mesophase structure is affected by strong confinement was also explored in this study. Inspiration for this lies in the rich structures and topological defects observed in lyotropic systems: the similarity in the textures observed in our thermotropic system highlights certain universal traits of topological defects. From an applications standpoint, this is of interest because topological defects can be recruited for the self-ordering of colloidal particles. In the case of a 2D system, this arrangement has the potential to yield monolayers of colloidal particles with specific positional constraints.

The 2D LC samples were confined within walls consisting of an array of fixed Lennard-Jones particles. Three different confinement scenarios were considered in this study: circular, square, and triangular. The mesogen packing fraction was kept approximately at $\eta = 0.75$ in all cases to ensure a nematic state point consistent with the bulk 2D phase diagram. As a point of

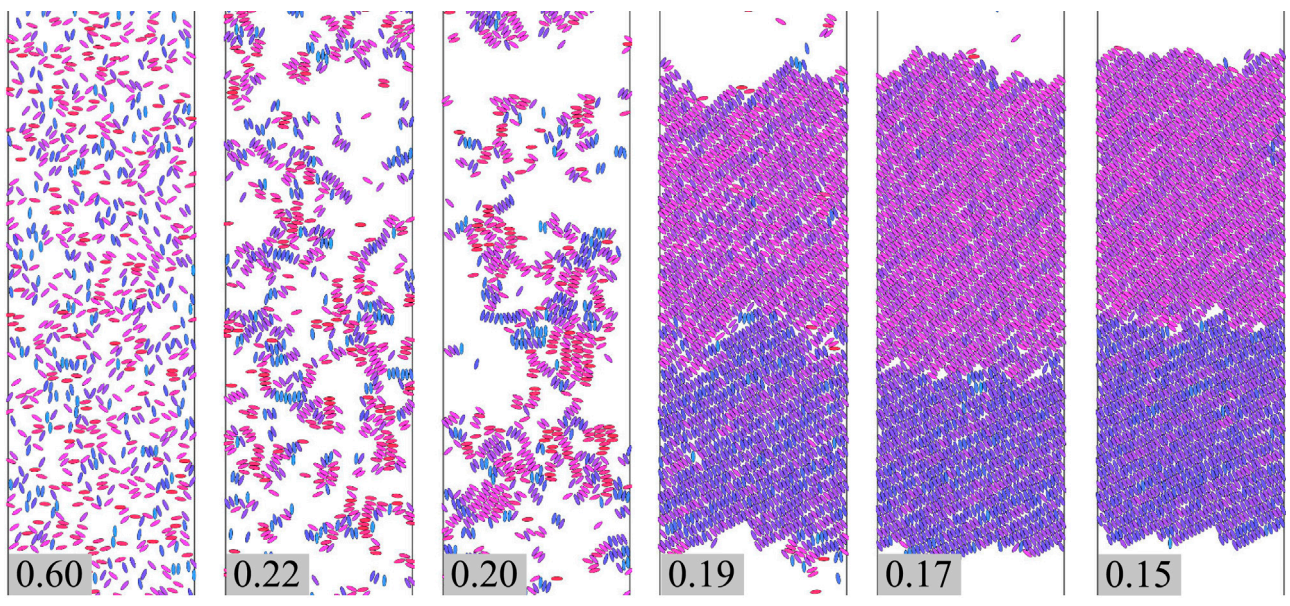

FIGURE 6 | A representative cooling sweep in the *NAT* ensemble. Configurations are shown for an ensemble with $N = 2,000$ and $\rho^* = 0.10$. The temperature T^* decreases going from left to right over a narrow temperature window as shown. Snapshots of the simulation box have been trimmed to improve the visual clarity of the more densely populated regions observed at lower temperature.

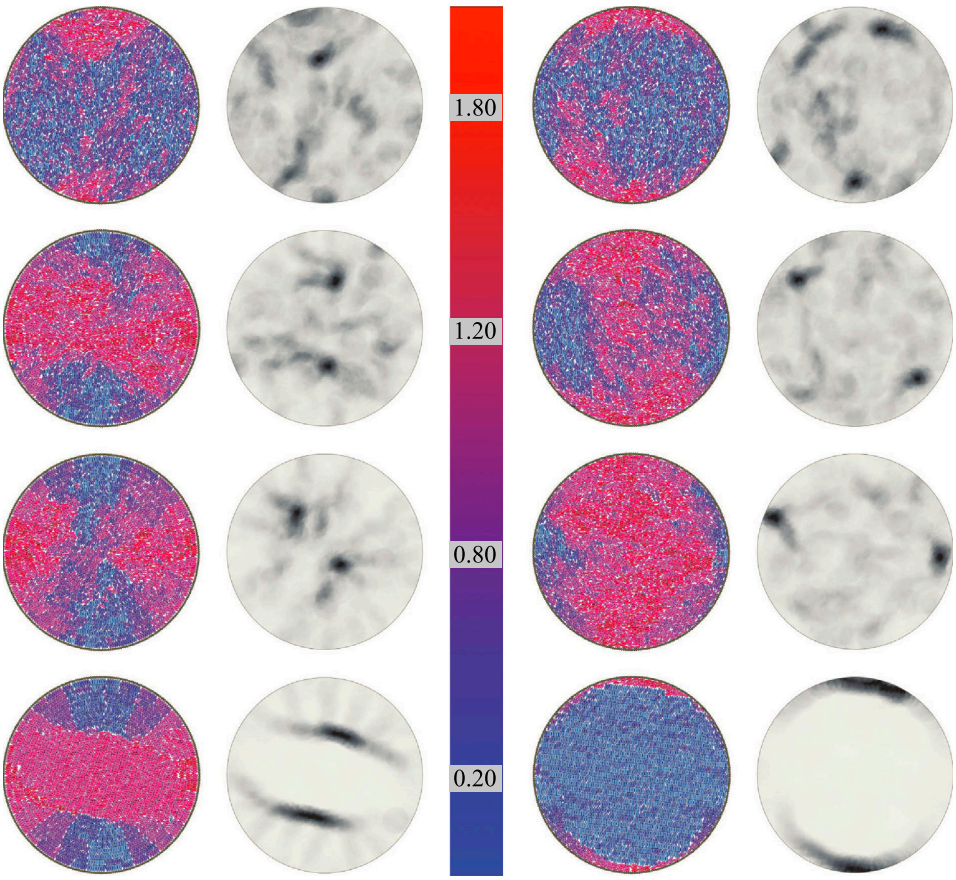

FIGURE 7 | The 2D GB(3, 5, 2, 1) mesogen system confined by a circular boundary. The series from top to bottom represents a cooling sweep: temperature is indicated by the centered temperature bar. Renditions are shown for homeotropic ($\varepsilon_h/\varepsilon_p$ = 5.0, two leftmost columns) and planar ($\varepsilon_h/\varepsilon_p$ = 0.2, two rightmost columns) anchoring. Each set of columns on either side of the temperature bar correspond as follows: configuration snapshots **(left)** and scalar field of the local order parameter **(right)**.

reference, the packing fraction for a 2D hexagonal lattice composed of circular units is $\eta \approx 0.907$ [165].

To characterize the way the confining walls exert a structuring effect on the mesogenic liquid, two anchoring conditions were considered: *homeotropic* ($\varepsilon_h/\varepsilon_p$ = 5.0) and *planar* ($\varepsilon_h/\varepsilon_p$ = 0.2) cases (**Eq. 10**). The nematic field emerging from the sample in the bulk region displays a dominant direction. However, the boundaries defining the confined area disrupt any such dominant alignment. The resulting director field persists in response to a delicate balance between anchoring conditions imposed by the confining walls and the strong tendency of neighboring mesogens to mutually align. As a result, this synergy has the effect of stabilizing topological defects within the confined region.

Data for circular confinement are shown in **Figure 7**. Topological defects are sharply sensitive to the type of anchoring. For homeotropic anchoring, the confinement radius in this work affords a low-temperature director field giving rise to two defects (with topological charge +1/2), localized away from the wall but separated in relation to one another. This behavior is consistent with density functional theory predictions [119]. As temperature increases, the defects move away from one another until they approach the wall: at sufficiently high temperature ($T^* \sim 1.80$), the defects dissipate to yield a single, isotropic configuration. Such an outcome is possible because the anchoring energies at the confining surfaces are of finite strength. As can be seen in the configuration snapshots, thermal fluctuations are sufficiently strong to overcome the orientation induced by anchoring.

The situation changes for planar anchoring: at low temperature, two defects are present, but they are located at opposite poles of the confining circle. As a result, the so-called polar nematic configuration is observed. This state is distinguished by a layered mesophase similar to the smectic-like state that dominates all but two thin surface shells on opposite ends ($T^* \sim 0.20$). Another configuration also observed at the lowest temperature possesses boundary disclinations, but the main topological defect consists of point defects appearing on opposite poles of the circular boundary (refer to the discussion on circular boundary confinement in **Section 3.4**). Radially oriented domains, like those observed in the case of homeotropic anchoring, are absent in planar

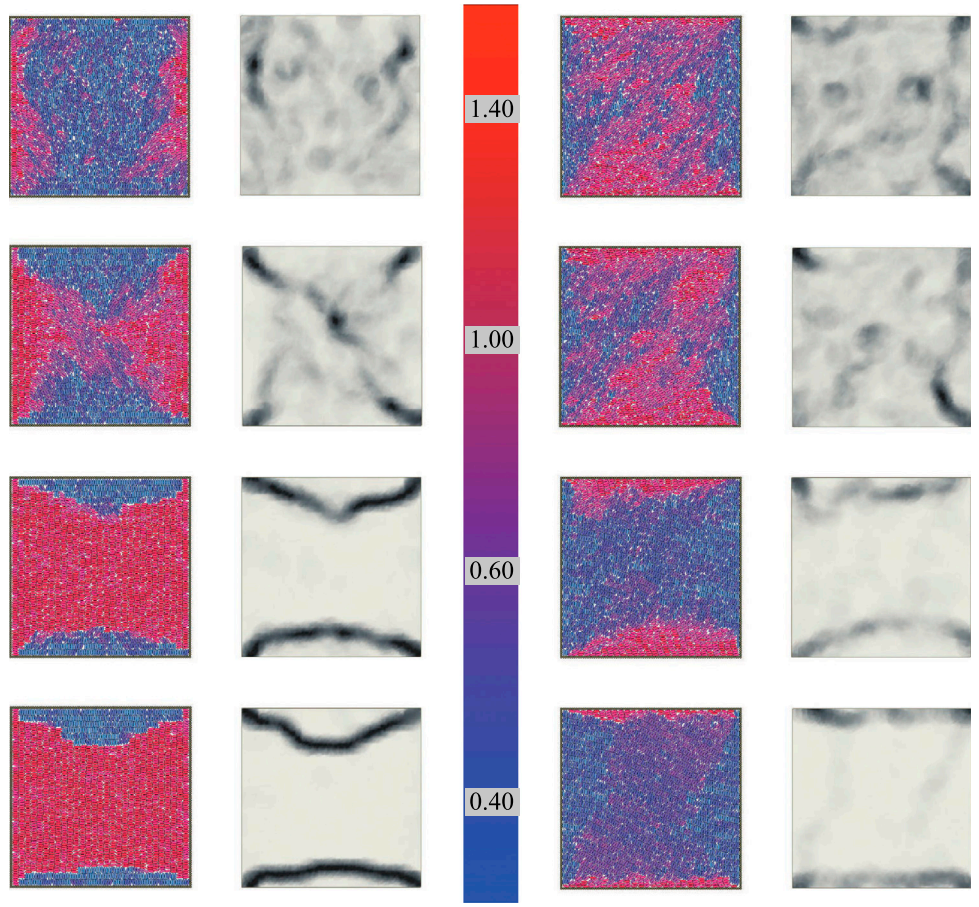

FIGURE 8 | The 2D GB(3, 5, 2, 1) mesogen system confined by a square boundary. Data are arranged as in **Figure 7**.

anchoring. Nematic-like order emerges as temperature increases for both anchoring modes under circular confinement. Although two polar defects persist at high temperature in the two systems ($T^* \sim 1.20$), the type of anchoring can be distinguished by probing the relative distance between defects: the separation between the two defects is always larger (nearing the boundary wall) for planar anchoring. As expected, internal order is mostly lost in both types of anchoring at sufficiently high temperatures. Our observations are consistent with those documented for a 2D fluid of hard rods in the high-density regime, with a sufficiently small aspect ratio [124].

Square confinement leads to more interesting textures as shown in **Figure 8**. The reduced symmetry of the boundary frustrates global mesophase order. For both anchoring conditions, domain walls (i.e., boundaries between different orientationally ordered domains) appear at sufficiently low temperature ($T^* \sim 0.60$). For homeotropic anchoring, domain walls define three regions: a large region with a local director rotated $\pi/2$ radians in relation to the local directors characterizing two small regions oriented in the same direction. Mesogens in the large region are highly oriented and form smectic-like layers. These domain walls signal domains possessing different orientations: the free energy is minimized in the system when curved interfaces develop. Moreover, two equivalent states are possible by symmetry: one shown in the snapshots and another obtained by rotating the snapshot $\pi/2$ radians. In this way, the system displays two-fold degeneracy. This effect was previously observed using a density-functional approach [166]. An external field can lead to an interchange between the two states dynamically, as previously reported [167].

When planar anchoring is operative under square confinement, four domain walls (i.e., five regions) appear. Four small regions display an orientation aligned with the confining walls and one interior region with a local director tilted slightly in relation to adjacent lateral domains. This arrangement is strikingly similar to the $W \sim 40L$ system studied by Cortes et al. [117]. It is plausible for the interior region to eventually reorient to create a single region where the local director matches that of two adjacent lateral domains. As temperature increases, those domain walls disappear and two point defects arise close to the corners of the square. The structural behavior of the LC sample under square confinement agrees with previous theoretical models [121].

The most severe confining geometry in this study is the triangular boundary, the results of which are shown in **Figure 9**. For either type of anchoring, three orientationally

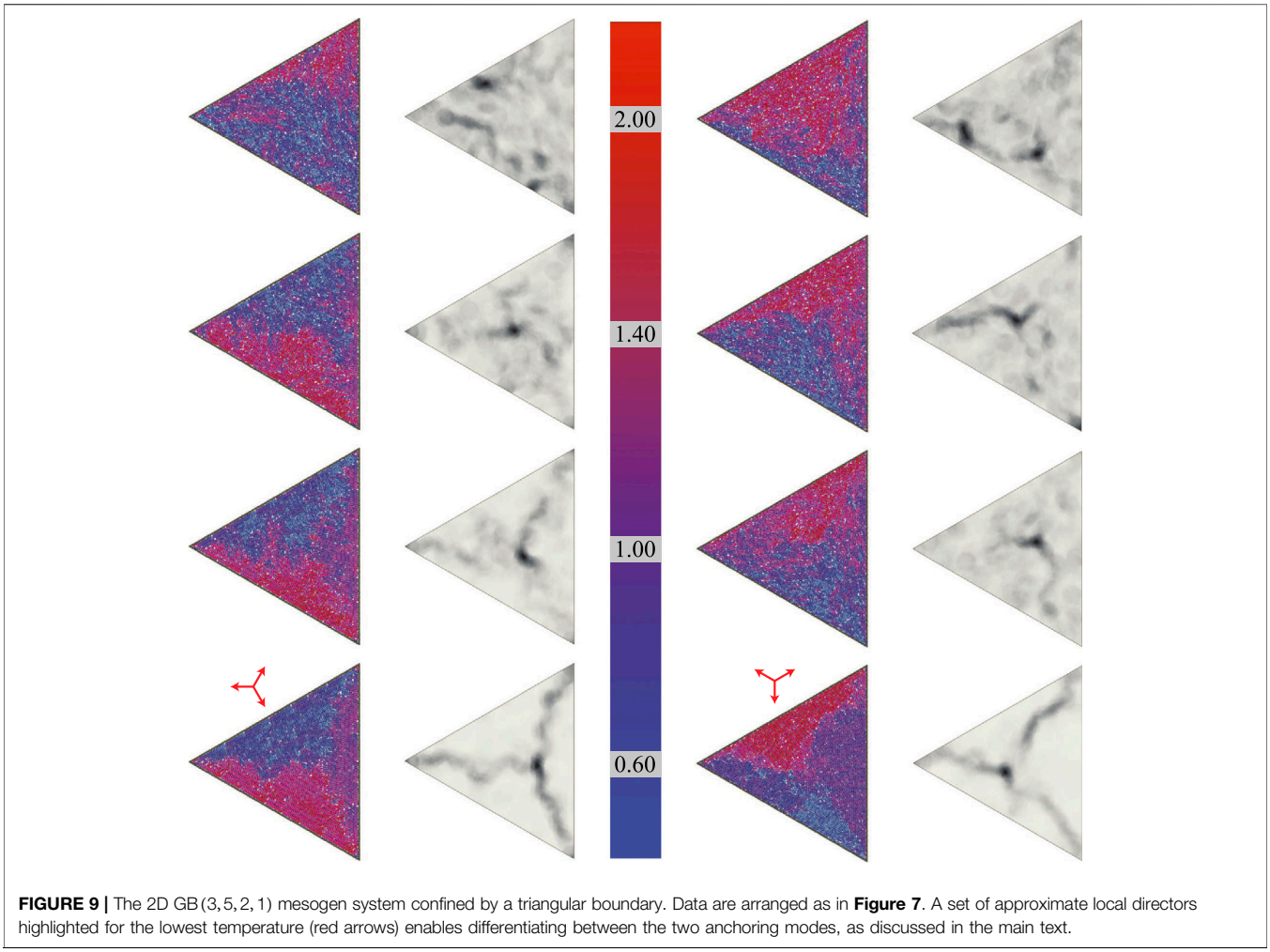

FIGURE 9 | The 2D GB(3, 5, 2, 1) mesogen system confined by a triangular boundary. Data are arranged as in **Figure 7**. A set of approximate local directors highlighted for the lowest temperature (red arrows) enables differentiating between the two anchoring modes, as discussed in the main text.

ordered regions are discernible at low temperature: the resulting topological defects are driven by an order that permeates from the boundary wall toward the center of the confining region. This effect promotes the formation of a near-centered defect in either anchoring case at fairly high temperature ($T^* \sim 2.00$). Streak disclinations radiate from the point defect, signaling the partition between distinctly oriented regions giving rise to three domain walls only when the temperature is sufficiently low ($T^* \sim 0.60$).

Although the scalar fields of the order parameter under triangular confinement for both anchoring cases are similar, the two samples can still be differentiated when accounting for local order. The approximate local directors corresponding to the three oriented domains highlighted in **Figure 9** are rotated $\pi/6$ radians with respect to one another. This difference arises from the coupling of the anisotropic shape of the calamitic mesogen and the underlying confining geometry. When placed at the center of the triangular region, the set of directors for the homeotropic sample point at the corners of the triangular boundary; the analogous set for planar anchoring results in the bisection of all sides of the triangular region. As expected, the orientationally ordered regions and the streak disclinations dissipate with increasing temperature, though the point defect persists even at high temperature ($T^* \sim 1.40$).

3.4 Dynamics of Confined Samples

Ancillary data from this work are ensemble trajectories given that systems were evolved with MD simulations. Although static information obtained from simulation snapshots is useful in characterizing orientational order and topological defects, it is equally important to probe the temporal behavior of mesophases. To this end, trajectories were leveraged to probe dynamical fluctuations in the fluid structure and the scalar field of the order parameter. The **Supplementary Material** includes trajectory visualizations for the systems in **Figures 7–9**. Each visualization is labeled by temperature and anchoring mode. The timescale in each case corresponds to approximately 3% of an entire simulation run.

The system under circular confinement with planar anchoring at reasonably high temperatures already exhibits features reminiscent of the polar defects stabilized at low temperatures. However, such defects are accompanied by strong fluctuations in intensity and positional alignment. As one point defect vanishes another emerges in the same pole. For homeotropic anchoring, point defects fluctuate in number, intensity, and position at high

temperatures. Upon further cooling, the homeotropic sample displays two point defects with minimal fluctuations in position and intensity, immediately after two radially oriented domains form. Before the central smectic-like region sets in, the separation between the two point defects reaches a minimum. Fluctuations in intensity are minimal at the lowest temperature studied: the separation between point defects stabilizes at a slightly larger distance ($T^* \sim 0.20$) than before ($T^* \sim 0.80$). In the case of planar anchoring, point defects appear on opposite poles of the circular boundary. Unlike the low-temperature configuration in **Figure 7**, textures in the bulk region of the confined area become richer when the smectic phase sets in: boundary defects of fleeting intensity appear upon further cooling for planar anchoring. However, polar defects persist prominently.

The behavior of topological defects upon sample cooling is similar for both anchoring modes under square confinement. In both cases, a highly fluctuating cross pattern with approximately two point-like defects on opposite corners of the square is observed. As soon as the sample reaches a temperature where the smectic mesophase becomes favorable, the fleeting point-like defects vanish: each anchoring case becomes distinguishable at this point ($T^* \sim 0.60$). For homeotropic anchoring, two prominent domain walls persist, giving rise to three distinct regions. For planar anchoring, four domain walls become stable, demarcating five distinct regions. The domain walls, although subdued when compared to the homeotropic case, yield a rhomboidal pattern.

When comparing the two anchoring modes for triangular confinement, the cooling history is very similar in both cases. A point defect is characteristic of either case upon the slightest hint of ordering. Three domain walls weakly form at high temperature ($T^* \sim 1.00$), although they are characterized by strong fluctuations in position and intensity. Upon further cooling, the domain walls assert their presence and a point defect becomes prominent in the sample ($T^* \sim 0.60$). As discussed in **Section 3.3**, due to the similarity between the two anchoring cases, it is only possible to distinguish the two samples by inspecting the relative arrangement of local directors in each sample.

4 CONCLUSION

Bulk and confined 2D samples were explored for the Gay-Berne mesogen with parameterization GB$(3, 5, 2, 1)$. This model calamitic exhibits a sharp isotropic-smectic (I-Sm) transition at lower pressures ($P^* < 2.0$); at higher pressures ($P^* \gtrsim 2.0$), the I-Sm transition involves an intermediate nematic phase. Clusters of locally ordered mesogens reach a threshold size, at sufficiently low temperatures, before the LC sample becomes smectic. The nematic phase shows an extended region of stability, nearly doubling in the temperature range at slightly lower densities. The critical point shifts to a lower temperature and a higher density compared to the analogous 3D system.

Confined samples were subjected to three boundary geometries: circular, square, and triangular. In *circular* geometry, two point defects emerge: for homeotropic anchoring, point defects are stable in the bulk region of the boundary and remain at a nearly constant separation. For planar anchoring, point defects gravitate toward opposite poles of the boundary. In *square* geometry, no stable point defects are observed at low temperatures. Instead, two distinct domain walls give rise to three regions under homeotropic anchoring; the structure under planar anchoring results in four interconnecting domain walls, rhomboidal in form, producing five regions. In *triangular* geometry, confinement yields similar defects when comparing anchoring modes: three domain walls "emanate" from a nearly centered point defect yielding three regions. In this case, local directors must be accounted for to differentiate between anchoring modes.

All systems were studied with MD simulations. The resulting trajectories of confined 2D LC samples were visualized, revealing a complex evolution of textures originating from topological defects. Ordered domains at low temperatures are prefaced with strong thermal fluctuations that cause spatial variations in the mesophase at sufficiently high temperatures. Within the mesophase, flickering in position and intensity of topological defects is minimized at sufficiently low temperatures. Both the confining geometry and anchoring mode contribute to the type of defects observed.

Confined 2D LC systems provide a rich and exciting outlook. An outstanding matter with an eye toward 3D metamaterials is how disclinations couple when colloidal slabs are stacked. Practicable systems could extend layer-by-layer protocols [7, 89, 90, 168–180], thus expanding the gamut of metamaterials attainable by conventional 3D-based methods. Studies on the switching mechanics by applying external fields (as opposed to thermal tempering) would be of interest in the production of devices and associated technologies. A characterization of relevant timescales would offer an important perspective on design principles. Structured colloidal assemblies *via* topological defects could be exploited to yield colloidal assemblies with screw/twist properties, thus amplifying the availability of chiral materials.

DATA AVAILABILITY STATEMENT

The numerical model simulations upon which this study is based are unwieldy to archive or to transfer. Instead, all information needed to replicate the simulations is provided.

AUTHOR CONTRIBUTIONS

AC-A and JM-V performed bulk simulations, wrote post-simulation analysis codes, and implemented data analysis. AC-A carried out simulations for small-scale bulk samples as well as strongly confined systems and visualized trajectories. JM-V performed large-scale simulations of bulk samples *via* parallelization. SH and AR-H contributed to the interpretation of results and drafted relevant sections of the analysis. ES verified results for bulk systems, interpreted dynamical trajectories of strongly confined systems, and completed writing the manuscript. JM-R conceived the study, wrote the Gay-Berne simulation code, drafted initial versions of the manuscript, and coordinated the direction of the project.

FUNDING

JM-V and JM-R are thankful for the computing time generously provided under grant LANCAD-UNAM-DGTI-344. SH is grateful for funding provided by projects UNAM-DGAPA-PAPIIT IA104319, LANCAD-UNAM-DGTIC-276, and LANCAD-UNAM-DGTIC-087.

ACKNOWLEDGMENTS

JM-R gratefully acknowledges the computing resources provided by the Laboratorio de Supercómputo y Visualización en Paralelo (LSVP) at UAM-I. SH gratefully acknowledges the technical support provided by Carlos Sair Flores Bautista, Alejandro de León Cuevas, and Luis Alberto Aguilar Bautista from the Laboratorio Nacional de Visualización Científica Avanzada (LAVIS-UNAM), as well as by Beatriz Marcela Millán Malo from CFATA-UNAM.

SUPPLEMENTARY MATERIAL

The Supplementary Material for this article can be found online at: https://www.frontiersin.org/articles/10.3389/fphy.2020.622872/full#supplementary-material.

REFERENCES

1. Fedotov V. Springer Handbook of Electronic and Photonic Materials. 2nd ed. Cham, Switzerland: Springer International Publishing (2017). 1351–77. chap. Metamaterials.
2. Liu Y, Zhang X. Metamaterials: a new frontier of science and technology. *Chem Soc Rev* (2011) 40:2494–507. doi:10.1039/c0cs00184h
3. Whitesides GM, Love JC. The art of building small. *Sci Am* (2001) 285:38–47. doi:10.1038/scientificamerican0901-38
4. Zhang S. Building from the bottom up. *Mater Today* (2003) 6:20–7. doi:10.1016/s1369-7021(03)00530-3
5. Shimomura M, Sawadaishi T. Bottom-up strategy of materials fabrication: a new trend in nanotechnology of soft materials. *Curr Opin Colloid Interface Sci* (2001) 6:11–6. doi:10.1016/s1359-0294(00)00081-9
6. Kotnala A, Zheng Y. Digital assembly of colloidal particles for nanoscale manufacturing. *Part Part Syst Charact* (2002) 36:1900152. doi:10.1002/ppsc.201900152
7. Borges J, Mano JF. Molecular interactions driving the layer-by-layer assembly of multilayers. *Chem Rev* (2014) 114:8883–942. doi:10.1021/cr400531v
8. Conti S, Cecchini M. Predicting molecular self-assembly at surfaces: a statistical thermodynamics and modeling approach. *Phys Chem Chem Phys* (2016) 18:31480–93. doi:10.1039/c6cp05249e
9. Israelachvili JN. Intermolecular and Surface Forces. Amsterdam, Netherlands: Academic Press (2011). 503–76 p.
10. Vilfan M, Osterman N, Čopič M, Ravnik M, Žumer S, Kotar J, et al. Confinement effect on interparticle potential in nematic colloids. *Phys Rev Lett* (2008) 101:237801. doi:10.1103/PhysRevLett.101.237801
11. Tasinkevych M, Andrienko D. Colloidal particles in liquid crystal films and at interfaces. *Condens Matter Phys* (2010) 13:33603. doi:10.5488/cmp.13.33603
12. Verstraete L, Greenwood J, Hirsch BE, De Feyter S. Self-assembly under confinement: nanocorrals for understanding fundamentals of 2D crystallization. *ACS Nano* (2016) 10:10706–15. doi:10.1021/acsnano.6b05954
13. Pfeiffer CR, Pearce N, Champness NR. Complexity of two-dimensional self-assembled arrays at surfaces. *Chem Commun* (2017) 53:11528–39. doi:10.1039/c7cc06110b
14. Nieckarz D, Szabelski P. Surface-confined self-assembly of asymmetric tetratopic molecular building blocks. *Chem Phys Chem* (2019) 20:1850–9. doi:10.1002/cphc.201900344
15. Całus S, Busch M, Kityk AV, Piecek W, Huber P. Chiral phases of a confined cholesteric liquid crystal: anchoring-dependent helical and smectic self-assembly in nanochannels. *J Phys Chem C* (2016) 120:11727–38. doi:10.1021/acs.jpcc.6b03553
16. Whitesides GM. The once and future nanomachine. *Sci Am* (2001) 285:78–83.doi:10.1038/scientificamerican0901-78
17. Tu RS, Tirrell M. Bottom-up design of biomimetic assemblies. *Adv Drug Deliv Rev* (2004) 56:1537–63. doi:10.1016/j.addr.2003.10.047
18. Min Y, Akbulut M, Kristiansen K, Golan Y, Israelachvili J. The role of interparticle and external forces in nanoparticle assembly. *Nat Mater* (2008) 7:527–38. doi:10.1038/nmat2206
19. Muševič I. Nematic colloids, topology and photonics. *Philos Trans A Math Phys Eng Sci* (2013) 371:20120266. doi:10.1098/rsta.2012.0266
20. Lavrentovich OD. Liquid crystals, photonic crystals, metamaterials, and transformation optics. *Proc Natl Acad Sci U S A* (2011) 108:5143–4. doi:10.1073/pnas.1102130108
21. Muševič I, Škarabot M, Tkalec U, Ravnik M, Žumer S. Two-dimensional nematic colloidal crystals self-assembled by topological defects. *Science* (2006) 313:954–8. doi:10.1126/science.1129660
22. Alexander GP, Chen BGG, Matsumoto EA, Kamien RD. Colloquium: disclination loops, point defects, and all that in nematic liquid crystals. *Rev Mod Phys* (2012) 84:497–514. doi:10.1103/revmodphys.84.497
23. Čopar S, Porenta T, Jampani VSR, Muševič I, Žumer S. Stability and rewiring of nematic braids in chiral nematic colloids. *Soft Matter* (2012) 8:8595–600. doi:10.1039/C2SM25952D
24. Ravnik M, Alexander GP, Yeomans JM, Žumer S. Three-dimensional colloidal crystals in liquid crystalline blue phases. *Proc Natl Acad Sci U S A* (2011) 108:5188–92. doi:10.1073/pnas.1015831108
25. Nych A, Ognysta U, Škarabot M, Ravnik M, Žumer S, Muševič I. Assembly and control of 3D nematic dipolar colloidal crystals. *Nat Commun* (2013) 4:1489. doi:10.1038/ncomms2486
26. Poulin P, Stark H, Lubensky TC, Weitz DA. Novel colloidal interactions in anisotropic fluids. *Science* (1997) 275:1770–3. doi:10.1126/science.275.5307.1770
27. González-Martínez AD, Chávez-Rojo MA, Sambriski EJ, Moreno-Razo JA. Defect-mediated colloidal interactions in a nematic-phase discotic solvent. *RSC Adv* (2019) 9:33413–27. doi:10.1039/c9ra05377h
28. Martinez A, Hermosillo L, Tasinkevych M, Smalyukh, II. Linked topological colloids in a nematic host. *Proc Natl Acad Sci U S A* (2015) 112:4546–51. doi:10.1073/pnas.1500998112
29. Wang X, Miller DS, de Pablo JJ, Abbott NL. Reversible switching of liquid crystalline order permits synthesis of homogeneous populations of dipolar patchy microparticles. *Adv Funct Mater* (2014) 24:6219–26. doi:10.1002/adfm.201400911
30. Cavallaro M, Jr., Gharbi MA, Beller DA, Čopar S, Shi Z, Kamien RD, et al. Ring around the colloid. *Soft Matter* (2013) 9:9099–102. doi:10.1039/c3sm51167g
31. Liu Q, Senyuk B, Tasinkevych M, Smalyukh, II. Nematic liquid crystal boojums with handles on colloidal handlebodies. *Proc Natl Acad Sci U S A* (2013) 110:9231–6. doi:10.1073/pnas.1301464110
32. Čopar S, Tkalec U, Muševič I, Žumer S. Knot theory realizations in nematic colloids. *Proc Natl Acad Sci U S A* (2015) 112:1675–80. doi:10.1073/pnas.1417178112
33. Senyuk B, Liu Q, He S, Kamien RD, Kusner RB, Lubensky TC, et al. Topological colloids. *Nature* (2013) 493:200–5. doi:10.1038/nature11710
34. Araki T, Tanaka H. Colloidal aggregation in a nematic liquid crystal: topological arrest of particles by a single-stroke disclination line. *Phys Rev Lett* (2006) 97:127801. doi:10.1103/PhysRevLett.97.127801
35. Ravnik M, Škarabot M, Žumer S, Tkalec U, Poberaj I, Babic D, et al. Entangled nematic colloidal dimers and wires. *Phys Rev Lett* (2007) 99:247801. doi:10.1103/PhysRevLett.99.247801
36. Jampani VS, Škarabot M, Ravnik M, Čopar S, Žumer S, Muševič I. Colloidal entanglement in highly twisted chiral nematic colloids: twisted loops, Hopf

links, and trefoil knots. *Phys Rev E—Stat Nonlinear Soft Matter Phys* (2011) 84: 031703. doi:10.1103/PhysRevE.84.031703
37. Hashemi SM, Ravnik M. Nematic colloidal knots in topological environments. *Soft Matter* (2018) 14:4935–45. doi:10.1039/c8sm00539g
38. Tkalec U, Ravnik M, Čopar S, Žumer S, Muševič I. Reconfigurable knots and links in chiral nematic colloids. *Science* (2011) 333:62–5. doi:10.1126/science.1205705
39. Lubensky TC, Pettey D, Currier N, Stark H. Topological defects and interactions in nematic emulsions. *Phys Rev E* (1998) 57:610–25. doi:10.1103/physreve.57.610
40. Loudet JC, Barois P, Poulin P. Colloidal ordering from phase separation in a liquid-crystalline continuous phase. *Nature* (2000) 407:611–3. doi:10.1038/35036539
41. Wang X, Miller DS, Bukusoglu E, de Pablo JJ, Abbott NL. Topological defects in liquid crystals as templates for molecular self-assembly. *Nat Mater* (2016) 15:106–12. doi:10.1038/nmat4421
42. Smalyukh II, Lavrentovich OD, Kuzmin AN, Kachynski AV, Prasad PN. Elasticity-mediated self-organization and colloidal interactions of solid spheres with tangential anchoring in a nematic liquid crystal. *Phys Rev Lett* (2005) 95: 157801–4. doi:10.1103/PhysRevLett.95.157801
43. Gharbi MA, Nobili M, Blanc C. Use of topological defects as templates to direct assembly of colloidal particles at nematic interfaces. *J Colloid Interface Sci* (2014) 417:250–5. doi:10.1016/j.jcis.2013.11.051
44. Pandey MB, Porenta T, Brewer J, Burkart A, Copar S, Žumer S, et al. Self-assembly of skyrmion-dressed chiral nematic colloids with tangential anchoring. *Phys Rev E—Stat Nonlinear Soft Matter Phys* (2014) 89:060502. doi:10.1103/PhysRevE.89.060502
45. Kim JH, Yoneya M, Yokoyama H. Tristable nematic liquid-crystal device using micropatterned surface alignment. *Nature* (2002) 420:159–62. doi:10.1038/nature01163
46. Machon T, Alexander GP. Knots and nonorientable surfaces in chiral nematics. *Proc Natl Acad Sci U. S. A* (2013) 110:14174–9.doi:10.1073/pnas.1308225110
47. Frydel D, Rice SA. Phase diagram of a quasi-two-dimensional colloid assembly. *Phys Rev E—Stat Nonlinear Soft Matter Phys* (2003) 68:061405. doi:10.1103/PhysRevE.68.061405
48. Fomin YD, Ryzhov VN, Tsiok EN. The influence of long-range interaction on the structure of a two-dimensional multi scale potential system. *J Phys Condens Matter* (2019) 31:315103. doi:10.1088/1361-648x/ab1df6
49. Fomin YD. The phase diagram of a two-dimensional core-softened system with purely repulsive monotonic potential. *Phys Stat Mech Appl* (2021) 565: 125519. doi:10.1016/j.physa.2020.125519
50. Li B, Xiao X, Wang S, Wen W, Wang Z. Real-space mapping of the two-dimensional phase diagrams in attractive colloidal systems. *Phys Rev X* (2019) 9:031032. doi:10.1103/physrevx.9.031032
51. Zhu X, Truskett TM, Bonnecaze RT. Phase diagram for two-dimensional layer of soft particles. *Soft Matter* (2019) 15:4162–9. doi:10.1039/c9sm00333a
52. Dudalov DE, Fomin YD, Tsiok EN, Ryzhov VN. How dimensionality changes the anomalous behavior and melting scenario of a core-softened potential system? *Soft Matter* (2014) 10:4966–76. doi:10.1039/c4sm00124a
53. Kryuchkov NP, Yurchenko SO, Fomin YD, Tsiok EN, Ryzhov VN. Complex crystalline structures in a two-dimensional core-softened system. *Soft Matter* (2018) 14:2152–62. doi:10.1039/c7sm02429k
54. Padilla LA, Ramírez-Hernández A. Phase behavior of a two-dimensional core-softened system: new physical insights. *J Phys Condens Matter* (2020a) 32: 275103. doi:10.1088/1361-648x/ab7e5c
55. Padilla LA, Ramírez-Hernández A. Phase diagrams of simple models of colloidal nanocrystals in two dimensions. *J Phys Mater* (2020b) 4:015006. doi:10.1088/2515-7639/abc7ed
56. Harth K, Stannarius R. Topological point defects of liquid crystals in quasi-two-dimensional geometries. *Front Physiol* (2020) 8:112. doi:10.3389/fphy.2020.00112
57. Hogan BT, Kovalska E, Craciun MF, Baldycheva A. 2D material liquid crystals for optoelectronics and photonics. *J Mater Chem C* (2017) 5:11185–95. doi:10.1039/c7tc02549a
58. Al-Zangana S, Iliut M, Turner M, Vijayaraghavan A, Dierking I. Properties of a thermotropic nematic liquid crystal doped with graphene oxide. *Adv Optical Mater* (2016) 4:1541. doi:10.1002/adom.201600351
59. Lavrič M, Cordoyiannis G, Tzitzios V, Lelidis I, Kralj S, Nounesis G, et al. Blue phase stabilization by CoPt-decorated reduced-graphene oxide nanosheets dispersed in a chiral liquid crystal. *J Appl Phys* (2020) 127:095101. doi:10.1063/1.5141930
60. Wang L, Urbas AM, Li Q. Nature-inspired emerging chiral liquid crystal nanostructures: from molecular self-assembly to DNA mesophase and nanocolloids. *Adv Mater* (2020) 32:1801335. doi:10.1002/adma.201801335
61. Li P, Wong M, Zhang X, Yao H, Ishige R, Takahara A, et al. Tunable lyotropic photonic liquid crystal based on graphene oxide. *ACS Photonics* (2014) 1: 79–86. doi:10.1021/ph400093c
62. Oaki Y. Intercalation and flexibility chemistries of soft layered materials. *Chem Commun* (2020) 56:13069–81. doi:10.1039/d0cc05931e
63. Querejeta-Fernández A, Chauve G, Methot M, Bouchard J, Kumacheva E. Chiral plasmonic films formed by gold nanorods and cellulose nanocrystals. *J Am Chem Soc* (2014) 136:4788–93. doi:10.1021/ja501642p
64. Atorf B, Funck T, Hegmann T, Kempter S, Liedl T, Martens K, et al. Liquid crystals and precious metal: from nanoparticle dispersions to functional plasmonic nanostructures. *Liq Cryst* (2017) 44:1929–47. doi:10.1080/02678292.2017.1359692
65. Boles MA, Engel M, Talapin DV. Self-assembly of colloidal nanocrystals: from intricate structures to functional materials. *Chem Rev* (2016) 116:11220–89. doi:10.1021/acs.chemrev.6b00196
66. Bedolla Pantoja MA, Abbott NL. Surface-controlled orientational transitions in elastically strained films of liquid crystal that are triggered by vapors of toluene. *ACS Appl Mater Interfaces* (2016) 8:13114–22. doi:10.1021/acsami.6b02139
67. Ishihara S, Lee JJ, Kek KJ. Detection of volatile organic chemicals by using liquid crystals. *IET Mater Circuits Devices Ser* (2019) 68:315–40. doi:10.1049/pbcs068g_ch19
68. Shibaev PV, Wenzlick M, Murray J, Tantillo A, Howard-Jennings J. Rebirth of liquid crystals for sensoric applications: environmental and gas sensors. *Adv Condens Matter Phys* (2015) 2015:729186. doi:10.1155/2015/729186
69. Chari K, Rankin CM, Johnson DM, Blanton TN, Capurso RG. Single-substrate cholesteric liquid crystal displays by colloidal self-assembly. *Appl Phys Lett* (2006) 88:043502. doi:10.1063/1.2167398
70. Draude AP, Kalavalapalli TY, Iliut M, McConnell B, Dierking I. Stabilization of liquid crystal blue phases by carbon nanoparticles of varying dimensionality. *Nanoscale Adv* (2020) 2:2404–9. doi:10.1039/d0na00276c
71. Ge Z, Rao L, Gauza S, Wu S-T. Modeling of blue phase liquid crystal displays. *J Disp Technol* (2009) 5:250–6. doi:10.1109/jdt.2009.2022849
72. Kakiuchida H, Ogiwara A. Smart windows. *IET Mater Circuits Devices Ser* (2019) 68:341–59. doi:10.1049/pbcs068g_ch20
73. Stratford K, Henrich O, Lintuvuori JS, Cates ME, Marenduzzo D. Self-assembly of colloid-cholesteric composites provides a possible route to switchable optical materials. *Nat Commun* (2014) 5:3954. doi:10.1038/ncomms4954
74. Ng AY, See CW, Somekh MG. Quantitative optical microscope with enhanced resolution using a pixelated liquid crystal spatial light modulator. *J Microsc* (2004) 214:334–40. doi:10.1111/j.0022-2720.2004.01323.x
75. Bergamini S, Darquié B, Jones M, Jacubowiez L, Browaeys A, Grangier P. Holographic generation of microtrap arrays for single atoms by use of a programmable phase modulator. *J Opt Soc Am B* (2004) 21:1889–94. doi:10.1364/josab.21.001889
76. Smith PJ, Taylor CM, Shaw AJ, McCabe EM. Programmable array microscopy with a ferroelectric liquid-crystal spatial light modulator. *Appl Optic* (2000) 39: 2664–9. doi:10.1364/ao.39.002664
77. Capeluto MG, La Mela C, Iemmi C, Marconi MC. Scanning mechanism based on a programmable liquid crystal display. *Optic Commun* (2004) 232:107–13. doi:10.1016/j.optcom.2003.12.080
78. Bunning TJ, Natarajan LV, Tondiglia VP, Sutherland RL. Holographic polymer-dispersed liquid crystals (H-PDLCs). *Annu Rev Mater Sci* (2000) 30:83–115. doi:10.1146/annurev.matsci.30.1.83
79. Qi J, Li L, De Sarkar M, Crawford GP. Nonlocal photopolymerization effect in the formation of reflective holographic polymer-dispersed liquid crystals. *J Appl Phys* (2004) 96:2443–50. doi:10.1063/1.1778480
80. Bowley CC, Kossyrev PA, Crawford GP, Faris S. Variable-wavelength switchable Bragg gratings formed in polymer-dispersed liquid crystals. *Appl Phys Lett* (2001) 79:9–11. doi:10.1063/1.1383566

81. Chen C-Y, Pan C-L, Hsieh C-F, Lin Y-F, Pan R-P. Liquid-crystal-based terahertz tunable Lyot filter. *Appl Phys Lett* (2006) 88:101107. doi:10.1063/1.2181271
82. Peierls R. Surprises in Theoretical Physics. Princeton, NJ: Princeton University Press (1979). p 85–91.
83. Ryzhov VN, Gaiduk EA, Tareyeva EE, Fomin YD, Tsiok EN. The Berezinskii-Kosterlitz-Thouless transition and melting scenarios of two-dimensional systems. *Phys Part Nucl* (2020) 51:786–90. doi:10.1134/s1063779620040632
84. Kosterlitz JM, Thouless DJ. Ordering, metastability and phase transitions in two-dimensional systems. *J Phys C Solid State Phys* (2002) 6:1181–203. doi:10.1088/0022-3719/6/7/010
85. Bak P, Paczuski M. Chapter 1 - Principles of Phase Transitions in Two-dimensional Systems. In: DA King DP. Woodruff, editors *Phase transitions and adsorbate restructuring at metal surfaces*. Amsterdam, Netherlands: Elsevier. The Chemical Physics of Solid Surfaces (1994), Vol. 7. p. 1–33. doi:10.1016/B978-0-444-81924-6.50006-0
86. Mermin ND. Crystalline order in two dimensions. *Phys Rev* (1968) 176:250–4. doi:10.1103/PhysRev.176.250
87. Kumari S, Ye F, Podgornik R. Ordering of adsorbed rigid rods mediated by the Boussinesq interaction on a soft substrate. *J Chem Phys* (2020) 153:144905. doi:10.1063/5.0022556
88. Wang W, Lin J-T, Su Y-S, I L. Micro-structure and motion of two-dimensional dense short spherocylinder liquids. *J Phys Condens Matter* (2018) 30:125102. doi:10.1088/1361-648x/aaaf03
89. Batys P, Nosek M, Weroński P. Structure analysis of layer-by-layer multilayer films of colloidal particles. *Appl Surf Sci* (1999) 332:318–27. doi:10.1016/j.apsusc.2015.01.171
90. Jalili R, Aboutalebi SH, Esrafilzadeh D, Konstantinov K, Moulton SE, Razal JM, et al. Organic solvent-based graphene oxide liquid crystals: a facile route toward the next generation of self-assembled layer-by-layer multifunctional 3D architectures. *ACS Nano* (2013) 7:3981–90. doi:10.1021/nn305906z
91. Jasieniak JJ, MacDonald BI, Mulvaney P. Nanocrystals, Layer-by-Layer Assembly, and Photovoltaic Devices. Wiley (2015). p. 357–94. Chap. 14. doi:10.1002/9781118867204.ch14
92. Gay JG, Berne BJ. Modification of the overlap potential to mimic a linear site-site potential. *J Chem Phys* (1981) 74:3316–9. doi:10.1063/1.441483
93. Memmer R, Kuball H-G, Schönhofer A. Computer simulation of chiral liquid crystal phases. I. The polymorphism of the chiral Gay-Berne fluid. *Liq Cryst* (1993) 15:345–60. doi:10.1080/02678299308029136
94. Memmer R, Janssen F. Computer simulation of chiral liquid crystal phases IX. Chiral induction in guest-host systems—calculation of the helical twisting power. *Z Naturforsch* (2014) 54:747–54. 10.1515/zna-1999-1212
95. Luckhurst GR, Stephens RA, Phippen RW. Computer simulation studies of anisotropic systems. XIX. Mesophases formed by the Gay-Berne model mesogen. *Liq Cryst* (1990) 8:451–64. doi:10.1080/02678299008047361
96. Satoh K, Mita S, Kondo S. Monte Carlo simulations on mesophase formation using dipolar Gay-Berne model. *Liq Cryst* (1996) 20:757–63. doi:10.1080/02678299608033169
97. Luckhurst GR, Luckhurst GR, Stephens RA, Phippen RW. The Gay-Berne mesogen: a paradigm shift? *Liq Cryst* (2006) 33:1389–405. doi:10.1080/02678290601140456
98. Bartsch H, Bier M, Dietrich S. Interface structures in ionic liquid crystals. *Soft Matter* (2019) 15:4109–26. doi:10.1039/c9sm00062c
99. Salgado-Blanco D, Díaz-Herrera E, Mendoza CI. Effect of the anchoring strength on the phase behaviour of discotic liquid crystals under face-on confinement. *J Phys Condens Matter* (2019) 31:105101. doi:10.1088/1361-648x/aaf843
100. Nozawa T, Brumby PE, Ayuba S, Yasuoka K. Ordering in clusters of uniaxial anisotropic particles during homogeneous nucleation and growth. *J Chem Phys* (2019) 150:054903. doi:10.1063/1.5064410
101. Segatti A, Snarski M, Veneroni M. Equilibrium configurations of nematic liquid crystals on a torus. *Phys Rev E—Stat Nonlinear Soft Matter Phys* (2014) 90:012501. doi:10.1103/PhysRevE.90.012501
102. Cañeda-Guzmán E, Moreno-Razo JA, Díaz-Herrera E, Sambriski EJ. Molecular aspect ratio and anchoring strength effects in a confined Gay-Berne liquid crystal. *Mol Phys* (2014) 112:1149–59. doi:10.1080/00268976.2013.837206
103. Margola T, Satoh K, Saielli G. Comparison of the mesomorphic behaviour of 1:1 and 1:2 mixtures of charged Gay-Berne GB(4.4,20.0,1,1) and Lennard-Jones particles. *Crystals* (2018) 8:3711–5.doi:10.3390/cryst8100371
104. de Miguel E, Martín del Río E, Blas FJ. Stability of smectic phases in the Gay-Berne model. *J Chem Phys* (2004) 121:11183–94. doi:10.1063/1.1810472
105. Cienega-Cacerez O, Moreno-Razo JA, Díaz-Herrera E, Sambriski EJ. Phase equilibria, fluid structure, and diffusivity of a discotic liquid crystal. *Soft Matter* (2014) 10:3171–82. doi:10.1039/c3sm52301b
106. Cienega-Cacerez O, García-Alcántara C, Moreno-Razo JA, Díaz-Herrera E, Sambriski EJ. Induced stabilization of columnar phases in binary mixtures of discotic liquid crystals. *Soft Matter* (2016) 12:1295–312. doi:10.1039/c5sm01959a
107. Caprion D, Bellier-Castella L, Ryckaert JP. Influence of shape and energy anisotropies on the phase diagram of discotic molecules. *Phys Rev E—Stat Nonlinear Soft Matter Phys* (2003) 67:041703. doi:10.1103/PhysRevE.67.041703
108. Bates MA, Luckhurst GR. Computer simulation studies of anisotropic systems. XXVI. Monte Carlo investigations of a Gay-Berne discotic at constant pressure. *J Chem Phys* (1996) 104:6696–709. doi:10.1063/1.471387
109. Patti A, Belli S, van Roij R, Dijkstra M. Relaxation dynamics in the columnar liquid crystal phase of hard platelets. *Soft Matter* (2011) 7:3533–45. doi:10.1039/c0sm01265c
110. Thompson IR, Coe MK, Walker AB, Ricci M, Roscioni OM, Zannoni C. Microscopic origins of charge transport in triphenylene systems. *Phys Rev Mater* (2018) 2:064601. doi:10.1103/physrevmaterials.2.064601
111. Cammidge AN, Bushby RJ. Handbook of liquid crystals, Synthesis and Structural Features. Chap. VII, Vol. 2B. Weinheim, Germany: Oxford University Press (1998). p. 703–5. doi:10.1002/9783527620623.ch4
112. Phillips TJ, Jones JC, McDonnell DG. On the influence of short range order upon the physical properties of triphenylene nematic discogens. *Liq Cryst* (1993) 15:203–15. doi:10.1080/02678299308031951
113. Kundu P, Mishra P, Jaiswal A, Ram J. Structures and phase transition in a two-dimensional system of Gay-Berne molecules. *J Mol Liq* (2019) 296:111769. doi:10.1016/j.molliq.2019.111769
114. Kundu P, Mishra P. Simulation of Gay-Berne liquid crystal molecules confined to a plane. *AIP Conf Proc* (2020) 2220:130016. doi:10.1063/5.0001132
115. Jordens S, Isa L, Usov I, Mezzenga R. Non-equilibrium nature of two-dimensional isotropic and nematic coexistence in amyloid fibrils at liquid interfaces. *Nat Commun* (2013) 4:1917. doi:10.1038/ncomms2911
116. Zheng Z, Wang F, Han Y. Glass transitions in quasi-two-dimensional suspensions of colloidal ellipsoids. *Phys Rev Lett* (2011) 107:065702. doi:10.1103/PhysRevLett.107.065702
117. Cortes LB, Gao Y, Dullens RP, Aarts DG. Colloidal liquid crystals in square confinement: isotropic, nematic and smectic phases. *J Phys Condens Matter* (2017) 29:064003. doi:10.1088/1361-648X/29/6/064003
118. Gârlea IC, Mulder P, Alvarado J, Dammone O, Aarts DG, Lettinga MP, et al. Finite particle size drives defect-mediated domain structures in strongly confined colloidal liquid crystals. *Nat Commun* (2016) 7:12112. doi:10.1038/ncomms12112
119. de las Heras D, Velasco E, Mederos L. Topological defects in a two-dimensional liquid crystal confined in a circular nanocavity. *Phys Rev E-Stat Nonlinear Soft Matter Phys* (2009) 79:061703. doi:10.1103/PhysRevE.79.061703
120. González-Pinto M, Martínez-Ratón Y, Velasco E. Liquid-crystal patterns of rectangular particles in a square nanocavity. *Phys Rev E-Stat Nonlinear Soft Matter Phys* (2013) 88:032506. doi:10.1103/PhysRevE.88.032506
121. Yao X, Zhang H, Chen JZY. Topological defects in two-dimensional liquid crystals confined by a box. *Phys Rev E* (2018) 97:052707. doi:10.1103/PhysRevE.97.052707
122. Walton J, Mottram NJ, McKay G. Nematic liquid crystal director structures in rectangular regions. *Phys Rev E* (2018) 97:022702. doi:10.1103/PhysRevE.97.022702
123. Foulaadvand ME, Yarifard M. Two-dimensional system of hard ellipses: a molecular dynamics study. *Phys Rev E-Stat Nonlinear Soft Matter Phys* (2013) 88:052504. doi:10.1103/PhysRevE.88.052504

124. de las Heras D, Velasco E. Domain walls in two-dimensional nematics confined in a small circular cavity. *Soft Matter* (2014) 10:1758–66. doi:10.1039/c3sm52650j
125. Geigenfeind T, Rosenzweig S, Schmidt M, de Las Heras D. Confinement of two-dimensional rods in slit pores and square cavities. *J Chem Phys* (2015) 142:174701. doi:10.1063/1.4919307
126. Gârlea IC, Mulder BM. Defect structures mediate the isotropic-nematic transition in strongly confined liquid crystals. *Soft Matter* (2015) 11: 608–14. doi:10.1039/c4sm02087a
127. Sidky H, Whitmer JK. Elastic properties of common Gay-Berne nematogens from density of states (DOS) simulations. *Liq Cryst* (2016) 43:2285–99. doi:10.1080/02678292.2016.1201869
128. de Miguel E, Rull LF, Chalam MK, Gubbins KE. Liquid crystal phase diagram of the Gay-Berne fluid. *Mol Phys* (1991) 74:405–24. doi:10.1080/00268979100102321
129. Brown JT, Allen MP, Martín del Río E, de Miguel E. Effects of elongation on the phase behavior of the Gay-Berne fluid. *Phys Rev E* (1998) 57:6685–99. doi:10.1103/physreve.57.6685
130. Bates MA, Luckhurst GR. Computer Simulation of Liquid Crystal Phases Formed by Gay-Berne Mesogens. Liquid Crystals I. Berlin, Heidelberg: Springer Berlin Heidelberg (1999). p. 65–137. doi:10.1007/3-540-68305-4_3
131. de Miguel E. Reexamining the phase diagram of the Gay-Berne fluid. *Mol Phys* (2002) 100:2449–59. doi:10.1080/00268970210121605
132. de Miguel E, Vega C. The global phase diagram of the Gay-Berne model. *J Chem Phys* (2002) 117:6313–22. doi:10.1063/1.1504430
133. Allen MP, Warren MA, Wilson MR, Sauron A, Smith W. Molecular dynamics calculation of elastic constants in Gay-Berne nematic liquid crystals. *J Chem Phys* (1996) 105:2850–8. doi:10.1063/1.472147
134. Joshi AA, Whitmer JK, Guzmán O, Abbott NL, de Pablo JJ. Measuring liquid crystal elastic constants with free energy perturbations. *Soft Matter* (2014) 10: 882–93. doi:10.1039/c3sm51919h
135. Humpert A, Allen MP. Elastic constants and dynamics in nematic liquid crystals. *Mol Phys* (2015) 113:2680–92.doi:10.1080/00268976.2015.1067730
136. Stillings C, Martin E, Steinhart M, Pettau R, Paraknowitsch J, Geuss M, et al. Nanoscaled discotic liquid crystal/polymer systems: confinement effects on morphology and thermodynamics. *Mol Cryst Liq Cryst* (2008) 495:285–292. doi:10.1080/15421400802430349
137. Caprion D. Discotic molecules in cylindrical nanopores: a Monte Carlo study. *Eur Phys J E Soft Matter* (2009) 28:305–13.doi:10.1140/epje/i2008-10412-6
138. Busselez R, Cerclier CV, Ndao M, Ghoufi A, Lefort R, Morineau D. Discotic columnar liquid crystal studied in the bulk and nanoconfined states by molecular dynamics simulation. *J Chem Phys* (2014) 141:134902. doi:10.1063/1.4896052
139. Sentker K, Zantop AW, Lippmann M, Hofmann T, Seeck OH, Kityk AV, et al. Quantized self-assembly of discotic rings in a liquid crystal confined in nanopores. *Phys Rev Lett* (2018) 120:067801. doi:10.1103/PhysRevLett.120.067801
140. Salgado-Blanco D, Mendoza CI, Chávez-Rojo MA, Moreno-Razo JA, Díaz-Herrera E. Influence of anchoring in the phase behaviour of discotic liquid crystals. *Soft Matter* (2018) 14:2846–59. doi:10.1039/c7sm02311a
141. Rull LF, Romero-Enrique JM. Nanodrops of discotic liquid crystals: a Monte Carlo study. *Langmuir* (2017a) 33:11779–87. doi:10.1021/acs.langmuir.7b02347
142. Humpert A, Masters AJ, Allen MP. Orientational dynamics in nematic liquid crystals. *Eur Phys J Spec Top* (2016) 225:1723–32. doi:10.1140/epjst/e2016-60118-1
143. Allen MP. Molecular simulation of liquid crystals. *Mol Phys* (2019) 117: 2391–417. doi:10.1080/00268976.2019.1612957
144. Rull LF, Romero-Enrique JM. Computer simulation study of the nematic-vapour interface in the Gay-Berne model. *Mol Phys* (2017b) 115:1214–24. doi:10.1080/00268976.2016.1274437
145. Wilson MR. Progress in computer simulations of liquid crystals. *Int Rev Phys Chem* (2005) 24:421–55. doi:10.1080/01442350500361244
146. Mishra P, Ram J. Effect of shape anisotropy on the phase diagram of the Gay-Berne fluid. *Eur Phys J E Soft Matter* (2005) 17:345–51.doi:10.1140/epje/i2005-10014-x
147. Berne BJ, Pechukas P. Gaussian model potentials for molecular interactions. *J Chem Phys* (1972) 56:4213–6. doi:10.1063/1.1677837
148. Cleaver DJ, Care CM, Allen MP, Neal MP. Extension and generalization of the Gay-Berne potential. *Phys Rev E* (1996) 54:559–67. doi:10.1103/physreve.54.559
149. Antypov D, Cleaver DJ. The effect of spherical additives on a liquid crystal colloid. *J Phys Condens Matter* (2004) 16:S1887–S1900. doi:10.1088/0953-8984/16/19/002
150. Frenkel D, Smit B, eds. Understanding Molecular Simulation: From Algorithms to Applications. 1st ed. Orlando, FL: Academic Press, Inc. (1996).
151. Gruhn T, Schoen M. Microscopic structure of molecularly thin confined liquid-crystal films. *Phys Rev E* (1997) 55:2861–75. doi:10.1103/physreve.55.2861
152. de Gennes PG. The Physics of Liquid Crystals. Oxford, United Kingdom: Clarendon Press (1993).
153. Cuesta JA, Frenkel D. Monte Carlo simulation of two-dimensional hard ellipses. *Phys Rev* (1990) 42:2126–36. doi:10.1103/physreva.42.2126
154. Illing B, Fritschi S, Kaiser H, Klix CL, Maret G, Keim P. Mermin-Wagner fluctuations in 2D amorphous solids. *Proc Natl Acad Sci U S A* (2017) 114: 1856–61. doi:10.1073/pnas.1612964114
155. Flenner E, Szamel G. Fundamental differences between glassy dynamics in two and three dimensions. *Nat Commun* (2015) 6:7392. doi:10.1038/ncomms8392
156. Verbeck B. 2D materials: amorphous and fluctuating. *Nat Phys* (2017) 13:205. doi:10.1038/nphys4065
157. Wegner FJ. Corrections to scaling laws. *Phys Rev B* (1972) 5:4529–36. doi:10.1103/physrevb.5.4529
158. Armas-Pérez JC, Quintana HJ, Chapela GA. Liquid-vapor equilibrium and interfacial properties of square wells in two dimensions. *J Chem Phys* (2013) 138:044508. doi:10.1063/1.4775342
159. Panagiotopoulos AZ. Direct determination of phase coexistence properties of fluids by Monte Carlo simulation in a new ensemble. *Mol Phys* (1987) 61: 813–26. doi:10.1080/00268978700101491
160. Bates MA, Frenkel D. Nematic-isotropic transition in polydisperse systems of infinitely thin hard platelets. *J Chem Phys* (1999) 110:6553–9. doi:10.1063/1.478558
161. Bianchi E, Tartaglia P, Zaccarelli E, Sciortino F. Theoretical and numerical study of the phase diagram of patchy colloids: ordered and disordered patch arrangements. *J Chem Phys* (2008) 128:144504. doi:10.1063/1.2888997
162. Kofke DA. Gibbs-Duhem integration: a new method for direct evaluation of phase coexistence by molecular simulation. *Mol Phys* (1993) 78:1331–6. doi:10.1080/00268979300100881
163. Ferrenberg AM, Swendsen RH. New Monte Carlo technique for studying phase transitions. *Phys Rev Lett* (1988) 61:2635–8. doi:10.1103/PhysRevLett.61.2635
164. Frenkel D, Ladd AJC. New Monte Carlo method to compute the free energy of arbitrary solids. Application to the fcc and hcp phases of hard spheres. *J Chem Phys* (1984) 81:3188–93. doi:10.1063/1.448024
165. Selinger JV. Introduction to the Theory of Soft Matter: From Ideal Gases to Liquid Crystals. Cham, Switzerland: Springer (2016). p 99.
166. Robinson M, Luo C, Farrell PE, Erban R, Majumdar A. From molecular to continuum modelling of bistable liquid crystal devices. *Liq Cryst* (2017) 44: 2267–84. doi:10.1080/02678292.2017.1290284
167. Guillamat P, Ignés-Mullol J, Sagués F. Control of active liquid crystals with a magnetic field. *Proc Natl Acad Sci U S A* (2016) 113:5498–502. doi:10.1073/pnas.1600339113
168. Wågberg L, Erlandsson J. The use of layer-by-layer self-assembly and nanocellulose to prepare advanced functional materials. *Adv Mater* (2020) 32:2001474. doi:10.1002/adma.202001474
169. Konopelnyk OI, Aksimentyeva OI, Horbenko YY, Poliovyi DO, Opaynych IY. Layer-by-layer assembly and thermal sensitivity of poly(3,4-ethylenedioxythiophene) nanofilms. *Mol Cryst Liq Cryst* (2016) 640: 158–64. doi:10.1080/15421406.2016.1257327
170. Amabilino DB. Supramolecular Chemistry at Surfaces (the Royal Society of Chemistry), chapter 6. Layer-by-layer growth. *Monographs Supramol Chem* (2016):303–39. doi:10.1039/9781782622161-00303
171. Lee T, Min SH, Gu M, Jung YK, Lee W, Lee JU, et al. Layer-by-Layer assembly for graphene-based multilayer nanocomposites: synthesis and applications. *Chem Mater* (2015) 27:3785–96. doi:10.1021/acs.chemmater.5b00491

172. Tjipto E, Cadwell KD, Quinn JF, Johnston AP, Abbott NL, Caruso F. Tailoring the interfaces between nematic liquid crystal emulsions and aqueous phases via layer-by-layer assembly. *Nano Lett* (2006) 6:2243–8. doi:10.1021/nl061604p
173. Richardson JJ, Björnmalm M, Caruso F. Multilayer assembly. Technology-driven layer-by-layer assembly of nanofilms. *Science* (2015) 348:aaa2491. doi:10.1126/science.aaa2491
174. Zhang X, Chen H, Zhang H. Layer-by-layer assembly: from conventional to unconventional methods. *Chem Commun* (2007) 1395–405. doi:10.1039/b615590a
175. Ariga K, Hill JP, Ji Q. Layer-by-layer assembly as a versatile bottom-up nanofabrication technique for exploratory research and realistic application. *Phys Chem Chem Phys* (2007) 9:2319–40. doi:10.1039/b700410a
176. Tian W, VahidMohammadi A, Wang Z, Ouyang L, Beidaghi M, Hamedi MM. Layer-by-layer self-assembly of pillared two-dimensional multilayers. *Nat Commun* (2019) 10:2558. doi:10.1038/s41467-019-10631-0
177. Wang AC, Pereira I, Ferreira C, Veiga F, Fakhrullin R. Chapter 1.4 - Layer-by-Layer Assembly for Nanoarchitectonics. In: K Ariga M. Aono, editors. Norwich, NY: William Andrew Publishing, Micro and Nano Technologies (2019). p. 89–121. doi:10.1016/B978-0-12-813341-5.00005-X
178. Zhao S, Caruso F, Dähne L, Decher G, De Geest BG, Fan J, et al. The future of layer-by-layer assembly: a tribute to ACS Nano associate editor Helmuth Möhwald. *ACS Nano* (2019) 13:6151–69. doi:10.1021/acsnano.9b03326
179. Oliveira DA, Gasparotto LHS, Siqueira JR, Jr. Processing of nanomaterials in Layer-by-Layer films: potential applications in (bio)sensing and energy storage. *An Acad Bras Cienc* (2019) 91:e20181343. doi:10.1590/0001-3765201920181343
180. Moon G, Jang W, Son I, Cho H, Park Y, Lee J. Fabrication of new liquid crystal device using layer-by-layer thin film process. *Processes* (2018) 6:108. doi:10.3390/pr6080108

Conflict of Interest: The authors declare that the research was conducted in the absence of any commercial or financial relationships that could be construed as a potential conflict of interest.

frontiers in Physics

ORIGINAL RESEARCH
published: 17 March 2021
doi: 10.3389/fphy.2021.636149

Thermodynamic and Mechanical Properties of DMPC/Cholesterol Mixed Monolayers at Physiological Conditions

Alan Bañuelos-Frias, Victor Manuel Castañeda-Montiel, Edgar Rogelio Alvizo-Paez, Emmanuel Antonio Vazquez-Martinez, Eduardo Gomez and Jaime Ruiz-Garcia**

Biological Physics Laboratory, Physics Institute, Universidad Autónoma de San Luis Potosí, San Luis Potosí, Mexico

One of the main known effects of cholesterol is to rigidify the cell membrane throughout the so-called condensing effect. Although many studies have been done in mixtures of cholesterol with different membrane lipids, there are not many studies in a wide concentration range of cholesterol or at physiological conditions. In this work, we studied mixtures of DMPC/Cholesterol monolayers to determine the effect of cholesterol, from very low to physiological concentrations and two pHs. We use a Langmuir balance and Brewster angle microscopy to study their thermodynamic behavior at 37.0 ± 0.1°C at the air/solution interface. From the analysis of the (π–A) isotherms, we determined the excess area and the compressibility elastic modulus to determine the monolayers mechanical properties. Surprisingly, we found three main effects of cholesterol: The first one is a fluidization effect of the monolayer at all cholesterol concentrations. The second effect is the so-called condensing effect that appears due to the non-ideality of the mixture. The third effect is a stiffness of the monolayer as the cholesterol concentration increases. These effects are stronger in pure water, pH ≈ 6.6, than on buffer at physiological pH = 7.4. We also found that all mixtures are thermodynamically stable at all concentrations at a surface pressure of 30.1 ± 1.6 and 27.4 ± 3.2 mN/m in pure water and buffer, respectively. Furthermore, we compared this stability with a fatty acid monolayer that shows a much lower surface pressure equilibrium value that DMPC or its mixtures with cholesterol, indicating a possibly reason why double chain lipids are better than single chain lipids to made up the cell membrane.

Keywords: cholesterol, DMPC, model membranes, brewster angle microscopy, Langmuir monolayers, isotherms, mechanical properties

OPEN ACCESS

Edited by:
Enrique Hernandez-Lemus, Instituto Nacional de Medicina Genómica (INMEGEN), Mexico

Reviewed by:
Luciano Caseli, Federal University of São Paulo, Brazil
Amir Darío Maldonado, Universidad Tecnológica del Sur de Sonora, Mexico

****Correspondence:***
Eduardo Gomez
egomez@mail.ifisica.uaslp.mx
Jaime Ruiz-Garcia
jaime@mail.ifisica.uaslp.mx

Specialty section:
This article was submitted to Soft Matter Physics, a section of the journal Frontiers in Physics

Received: *01 December 2020*
Accepted: *05 February 2021*
Published: *17 March 2021*

Citation:
Bañuelos-Frias A, Castañeda-Montiel VM, Alvizo-Paez ER, Vazquez-Martinez EA, Gomez E and Ruiz-Garcia J (2021) Thermodynamic and Mechanical Properties of DMPC/Cholesterol Mixed Monolayers at Physiological Conditions. Front. Phys. 9:636149. doi: 10.3389/fphy.2021.636149

INTRODUCTION

Cholesterol is a very important component in all membranes of mammalian cells and it is critical to human health: It is known that cholesterol is responsible for the modulation of physical properties of cell membranes, because the bulky molecular structure of cholesterol interferes with the movement of the phospholipid tails [1]. It constitutes up to 40% of the plasma membrane in some type of cells

[2] and the cholesterol concentration seems to be involved in the regulation of microphase separation (lipid rafts), rigidity, membrane thickness and permeability [3–5].

One effect of adding cholesterol is to reduce the L_β/L_α phase transition temperature, and it removes completely the transition at 50% of cholesterol concentration [6], by inducing the formation of an intermediate phase known as the liquid crystalline ordered or liquid ordered phase [5, 7]. The transition temperatures are correlated with the chain melting temperature (0°C for some glycerophospholipids and 37°C for sphingolipids). Other effects of adding cholesterol include changes in the lipid molecule cross sectional area, the thickness of the bilayer, the orientational order of the lipids and the motion of the hydrocarbon chains [1, 3, 5].

Cholesterol mixed with phospholipids can form oligomeric chemical complexes with a fundamental stoichiometry 3:2 and 6:1 phospholipids per cholesterol molecule [8, 9]. The formation of these phospholipid/cholesterol complexes produce the so-called cholesterol condensing effect [4, 7, 10, 11] where the area occupied by the molecules is decreased. As stated by the umbrella model, the lipid acyl chains and the nonpolar cholesterol part become densely packed as they share the limited space below the phospholipid head groups. At a particular concentration, the head groups cannot protect additional cholesterol molecules from contact with water and they form a separated and immiscible monohydrated cholesterol phase [12–14]. The solubility limit for cholesterol in phosphatidilcholines (PC) bilayers is known to be around 66% [7, 10, 12].

Recent monolayer studies of the interaction of phospholipids and cholesterol have shown that the molecular area of the mixture is typically smaller than the weighted molecular areas of the pure components [4, 15, 16]. It was found that cholesterol interacts preferentially with phospholipids containing fully saturated chains and this interaction decreases significantly with unsaturated chains [1, 5, 15, 17]. Cholesterol interacts more strongly with sphingolipids than with phosphatidylcholines of similar chain length [8, 11, 17, 18]. Monolayers mixtures of phosphatidilcholines and cholesterol have a higher collapse pressure (π_c) than monolayers of single components, indicating that a mixed monolayer is more stable [16, 19, 20].

Model systems with only a few components have been extensively used to study the properties of biological membranes [8, 17, 19]. Giant unilamellar vesicles have been used to study mechanical properties and interactions between lipids and DNA, peptide and proteins in a simple model system composed of a single phospholipid bilayer [21, 22]. Langmuir monolayers have also been used as 2D model systems to study interactions present in biomembranes [3, 18], since the physicochemical and mechanical characterization of the monolayers can be obtained from surface pressure-area (π–A) measurements [17, 23, 24]. Furthermore, phase transitions, morphologies and textures can be obtained by combining additional characterization techniques such as neutron and X-ray scattering, polarized fluorescence, Brewster angle microscopy (BAM) or atomic force microscopy (AFM) [12, 18, 25].

Phosphatidylcholines play an important role in cell membranes since they represent more than 50% of the lipids of the plasma membrane in most eukaryotic cells [26]. The interaction of DMPC and other phosphatidylcholines of different acyl chain length and saturation degree with cholesterol has been studied at pH 6.6 and 24°C, and found that cholesterol cannot condense in the same way unsaturated lipids as it does saturated lipids, due to the kinks of the double bonds on the acyl chains [27]. In a similar study, at different temperatures from 10–30°C, it was found that acyl chain asymmetry modifies the interfacial elasticity of the lipid monolayers [28]. The condensation effect in DMPC and DPPC induced by different sterols at 23°C has been determined by mean of the analysis of the excess free energy; it was found that the mixture of phosphatidylcholines with cholesterol produced the most stable monolayers in comparison when cholesterol is replaced by ergosterol or lanosterol [29]. The effect of the subphase pH on the condensation effect in mixed monolayers of DPPC/cholesterol in a wide range of cholesterol fraction (10–90%) has been studied by Gong et al, at 25°C. They found that the monolayer is more stable at neutral pH and at 60% of cholesterol fraction [11]. Kim et al. observed that at 23°C a very low fraction of cholesterol (≈0.2%) modifies dramatically the morphology and the dynamic properties of a DPPC monolayer by reducing the surface viscosity due to the formation of 6:1 phospholipid/cholesterol complexes. This complexes decorates the boundaries of the DPPC lipid domains [9].

In this work, we study the interaction between DMPC and cholesterol from very low to physiological cholesterol mole fractions (0.01–0.40) and at physiological conditions of temperature, 37 ± 0.1°C and pH, ≈ 6.6 and 7.4. We use the Langmuir balance technique to study the model membrane monolayers, and we obtain the mechanical properties of the membranes from the isotherms. We show that cholesterol have three effects i) It fluidizes the monolayer at low surface pressures and at all concentrations studied, ii) When the pure condensed phase appears, it shows the so-called condensing effect, and iii) Upon increasing the concentration of cholesterol the monolayers stiffens.

EXPERIMENTAL

Materials

DMPC (1,2-Dimyristoyl-sn-glycero-3-phosphocholine, > 99%, Sigma-Aldrich, United States), Cholesterol (>99% Sigma-Aldrich, United States) and Arachidic acid (≥99% Sigma-Aldrich, United States) were used without further purification. DMPC, Cholesterol and Arachidic acid were dissolved in HPLC grade chloroform (>99%, Fermont, Mexico). Then DMPC and Cholesterol were mixed in different molar ratios (0, 0.01, 0.02, 0.03, 0.04, 0.10, 0.15, 0.20, 0.30, 0.35, 0.40, and 1.0) of cholesterol and stored at −20°C.

Methods

Langmuir-Blodgett Trough

A Langmuir-Blodgett trough (model 611, NIMA Technology LTD., Coventry, England) was used to measure the pressure-area isotherms, using a filter paper as the Wilhelmy plate for the surface pressure determination (with a precision of ±0.1 mN/m). The trough was filled with deionized water (bioresearch grade water, >18.0 MΩ-cm of resistivity, Barnstead/Thermolyne, Dubuque, Iowa, United States) and deionized water was used to prepare the pH 7.4 phosphate buffer solution. The temperature was kept at 37.0 ± 0.1°C, during the experiments in order to have human physiological temperature conditions, using a water recirculator bath (Neslab, United States). Before starting each experiment, the subphase and trough cleanliness were tested by closing the barriers and checking that the pressure sensor readings were less than 0.1 mN/m when the barriers of the Langmuir through were fully closed (and by the presence of a dark background only, observed by Brewster angle microscopy, see below). Using a 50 µl Hamilton glass microsyringe, the lipid/Cholesterol mixtures were gently deposited on the air/water interface and waited at least 30 min to allow for the evaporation of the solvent before starting each experiment. The monolayer was then compressed at 20 cm^2/min. The average area per molecule was calculated by the NIMA software based upon the average molecular weight, concentration and volume of the deposited sample.

Brewster Angle Microscope

During the compression, images of the monolayer were acquired using a Brewster Angle Microscope BAM (Nanofilm EP4, Accurion GmbH, Germany) in order to see morphologies of the monolayer and phase transitions, along the obtained isotherms in the whole surface pressure range.

Mixed Monolayer Stability Study

We studied the stability of the DMPC/cholesterol mixed monolayers by slowly compressing them up to 35 mN/m and maintaining the area per molecule constant by using the area control function of the NIMA trough software. The surface pressure was recorded for approximately 300 min, in order to determine changes in surface pressure as consequence of the monolayer relaxation until its equilibrium value. The experiments were done both in ultrapure water (pH ≈ 6.6) and in a buffer subphase at pH 7.4.

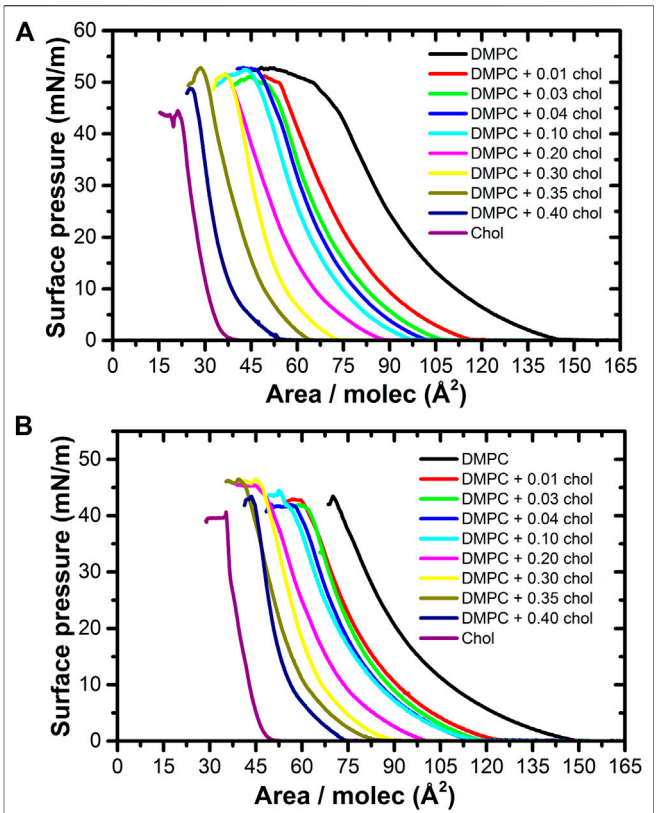

FIGURE 1 | Pressure-area isotherms of the DMPC/Cholesterol mixtures at 37.0 ± 0.1°C, on **(A)** ultrapure water at pH ≈ 6.6 and **(B)** PBS Buffer at pH 7.4 subphases. As the cholesterol mole fraction increases, the take-off pressure moves to lower areas per molecule, extending the presence of the gas phase.

RESULTS AND DISCUSSION

Isotherms

The addition of even a very small amount of cholesterol produces a considerable shift in the take-off pressure area [12]. Considering an ideal mixture behavior between DMPC and cholesterol, each isotherm should give a take-off pressure area equal to $A = X_{DMPC} A_{DMPC} + X_{Chol} A_{Chol}$, where A_i and X_i are the molecular take-off area and the mole fraction of the "i" component, respectively. Taking a 0.01 cholesterol fraction gives A = 0.99 (142) +0.01 (40) = 141.0 $Å^2$/molecule, which is much larger than the experimental value of 115.3 ± 0.1 $Å^2$/molecule obtained. In fact, this is reflected at all cholesterol concentrations studied here, as it is shown in **Figure 1**. This difference implies that cholesterol interacts strongly with the liquid expanded (LE) DMPC phase, disrupting its formation and making the gas phase to disappear at much lower areas per molecule. Here, we are taking the take-off pressure as a reference for the "disappearing" of the gas phase, although in a mixture this is not completely correct, especially when the concentration of cholesterol becomes high. However, at the higher concentration of cholesterol in the mixture, we notice that the gas phase disappeared at about 5–8 mN/m and at lower cholesterol concentrations the gas phase disappear at even lower surface pressure; therefore we are taking the take-off pressure area as a reference for this case.

So, taking the take-off pressure as a reference of the condensed phase of pure DMPC, the molecules are arranged with a particular tilt azimuthal order parameter [30]. However, the bulky cholesterol molecule disrupts this order, shifting the appearance of the pure condense phase to lower areas per molecule, as denoted by a smaller take-off area of the surface pressure, as shown in **Figure 2**. A cholesterol molecule changes the tilt angle of the DMPC molecules around it, making them

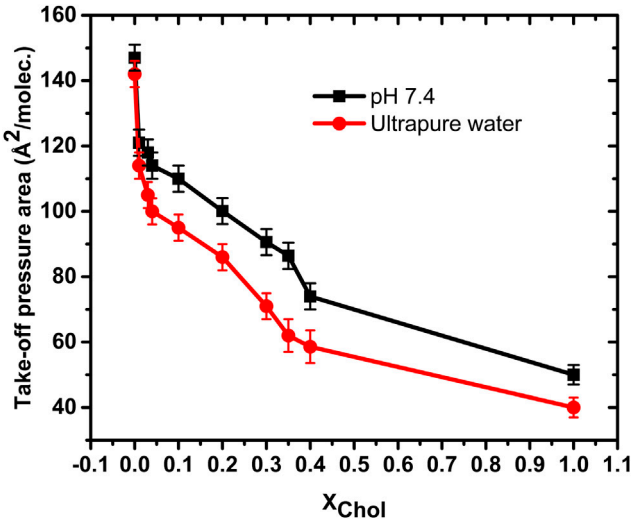

FIGURE 2 | Take-off pressure area of the studied isotherms on ultrapure water at pH ≈ 6.6 and on PBS Buffer pH 7.4 subphases. In both cases, the cholesterol delays the appearance of the pure condensed phase to lower areas/molec.

more vertical with respect to the surface, so that they occupy a smaller effective area. The LE – G coexistence region is thus extended, decreasing the take-off pressure area by more than just the difference in areas of the individual components [16, 17, 31]. Cholesterol have therefore the effect of fluidizing the monolayer, preventing the appearance of the pure condensed phase.

Figure 3 shows representative BAM images along various isotherms. The images show the coexistence of the gaseous (G) phase (darker regions) and the more condensed (LE) phase (brighter regions) at relatively low surface pressures (**Figures 3A–D**). In the pure DMPC isotherm, the G phase disappears at the take-off surface pressure, as it is noticeable absent at a pressure of 5 mN/m (**Figure 3E**), something typical for a pure component system [18, 32, 33]. As we increase the amount of cholesterol there is a residual amount of gaseous phase at the same pressure of 5 mN/m, see **Figures 3F–H** [17, 34]. But at the surface pressure of 15 mN/m, the gaseous phase disappears at all mixture concentrations but in fact it disappears even a lower surface pressures, rendering a homogenous monolayer in the condensed phase (**Figures 3I–L**). At an even higher pressure value of 32.5 mN/m, we notice the presence of small 3D crystals which become more noticeable at higher pressures particularly close to the collapse pressure (IIc). The amount and size of the 3D crystals increase with the cholesterol concentration. It has been proposed [35] that the properties of a lipid monolayer can be correlated to those of a bilayer around a surface pressure of 32–35 mN/m.

Excess Area Analysis

A way to estimate the miscibility and the interactions between molecules present in a two-component monolayer mixture is by the determination of the excess area [11, 16]:

$$A_{ex} = A_{12} - (X_1A_1 - X_2A_2) \quad (1)$$

where A_{12} is the average area per molecule of the mixture and A_i and X_i as defined above. A negative excess area indicates attractive forces between the two kind of molecules of the mixture [11, 20, 23, 31]. **Figure 4** shows the excess area determined at different surface pressures in the cholesterol range studied. The excess area is negative in all cases, indicating attractive interactions in the condensed phase between DMPC and cholesterol. At a given pressure the excess area is fairly constant at all cholesterol fractions; showing a clear effect that is noticeable even at the smaller amount of cholesterol studied. The effect is more evident at lower surface pressures, possible due to there is more space between the phospholipid molecules where cholesterol can be intercalated. As the surface pressure increases, this space is reduce making the presence of cholesterol between the lipids more difficult, until it is expelled at even higher surface pressures. The strongest attractive interaction (most negative excess area) occurs in the range of 0.30–0.40 M fraction of cholesterol. It is worth noting that this range of cholesterol concentration coincides with the physiological value in most cell membranes [11, 17, 26].

Thermodynamic Properties

Thermodynamic stability of mixed monolayers can be obtained by comparing the pure monolayer using the excess Gibbs free energy [23],

$$\Delta G_{exc} = \int_0^{\pi} [A_{12} - (x_1A_1 + x_2A_2)]d\pi \quad (2)$$

It can be noticed from **Figure 5** that the excess Gibbs-free energy for all the mixtures is negative, therefore it can be concluded that the DMPC and cholesterol molecules form a stable mixed monolayer at all conditions. The lowest energy happens again at a concentration between 30–40% of cholesterol concentration and at surface pressures of 30–40 mN/m that correspond to the values present in mammalian cell membranes [2, 26, 35].

Mechanical Properties and Equilibrium Spreading Pressure

Monolayer mechanical properties can be analyzed by calculating the isothermal compressibility or rather its inverse, the area compressibility elastic modulus given by [15, 23, 24],

$$C_s^{-1} = -A\left(\frac{d\pi}{dA}\right) \quad (3)$$

Figure 6 shows a plot of C_s^{-1} as a function of the area per molecule for different cholesterol fractions. Note that C_s^{-1} start at a very low value when the monolayer is at the coexistence region of the condensed and gaseous phases (see **Figure 3A**). In this situation, the high compressibility of the gas phase gives a low value for C_s^{-1}. The value of C_s^{-1} rises sharply at the take-off pressure area, mainly due to the compression force required to overcome the repulsive interactions of the condensed domains

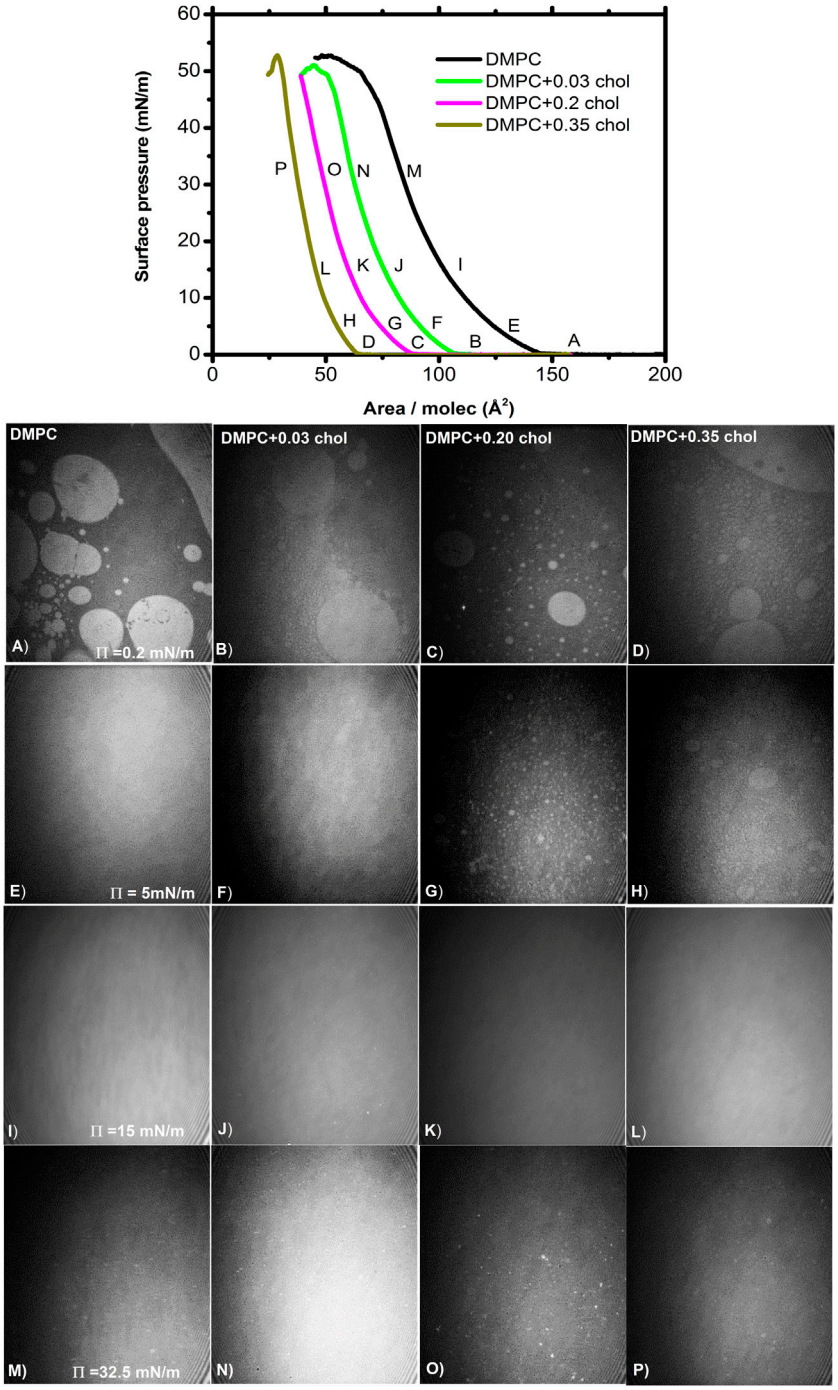

FIGURE 3 | BAM images of DMPC/chol mixed monolayer at different surface pressures at 37.0°C. The images are 462 × 564 μm2. All the images in a row (column) correspond to the surface pressure (cholesterol fraction) indicated in the first image.

during domain coalescence [8]. The sharp rise stops once we reach a uniform monolayer and here we see two different slopes for pure DMPC (Area/molecule between 90 and 130 $Å^2$), indicating a phase transition between two different condensed phases with different compressibility values. That transition is not as evident with a small fraction of cholesterol, probably due to the fact that cholesterol introduces some disorder in the monolayer [36]. As it was discussed before, the cholesterol changes the tilt angle of the DMPC molecules around it, moving the system away from a well-defined phase. At higher molar fractions (>0.10), the C_s^{-1} curve start showing again two slopes; this is the monolayer becomes stiffer at higher surface pressures due to a rise in

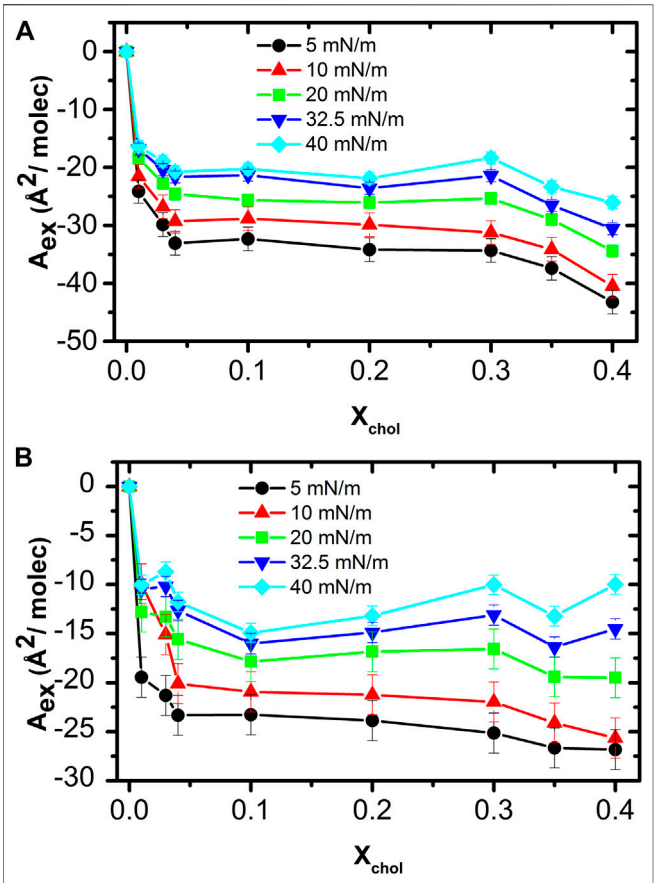

FIGURE 4 | Excess area as function of cholesterol concentration at different surface pressures in ultrapure water **(A)** and in pH 7.4 subphase **(B)**.

molecule packing driven by the well-known cholesterol condensation effect, where the phospholipid acyl chains interact strongly with cholesterol as reported in the literature [5, 11, 16]. This condensing effect does not mean that the monolayer becomes more ordered, in fact there are reports that the molecular correlation is short range [36]. Even more, at around physiological concentration of cholesterol (0.3–0.4), the C_s^{-1} curve still show two slopes. However, the lower slope region has shrunk while the upper one has increased. The pure cholesterol C_s^{-1} curve only show one high slope indicating a low compressibility of the condensed phase, in good agreement with its corresponding isotherm [37]. All C_s^{-1} the curves reached a maximum value until collapse occurs; after the maximum, the value of C_s^{-1} decreases rapidly to zero because the film becomes highly compressible due to collapse.

On the other hand, the behavior of both type isotherms, and therefore C_s^{-1}, is quite different at pH 7.4 than in ultrapure water (pH ≈ 6.6). First of all, the take-off surface pressure occurs at higher molecular areas at pH 7.4. This means that the condensed phase appears at larger areas per molecule, due to the interactions between the head groups and the phosphate ions of the buffer solution expands the condensed phase [25, 38]. This difference in the take-off surface pressure might change the phase order compared to those present at lower pH, it could result in a more tilted phase; this result in a more expanded phase but also somewhat more compressible, as can be observed by both type of isotherms and C_s^{-1}, since the latter is significantly larger for the pure DMPC and the higher cholesterol concentration at the higher pH. In addition, the change in pH has an effect in the behavior of C_s^{-1}, for example, for the pure DMPC monolayer it shows three different slopes before collapse at pH 7.4 while at pH ≈ 6.6 it shows only two slopes, indicating that the monolayer might have three and two different phase regions, respectively. In addition, the maximum of the C_s^{-1} value at the intermediate concentrations of cholesterol is similar at 0.01 M fraction of cholesterol, but at 0.1 M cholesterol concentration is significantly higher at the lower pH. However, an addition of a small amount of cholesterol has a more noticeable effect at the higher pH than at lower pH. As mentioned above, the C_s^{-1} values change strongly with the addition of only 0.01 cholesterol fractions even more at 0.1 cholesterol fraction the C_s^{-1} curve becomes more shallow, with not very well defined regions. But at around physiological concentration of cholesterol, e.g., 0.35–0.40, the C_s^{-1} curve behavior changes strongly; the slope is very high, especially at physiological pH, and closer to the behavior of the

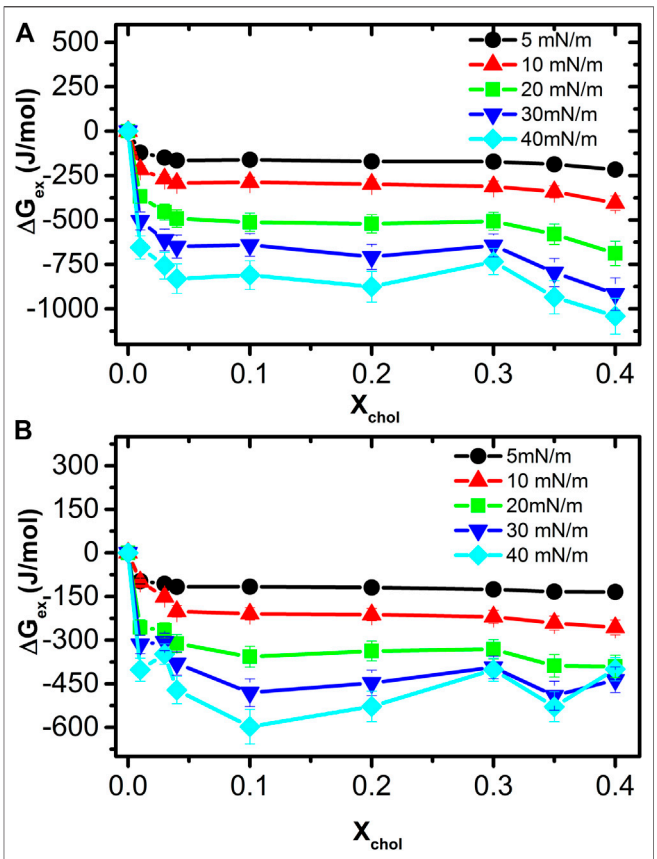

FIGURE 5 | Excess Gibbs free energy for the mixed monolayer at different cholesterol concentrations and surface pressures in ultrapure water **(A)** and in pH 7.4subphase **(B)**. For all the isotherms, the ΔG_{ex} is negative, indicating that the molecules mix spontaneously.

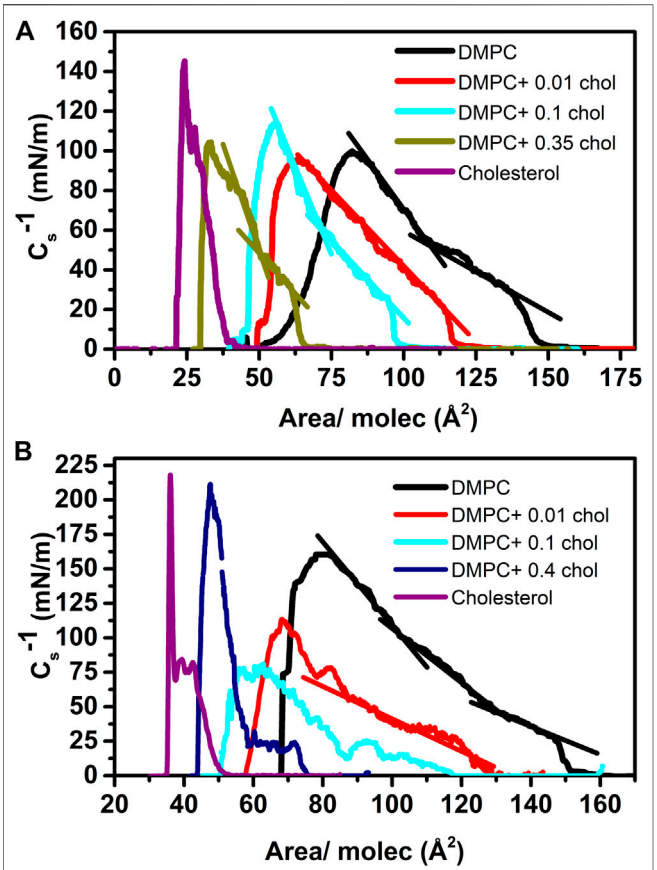

FIGURE 6 | Area compressibility elastic modulus at different cholesterol fractions at 37.0 ± 0.1°C on ultrapure water subphase **(A)** and on pH 7.4 **(B)**.

pure cholesterol curve, indicating that the monolayer becomes very stiff.

It is worth noticing that the maximum of the C_s^{-1} curves at high concentration of cholesterol and also for pure cholesterol, is much higher at higher pH, indicating that the monolayer is stiffer. This behavior is easily observed in **Figure 7**, where for different concentrations of cholesterol, the C_s^{-1} values are slightly lower at low surface pressures for the higher pH. But as the surface pressure is increased, the monolayer behavior is reversed since at higher pH shows higher values of C_s^{-1} than a lower pH, which again indicates that the monolayer becomes stiffer.

Figure 8 shows a monolayer stability analysis as a function of time at pH ≈ 6.6 (**Figure 8A**) and physiological pH (**Figure 8B**). In this study, we prepare again Langmuir monolayers with different concentrations of cholesterol and compared their relaxation with that of pure DMPC. We also include for comparison, the relaxation behavior of pure arachidic acid and pure cholesterol. It has been proposed [13, 34] that the behavior of a monolayer in a surface pressure range of 32–35 mN/m is equivalent to the behavior of a bilayer in a cell membrane at 20°C. To test this hypothesis, the monolayers were slowly compressed (20 cm^2/min) up to 35 mN/m and allowed to relax to its equilibrium surface pressure.

Our relaxation studies indicate that all monolayers have a pressure drop as a function of time. However, both DMPC and DMPC + cholesterol relax to an equilibrium surface pressure of about 30.2 ± 1.4 and 27.4 ± 3.2 mN/m in pure water (pH ≈ 6.6) and buffer at pH 7.4, respectively. It is surprising that at pH ≈ 6.6 the equilibrium surface pressure in quite similar for all the cholesterol concentration range, the surface pressure drop was between 3.8 and 6.2 mN/m, while at pH 7.4 the surface pressure drop is somewhat larger, between 4.4 and 11.5 mN/m. Therefore, the equilibrium surface pressure values at pH 6.6 are not very different for all DPPC-Cholesterol mixtures, but at pH 7.4 the equilibrium surface pressure values are not as homogeneous. The pressure drop indicates that the monolayer is slowly collapsing; that is, forming three-dimensional structures, but it is worth noting that the equilibrium surface pressure at pH 7.4 of pure DMPC and its mixture with a cholesterol mole fraction of 0.35 falls in the range of the equilibrium surface pressure at pH 6.6. In addition, we can state that at 37.0°C and physiological pH 7.4 that any of these monolayers could be equivalent to a bilayer below 27 mN/m, in terms of their equilibrium properties. Remarkably, pure cholesterol has a quick and very large surface pressure drop at physiological pH, to about 17 mN/m, as shown in **Figure 8B**). This indicates that the equilibrium surface pressure of the mixture is mostly due to the DMPC. Moreover, the surface

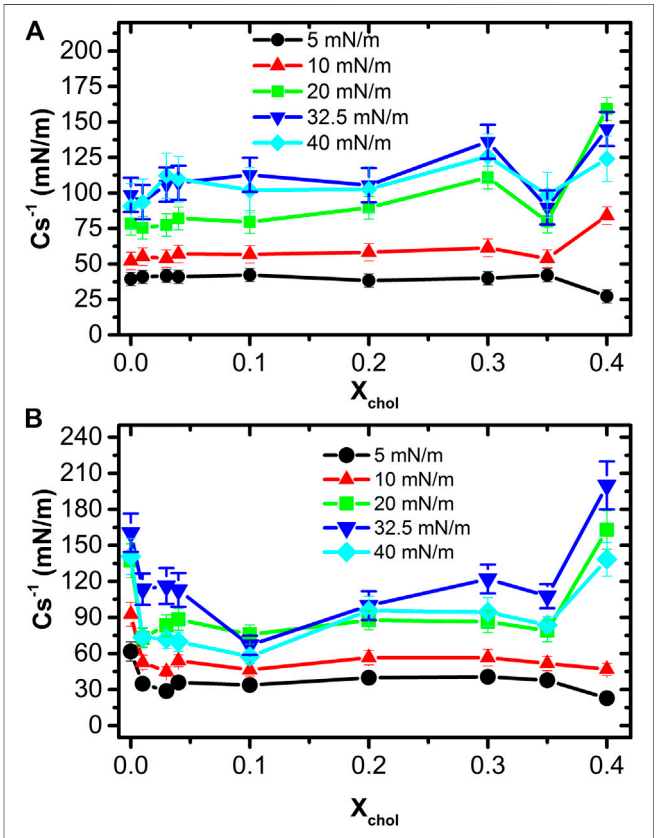

FIGURE 7 | Comparison between area compressibility elastic modulus at different surface pressures on ultrapure water subphase **(A)** and pH 7.4 subphase **(B)**.

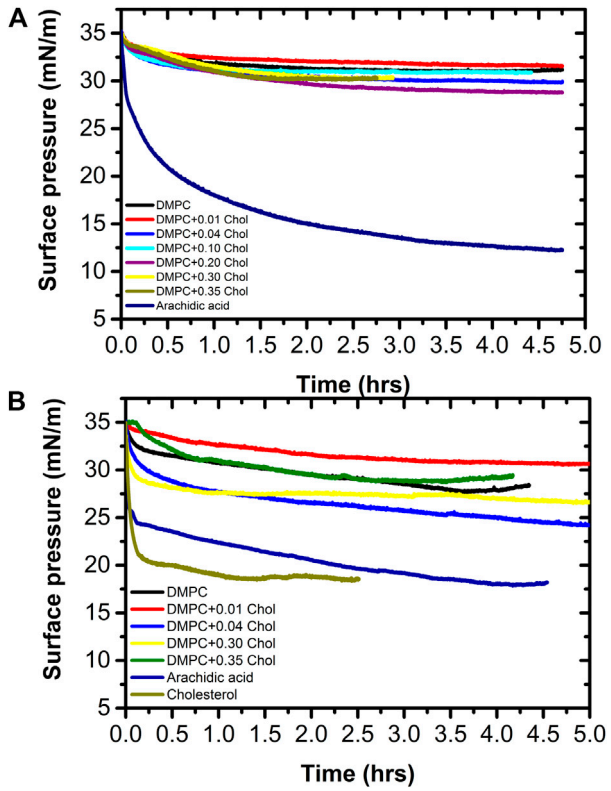

FIGURE 8 | Monolayer equilibrium surface pressure comparison as a function of the cholesterol concentration at **(A)** pH 6.6 and **(B)** pH 7.4 determined at 37.0 ± 0.1°C. In addition, the equilibrium surface pressure of arachidic acid is shown at both conditions.

pressure of arachidic acid shows two behaviors at pH 7.4; first, a rapid decay of about 11 mN/m in a short time, followed by a much slower decay of about 6 mN/m more toward the final equilibrium spreading pressure of about 18 mN/m. This is, the equilibrium spreading pressure value of arachidic acid is similar to that of pure cholesterol and almost half the initial surface pressure value. Even more, at pH 6.6, the equilibrium pressure of arachidic acid decays more slowly that at pH 7.4, but it decays even to a lower value of about 12.5 mN/m. This give us a good indication that monolayers formed by single chain lipids have a much lower equilibrium surface pressure than monolayers formed by double chain lipids, such as phospholipids. This also might indicate why nature chose double chain lipids, such as phospholipids, to be the main lipid components in cell membranes. Due to energetic considerations, single chain lipids tend to form micelles while double chain lipids tend to form vesicles that are associated with the formation of cell membranes [39]. However, even if single chain lipids could form vesicles, they could not form thermodynamically stable unilamellar vesicles but rather multiwall vesicles; for the case of arachidic acid they will be 4 to 5 bilayers thick [32].

Figure 9 shows a series of representative Brewster angle microscopy images of the equilibrium spreading pressure experiments of the monolayers. First at a surface pressure of 35 mN/m (left) and then at the equilibrium surface pressure

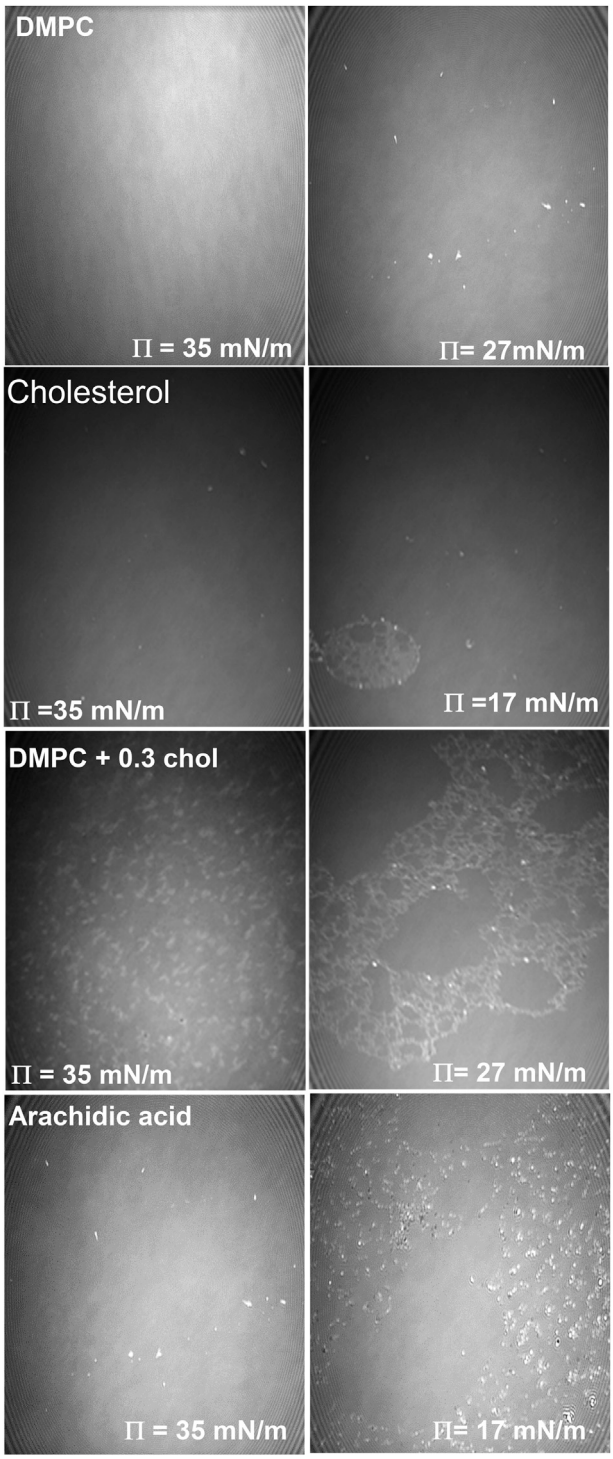

FIGURE 9 | Relaxation of lipid monolayers for pure DMPC (first row) and arachidic acid (second row) monolayers at the beginning of the experiment (left column) and at the end of the experiment (right column) at pH 7.4 subphase at 37.0 ± 0.1°C. The images are 462 × 564 μm^2.

(right) of the corresponding sample. The first row corresponds to the DMPC monolayer, at 35 mN/m where a homogeneous monolayer can be observed. While at 27 mN/m a few 3D

structures can be noted over the homogeneous DMPC monolayer, this is due to the relaxation of the monolayer. In the second row, a homogeneous Cholesterol monolayer can be noted at 35 mN/m and then when the equilibrium surface pressure is reached (17 mN/m), after 2.5 hours, some 3D structures can be noted floating on a homogeneous monolayer. In the third row the DMPC+0.3 cholesterol mixed monolayer is shown. At the start of the experiment at 35 mN/m, separated 3D structures can be noted due to the condensing effect induced by the cholesterol molecules. While at the equilibrium surface pressure (27 mN/m), 3D structure domains can be noted as well, forming a foam-like structure. Finally, the fourth row shows the images corresponding to the arachidic acid monolayer. At the beginning of the surface pressure relaxation experiment (35 mN/m) some 3D structures can be observed. But at the equilibrium surface pressure (17 mN/m), a large amount of arachidic acid crystals can be noticed due to the collapse of the monolayer by the relaxation process. It is important to notice that the arachidic acid monolayer achieves stability at a surface pressure value 37 % lower than the DMPC monolayer and its mixtures with cholesterol. Therefore, the phospholipid monolayer has a stable surface pressure much higher than the single-chain fatty acid.

CONCLUSION

The analysis of the thermodynamics and mechanical properties of Langmuir monolayers of DMPC/cholesterol as a function of the concentration of cholesterol and at two pH values at physiological temperature gave interesting results. For example, we found that the isotherms of DMPC/cholesterol monolayers mixtures show an increase in the monolayer fluidity at all cholesterol concentrations. Cholesterol is a bulky molecule that makes the take-off surface pressure of the monolayer appears at lower areas per molecule. This means that the presence of the gas phase remains at much lower area per molecule compared to that of the pure DMPC monolayer due to the effect of cholesterol, thus fluidizing the monolayer. However, this effect is much less pronounced as the concentration of cholesterol increases, and near physiological cholesterol concentration the monolayer is less compressible, as observed by an increased in slope of the compression modulus, C_s^{-1}, more noticeable at physiological pH than at the lower pH of pure water.

On the other hand, it is important to notice that the excess free energy is the lowest at physiological concentrations of cholesterol at both pH and surface pressure, this is, it becomes more negative not only as the concentration of cholesterol increases but also as the surface pressure increases as well, close to the equilibrium surface pressure determined at both pH. This indicates that DMPC and cholesterol mix better at higher cholesterol concentrations as well as at higher surface pressures. In general, in agreement to the excess area and Gibbs free energy analysis, this results showed the presence of attractive interactions that form thermodynamically stable monolayers in the whole cholesterol fraction range studied [17], and where more stable monolayers were observed when the mixture contained about the average physiological cholesterol fraction (≈0.35) that resulted to be energetically favored and gives more stable monolayers [11]. Furthermore, we show that monolayers formed by either pure DMPC or a mixture of DMPC with cholesterol relax to about the same equilibrium surface pressure, although the final surface pressure relaxation value is different depending on the pH. Furthermore, we also show that a monolayer formed by a single chain lipid, such as arachidic acid, is much less stable than the pure DMPC or the DMPC/cholesterol mixture; this results clearly indicates a possible reason on why nature uses double chain lipids as its mayor component in cell membranes.

DATA AVAILABILITY STATEMENT

The raw data supporting the conclusions of this article will be made available by the authors, without undue reservation.

AUTHOR CONTRIBUTIONS

AB-F, VMC-M, ERA-P, and EAV-M performed the experiments and data analysis. AB-F, EG, and JR-G wrote and discussed the paper funding acquisition. All authors discussed the data, conclusions and proof read the manuscript. EG and JR-G were responsible for the funding acquisition JR-G directed the project and experiments. All authors contributed in the revision of the manuscript.

FUNDING

This work was supported by CONACYT through grants FC-341, FC-157, CB-254981, CB-237439 and CB-254460. Part of the work was also supported by the UASLP through the Fondos Concurrentes program.

REFERENCES

1. McMullen TPW, Lewis RNAH, McElhaney RN. Cholesterol-phospholipid interactions, the liquid-ordered phase and lipid rafts in model and biological membranes. *Curr Opin Colloid Interf Sci* (2004) 8(6):459–68. doi:10.1016/j.cocis.2004.01.007
2. van Meer G. Lipid traffic in animal cells. *Annu Rev Cell Biol* (1989) 5(1):247–75. doi:10.1146/annurev.cb.05.110189.001335
3. Simons K, Toomre D. Lipid rafts and signal transduction. *Nat Rev Mol Cell Biol* (2000) 1:31–9. doi:10.1038/35036052
4. Bacia K, Schwille P, Kurzchalia T, Bacia K, Schwille P, Kurzchalia T. Sterol structure determines the separation of phases and the curvature of the liquid-ordered phase in model membranes. *Proc Natl Acad Sci USA* (2005) 102(9):3272–7. doi:10.1073/pnas.0408215102
5. Stottrup BL, Hernandez-Balderrama LH, Kunz JC, Nguyen AH, Sonquist BJ. Comparison of cholesterol and 25-hydroxycholesterol in phase-separated Langmuir monolayers at the air-water interface. *J Phys Chem B* (2014) 118(38):11231–7. doi:10.1021/jp506592k
6. McMullen TP, Lewis RN, McElhaney RN. Comparative differential scanning calorimetric and FTIR and 31P-NMR spectroscopic studies of the effects of cholesterol and androstenol on the thermotropic phase behavior and

organization of phosphatidylcholine bilayers. *Biophys J* (1994) 66(3):741–52. doi:10.1016/S0006-3495(94)80850-1
7. Simons K, Vaz WL. Model systems, lipid rafts, and cell membranes. *Annu Rev Biophys Biomol Struct* (2004) 33:269–95. doi:10.1146/annurev.biophys.32.110601.141803
8. McConnell HM, Radhakrishnan A. Condensed complexes of cholesterol and phospholipids. *Biochim Biophys Acta* (2003) 1610:159–73. doi:10.1016/S0005-2736(03)00015-4
9. Kim K, Choi SQ, Zell ZA, Squires TM, Zasadzinski JA. Effect of cholesterol nanodomains on monolayer morphology and dynamics. *Proc Natl Acad Sci USA* (2013) 110:E3054–60. doi:10.1073/pnas.1303304110
10. Tierney KJ, Block DE, Longo ML. Elasticity and phase behavior of DPPC membrane modulated by cholesterol, ergosterol, and ethanol. *Biophys J* (2005) 89:2481–93. doi:10.1529/biophysj.104.057943
11. Gong K, Feng S-S, Go ML, Soew PH. Effects of pH on the stability and compressibility of DPPC/cholesterol monolayers at the air-water interface. *Colloids Surf A: Physicochem Eng Aspects* (2002) 207:113–25. doi:10.1016/S0927-7757(02)00043-2
12. Huang J, Feigenson GW. A microscopic interaction model of maximum solubility of cholesterol in lipid bilayers. *Biophys J* (1999) 76:2142–57. doi:10.1016/S0006-3495(99)77369-8
13. Brezesinski G, Möhwald H. Langmuir monolayers to study interactions at model membrane surfaces. *Adv Colloid Interf Sci* (2003) 100-102:563–84. doi:10.1016/s0001-8686(02)00071-4
14. Barrett MA, Zheng S, Toppozini LA, Alsop RJ, Dies H, Wang A, et al. Solubility of cholesterol in lipid membranes and the formation of immiscible cholesterol plaques at high cholesterol concentrations. *Soft Matter* (2013) 9:9342–51. doi:10.1039/C3SM50700A
15. de Meyer F, Smit B. Effect of cholesterol on the structure of a phospholipid bilayer. *Proc Natl Acad Sci* (2009) 106:3654–8. doi:10.1073/pnas.0809959106
16. Ohvo-Rekilä H, Ramstedt B, Leppimäki P, Slotte JP. Cholesterol interactions with phospholipids in membranes. *Prog Lipid Res* (2002) 41:66–97. doi:10.1016/S0163-7827(01)00020-0
17. Wydro P. The magnitude of condensation induced by cholesterol on the mixtures of sphingomyelin with phosphatidylcholines-study on ternary and quaternary systems. *Colloids Surf B Biointerfaces* (2011) 82:594–601. doi:10.1016/j.colsurfb.2010.10.023
18. Wydro P, Flasiński M, Broniatowski M. Does cholesterol preferentially pack in lipid domains with saturated sphingomyelin over phosphatidylcholine? A comprehensive monolayer study combined with grazing incidence X-ray diffraction and Brewster angle microscopy experiments. *J Colloid Interf Sci* (2013) 397:122–30. doi:10.1016/j.jcis.2013.01.060
19. Silvius JR, del Giudice D, Lafleur M. Cholesterol at different bilayer concentrations can promote or antagonize lateral segregation of phospholipids of differing acyl chain length. *Biochemistry* (1996) 35:15198–208. doi:10.1021/bi9615506
20. Dynarowicz-Łątka P, Hąc-Wydro K. Interactions between phosphatidylcholines and cholesterol in monolayers at the air/water interface. *Colloids Surf B: Biointerfaces* (2004) 37:21–5. doi:10.1016/j.colsurfb.2004.06.007
21. Montes LR, Alonso A, Goñi FM, Bagatolli LA. Giant unilamellar vesicles electroformed from native membranes and organic lipid mixtures under physiological conditions. *Biophys J* (2007) 93:3548–54. doi:10.1529/biophysj.107.116228
22. Menger FM, Keiper JS. Chemistry and physics of giant vesicles as biomembrane models. *Curr Opin Chem Biol* (1998) 2:726–32. doi:10.1016/S1367-5931(98)80110-5
23. Nichols-Smith S, Teh SY, Kuhl TL. Thermodynamic and mechanical properties of model mitochondrial membranes. *Biochim Biophys Acta* (2004) 1663:82–8. doi:10.1016/j.bbamem.2004.02.002
24. Wydro P. Sphingomyelin/phosphatidylcholine/cholesterol monolayers--analysis of the interactions in model membranes and Brewster Angle Microscopy experiments. *Colloids Surf B Biointerfaces* (2012) 93:174–9. doi:10.1016/j.colsurfb.2011.12.035
25. Qiu X, Ruiz-Garcia J, Stine KJ, Knobler CM, Selinger JV. Direct observation of domain structure in condensed monolayer phases. *Phys Rev Lett* (1991) 67:703–6. doi:10.1103/PhysRevLett.67.703
26. Van Meer G, Voelker DR, Feigenson GW. Membrane lipids: where they are and how they behave. *Nat Rev Mol Cell Biol* (2008) 9:112–24. doi:10.1038/nrm2330
27. Smaby JM, Momsen MM, Brockman HL, Brown RE. Phosphatidylcholine acyl unsaturation modulates the decrease in interfacial elasticity induced by cholesterol. *Biophys J* (1997) 73:1492–505. doi:10.1016/S0006-3495(97)78181-5
28. Ali S, Smaby JM, Momsen MM, Brockman HL, Brown RE. Acyl chain-length asymmetry alters the interfacial elastic interactions of phosphatidylcholines. *Biophys J* (1998) 74:338–48. doi:10.1016/S0006-3495(98)77791-4
29. Sabatini K, Mattila JP, Kinnunen PK. Interfacial behavior of cholesterol, ergosterol, and lanosterol in mixtures with DPPC and DMPC. *Biophys J* (2008) 95:2340–55. doi:10.1529/biophysj.108.132076
30. Kaganer VM, Peterson IR, Kenn RM, Shih MC, Durbin M, Dutta P. Tilted phases of fatty acid monolayers. *J Chem Phys* (1995) 102:9412–22. doi:10.1063/1.468809
31. Dynarowicz-Łątka P, Kita K. Molecular interaction in mixed monolayers at the air/water interface. *Adv Colloid Interf Sci* (1999) 79:1–17. doi:10.1016/S0001-8686(98)00064-5
32. Valdes-Covarrubias MA, Cadena-Nava RD, Vásquez-Martínez E, Valdez-Pérez D, Ruiz-García J. Crystallite structure formation at the collapse pressure of fatty acid Langmuir films. *J Phys Condens Matter* (2004) 16:S2097–107. doi:10.1088/0953-8984/16/22/008
33. Kubo I, Adachi S, Maeda H, Seki A. Phosphatidylcholine monolayers observed with Brewster angle microscopy and π-A isotherms. *Thin Solid Films* (2001) 393:80–5. doi:10.1016/S0040-6090(01)01101-4
34. Subramaniam S, McConnell HM. Critical mixing in monolayer mixtures of phospholipid and cholesterol. *J Phys Chem* (1987) 91:1715–8. doi:10.1021/j100291a010
35. Marsh D. Lateral pressure in membranes. *Biochim Biophys Acta* (1996) 1286:183–223. doi:10.1016/s0304-4157(96)00009-3
36. Ege C, Ratajczak MK, Majewski J, Kjaer K, Lee KY. Evidence for lipid/cholesterol ordering in model lipid membranes. *Biophys J* (2006) 91:L01–3. doi:10.1529/biophysj.106.085134
37. Cadena-Nava RD, Martin-Mirones JM, Vázquez-Martínez EA, Roca JA, Ruiz-Garcia J. Direct observations of phase changes in Langmuir films of cholesterol. *Rev Mexi Fís* (2006) 52:32–40.
38. Castillo-Santaella D, Maldonado-Valderrama J, Faraudo J, Martín-Molina A. Specific ion effects in cholesterol monolayers. *Materials* (2016) 9:340–54. doi:10.3390/ma9050340
39. Israelachvili JN. *Intermolecular and surface forces*. 3rd Edn. Cambridge, MA: Academic Press (2011).

Conflict of Interest: The authors declare that the research was conducted in the absence of any commercial or financial relationships that could be construed as a potential conflict of interest.

frontiers in Physics

ORIGINAL RESEARCH
published: 25 March 2021
doi: 10.3389/fphy.2021.634792

Entropic Effects of Interacting Particles Diffusing on Spherical Surfaces

*Aldo Ledesma-Durán[1], J. Munguía-Valadez[2], J. Antonio Moreno-Razo[2], S. I. Hernández[3] and I. Santamaría-Holek[3]**

[1]Departamento de Matemáticas, Universidad Autónoma Metropolitana-Iztapalapa, Avenida San Rafael Atlixco No.186 Colonia Vicentina, Delegación Iztapalapa, México City, México, [2]Departamento de Física, Universidad Autónoma Metropolitana-Iztapalapa, Avenida San Rafael Atlixco No.186 Colonia Vicentina, Delegación Iztapalapa, México City, México, [3]Unidad Multidiciplinaria de Docencia e Investigación-Juriquilla, Facultad de Ciencias, Universidad Nacional Autónoma de México (UNAM), Boulevard Juriquilla, Querétaro, México

We present a molecular dynamics and theoretical study on the diffusion of interacting particles embedded on the surface of a sphere. By proposing five different interaction potentials among particles, we perform molecular dynamics simulations and calculate the mean square displacement (MSD) of tracer particles under a crowded regime of high surface density. Results for all the potentials show four different behaviors passing from ballistic and transitory at very short times, to sub-diffusive and saturation behaviors at intermediary and long times. Making use of irreversible thermodynamics theory, we also model the last two stages showing that the crowding induces a sub-diffusion process similar to that caused by particles trapped in cages, and that the saturation of the MSD is due to the existence of an entropic potential that limits the number of accessible states to the particles. By discussing the convenience of projecting the motions of the particles over a plane of observation, consistent with experimental capabilities, we compare the predictions of our theoretical model with the simulations showing that these stages are remarkably well described in qualitative and quantitative terms.

Keywords: molecular simulations, mean square displacement, surface sphere, diffusion coefficient, curved surfaces

OPEN ACCESS

Edited by:
Ramon Castañeda-Priego, University of Guanajuato, Mexico

Reviewed by:
Leonardo Dagdug, Metropolitan Autonomous University, Mexico
Pavel Castro-Villarreal, Autonomous University of Chiapas, Mexico
Andrey Cherstvy, University of Potsdam, Germany

****Correspondence:***
I. Santamaria Holek
isholek.fc@gmail.com

Specialty section:
This article was submitted to Interdisciplinary Physics, a section of the journal Frontiers in Physics

Received: *28 November 2020*
Accepted: *08 January 2021*
Published: *25 March 2021*

Citation:
Ledesma-Durán A, Munguía-Valadez J, Moreno-Razo J A, Hernández SI and Santamaría-Holek I (2021) Entropic Effects of Interacting Particles Diffusing on Spherical Surfaces. Front. Phys. 9:634792. doi: 10.3389/fphy.2021.634792

1 INTRODUCTION

In several physical and biological systems the mass transport phenomena is carried out in surfaces with non vanishing curvatures. The diffusion of bio-molecules and other particles on the surface of liposomes, drops and other curved entities is of high relevance due to its potential applications in biomedicine and technology [1–4]. Characteristic examples of this phenomena can be found in the diffusion of proteins on curved membranes or in the surface diffusion of molecules and chemical solvents in catalytic surfaces [5–8].

In these curved domains, many geometric aspects relating the motion of the particles on surfaces have been studied in recent years [9–14]. These studies are relevant in the understanding of applied problems such as nucleation, spinodal decomposition, adsorption, and phase transitions, since the dynamics of the particles is modified due to the curvature of the surface on which the molecules are embedded [15–18].

In particular, the most relevant quantity to measure in these particle motions is the mean square displacement (MSD). However, most of the previously refereed studies provide geometric

information of the MSD and the effective diffusion coefficient only for the case where the interaction of the particles occurs with the surface and not among particles themselves. In this simplification, many expressions can be found in the literature for approximating the short and long time behavior of the MSD, see Ref. [9] and references therein. However, for the case of interacting particles, there are only few numerical works studying the influence of interaction and confinement in the MSD [19–21].

In this work we will consider how the surface diffusion displacements are influenced by the interaction of the particles and the projection of their displacement in a plane of observation. This is because for most experimental cases of interest, the geodesic trajectories of the particles cannot be followed at all times, and only the projection in a plane of observation can be measured [11, 22, 23]. This fact emphasizes that for diffusion over closed surfaces, the observed motility depends on the curvature of the surface and on the plane of observation [24–26].

We present the results of the MSD for interacting particles in a crowded spherical surface by using Molecular Dynamics (MD) simulations and implementing five different pairwise-interaction potentials between the particles in a relatively high surface density medium ($\rho^* = 0.92$). The particles are free to move on the entire spherical surface of radius R. To keep the particles on the surface, we use the algorithm described by Juffer et al. [27]. The continuous interaction potentials used are different cases of the generalized form of the Mie potentials [28]: *LJTS*, *WCA* (12.6), *WCA* (50.49). Besides, some simple discontinuous potentials like the shoulder-square (*SS*) and the well-square (*SW*) were adapted to their continuous-mathematical form described by Munguía-Valadez et al.[1]

With the aim to provide a physical interpretation of the results of these numerical calculations, we formulate an analytic model based on the generalized Smoluchowski equation with time-dependent coefficients [29–34]. Using this tool, we can identify how the change of perspective, confinement and crowding are incorporated in an effective diffusion coefficient that takes into account the entropic confinement and the anomalous diffusion. The model used here was derived in the context of mesoscopic non-equilibrium thermodynamics (MNET) and has been widely used in order to obtain kinetic equations for transport phenomena, like diffusion-adsorption processes, anomalous diffusion, activated processes, diffusion in pores, and diffusion in the presence of entropic barriers [35–39]. In particular for our purposes, MNET has been successful in describing diffusion on other confined systems [38, 40–42].

The comparison between our numerical simulations and thermodynamic-based model allows us to propose a new interpretation of the observed dynamics of the MSD for diffusion of interacting particles over a sphere, and to compare the different subdiffusive regimes associated with the hardness or softness of the particle collisions. We have chosen a spherical geometry in order to rule out the effects of different local curvatures in the surface. This will also allow us to recover previous theoretical results deduced for the sphere in absence of interaction.

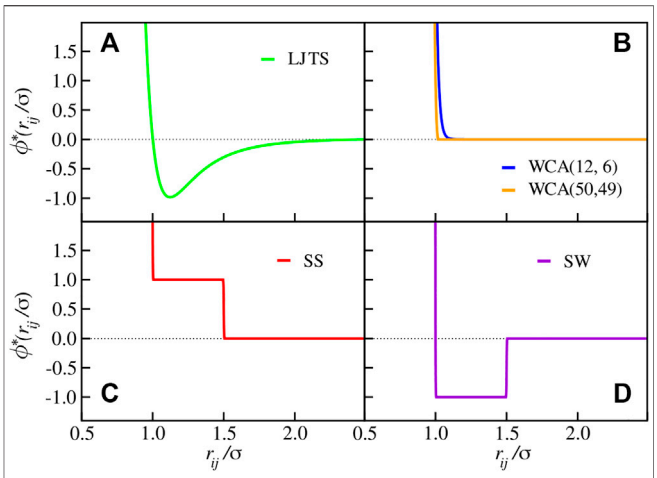

FIGURE 1 | Potentials of interacting particles used for the simulations. **(A)** Potential of Truncated and Shifted Lennard-Jones. **(B)** *WCA* (12, 6) potential and the hard sphere pseudo-potential *WCA* (50, 49). **(C)** and **(D)** Square-Shoulder potential continuous and continuous Square-Well respectively, given by **Eq. 4**.

Regarding the organization of work, in **Section 2** we present our Molecular Dynamics simulations on the diffusion of finite sized-particles over an spherical surface for different interaction potentials among particles. Then, we study the dynamics of the diffusion and the behavior of the MSD using the results provided by a Smoluchowski description which is presented in **Sections 3.1** and **3.2**, for free and interacting particles, respectively. Comparison between simulations and model is presented in **Section 4**. Finally, discussion and concluding remarks are provided in **Section 5**.

2 MOLECULAR DYNAMICS SIMULATIONS

We present the details of the simulations as well as a brief description of the interaction potentials used in this work.

2.1 Interaction Potentials

The continuous interaction potentials are defined through:

$$\phi_{n,m}(r_{ij}) = \left(\frac{n}{n-m}\right)\left(\frac{n}{m}\right)^{m/(n-m)}\varepsilon\left[\left(\frac{\sigma}{r_{ij}}\right)^n - \left(\frac{\sigma}{r_{ij}}\right)^m\right], \quad (1)$$

where $\phi_{n,m}(r_{ij})$ is the most general form of the Mie potential [28]. For example, we can write the Truncated and Shifted Lennard-Jones (*LJTS*) interaction by choosing n, $m = 12$, 6, and then

$$\phi_{LJTS}(r_{ij}) = \begin{cases} \phi_{12,6}(r_{ij}) - \phi_{12,6}(r_c), & r_{ij} \le r_c, \\ 0, & r_{ij} > r_c, \end{cases} \quad (2)$$

[1]Munguía-Valadez J, Chávez-Rojo MA, Moreno-Razo JA, Sambriski EJ (under review). The generalized continuous multiple step potential: model systems and related properties. J Chem Phys.

where $\sigma(=2a)$ is the particle diameter, $r_{ij} = |\mathbf{r}_i - \mathbf{r}_j|$ the distance between the centers of mass of the i-th and the j-th particles, ϵ the potential well depth, and $r_c(=2.5\sigma)$ the cutoff radius. On the other hand, a generalization of the Weeks-Chandler-Anderson potential (WCA) [43, 44] can be written as

$$\phi_{WCA(n,m)}\left(r_{ij}\right) = \begin{cases} \phi_{n,m}\left(r_{ij}\right) + \epsilon, & r_{ij} \leq \left(\frac{n}{m}\right)^{1/n-m}\sigma, \\ 0, & r_{ij} > \left(\frac{n}{m}\right)^{1/n-m}\sigma, \end{cases} \quad (3)$$

where $r_{ij} = (n/\mathrm{m})^{1/\mathrm{n-m}}\sigma$ is the value that corresponds to the minimum potential. In our case, we use the parameters n, $m = 12, 6$, $[WCA(12, 6)]$ and n, $m = 50, 49$, $[WCA(50, 49)]$ to incorporate pseudo hard-sphere interaction models into the study, see **Figure 1B** [44].

The Square-Well (SW) and Square-Shoulder (SS) potentials can be approximated with the Generalized Continuous Multiple Step Potential ($GCMS$), which incorporates a contribution of excluded volume followed by multiple steps that model repulsive barriers or attractive wells as the case may be. Its simplified form can be written as:

$$\phi_{GCMS}\left(\sigma, \omega, q, a_0, r_{ij}\right) = \epsilon\left[\left(\frac{\omega}{r_{ij} - \sigma + \omega}\right)^q + \frac{a_0}{1 + \exp\left[q\left(r_{ij} - \sigma - \omega\right)/\omega\right]}\right], \quad (4)$$

where ω defines the spatial extent of the particle core in units of σ, q is related to the hardness of the potential, and a_0 is a factor that defines an attractive step ($a_0 < 0$) or a repulsive one ($a_0 > 0$). The parameters used to reproduce the SS and SW are: $\omega = 0.5$, $q = 500$, $a_0 = 1$ and $a_0 = -1$, respectively, see **Figure 1C** y **Figure 1D**.

2.2 Simulation Method

In this work all quantities are assumed to be expressed in conventional reduced units, with m, σ and ϵ as the units of mass (set equal to 1), distance, and energy, respectively. According to this convention, the temperature (T^*) is in units of k_BT/ϵ where k_B is Boltzmanns constant, the density (ρ^*) in units of $\rho\sigma^2$, the time (δt^*) in units of $\delta t(\epsilon/\mathrm{m}\sigma^2)^{1/2}$, and the energy ($\phi^*$) in units of ϕ/ϵ. A monodisperse system of spherical particles was studied with the restriction of moving on the surface of a sphere of radius $R = 9.3\sigma$. To study the dynamic behavior of each system, Molecular Dynamics simulations were performed in the canonical assembly (NVT) for a total of $N = 1000$ particles embedded in the spherical surface, with a surface density given by $\rho^*(=\mathrm{N/A}) = 0.92$. The R and ρ^* values were taken for compatibility with previous studies by Vest et al. [45–47]. The system was placed in a thermal bath at a temperature $T^* = 1.0$ set constant by using the isokinetic method; the integration of the equations of motion was carried out using the velocity-Verlet algorithm [48], with the restriction $f_i(\mathbf{r}_i) = |\mathbf{r}_i|^2 - R^2 = 0$ (see Ref. [27]) and a time-step $\delta t^* = 10^{-3}$ for $LJTS$, $WCA(50, 49)$ and $WCA(12, 6)$ systems, and with $\delta t^* = 10^{-4}$ for SS and SW systems.

The simulations were run by 10^6 time-steps for $LJTS$, $WCA(50, 49)$ and $WCA(12, 6)$, and by 10^7 time-steps for SS and SW to reach thermodynamic equilibrium, then for 3×10^7 and 4×10^8 time-steps, respectively, for the calculation of the mean square displacement. Some representative trajectories of a tracer particle for each potential are plotted in **Figure 2**.

The results of our simulations for the MSD are plotted in **Figure 3**. At the right side we plot the geodesic MSD over the sphere with the saturation valor of $(\pi^2 - 4)R^2/2$. At the left, we plot the MSD measured when the displacements of the particles are projected the plane of observation XY, giving the saturation value of $2R^2/3$. These saturation values for long times only depend on the geometric configuration and therefore are the same for free and interacting diffusing particles [10].

The MSD plotted in **Figure 3** shows four different stages: 1) the ballistic regime where the MSD increases as t^2, 2) a transition between ballistic and diffusive regime where the slope of the MSD decreases and changes of concavity, 3) the subdiffusive regime where, as we will calculate below, the MSD increases as t^α with $\alpha \lesssim 1$ and, finally, for long times, 4) the saturation regime where the MSD no longer increases since the domain of the sphere is finite. These four regimes are seen in the geodesic and projected version of the MSD plotted at right and left of **Figure 3**, respectively. Some or all of these four stages have been found both in numerical simulations [9, 49–52] and experiments, mainly for protein and lipid diffusion on cell membranes [53–56].

The form of the plots for the MSD in **Figure 3** depends on the combined effect of the curvature of the surface, the interaction of the particles and, in the case of the projected displacement, the projection on the observation plane. In the next section we will deal with the connection between these different effects and their effect in the measured effective diffusion coefficient.

3 THE MSD OF FREE AND INTERACTING PARTICLES

Commonly, experimental setups for measuring the diffusion of particles on curved surfaces use confocal microscopy techniques [33, 57, 58]. Due to the focal length inherent to these techniques, the measure of the motions of the particles under study is preferentially performed in terms of their projection to the focal plane [22, 23]. In view of this, in the present section we study the equivalence between the description of the free diffusion over the surface (the geodesic displacement) and compare with the evolution of its projection in the planar disk constrained by the sphere, see **Figure 4**. First, we will deduce an expression for the MSD of free particles moving at a flat disk by considering how the entropic restriction of the movement (imposed by the fact that the particles cannot travel beyond the radius of the disk) is reflected in the transport properties that are used to describe the motion. Then, we will modify the MNET description to include the interaction and crowding of particles.

3.1 The MSD of Free Punctual Particles

From a thermodynamic point of view, the problem can be tackled by estimating the equivalent force keeping the system confined to diffuse in the planar disk delimited by the surface of the sphere of radius R, see **Figure 4**. This equivalent force can be written in

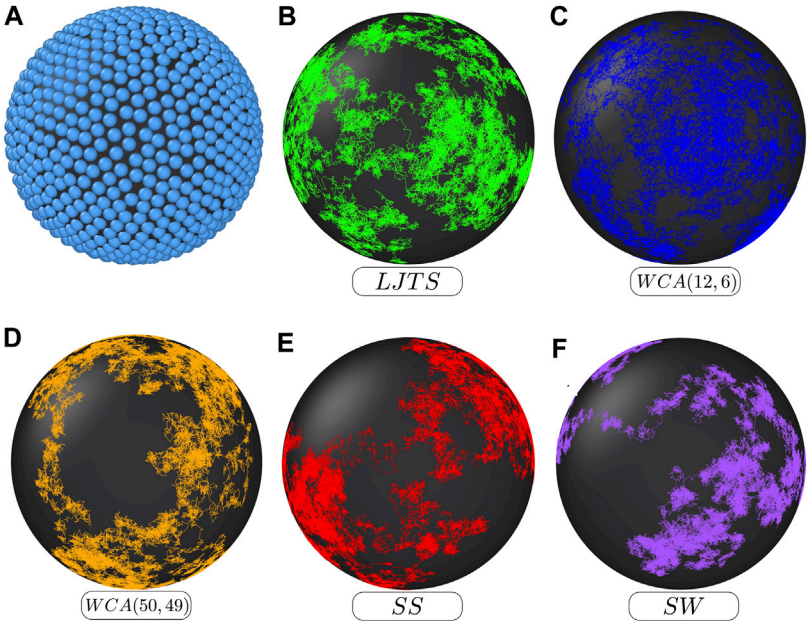

FIGURE 2 | (A) Representative instantaneous configuration of the system with N = 1,000 particles on the spherical surface of density ρ^* (= N/A) = 0.92 and with a radius of $R = 9.3\sigma$. **(B–F)** Path of a tracer particle over the spherical surface for the different interaction potentials.

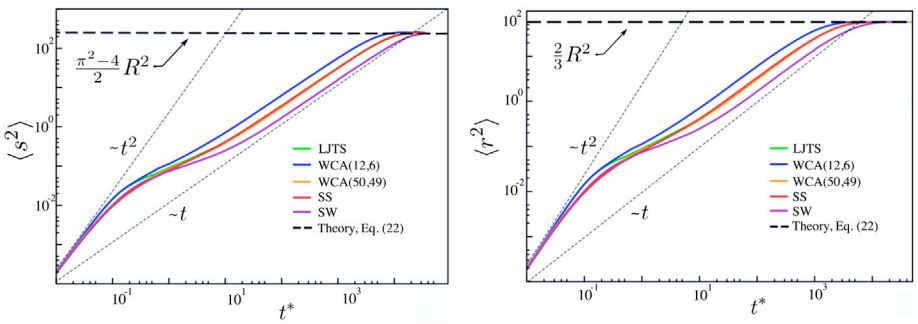

FIGURE 3 | MSD of interacting particles over the sphere with the potentials given in **Figure 1**. The geodesic arc, $\langle s^2 \rangle$, and the projected displacement in the XY plane, $\langle r^2 \rangle$, are plotted at left and right, respectively.

terms of a Taylor expansion. To first order, this correspond to an harmonic-like potential of the form

$$U(r) \simeq \frac{1}{2}\kappa_0 r^2. \tag{5}$$

The potential here is of an entropic origin, since it is due to the fact that the particles cannot leave the sphere projection or, equivalently, the planar disk. The maximum value of this potential, associated with the equivalent force, can be estimated by using the equipartition theorem [59]. Comparing the mean kinetic energy of the particles, $K = (3/2)kT$ (which corresponds to one half for each degree of freedom in the three dimensional description), with the maximum potential energy available for the trapped particles, $U_{max} = (1/2)\kappa_0 R^2$, we can estimate the value of the effective restorative coefficient κ_0 as

$$\kappa_0(R) = \frac{3k_B T}{R^2}. \tag{6}$$

Hence, the projected motion of the particles constrained to diffuse in a disk under the influence of the equivalent harmonic force can be described by means of the Smoluchowsky equation

$$\frac{\partial P}{\partial t} = D_0 \nabla^2 P - \frac{D_0}{k_B T}\nabla \cdot (P\mathbf{F}), \tag{7}$$

where k_B and T are Boltzmann constant and temperature, respectively. Since the equivalent force has radial symmetry, assuming an initial configuration with the same symmetry allow us to reduce the calculation of the MSD to the contribution in the radial coordinate r. In this case, we have

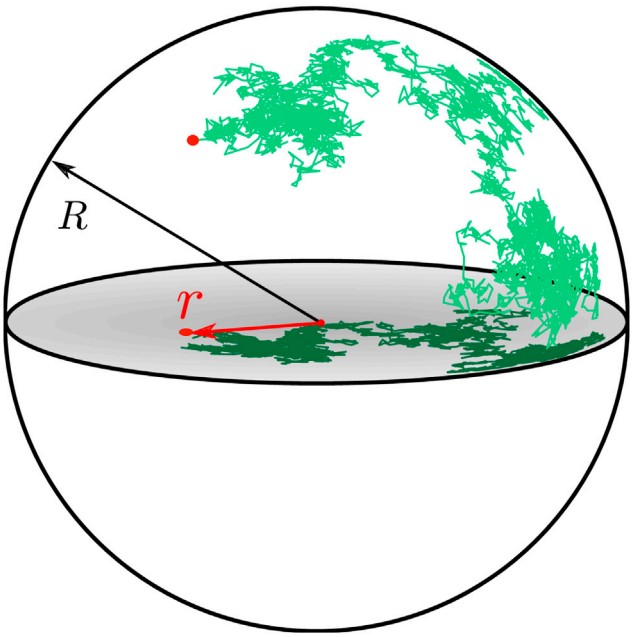

FIGURE 4 | Projection on an equatorial plane of the Brownian motion which takes place over the surface of a sphere of radius *R*. The polar radial coordinate of the particle *r* is measured on the plane.

$$\frac{\partial p}{\partial t} = \frac{D_0}{r}\frac{\partial}{\partial r}\left[r\frac{\partial p}{\partial r} + \frac{\kappa_0 r^2}{k_B T}p\right] \tag{8}$$

where the force that constraint the particles motions is $\mathbf{F} = -\nabla U$, with U given by **Eq. 5**, and the gradient and Laplacian operators are represented in polar coordinates.

The mean square displacement in the constrained disk system is therefore given by

$$\langle r^2\rangle = \int_0^R \int_0^{2\pi} r^2 p r dr. \tag{9}$$

The time evolution of the MSD is obtained by taking the derivative

$$\frac{d\langle r^2\rangle}{dt} = \int r^2 \frac{\partial p}{dt} dA, \tag{10}$$

And substituting **Eq. 8**. Assuming zero flux boundary condition: $\partial p/\partial r\,(R) = 0$ in the border of the disk and the conservation normalization equation, $\int_0^R p r dr = 1$, we can prove, using successive integration by parts, that

$$\frac{d\langle r^2\rangle}{dt} = 4D_0 - \frac{2D_0}{k_B T}\kappa_0\langle r^2\rangle. \tag{11}$$

The comparison of the previous result with the result of diffusion in an infinite planar surface, $\langle r^2\rangle = 4D_0 t$, shows that the effect of the confinement is proportional to the ratio of the potential and kinetic energies:

$$\frac{d\langle r^2\rangle}{dt} = 4D_0\left(1 - \frac{3}{2}\frac{\langle U\rangle}{\langle K\rangle}\right), \tag{12}$$

where the average here is over the ensemble of non-interacting particles. **Eq. 11** is readily solved using that $\langle r^2\rangle \to 0$ when $t \to 0$ as

$$\langle r^2\rangle = \frac{2k_B T}{\kappa_0}\left[1 - e^{-2\kappa_0 D_0 t/k_B T}\right]. \tag{13}$$

Substituting the estimated value of κ_0 given in **Eq. 6**, valid when particle interactions are negligible, we obtain

$$\langle r^2\rangle = \frac{2R^2}{3}\left[1 - e^{-6D_0 t/R^2}\right]. \tag{14}$$

This result has been obtained by using different methods in Ref. [10] and, as expected, only depends upon geometrical considerations resulting from averaging methodologies applied directly to the Laplace-Beltrami diffusion equation.

This result describing the projection of the surface to the disk can be contrasted to the result of particles really moving on a planar disk of radius R, where $K = k_B T$ (since there are only two freedom degrees), $\kappa_0 = 2k_B T/R^2$, and therefore, from **Eq. 11**, we have

$$\langle r^2\rangle_{2D} = R^2\left[1 - e^{-4D_0 t/R^2}\right]. \tag{15}$$

Comparison between **Eqs 14**, **15** shows that the displacement in a sphere respect to a planar projection has an average reduction by a factor of 2/3 for long times. This reduction factor in the displacements can be deduced also by evaluating the ratio between the effective diffusion coefficient measured on a planar region, D_0, with respect to that measured in the observation plane, $D_\perp$. The result is

$$\frac{D_\perp}{D_0} = \frac{1}{2}\left(1 + \langle n_z^2\rangle\right), \tag{16}$$

Where $\langle n_z^2\rangle$ is the geometric average of the quadratic vertical component of the normal vector [10, 59]. For the sphere we have $n_z = \cos\theta$, from where it is straightforward deduced that $\langle n_z^2\rangle = 1/3$ giving the expected result $D_\perp/D_0 = 2/3$.

3.2 The MSD of Interacting Non-punctual Particles

In the previous subsection we have shown that the entropic restrictions, present by the fact that tracer particles move over a surface with a finite number of accessible states, are responsible for the observed saturation value reached by the MSD at long times. However, as we have seen in **Figure 3**, the simulations show that the time behavior of the MSD at intermediate times scales with a time dependence t^α with $\alpha \leq 1$. Therefore, for certain interaction potentials, anomalous diffusion is observed. This fact requires that the model developed in **Section 3.1** should be generalized to cope with particle interaction.

This generalization goes along the same lines of Santamaría-Holek et al. [32], where a Smoluchowski description with

time-dependent coefficients was used to demonstrate that the exponent characterizing the sub-diffusion is controlled by the nature of the local cages and the free space at disposal for their motion. In our case, since the single particle MSD reported here accounts for the motion of independent particles in a crowded media, the description of the diffusion can be given also in terms of the generalized Smoluchowski equation for the single-particle distribution function [61]. This equation for the probability is the counterpart of the respective generalized Langevin equation with memory effects, commonly used to describe microrheological experiments and has the peculiarity of being equivalent in the long-time regime to the Smoluchowski equation with time dependent coefficients [29, 30]. This fact was generalized in Refs. [31, 33, 62] for the case of power-law dependent memory kernels which are equivalent to time dependent diffusion coefficients of the form

$$D_s(t) \approx D_0\left(\frac{t}{\tau}\right)^{\alpha-1}, \tag{17}$$

where τ is a characteristic time of the anomalous diffusion process. In this equation, the exponent $\alpha \in (0, 1]$ characterizes how strong sub-diffusion is and, as it was shown in Ref. [32], has the general form

$$\alpha = \left(1 - B_1\frac{a}{\xi}\right)\frac{3k_BT}{\kappa_0 R^2}. \tag{18}$$

Besides the entropic effect introduced through the ratio k_BT/κ_0R^2, the **Eq. 18**, through the factor $1 - B_1(a/\xi)$, contains the two main ingredients mentioned previously, namely, the free-area at disposal to perform diffusion a/ξ, and the nature of the local cages through the coefficient B_1. The characteristic length ξ is related with the free-area in which the finite particles can move in a surface of total area A: $\xi = A_{free}^{1/2} \simeq R(1 - Ma^2/\mathrm{R}^2)^{1/2}$ where M is the number of particles forming the cage. In this case, we have

$$\alpha = \left(1 - B_1\frac{aR}{R^2 - Ma^2}\right), \tag{19}$$

This expression for the sub-diffusion exponent shows that it only depends in the radii of the particles and sphere, and on the parameter B_1. This parameter indirectly depends in the nature of the interaction potentials used. In the context of hydrodynamics [63], it was related with the correction introduced by hydrodynamic interactions over the motion of a particle when this motion takes places near to a solid wall. Since these interactions are related to the potential interactions among particles, one may conjecture that the parameter B_1 is a measure of the effect that different interaction potentials have on the cages' dynamic structure and, therefore, of the different values that the sub-diffusion exponent may take.

Even in this approximation, it results difficult to estimate theoretically the parameters in **Eq. 18**. However, it is clear that the exponent of the subdiffusive process is linked to the shape of the interacting potential, the curvature of the surface and the projection of the forces to the observation plane. In order to find its value for the different potentials in **Figure 1**, we will adjust the data of the numerical simulations, using the Smoluchowski equation, but now in terms of this time dependent diffusion coefficient as we detail below.

Therefore, we will consider that the single particle Smoluchowski equation describing the dynamics of a tracer particle in an effective medium of $N - 1$ interacting non-punctual particles takes the form

$$\frac{\partial p}{\partial t} = \frac{D_s(t)}{r}\frac{\partial}{\partial r}\left[r\frac{\partial p}{\partial r} + \frac{1}{k_BT}\kappa_0 r^2 p\right], \tag{20}$$

Where now the time dependent coefficient is given through **Eqs. 17**, **19**. From the last equation, repeating the same procedure of the last section, the temporal evolution of the MSD is obtained to be

$$\langle r^2\rangle = \frac{2k_BT}{\kappa_0}\left\{1 - \exp\left[-\frac{2\kappa_0}{k_BT}\left(\int_0^t D_s(t')dt'.\right)\right]\right\}. \tag{21}$$

Using **Eq. 6** we finally have

$$\langle r^2\rangle = \frac{2}{3}R^2\left\{1 - \exp\left[-\frac{6}{R^2}\left(\int_0^t D_s(t')dt'\right)\right]\right\}, \tag{22}$$

Which is the general expression for the MSD of the tracer particles valid for the whole time interval. From this equation, it is possible to deduce the temporal behavior of the diffusion coefficient for all the stages of the process in terms of the numerical data provided by the simulations as

$$D_s(t) = \frac{R^2}{6}\frac{\left(d\langle r^2\rangle/dt\right)(t)}{\left((2/3)R^2 - \langle r^2\rangle(t)\right)}. \tag{23}$$

Notice that this equation reproduces the expected behavior for short and long times. For short times $\langle r^2\rangle \to 0$ and $d\langle r^2\rangle/dt \to 4D_0$ and therefore $D_s \to D_0$. For long times, it is expected that the MSD saturates and, therefore, $d\langle r^2\rangle/dt \to 0$ with $D_s \to 0$.

At the other hand, when (**Eq. 22**) is used in combination with the diffusion coefficient in **Eq. 17**, it accounts only for the process once the sub-diffusion stage has started. At intermediary times, it accounts for the sub-diffusion associated with particle interactions and cage diffusion effects and, for long times, it account for the fact that the particles have a restricted number of accessible states in a finite domain. In the next section we will use the numerical simulation in order to find the general behavior of the temporal diffusion coefficient and the exponents of sub-diffusion for the potentials we have considered in **Section 2**.

4 COMPARISON BETWEEN MODEL AND SIMULATIONS

We have shown that the projection on the equatorial plane of the geodesic MSD, directly measured in the numerical simulations, is an equivalent form to characterize the diffusive dynamics of the particles. We have explained how the saturation value of the MSD rescales due to the restricted number of accessible states, giving rise to entropic constrictions on the dynamics of the particles.

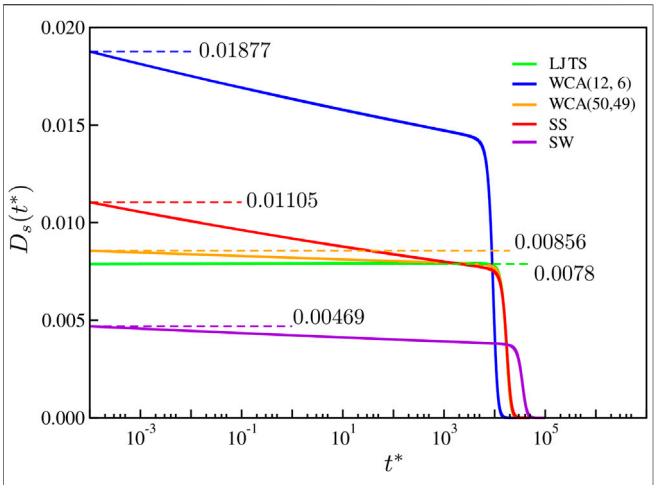

FIGURE 5 | Projected surface diffusion coefficient $D_s(t)$ as a function of the time for the interacting particles with potentials given in **Figure 1**. The dashed lines represent the reference value D_0 in a planar surface.

For short and intermediate times, our methodology allows us to consider how different aspects modify the behavior of the MSD of interacting particles forced to diffuse in the surface of the sphere. All these aspects are clearly represented in **Figure 5**, where we plot the time-dependent diffusion coefficient, D_s, given in **Eq. 23** for the potentials chosen, and illustrated in **Figure 1**. For constructing this plot, the data from the functions $\langle r^2\rangle(t)$ and $d\langle r^2\rangle/dt$ obtained from numerical simulations are directly substituted in (**Eq. 17**) for $D_s(t)$.

The first aspect to notice is the reference diffusion coefficient, D_0. This is marked as a dashed line in **Figure 5** and represents the surface diffusion coefficient in an infinite planar surface, and negligible interaction potential among particles. In **Figure 5** it is seen that, for the used potentials, the value of the diffusion coefficients augments according to the order: *SW*, *LJTS*, *SS*, and *WCA*(12, 6). The color key is the same as in **Figure 1**.

The second aspect to notice in the temporal dependence of the diffusion coefficient $D_s(t)$ is the emergence of sub-diffusion due to the crowding effects. This results in different slopes of the curve $D_s(t)$ at intermediary times and, therefore, corresponds to different values of the sub-diffusion exponent α. In order to compare quantitatively the sub-diffusion for the different potentials, in **Figure 6**, we adjust the data from numerical simulations using (**Eq. 22**) with the temporal dependence of the diffusion coefficient in (**Eq. 17**) using the least squares method. The value of the local diffusion coefficient D_0 and the sub-diffusion exponent α together with the fits of the data are given in **Figure 6**.

Figure 5, show that the value of the diffusion constant D_0 is smaller for hardest potentials (*WCA*(12, 6) and *SS*) than for softer potentials (*WCA*(50, 49), *LJTS* and *SW*). The potentials having wells also show this tendency since the diffusion constant for the *LJTS* is larger that of the SW potential. The attractive part of the potentials decreases, in turn, the kinetic energy of the particles surrounding the tracer particle and, therefore, the energy availability to perform position fluctuations. This interpretation is clear after a comparison between the potentials *WCA*(50, 49) and *WCA*(12, 6), which have a similar functional form but different degree of penetrability. Another aspect to be noticed is the steepest drop of the diffusion coefficients (lower α) for the potentials with a tilted repulsive part after $r = 1$, that is, *SS* and *WCA*(12, 60). A better understanding of the effect of the shape and hardness of the interaction potentials on the diffusion constants and the sub-diffusion process will require its own work.

Finally, the third aspect to notice is that both the ballistic and long-time behaviors of the MSD appear in all cases since not depend on the interaction potential. Because of this, they do not provide information of the fluid medium where the diffusion occurs. As it is seen in **Figure 5**, the final drop of the diffusion coefficient to zero occurs earlier as the diffusion coefficient is lower, as expected.

Our work shows that the deviations of the MSD relative to the planar behavior represent the effect that the particle interaction and crowding effects have on the dynamics. This effect is coupled with the presence of an entropic force restricting the number of accessible states. We prove that these two effects are well captured by the projected diffusion coefficient D_s, given in **Figure 5** and which has been reported in previous numerical simulations and experiments [53, 64].

The excellent agreement in **Figure 6** among simulation results and the theory proposed indicates that particle interactions control the cage effect and the sub-diffusion regime. The delay induced by the crowded scenario appears since the transient stage, and its influence is captured by the memory effects that the effective diffusion coefficient $D_s(t)$ incorporates. We have found that the value of the parameters used for fitting the MSD curves depend upon the used potentials and further numerical and theoretical studies are necessary in order to show the relation between the form of the potential interaction and the surface diffusion coefficient. Similar commentaries can be done concerning the specific value for the radii of the particles and the surface density. These values allowed us to capture the effect of the surface density and the form of the potential on the sub-diffusion observed. Nonetheless, a more detailed study on the dependence of the diffusion properties on this factor will require a future work.

5 CONCLUSION

We have studied the statistical and dynamical properties of a system of interacting particles constituting a fluid embedded on a sphere's surface. To understand the link between the microscopic properties of the fluid and the observed MSD, we have proposed a diffusion model incorporating memory and entropic effects that allowed us to derive a simple and powerful expression for the projected time-dependent diffusion coefficient. This expression allows us to characterize the dependence of the diffusive dynamics on the particle interactions and surface curvature. This approach takes into account the change of perspective

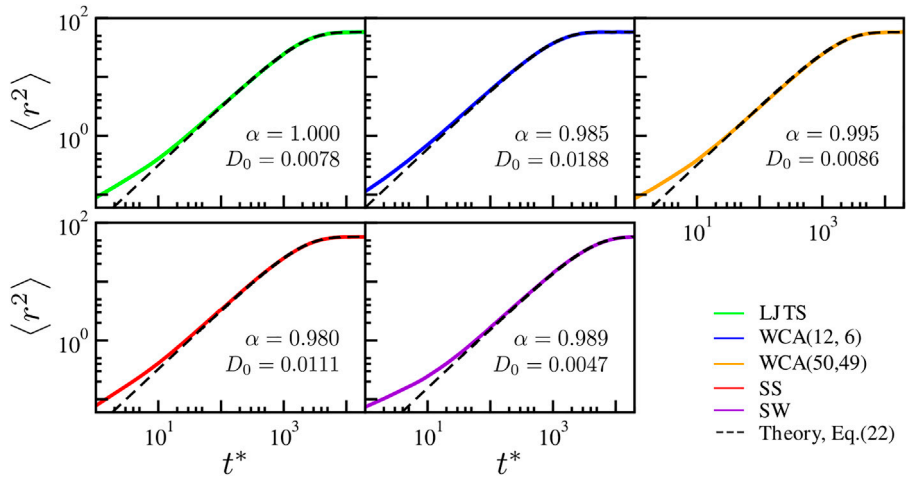

FIGURE 6 | Comparison between the projected MSD obtained from simulations (colored solid lines) and theory (black lines) according to **Eq. 22**. The values of the parameters used are included in each plot. The scaling factor in **Eq. 17** is $\tau = 1$ for all cases.

inherent to the experimental measure of diffusion of particles on closed surfaces. The formalism proposed in this work reproduces also some limiting cases previously studied in the literature and exemplifies, with the use of ideas emerging from irreversible thermodynamics, how we can provide a more flexible description that helps to interpret complex phenomena occurring at the surface.

In this work, we have shown in **Figure 3** that the dynamics of the MSD reflects four stages. Two, at short times $t^* \leq 10^{-1}s$, are associated with the ballistic regime and how it ceases; and other two ($t^* \geq 10^{-1}s$) associated with the diffusion regime in presence of cages at the intermediate and long time regimes, corresponding to anomalous diffusion and saturation, respectively. Using the ideas of the MNET we use the Smoluchowski equation for describing the process once the diffusion regime starts and this is shown **Figure 6** for the intermediary and long time behaviors of the MSD. In contrast, modeling the regimes at short times will require another kind of kinetic mechanism. However, it is worth mentioning that, under the perspective of biological applications of surface diffusion in crowded membrane environments we discuss below, only the subdiffusive regime is accessible to measurements with the actual experimental time-resolution capabilities and therefore, this does not constitute a limitation to our conclusions.

In the realm of applications, this study allows us to establish a connection with models and experiments studying the diffusion of several tracers in the cytoplasm of living cells which often exhibit heterogeneous distribution of macromolecular crowders [65–67]. This crowding is extremely important in the surface membrane and might affect the properties of anomalous diffusion. It is known, for example, that going from a less to a more crowded region will slow down the dynamics, both in terms of the exponent and diffusivity [68–70]. This results very important since the slow transport in the cell membrane of lipids and proteins is linked with protein cluster formation, phase segregation, lipid droplet formation, signal propagation and other crucial functions occurring on the cell surface which can be enhanced by the presence of sub-diffusion [71, 72].

DATA AVAILABILITY STATEMENT

The original contributions presented in the study are included in the article/Supplementary Material, further inquiries can be directed to the corresponding author.

AUTHOR CONTRIBUTIONS

IS-H, AL-D and JM-R designed the research. AL-D and JM-V performed the calculations and methology. IS-H, JM-R, AL-D and JM-V performed analysis. IS-H, JM-R, AL-D and SH wrote the original draft. All authors contributed to the analysis and discussion of the data and the writing of the paper.

FUNDING

SIH is grateful to projects UNAMDGAPA-PAPIIT IN114721 and LANCAD-UNAM-DGTIC-276. ISH acknowledges UNAM-DGAPA for financial support under grant number IN117419.

ACKNOWLEDGMENTS

Authors appreciate the technical support of Carlos Sair Flores Bautista, Alejandro de León Cuevas, Jair Santiago García Sotelo and Luis Alberto Aguilar Bautista from Laboratorio Nacional de Visualización Científica Avanzada (LAVIS-UNAM)

REFERENCES

1. Moreno-Razo JA, Sambriski EJ, Abbott NL, Hernández-Ortiz JP, de Pablo JJ. Liquid-crystal-mediated self-assembly at nanodroplet interfaces. *Nature* (2012) 485(7396):86. doi:10.1038/nature11084
2. Holly C. Gaede and Klaus Gawrisch. Lateral diffusion rates of lipid, water, and a hydrophobic drug in a multilamellar liposome. *Biophys J* (2003) 85(3):1734–40. doi:10.1016/S0006-3495(03)74603-7
3. Nuytten N, Hakimhashemi M, Ysenbaert T, Defour L, Trekker J, Soenen SJ, et al. Pegylated lipids impede the lateral diffusion of adsorbed proteins at the surface of (magneto)liposomes. *Colloids Surf B Biointerfaces* (2010) 80(2): 227–31. doi:10.1016/j.colsurfb.2010.06.009
4. Danelian E, Karlén A, Karlsson R, Winiwarter S, Hansson A, Löfås S, et al. Spr biosensor studies of the direct interaction between 27 drugs and a liposome surface: correlation with fraction absorbed in humans. *J Med Chem* (2000) 43(11):2083–6. doi:10.1021/jm991156g
5. Ledesma-Durán A, Hernández SI, Santamaría-Holek I. Effect of surface diffusion on adsorption-desorption and catalytic kinetics in irregular pores. I. Local kinetics. *J Phys Chem C* (2017) 121(27):14544. doi:10.1021/acs.jpcc.7b03652
6. Ledesma-Durán A, Hernández SI, Santamaría-Holek I. Effect of surface diffusion on adsorption-desorption and catalytic kinetics in irregular pores. II. Macro-kinetics. *J Phys Chem C* (2017) 121(27):14557. doi:10.1021/acs.jpcc.7b03653
7. Faraudo J. Diffusion equation on curved surfaces. I. Theory and application to biological membranes. *J Chem Phys* (2002) 116(13):5831. doi:10.1063/1.1456024
8. Reister-Gottfried E, Leitenberger S, Seifert U. Diffusing proteins on a fluctuating membrane: analytical theory and simulations. *Phys Rev E - Stat Nonlinear Soft Matter Phys* (2010) 81(3):031903. doi:10.1103/PhysRevE.81.031903
9. Castro-Villarreal P, Villada-Balbuena A, Méndez-Alcaraz JM, Castañeda-Priego R, Estrada-Jiménez S. A brownian dynamics algorithm for colloids in curved manifolds. *J Chem Phys* (2014) 140(21):214115. doi:10.1063/1.4881060
10. Castro-Villarreal P. Intrinsic and extrinsic measurement for brownian motion. *J Stat Mech* (2014) 2014(5):P05017. doi:10.1088/1742-5468/2014/05/p05017
11. Reister-Gottfried E, Leitenberger SM, Seifert U. Hybrid simulations of lateral diffusion in fluctuating membranes. *Phys Rev E - Stat Nonlinear Soft Matter Phys* (2007) 75(1):011908. doi:10.1103/PhysRevE.75.011908
12. Castro-Villarreal P. Brownian motion meets riemann curvature. *J Stat Mech* (2010) 2010(8):P08006. doi:10.1088/1742-5468/2010/08/p08006
13. Apaza L, Sandoval M. Brownian self-driven particles on the surface of a sphere. *Phys Rev E* (2017) 96(2):022606. doi:10.1103/PhysRevE.96.022606
14. Petersen CF, Schrack L, Franosch T. Static properties of quasi-confined hard-sphere fluids. *J Stat Mech* (2019) 2019(8):083216. doi:10.1088/1742-5468/ab3342
15. Jinnai H, Koga T, Nishikawa Y, Hashimoto T, Hyde ST. Curvature determination of spinodal interface in a condensed matter system. *Phys Rev Lett* (1997) 78(11):2248. doi:10.1103/physrevlett.78.2248
16. Saito A, Foley HC. Curvature and parametric sensitivity in models for adsorption in micropores. *AIChE J* (1991) 37(3):429. doi:10.1002/aic.690370312
17. Tvergaard V. Effect of yield surface curvature and void nucleation on plastic flow localization. *J Mech Phys Solid* (1987) 35(1):43. doi:10.1016/0022-5096(87)90027-5
18. Roux A, Cuvelier D, Nassoy P, Prost J, Bassereau P, Goud B. Role of curvature and phase transition in lipid sorting and fission of membrane tubules. *EMBO J* (2005) 24(8):1537. doi:10.1038/sj.emboj.7600631
19. Resende FJ, Costa BV. Molecular-dynamics study of the diffusion coefficient on a crystal surface. *Phys Rev B* (2000) 61(19):12697. doi:10.1103/physrevb.61.12697
20. Wang D, He C, Stoykovich MP, Schwartz DK. Nanoscale topography influences polymer surface diffusion. *ACS Nano* (2015) 9(2):1656. doi:10.1021/nn506376n
21. Bulnes FM, Pereyra VD, Riccardo JL. Collective surface diffusion: n-fold way kinetic Monte Carlo simulation. *Phys Rev E* (1998) 58(1):86. doi:10.1103/physreve.58.86
22. Benavides-Parra JC, Jacinto-Méndez D, Brotons G, Carbajal-Tinoco MD. Brownian motion near a liquid-gas interface. *J Chem Phys* (2016) 145(11): 114902. doi:10.1063/1.4962746
23. Sandoval-Jiménez IM, Jacinto-Méndez D, Toscano-Flores LG, Carbajal-Tinoco MD. Brownian-particle motion used to characterize mechanical properties of lipid vesicles. *J Chem Phys* (2020) 152(1):014901. doi:10.1063/1.5133092
24. King MR. Apparent 2-d diffusivity in a ruffled cell membrane. *J Theor Biol* (2004) 227(3):323–6. doi:10.1016/j.jtbi.2003.11.010
25. Naji A, Brown FL. Diffusion on ruffled membrane surfaces. *J Chem Phys* (2007) 126(23):235103. doi:10.1063/1.2739526
26. Gov NS. Diffusion in curved fluid membranes. *Phys Rev E-Stat Nonlinear Soft Matter Phys* (2006) 73(4):041918. doi:10.1103/PhysRevE.73.041918
27. Juffer AH, Berendsen HJC. Dynamic surface boundary conditions. *Mol Phys* (1993) 79(3):623. doi:10.1080/00268979300101501
28. Mie G. Zur kinetischen Theorie der einatomigen Körper. *Ann Phys* (1903) 316(8):657. doi:10.1002/andp.19033160802
29. Adelman SA. Fokker-Planck equations for simple non-Markovian systems. *J Chem Phys* (1976) 64(1):124–30. doi:10.1063/1.431961
30. Tokuyama M, Mori H. Statistical-mechanical theory of random frequency modulations and generalized brownian motions. *Prog Theor Phys* (1976) 55(2): 411–29. doi:10.1143/ptp.55.411
31. Metzler R, Barkai E, Klafter J. Deriving fractional fokker-planck equations from a generalised master equation. *Europhys Lett* (1999) 46(4):431. doi:10.1209/epl/i1999-00279-7
32. Santamaría-Holek I, Rubi JM. Finite-size effects in microrheology. *J Chem Phys* (2006) 125(6):64907. doi:10.1063/1.2241190
33. Santamaría-Holek I, Rubí JM, Gadomski A. Thermokinetic approach of single particles and clusters involving anomalous diffusion under viscoelastic response. *J Phys Chem B* (2007) 111(9):2293. doi:10.1021/jp0675375
34. Sevilla FJ, Rodríguez RF, Gómez-Solano JR. Generalized ornstein-uhlenbeck model for active motion. *Phys Rev E* (2019) 100:032123. doi:10.1103/PhysRevE.100.032123
35. Reguera D, Rubí JM, Vilar JM. The mesoscopic dynamics of thermodynamic systems. *J Phys Chem B* (2005) 109(46):21502. doi:10.1021/jp052904i
36. Pan W, Vekilov PG, Lubchenko V. Origin of anomalous mesoscopic phases in protein solutions. *J Phys Chem B* (2010) 114(22):7620. doi:10.1021/jp100617w
37. Dekker H. Nonisothermal activation: nonequilibrium thermodynamics of metastable mesoscopic systems. *Phys Rev, A* (1991) 43(8):4224. doi:10.1103/physreva.43.4224
38. Santamaría-Holek I, Hernández S, García-Alcántara C, Ledesma-Durán A. Review on the macro-transport processes theory for irregular pores able to perform catalytic reactions. *Catalysts* (2019) 9(3):281. doi:10.3390/catal9030281
39. Santamaría-Holek I, Grzywna ZJ, Rubi JM. Entropic effects in diffusion-adsorption processes in micropores. *Eur Phys J Spec Top* (2013) 222(1):129. doi:10.1140/epjst/e2013-01831-2
40. Reguera D, Rubí JM. Kinetic equations for diffusion in the presence of entropic barriers. *Phys Rev E-Stat Nonlinear Soft Matter Phys* (2001) 64(6):061106. doi:10.1103/PhysRevE.64.061106
41. Chacón-Acosta G, Pineda I, Dagdug L. Diffusion in narrow channels on curved manifolds. *J Chem Phys* (2013) 139(21):214115. doi:10.1063/1.4836617
42. Santamaría-Holek I, Ledesma-Durán A, Hernández SI, García-Alcántara C, Andrio A, Compañ V. Entropic restrictions control the electric conductance of superprotonic ionic solids. *Phys Chem Chem Phys* (2020) 22(2):437. doi:10.1039/c9cp05486c
43. Andersen HC, Weeks JD, Chandler D. Relationship between the hard-sphere fluid and fluids with realistic repulsive forces. *Phys Rev A* (1971) 4(4):1597. doi:10.1103/physreva.4.1597
44. Jover J, Haslam AJ, Galindo A, Jackson G, Müller EA. Pseudo hard-sphere potential for use in continuous molecular-dynamics simulation of spherical and chain molecules. *J Chem Phys* (2012) 137(14):144505. doi:10.1063/1.4754275
45. Julien-Piera V, Gilles T, Pascal V. Dynamics of a monodisperse Lennard-Jones system on a sphere. *Mol Phys* (2014) 112(9–10):1330. doi:10.1080/00268976.2014.901568
46. Julien-Piera V, Gilles T, Pascal V. Mode-coupling approach for the slow dynamics of a liquid on a spherical substrate. *J Chem Phys* (2015) 143(8): 084505. doi:10.1063/1.4928513
47. Julien-Piera V, Gilles T, Pascal V. Glassy dynamics of dense particle assemblies on a spherical substrate. *J Chem Phys* (2018) 148(16):164501. doi:10.1063/1.5027389
48. Swope WC, Andersen HC, Berens PH, Wilson KR. A computer simulation method for the calculation of equilibrium constants for the formation of

physical clusters of molecules: application to small water clusters. *J Chem Phys* (1982) 76(1):637. doi:10.1063/1.442716
49. Yamamoto E, Akimoto T, Yasui M, Yasuoka K. Origin of subdiffusion of water molecules on cell membrane surfaces. *Sci Rep* (2014) 4:4720. doi:10.1038/srep04720
50. Chipot C, Comer J. Subdiffusion in membrane permeation of small molecules. *Sci Rep* (2016) 6:35913. doi:10.1038/srep35913
51. Tan P, Liang Y, Xu Q, Mamontov E, Li J, Xing X, et al. Gradual crossover from subdiffusion to normal diffusion: a many-body effect in protein surface water. *Phys Rev Lett* (2018) 120(24):248101. doi:10.1103/PhysRevLett.120.248101
52. Ghosh SK, Cherstvy AG, Grebenkov DS, Metzler R. Anomalous, non-Gaussian tracer diffusion in crowded two-dimensional environments. *New J Phys* (2016) 18(1):013027. doi:10.1088/1367-2630/18/1/013027
53. Schwille P, Korlach J, Webb WW. Fluorescence correlation spectroscopy with single-molecule sensitivity on cell and model membranes. *Cytometry* (1999) 36(3):176–82. doi:10.1002/(sici)1097-0320(19990701)36:3<176::aid-cyto5>3.0.co;2-f
54. Golan Y, Sherman E. Resolving mixed mechanisms of protein subdiffusion at the t cell plasma membrane. *Nat Commun* (2017) 8(1):15851–15. doi:10.1038/ncomms15851
55. Ehrig J, Petrov EP, Schwille P. Near-critical fluctuations and cytoskeleton-assisted phase separation lead to subdiffusion in cell membranes. *Biophys J* (2011) 100(1):80–9. doi:10.1016/j.bpj.2010.11.002
56. Weiss M, Elsner M, Kartberg F, Nilsson T. Anomalous subdiffusion is a measure for cytoplasmic crowding in living cells. *Biophys J* (2004) 87(5):3518–24. doi:10.1529/biophysj.104.044263
57. Zhong Y, Zhao L, Tyrlik PM, Wang G. Investigating diffusing on highly curved water-oil interface using three-dimensional single particle tracking. *J Phys Chem C* (2017) 121(14):8023–32. doi:10.1021/acs.jpcc.7b01721
58. Sarmiento-Gomez E, Santamaría-Holek I, Castillo R. Mean-square displacement of particles in slightly interconnected polymer networks. *J Phys Chem B* (2014) 118(4):1146. doi:10.1021/jp4105344
59. Mendoza CI, Santamaría-Holek I, Pérez-Madrid A. Effective temperatures and the breakdown of the Stokes-einstein relation for particle suspensions. *J Chem Phys* (2015) 143(10):104506. doi:10.1063/1.4930550
60. Gustafsson S, Halle B. Diffusion on a flexible surface. *J Chem Phys* (1997) 106(5):1880–7. doi:10.1063/1.473326
61. Mason TG, Ganesan K, van Zanten JH, Wirtz D, Kuo SC. Particle tracking microrheology of complex fluids. *Phys Rev Lett* (1997) 79(17):3282. doi:10.1103/physrevlett.79.3282
62. Rodríguez RF, Salinas-Rodríguez E, W Dufty J. Fokker-Planck and Langevin descriptions of fluctuations in uniform shear flow. *J Stat Phys* (1983) 32(2):279–98. doi:10.1007/BF01012711
63. Happel J, Brenner H. *Low Reynolds number hydrodynamics: with special applications to particulate media*, Vol. 1. Berlin, Germany: Springer Science & Business Media (2012).
64. Saxton MJ. A biological interpretation of transient anomalous subdiffusion. i. qualitative model. *Biophys J* (2007) 92(4):1178–91. doi:10.1529/biophysj.106.092619
65. Szymanski J, Weiss M. Elucidating the origin of anomalous diffusion in crowded fluids. *Phys Rev Lett* (2009) 103(3):038102. doi:10.1103/PhysRevLett.103.038102
66. Sharonov A, Bandichhor R, Burgess K, Petrescu AD, Schroeder F, Kier AB, et al. Lipid diffusion from single molecules of a labeled protein undergoing dynamic association with giant unilamellar vesicles and supported bilayers. *Langmuir* (2008) 24(3):844–50. doi:10.1021/la702600w
67. Javanainen M, Hammaren H, Monticelli L, Jeon JH, Miettinen MS, Martinez-Seara H, et al. Anomalous and normal diffusion of proteins and lipids in crowded lipid membranes. *Faraday Discuss* (2013) 161:397–59. doi:10.1039/c2fd20085f
68. Guigas G, Weiss M. Sampling the cell with anomalous diffusion - the discovery of slowness. *Biophys J* (2008) 94(1):90–4. doi:10.1529/biophysj.107.117044
69. Jeon JH, Monne HM, Javanainen M, Metzler R. Anomalous diffusion of phospholipids and cholesterols in a lipid bilayer and its origins. *Phys Rev Lett* (2012) 109(18):188103. doi:10.1103/PhysRevLett.109.188103
70. Goose JE, Sansom MS. Reduced lateral mobility of lipids and proteins in crowded membranes. *PLoS Comput Biol* (2013) 9(4):e1003033. doi:10.1371/journal.pcbi.1003033
71. Metzler R, Jeon JH, Cherstvy AG. Non-brownian diffusion in lipid membranes: experiments and simulations. *Biochim Biophys Acta* (2016) 1858(10):2451–67. doi:10.1016/j.bbamem.2016.01.022
72. Guigas G, Weiss M. Effects of protein crowding on membrane systems. *Biochim Biophys Acta* (2016) 1858(10):2441–50. doi:10.1016/j.bbamem.2015.12.021

Conflict of Interest: The authors declare that the research was conducted in the absence of any commercial or financial relationships that could be construed as a potential conflict of interest.

frontiers in Physics

ORIGINAL RESEARCH
published: 29 March 2021
doi: 10.3389/fphy.2021.643333

Work Extraction and Performance of Colloidal Heat Engines in Viscoelastic Baths

*Juan Ruben Gomez-Solano**

Departamento de Sistemas Complejos, Instituto de Física, Universidad Nacional Autónoma de México, Ciudad de México, Mexico

A colloidal particle embedded in a fluid can be used as a microscopic heat engine by means of a sequence of cyclic transformations imposed by an optical trap. We investigate a model for the operation of such kind of Brownian engines when the surrounding medium is viscoelastic, which endows the particle dynamics with memory friction. We analyze the effect of the relaxation time of the fluid on the performance of the colloidal engine under finite-time Stirling cycles. We find that, due to the frequency-dependence of the friction in viscoelastic fluids, the mean power delivered by the engine and its efficiency can be highly enhanced as compared to those in a viscous environment with the same zero-shear viscosity. In addition, with increasing fluid relaxation time the interval of cycle times at which positive power output can be delivered by the engine broadens. Our results reveal the importance of the transient behavior of the friction experienced by a Brownian heat engine in a complex fluid, which cannot be neglected when driven by thermodynamic cycles of finite duration.

Keywords: stochastic thermodynamics, heat engine, fluctuations, noise, viscoelasticity, memory effects, non-equilibrium processes, colloids

OPEN ACCESS

Edited by:
Ramon Castañeda-Priego, University of Guanajuato, Mexico

Reviewed by:
Roberto Cerbino, University of Vienna, Austria
Erick Sarmiento-Gomez, University of Guanajuato, Mexico

***Correspondence:**
Juan Ruben Gomez-Solano
r_gomez@fisica.unam.mx

Specialty section:
This article was submitted to Soft Matter Physics, a section of the journal Frontiers in Physics

Received: *17 December 2020*
Accepted: *04 March 2021*
Published: *29 March 2021*

Citation:
Gomez-Solano JR (2021) Work Extraction and Performance of Colloidal Heat Engines in Viscoelastic Baths. Front. Phys. 9:643333. doi: 10.3389/fphy.2021.643333

1. INTRODUCTION

Historically, the study of heat engines has played a fundamental role in the general understanding of energy exchanges in macroscopic systems. For instance, the conception of the well-known Carnot cycle almost two centuries ago was motivated by the design of efficient engines capable of performing mechanical work by extracting energy from a hot reservoir and transferring heat to a cold reservoir, which finally led to the formulation of the second law of thermodynamics. Carnot theorem imposes a universal bound for the maximum efficiency that can be ideally achieved by any heat engine working reversibly in the quasi-static limit. Since then, further theoretical results on the efficiency of irreversible heat engines under finite-time thermodynamic cycles with non-zero power output have been obtained [1–6], which turn out to be important for practical applications.

In more recent years, advances in miniaturization technologies have allowed researchers in both basic and applied science to conceive the design of micron- and submicron-sized machines with the ability to perform specific tasks in the mesoscopic realm, e.g., controlled cargo transport through microchannels and nanopores, *in situ* cell manipulation, assembly of functional microstructures, micropumping, microflow rectification, micromixing of fluids, and bio-inspired artificial locomotion [7–9]. This has triggered an increasing interest in investigating the energetics and performance of mesoscopic heat engines, which, similar to their macroscopic counterparts, must be able to convert in an efficient manner the energy absorbed from their environment into useful work [10, 11]. An important issue that arises in the theoretical description

and implementation of such devices is that they must operate under highly non-equilibrium conditions with pronounced thermal fluctuations, which poses important conceptual and practical challenges [12]. A significant progress in the theoretical analysis of mesoscopic heat engines has been made in the last two decades with the advent of stochastic thermodynamics, which extends concepts of classical thermodynamics such as heat, work and entropy production to the level of single stochastic trajectories for both equilibrium and driven systems [13–16]. Within this theoretical framework, it is possible to carry out a comprehensive analysis of the performance of stochastic heat engines based on Brownian particles subject to periodically time-dependent potentials and temperatures [17–21]. Along the same lines, optical micromanipulation techniques have facilitated during the last decade the experimental realization of simple colloidal heat engines, which are composed of a single colloidal particle as a working substance, embedded in water as a heat reservoir, undergoing thermodynamic cycles controlled by a harmonic optical potential [22–26]. In such colloidal systems, expansions and compressions during Stirling- and Carnot-like cycles are achieved by decreasing and increasing the trap stiffness, respectively, while a hot reservoir is realized either by an actual increase of the local temperature of the around the particle or by addition of synthetic noise of non-thermal origin. These experiments have paved the way for the investigation of stochastic models of colloidal heat engines in more intricate and realistic situations, such as passive Brownian engines operating in contact with active baths [27–32], Brownian engines with a self-propelled particle as working substance in contact with a viscous fluid [32–35] or in a suspension of passive Brownian particles [36] as a heat bath, as well as the realization of a colloidal Stirling engine in bacterial baths with tunable activity [37].

It must be pointed out that, in most of the situations envisaged for biological and technological applications, the fluid environment of a colloidal heat engine is not perfectly Newtonian with a constant viscosity, but possesses a complex viscoelastic microstructure because of the presence of macromolecules, e.g., biomolecular chains, polymers and wormlike micelles, or colloids suspended in a solvent, thus exhibiting time-dependent flow properties [38]. Therefore, the motion of a colloidal particle in such materials lacks a clear-cut separation from timescales of the surroundings, which results in memory effects with large relaxation times. All these features give rise to a wealth of intriguing transient effects that markedly manifest themselves when time-dependent driving forces are exerted on an embedded particle [39–44], and are absent in the case of purely viscous fluids. Although all these conditions are met by a colloidal heat engine operating in a complex fluid, to the best of our knowledge they have never been examined in the context of stochastic thermodynamic cycles. Therefore, it is of paramount importance to assess the role of viscoelasticity in the performance of this kind of engines, since the resulting frequency-dependent friction experienced by a colloidal particle can significantly impact the rate at which energy is dissipated into a viscoelastic bath [45–48].

Here, we investigate a model based on the generalized Langevin equation for the operation of a stochastic Stirling engine composed of a Brownian particle embedded in a viscoelastic fluid bath, which includes a memory kernel and colored noise to account for retarded friction effects and thermal fluctuations of the medium on the particle motion. By numerically solving the corresponding non-Markovian equation of motion, we analyze the effect of the characteristic relaxation time of the fluid on the performance of the engine under finite-time Stirling cycles, and compare our results with those found in the case of Brownian particle in a Markovian bath. We uncover a significant increase in the power output and the efficiency of the engine operating in a viscoelastic environment with respect to the corresponding values in a viscous bath at a given cycle time. Moreover, with increasing relaxation time of the fluid, the convergence to the quasi-static Stirling efficiency is shifted to monotonically decreasing values of the cycle period, thereby expanding the interval at which the engine is able to efficiently deliver positive power.

2. MODEL

We consider a stochastic heat engine consisting of a Brownian particle embedded in a viscoelastic fluid as a heat bath, whose motion is confined by a harmonic potential. Both the curvature of the confining potential and the temperature of the system can be varied in time according to a well-specified periodic protocol that mimics a macroscopic thermodynamic cycle. Therefore, a stochastic model of the particle dynamics that allows for temporal variations of the temperature is needed. Based on Zwanzig's pioneering work [49], Brey et al. [50] and Romero-Salazar et al. [51] derived the simplest equations of motion of a Brownian particle coupled to a heat bath with temperature changing in time. Their approach incorporates linear dissipative terms in the equations of motion of the surrounding bath particles, which account for continuous cooling or heating of the system controlled by some external mechanism in such a way that the bath particles are always in a canonical equilibrium at a well-behaved temperature dependent on time. In particular, in one dimension the generalized Langevin equation for the position $x(t)$ at time $t > 0$ of the Brownian particle subject to a potential $U(x(t), t)$, reads [50, 51].

$$m\frac{d^2x(t)}{dt^2} = -\int_0^t ds\, K(t-s)\frac{d}{ds}\left[\sqrt{\frac{T(t)}{T(s)}}x(s)\right] - \frac{dU(x(t),t)}{dx} + \zeta(t), \tag{1}$$

where m is the mass of the particle, $T(s)$ is the temperature of the system at time $0 \leq s \leq t$, and $K(t-s)$ is a memory kernel that weights the effect of the previous history of the particle motion at time s on its current drag force at time t due to the temporal correlations induced by the surrounding medium. In addition, in Equation (1), $\zeta(t)$ is a Gaussian stochastic force which accounts for thermal fluctuations in the system and satisfies

$$\begin{aligned} \langle \zeta(t) \rangle &= 0, \\ \langle \zeta(t)\zeta(s) \rangle &= k_B\sqrt{T(t)T(s)}K(|t-s|). \end{aligned} \tag{2}$$

Extensions of Equation (1) to the three dimensional case, $\boldsymbol{r} = (x, y, z)$, which are relevant in many experimental situations using

optical trapping techniques [52], are possible by a proper choice of the potential $U(\boldsymbol{r},t)$ and a tensorial form of the memory kernel for particles of arbitrary shape [53]. Here, for the sake of simplicity we focus on the dynamics of a single coordinate of a spherical particle of radius a, which is confined by a harmonic potential $U(x,t) = \frac{1}{2}\kappa(t)x(t)^2$, where $\kappa(t)$ is the stiffness at time t of the corresponding restoring force. Moreover, we assume that the fluid bath is incompressible and the time-dependent variation of $\kappa(t)$ and $T(t)$ are such that its rheological properties remain in the linear viscoelastic regime, which is completely characterized by the stress relaxation modulus $G(t)$, or equivalently, by the complex dynamic shear modulus at frequency $\omega > 0$, $G^*(\omega) = i\omega\eta^*(\omega)$, where $i = \sqrt{-1}$ and $\eta^*(\omega)$ is the complex viscosity given by the Fourier transform of $G(t)$, i.e., $\eta^*(\omega) = \int_{-\infty}^{\infty} dt\, e^{-i\omega t}G(t)$ [54]. In general, $G(t)$ is a function that decays to zero over a finite time-scale whose value is many orders of magnitude greater than those of simple viscous fluids [38]. For a larger than the characteristic length-scales of the fluid microstructure, the Fourier transform of the memory kernel, $\hat{K}(\omega) = \int_{-\infty}^{\infty} dt\, e^{-i\omega t}K(t)$, is related to $\eta^*(\omega)$ by the generalized Stokes relation [55, 56].

$$\hat{K}(\omega) = 6\pi a\eta^*(\omega)\left[1 + a\sqrt{\frac{i\rho\omega}{\eta^*(\omega)}}\right], \tag{3}$$

with ρ the density of the fluid. Furthermore, when a is much smaller than the so-called viscoelastic penetration depth, $\sqrt{\frac{|\eta^*(\omega)|}{\rho\omega}}$, as typically occurs for micron-sized particles suspended in most viscoelastic fluids, inertial flow effects are negligible [57]. In such a case, Equation (3) can be approximated to $\hat{K}(\omega) = 6\pi a\eta^*(\omega)$ [58], which yields the simple relation $K(t) = 6\pi aG(t)$ by Fourier inversion. This leads to the following Langevin equation for the position of the Brownian heat engine in the overdamped limit

$$6\pi a\int_0^t ds\, G(t-s)\frac{d}{ds}\left[\sqrt{\frac{T(t)}{T(s)}}x(s)\right] = -\kappa(t)x(t) + \zeta(t). \tag{4}$$

In the following, we focus on a fluid relaxation modulus consisting of a Dirac delta function plus an exponential decay

$$G(t) = 2\eta_\infty\delta(t) + \frac{\eta_0 - \eta_\infty}{\tau_0}\exp\left(-\frac{t}{\tau_0}\right), t \geq 0, \tag{5}$$

which models the rheological response of several viscoelastic fluids, such as wormlike micelles [42, 59, 60], some polymer solutions [61, 62], and to a great extent, the linear viscoelasticity over certain time intervals of intracellular fluids [63, 64], block copolymers [65], and λ-phage DNA [42, 66], where τ_0 is the relaxation time of their elastic microstructure, whereas η_0 and η_∞ represent the zero-shear viscosity and the background solvent viscosity, respectively. Therefore, the corresponding friction memory kernel is

$$K(t) = 2\gamma_\infty\delta(t) + \frac{\gamma_0 - \gamma_\infty}{\tau_0}\exp\left(-\frac{t}{\tau_0}\right), t \geq 0, \tag{6}$$

where the complex conjugate of its Fourier transform, $\hat{K}^*(\omega) = 6\pi a\eta(\omega)$, represents a frequency-dependent friction

$$\hat{K}^*(\omega) = \frac{\gamma_0 + \gamma_\infty\omega^2\tau_0^2}{1+\omega^2\tau_0^2} + i\frac{(\gamma_0 - \gamma_\infty)\omega\tau_0}{1+\omega^2\tau_0^2}. \tag{7}$$

In Equations (6) and (7), $\gamma_\infty = 6\pi r\eta_\infty$ and $\gamma_0 = 6\pi r\eta_0 \geq \gamma_\infty$ are friction coefficients characterizing dissipation at short and long timescales, respectively, whereas elastic effects are quantified by $(\gamma_0 - \gamma_\infty)\tau_0$. Hence, in this case, Equation (4) takes the form

$$\gamma_\infty\frac{dx(t)}{dx} + \frac{\gamma_0 - \gamma_\infty}{\tau_0}\int_0^t ds\,\exp\left(-\frac{t-s}{\tau_0}\right)\frac{d}{ds}\left[\sqrt{\frac{T(t)}{T(s)}}x(s)\right] = -\kappa(t)x(t) + \zeta(t). \tag{8}$$

It is noteworthy that, at constant temperature T and in absence of a trapping potential, the mean square displacement of a particle whose motion is described by Equation (8), is

$$\langle\Delta x(t)^2\rangle = \frac{2k_BT}{\gamma_0}\left\{t + \left(1 - \frac{\gamma_\infty}{\gamma_0}\right)\tau_0\left[1 - \exp\left(-\frac{\gamma_0}{\gamma_\infty\tau_0}t\right)\right]\right\}, \tag{9}$$

which implies that in the long-time limit, $t \gg \gamma_\infty\tau_0/\gamma_0$, it would perform free diffusion like in a Newtonian fluid with constant viscosity η_0 [67–69], i.e., $\langle\Delta x(t)^2\rangle \approx \frac{2k_BT}{\gamma_0}t$. This provides a clear criterion for a direct comparison of the performance of a Brownian engine in a viscoelastic fluid bath with that in a viscous medium of the same zero-shear viscosity, i.e., $\eta = \eta_0$, under identical time-dependent variations of $\kappa(t)$ and $T(t)$. Furthermore, we introduce the dimensionless parameter

$$\alpha = \frac{\gamma_0}{\gamma_\infty} - 1 \geq 0, \tag{10}$$

in such a way that, for either $\alpha = 0$ or $\tau_0 \to 0$, the memory kernel becomes $K(t) = 2\gamma\delta(t)$, with constant friction coefficient $\gamma = \gamma_0 = \gamma_\infty$. Consequently, in these cases Equation (4) reduces to

$$\gamma\frac{dx(t)}{dt} = -\kappa(t)x(t) + \zeta(t), \tag{11}$$

where the thermal noise $\zeta(t)$ simply satisfies [50].

$$\begin{aligned}\langle\zeta(t)\rangle &= 0,\\ \langle\zeta(t)\zeta(s)\rangle &= 2k_BT(t)\gamma\delta(t-s),\end{aligned} \tag{12}$$

Equation (11) describes the motion of a Brownian particle coupled to a viscous heat bath with time dependent temperature $T(t)$ through the frictional force $-\gamma\frac{dx(t)}{dt}$ and the thermal stochastic force, subject to a restoring force $-\kappa(t)x(t)$. It should be noted that this situation was explicitly considered in many of the models of single-particle heat engines reported in the literature [18, 20, 27, 28, 31–35].

We point out that the rheological properties of viscoelastic fluids are generally dependent on their temperature, which under a thermodynamic cycle would also become time-dependent.

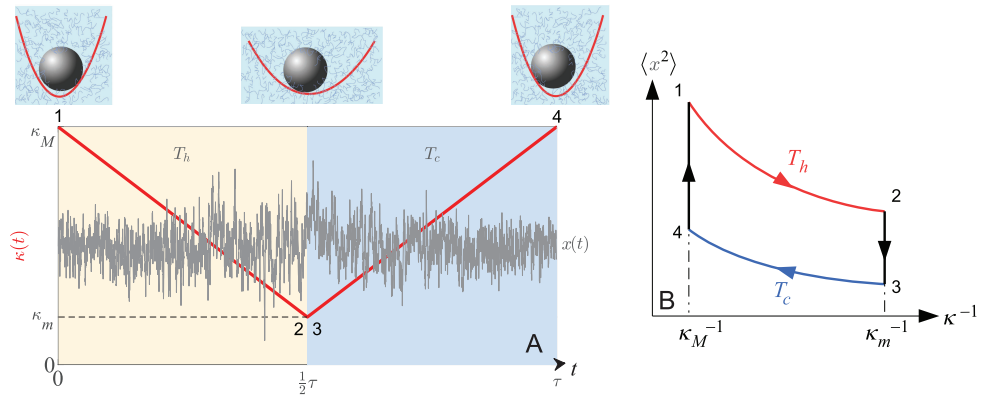

FIGURE 1 | (A) Schematic representation of a Stirling cycle of period τ performed by a colloidal heat engine, embedded in a viscoelastic fluid, by means of the temporal variation of the stiffness $\kappa(t)$ of a trapping harmonic potential $U(x,t) = \frac{1}{2}\kappa(t)x(t)^2$ and of the bath temperature $T(t)$. At time $0 \leq t < \tau/2$, the trap stiffness is linearly decreased from κ_M to $\kappa_m < \kappa_M$ while keeping the temperature of the surroundings at high temperature T_h (step $1 \to 2$). At $t = \tau/2$, the temperature is suddenly decreased to $T_c < T_h$ (step $2 \to 3$), and kept at that value for $\tau/2 < t < \tau$, while linearly increasing the trap stiffness from κ_m to κ_M (step $3 \to 4$). The cycle is completed at $t = \tau$, at which the temperature is again increased to T_h (step $4 \to 1$). For a given realization of the cycle, the particle position $x(t)$ encodes the information of the stochastic energy exchange between the particle and the surrounding fluid, as depicted by the noisy trajectory obtained by numerical simulations of Equation (8). **(B)** Schematic representation of the Brownian Stirling cycle in a $\langle x^2 \rangle$-κ^{-1} diagram, similar to the pressure-volume diagram of a gas.

The inclusion of such thermal effects in the minimal Langevin model (8) is not trivial and even a phenomenological description through additional rheological parameters and time-scales would render it little useful for a clear interpretation of the memory effects of a frequency-dependent friction in the performance of the Brownian engine. Therefore, similar to the simplifications made in most single-particle models of heat engines working in purely viscous fluids, as a first approximation we assume that η_0, η_∞ and τ_0 remain constant over time. The effect of the temperature dependence of these parameters is out of the scope of the present paper and will be the subject of further work.

The operation of the Brownian engine during a Stirling cycle of duration τ is depicted in **Figure 1A**, where the trap stiffness and the temperature are varied in time t according to the following protocols

$$\kappa(t) = \begin{cases} \kappa_M - \frac{2}{\tau}\delta\kappa t, & 0 \leq t \leq \frac{\tau}{2}, \\ \kappa_m - \delta\kappa\left(1 - \frac{2}{\tau}t\right), & \frac{\tau}{2} < t \leq \tau, \end{cases} \tag{13}$$

and

$$T(t) = \begin{cases} T_h, & 0 \leq t < \frac{\tau}{2}, \\ T_c, & \frac{\tau}{2} \leq t < \tau, \\ T_h, & t = \tau, \end{cases} \tag{14}$$

respectively, where $\delta\kappa = \kappa_M - \kappa_m > 0$ and $T_h > T_c$. More specifically, a full cycle consists of a sequence of four steps:

$1 \to 2$: For $0 \leq t < \tau/2$, the colloidal engine undergoes an isothermal expansion at high temperature T_h by linearly decreasing the trap stiffness from κ_M to κ_m.

$2 \to 3$: At $t = \tau/2$, the temperature is suddenly decreased to T_c, while keeping the trap stiffness at $\kappa(t = \tau/2) = \kappa_m$, thus corresponding to a isochoric-like process.

$3 \to 4$: For $\tau/2 < t < \tau$, the engine undergoes an isothermal compression at low temperature T_c by linearly increasing the trap stiffness from κ_m to κ_M.

$4 \to 1$: At $t = \tau$, the temperature is suddenly raised to T_h, while keeping the trap stiffness at $\kappa(t = \tau) = \kappa_M$, i.e., an isochoric-like process, thus completing the full cycle.

Then, the cycle is repeated until the system reaches a time-periodic steady state, which becomes independent of the choice of the initial condition $x(t = 0) = x_0$. Note that, by analogy with a macroscopic Stirling cycle of a gas as a working substance, here the inverse of the trap stiffness and the variance of the particle position play the role of the volume and pressure, respectively, as depicted in **Figure 1B**.

According to stochastic thermodynamics [14], the work done on the system by the time variation of the optical trap over a single stochastic realization of the $(n+1)-$th cycle starting at $t_n = n\tau$, with $n = 0, 1, 2, \ldots$, is

$$\begin{aligned} W_\tau &= \frac{1}{2}\int_{t_n}^{t_n+\tau} dt\, \frac{d\kappa(t)}{dt} x(t)^2, \\ &= \frac{\delta\kappa}{\tau}\left[-\int_{t_n}^{t_n+\frac{\tau}{2}} dt\, x(t)^2 + \int_{t_n+\frac{\tau}{2}}^{t_n+\tau} dt\, x(t)^2\right], \end{aligned} \tag{15}$$

whereas the heat dissipated into the bath during the first half period of the cycle is given by

$$\begin{aligned} Q_{\tau/2} &= W_{\tau/2} - \Delta U_{\tau/2} \\ &= -\frac{\delta\kappa}{\tau}\int_{t_n}^{t_n+\frac{\tau}{2}} dt\, x(t)^2 - \frac{1}{2}\left[\kappa_m x\left(t_n + \frac{\tau}{2}\right)^2 - \kappa_M x(t_n)^2\right]. \end{aligned} \tag{16}$$

In Equation (16), $W_{\tau/2}$ is the work done during the first half of the cycle, and $\Delta U_{\tau/2}$ is the corresponding variation of the

potential energy in the harmonic trap, $U(x,t)$, in accordance with the stochastic extension of the first law of thermodynamics. Positive and negative values of W_τ correspond to work done on the particle and work performed by the particle, respectively, whereas positive and negative values of $Q_{\tau/2}$ represent heat transferred from the particle to the bath and heat absorbed by the particle, respectively. It must be noted that the mean steady-state values of the two stochastic variables given by Equations (15) and (16), which will be denoted as $\langle W_\tau\rangle$ and $\langle Q_{\tau/2}\rangle$, respectively, are the ones needed for the calculation of the efficiency of the Stirling heat engine [17]. They involve the variance of the particle position at an arbitrary time $t \geq 0$, $\langle x(t)^2\rangle$, with $t = 0$ the time defining the initial condition, computed over an ensemble of independent realizations of the colored noise $\zeta(t)$ defined by Equations (2). An analytical treatment of this problem requires the explicit solution of the generalized Langevin Equation (8), which is not trivial even in the simpler case of a constant trap stiffness and constant temperature [48]. Therefore, to address the problem of the performance of a Brownian Stirling heat engine described by Equations (2), (8), (13) and (14), we opt for numerical simulations of the corresponding stochastic dynamics.

2.1. Numerical Solution

In order to compute the probability distributions of the work and the heat defined in Equations (15) and (16), as well as their corresponding mean values, the non-Markovian Langevin Equation (8) must be numerically solved. To this end, we express it in an equivalent Markovian form by introducing an auxiliary stochastic variable, $z(t)$, defined as

$$z(t) = \frac{1}{\tau_0}\int_0^t ds\, \exp\left(-\frac{t-s}{\tau_0}\right)\sqrt{\frac{T(t)}{T(s)}}\left[x(s) + \tau_0\sqrt{2\Delta(s)}\xi_z(s)\right], \tag{17}$$

where

$$\Delta(s) = \frac{k_B T(s)}{\gamma_0 - \gamma_\infty}, \tag{18}$$

represents a diffusion coefficient associated to the effective friction $\gamma_0 - \gamma_\infty$, which depends on the instantaneous value of the temperature at time s, $T(s)$, and $\xi_z(s)$ is a Gaussian noise satisfying

$$\begin{aligned}\langle \xi_z(s)\rangle &= 0,\\ \langle \xi_z(s)\xi_z(s')\rangle &= \delta(s-s').\end{aligned} \tag{19}$$

Consequently, the non-Markovian Langevin Equation (4) for $x(t)$ can be written as a linear system of two coupled Markovian Langevin equations

$$\frac{dx(t)}{dt} = -\frac{\alpha+1}{\gamma_0}\kappa(t)x(t) - \frac{\alpha}{\tau_0}\left[x(t)-z(t)\right] + \sqrt{2D_\infty(t)}\xi_x(t), \tag{20}$$

$$\frac{dz(t)}{dt} = -\frac{1}{\tau_0}\left[z(t)-x(t)\right] + \frac{1}{2T(t)}\frac{dT(t)}{dt}z(t) + \sqrt{2\Delta(t)}\xi_z(t), \tag{21}$$

with α defined in Equation (10). In Equation (20), $D_\infty(t)$ is a short-time diffusion coefficient associated to the infinite-frequency friction coefficient $\lim_{\omega\to\infty}\hat{K}^*(\omega) = \gamma_\infty$, see Equation (7), at temperature $T(t)$, and is given by

$$D_\infty(t) = \frac{k_B T(t)}{\gamma_\infty}, \tag{22}$$

whereas $\xi_x(t)$ is a Gaussian noise which satisfies

$$\begin{aligned}\langle \xi_x(t)\rangle &= 0,\\ \langle \xi_x(t)\xi_x(s)\rangle &= \delta(t-s),\end{aligned} \tag{23}$$

Note that, apart from the step-like changes at $t = t_n$ and $t = t_n + \frac{\tau}{2}$, $T(t)$ remains constant. Accordingly, the rate of change of the time-dependent temperature in Equation (20) vanishes during each half a Stirling cycle, i.e., $\frac{d}{dt}\left[\ln T(t)\right] = 0$.

To compute the probability distributions of W_τ and $Q_{\tau/2}$, we carry out numerical simulations of the stochastic process $[x(t), z(t)]$ starting from the initial condition $[x(t=0) = 0, z(t=0) = 0]$ with a total length of 2×10^4 times the period τ. To ensure that the system is always in a time-periodic non-equilibrium steady state independent of the choice of the initial condition, the first 10^4 cycles are left out and the origin of time is shifted to the beginning of the $(10^4+1)-$st cycle. Furthermore, without loss of generality we choose constant values of the low and high-frequencies viscosities that are typical of viscoelastic fluids prepared in aqueous solution in semidilute regimes [42, 62, 66, 70, 71]: $\eta_0 = 0.040$ Pa s and $\eta_\infty = 0.004$ Pa s, which correspond to $\alpha = 9$. The diameter of the colloidal particle is set to $a = 0.5\,\mu$m, while the maximum and minimum values of the trap stiffness during the Stirling cycle are chosen as $\kappa_M = 5\,\text{pN}\,\mu\text{m}^{-1}$ and $\kappa_m = 1\,\text{pN}\,\mu\text{m}^{-1}$, respectively, which are easily accessible with optical tweezers [52]. The temperatures of the reservoir during the hot and cold part of the cycle are $T_c = 5^\circ$C and $T_h = 90^\circ$C, which are selected in such a way that they are within the temperature range in which water, which is a common solvent component of many viscoelastic fluids, remains liquid. On the other hand, to study the influence of the fluid relaxation time on the performance of the colloidal Stirling engine, τ_0 is varied in the range of 0.01–100 s, which also covers characteristic values in actual experimental systems. We solve Equations (20) by means of an Euler–Cromer scheme with time step $\delta t = 10^{-4}$ s, which is about 75 times smaller than the shortest relaxation time of the system, γ_∞/κ_M. In the case of the Stirling heat engine in a Newtonian viscous fluid, we solve numerically Equation (11) with constant friction coefficient $\gamma = 6\pi a\eta$, where $\eta = \eta_0 = 0.040$ Pa s and the rest of the involved parameters, namely, κ_m, κ_M, a, T_c, T_h, and δt, are selected with the same values as described before for the viscoelastic case for a direct comparison between both systems. We also explore different values of the cycle period, $0.01\text{ s} \leq \tau \leq 50$ s, which allows us to examine the approach of the computed quantities to the quasi-static values $\tau \to \infty$. We note that $\tau_\kappa \equiv \gamma_0/\kappa_m$ represents the slowest dissipation time-scale of the system [26], and appears explicitly in the analytical expressions for the variance of a Brownian particle undergoing a finite-time Stirling cycle in contact with a

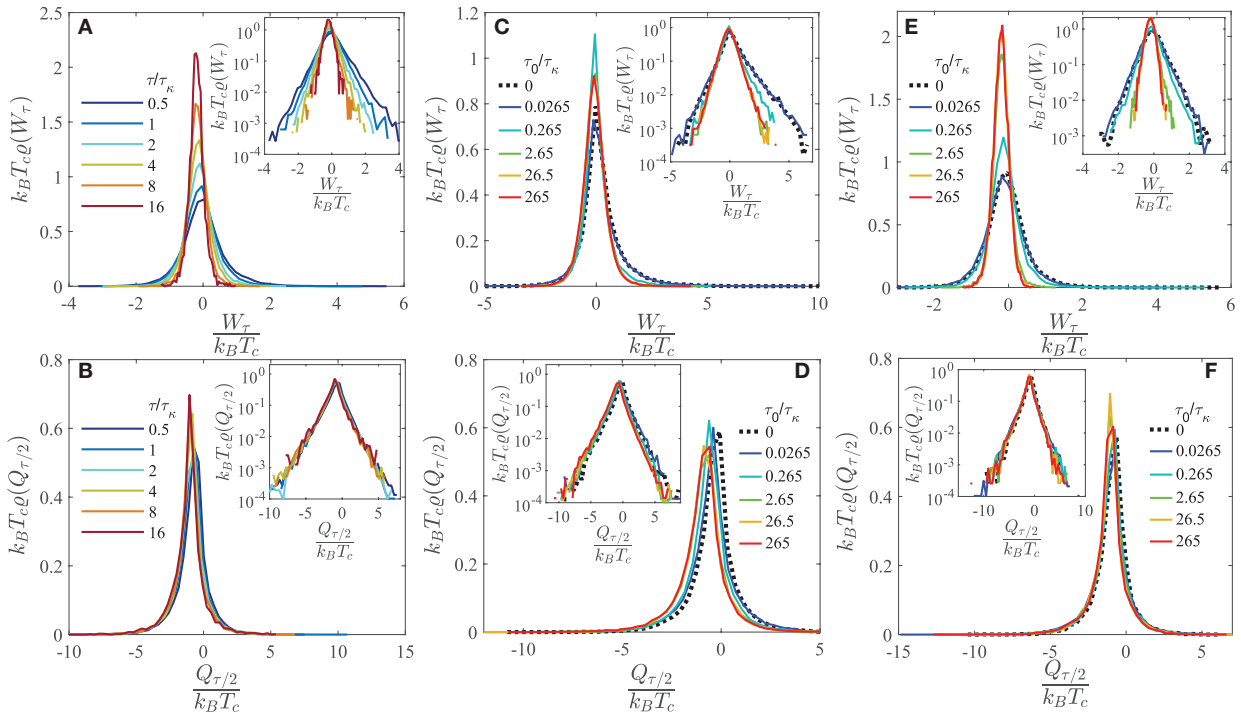

FIGURE 2 | (A) Probability density function of the work W_τ, and **(B)** the heat $Q_{\tau/2}$, for a Brownian Stirling engine in contact with a viscoelastic fluid bath with relaxation time $\tau_0 = 2.65\tau_\kappa$, for different values of the cycle time τ. **(C)** Probability density function of the work W_τ, and **(D)** the heat $Q_{\tau/2}$, for a Brownian Stirling engine during a cycle of duration $\tau = \tau_\kappa$, in contact with viscoelastic fluid baths with the same zero-shear viscosity $\eta_0 = 0.040$ Pa a, and distinct relaxation times τ_0 spanning 5 orders of magnitude (solid lines). **(E)** Probability density function of the work W_τ, and **(F)** the heat $Q_{\tau/2}$, for a Brownian Stirling engine during a cycle of duration $\tau = 10\tau_\kappa$, in contact with viscoelastic fluid baths with the same zero-shear viscosity $\eta_0 = 0.040$ Pa s and distinct relaxation times τ_0 spanning 5 orders of magnitude (solid lines). In **(C–F)**, the dotted lines represents the corresponding curves for a Brownian engine in a Newtonian fluid ($\tau_0 = 0$) with constant viscosity $\eta_0 = 0.040$ Pa s. The insets are semilogarithmic representations of the main plots.

viscous heat bath [34]. Therefore, in both cases of the viscous and viscoelastic baths analyzed here, all the timescales are normalized by τ_κ, whereas energies are normalized by k_BT_c.

3. RESULTS AND DISCUSSION

Since W_τ and $Q_{\tau/2}$ are stochastic variables, we first present the results for their probability distributions, $\varrho(W_\tau)$ and $\varrho(Q_{\tau/2})$, respectively, for different values of the time-scales τ and τ_0. In **Figures 2A,B**, we plot such distributions for a value of the fluid relaxation time that is comparable to the largest dissipation time-scale of the system: $\tau_0 = 2.65\tau_\kappa$, at which memory effects due to the frequency-dependent friction must be important. In such a case, we observe that for fast Stirling cycles with period τ smaller or comparable to τ_κ the work distribution is asymmetric with respect to its maximum and exhibits pronounced exponential tails, as illustrated in the inset of **Figure 2A**. In addition, large positive work fluctuations occur for small τ, which indicates the existence of rare events where work is done on the particle during a cycle, thus effectively consuming energy as a heat pump. As τ increases, the exponential tails and their asymmetry vanish, thus giving rise to a narrower Gaussian-like shape for $\tau \gg \tau_k$. This shows that the probability of finding positive work fluctuations decreases by increasing τ, i.e., the Brownian particle behaves more and more like a macroscopic Stirling engine, which on average is able to convert the heat absorbed from the viscoelastic bath into work. On the contrary, the heat distribution does not significantly change with the cycle time τ, as shown in **Figure 2B**. In this case, clear exponential tails remain even for large values of τ, as revealed in the inset of **Figure 2B**. where the probability of occurrence of negative heat fluctuations is higher than that of positive ones. Hence, regardless of the cycle period τ, it is more likely that heat is absorbed by the particle than dissipated into the bath during the isothermal expansion at temperature T_h.

In **Figures 2C,D**, we analyze the dependence on the fluid relaxation time τ_0 of the work and heat distributions, respectively, for Stirling cycles of period $\tau = \tau_\kappa$, i.e., similar to the largest viscous dissipation time-scale of the system. For comparison, we also plot as dotted lines the corresponding probability distributions for a colloidal engine in a fluid with constant viscosity $\eta = \eta_0$, for which $\tau_0 = 0$. Remarkably, we find that the fluid viscoelasticity, through the parameter τ_0, has a strong influence on the resulting shape of the distributions. For a viscous bath, the work has large exponential tails with a highly asymmetric shape. A similar shape is observed for a viscoelastic

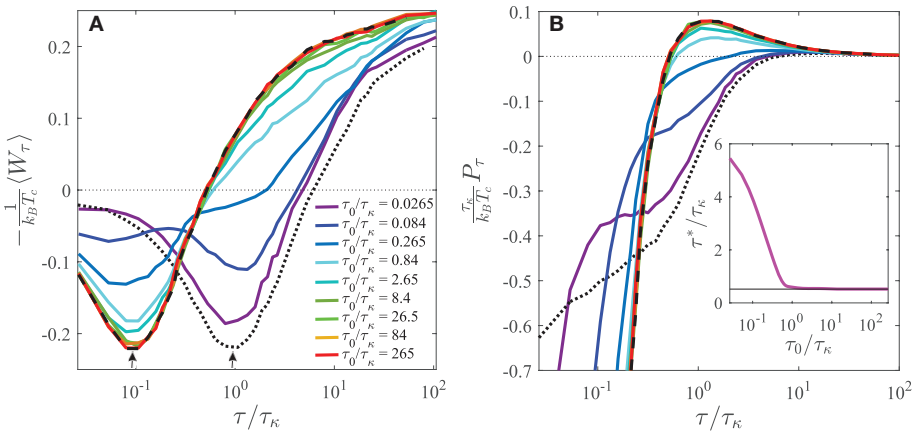

FIGURE 3 | (A) Mean work done by the Brownian Stirling engine during a cycle, $-\langle W_\tau \rangle$, as a function of the cycle time τ, for different values of the fluid relaxation time τ_0 (solid lines). The dotted and dashed lines represent the mean power output of a Brownian Stirling engine in Newtonian fluids with constant viscosities $\eta = \eta_0$ and $\eta = (1+\alpha)^{-1}\eta_0 = \eta_\infty$, respectively. The arrows depict the location of the corresponding minima. **(B)** Mean power output per cycle of the colloidal Stirling engine, P_τ, as a function of the cycle duration τ, for different values of the fluid relaxation time τ_0 (solid lines). The dotted and dashed lines represent the mean power output of a Brownian Stirling engine in Newtonian fluids with constant viscosities $\eta = \eta_0$ and $\eta = (1+\alpha)^{-1}\eta_0 = \eta_\infty$, respectively. Same color code as in **(A)**. Inset: stall time of the engine defined in Equation (26), τ^*, as a function of the fluid relaxation time, τ_0 (thick line). The thin line represents the value of τ^* for an engine operating in a Newtonian fluid with constant viscosity $\eta = \eta_\infty$.

bath at sufficiently small τ_0, but the width and the asymmetry of the distribution gradually decrease as τ_0 increases, then converging to a single limiting curve with a rather symmetric profile for sufficiently large values of the fluid relaxation time $\tau_0 \gtrsim \tau_\kappa$, as shown in the inset of **Figure 2C**. In addition, the heat distribution also has exponential tails with a width that does not strongly depend on the fluid relaxation time τ_0, but the location of the maximum is slightly shifted to more and more negative values of $Q_{\tau/2}$ with increasing τ_0, as shown in **Figure 2D**. Finally, for values of the cycle duration τ larger than τ_κ, the shape of $\varrho(W_\tau)$ changes from a rather symmetric exponentially-tailed distribution to a limiting Gaussian curve with increasing τ_0, whereas $\varrho(Q_{\tau/2})$ exhibits a symmetric profile with exponential tails peaked at a negative value of $Q_{\tau/2}$, which remains unaffected by the τ_0, as respectively shown in **Figures 2E,F** for $\tau = 10\tau_\kappa$. It is important to realize that for $\tau > \tau_\kappa$, the work distribution of the Brownian engine is narrower in a viscoelastic bath as compared to that in a viscous bath with the same zero-shear viscosity. This can be attributed the elastic response in the former case, which prevents large instantaneous heat losses into the bath by viscous dissipation, thus resulting in a more efficient conversion into work of the energy extracted from the surroundings. This observation underlines the importance of the friction memory kernel of the particle motion in the viscoelastic fluid, which becomes strongly dependent on the frequency imposed by the Stirling cycle. Thus, for sufficiently small $\tau_0 < \tau_\kappa$ the energy exchanges between the Brownian particle and the viscoelastic bath must not be that different from those occurring in a viscous fluid, while for sufficiently large $\tau_0 > \tau_\kappa$ significant deviations must take place, as verified in **Figures 2C,E** for $\tau_0 = 0.0265\tau_\kappa$ and $\tau_0 = 265\tau_\kappa$, respectively.

To investigate the performance of a Brownian engine operating in a viscoelastic bath, in **Figure 3A** we plot the mean work *done by the Brownian engine* during a cycle, i.e., $-\langle W_\tau \rangle$. In a Newtonian fluid, $-\langle W_\tau \rangle$ is positive at sufficiently large τ and monotonically saturates to a constant positive value in the quasi-static limit $\tau \to \infty$ [34].

$$-\langle W_{\tau\to\infty}\rangle = \frac{1}{2}k_B(T_h - T_c)\ln\left(\frac{\kappa_M}{\kappa_m}\right), \tag{24}$$

whereas it becomes negative at small values of τ and tends to zero as $\tau \to 0$ according to Equation (15), thus implying that it has a minimum at a certain value of τ. This is verified in **Figure 3A**, where we plot as dotted and dashed lines the curves corresponding to the work done by a particle in viscous fluids with constant viscosities $\eta = \eta_0 = 0.040$ Pa s and $\eta = \eta_\infty = 0.004$ Pa s, respectively, i.e., equal to the viscosities characterizing the long-time and short-time dissipation of the viscoelastic fluid. The location of the minimum, which is depicted by arrows, depends on the specific value of η, but the general shape of the curve in a linear-logarithmic representation is the same, as observed in **Figure 3A**. Interestingly, in the case of viscoelastic fluids with non-zero values of τ_0, the work done by the particle exhibits an intermediate behavior between these two curves. For instance, for $\tau_0 = 0.0265\tau_\kappa \ll \tau_\kappa$, the dependence of $-\langle W_\tau \rangle$ on τ is very similar to that in a Newtonian fluid with viscosity $\eta = \eta_0$, with a single minimum at the same location ($\tau \approx \tau_\kappa$) and only small deviations of the respective values along the vertical axis. Nevertheless, as τ_0 increases, a second local minimum emerges at $\tau \approx 0.1\tau_\kappa$, i.e., at the location of the minimum of the curve corresponding to the Newtonian fluid of viscosity $\eta = \eta_\infty$, as observed in **Figure 3A** for $\tau_0 = 0.084\tau_\kappa$. Such a second minimum becomes more and more apparent with increasing τ_0, whereas the first minimum at $\tau \approx \tau_\kappa$ becomes less and less dominant, as seen for $\tau_0 \geq 0.265\tau_\kappa$. Unexpectedly, for $\tau_0 \gg \tau_\kappa$, the curves for the

viscoelastic case converge to that for a Newtonian fluid with a viscosity $\eta = \eta_\infty$. These observations suggest that, depending of the specific values of the fluid relaxation time and the cycle time with respect to τ_κ, different dissipation mechanisms take place in order for the particle to convert the energy taken from the bath into work by means of the applied thermodynamic cycle.

Next, we compute the mean power produced by the engine during a cycle

$$P_\tau = -\frac{\langle W_\tau \rangle}{\tau}, \tag{25}$$

whose dependence on the cycle time τ is plotted as solid lines in **Figure 3B** for some exemplary values of the fluid relaxation time τ_0. Besides, we also plot in **Figure 3B** as a dotted line the mean power for a Brownian engine in a Newtonian fluid bath with viscosity $\eta = \eta_0$. It is important to note that, for all values of τ_0, P_τ exhibits a non-monotonic behavior as a function of τ, which gradually deviates from the behavior in a Newtonian fluid with viscosity $\eta = \eta_0$ as τ_0 increases. This is the result of the pronounced non-monotonic dependence of $-\langle W_\tau \rangle$ on τ shown in **Figure 3A**. In particular, P_τ has a maximum that originates from the trade-off between high energy dissipation at small cycle times τ (high frequency operation) and large τ (slow operation), at which net work is produced by the engine with low dissipation. Additionally, the general shape of all power curves displays three different operation regimes. For sufficiently slow Stirling cycles (large τ), the engine is able to deliver net power on average ($P_\tau > 0$), where the irreversible energy dissipation into the bath becomes negligible. On the other hand, there is a specific value of the cycle time at which the engine stalls, i.e., both the mean work and the power output vanish: $\langle W_\tau \rangle = 0$, $P_\tau = 0$ [17]. Finally, for sufficiently fast cycles (small τ), the engine absorbs energy ($P_\tau < 0$) rather than delivering it, thus behaving like a heat pump. This regime is the consequence of the large amount of energy irreversibly dissipated when the particle is quickly driven by the periodic variation of $\kappa(t)$ and $T(t)$. Interestingly, in **Figure 3B**, we show that the value of the fluid relaxation time τ_0 has a considerable impact on the mean power output, and in particular, on the value of the cycle time at which the Brownian engine stalls, which we denote as τ^*

$$P_{\tau^*} = 0. \tag{26}$$

For instance, in the case of the Newtonian fluid ($\tau_0 = 0$) with $\eta = \eta_0$, we find $\tau^* = 6.15\tau_\kappa$, while for a viscoelastic fluid ($\tau_0 > 0$), τ^* is smaller and decreases with increasing τ_0. In the inset of **Figure 3B**, we plot the dependence of τ^* on τ_0, where we can see that for sufficiently short fluid relaxation times, the stall time is close to that for a Newtonian fluid bath ($\tau^* = 6.15\tau_\kappa$), and monotonically decreases with increasing τ_0. In this short-τ_0 regime, the performance of the engine is very sensitive to the specific value of τ_0, as shown by the strong variation of the shape of the power curves plotted in **Figure 3B** for $\tau_0 = 0.0265\tau_\kappa, 0.084\tau_\kappa, 0.265\tau_\kappa, 0.84\tau_\kappa$. Around $\tau_0 = \tau_\kappa$, a conspicuous change in the dependence on τ_0 of the operation of the engine happens. Indeed, as τ_0 increases the stall time converges to the constant value $\tau^* = 0.52\tau_\kappa$, as verified in the inset of **Figure 3A** for $\tau_0 > \tau_\kappa$. The monotonic decrease of τ^* implies that the interval of cycle times at which the engine is able to efficiently deliver positive power output is expanded with increasingly larger τ_0. Moreover, with increasing fluid relaxation times $\tau_0 > \tau_\kappa$, which is consistent with increasingly pronounced viscoelastic behavior of the bath, the power output curves converge to a limiting curve, as shown in **Figure 3B** for $\tau_0 = 2.65\tau_\kappa, 8.4\tau_\kappa, 26.5\tau_\kappa, 84\tau_\kappa, 265\tau_\kappa$. Remarkably, we find that such a limiting curve corresponds to the power curve of a Brownian Stirling engine in a Newtonian bath with viscosity equal to high frequency value $\eta = \eta_\infty = 0.004$ Pa s, i.e., the viscosity of the solvent component in the viscoelastic fluid, which is represented as a dashed line in **Figure 3B**. As a consequence, the limit of the stall time of an engine working in a viscoelastic fluid with increasing τ_0 corresponds to the stall time of a Brownian engine operating in a Newtonian one with constant viscosity $\eta = \eta_\infty$, $\tau^* = 0.52\tau_\kappa$, as verified in the inset of **Figure 3B**, see the horizontal solid line. Furthermore, in **Figure 3B**, we check that, for a given cycle of finite duration τ, the mean power output of the engine operating in a viscoelastic fluid is enhanced with increasing values of τ_0 with respect to the power output in a Newtonian fluid of the same zero-shear viscosity. We also find that the location of the global maximum of each power output is shifted to smaller and smaller values of τ with increasing τ_0, whereas the value of P_τ at the maximum increases with increasing τ_0 because of the decreasing irreversible dissipation taking place in a fluid with pronounced viscoelastic behavior.

These findings allows us to uncover the underlying mechanism behind the influence of fluid viscoelasticity on the performance of the engine. In a Newtonian fluid with constant viscosity η_0, the largest time-scale associated to viscous dissipation due to temporal changes in the trap stiffness is precisely τ_κ, which is proportional to η_0, and represents the largest relaxation time in the system. In this case, the viscous bath simply acts as a mechanically inert element of the engine which equilibrates instantaneously in response to the particle motion under the variations of the trap stiffness. On the other hand, when the bath is a viscoelastic fluid, the hidden degrees of freedom of its elastic microstructure, e.g., entangled micelles, polymers, interacting colloids, etc., also come into play in the dynamics and mechanically respond within a characteristic time $\tau_0 > 0$ to the temporal changes periodically imposed on the particle. Therefore, the interplay between τ_κ and τ_0 determines the resulting energetic behavior of the system:

- If $\tau_0 \ll \tau_\kappa$, the fluid microstructure fully relaxes before the energy dissipation into the bath takes place on a time-scale τ_κ. In such circumstances, the Brownian particle has enough time to probe the long-time (low frequency) properties of the fluid environment with friction coefficient $\hat{K}^*(\omega \to 0) = \gamma_0 = 6\pi a\eta_0$, see Equation (7), thereby leading to a stochastic energetic behavior similar to that in a Newtonian fluid with constant viscosity $\eta = \eta_0$.
- If $\tau_0 \lesssim \tau_\kappa$, excessive irreversible energy losses by viscous dissipation are counterbalanced by the transient energy storage in the elastic structure of the bath, because at frequencies $\omega \sim \tau_0^{-1}$ the imaginary part of $\hat{K}^*(\omega)$ is not

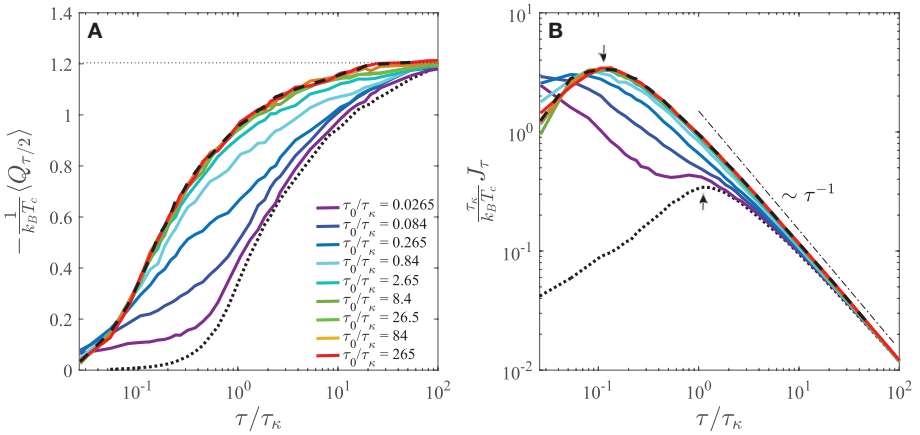

FIGURE 4 | (A) Mean heat absorbed by the Brownian Stirling engine during the isothermal expansion at high temperature, $-\langle Q_{\tau/2}\rangle$, as a function of the cycle time τ, for different values of the fluid relaxation time τ_0 (solid lines). The dotted and dashed lines corresponds to the mean heat absorbed by the colloidal engine in Newtonian fluids with constant viscosities $\eta = \eta_0$ and $\eta = (1+\alpha)^{-1}\eta_0 = \eta_\infty$, respectively. The horizontal thin dotted line represents the quasi-static value given by Equation (27). **(B)** Mean rate of heat absorption by the colloidal engine during the isothermal expansion at high temperature, J_τ, as a function of the duration of the cycle τ, for different values of the fluid relaxation time τ_0 (solid lines). Same color code as in **(A)**. The dotted and dashed lines correspond to mean rate of heat absorption in Newtonian fluids with constant viscosities $\eta = \eta_0$ and $\eta = \eta_\infty$, respectively. The arrows depict the location of the corresponding maxima. The dotted-dashed line depicts the behavior $\sim \tau^{-1}$.

negligible. Therefore, the value $\tau_0 \approx \tau_\kappa$ marks a qualitative change in the energy exchange between the particle and bath.

- If $\tau_0 > \tau_\kappa$, the elastic fluid microstructure does not have enough time to mechanically relax to the temporal changes of the cycle, thus preventing the particle from undergoing the long-time friction characterized by the coefficient γ_0. Therefore, the particle can only probe the short-time response of the surrounding fluid through the high-frequency components of the friction, which correspond to $\hat{K}^*(\omega \to \infty) = \gamma_\infty = 6\pi a \eta_\infty$ for $\tau_0 \gg \tau_\kappa$ according to Equation (7). As a consequence, in this limit the relevant dissipation timescale is γ_∞/κ_m, which is in general smaller than τ_κ because $\eta_\infty = \eta_0(1+\alpha)^{-1} \leq \eta_0$. For instance, for the numerical values chosen in the simulations presented here, $\gamma_\infty/\kappa_m = 0.1\tau_\kappa$. Accordingly, less irreversible dissipation must take place in the viscoelastic fluid under finite-time Stirling cycles, thus enhancing the net power output of the engine at a given cycle time τ as compared to that in a Newtonian fluid with the same zero-shear viscosity η_0.

To confirm the previously described mechanism of energy storage and dissipation during the Stirling cycle, in **Figure 4A**, we plot the mean heat absorbed by the particle during the hot step of the cycle, $-\langle Q_{\tau/2}\rangle$, as a function of the total duration τ of a full cycle. We find that, for all values of τ and of the fluid relaxation time τ_0, $-\langle Q_{\tau/2}\rangle \geq 0$, which means that the particle absorbs heat on average during the first half of the cycle. In particular, for a given τ_0 the mean absorbed heat increases monotonically from the value $-\langle Q_{\tau=0}\rangle = 0$, and saturates to a constant value corresponding to a quasi-static process as $\tau \to \infty$. For comparison, in **Figure 4A**, we also plot as a dotted line the mean heat absorbed by the Brownian engine when operating in a Newtonian fluid with viscosity $\eta = \eta_0$. In such a case, it can be readily demonstrated from Equation (16) that $-\langle Q_{\tau/2}\rangle$ actually approaches a quasi-static value, which is explicitly given by [34]

$$-\langle Q_{(\tau\to\infty)/2}\rangle = \frac{1}{2}k_B(T_h - T_c) + \frac{1}{2}k_B T_h \ln\left(\frac{\kappa_M}{\kappa_m},\right) \tag{27}$$

For the numerical values of the parameters investigated here, $-\langle Q_{(\tau\to\infty)/2}\rangle = 1.203 k_B T_c$, see horizontal thin dotted line in **Figure 4A**. We observe that, regardless of τ_0, all heat curves converge to such a value for $\tau \gg \tau_\kappa$, but depending on the specific value of the fluid relaxation time, different behaviors occur at short and intermediate cycle durations. Once again, we find that with increasing τ_0, the mean-heat curves gradually deviate from the behavior in a Newtonian fluid with viscosity $\eta = \eta_0$, and for $\tau_0 \gg \tau_\kappa$ they converge to that in a Newtonian fluid with $\eta = \eta_\infty$, see dashed line in **Figure 4A**. This provides another evidence that, as τ_0 increases, the energy dissipation of an engine operating in a viscoelastic fluid is mainly determined by the friction with the solvent.

In **Figure 4B**, we plot as solids lines the mean rate of heat absorption by the engine from the bath during the isothermal expansion at temperature T_h

$$J_\tau = -\frac{\langle Q_{\tau/2}\rangle}{\tau}, \tag{28}$$

as a function of the cycle duration τ for some representative values of $\tau_0 > 0$. The corresponding curves for a particle in Newtonian fluids with $\eta = \eta_0$ and $\eta = \eta_\infty$ are represented as dotted and dashed lines, respectively. In such cases, we find that J_τ exhibits a maximum, which corresponds approximately

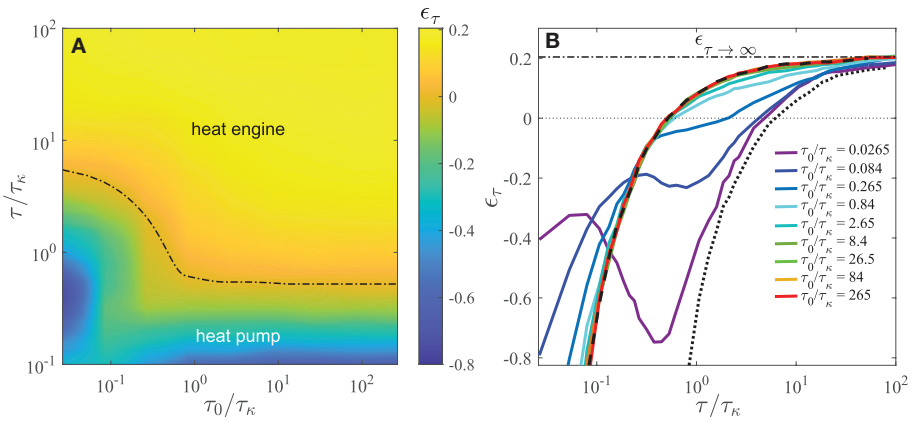

FIGURE 5 | (A) 2D color map representation of the efficiency of the colloidal Stirling engine, ϵ_τ, as a function of the fluid relaxation time, τ_0, and the duration of a Stirling cycle, τ. The dotted-dashed line corresponds to the stall time τ^*, which separates the values of the parameters τ_0 and τ for which the system operates as a heat engine ($\epsilon_\tau > 0$) from those for which it behaves as a heat pump ($\epsilon_\tau < 0$). **(B)** Examples of efficiency curves as function of the duration of a Stirling cycle, τ, for some particular values of the fluid relaxation time (solid lines). The dotted and dashed lines represent the efficiency curves of a Brownian Stirling engine in Newtonian fluids with constant viscosity $\eta = \eta_0$ and $\eta = \eta_\infty$, respectively. The dotted-dashed line depicts the quasi-static value of the Stirling efficiency, $\epsilon_{\tau\to\infty}$, given by Equation (30).

to the location of the minima in $-\langle W_\tau\rangle$ shown in **Figure 3A**. For $\tau \lesssim \tau_\kappa$, a marked dependence on the fluid relaxation time is observed if $\tau_0 \lesssim \tau_\kappa$, while for $\tau \gg \tau_\kappa$ a dependence $J_\tau \sim \tau^{-1}$ on the Stirling cycle time emerges for all values of τ_0, thus indicating the onset of the quasi-static thermodynamic behavior.

The previous findings reveal that, unlike the performance of Brownian heat engines in a Newtonian environment with a single relevant time-scale γ_0/κ_m of energy dissipation, in a viscoelastic fluid bath the low-frequency and the high-frequency values of the friction, γ_0 and γ_∞, give rise two meaningful dissipation time-scales, namely $\tau_\kappa = \gamma_0/\kappa_m$ and the apparently hidden time-scale $(1+\alpha)^{-1}\tau_\kappa = \gamma_\infty/\kappa_m$ due to the friction of the particle with the solvent. When the Stirling cycle time τ is comparable to one of such time-scales, the corresponding channel of irreversible dissipation is strongly activated. This in turn leads to a large amount of energy absorbed by the particle from the heat bath at a very high rate, as manifested by the minima and maxima depicted by arrows in **Figures 3A**, **4B**, respectively. For an arbitrary cycle time, the interplay between the two channels of irreversible dissipation along with the transient energy storage by the elastic microstructure of the fluid determine the resulting performance of the Brownian engine.

Finally, we determine the efficiency of the Brownian Stirling engine, defined as

$$\epsilon_\tau = \frac{-\langle W_\tau\rangle}{-\langle Q_{\tau/2}\rangle}, \tag{29}$$

as a function of the cycle time, τ, and the relaxation time of the viscoelastic fluid, τ_0. The results are represented as a 2D color map in **Figure 5A**, with some efficiency curves plotted in **Figure 5B** as a function of τ for exemplary values of τ_0. Additionally, in **Figure 5A**, we also plot the stall time τ^* defined in Equation (26) as a function of the fluid relaxation time. As a consequence of the energy exchange with a viscoelastic bath discussed in the previous paragraphs, τ^* divides the efficiency diagram into two regions. For $\tau < \tau^*$ the Brownian particle behaves a heat pump, where $\epsilon_\tau < 0$ exhibits a rather intricate dependence on τ_0 and τ due to the competition between the different energy storage and dissipation channels of the bath, which results on average in net energy absorption from the bath. On the other hand, for $\tau > \tau^*$, the efficiency is positive, $\epsilon_\tau > 0$, i.e., the Brownian particle behaves as a heat engine with positive power output. In this case, the efficiency is a monotonic increasing function of both τ and τ_0. Note that for the investigated values of the cycle time τ, the interval at which the engine has a positive efficiency is rather narrow for small fluid relaxation times $\tau_0 < \tau_\kappa$, because for the large value of the zero-shear viscosity considered in the simulations ($\eta_0 = 0.040$ Pa s, typical of biological fluids), there is a large amount of heat dissipation even at comparatively slow Stirling cycles. However, when the value of τ_0 is similar or larger than τ_κ, the elastic response of the fluid takes effect, hence the decrease in energy dissipation with a subsequent broadening of the interval of cycle times by one order magnitude for which $\epsilon_\tau > 0$.

Because in the model (4), we assume that the only source of stochasticity of the system is the thermal fluctuations of the fluid, apart from the driving potential of the harmonic trap there are no other sources of energy that affect the performance of the Brownian engine. Therefore, it is expected that the quasi-static Stirling efficiency

$$\epsilon_{\tau\to\infty} = \frac{\epsilon_C}{1+\frac{\epsilon_C}{\ln\left(\frac{\kappa_M}{\kappa_m}\right)}}, \tag{30}$$

which can be determined from the ratio of Equations (24) and (27), is never exceeded at finite τ regardless of the relaxation time of the viscoelastic fluid. In Equation (30), $\epsilon_C = 1 - \frac{T_c}{T_h}$

TABLE 1 | Mean power output produced by a Brownian Stirling engine during a cycle $\tau = \tau_{MP} = 18.6\tau_\kappa$ and corresponding efficiency for distinct values of the fluid relaxation time τ_0.

τ_0/τ_κ	$\frac{\tau_\kappa}{k_B T_c} P_{\tau=\tau_{MP}}$	$\epsilon_{\tau=\tau_{MP}}$
0	0.00679	0.1218
0.1	0.00867	0.1484
1	0.00994	0.1667
10	0.01142	0.1829
100	0.01183	0.1893

In all cases, the zero shear viscosity is the same, $\eta_0 = 0.040$ Pa s.

corresponds to the efficiency of a Carnot engine operating quasi-statically between two reservoirs at temperatures T_c and T_h. For the numerical values of the parameters characterizing the Stirling cycle considered here, we find $\epsilon_{\tau\to\infty} = 0.2043$. In **Figure 5B**, we demonstrate that, indeed, all the efficiency curves are bounded by such a value and approach it as the cycle time τ increases. The typical value of cycle period at which such efficiency is reached strongly depends on τ_0. While for a Brownian engine in a Newtonian fluid of viscosity η_0 the convergence is very slow, the quasi-static Stirling efficiency can be reached in a viscoelastic bath for typical experimental values of the parameters of the system, as shown in **Figure 5B** for $\tau_0 > \tau_\kappa$.

To compare the performance of a Stirling Brownian engine in a viscoelastic bath with other situations of practical interest, we first determine its efficiency at maximum power in a Newtonian fluid bath with the same zero-shear viscosity $\eta = \eta_0$. Although not as general as the Carnot efficiency, under some circumstances the so-called Curzon-Ahlborn efficiency [1, 2] represents a good approximation for the upper bound of the efficiency of stochastic heat engines working at maximum power [4, 6, 17, 19]. For the values of the parameters investigated in this work, we find that the power output P_τ in a purely viscous fluid reaches the maximum value $P_{\tau_{MP}} = 0.00679 k_B T_c {\tau_\kappa}^{-1}$ at a cycle time of $\tau_{MP} = 18.6\tau_\kappa$, at which the efficiency is $\eta_{\tau_{MP}} = 0.1218$. This value compares well with the Curzon-Ahlborn efficiency, $\epsilon_{CA} = 1 - \sqrt{\frac{T_c}{T_h}} = 0.1248$, and is approximately 60% the Carnot efficiency $\eta_C = 0.2043$. In **Table 1**, we list some exemplary values of the mean power output over a cycle, $P_{\tau=\tau_{MP}}$, and the corresponding efficiencies of the Brownian engine, $\epsilon_{\tau=\tau_{MP}}$, operating at the same Stirling cycle time $\tau_{MP} = 18.6\tau_\kappa$ in viscoelastic fluid baths with distinct values of their relaxation time τ_0. We verify that with increasing τ_0, both the absolute power delivered by engine and its efficiency are enhanced with respect to those in a Newtonian fluid. In particular, the efficiency at $\tau_{MP} = 18.6\tau_\kappa$ converges to approximately 93% the Carnot efficiency for $\tau_0 \gg \tau_\kappa$.

4. SUMMARY AND FINAL REMARKS

In this work, we have investigated a stochastic model based on the generalized Langevin equation for a Brownian Stirling engine in contact with a viscoelastic fluid bath. The slow rheological behavior of the fluid is taken into account in the model by an exponentially decaying memory kernel, which captures the basic features of the linear viscoelastic behavior of many non-Newtonian fluids. Our findings demonstrate that the memory friction exerted by the surrounding fluid has a tremendous impact on the performance of the heat engine in comparison with its operation in a viscous environment with the same zero-shear viscosity. In particular, a pronounced enhancement of the power output and the efficiency of the engine occurs as a result of the frequency-dependent response of the fluid under finite-time Stirling cycles, thus converging to limiting curves determined by the high frequency component of the friction of the particle as the fluid relaxation time increases. Moreover, the minimum value of the duration of the Stirling cycle at which the Brownian engine can convert energy from the medium into work becomes monotonically shorter with increasing fluid relaxation time, which broadens the interval of possible values of the Stirling cycle duration over which the engine is able to efficiently deliver positive power. From a wider perspective, our results highlight the importance of the non-equilibrium transient nature of the particle friction under temporal cycles of finite duration. We point out that, although in a different context, qualitatively similar effects have been discussed in systems with frequency-dependent properties due to their coupling to non-Markovian baths, such as Brownian particles driven into periodic non-equilibrium steady states [72] and quantum Otto refrigerators [73]. Furthermore, the link between a frequency dependent friction and the noise correlations of the bath is in turn an important issue for the correct interpretation of the efficiency of stochastic heat engines operating in non-equilibrium baths, as recently examined in the case of underdamped active Brownian particles [74].

To the best of our knowledge, our work represents the first investigation on the effect of memory friction in the performance of a Brownian Stirling engine in contact with a viscoelastic fluid reservoir. Thus, we expect that the results presented in this paper will contribute to a better understanding and potential applications of efficient work extraction and heat dissipation in other types of mesoscopic engines operating in complex fluids. Further steps of our work aim at addressing long-term memory effects during stochastic thermodynamic cycles with finite period, as those described by stretched exponentials [75] and power law kernels and fractional Brownian noise [76–79], which describe the mechanical response of diverse soft matter systems such as glasses and biological materials [80, 81]. One further aspect that could be investigated in the future is the effect of temporal changes in the fluid parameters, as it is well-known that the rheological properties of viscoelastic fluids are dependent on their temperature, which under a thermodynamic cycle would become time-dependent. We would like to point out that, since the parameters characterizing the operation of the heat engine presented in this paper are representative of typical soft matter systems, we expect that this process can be realized in a straightforward manner by use of optical tweezers [52]. Similar ideas could be extended to Brownian particles in non-linear potentials [82], and active Brownian heat engines [32] functioning in complex fluids, which

could be implemented by means of light-activated colloids in non-Newtonian liquids [69, 83–86] and hot Brownian particles [87–89].

DATA AVAILABILITY STATEMENT

The raw data supporting the conclusions of this article will be made available by the authors, without undue reservation.

AUTHOR CONTRIBUTIONS

JG-S conceived the model, carried out the numerical simulations, analyzed the results, and wrote the manuscript.

FUNDING

This work was supported by UNAM-PAPIIT IA103320.

REFERENCES

1. Novikov II. The efficiency of atomic power stations (a review). *J Nuclear Energy*. (1958). 7:125–28. doi: 10.1016/0891-3919(58)90244-4
2. Curzon FL, Ahlborn B. Efficiency of a Carnot engine at maximum power output. *Am J Phys*. (1975) 43:22–4. doi: 10.1119/1.10023
3. Leff HS. Thermal efficiency at maximum work output: new results for old heat engines. *Am J Phys*. (1987) 55:602–10. doi: 10.1119/1.15071
4. Van den Broeck C. Thermodynamic efficiency at maximum power. *Phys Rev Lett*. (2005) 95:190602. doi: 10.1103/PhysRevLett.95.190602
5. Izumida Y, Okuda K. Molecular kinetic analysis of a finite-time Carnot cycle. *Europhys Lett*. (2008) 83:60003. doi: 10.1209/0295-5075/83/60003
6. Esposito M, Lindenberg K, Van den Broeck C. Universality of efficiency at maximum power. *Phys Rev Lett*. (2009) 102:130602. doi: 10.1103/PhysRevLett.102.130602
7. Ozin GA, Manners I, Fournier-Bidoz S, Arsenault A. Dream nanomachines. *Adv Mater*. (2005) 17:3011–8. doi: 10.1002/adma.200501767
8. Hänggi P, Marchesoni F. Artificial Brownian motors: controlling transport on the nanoscale. *Rev Mod Phys*. (2009) 81:387–442. doi: 10.1103/RevModPhys.81.387
9. Kim K, Guo J, Liang ZX, Zhu FQ, Fan DL. Man-made rotary nanomotors: a review of recent developments. *Nanoscale*. (2016). 8:10471–90. doi: 10.1039/C5NR08768F
10. Martinez IA, Roldan D, Dinis L, Rica RA. Colloidal heat engines: a review. *Soft Matter*. (2017). 13:22–36. doi: 10.1039/C6SM00923A
11. Pietzonka P, Fodor E, Lohrmann C, Cates ME, Seifert U. Autonomous engines driven by active matter: energetics and design principles. *Phys Rev X*. (2019) 9:041032. doi: 10.1103/PhysRevX.9.041032
12. Ciliberto S, Gomez-Solano R, Petrosyan A. Fluctuations, linear response, and currents in out-of-equilibrium systems. *Annu Rev Cond Matter Phys*. (2013) 4:235–61. doi: 10.1146/annurev-conmatphys-030212-184240
13. Sekimoto K. Langevin equation and thermodynamics. *Prog Theor Phys Suppl*. (1998) 130:17–27. doi: 10.1143/PTPS.130.17
14. Seifert U. Stochastic thermodynamics, fluctuation theorems and molecular machines. *Rep Prog Phys*. (2012) 75:126001. doi: 10.1088/0034-4885/75/12/126001
15. Speck T. Stochastic thermodynamics for active matter. *Europhys Lett*. (2016) 114:30006. doi: 10.1209/0295-5075/114/30006
16. Ciliberto S. Experiments in stochastic thermodynamics: short history and perspectives. *Phys Rev X*. (2017) 7:021051. doi: 10.1103/PhysRevX.7.021051
17. Schmiedl T, Seifert U. Efficiency at maximum power: an analytically solvable model for stochastic heat engines. *Europhys. Lett*. (2007) 81:20003. doi: 10.1209/0295-5075/81/20003
18. Rana S, Pal PS, Saha A, Jayannavar AM. Single-particle stochastic heat engine. *Phys Rev E*. (2014) 90:042146. doi: 10.1103/PhysRevE.90.042146
19. Holubec V. An exactly solvable model of a stochastic heat engine: optimization of power, power fluctuations and efficiency. *J Stat Mech Theory Exp*. (2014) 2014:P05022. doi: 10.1088/1742-5468/2014/05/P05022
20. Tu ZC. Stochastic heat engine with the consideration of inertial effects and shortcuts to adiabaticity. *Phys Rev E*. (2014) 89:052148. doi: 10.1103/PhysRevE.89.052148
21. Bauer M, Brandner K, Seifert U. Optimal performance of periodically driven, stochastic heat engines under limited control. *Phys Rev E*. (2016) 93:042112. doi: 10.1103/PhysRevE.93.042112
22. Blickle V, Bechinger C. Realization of a micrometre-sized stochastic heat engine. *Nat Phys*. (2012) 8:143–46. doi: 10.1038/nphys2163
23. Quinto-Su PA. A microscopic steam engine implemented in an optical tweezer. *Nat Commun*. (2014) 5:5889. doi: 10.1038/ncomms6889
24. Martinez IA, Roldan, Dinis L, Petrov D, Parrondo JMR, Rica RA. Brownian Carnot engine. *Nat Phys*. (2016) 12:67–70. doi: 10.1038/nphys3518
25. Argun A, Soni J, Dabelow L, Bo S, Pesce G, Eichhorn R, et al. Experimental realization of a minimal microscopic heat engine. *Phys Rev E*. (2017) 96:052106. doi: 10.1103/PhysRevE.96.052106
26. Albay JAC, Zhou ZY, Chang CH, Jun Y. Shift a laser beam back and forth to exchange heat and work in thermodynamics. *Sci Rep*. (2021) 11:4394. doi: 10.1038/s41598-021-83824-7
27. Zakine R, Solon A, Gingrich T, Van Wijland F. Stochastic stirling engine operating in contact with active baths. *Entropy*. (2017) 19:193. doi: 10.3390/e19050193
28. Saha A, Marathe R, Pal PS, Jayannavar AM. Stochastic heat engine powered by active dissipation. *J Stat Mech Theory Exp*. (2018) 2018:113203. doi: 10.1088/1742-5468/aae84a
29. Chaki S, Chakrabarti R. Entropy production and work fluctuation relations for a single particle in active bath. *Phys A Stat Mech Appl*. (2018) 511:302–15. doi: 10.1016/j.physa.2018.07.055
30. Chaki S, Chakrabarti R. Effects of active fluctuations on energetics of a colloidal particle: Superdiffusion, dissipation and entropy production. *Phys A Stat Mech Appl*. (2019) 530:121574. doi: 10.1016/j.physa.2019.121574
31. Saha A, Marathe R. Stochastic work extraction in a colloidal heat engine in the presence of colored noise. *J Stat Mech Theory Exp*. (2019) 2019:094012. doi: 10.1088/1742-5468/ab39d4
32. Holubec V, Steffenoni S, Falasco G, Kroy K. Active Brownian heat engines. *Phys Rev Research*. (2020) 2:043262. doi: 10.1103/PhysRevResearch.2.043262
33. Ekeh T, Cates ME, Fodor E. Thermodynamic cycles with active matter. *Phys Rev E*. (2020) 102:010101. doi: 10.1103/PhysRevE.102.010101
34. Kumari A, Pal PS, Saha A, Lahiri S. Stochastic heat engine using an active particle. *Phys Rev E*. (2020) 101:032109. doi: 10.1103/PhysRevE.101.032109
35. Szamel G. Single active particle engine utilizing a nonreciprocal coupling between particle position and self-propulsion. *Phys Rev E*. (2020) 102:042605. doi: 10.1103/PhysRevE.102.042605
36. Martin D, Nardini C, Cates ME, Fodor É. Extracting maximum power from active colloidal heat engines. *Europhys Lett*. (2018) 121:60005. doi: 10.1209/0295-5075/121/60005
37. Krishnamurthy S, Ghosh S, Chatterji D, Ganapathy R, Sood AK. A micrometre-sized heat engine operating between bacterial reservoirs. *Nat Phys*. (2016) 12:1134–8. doi: 10.1038/nphys3870
38. Larson RG. *The Structure and Rheology of Complex Fluids*. New York, NY: Oxford University Press (1999).
39. Wilson LG, Harrison AW, Poon WCK, Puertas AM. Microrheology and the fluctuation theorem in dense colloids. *Europhys Lett*. (2011) 93:58007. doi: 10.1209/0295-5075/93/58007
40. Démery V, Bénichou O, Jacquin H. Generalized Langevin equations for a driven tracer in dense soft colloids: construction and applications. *N J Phys*. (2014) 16:053032. doi: 10.1088/1367-2630/16/5/053032
41. Gomez-Solano JR, Bechinger C. Probing linear and nonlinear microrheology of viscoelastic fluids. *Europhys Lett*. (2014) 108:54008. doi: 10.1209/0295-5075/108/54008

42. Gomez-Solano JR, Bechinger C. Transient dynamics of a colloidal particle driven through a viscoelastic fluid. *N J Phys*. (2015) 17:103032. doi: 10.1088/1367-2630/17/10/103032
43. Berner J, Müller B, Gomez-Solano JR, Krüger M, Bechinger C. Oscillating modes of driven colloids in overdamped systems. *Nat Commun*. (2018) 9:999. doi: 10.1038/s41467-018-03345-2
44. Mohanty RP, Zia RN. Transient nonlinear microrheology in hydrodynamically interacting colloidal dispersions: flow cessation. *J Fluid Mech*. (2020) 884:A14. doi: 10.1017/jfm.2019.912
45. Toyabe S, Sano M. Energy dissipation of a Brownian particle in a viscoelastic fluid. *Phys Rev E*. (2008) 77:041403. doi: 10.1103/PhysRevE.77.041403
46. Vishen AS. Heat dissipation rate in a nonequilibrium viscoelastic medium. *J Stat Mech Theory Exp*. (2020) 2020:063201. doi: 10.1088/1742-5468/ab7e2f
47. Di Terlizzi I, Baiesi M. A thermodynamic uncertainty relation for a system with memory. *J Phys A Math Theor*. (2020) 53:474002. doi: 10.1088/1751-8121/abbc7d
48. Di Terlizzi I, Ritort F, Baiesi M. Explicit solution of the generalised Langevin equation. *J Stat Phys*. (2020) 181:1609–35. doi: 10.1007/s10955-020-02639-4
49. Zwanzig R. Nonlinear generalized Langevin equations. *J Stat Phys*. (1973) 9:215–20. doi: 10.1007/BF01008729
50. Brey JJ, Casado J. Generalized Langevin equations with time-dependent temperature. *J Stat Phys*. (1990) 61:713–22. doi: 10.1007/BF01027298
51. Romero-Salazar L, Velasco RM. Generalized Fokker-Planck equation with time dependent temperature. *Revista Mexicana de Fisica*. (1995) 41:358–64.
52. Gieseler J, Gomez-Solano JR, Magazzù A, Castillo IP, García LP, Gironella-Torrent M, et al. Optical tweezers: a comprehensive tutorial from calibration to applications. *Appl Opt Photon*. (2021) 13:74–241. doi: 10.1364/AOP.394888
53. Squires TM, Mason TG. Tensorial generalized Stokes-Einstein relation for anisotropic probe microrheology. *Rheol Acta*. (2010) 49:1165–77. doi: 10.1007/s00397-010-0490-5
54. Bird R, Armstrong R, Hassager O. *Dynamics of Polymeric Liquids, Volume 1: Fluid Mechanics*. 2nd ed. New York, NY: Wiley (1987).
55. Felderhof BU. Estimating the viscoelastic moduli of a complex fluid from observation of Brownian motion. *J Chem Phys*. (2009) 131:164904. doi: 10.1063/1.3258343
56. Indei T, Schieber JD, Córdoba A, Pilyugina E. Treating inertia in passive microbead rheology. *Phys Rev E*. (2012) 85:021504. doi: 10.1103/PhysRevE.85.021504
57. Xu K, Forest MG, Klapper I. On the correspondence between creeping flows of viscous and viscoelastic fluids. *J NonNewtonian Fluid Mech*. (2007). 145:150–72. doi: 10.1016/j.jnnfm.2007.06.003
58. Cordoba A, Indei T, Schieber JD. Elimination of inertia from a Generalized Langevin Equation: Applications to microbead rheology modeling and data analysis. *J Rheol*. (2012) 56:185–212. doi: 10.1122/1.3675625
59. Fischer P, Rehage H. Rheological master curves of viscoelastic surfactant solutions by varying the solvent viscosity and temperature. *Langmuir*. (1997) 13:7012–20. doi: 10.1021/la970571d
60. Ezrahi S, Tuval E, Aserin A. Properties, main applications and perspectives of worm micelles. *Adv Coll Interface Sci*. (2006) 128–30:77–102. doi: 10.1016/j.cis.2006.11.017
61. Paul S, Kundu A, Banerjee A. Active microrheology to determine viscoelastic parameters of Stokes-Oldroyd B fluids using optical tweezers. *J Phys Commun*. (2019) 3:035002. doi: 10.1088/2399-6528/ab0833
62. Paul S, Narinder N, Banerjee A, Nayak KR, Steindl J, Bechinger C. Bayesian inference of the viscoelastic properties of a Jeffrey's fluid using optical tweezers. *Sci Rep*. (2021) 11:2023. doi: 10.1038/s41598-021-81094-x
63. Wilhelm C, Gazeau F, Bacri JC. Rotational magnetic endosome microrheology: viscoelastic architecture inside living cells. *Phys Rev E*. (2003) 67:061908. doi: 10.1103/PhysRevE.67.061908
64. Vaippully R, Ramanujan V, Bajpai S, Roy B. Measurement of viscoelastic properties of the cellular cytoplasm using optically trapped Brownian probes. *J Phys Cond Matter*. (2020) 32:235101. doi: 10.1088/1361-648X/ab76ac
65. Raspaud E, Lairez D, Adam M, Carton JP. Triblock copolymers in a selective solvent. 2. Semidilute solutions. *Macromolecules*. (1996) 29:1269–77. doi: 10.1021/ma951172x
66. Zhu X, Kundukad B, van der Maarel JRC. Viscoelasticity of entangled lambda-phage DNA solutions. *J Chem Phys*. (2008) 129:185103. doi: 10.1063/1.3009249
67. Bellour M, Skouri M, Munch JP, Hébraud P. Brownian motion of particles embedded in a solution of giant micelles. *Eur Phys J E*. (2002) 8:431–6. doi: 10.1140/epje/i2002-10026-0
68. Grimm M, Jeney S, Franosch T. Brownian motion in a Maxwell fluid. *Soft Matter*. (2011) 7:2076–84. doi: 10.1039/c0sm00636j
69. Narinder N, Gomez-Solano JR, Bechinger C. Active particles in geometrically confined viscoelastic fluids. *N J Phys*. (2019) 21:093058. doi: 10.1088/1367-2630/ab40e0
70. Handzy NZ, Belmonte A. Oscillatory rise of bubbles in wormlike micellar fluids with different microstructures. *Phys Rev Lett*. (2004) 92:124501. doi: 10.1103/PhysRevLett.92.124501
71. Chapman CD, Robertson-Anderson RM. Nonlinear microrheology reveals entanglement-driven molecular-level viscoelasticity of concentrated DNA. *Phys Rev Lett*. (2014) 113:098303. doi: 10.1103/PhysRevLett.113.098303
72. Wulfert R, Oechsle M, Speck T, Seifert U. Driven Brownian particle as a paradigm for a nonequilibrium heat bath: effective temperature and cyclic work extraction. *Phys Rev E*. (2017) 95:050103. doi: 10.1103/PhysRevE.95.050103
73. Camati PA, Santos JFG, Serra RM. Employing non-Markovian effects to improve the performance of a quantum Otto refrigerator. *Phys Rev A*. (2020) 102:012217. doi: 10.1103/PhysRevA.102.012217
74. Holubec V, Marathe R. Underdamped active Brownian heat engine. *Phys Rev E*. (2020) 102:060101. doi: 10.1103/PhysRevE.102.060101
75. Cui B, Yang J, Qiao J, Jiang M, Dai L, Wang YJ, et al. Atomic theory of viscoelastic response and memory effects in metallic glasses. *Phys Rev B*. (2017) 96:094203. doi: 10.1103/PhysRevB.96.094203
76. Qian H. Fractional Brownian motion and fractional Gaussian noise. In: Rangarajan G, Ding M, editors. *Processes with Long-Range Correlations: Theory and Applications*. Berlin; Heidelberg: Springer-Verlag (2003) p. 22–33. doi: 10.1007/3-540-44832-2_2
77. Rodriguez RF, Fujioka J, Salinas-Rodriguez E. Fractional correlation functions in simple viscoelastic liquids. *Phys A Stat Mech Appl*. (2015) 427:326–40. doi: 10.1016/j.physa.2015.01.060
78. Sevilla FJ, Rodríguez RF, Gomez-Solano JR. Generalized Ornstein-Uhlenbeck model for active motion. *Phys Rev E*. (2019) 100:032123. doi: 10.1103/PhysRevE.100.032123
79. Gomez-Solano JR, Sevilla FJ. Active particles with fractional rotational Brownian motion. *J Stat Mech Theory Exp*. (2020) 2020:063213. doi: 10.1088/1742-5468/ab8553
80. Balland M, Desprat N, Icard D, Féréol S, Asnacios A, Browaeys J, et al. Power laws in microrheology experiments on living cells: comparative analysis and modeling. *Phys Rev E*. (2006) 74:021911. doi: 10.1103/PhysRevE.74.021911
81. Kobayashi Y, Tsukune M, Miyashita T, Fujie MG. Simple empirical model for identifying rheological properties of soft biological tissues. *Phys Rev E*. (2017) 95:022418. doi: 10.1103/PhysRevE.95.022418
82. Ferrer BR, Gomez-Solano JR, Arzola AV. Fluid viscoelasticity triggers fast transitions of a Brownian particle in a double well optical potential. *Phys Rev Lett*. (2021) 126:108001. doi: 10.1103/PhysRevLett.126.108001
83. Gomez-Solano JR, Samin S, Lozano C, Ruedas-Batuecas P, van Roij R, Bechinger C. Tuning the motility and directionality of self-propelled colloids. *Nat Commun*. (2017) 7:14891. doi: 10.1038/s41598-017-14126-0
84. Gomez-Solano JR, Roy S, Araki T, Dietrich S, Maciolek A. Transient coarsening and the motility of optically heated Janus colloids in a binary liquid mixture. *Soft Matter*. (2020) 16:8359–71. doi: 10.1039/D0SM00964D
85. Narinder N, Bechinger C, Gomez-Solano JR. Memory-induced transition from a persistent random walk to circular motion for achiral microswimmers. *Phys Rev Lett*. (2018) 121:078003. doi: 10.1103/PhysRevLett.121.078003
86. Lozano C, Gomez-Solano JR, Bechinger C. Active particles sense micromechanical properties of glasses. *Nat Mater*. (2019) 18:1118–23. doi: 10.1038/s41563-019-0446-9
87. Rings D, Schachoff R, Selmke M, Cichos F, Kroy K. Hot Brownian motion. *Phys Rev Lett*. (2010) 105:090604. doi: 10.1103/PhysRevLett.105.090604
88. Rings D, Chakraborty D, Kroy K. Rotational hot Brownian motion. *N J Phys*. (2012) 14:053012. doi: 10.1088/1367-2630/14/5/053012
89. Kumar S, Kumar A, Gunaseelan M, Vaippully R, Chakraborty D, Senthilselvan J, et al. Trapped in out-of-equilibrium stationary state: hot Brownian motion

in optically trapped upconverting nanoparticles. *Front Phys*. (2020) 8:429. doi: 10.3389/fphy.2020.570842

Conflict of Interest: The author declares that the research was conducted in the absence of any commercial or financial relationships that could be construed as a potential conflict of interest.

frontiers in Physics

ORIGINAL RESEARCH
published: 15 April 2021
doi: 10.3389/fphy.2021.643355

Spontaneous Pattern Growth on Chocolate Surface: Simulations and Experiments

Jorge Delgado[1]*, *Claudia Ferreiro-Córdova*[2] *and Alejandro Gil-Villegas*[1]

[1] *División de Ciencias e Ingenierías, Universidad de Guanajuato, León, Mexico,* [2] *Tecnologico de Monterrey, Escuela de Ingeniería y Ciencias, Querétaro, Mexico*

The natural variation of temperature at ambient conditions produces spontaneous patterns on the surface of chocolate, which result from fat bloom. These metastable patterns are peculiar because of their shape and cannot be obtained by controlled temperature conditions. The formation of these spontaneous grains on the surface of chocolate is studied on experimental and theoretical grounds.Three different kinds of experiments were conducted: observation of formed patterns in time, atomic force microscopy of the initial events on the grain formation and rheology of the melted chocolate. The patterns observed in our experiments follow the trends described by the Avrami model, which considers a constant value at all spatial scales of the rate of linear growth α that governs the formation of isolated grains, starting from molecular clusters. Through NVT-ensemble computer simulations, using a Mie-segmented coarse-grained model of triacylglycerides molecules, we studied the process of nucleation that starts the pattern growth. From simulation and experiment results it is possible to derive a realistic value of α.

Keywords: chocolate, cocoa butter, nucleation, fat bloom, Avrami equation

OPEN ACCESS

Edited by:
Enrique Hernandez-Lemus, Instituto Nacional de Medicina Genómica (INMEGEN), Mexico

Reviewed by:
Martin Kröger, ETH Zürich, Switzerland
Vagelis Harmandaris, University of Crete, Greece

***Correspondence:**
Jorge Delgado
jorgedel@fisica.ugto.mx

Specialty section:
This article was submitted to Soft Matter Physics, a section of the journal Frontiers in Physics

Received: *18 December 2020*
Accepted: *16 March 2021*
Published: *15 April 2021*

Citation:
Delgado J, Ferreiro-Córdova C and Gil-Villegas A (2021) Spontaneous Pattern Growth on Chocolate Surface: Simulations and Experiments. Front. Phys. 9:643355. doi: 10.3389/fphy.2021.643355

1. INTRODUCTION

The study of chocolate is interesting for many reasons. Despite its evident importance in the food industry, this complex mixture is also a good example of some scientific curiosities [1]. For sure, some of these curiosities were found because of its technological importance and this is the case of our research: if a chocolate bar on a lab table had not become aged by chance, the observation of beautiful patterns on its surface had not inspired this ongoing study. Most of us have seen the appearance of patterns on a chocolate bar when left unperturbed for a long enough period of time, allowing it to age, some examples of such patterns are shown in **Figure 1**. It is easy to see that the contours formed call for the use of fractals to explain them, but shape generalities might not be easy to describe in scientific terms. On a close inspection of patterns in **Figure 1**, in the same sample, one finds a variety of shapes as different as "mostly circular," "snowflake-like," "almost circular," and "hexagonal-like".

The formation of chocolate phases and their properties can be revised extensively in the literature [2]. **Figure 2** summarizes the phases observed as function of temperature [3, 4]. In the temperature range of 50–60°, all the history of the sample can be erased. The volume change in the cooling-heating processes presents an important hysteresis. On one side, under cooling it is understood that the polymorphic forms β(V) and β(VI) form low temperature phases without a clear formation of the phases α and β'. In contrast, under heating, volume changes are noticeable

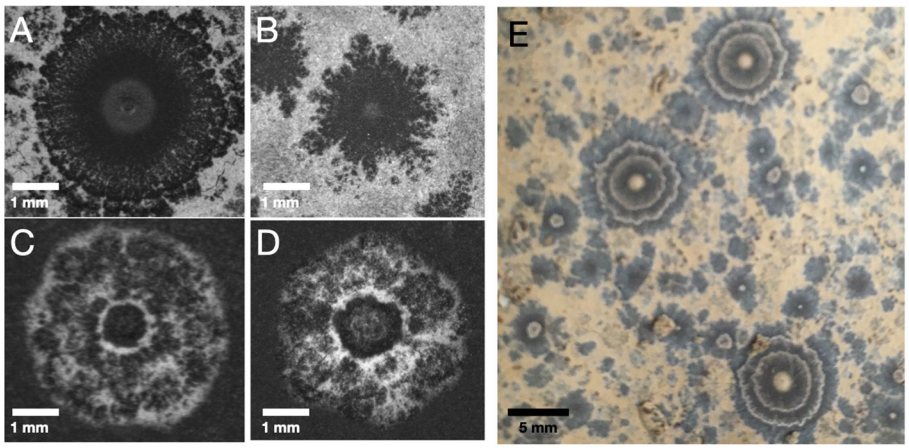

FIGURE 1 | (A–E) Spontaneous patterns on chocolate surfaces obtained at ambient temperature after several days.

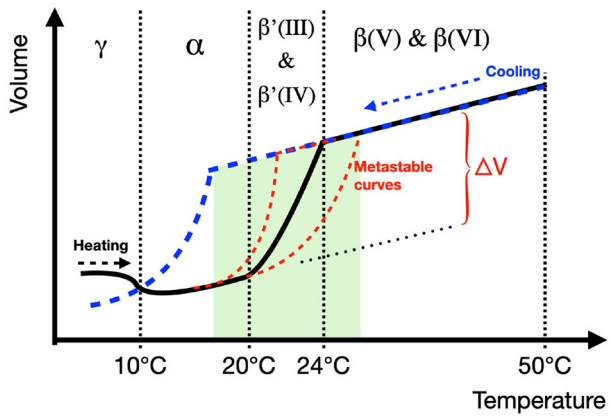

FIGURE 2 | Illustrative diagram of the volume change for the different phases observed under heating (black continuous line) and cooling (blue segmented line) ramps for cocoa butter. The phases more commonly described and named in the literature are annotated at the top of the different sections separated by vertical segmented lines. The intervals marked for each phase are approximated. The green region marks a common range of dispersion data associated to different phase transition and glass transition temperature values reported in literature. Metastable curves and melt expansion volume are suggested accordingly.

when different phases are formed. As depicted in **Figure 2**, previous works suggest that volume changes are not monotonous [4]. Phase change temperatures are approximate and, in general, temperatures reported differ by several degrees. Moreover, glass transition temperatures are also reported in the same ranges as the ones for phase change temperatures [5]. As a consequence, it is easy to suggest metastable lines that practically span all over the volume temperature diagram due to the proximity between the phase change temperatures [6, 7].

The story is a little different for the formation of patterns on the surface of chocolate, the phenomenon is not clearly understood, and few studies analyze the shape of these patterns [8]. In addition, from the collection of patterns previously reported, it is difficult to draw conclusions about the shapes formed, or about the reasons that gave rise to them. However, it is a consensus to consider the onset of the whitish color on the chocolate surface a consequence of the "fat bloom" event: the physical separation between β(V) and β(VI) phases during the aging process of chocolate. In the literature, one can find some "recipes" to produce "fat bloom," most of them involve the use of temperature cycles [3, 9]. However, in our initial attempts to create such patterns, we had difficulties obtaining them using periodic cycles or constant temperatures as it happens in literature [10]. As a consequence, the patterns observed in **Figure 1** were produced using a different procedure to what is usually reported in the literature.

In this paper, we reproduce the common patterns observed during the aging of chocolate at ambient conditions and give a glimpse on the reasons for obtaining them, based on a theoretical description given by the Avrami model for aggregation [11, 12]. For our study we use both experiments and simulations. Definitively, the complex mixture of at least triglycerides, polyphenols, and carbohydrates of high molecular weight, called "chocolate," represents a challenge for experimental reproducibility [3, 13]. Despite being difficult to conduct an experiment expecting the same pattern twice, it is possible to reproduce some trends of events necessary to obtain patterns that share some common characteristics. Here, it is crucial to identify, as is going to be discussed, that different events play a role in the final shape observed.

2. EXPERIMENTAL AND THEORETICAL METHODS

2.1. Sample Preparation

Two types of commercial chocolate were used in this work: a commercial 100% cacao product from the brand Mayordomo without added sugar or soy lecithin (https://chocolatemayordomo.com.mx) and a chocolate

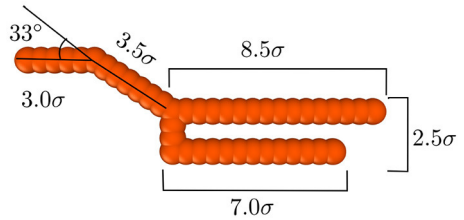

FIGURE 3 | Illustration of the particles used to model β(V) molecules. Each particle is composed of 43 fused spheres of diameter σ that form a chair-shaped molecule. The length of each segment of the molecule is shown in the diagram.

from the brand New Art Xocolatl with 85% cacao (www.newartxocolatl.com). The latter has added sugar and soy lechitin. These two extra components are usually the main difference between pure cacao and the mixture called "chocolate." In these mixtures, soy lechitin allows emulsification of the product with water and milk while sugar provides sweetness, which is completely absent in pure cacao. Despite the differences in composition between the two chocolates used, the experimental results were similar when changing the type of chocolate used.

Three different kinds of experiments were conducted: observation of formed patterns in time on chocolate surfaces at different temperatures, atomic force microscopy of the initial events on the pattern formation and rheology of melted chocolate. Patterns on chocolate surfaces were obtained by heating up samples of chocolate up to 60°C and pouring the viscous liquid in pre-heated petri dishes, which were then subjected to different temperature conditions. Time and temperature were recorded during pattern formation. The images analyzed in this paper were captured from these petri dishes during the evolution of the patterns. The topography Atomic Force Microscopy (AFM) images were also obtained from the petri dishes samples using a Witec alpha-300 microscope in a tapping mode ($100 \times 100\,\mu$m and 150×150 lines). Rheology was performed in a HR-3 Discovery Hybrid Rheometer (TA Instruments) using a cone-plate geometry of 40 mm diameter and 0.5°. The temperature was controlled in the rheometer using a Peltier plate.

2.2. Computer Simulations

We have developed a two-dimensional (2D) model for the experimental system which allow us to have a glance at the self assembly of the β(V) molecules. Our system consist of rigid bodies, each made with spheres of diameter σ, that have a shape close to one of a β(V) molecule [14–16] (see **Figure 3**). We have chosen a Mie-type potential to model the short-range attractive behavior between fat molecules. Lennard-Jones interaction potentials have been previously used to model units of fat crystals and its assembly into bigger systems [17]. Here, we chose to impose a shorter attractive range as a first attempt to model the fat crystal formation. In our model, the spherical units in each molecule interact only with the spheres of neighboring molecules via the pair potential,

$$U_{ij}(r) = \begin{cases} C\epsilon\left[\left(\frac{\sigma}{r}\right)^m - \left(\frac{\sigma}{r}\right)^n\right] + U_0 & r < r_{cut} \\ 0 & r \geq r_{cut} \end{cases}. \quad (1)$$

Where r is the center-of-mass distance between two spheres, ij indicates interaction between the spherical units i and j in two different molecules, σ is the approximated diameter of the repulsive core and ϵ is the strength of the interaction in k_BT units. The exponents m and n in Equation (1) define the range of the attractions, and are set to $m = 36$ and $n = 24$. The constant $C = m\,(m/n)^{n/(m-n)}/(m-n)$ ensures that the minimum of the potential is at $\epsilon = 1$. The range of the interaction between molecules is set with the cut-off parameter $r_{cut} = 1.9\sigma$. The shift value U_0 is chosen accordingly such that $U_{ij}(r_{cut}) = 0$. For simplicity, we have set $\epsilon = 1$, $\sigma = 1$ and the unit time $\tau_{sim} = \sqrt{m\sigma^2/k_B}$. Our simulation model does not considers the explicit presence of other compounds of the cocoa fat, i.e., these molecules are described as a continuous solvent, like a primitive model of the system, an approach that has been used in computer simulations of asphaltenes [18]. The properties of this effective solvent can be introduced by a dielectric constant, that can be incorporated within the strength of the interaction or the reduced temperature used in the simulation.

All simulations have been performed with the open-source MD simulation package LAMMPS [19], which has a dynamical integrator for rigid bodies [20, 21]. In our 2D simulations, the spherical units that form our molecules are restricted to a plane and keep the same initial z position. Each molecule segment of length 1σ is composed of two spheres, with a total of $N_p = 43$ spheres per molecule and $N_M = 1,020$ molecules in our 2D simulation box. To explore the assembly of our molecules, we use the packing fractions $\phi = 0.22$, $\phi = 0.36$, and $\phi = 0.48$. For each case, we start with a 2D box with an initial isotropic configuration, which was created with purely repulsive molecules ($r_{cut} = \sigma$). The interaction between the molecules is turned on in a constant number, volume, and temperature (NVT) ensemble using a Nose-Hoover thermostat [22]. We have set the temperature of the systems to $k_BT/\epsilon = 1$. The simulation time step was taken as $\delta t = 0.005\tau_{sim}$ and the total simulation times used were of $2 \times 10^5\ \tau_{\rm sim}$ to $5 \times 10^5\ \tau_{\rm sim}$.

3. RESULTS

3.1. Pattern Formation

Figure 4 shows several attempts to obtain the patterns observed in **Figure 1** with different cycles of temperature, as explained in the figure caption. As it can be observed, the patterns formed by controlled cycles, or just by maintaining a constant temperature, do form different types of patterns, but they are qualitatively different from those in **Figure 1**. Examples of these differences can be seen also in literature [3, 10]. Perhaps the main phenomenological differences between patterns in both figures are the occurrence of clear circular centers and more symmetric shapes, see the two patterns presented in **Figure 1**. What we observe in **Figure 1** is the most commonly observed

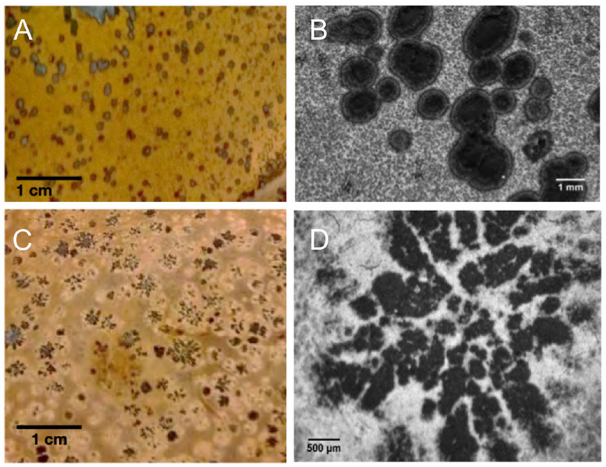

FIGURE 4 | Patterns on chocolate surfaces produced with a cycle or a constant temperature value. **(A,B)** Patterns obtained with a temperature cycle from 17 to 35°C in 12 h during 4 days. **(C,D)** Patterns obtained using a constant temperature of 26°C for three days. In both cases, the samples are cooled down from 60°C and poured on petri dishes thermalized at the minimum temperature tested.

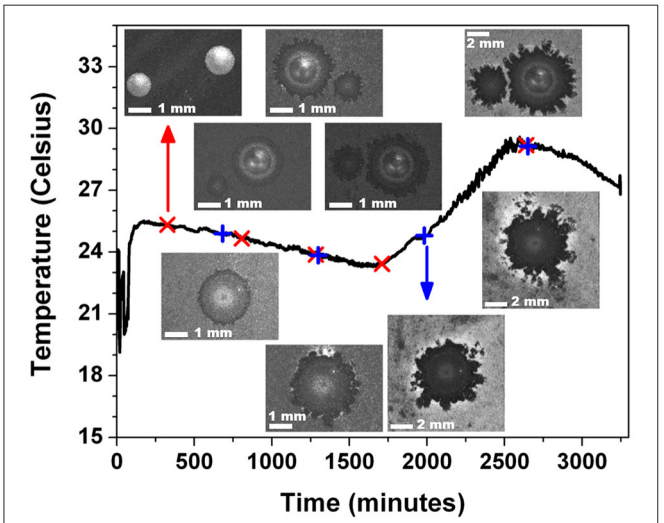

FIGURE 5 | Ambient temperature fluctuation in time and spontaneous patterns obtained in these conditions on a chocolate surface. Upper patterns correspond with red crosses and lower patterns with blue plus signs on the temperature curve. Patterns on the left, before 2,000 min, are 5.15 mm width and the last three patterns on the right are 10.55 mm width.

phenomenology and it can only be produced when temperature fluctuates in the range between 20 and 30°C, as observed in the sequence of pictures presented in **Figure 5** with the corresponding registry of temperature. These fluctuations are, apparently, necessary to obtain the characteristic morphology of these patterns. The initial steps to obtain this morphology are shown in **Figure 5**. At the very beginning, a circular center acts as a germ nucleus for a new phase, and in this way the polymorphic forms evolve from β' to β, as reported in the literature [4]. Some of the pictures suggest correctly that the center is a dome with an associated change in volume. In Fact, during all the formation of patterns, volume changes modify and produce patterns with uneven surfaces. The blooming is dusty, making difficult a measure with AFM, but interestingly, the beginning of the pattern can be measured with this technique as observed in **Figure 6**. Here, we show the first steps of the pattern formation, where we see a clear circle of a different phase rising up from the surface.

Using rheology, it is possible to correlate volume changes and reproducibility of the melting process. **Figure 7** shows shear apparent viscosity and the first normal stress coefficient of a sample under temperature cycles. For the two chocolate types, the viscosities rise up under cooling clearly because of the formation of the melting phase. The first time that the sample was cooled, the viscosity of the samples raised up at a temperature around 18°C, but the temperature at which the maximum occurs is not the same. Remarkably, because of the pre-history of the samples, this difference exacerbates under heating. Moreover, between two different experiments with the same cooling or heating history, it was impossible to obtain reproducible temperatures where the same viscosity rose up. Interestingly, the temperatures around which we observe the rise of both viscosities (18 and 25°C) have been described as glass-transition temperatures, which is possibly related to traces of unstable polymorphic forms of monounsaturated triacylglycerides [5]. It is important to point out that, in our case, the fact that the first normal stress coefficient, related with the change in volume, could rise up in different moments even for the same conching history, might be one of the reasons for the wide range of pattern shapes observed on the chocolate surfaces.

3.2. Simulation Results

An effective packing fraction for a model of pure cocoa butter can be obtained using the unit cell length values in crystalline polymorphic forms of triglycerides and the elongated shape of the molecules. With this, we calculated a packing fraction close to $\phi = 0.30$. Thus, we used this value as a reference for our simulation systems and selected the range of packing fraction values $0.22 \leq \phi \leq 0.36$. **Figure 8** shows snapshots of the typical configurations obtained for the concentrations explored. The colors indicate clusters of molecules with the same local orientation. The clusters were obtained using the criterion for nematic droplets made of hard spherocylinders developed by Cuetos and Dijkstra [23], which uses the local order parameter of each particle. This parameter is obtained for each particle i by setting a surface-to-surface cutoff distance of $\rho_{ij} = 0.5\sigma$ to all the j particles in this range. The local orientation order parameter $S(i)$ of each i particle is calculated using all the j particles that follow the restriction imposed by ρ_{ij}. Two particles, i and j, belong to the same cluster if they obey three conditions: $S(i) > 0.4$ and $S(j) > 0.4$, their surface-to-surface distance is $\rho_{ij} < 0.5\,\sigma$, and the product of their main axis orientation vectors is $|\,\mathbf{u}_i \cdot \mathbf{u}_j\,| > 0.85$. The separation restriction $\rho_{ij} < 0.5\,\sigma$ accounts for the fact that the potential imposes a short range attraction

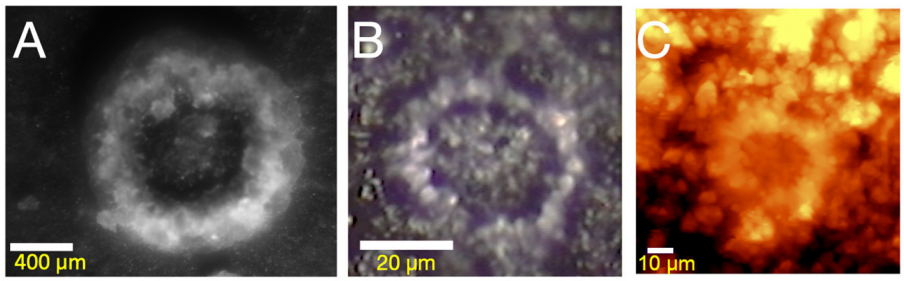

FIGURE 6 | (A,B) Beginning of the pattern formation at different spatial scales. **(C)** Topographic image of the pattern observed in **(B)** by AFM microscopy. Brighter zones correspond with upper regions in space.

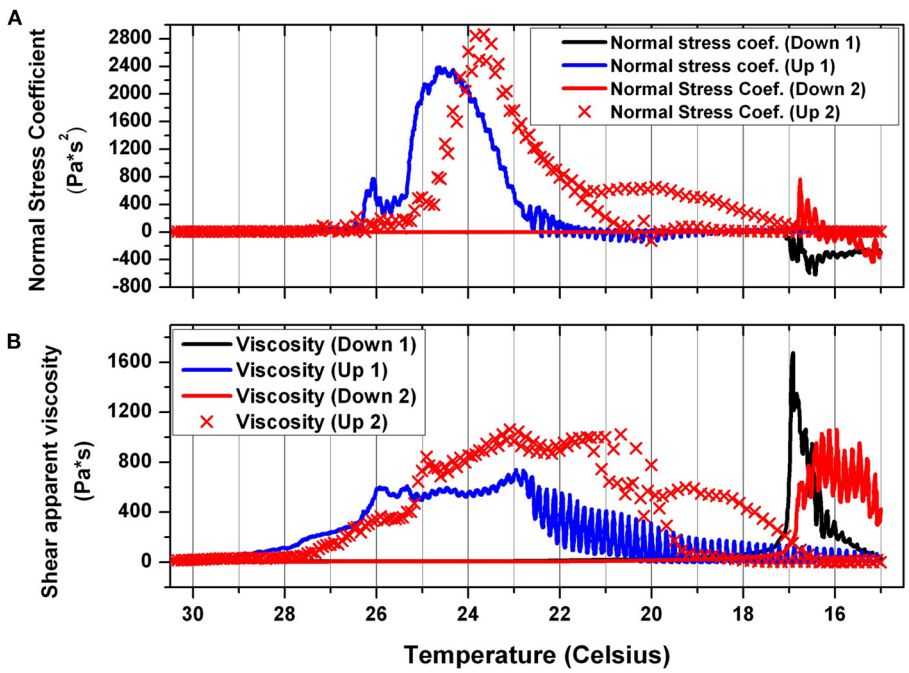

FIGURE 7 | First Normal Stress Coefficient **(A)** and Shear Apparent Viscosity **(B)** for chocolate in a temperature cycle using a rate of 0.25°C/min. The sample was first conditioned 5 min at 60°C prior to the beginning of the experiment. Then, the sample was cooled down from 40°C to 15°C ("Down" in the legend) and immediately heated up again until 40°C ("Up" in the legend). The experiment was performed twice with two different samples ("1" and "2" in the legend).

between particles; particles in a fat crystal will be at short surface-to-surface separations. With this procedure we identify all the clusters in our simulation box, and assign the same color to all the particles in each cluster.

In this work, the analysis of the systems is purely qualitatively, and focuses only on the cluster sizes and connectivity, but relevant information can be extracted from it. In **Figure 8A**, only two different clusters are found, but when the concentration is increased, the connectivity of the molecules is reduced and several small clusters appear (see **Figure 8C**). In fact, we have measured the average size of clusters for a bigger simulation box (8,500 particles) in a wider packing fraction range ($0.12 \leq \phi \leq 0.48$), and found that the clusters have an average size of around 480σ up to concentrations close to $\phi \approx 0.20$. Above this concentration, the average size decreases to about 85σ at $\phi = 0.48$. These sizes were calculated by averaging the length of several clusters in more than one direction and can be interpreted as average diameters. Thus, clusters become smaller as the concentration increases. The size of the clusters is relevant because our systems are consistent with the process of aggregation described by the Avrami model, characterized by two stages: a microscopic nucleation of molecules in order to form active germ nuclei, which consequently aggregate to induce growth grains. The simulations give insights into the first stage, where the clustering of particles give rise to the germ nuclei, corresponding to the aggregation nuclei that will induce

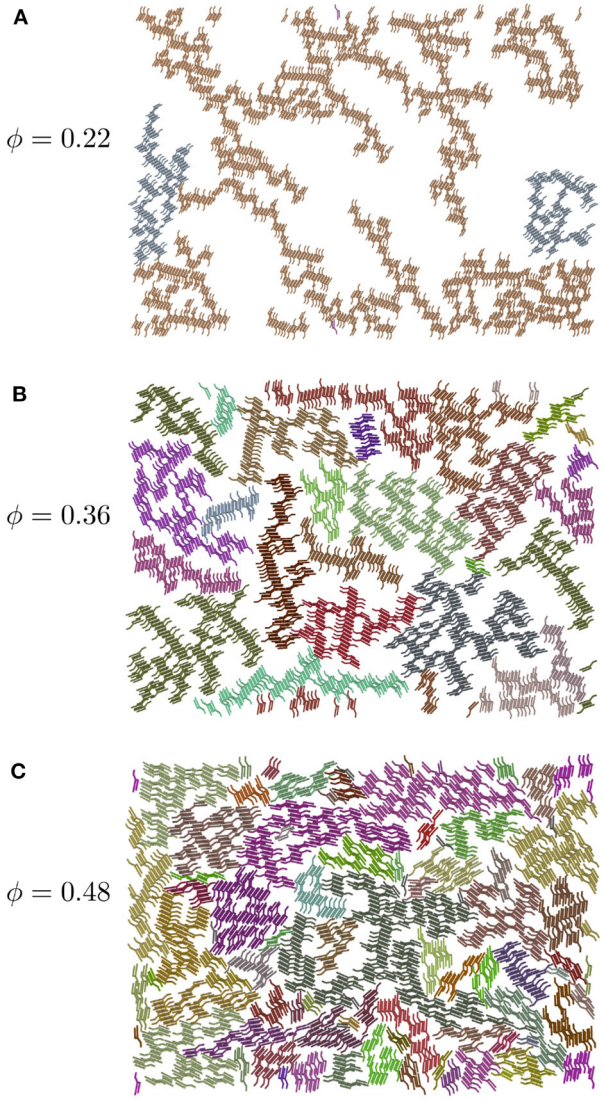

FIGURE 8 | Snapshots of typical final configurations of simulation boxes at packing fractions **(A)** $\phi = 0.22$, **(B)** $\phi = 0.36$, and **(C)** $\phi = 0.48$. Colors indicate different clusters, the preferred orientation of the molecules changes between clusters.

the formation of grains in chocolate samples. The size of these clusters might also have an effect on the final shape of the patterns formed on chocolate surfaces.

3.3. Pattern Growth

The nucleation process observed in experiments and simulations can be theoretically described using the Avrami model [11, 12], which is based on a statistical description of the formation of grains starting from initial or germ nuclei. The basic assumption behind this model is that the factors that govern the tendency of the growth nuclei are similar to those which govern further growth, i.e., what Avrami described as an *isokinetic process*. If $p(t)$ describes the probability of formation of growth nuclei per germ nucleus per unit time at temperature T, then

$$p(t) = Ke^{-(Q+A)/RT} \tag{2}$$

where Q is the energy of activation per gram molecule, A is the work per gram molecule required for a germ nucleus to become a growth nucleus, R is the gas constant and K is a normalization constant. The probability $p(t)$ is used to introduce a characteristic time τ of the growth process, defined as

$$\frac{d\tau}{dt} = p(t). \tag{3}$$

In a similar way, the size or linear dimension of the grain, denoted by $r(t)$, is given in terms of a rate of growth, $G(t)$, according to the expression

$$\frac{dr}{dt} = G(t). \tag{4}$$

Both equations imply that

$$G(t) = \frac{dr}{d\tau}p(t), \tag{5}$$

where $\frac{dr}{d\tau}$ is the speed of linear growth in the characteristic time. By integrating we obtain

$$r(\tau) = \int_0^\tau \frac{G(x)}{p(x)}dx \tag{6}$$

In the isokinetical regime, it is assumed that the speed of linear growth is a constant over concentrations and temperatures, denoted by α, i.e., $G(t) = \alpha p(t)$. Consequently,

$$r(\tau) = \alpha\tau \tag{7}$$

The volume V and surface area S of a grain are then given as,

$$V(\tau) = \sigma_{3D}r^3 \tag{8}$$

and

$$S(\tau) = \sigma_{2D}r^2. \tag{9}$$

Where $\sigma_{3D} = 4\pi/3$ and $\sigma_{2D} = \pi$ are 3D and 2D shape factors, respectively.

These expressions correspond to isolated growth nuclei. By considering two associating mechanisms for the growth of a grain, via the nucleation around a germ nucleus or the nucleation around an already growth nucleus, and using the expressions obtained for the V and S, as initial values for the grain sizes, Avrami [11] derives rate equations for the number density of nuclei germs $N(t)$ and for the total extended volume of the grain. By coupling these equations and solving them in the general case of a random distribution of initial germ nuclei, a general equation for the actual value of $V(t)$ is obtained, known in the literature as the Avrami equation, given by

$$V(t) = V_0(1 - e^{-bt^d}). \tag{10}$$

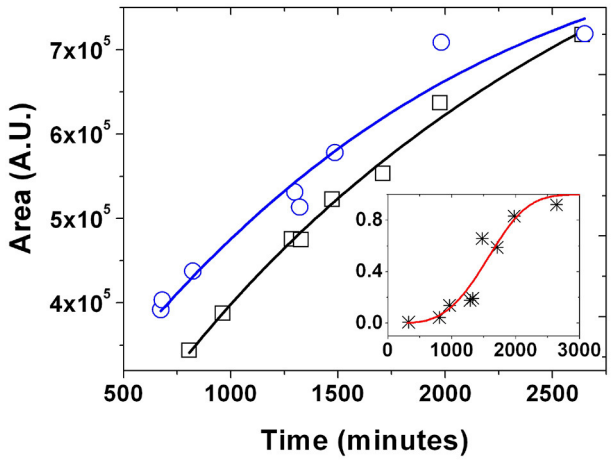

FIGURE 9 | Growing area vs. time for the patterns observed in the two series of **Figure 4**. The solid line is the fitting of the data to the 2D Avrami equation. The temporal Avrami exponent obtained is $d = 0.905 \pm 0.14$ (open black squares) and $d = 1.142 \pm 0.28$ (open blue circles). The corresponding values for parameter b are 0.00043 ± 0.00020 and 0.00059 ± 0.00028, respectively. The square correlation coefficient is higher than 0.96 in both cases. Inset: Normalized fat bloom growing area from binarized images vs. time of a section of the chocolate surface where no patterns were formed; data were also fitted with the Avrami equation (solid red line) obtaining $d = 4.055 \pm 1.406$ and $b = 8.1 \times 10^{-14} \pm 8.3 \times 10^{-13}$.

Where b is a coefficient that depends on $G(t)$ and $p(t)$ and d is the Avrami exponent. Both quantities depend also on the geometric dimension of the grain. Typical theoretical values obtained for d vary within the range $1 \leq d \leq 4$, depending on the value of the probability of formation of growth nuclei $p(t)$, which is set by the energy of activation Q and the work required to form a growth grain A [12]. In the case of quasi two-dimensional, plate-like, grains, $d \approx 3$ if $p(t)$ is small (i.e., a high total energy $E = Q + A$ per mole required for a germ nucleus to become a growth one) whereas for high values of $p(t)$ (i.e., small values of E), $d \approx 2$. Linear-like grains will have $1 \leq d \leq 2$, although it is important to bear in mind that the key factor that determines d is a complex one since not only depends on E but on G. For fluctuations in temperature, we could expect that Q becomes a determinant factor in the way that the grain growth formation is induced.

The growing area $S(t)$ of the two pattern series observed in **Figure 5** was analyzed using the Avrami equation for the corresponding 2D case, written as

$$\frac{S(t)}{S_0} = 1 - e^{-bt^d}, \tag{11}$$

where S_0 is the saturation area. This 2D version of Avrami model has been used previously to study crystallization by clustering of disk nuclei, using computer simulation [24]. For each time step, the pattern was drawn on a mask and the corresponding area, in pixels, was plotted vs. time. Results of the pattern growth for the two series, observed in the, show a remarkable similarity. For this image analysis, the fitting of the data to the Avrami equation gives an exponent $d \approx 1$. Furthermore, we analyzed the fat bloom homogeneous phenomena by performing a binarization that identifies regions of higher fat content, which presumably corresponds to β(V)-β(VI) rich regions and have a lighter typical color. We focused on sections of the images where no patterns grow, to avoid regions with holes on the surface. From these data, we obtained an Avrami exponent $d \approx 4$ (see inset in **Figure 9**). From the Avrami fitted expression in Equation (11), and assuming the formation of effective disk grains, the statistical quantities involved in the Avrami model, described by Equations (2–9), can be given as explicit functions of time and model constants. For example, the effective radius of the grains is given by

$$r(t) = r_0\sqrt{1 - e^{-bt^d}} \tag{12}$$

where r_0 is the grain's radius for the saturation time

$$\theta = (1/b)^{1/d} \tag{13}$$

On the other hand, the energy formation for a grain can be given by two different terms,

$$\frac{Q + A}{RT} = \ln\left[\frac{2\alpha\theta}{r_0 d}\right] + \ln\left[\frac{\sqrt{1 - e^{-bt^d}}}{\theta b t^{d-1} e^{-bt^d}}\right], \tag{14}$$

where θ is used in order to split the logarithm into two terms with dimensionless arguments. In this equation, the work per gram molecule required for the formation of the growth nucleus (A) is the time dependent term in the right side of the equation, and the energy of activation per gram molecule (Q) is the constant term, i.e.,

$$\frac{Q}{RT} = \ln\left[\frac{2\alpha\theta}{r_0 d}\right]. \tag{15}$$

From computer simulations, Q/RT can be obtained from the minimum value of the potential energy required by a pair of clusters in order to associate into a grain disk. This energy $E^* = E/\epsilon$ is determined from MD simulations. We can estimate ϵ and σ using data from a previous work on modeling biodiesel phase diagrams with a Molecular Thermodynamic approach [25]. Biodiesel molecules and triglyceride molecules have the same fatty acids. The triglyceride molecule in our model, observed in **Figure 3**, is formed by two units of stearic acid and one unit of oleic acid. The size of the oleic acid residue, linked to one of the three hydroxymethyl residues of the glycerol with a size of 6.5σ, can be compared with the size of the methyl oleate in reference [25], in order to estimate the total size and interaction energy of our triglyceride molecule. In this way, each molecule is formed by N_p segments and each segment has an average energy ϵ. The activation energy per molecule is set by the molecules at the border of each cluster, according to the short-ranged Mie potential model used in the simulations. The average energy per molecule is then approximated by $E = N_p\epsilon_f$, where ϵ_f is an average energy term per segment that only has contributions from interactions in the border of the clusters. The molar

TABLE 1 | Rates of linear size growth for different sets of Avrami parameters d and b. Values are also given for the saturation time and predicted diameters of chocolate grains after 2,000 min.

d	b	θ/min	α/(mm/min)	Diameter/mm
0.905	$4.3\ 10^{-4}$	5247.1606	$3.3279\ 10^{-5}$	0.1331
1.142	$5.9\ 10^{-4}$	672.3961	$3.2771\ 10^{-4}$	1.3108
4.055	$8.1\ 10^{-14}$	1696.4375	$4.6115\ 10^{-4}$	1.8446

activation energy Q/RT is here given by E/kT. Together with the constants d and b determined from fitting of experimental data $S(t)$, we obtained the value of the isokinetical parameter α that links the energetic process involved in the growth of grains with the rate of change with time of the radius of the grain,

$$\begin{aligned} \alpha &= \frac{r_0 d}{2\theta} e^{Q/RT} \\ &= \frac{r_0 d}{2\theta} e^{N_p \epsilon_f^* \epsilon / kT}. \end{aligned} \tag{16}$$

As described in detail in the **Supplementary Material**, from this expression we can predict a value for α considering the saturation time θ, and the corresponding typical value of 1 mm for the diameter of a grain. The simulation value obtained for $\epsilon_f^* = \epsilon_f/\epsilon$ for a packing fraction $\phi = 0.36$ is -0.015, and with the Molecular Thermodynamic value of energy for the biodiesel parameter [25], we obtained the results for θ and α reported in **Table 1**. Furthermore, we calculated a predicted value of the diameter of a grain after 2,000 min, obtained from α, that allows comparisons with the experimental results from **Figure 5**. We observe that the model can predict accurately the effective diameter of the chocolate grains.

4. DISCUSSION

We have presented the different aspects required to obtain the most common patterns observed during the aging on the surface of the chocolate. One basic aspect is the necessity of having temperature fluctuations in the range of 20–30°C, as observed in **Figure 5**. Without them, it is practically impossible to obtain metastable patterns with circular centers and high radial and angular symmetry. Ambient temperature fluctuations apparently allow to reshape constantly the pattern; following metastable paths that produce more frequently and more efficiently patterns with radial symmetry than the symmetry produced in situations where temperature is fixed or cyclic. It is important to point out that the different phases observed with the variation of temperature have differences in volume and crystallinity (orientation). In the literature there are descriptions of typical hysteresis in volume between the cooling and the heating histories, as depicted in **Figure 2**, which is similar to what it is suggested from hysteresis in the normal stress coefficient vs. temperature (**Figure 7**). Following **Figure 2**, we can also suggest that the proximity among the different stable and metastable chocolate phases produces easily different shapes or patterns on its surface, that depend on temperature fluctuations and on the previous history of the sample. However, the patterns are completely reproducible; considering that the first events are always circular patterns that, as time goes on, develop ruffles and small scarce islands. Clearly, more than two phases could be involved to create a pattern, but interestingly the pattern growing can be captured using the Avrami model (**Figure 9**). An Avrami exponent d in the range of one is obtained and, as previously mentioned, it can be linked, via the probability of formation of growth nuclei $p(t)$, with a low value of energy E of the fat bloom event triggered in a pattern. By contrast, the homogeneous fat bloom formation also analyzed according to the Avrami model (**Figure 9**, inset), presents an exponent near 4, that corresponds to an energy higher than the one necessary to form a pattern.

Although the time and size scales involved in experiments and simulations are very different, the fact that the spontaneous pattern growth observed on the chocolate surface can be closely described by the Avrami equation suggests that the isokinetical approach intrinsic to this model, i.e., the proportionality between the growth rate $G(t)$ and the probability of formation growth of nuclei, $p(t)$, can be linked to the way the triacylglycerides molecules interact to form active germ nuclei, as observed in simulations, and then the clustering of these nuclei in order to form grains with an increasing radius. In other words, the associating mechanisms that induce the formation of grains can be described using the coarse-grained model of molecules in our NVT simulations scale accordingly to the Avrami model. Within their uncertainty values, the Avrami constants b and d obtained for the experimental system can be used, in combination with the activation energy determined from computer simulations at an equivalent packing fraction of the experiments, in order to determine the isokinetical parameter α (or speed of linear growth of the formation) of chocolate grains. We have found that the predicted sizes for chocolate grains compare accurately with real sizes. In future works we will address the correlation between the parameters of the Mie pair-interaction used in the simulations and the actual value of Q required to form a growth nucleus from germ nuclei. It is important to stress here that a proper modeling of the grain formation, according to the second stage of aggregation described by Avrami, requires the consideration of the surface tension of the system. However, at the level of the scale described by the simulations presented here, our simulations are restricted to the description of the first stage of the aggregation process, that only considers the formation of active germ nuclei. A more detailed analysis will also require to consider the role played by other molecules present in chocolate.

In spite of the complexity of the behavior of real patterns on the chocolate surface, it is interesting that a coarse-grained model of the molecular behavior involved can be accomplished through the Avrami model in order to give information of the associating mechanisms that determine the actual growth process of chocolate grains. Furthermore, the alignment of the nuclei observed in the simulations resembles what is expected in the formation of fat crystals [14, 17, 26]. The difference in the connectivity for different packing fractions might be another

crucial factor in fat bloom. Further issues that we would like to answer are how the fluctuation of temperature is correlated to the activation energy for the formation of grains, and the characterization of the rheological behavior of experimental samples in terms of the molecular model used in the simulation and its dependence on the Mie potential parameters, as well as the role played by the solvent molecules.

DATA AVAILABILITY STATEMENT

The raw data supporting the conclusions of this article will be made available by the authors, without undue reservation.

AUTHOR CONTRIBUTIONS

JD carried out the experiments and data analysis. CF-C carried out simulations and data analysis. AG-V was involved in the theoretical analysis. All authors designed the research and wrote the paper.

FUNDING

JD and AG-V thank SEP-CONACYT for the funding of the project No. 237425 Materia Blanda Coloidal.

ACKNOWLEDGMENTS

We thank Jacqueline Chávez for her help with some experiments.

SUPPLEMENTARY MATERIAL

The Supplementary Material for this article can be found online at: https://www.frontiersin.org/articles/10.3389/fphy.2021.643355/full#supplementary-material

REFERENCES

1. Blanco E, Hodgson DJM, Hermes M, Besseling R, Hunter GL, Chaikin PM, et al. Conching chocolate is a prototypical transition from frictionally jammed solid to flowable suspension with maximal solid content. *Proc Natl Acad Sci USA*. (2019) 116:10303–8. doi: 10.1073/pnas.1901858116
2. Sato K. Crystallization behaviour of fats and lipids—a review. *Chem Eng Sci*. (2001) 56:2255–65. doi: 10.1016/S0009-2509(00)00458-9
3. Marangoni AG, McGauley SE. Relationship between crystallization behavior and structure in cocoa butter. *Cryst Growth Des*. (2003) 3:95–108. doi: 10.1021/cg025580l
4. Gouveia JR, De Lira Lixandr ao KC, Tavares LB, Fernando PHL, Garcia GES, Dos Santos DJ. Thermal transitions of cocoa butter: a novel characterization method by temperature modulation. *Foods*. (2019) 8:1–9. doi: 10.3390/foods8100449
5. Calva-Estrada SJ, Utrilla-Vázquez M, Vallejo-Cardona A, Roblero-Pérez DB, Lugo-Cervantes E. Thermal properties and volatile compounds profile of commercial dark-chocolates from different genotypes of cocoa beans (*Theobroma cacao* L.) from Latin America. *Food Res Int*. (2020) 136:109594. doi: 10.1016/j.foodres.2020.109594
6. Van Krevelen DW, Te Nijenhuis K. *Properties of Polymers*. Amsterdam: Elsevier (2009).
7. Simha R, Boyer RF. On a general relation involving the glass temperature and coefficients of expansion of polymers. *J Chem Phys*. (1962) 37:1003–7. doi: 10.1063/1.1733201
8. Marangoni AG, Ollivon M. Fractal character of triglyceride spherulites is a consequence of nucleation kinetics. *Chem Phys Lett*. (2007) 442:360–4. doi: 10.1016/j.cplett.2007.05.098
9. Rodriguez Furlán LT, Baracco Y, Lecot J, Zaritzky N, Campderrós ME. Effect of sweetener combination and storage temperature on physicochemical properties of sucrose free white chocolate. *Food Chem*. (2017) 229:610–20. doi: 10.1016/j.foodchem.2017.03.002
10. Sonwai S, Rousseau D. Controlling fat bloom formation in chocolate—impact of milk fat on microstructure and fat phase crystallisation. *Food Chem*. (2010) 119:286–97. doi: 10.1016/j.foodchem.2009.06.031
11. Avrami M. Kinetics of phase change. I. General theory. *J Chem Phys*. (1939) 7:1103–12. doi: 10.1063/1.1750380
12. Avrami M. Kinetics of phase change. II. Transformation-time relations for random distribution of nuclei. *J Chem Phys*. (1940) 8:212–24. doi: 10.1063/1.1750631
13. Tremeac B, Hayert M, Le-Bail A. Mechanical properties of Tylose gel and chocolate in the freezing range. *Int J Refriger*. (2008) 31:867–73. doi: 10.1016/j.ijrefrig.2007.10.005
14. van Mechelen JB, Peschar R, Schenk H. Structures of mono-unsaturated triacylglycerols. II. The β_2 polymorph. *Acta Crystallogr Sect B*. (2006) 62:1131–8. doi: 10.1107/S0108768106037086
15. Peschar R, Pop MM, De Ridder DJA, van Mechelen JB, Driessen RAJ, Schenk H. Crystal structures of 1,3-distearoyl-2-oleoylglycerol and cocoa butter in the β(V) phase reveal the driving force behind the occurrence of fat bloom on chocolate. *J Phys Chem B*. (2004) 108:15450–3. doi: 10.1021/jp046723c
16. Hernqvist L. Polymorphism of triglycerides a crystallographic review. *Food Struct*. (1990) 9:5.
17. Marangoni AG, Acevedo N, Maleky F, Co E, Peyronel F, Mazzanti G, et al. Structure and functionality of edible fats. *Soft Matter*. (2012) 8:1275–300. doi: 10.1039/C1SM06234D
18. Ortega-Rodríguez A, Cruz SA, Gil-Villegas A, Guevara-Rodríguez F, Lira-Galeana C. Molecular view of the asphaltene aggregation behavior in asphaltene-resin mixtures. *Energy Fuels*. (2003) 17:1100–8. doi: 10.1021/ef030005s
19. Plimpton S. Fast parallel algorithms for short-range molecular dynamics. *J Comput Phys*. (1995) 117:1–19. doi: 10.1006/jcph.1995.1039
20. Miller Iii T, Eleftheriou M, Pattnaik P, Ndirango A, Newns D, Martyna G. Symplectic quaternion scheme for biophysical molecular dynamics. *J Chem Phys*. (2002) 116:8649–59. doi: 10.1063/1.1473654
21. Kamberaj H, Low RJ, Neal MP. Time reversible and symplectic integrators for molecular dynamics simulations of rigid molecules. *J Chem Phys*. (2005) 122:224114. doi: 10.1063/1.1906216
22. Martyna GJ, Klein ML, Tuckerman M. Nosé-Hoover chains: the canonical ensemble via continuous dynamics. *J Chem Phys*. (1992) 97:2635–43. doi: 10.1063/1.463940
23. Cuetos A, Dijkstra M. Kinetic pathways for the isotropic-nematic phase transition in a system of colloidal hard rods: a simulation study. *Phys Rev Lett*. (2007) 98:095701. doi: 10.1103/PhysRevLett.98.095701
24. Weinberg MC. A test of the Johnson-Mehl-Avrami equation. *J Cryst Growth*. (1987) 2:779–80. doi: 10.1016/S0022-0248(87)80025-8
25. Perdomo FA, Gil-Villegas A. Molecular thermodynamics of biodiesel fuel compounds. *Fluid Phase Equil*. (2010) 293:182–9. doi: 10.1016/j.fluid.2010.03.011

26. Fernandes VA, Müller AJ, Sandoval AJ. Thermal, structural and rheological characteristics of dark chocolate with different compositions. *J Food Eng.* (2013) 116:97–108. doi: 10.1016/j.jfoodeng.2012.12.002

Conflict of Interest: The authors declare that the research was conducted in the absence of any commercial or financial relationships that could be construed as a potential conflict of interest.

frontiers in Physics

ORIGINAL RESEARCH
published: 15 April 2021
doi: 10.3389/fphy.2021.637138

Cluster Morphology of Colloidal Systems With Competing Interactions

Néstor E. Valadez-Pérez[1]*, *Yun Liu*[2,3] *and Ramón Castañeda-Priego*[4]

[1]Facultad De Ciencias en Física y Matemáticas, Universidad Autonoma De Chiapas, Tuxtla Gutiérrez, México, [2]NIST Center for Neutron Research, National Institute of Standards and Technology, Gaithersburg, MD, United States, [3]Department of Chemical and Biomolecular Engineering, University of Delaware, Newark, DE, United States, [4]División De Ciencias e Ingenierías, Campus León, Universidad De Guanajuato, León, México

Reversible aggregation of purely short-ranged attractive colloidal particles leads to the formation of clusters with a fractal dimension that only depends on the second virial coefficient. The addition of a long-ranged repulsion to the potential modifies the way in which the particles aggregate into clusters and form intermediate range order structures, and have a strong influence on the dynamical and rheological properties of colloidal dispersions. The understanding of the effect of a long-ranged repulsive potential on the aggregation mechanisms is scientifically and technologically important for a large variety of physical, chemical and biological systems, including concentrated protein solutions. In this work, the equilibrium cluster morphology of particles interacting through a short-ranged attraction plus a long-ranged repulsion is extensively studied by means of Monte Carlo computer simulations. Our findings point out that the addition of the repulsion affects the resulting cluster morphology and allows one to have a full control on the compactness or fractal dimension of the aggregates at a given thermodynamic condition. This allows us to manipulate the reversible aggregation process and, therefore, to finely tune the resulting building blocks of materials at large length scales.

Keywords: competing interactions, reversible aggregation, clustering, cluster morphology, fractal dimension

OPEN ACCESS

Edited by:
Giancarlo Ruocco,
Italian Institute of Technology (IIT), Italy

Reviewed by:
Emanuela Zaccarelli,
National Research Council (CNR), Italy
Patrick Charbonneau,
Duke University, United States

***Correspondence:**
Néstor E. Valadez-Pérez
nestor.valadez@unach.mx
enextv@gmail.com

Specialty section:
This article was submitted to Soft Matter Physics, a section of the journal Frontiers in Physics

Received: *02 December 2020*
Accepted: *03 February 2021*
Published: *15 April 2021*

Citation:
Valadez-Pérez NE, Liu Y and Castañeda-Priego R (2021) Cluster Morphology of Colloidal Systems With Competing Interactions. Front. Phys. 9:637138. doi: 10.3389/fphy.2021.637138

1 INTRODUCTION

Many body systems composed of particles interacting via a short-range attraction and a long-range repulsion (SALR) have attracted attention in the past decade due to their rich phase behavior not observed for systems interacting with purely attractive potentials. One of these is the clustered fluid phase resulting from the frustration of the gas-liquid separation. This phase has been observed in experiments, as well as in molecular simulations, see, *e.g.*, references [1–14]. Understanding the clustering of particles is necessary to explain changes in the dynamics and rheology of colloidal systems with competing interactions, see [15, 16].

The competition between attraction and repulsion over different length scales makes possible to have different phase diagrams depending on the parameters that control both the range and strength of each potential feature. [17] presented an empirical classification for systems with competing interactions based on the range of the repulsion and attraction. When the attraction range is smaller than 20% of the particle diameter σ and a repulsion range is slightly larger than that of the attraction, these systems are considered as type I system. Particles in type II systems have a longer range repulsion while the attraction range is similar to that of the type I systems. However, the range of the repulsion is still at the order of σ. Both the type I and II SALR systems have been studied see Table 1 in reference [17]. Type I and II systems present a similar phase diagram, which includes phases as: the

dispersed fluid, clustered fluid, and percolated states. One difference of these two types of systems is that type I is believed to present a gas-liquid separation below the cluster temperature if the repulsion range is short enough, as is speculated by [17]. In type II systems, the repulsion prevents the equilibrium clustering of particles beyond some limit, see, *e.g.* [3]. In reference [11] it is found that it is possible to find a fluid-crystal coexistence in type II systems. Finally, a type III system the attraction range is much longer than that of type I and II systems, and comparable to σ with an even longer-ranged repulsion. For those systems, some theoretical study show that there can be some very interesting gas-liquid transition behavior, see, *e.g.*, [18, 19].

In this work, we focus on the cluster morphology of type I systems, since the features of the interaction are more similar to the estimated potential for colloidal systems and protein solutions, see for example references [2, 4, 5, 20–23]. Besides, the structural properties of clusters have not been studied systematically yet.

The phase diagram of particles with only short-ranged attractions has been studied intensively, see *e.g.* [24–30]; and it is widely accepted that their thermodynamic behavior is determined by the extended law of corresponding states, [31]. In a similar spirit [10], proposed a generalized phase diagram for particles with competing interactions after studying type I and II systems through Monte Carlo computer simulations. According to the generalized phase diagram, particles at low and moderate concentrations form a dispersed fluid state at high temperatures, and an equilibrium clustered fluid state at temperatures below T_c^{ref}, where T_c^{ref} is the critical temperature of a reference system. Particles in the reference system interact through only the attractive part of the full SALR potential, the repulsive part, beyond σ, plays the role of a perturbation. At high enough concentrations, the dispersed fluid state percolates to form the random percolated state similar to particles with only attractions. However, when increasing the concentration, clustered fluid state can transition into a different percolating network, the cluster percolated state. Below the equilibrium clustered fluid state, it has been identified a non-equilibrium region related to the gel transition, [11]; but it is out of scope of the generalized phase diagram proposed by [10].

The manuscript is organized as follows. In **Section 2**, the interaction potential, as well as the computer simulation protocol are described. In **Section 3**, the structural signature of competing interaction systems is discussed and intimately related to the properties of clusters, which are studied in **Section 5**. **Section 4** presents the phase diagram, where the region relevant for this work is explicitly pointed out. Finally, in **section 6** the main conclusions of this work and some perspectives are presented.

2 COMPETING INTERACTION POTENTIAL AND MONTE CARLO COMPUTER SIMULATIONS

We have performed extensive Monte Carlo (MC) computer simulations in the canonical ensemble *NVT* for a system made up of spherical particles with a diameter σ, interacting through a short-ranged attraction plus a long-ranged repulsion given by the expression,

$$u(r) = \begin{cases} \infty & r < \sigma \\ -\epsilon & \sigma \le r \le \lambda\sigma \\ A\epsilon \dfrac{\exp\left(-\kappa\left(r-\lambda\sigma\right)\right)}{r/\sigma - 0.1} & r > \lambda\sigma \end{cases} \tag{1}$$

the range and strength of the attraction are well determined by λ and ϵ, respectively, while the maximum repulsion strength (in units of ϵ) is given by A and the corresponding range is approximately κ^{-1}. The potential well is related to the reduced temperature by $T^* = k_B T/\epsilon$, with k_B being the Boltzmann's constant and T the absolute temperature. This potential form was chosen because the contribution of the attraction, as well as the repulsion, are easily distinguishable. We have also chosen the range parameters as: $\lambda = 1.1$ and $\kappa = 3$ to have a simple representation of the interaction between proteins in aqueous solution, see, for example [10]. We are mainly interested in the effect of the repulsion strength on the structure and aggregate morphology. For that reason, we systematically vary the values of $A = 0.2$, 0.5, 0.7 and 1.0.

MC computer simulations were carried out at the same packing fraction, $\phi = 0.1$; this is related with the number density $\rho^* = \frac{6\phi}{\pi}$. We particularly chose this particle concentration to avoid the percolation threshold, which is reached when $\phi \gtrsim 0.15$, see [32, 33]. A typical simulation consists of 10^8 MC steps to reach the equilibrium and 10^8 extra MC steps to measure the structural properties of the system. At the lowest temperatures, additional MC steps where required to reach thermodynamic equilibrium; 10^9 MC steps before the structure was measured. In some simulations, we were not able to reach the equilibrium since particles tend to aggregate in large clusters, this situation is similar to the usual gas-liquid phase separation. In the **Supplementary Material**, we show the calculation of the binodal line; those results indicate that the non-equilibrium states observed in simulations are close to the binodal.

To characterize the microstructure, we calculate the so-called structure factor, $S(q)$, which quantifies the density fluctuation correlations [34]. We have simulated a system of 11,000 particles to resolve the $S(q)$ at small q-values, *i.e.*, long wavelengths. Once the structure of a system was determined, the cluster size distribution, $P(s)$, as well as the radius of gyration, $R_g(s)$, were calculated. Those quantities represent the normalized probability of finding a cluster made of s particles and the corresponding effective radius. In this second calculation, the number of particles in the simulations was decreased to 4,000, since the computational cost of larger systems is quite expensive.

3 STRUCTURAL SIGNATURE OF THE INTERMEDIATE RANGE ORDER STRUCTURES AND CLUSTERED PHASE

The hallmark of many SALR systems, is found in the structure factor, [10]. The $S(q)$ presents a peak at some q-value smaller than the typical one related to the correlation between pairs of particles,

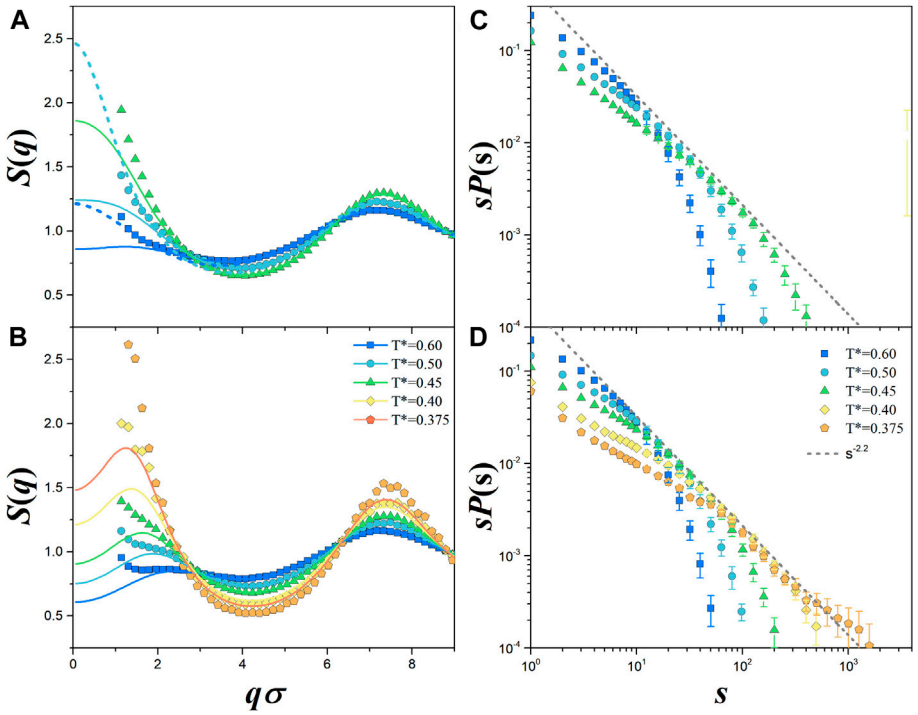

FIGURE 1 | Structure factor for competing interaction systems whose repulsion strength is **(A)** $A = 0.2$ and **(B)** $A = 0.5$ at $\phi = 0.1$ and different temperatures. **(C,D)** display the cluster size distributions for **(A,B)**, respectively. Computer simulation results are denoted by symbols, while solid lines are the theoretical solution of the Ornstein-Zernike equations with the Percus-Yevick closure. In **(A)** we also include the $S(q)$ for the reference system the SW potential, *i.e.*, $A = 0$ (dashed lines). In **(C,D)** we also include $P(s) \sim s^{-2.2}$ (solid line), the limit case for random percolation, see [35].

usually around $2\pi/\sigma$. Such low-q peak has been observed in protein solutions, see, for example, [1, 2, 5, 15, 22]. However, this peak is not only due to the appearance of a clustered phase, but to a more general intermediate range order (IRO) structure, see [8–10, 22]. For example, the IRO peak has also been observed at high concentrations where particles are already forming a percolating network, see [8].

[10] defined the clustered fluid state as that thermodynamic state of a system at which the cluster size distribution, $P(s)$, displays a well-defined peak or maximum around $s \sim 20$. This state is easily detected since $P(s)$ decreases faster than a power law, when the system is below the percolation threshold. Also, according to [10] the clustered state is reached when the low q-peak takes a value above the critical value of 2.7. This empirical criterion works well for type II SALR systems, although there is not a physical explanation for such a value. Another criterion to identify the clustered phase has been proposed by [13] based on the value of the thermal correlation length.

In **Figures 1A,B** the structure factor for the systems with the lower repulsion, obtained through MC simulation (symbols) and by solving the Ornstein-Zernike equation with the Percus-Yevick closure (solid lines), is shown. In (A) it is also included the $S(q)$ for the reference system, $A = 0$ (dashed lines). The structure factor for $A = 0$ and $A = 0.2$ is equal for all temperatures considered, except for $q\sigma < 2$, that means the repulsion is too weak to affect the short-ranged correlations at separations around σ but is large enough to break up the large-ranged correlations responsible of the gas-liquid phase separation, as q goes to 0. For the system with $A = 0.5$, the low-q peak emerges as indicated in both simulation and theory, see **Figure 1B**. The localization of this peak shifts to lower values as T^* is lowered. It is worth to mention that the theory does not agree with the simulation at low-q values however the information provided is useful to distinguish between systems close to the phase separation, panel (A) and systems with a true clustered phase, panel (B). In panel (B) the low-q peak for the lowest temperatures is close to the limit imposed to the periodic boundary conditions, but the theory can give the trend of simulation as it does at the highest temperatures.

Figures 1C,D show the cluster size distribution for systems with $A = 0.2$ and 0.5, respectively, where $P(s)$ is multiplied by s to avoid the biasing to monomers. The probability of finding large clusters increases as the temperature gets lower, as expected, see [8]. For example, for the system with $A = 0.2$ at $T^* = 0.4$, that is inside the phase separation region, the distribution presents two peaks, at $s = 1$ and ~ 4000 (data not shown). By increasing the repulsion strength to $A = 0.5$, $P(s)$ indicates that the probability of finding large clusters is higher for $A = 0.2$ than for $A = 0.5$, since the repulsion impedes the clustering. At $T^* = 0.375$ the distribution looks different than the one obtained for other temperatures. In fact, there is a small shoulder at around 60 particles, a value larger than the reported for the clustered phase in reference [10]. Also, for this temperature, the low-q peak exceeds the value of 2.5, which is closer to the expected for a clustered fluid. Then, this case is somehow in the middle of the

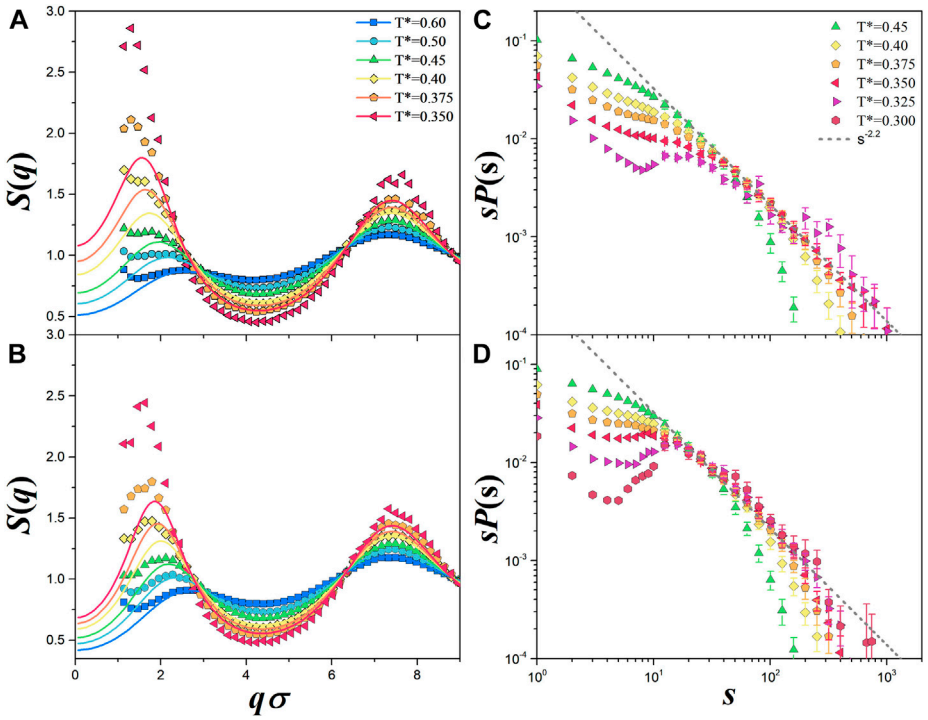

FIGURE 2 | Structure factor for competing interaction systems whose repulsion strength is **(A)** $A = 0.7$ and **(B)** $A = 1.0$ at $\phi = 0.1$ and different temperatures. **(C,D)** show the corresponding cluster size distributions. Computer simulation results are denoted by symbols, while solid lines are the theoretical solution to the Ornstein-Zernike equation with the Percus-Yevick closure. In **(C,D)** we also include $P(s) \sim s^{-2.2}$ (solid line), the limit case for random percolation, see [35].

full phase separation and the formation of a clustered phase. This observation thus indicates that for a type I SALR system, the transition temperature from a dispersed fluid state to a clustered fluid state may start shift away from the gas-liquid transition line for a reference potential system. This is qualitatively different from that of a type II SALR system. Hence, for the SALR system, the strength of the repulsion can affect the transition temperature from a dispersed fluid to the clustered fluid state.

The relationship between the low-q peak and the shoulder in $sP(s)$ is clearer for the remaining cases. **Figure 2** contains the same information as in **Figure 1** for systems with $A = 0.7$ and 1.0. At low temperatures, $T^* < 0.375$, the low-q peak of the structure factor is about 2.0, and the cluster size distribution in panels (C) and (D) present a shoulder between 20 and 30 particles, which indicates the formation of the clustered fluid. Here the maximum of the $S(q)$ is not that close to the 2.7 threshold value, however systems are forming a clustered fluid. An important observation here is that at high s values the size distribution follows the power law $P(s) \sim s^{-2.2}$ observed in random percolation and previously noted in reference [8]. Here, clusters must form larger clusters that eventually percolate in the cluster percolated phase, see reference [10].

4 PHASE DIAGRAM

In **Figure 3A** the phase diagram for the SW fluid with an interaction range $\lambda = 1.1$ is displayed; it shows the gas-liquid coexistence (blue circles) and the percolation threshold (orange diamonds). The main effect having a repulsive potential coupled with the SW is either to lower the critical temperature or to inhibit the gas-liquid phase separation, favoring the formation of the so-called intermediate range order (IRO) structure, as is discussed in references [8–10]. For the lowest repulsion considered here, $A = 0.2$, we did not observed the IRO peak, as well as the clustered phase, but for the larger repulsion the simulations predict the existence of the IRO peak at all temperatures considered.

The information presented in the previous section allows us to establish the boundary between a disperse fluid, the clustered one and the phase separation. Nonetheless, the exact location of this boundary depends on the specific value of the repulsive potential, see **Figure 3B**. Competing interaction systems at low temperatures resemble the gas-liquid phase separation for $A > 0.2$, however, it is difficult to establish this from the simulation results. In the **Supplementary Material**, we show the calculation of the binodal corresponding for different A-values by using an approximate perturbation approach developed by [36]. This approach predicts the occurrence of the gas-liquid phase separation for all repulsive potentials considered here, which agrees well with the proposal discussed in reference [17] concerning the phase diagram of type I SALR systems. For $A = 0.2$, the separation is predicted at $T^* \sim 0.4$, which agrees well with the findings of our simulations. Thus, the most interesting region to analyze the clustering is localized below the percolation threshold and at temperatures around the

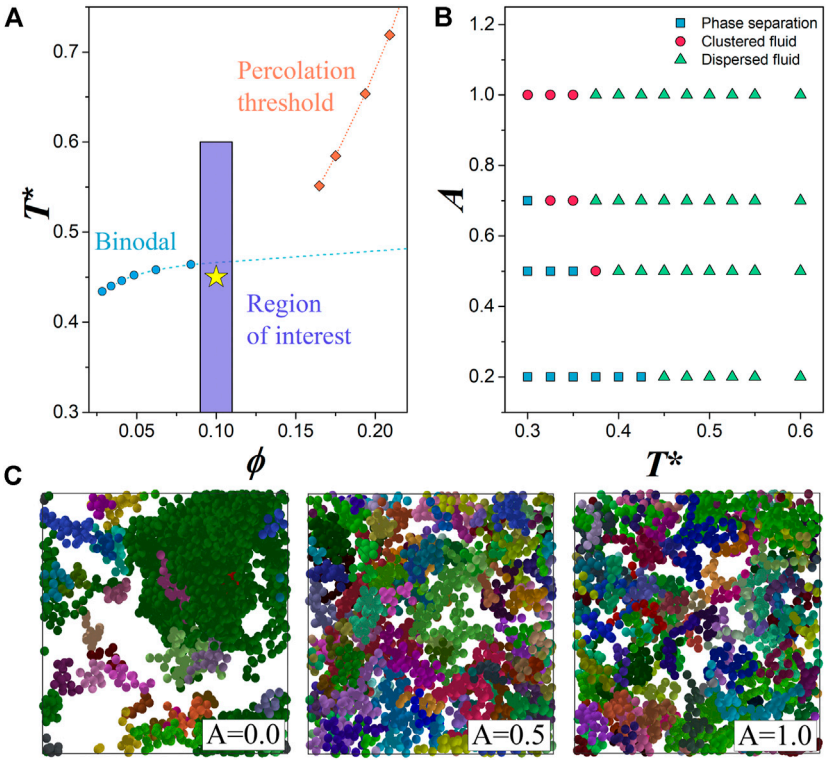

FIGURE 3 | (A) phase diagram for the SW fluid with $\lambda = 1.1$, our reference system. Circles correspond to the gas-liquid phase separation taken from reference [29]; diamonds point out the percolation threshold, from reference [33]; using the extended law of corresponding states to map the SW with $\lambda = 1.05$ data. **(B)** State for particles interacting through the full SALR potential, here we identify the dispersed fluid, the clustered fluid and those states in the phase separation, see **Supplementary Material**. **(C)** Snapshots corresponding to the yellow star for different repulsion strengths. Clusters are colored randomly to be easily identified. For clarity, clusters with 10 or more particles are the only ones displayed.

binodal, colored region in **Figure 3A**. This temperature window includes states where the systems could be either a disperse or a clustered fluid and close to the expected phase separation.

Figure 3C shows some snapshots of the simulated system at $\phi = 0.1$ and $T^* = 0.45$ for different values of A, this corresponds to the yellow star in (A). For clarity, only clusters with 10 and more particles are shown. The system with purely attractive particles, case $A = 0$, presents the expected gas-liquid phase separation, a large cluster surrounded by small clusters and monomers. As the repulsion strength increases, the liquid phase disappears and a clustered phase emerges. It can be observed that the cluster morphology depend of the value of A as we will see below.

5 CLUSTER MORPHOLOGY

The cluster morphology of competing interactions systems has been studied in experiments and simulations [13]. found that equilibrium clusters are more compact than those out of equilibrium. Experiments made by [7] indicate that cluster morphology is affected by the attractive contribution. Also [37], found that equilibrium clusters tend to be elongated structures. In a previous publication, [38]; we studied the morphology of clusters made of purely attractive particles at the same ϕ-value and for temperatures above the binodal. There, we found that the morphology of clusters with more than 10 particles is determined by the strength of the attraction via the second virial coefficient, while the morphology of small clusters is insensitive to the state of the system.

In this work, we have performed a systematic study of the cluster morphology. The radius of gyration is fitted using the equation: $R_g = Cs^{1/d_f}$, where d_f is the well-known fractal dimension; this definition has been used to characterize the morphology in similar systems [39]. **Figure 4** shows the results for systems at different temperatures and for repulsion strengths (A) A = 0.5 and (B) 1.0. It is worth to mention that we have only considered the R_g of clusters observed at least 100 times in the simulation to have a more reliable and accurate statistics. For $A = 0.5$, systems at high temperatures follow a similar trend as the one observed for attractive particles. Small clusters have almost the same shape independent of the temperature and large clusters become more compact as the attraction becomes stronger, see Reference [38]. The changes in d_f of large clusters are smaller than the ones observed in systems with purely attractive interactions and clusters keep a fractal dimension close to 2.0.

From **Figure 1** it was noted the presence of small shoulder at $s \sim 60$ particles, at the same value there is a small change in the

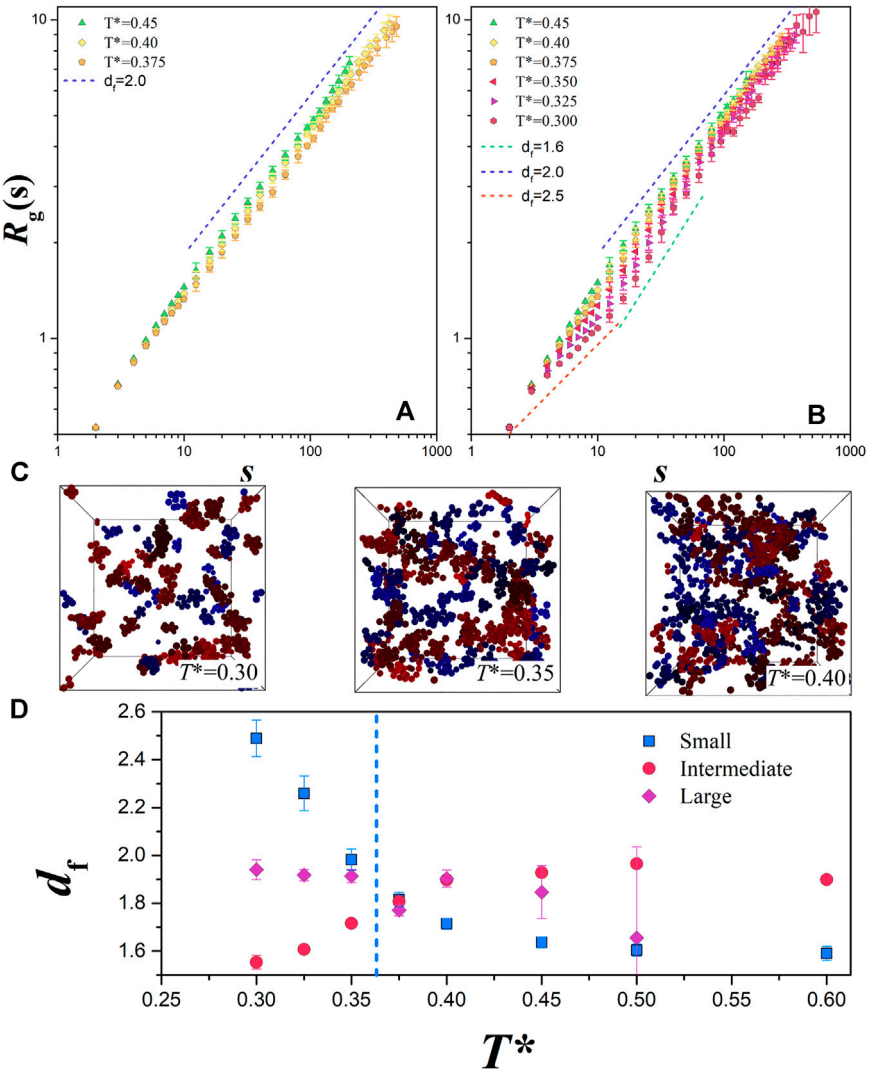

FIGURE 4 | Radius of gyration for competing interaction systems at $\phi = 0.1$ with different repulsion strengths **(A)** $A = 0.5$ and **(B)** $A = 1.0$ at different temperatures. We plot, along the expected R_g, the radius of gyration for clusters with a fractal dimension of 2 (blue lines), 2.5 (red lines) and 1.6 (green lines). **(C)** Snapshots of the system with $A = 1.0$ at different temperatures are displayed. Clusters with 5 up to 12 particles are colored in blue and clusters with $15 \leq s \leq 30$ in red. **(D)** Fractal dimension for systems with $A = 1.0$, we classify clusters in small ($s \leq 12$), intermediate ($13 \leq s \leq 60$) and large ($s \geq 100$), see [40]. Vertical line is the boundary between dispersed and clustered fluid.

slope of R_g; this behavior is more pronounced for the case $A = 1.0$ where also the localization of the shoulder is shifted to $s \sim 20$. Such case is shown in 4 (B), the behavior or R_g is completely different from that reported in reference [38]. Firstly, the morphology of small clusters with less than approximately 15 particles becomes more compact as the temperature gets lower, the fractal dimension at the lowest temperature is around 2.5. Secondly, clusters with a larger number of particles, until ~ 60, present a lower fractal dimension as the temperature gets lower. A similar morphology has been previously reported by [23]; they simulated a system of particles interacting through a potential fitted from experimental data for a lysozyme immersed in an aqueous solution. This means that at low temperatures compact clusters join together without merging completely, that makes possible the arrangement of these clusters in elongated structures with a lower fractal dimension, in agreement to [23]. It is important to note that for those clusters $2.5 < 2R_g/\sigma < 4$, this size is comparable with $1.5 < q\sigma < 2.5$, which is the interval where the low-q peak was located. Finally, clusters with more than approximately 60 particles seem to have the same d_f, regardless the temperature of the system. The latter could be related to the fact that at all temperatures, the $S(q)$ is very similar at low wavelengths, *i.e.*, $q \to 0$, see **Figure 2B**.

Figure 4C shows snapshots for systems with $A = 1.0$ at different temperatures. In these cases, small clusters ($5 < s \leq 12$) are colored in blue and intermediate clusters ($15 \leq s \leq 30$) in red. Small clusters at low temperatures tend to be compact structures, they are less compact as the temperature increases. The intermediate size clusters

at low temperatures are still compact, but adopt an elongated configuration while at high temperatures some particles look as branches. Besides, at $T^* = 0.4$ small and intermediate clusters do not have a distinctive shape as for the lower temperatures, which agree with the fact that R_g does not change its slope at 15 particles. These qualitative observations are supported by the information given in **Figure 4D**. There, we have computed the fractal dimension of clusters at different temperatures, they are classified as small ($s \leq 12$), intermediate ($13 \leq s \leq 60$) and large ($s \geq 100$), this classification agrees with the different fractal regimes shown by [40]. Since the boundary between intermediate and large clusters does not have a well-defined location, we have decided to skip some of the data. From the figure, it is clear how small clusters become more compact as the temperature gets lower than $T^* = 0.375$, *i.e.*, the boundary between the dispersed and clustered phases. Intermediate clusters become more elongated, while the morphology of large clusters only changes slightly.

6 CONCLUSION

In this work, we investigated the cluster formation for systems with competing interactions. The potential parameters were chosen to represent the interactions between proteins in an aqueous solution at low salinity. The analysis of the structure factor, as well as the cluster morphology, reveals that due to the addition of the long-ranged repulsion, the gas-liquid phase separation is shifted to lower temperatures compared with that of systems with pure attractive potential. For the case $A = 0.2$, it was evident that the phase separation happens at $T^* = 0.4$ and there is no clearer IRO peak in the structure factor. For stronger repulsion, the development of the IRO states as indicated by the IRO peak is very obvious in the structure factor. And the cluster morphology showed more complex structures due to the competition of the attraction and repulsion. At the lowest temperature analyzed here, $T^* = 0.35$, the system with $A = 0.5$ reached a non-equilibrium state, which made difficult to state if it is a gas-liquid phase transition or a non-equilibrium cluster phase. Systems with the largest repulsion strength remained in equilibrium within the simulation window.

The analysis of the cluster size percolation for systems in the clustered fluid state revealed that there is cluster formation with a preferential size in clustered fluid states. This optimal size depends also on the strength of the repulsive potential. Thus for the type I SALR systems, it is possible to produce clustered states with specific cluster size by controlling the potential parameters.

At the lowest temperatures for the stronger repulsion, particles are locally organized in very compact structures. Small clusters with less than 12 particles tend to adopt the minimum energy configuration, while intermediate size clusters have elongated configurations when these compact clusters join together with certain specific configurations. This cluster formation is different from that observed in systems made of purely attractive particles, [38]. For the SALR systems studied here, the scales at which the intermediate size clusters are observed can be related with the value at which the IRO peak appears in the structure factor. An interesting future work is the analysis of the dynamics of the clustering process at different concentrations in both the cluster fluid states and the cluster percolated states.

DATA AVAILABILITY STATEMENT

The original contributions presented in the study are included in the article/**Supplementary Material**, further inquiries can be directed to the corresponding authors.

AUTHOR CONTRIBUTIONS

All authors contributed to the design and implementation of the research, to the analysis of the results and to the writing of the manuscript.

FUNDING

NV-P acknowledges support by CONACyT through the scholarship Retenciones 2019–1. RC-P. also acknowledges the financial support provided by the Consejo Nacional de Ciencia y Tecnología (CONACYT, Mexico) through Grants Nos. 237,425 and 287,067. YL acknowledge the support by the Center for High Resolution Neutron Scattering (CHRNS), a partnership between the National Institute of Standards and Technology and National Science Foundation under Agreement No. DMR-1508249.

SUPPLEMENTARY MATERIAL

The Supplementary Material for this article can be found online at: https://www.frontiersin.org/articles/10.3389/fphy.2021.637138/full#supplementary-material.

REFERENCES

1. Baglioni P, Fratini E, Lonetti B, and Chen SH. Structural arrest in concentrated cytochrome c solutions: the effect of pH and salts. *J Phys Condens Matter* (2004) 16:S5003. doi:10.1088/0953-8984/16/42/016
2. Stradner A, Sedgwick H, Cardinaux F, Poon WCK, Egelhaaf SU, and Schurtenberger P. Equilibrium cluster formation in concentrated protein solutions and colloids. *Nature* (2004) 432:492–495. doi:10.1038/nature03109
3. Sciortino F, Mossa S, Zaccarelli E, and Tartaglia P. Equilibrium cluster phases and low-density arrested disordered states: the role of short-range attraction and long-range repulsion. *Phys Rev Lett* (2004) 93(5):055701. doi:10.1103/PhysRevLett.93.055701
4. Campbell AI, Anderson VJ, van Duijneveldt JS, and Bartlett P. Dynamical arrest in attractive colloids: the effect of long-range repulsion. *Phys Rev Lett* (2005) 94(20):208301. doi:10.1103/PhysRevLett.94.208301
5. Cardinaux F, Stradner A, Schurtenberger P, Sciortino F, and Zaccarelli E. Modeling equilibrium clusters in lysozyme solutions. *Europhys Lett* (2007) 77:48004. doi:10.1209/0295-5075/77/48004
6. Toledano JCF, Sciortino F, and Zaccarelli E. Colloidal systems with competing interactions: from an arrested repulsive cluster phase to a gel. *Soft Matter* (2009) 5:2390–8. doi:10.1039/B818169A

7. Zhang TH, Klok J, Hans Tromp R, Groenewold J, and Kegel WK. Non-equilibrium cluster states in colloids with competing interactions. *Soft Matter* (2012) 8:667–72. doi:10.1039/C1SM06570J
8. Valadez-Pérez NE, Castañeda Priego R, and Liu Y. Percolation in colloidal systems with competing interactions: the role of long-range repulsion. *RSC Adv* (2013) 3:25110–9. doi:10.1039/C3RA44588G
9. Godfrin PD, Castañeda Priego R, Liu Y, and Wagner NJ. Intermediate range order and structure in colloidal dispersions with competing interactions. *J Chem Phys* (2013) 139:154904. doi:10.1063/1.4824487
10. Godfrin PD, Valadez-Pérez NE, Castañeda Priego R, Wagner NJ, and Liu Y. Generalized phase behavior of cluster formation in colloidal dispersions with competing interactions. *Soft Matter* (2014) 10:5061–71. doi:10.1039/C3SM53220H
11. Mani E, Lechner W, Kegel WK, and Bolhuis PG. Equilibrium and non-equilibrium cluster phases in colloids with competing interactions. *Soft Matter* (2014) 10:4479–86. doi:10.1039/C3SM53058B
12. Sweatman MB, Fartaria R, and Lue L. Cluster formation in fluids with competing short-range and long-range interactions. *J Chem Phys* (2014) 140:124508. doi:10.1063/1.4869109
13. Jadrich RB, Bollinger JA, Johnston KP, and Truskett TM. Origin and detection of microstructural clustering in fluids with spatial-range competitive interactions. *Phys Rev E* (2015) 91:042312. doi:10.1103/PhysRevE.91.042312
14. Santos AP, Pękalski J, and Panagiotopoulos AZ. Thermodynamic signatures and cluster properties of self-assembly in systems with competing interactions. *Soft Matter* (2017) 13:8055–63. doi:10.1039/C7SM01721A
15. Riest J, Nägele G, Liu Y, Wagner NJ, and Godfrin PD. Short-time dynamics of lysozyme solutions with competing short-range attraction and long-range repulsion: experiment and theory. *J Chem Phys* (2018) 148:065101. doi:10.1063/1.5016517
16. Ruiz-Franco J, Camerin F, Gnan N, and Zaccarelli E. Tuning the rheological behavior of colloidal gels through competing interactions. *Phys Rev Mater* (2020) 4:045601. doi:10.1103/PhysRevMaterials.4.045601
17. Liu Y, and Xi Y. Colloidal systems with a short-range attraction and long-range repulsion: phase diagrams, structures, and dynamics. *Curr Opin Colloid Interf Sci* (2019) 39:123–36. doi:10.1016/j.cocis.2019.01.016
18. Archer AJ, and Wilding NB. Phase behavior of a fluid with competing attractive and repulsive interactions. *Phys Rev E* (2007) 76:031501. doi:10.1103/PhysRevE.76.031501
19. Zhuang Y, and Charbonneau P. Equilibrium phase behavior of the square-well linear microphase-forming model. *J Phys Chem B* (2016) 120:6178–88. doi:10.1021/acs.jpcb.6b02167
20. Shukla A, Mylonas E, Di Cola E, Finet S, Timmins P, and Narayanan T. Absence of equilibrium cluster phase in concentrated lysozyme solutions. *Pnas* (2008) 105:5075–80. doi:10.1073/pnas.0711928105
21. Godfrin PD, Hudson SD, Hong K, Porcar L, Falus P, and Wagner NJ . Short-time glassy dynamics in viscous protein solutions with competing interactions. *Phys Rev Lett* (2015) 115:228302. doi:10.1103/PhysRevLett.115.228302
22. Liu Y, Porcar L, Chen J, Chen WR, Falus P, and Faraone A . Lysozyme protein solution with an intermediate range order structure. *J Phys Chem B* 115 (2011) 7238–47. doi:10.1021/jp109333c
23. Baumketner A, and Cai W. Clusters of lysozyme in aqueous solutions. *Phys Rev E* (2018) 98:032419. doi:10.1103/PhysRevE.98.032419
24. Dijkstra M. Phase behavior of hard spheres with a short-range yukawa attraction. *Phys Rev E* (2002) 66:021402. doi:10.1103/PhysRevE.66.021402
25. Schöll-Paschinger E, Benavides AL, and Castañeda-Priego R. Vapor-liquid equilibrium and critical behavior of the square-well fluid of variable range: a theoretical study. *J Chem Phys* (2005) 123:234513. doi:10.1063/1.2137713
26. Largo J, Solana JR, Yuste SB, and Santos A. Pair correlation function of short-ranged square-well fluids. *J Chem Phys* (2005) 122:084510. doi:10.1063/1.1855312
27. Pagan DL, and Gunton JD. Phase behavior of short-range square-well model. *J Chem Phys* (2005) 122:184515. doi:10.1063/1.1890925
28. Espíndola-Heredia R, del Río F, and Malijevsky A. Optimized equation of the state of the square-well fluid of variable range based on a fourth-order free-energy expansion. *J Chem Phys* (2009) 130:024509. doi:10.1063/1.3054361
29. Valadez-Pérez NE, Benavides AL, Schöll-Paschinger E, and Castañeda Priego R. Phase behavior of colloids and proteins in aqueous suspensions: theory and computer simulations. *J Chem Phys* (2012) 137:084905. doi:10.1063/1.4747193
30. Orea P, Romero-Martínez A, Basurto E, Vargas CA, and Odriozola G. Corresponding states law for a generalized Lennard-Jones potential. *J Chem Phys* (2015) 143:024504. doi:10.1063/1.4926464
31. Noro MG, and Frenkel D. Extended corresponding-states behavior for particles with variable range attractions. *J Chem Phys* (2000) 113:2941–4. doi:10.1063/1.1288684
32. Heyes DM. Monte Carlo simulations of continuum percolation of 3d well fluids. *J Phys Condens Matter* (1990) 2:2241–9. doi:10.1088/0953-8984/2/9/013
33. Wei J, Xu L, and Song F. Range effect on percolation threshold and structural properties for short-range attractive spheres. *J Chem Phys* (2015) 142:034504. doi:10.1063/1.4906084
34. Hansen JP, and McDonald IR. *Static properties of liquids: thermodynamics and structure*. 4th ed. Oxford: Academic Press (2013). 61–104 p.
35. Stauffer D. Scaling theory of percolation clusters. *Phys Rep* (1979) 54:1–74. doi:10.1016/0370-1573(79)90060-7
36. Benavides AL, and Gil-Villegas A. The thermodynamics of molecules with discrete potentials. *Mol Phys* (1999) 97:1225–32. doi:10.1080/00268979909482924
37. Kowalczyk P, Ciach A, Gauden P, and Terzyk A. Equilibrium clusters in concentrated lysozyme protein solutions. *J Colloid Interf Sci* (2011) 363:579–84. doi:10.1016/j.jcis.2011.07.043
38. Valadez-Pérez NE, Liu Y, and Castañeda Priego R. Reversible aggregation and colloidal cluster morphology: the importance of the extended law of corresponding states. *Phys Rev Lett* (2018) 120:248004. doi:10.1103/PhysRevLett.120.248004
39. Sciortino F, Tartaglia P, and Zaccarelli E. One-dimensional cluster growth and branching gels in colloidal systems with short-range depletion attraction and screened electrostatic repulsion. *J Phys Chem B* (2005) 109:21942–53. doi:10.1021/jp052683g
40. Ruiz-Franco J, and Zaccarelli E. On the role of competing interactions in charged colloids with short-range attraction. *Annu Rev Condens Matter Phys* (2021) 12:51. doi:10.1146/annurev-conmatphys-061020-053046

Conflict of Interest: The authors declare that the research was conducted in the absence of any commercial or financial relationships that could be construed as a potential conflict of interest.

frontiers in Physics

REVIEW
published: 15 April 2021
doi: 10.3389/fphy.2021.641859

Random Fields in Physics, Biology and Data Science

Enrique Hernández-Lemus[1,2]*

[1]Computational Genomics Division, National Institute of Genomic Medicine, Arenal Tepepan, Mexico, [2]Centro de Ciencias de La Complejidad, Universidad Nacional Autónoma de México, Coyoacán, Mexico

A random field is the representation of the joint probability distribution for a set of random variables. Markov fields, in particular, have a long standing tradition as the theoretical foundation of many applications in statistical physics and probability. For strictly positive probability densities, a Markov random field is also a Gibbs field, i.e., a random field supplemented with a measure that implies the existence of a regular conditional distribution. Markov random fields have been used in statistical physics, dating back as far as the Ehrenfests. However, their measure theoretical foundations were developed much later by Dobruschin, Lanford and Ruelle, as well as by Hammersley and Clifford. Aside from its enormous theoretical relevance, due to its generality and simplicity, Markov random fields have been used in a broad range of applications in equilibrium and non-equilibrium statistical physics, in non-linear dynamics and ergodic theory. Also in computational molecular biology, ecology, structural biology, computer vision, control theory, complex networks and data science, to name but a few. Often these applications have been inspired by the original statistical physics approaches. Here, we will briefly present a modern introduction to the theory of random fields, later we will explore and discuss some of the recent applications of random fields in physics, biology and data science. Our aim is to highlight the relevance of this powerful theoretical aspect of statistical physics and its relation to the broad success of its many interdisciplinary applications.

Keywords: random fields, probabilistic graphical models, Gibbs fields, Markov fields, Gaussian random fields

OPEN ACCESS

Edited by:
Umberto Lucia,
Politecnico di Torino, Italy

Reviewed by:
Farrukh Mukhamedov,
United Arab Emirates University,
United Arab Emirates
Luca Martino,
Rey Juan Carlos University, Spain

***Correspondence:**
Enrique Hernández-Lemus
ehernandez@inmegen.gob.mx

Specialty section:
This article was submitted to Interdisciplinary Physics, a section of the journal Frontiers in Physics

Received: *15 December 2020*
Accepted: *01 February 2021*
Published: *15 April 2021*

Citation:
Hernández-Lemus E (2021) Random Fields in Physics, Biology and Data Science. Front. Phys. 9:641859. doi: 10.3389/fphy.2021.641859

1 INTRODUCTION

The theory and applications of random fields born out of the fortunate marriage of two simple but deep lines of reasoning. On the one hand, physical intuition, strongly founded in the works of Boltzmann and the Ehrenfests, but also in other originators of the kinetic theory of matter, was that large scale, long range phenomena may originate from (a multitude of) local interactions. On the other hand, probabilistic reasoning induced us to think that such multitude of local interactions would be stochastic in nature. These two ideas, paramount to statistical mechanics, have been extensively explored and develop into a full theoretical subdiscipline, the theory of random fields. Perhaps the archetypal instance of a random field was laid out in the doctoral thesis of Ernst Ising, the Ising model of ferromagnetism [1]. However, although the physical ideas have been laid out mainly by physicists, much of the further mathematical development was made by the Russian school of probability. In particular, by the works of Averintsev [2, 3], which–along with the measure theoretical-inspired formalization of statistical mechanics by J.W. Gibbs–, was able to specify a general class of fields described only by pair potentials [4]. Theoretical advances were given by Stavskaya who studied random fields by measure theory considering them as invariant states for local

processes [5, 6], by Vasilyev who consider stationary measures as derived from local interactions in discrete mappings [7] and others.

The formal establishment of the theory of Markov-Gibbs random fields, however, is often attributed to the works of Dobruschin, Lanford and Ruelle [8, 9], in particular to their DLR equations for the probability measures. Also remarkable is the contribution of Hammersley and Clifford, who developed a proof of the equivalence of Gibbs random fields and Markov random fields, provided positive definite probabilities [10]. Although the authors never officially published this work, that they thought to be incomplete given the–now known to be essential–requirement of positive definite probabilities, several published works have been made on top of it and even alternative proofs have been published [11–13].

Aside from the extensive use of the Ising model and other random fields in statistical mechanics–too many contributions to mention here, but most of them comprehensively reviewed in the monographs by Baxter [14], Cipra [15], McCoy and Wu [16], Thompson [17] and in the simulation-oriented book by Adler [18]–; there has been also a deep interest in development in models in biophysics, computer science and other fields. The development of Hopfield networks as models of addressable memory in neurophysiology (and artificial neural networks) [19] is perhaps one of the earliest examples. Followed by the implementation if the so-called Boltzmann machines in artificial intelligence (AI) applications [20, 21] paved the way to a plethora of theoretical, computational and representational applications of random fields.

In the rest of this review paper, we will present some general grounds of the theory of Markov random fields to serve as a framework to elaborate on many of its relevant applications inside and outside physics. Our emphasis here will not be to be comprehensive but illustrative of some relevant features that have made this quintessential model of statistical physics so pervasive in our discipline and in many others (*Markov Random Fields: A Theoretical Framework*). We will also discuss how methodological and computational advances in these areas may be implemented to improve on the applications of random fields in physical models. We have chosen to focus on applications in Physics (*Markov Random Fields in Physics*), Biology (*Markov Random Fields in Biology*) and Data Science (*Markov Random Fields in Data Science and Machine Learning*). We are aware that by necessity (finiteness), we are leaving out contributions in fields such as sociology (Axelrod models, for instance), finance (volatility maps, Markov switching models, etc.) and others. However, we believe this panoramic view will make easier for the interested reader to look into these other applications. Finally, in *Concluding Remarks* we will outline some brief concluding remarks.

2 MARKOV RANDOM FIELDS: A THEORETICAL FRAMEWORK

Here we will define and describe Markov random fields [8, 12] (MRFs) as an appropriate theoretical framework useful for systematic probabilistic analysis in various settings. An MRF represents, in this context, the joint probability distribution for a set (as large as desired) of real-valued random variables. There are several extensions of the general ideas presented here, that will be presented and briefly addressed as needed.

Let $X = X_\alpha$ be a vector of random variables (i.e., the features or characteristic functions used to describe a system of interest). An MRF may be represented as an undirected graph depicting the statistical dependency structure of X, as given by the joint probability distribution $\mathbb{P}(X)$ [22].

Let this graph be embodied in the form of a duplex $G = (V, E)$ consisting of a set V of vertices or nodes (the random variables X_i's) and a set $E \subseteq V \times V$ of edges connecting the nodes (thus representing the statistical dependencies between random variables). E also represents a neighborhood law N stating which vertex is connected (i.e., dependent) to which other vertex in the graph. With this in mind, an MRF can be also represented as $G = (V, N)$. The set of neighbors of a given point X_i is denoted N_{X_i}.

2.1 Configuration

We can assign each point in the graph, one of a finite set S of labels. Such assignment, it is often called a *configuration*. We can then assign probability measures to the set Ω of all possible configurations ω. Hence, ω_A represents the configuration ω restricted to the subset A of V. We may think of ω_A as a configuration on the subgraph G_A restricting V to points of A.

2.2 Local Characteristics

We can define *local characteristics* on MRFs. The local characteristics of a probability measure $\mathbb{P}$ defined on Ω are the conditional probabilities:

$$\mathbb{P}(\omega_t \mid \omega_{T\setminus t}) = \mathbb{P}(\omega_t \mid \omega_{N_t}) \tag{1}$$

This represents the probability that the point t is assigned the value ω_t, given the values at all other points of the graph. Let us re-write **Eq. 1**. Since the probability measure will define an MRF if the local characteristics depend only on the outcomes at neighboring points, i.e., if for every ω

$$\mathbb{P}(\omega_{X_i} \mid \omega_{G\setminus X_i}) = \mathbb{P}(\omega_{X_i} \mid \omega_{N_{X_i}}) \tag{2}$$

2.3 Cliques

Given an arbitrary graph, we may refer to a set of points C, as a *clique*, if every pair of points in C are neighbors. This includes the empty set as a clique. A clique is then a set whose *induced subgraph* is complete. Cliques are also called *complete induced subgraphs* or *maximal subgraphs*.

2.4 Configuration Potentials

A *potential* η is an assignment of a number $\eta_A(\omega)$ to every subconfiguration ω_A of a configuration ω in the graph G. A given η, induces an *energy* $U(\omega)$ on the set of all configurations ω as follows:

$$U(\omega) = \sum_A \eta_A(\omega) \tag{3}$$

Here, for fixed ω, the sum is taken over all subsets $A \subseteq V$ including the empty set. It is possible to define a probability measure, called the *Gibbs measure induced* by U as

$$\mathbb{P}(\omega) = \frac{e^{-U(\omega)}}{Z} \tag{4}$$

Z (taken from the German word *zustanssumme* or *sum over states*) is a normalization constant called the *partition function*. As it is known, explicit computation of the partition function is in many cases a very challenging endeavor. There is a great deal of work in the development of methods and approaches to overcome some (but not all) challenges in this regard. Some of these approximations will be discussed later on.

$$Z = \sum_{\omega} e^{-U(\omega)} \tag{5}$$

The term *potential* is often used in connection with potential energies. In this context η_A is commonly termed a *potential energy* in physics applications. $\phi_A = e^{-\eta_A}$ is then called a potential.

Equations 4, **5** can be thus rewritten as:

$$\mathbb{P}(\omega) = \frac{\prod_A \phi_A(\omega)}{Z} \tag{6}$$

$$Z = \sum_{\omega} \prod_A \phi_A(\omega) \tag{7}$$

Since this latter use is more common in probability and graph theory, and it is also used in theoretical physics, we will refer to **Eqs. 6**, **7** as the definitions of Gibbs measure and partition function (respectively) unless otherwise stated. This will also be justified given that **Eq. 6** is a form of probability factorization (in this case a *clique factorization*) [11].

2.5 Gibbs Fields

A potential is termed a nearest neighbor Gibbs potential if $\phi_A(\omega) = 1$ whenever A is not a clique. We often call a *Gibbs measure* to any regular measure induced by a nearest neighbor Gibbs potential. However, we may define more general Gibbs measures by considering different classes of potentials.

The inclusion of all cliques in the calculation of the Gibbs measure is needed to establish the equivalence between Gibbs random fields and Markov random fields. A nearest neighbor Gibbs measure on a graph determines an MRF as follows [22]:

Let $\mathbb{P}(\omega)$ be a probability measure determined on Ω by a nearest neighbor Gibbs potential ϕ:

$$\mathbb{P}(\omega) = \frac{\prod_C \phi_C(\omega)}{Z} \tag{8}$$

With the product taken over all cliques C on the graph G. Then,

$$\mathbb{P}\left(\omega_{X_i} \middle| \omega_{G \setminus X_i}\right) = \frac{\mathbb{P}(\omega)}{\sum_{\omega_r} \mathbb{P}(\omega')} \tag{9}$$

Here ω' is any configuration which agrees with ω at all points except X_i.

$$\mathbb{P}\left(\omega_{X_i} \middle| \omega_{G \setminus X_i}\right) = \frac{\prod_C \phi_C(\omega)}{\sum_{\omega_r} \prod_C \phi_C(\omega')} \tag{10}$$

For any clique C that does not contain X_i, $\phi_C(\omega) = \phi_C(\omega')$, So that all the terms that correspond to the cliques that do not contain the point X_i cancel both from the numerator and the denominator in **Eq. 10**, therefore this probability depends only on the values x_i at X_i and its neighbors. $\mathbb{P}$ defines thus an MRF. A more general proof of this equivalence was given by Hammersley-Clifford theorem (see for instance [11]).

In essence, we can state that among the general class of random fields, Markov random fields are defined by obeying the Markov neighborhood law. Gibbs fields are usually understood as Markov fields with strictly positive probability measures (in particular, a strictly positive joint probability density). These Markov-Gibbs fields are thus defined by the Markov property and the positive definite probabilities and are the ones that follow the Hammersley-Clifford theorem. More general Gibbs fields can be defined by other neighborhood laws than the Markov property [23], but these will not be addressed in the present work.

2.6 Conditional Independence in Markov Random Fields

To discuss the conditional independence structure induced by MRFs, let us consider the following: An adjacency matrix A_{ij} represents the neighborhood law (as given by the Markov property) on the graph G. Every non-zero entry in this matrix represents a statistical dependency relation between two elements on X. The conditional dependence structure on MRFs is related not only to the *local* statistical independence conditions, but also to the dependency structure of the whole graph [11, 24].

A definition of conditional independence (CI) for the set of random variables can be given as follows:

$$\begin{aligned} \left(X_i \perp\!\!\!\perp X_j\right) \middle| X_l &\Leftrightarrow \mathbb{F}_{X_i, X_j | X_l = X_l^*}\left(X_i^*, \mathrm{X_j}^*\right) \\ &= \mathbb{F}_{X_i | X_l = X_l^*}(X_i^*) \cdot \mathbb{F}_{X_j | X_l = X_l^*}\left(X_j^*\right) \\ &\forall X_i, X_j, X_l \in X \end{aligned} \tag{11}$$

Here $\perp\!\!\!\perp$ refers to conditional independence between two random variables. $\mathbb{F}_{X_i, X_j | X_l = X_l^*}(X_i^*, \mathrm{X_j}^*) = Pr\left(X_i \leq X_i^*, \mathrm{X_j} \leq \mathrm{X_j}^* \middle| \mathrm{X_l} = \mathrm{X_l}^*\right)$ is the joint conditional cumulative distribution of X_i and X_j given X_l. X_i^*, X_j^* and X_l^* are realizations of the corresponding random variables.

In the case of MRFs, CI is defined by means of graph separation: Hence $X_i \perp\!\!\!\perp_G X_j \middle| X_l$ iff X_l separates X_i from X_j in G. This means that if we remove node X_l there are no undirected paths from X_i to X_j in G.

Conditional independence in random fields can be considered in terms of subsets of V. Let A, B and C be subsets of V. The statement $X_A \perp\!\!\!\perp_G X_B \middle| X_C$, which holds only iff C separates A from B in G, means that if we remove all vertices in C there will be no paths connecting any vertex in A to any vertex in B. This is customarily called the *global Markov property* of TMFs [11, 24].

The smallest set of vertices that renders a vertex X_i conditionally independent of all other vertices in the graph is called its *Markov blanket*, denoted $mb(X_i)$. If we define the *closure* of a node X_i as $\mathcal{C}(X_i)$ then $X_i \perp\!\!\!\perp G \backslash \mathcal{C}(X_i) | mb(X_i)$.

In an MRF, the Markov blanket of a vertex is its set of first neighbors. This statement is the so-called *undirected local Markov property*. Starting from the local Markov property, it is possible to show that two vertices X_i and X_j are conditionally independent given the rest if there is no direct edge between them. This is the *pairwise Markov property*.

If we denote by $G_{X_i \to X_j}$ the set of undirected paths in the graph G connecting vertices X_i and X_j, then the pairwise Markov property of an MRF is given by:

$$X_i \perp\!\!\!\perp X_j \left| G \backslash \left\{ X_i, X_j \right\} \right. \Leftrightarrow G_{X_i \to X_j} = \varnothing \tag{12}$$

Hence the global Markov property implies the local Markov property which, in turn, implies the pairwise Markov property. For systems with positive definite probability densities, it has been proved that pairwise Markov actually implied global Markov (See [11] p. 119 for a proof). This is important for applications since it is easier to assess pairwise conditional independence statements.

2.6.1 Indepence Maps

Let I_G denote the set of all conditional independence relations encoded by the graph G (i.e., those CI relations given by the Global Markov property). Let $I_{\mathbb{P}}$ be the set of all CI relations implied by the probability distribution $\mathbb{P}(X_i)$. A graph G will be called an *independence map* (*I-map*) for a probability distribution $\mathbb{P}(X_i)$, if all CI relations implied by G hold for $\mathbb{P}(X_i)$, i.e., $I_G \subseteq I_{\mathbb{P}}$ [11].

The converse statement is however not necessarily true, i.e., there may be some CI relations implied by $\mathbb{P}(X_i)$ that are not coded in the graph G. We may often be interested in the so-called *minimal I-maps*, i.e., I-maps from which none of the edges could be removed without destroying its CI properties.

Every distribution has a unique minimal I-map (and a given graph representation). Let $\mathbb{P}(X_i) > 0$. Let $G^{\dagger}$ be the graph obtained by introducing edges between all pairs of vertices X_i, X_j such that $X_i \perp\!\!\!\perp X_j \left| X \backslash \{X_i, X_j\} \right.$, then $G^{\dagger}$ is the unique minimal I-map. We call G a *perfect map* of $\mathbb{P}$ when there are no dependencies G which are not indicated by $\mathbb{P}$, i.e., $I_G = I_{\mathbb{P}}$ [11].

2.6.2 Conditional Independence Tests

Conditional independence tests are useful to evaluate whether CI conditions apply either exactly or in the case of applications under a certain bounded error [24]. In order to be able to write down expressions for C.I. tests let us introduce the following *conditional kernels* [25]:

$$\mathbb{C}_A(B) = \mathbb{P}(B|A) = \frac{\mathbb{P}(AB)}{\mathbb{P}(A)} \tag{13}$$

As well as their generalized recursive relations:

$$\mathbb{C}_{ABC}(D) = \mathbb{C}_{AB}(D|C) = \frac{\mathbb{C}_{AB}(CD)}{\mathbb{C}_{AB}(C)} \tag{14}$$

The conditional probability of X_i given X_j can be thus written as:

$$\mathbb{C}_{X_j}(X_i) = \mathbb{P}\left(X_i \middle| X_j\right) = \frac{\mathbb{P}\left(X_i, X_j\right)}{\mathbb{P}\left(X_j\right)} \tag{15}$$

We can then write down expressions for Markov conditional independence as follows:

$$X_i \perp\!\!\!\perp X_j \left| X_l \Rightarrow \mathbb{P}\left(X_i, X_j \middle| X_l\right) = \mathbb{P}(X_i|X_l) \times \mathbb{P}\left(X_j \middle| X_l\right) \right. \tag{16}$$

Following Bayes' theorem, CI conditions–in this case–will be of the form:

$$\mathbb{P}\left(X_i, X_j \middle| X_l\right) = \frac{\mathbb{P}(X_i, X_l)}{\mathbb{P}(X_l)} \times \frac{\mathbb{P}\left(X_j, X_l\right)}{\mathbb{P}(X_l)} = \frac{\mathbb{P}(X_i, X_l) \times \mathbb{P}\left(X_j, X_l\right)}{\mathbb{P}(X_l)^2} \tag{17}$$

Equation 17 is useful since in large scale data applications is computationally cheaper to work with joint and marginal probabilities rather than conditionals.

Now let us consider the case of conditional independence given several conditional variables. The case for CI given two variables could be written–using conditional kernels–as follows:

$$X_i \perp\!\!\!\perp X_j \left| X_l, X_n \Rightarrow \mathbb{P}\left(X_i, X_j \middle| X_l, X_n\right) = \mathbb{P}(X_i|X_l, X_n) \times \mathbb{P}\left(X_j \middle| X_l, X_n\right) \right. \tag{18}$$

Hence,

$$\mathbb{P}\left(X_i, X_j \middle| X_l, X_n\right) = \mathbb{C}_{X_l, X_n}(X_i) \times \mathbb{C}_{X_l, X_n}\left(X_j\right) \tag{19}$$

Using Bayes' theorem,

$$\mathbb{P}\left(X_i, X_j \middle| X_l, X_n\right) = \frac{\mathbb{P}(X_i, X_l, X_n)}{\mathbb{P}(X_l, X_n)} \times \frac{\mathbb{P}\left(X_j, X_l, X_n\right)}{\mathbb{P}(X_l, X_n)} \tag{20}$$

Or

$$\mathbb{P}\left(X_i, X_j \middle| X_l, X_n\right) = \frac{\mathbb{P}(X_i, X_l, X_n) \times \mathbb{P}\left(X_j, X_l, X_n\right)}{\mathbb{P}(X_l, X_n)^2} \tag{21}$$

In order to generalize the previous results to CI relations given an arbitrary set of conditionals, let us consider the following *sigma-algebraic* approach:

Let Σ_{ij} be the σ-algebra of all subsets of X that do not contain X_i or X_j. A relevant problem for network reconstruction is that of establishing the more general Markov pairwise CI conditions, i.e., the CI relations for every edge not drawn on the graph. Two arbitrary nodes X_i and X_j are conditionally independent given the rest of the graph iff:

$$X_i \perp\!\!\!\perp X_j \left| \Sigma_{ij} \Rightarrow \mathbb{P}\left(X_i, X_j \middle| \Sigma_{ij}\right) = \mathbb{P}\left(X_i \middle| \Sigma_{ij}\right) \times \mathbb{P}\left(X_j \middle| \Sigma_{ij}\right) \right. \tag{22}$$

By using conditional kernels, the recursive relations and Bayes' theorem it is possible to write down:

$$\mathbb{P}\left(X_i, X_j \middle| \Sigma_{ij}\right) = \frac{\mathbb{P}\left(X_i, \Sigma_{ij}\right) \times \mathbb{P}\left(X_j, \Sigma_{ij}\right)}{\mathbb{P}\left(\Sigma_{ij}\right)^2} \tag{23}$$

The family of **Eq. 23** represent the CI relations for all the non-existing edges in the graph G, i.e., every pair of nodes X_i and X_j not-connected in G must be conditionally independent given the rest of the nodes in the graph. This is perhaps the most important features of MRFs in connection with potential applications as probabilistic graphical models. CI conditions often lead to simpler (or at least computationally tractable) ways to factorize the PDF or compute the partition function.

The algorithmic complexity of doing so *in general* (since the number of CI relations grows combinatorially with the size of the graph), makes it prohibitive in the case of a large number of variables/relationships, in spite of recent advances on optimizing large dimensional space CI testing for discrete distributions [26]. This is the biggest advantage of the present approach. As long as one deals with strictly positive probabilities (that one can often attain *via* regularization) and Hammersley-Clifford conditions apply, modeling with nearest neighbor Gibbs potentials ensure CI conditions in the graph (recall that global Markov property implies pairwise Markov property and vice versa).

Now that we have presented the fundamentals of MRFs at an introductory level, this may allow to discuss on how these features have impact on their wide range of applications, as the basis for probabilistic graphical models. Let us start by considering some recent applications in physics.

3 MARKOV RANDOM FIELDS IN PHYSICS

From the pioneering work of the Ehrenfests, to the foundational Izing models and its extensions (Potts, XY, etc.), MRFs have been thoroughly used and developed in many subdisciplines of physics, ranging from condensed matter and mathematical physics to geophysics, econophysics and more. There are numerous in-depth reviews and monographs summarizing research along these lines (see, for instance [27–30]). Since the main goal here is to present some of the characteristic features of the usefulness of MRFs as probabilistic graphical models, in terms of their mathematical properties and broad scope of applicability, both within and outside physics; our discussion will be somehow biased toward work showing one or more of such features.

3.1 MRFs in Statistical Mechanics and Mathematical Physics

Due to their intrinsic simplicity and generality, MRFs have attracted the attention of mathematical physicists and probability theorists looking to extend their associated theoretical foundations. Important work has been done, for instance, to incorporate geometrical properties and generalized embeddings to the theory of random fields. Extremely relevant in this regard is the monumental work presented in the monograph by Adler and Taylor [31]. There, the authors expand on the consideration of a random field as a stochastic process in a metric space (discrete, Euclidean, etc.) to consider random fields as stochastic mappings over manifolds. This extension is given *via* writing down differential geometry characterizations of the fields based on a measure-theoretic definition of probability. Though this work may seem quite abstract, it was indeed born out of an idea for an application of random fields to neuroscience. Nurturing from similar ideas, recent work by Ganchev [32] has expanded the notion of locality of MRFs and assimilate it to the geometric features present in lattice quantum gauge theories, to generate a *gauge theory of Markov-Gibbs fields*. Again, even if the setting seems to be quite theoretical, an application to the modeling of trading networks in finance is given.

Other mathematical extensions of Markov random fields are related to the nature of the graphical model considered. In general, probabilistic graphical models may belong to one of two quite general classes: Markov networks (such as MRFs) which are *undirected* graphs or Bayesian networks which are *directed* graphs. The difference between undirected and directed graphical models impose consequences in the kind of fundamental mathematical objects of the theory: joint probabilities or conditional probabilities, loopy graphs or trees–directed acyclic graphs–, clique factorization vs. conditional probability factorization *via* the chain rule, etc. Whether the model is undirected or directed also has modeling and computational consequences. To be fair, both models have pros and cons.

Trying to overcome the limitations of both general approaches, Freno and Trentin [33] developed a more general approach to random fields termed *Hybrid random fields* (HRFs). The purpose of HRFs is to allow the systems to present a wider variety of conditional independence structures. As we will discuss later, allowing for a systematic incorporation of more general classes of conditional independence structures in indeed one of the current *hot topics* in computational intelligence and machine learning. Actually, even when HRFs are theoretical constructs (much alike MRFs) they were designed to be *learning machines*, i.e., to be supplemented with training algorithms to deal with high dimensional data. HRFs were developed for logical inference in the presence of partial information or noise. As in the case of MRFs and of their gauge extensions just mentioned, HRFs were developed to rely on a *principle of locality* which is an extension of the Markov property that allows for sparse stochastic matrix representations amenable for the computation on actual applications. Once a (graph) structure has been given (or inferred) HRFs are able (as is the case of MRFs) to learn the local (conditional or joint-partial) probability distributions from empirical data, a task commonly known in statistics as *parameter learning* [34]. Hence HRFs are theoretically founded, but developed thinking in applications. The scope of applicability of MRFs has also become broader by expanding its applicability to model tensor valued quantities [35], giving rise to the so-called multilayer graphical models, also called multilayer networks [36–39].

Aside from expanding the fundamental structure of MRFs, mathematical physics applications of Gibbs random fields are abundant. In particular, the so-called Random Field Ising model (RFIM) has gained a lot of attention in the recent years. By using the monotonicity properties of the associated stochastic field, Aizenmann and Peled [40] were able to prove that there is a power law upper bound on the correlations on a two-dimensional Ising model, supplemented with a quenched random magnetic

field. The fact that by combining random fields (the intrinsic Ising field and the quenched magnetic field), the nature of the phase transitions may drastically change has made the RFIM a current topic of discussion in mathematical statistical mechanics. The consequences of the induction of long range order in the RFIM, leading to the emergence of the so-called Imry-Ma phase or Imry-Ma states (named so since Imry and Ma were actually behind the first proposal of the RFIM [41]) have been the object of intense study recently. Berzin and co-workers [42] used MRFs to analyze the dynamic fluctuations of the order parameter in the Imry-Ma RFIM and its coupling with the static fluctuations of the structural random field (accounting for the defects). Interestingly, anisotropic coupling arises from two non-absolutely overlapping local fields [43]. The effects of the non-overlapping fields in anisotropy and disorder has been studied since several decades ago [44], but the actual relationship with non-locality was established relatively recently. For instance, it was until 2018 that Chatterjee was able to quantitatively describe the decay of correlations of the 2D RFIM [45] in a relevant paper that led Aizenmann to re-analyze his former, mostly qualitative proposal [40, 46].

Local stochastic phenomena in non-homogeneous and disordered media in the context of the RFIM has also attracted attention in relation to critical exponents and scaling. Trying to expand on the origins of long range order from local interactions, Fytas and coworkers have studied the 4D RFIM and its hyperscaling coefficients [47]. This is particularly interesting since it has been shown, *via* perturbative renormalization group calculations, that the critical exponents of the RFIM in D dimensions are the same as the exponents of the pure Ising model in $D-2$ dimensions [48]. Related work has been carried out by Tarjus and Tissier, but they instead resort to the use of the so-called *functional renormalization group* approach in the multi-copy formalism setting [49]. Their work has extended the predictive capabilities of MRFs by incorporating ideas from symmetry breaking allowing to characterize not just long-range order (LRO) but also intermediate states characterized by quasi-long range order (QLRO). The fact that QLRO may be attained from purely Markov statistics (localized interactions) is in itself appealing for statistical physics. The fact that local dependencies may suffice to account for LRO and QLRO under certain conditions that do not violate the Markov property of the MRFs, will have relevant consequences for the applications of MRFs outside physics, such as in the case of image reconstruction and pattern recognition in machine learning. We will come back to these ideas later on.

Locality as depicted in MRFs can also have important consequences for the theory of fluctuations in fields of interacting particles. Reconstructing Boltzmann statistics from local Gibbs fields (that as we have repeatedly stated are formally equivalent to MRFs, provided strictly positive probability measures) imply that under central limit scales the fluctuation field of local functions can be represented instead as a function of the density fluctuation field, in what is known as the Boltzmann-Gibbs principle (BGP). It has been shown that the BGP induces a duality whose origins are purely probabilistic, i.e., is independent of the nature of the interactions provided their compliance with the tenets of MRFs [50].

It is worth noticing that these contemporary developments in the formal theory of MRFs are actually founded on seminal work by probability theorists and mathematical physicists such as Dobrushin, Ruelle, Gudder, Kessler and others. For instance, Dobrushin laid out the essential conditions of regularity that allow to make explicit the conditional probabilities in MRF models [8]. This work, further developed by Lanford and Ruelle [9] gives rise to the so called Dobrushin-Lanford-Ruelle (DLR) equations that established, in a formal way, the properties of general Gibbs measures. Later on, Dobrushin expanded on these ideas by applying perturbation methods to generalize Gibbs measures to even wider classes of interactions (i.e., to include other families of potentials) [51]. An application of these ideas in quantum field theory can be found in [52] within the context of (truncated) generalized Gibbs ensembles.

Aside from measure-theoretical and algebraic foundations of MRFs, important developments were made by considering explicit dependency structures. In particular, the introduction of strong independence properties led to the formal definition of Gaussian random fields by Gudder [53]. Much of this earlier work has been summarized in the monograph by Kindermann and Laurie Snell [22]. The fact that MRFs are characterized by Gibbs measures even for many-body interactions (under special conditions), and not only for paired-potentials, was already envisioned by Sherman [54], though it remained an unfinished task for decades. Many body effects have actually been reported in the context of localization in the random field Heisenberg chain [55]. One step ahead toward generalizing MRFs consisted in exploring the equivalence of some properties of random fields in terms of *sample functions*. In this regard, Starodubov [56] proved that there are random fields stochastically equivalent to an MRF, but defined on another probability triple whose sample functions belong to a map associated with the original MRF. The existence of such mappings has relevant implications for applications, in particular in cases in which explicit computation of the partition function is intractable.

3.2 MRFs in Condensed Matter Physics and Materials Science

Discrete and continuous versions of random fields have been applied to model systems in condensed matter physics and materials science (CMP/MS). The relevance of MRFs and its extensions relies on their suitability to describe the onset of spatio-temporal phenomena from localized interactions. Acar and Sundararaghavan [57] have used MRFs to model the spatio-temporal evolution of microstructures, such as grain growth in polychrystalline microstructures as captured by videomicroscopy experiments. Experimental data is the foundation for explicit calculations of the (empirical) conditional probability distributions.

Gaussian random fields have been used to model quenched random potentials in fluids *via* mode-coupling by Konincks and Krakoviack [58], and to model beta-distributed material properties by Liu and coworkers [59]. These and other extensions in CMP/MS made use of continuous, piecewise continuous or lattice fluid extensions of Gibbs random fields.

Such is also the case of the work of Chen and coworkers [60] who introduced stochastic harmonic potentials in random fields to account for the effects of local interactions on the properties of structured materials; of the work by Singh and Adhilari [61] on Brownian motion in confined active colloids and of the work of Yamazaki [62] on stochastic Hall magnetohydrodynamics. A semi-continuous approach (called smoothed particle hydrodynamics, SPH), using discrete MRFs and extension theorems, was used by Ullah and collaborators [63] in their density dependent *hydrodynamic* model for crowd coherency detection in active matter.

Extending the ideas of the classic RFIM, Tadic and collaborators [64] were able to describe critical Barkhausen avalanches in quasi-2D ferromagnets with an open boundary. The use of MRFs with disordered field components has also allowed to characterize embedded inhomogeneities in the spectral properties of Rayleigh waves with application to the study of the Earth's microseismic field [65]. Geoacustic measurements and its MRF modeling allowed these researchers to estimate the mechanical and structural properties of the Earth's crust and upper mantle. Accurate estimates of these properties are foundational to develop seismic-resistant devices and structures.

3.3 Applications of MRFs in Other Areas of Physics

MRFs have also been applied in other areas of physics aside from statistical mechanics and condensed matter. MRFs were applied for instance, in geophysical models of marine climate patterns [66], to study reservoir lithology [67] and subsurface soil patterns [68] from remote sensing data. Aside from geophysics, optics and acoustics have also incorporated MRF applications. In acoustics, for instance, an MRF formalism can be used for the isolation of selected signals [69]; or for the segmentation of sonar pulses [70]. In chemical physics, MRFs are applied for the analysis of molecular structures [71], and in the implementation of quantum information algorithms for molecular physics modeling [72].

Disparate as the applications of MRF in the physical sciences just presented may be, these are neither a comprehensive nor even a representative list. However, we expect that some of the essential aspects of its wide range of applicability and the large room for theoretical development still available for these types of models were captured in the previous discussion. Moving on to applications and developments in other disciplines, such as Biology/Biomedicine and the Data Sciences, we will try to convey, not just the usefulness of a quintessential model in statistical physics in other realms–which is huge, indeed–. We also intend to show how some of the implementations and theoretical improvements in other disciplines, can be exported back to physics and may help to solve some of the many remaining conundrums of the theory and applications of random fields in the physical sciences.

4 MARKOV RANDOM FIELDS IN BIOLOGY

Biology and Biomedicine are also disciplines in which MRFs have flourished in applications and theoretical development. The abundance of research problems and practical cases in which stochastic phenomena dependent in spatio-temporal localization is most surely behind. From the reconstruction of complex imaging patterns (not far from applications in geophysics/astrophysics imaging), to resolution of molecular maps in structural biology, to disentangling molecular interaction networks and ecological interactions; there are many outstanding advances involving random fields in biology. Again, we will discuss here just a few examples that will likely provide us with a panoramic view and perhaps spark interest and curiosity.

4.1 Applications of MRFs in Biomedical Imaging

One somehow natural application of MRFs is imaging de-noizing or *segmentation*. This is a quite general problem in which one wishes to discern patterns from a *blurred* image. In particular an MRF is built to discern which points in imaging space (pixels, voxels) are locally correlated with each other, pointing out to their *membership* to the same object in the image. The Markov neighborhood structure of the MRF is hence used to *un-blur* patterns and being able to accurately interpret the images. Often MRFs (or its associated conditional Random fields) are used in conjunction with inference machines such as Convolutional Neural Networks (CNNs). This is the case of the work by Li and Ping [73] who used a neural conditional random field (NCRF) for metastasis detection from lymph node slide images. Their NCRF approach infers the spatial correlations among neighboring patches *via* a fully connected conditional MRF incorporated on top of a CNN feature extractor. Their modeling approach used a conditional distribution of an MRF with a Gibbs distribution. As is often the case the *energy function* (i.e., the *Hamiltonian*) consists of two terms, one summarizing the contributions from unary potentials characteristic for each patch, and the other one summing the pairwise potentials measuring the *cost* of jointly assigning two neighboring patches (i.e., the *interaction* potentials).

As is common in physics, estimating the marginals is an intractable problem. Li and Ping resorted to using a *mean-field* approach and then conditioning their results on this mean field calculations. In order to do this, they trained a CNN with the empirical data. CNN-MRF approaches have also been recently applied to successfully discern computerized tomography imaging (CT scans) [74] for prostate and other pelvic organs at risk. After processing the data with an encoder/decoder scheme, the output of CNN was used as the unary potential of the MRF. Then *via* a MRF block model based on local convolution layers, a global convolution layer, and a 3D max-pooling layer the authors were able to calculate the pairwise potential. The maximum likelihood optimization problem was then solved *via* an adaptive loss function.

A similar approach was followed by Fu and collaborators [75] to solve the retinal vessel segmentation problem, fundamental in the diagnostics and surgery of ophthalmological diseases, and, until quite recently *manually* performed by an ocular pathologist. The authors also used a two term energy function within a mean

field approach. To minimize the energy function subject to empirical constraints they used a recurrent neural network based on Gaussian kernels on the feature vectors applying standard gradient descent methods. Blood vessel segmentation was also studied using conditional MRFs by Orlando and coworkers [76]. However, instead of using a mean-field approach and inferring the marginals using neural networks, these authors chose to perform Maximum a Posteriori (MAP) labeling with likelihood functions optimized *via* Support Vector Machines (SVMs). Imaging segmentation *via* MRFs can be applied not only at the tisular level, but also on cellular (and even supramolecular) scales. Several blood diseases, for instance, are diagnosed by discerning the quantity, morphology and other aspects of leukocytes as well as their nuclear and cytoplasmic structure. To this end, Reta and coworkers used unsupervised binary MRFs (i.e., classical Ising-like fields) to study leukocyte segmentation [77]. A Markov neighborhood and clique potential approach was followed. This *classic* approach has been enough since from their high quality colored imaging data, it was possible to define an energy function based on *a priori* Gaussian-distributed probabilities, then applying a maximum likelihood approach to calculate the posterior probability. Related ideas were used to study microvasculature disorders in glioblastomas by the group of Kurz [78].

Application Box I: Metastasis Detection

General problem statement: Accurate detection of metastatic events is key to proper diagnostics in cancer patients. Pathologists often resort to the analysis of whole slide images (WSI). Computational histopathology aims for the automated modeling and classification of WSI to distinguish between normal and tumor cells, thus alleviating the heavy burden of manual image classification. Li and Ping [73] used Conditional Random Fields together with deep convolutional neural networks to approach this problem.

Theoretical/Methodological approach: The approach developed by the authors consisted in using a deep convolutional neural network (CNN) for the automated detection of the relevant variables (feature extraction or feature selection). Once these relevant variables have been determined, a conditional random field (CRF) was used to consider the spatial correlations between neighboring patches. The approach used to determine tumor and non-tumor regions is similar to the one used in statistical physics of condensed matter for the determination of ferromagnetic/anti-ferromagnetic domains.

Improvements/advantages: The use of CNNs to reduce the number of variables (and to find the optimal ones) is gaining relevance in computational biology and data analysis applications of random fields. It may result useful in any setting in which there are no *a priori* determined relevant variables. By conditioning these variables on the spatial location, the authors have turn the configuration problem into a classifier thus solving their problem.

Limitations: Though not an actual limitation for their particular problem, the authors resort to the use of a mean field approach to infer the marginals. This condition can be strengthened by using approaches such as perturbative expansions or maximum entropy optimization with a suitable set of constraints.

MRFs have also been used in conjunction with deep learning approaches for the topographical reconstruction of colon structures from conventional endoscopy images. Since the colon is a deeply complex anatomical structure, accurately reconstructing its structure to detect anomalies related to, for instance, colorectal cancer is of paramount importance. Mahmmod and Durr [79] developed a deep convolutional neural network-conditional random field method, which uses a two-term energy function whose parameters are optimized *via* stochastic-descent back-propagation. Several convolution maps were used since their goal was also to estimate depth from photographic (2D) images *via* MAP (i.e., by an a posteriori maximum likelihood) optimization. This was actually possible since the authors trained their model with over 200,000 synthetic images of an anatomically realistic colon.

To improve the automated evaluation of mammography, Sari and coworkers [80] developed an MRF approach supplemented with simulated annealing optimization (MRF/SA). Improved performance was actually attained by using pre-processing filters leading to AUC/ROC of up to 0.84, which is considered quite high since mammograms have proved to be especially hard to interpret with computer aided diagnostics. MRFs have also helped improve the estimation of cardiac strain from magnetic resonance imaging data, a relatively non-invasive test to analyze cardiac muscle mechanics [81].

4.2 Applications of MRFs in Computational Biology and Bioinformatics

Computational biology and bioinformatics are also disciplines that have widely adopted the random field formalism as a relevant component of their toolkits. There are several instances in which MRFs can be adapted to solve problems in these domains: from structural biology problems in which the spatio-temporal locality is naturally mapped onto random fields, to molecular regulatory networks in which the graph structure of the MRFs mimic the underlying connectivity of the networks, to *semantic* and *linguistic* segmentation problems in genomic sequences or biomedical texts.

Regarding computational models in structural biology, Rosenberg-Johansen and his group [82] used a combination of deep neural networks and conditional random fields to improve predictions on the secondary structure of proteins (i.e., the three dimensional conformation of local protein segments, the formation of alpha helices, beta sheets and so on). The CRF approach was quite useful in this case (in general non-computationally tractable), since in protein secondary structure, there is a high degree of crosstalk between neighboring elements (residues), then the local dependency structure greatly shrinks the *search space*. Previously, Yanover and Fromer [83] applied an MRF formalism for the prediction of low energy, protein side configurations, a relevant problem fro several aspects of structural biology such as *de novo* protein

folding, homology modeling and protein-protein docking. The different types of local interactions among amino acid residues: hydrophobic, hydrophilic, charged, polar, etc.) modeled as pairwise potentials let to semi-empirical expressions for the potential energies used in the MRF formalism. Once explicit expressions for the field have been written, the authors resort to a belief-propagation algorithm to find the optimal solution to the MRF problem given the constraints. Several improvements were actually applied to the message-passing algorithm that allow the authors to find a method to obtain the lowest energy amino acid chain configurations. This kind of approach may also be relevant to improve solving methods of random fields in statistical physics problems since it led to approximate explicit forms of the partition function.

Improving methods to discern the structural properties of proteins are also quite used in the context of protein homology, i.e., to investigate on the functions of proteins related to their structural similarity to other proteins, perhaps in different organisms. Local homology relationships can also be investigated by means of Markov random field methods. Xu and collaborators developed a method (or better, a *family* of methods) called MRFalign for protein homology detection based on the alignment of MRFs [84, 85]. Aside from purely *Ising* approaches, other methods of random fields of statistical mechanics have been adopted in the computational biology community. One of them is the Potts model. Recently, Wilburn and Eddy used a Potts model with latent variables for the prediction of *remote* protein homology (involving changes such as insertions and deletions) [86] importance sampling from extensive databases was used to perform MAP optimization as commonly done in computational biology and computer science.

A topic related to homology, but also involving space-dependent electrostatic interactions (protein-protein interactions, in particular) is protein function prediction. Networked models of protein prediction have been developed: primitive models can be used to associate a function to a given protein given the functions of proteins in their interaction neighborhood and probabilistic models may do this by weighting interactions with an associated probability. Gehrman and collaborator devised a CRF method fro protein function prediction based on these premises [87]. To solve the CRF, they resort to a factor graph approach [88] to write down explicit contributions to the cliques [89] and then using an approximate Gibbs measure calculated from this clique factorization. The approximation is based on other relevant feature of Markov random fields, which we will discuss later in the context of statistics and computer science: the use of the so-called *Gibbs sampler* or Gibbs sampling algorithm [90]. The Gibbs sampler is a Markov chain Monte Carlo (MCMC) method used to obtain a sequence of observations–approximated from a specified multivariate probability distribution–, in those cases for which direct sampling is difficult or even impossible (e.g., NP-hard or super-combinatorial problems).

Perhaps not so well known as a relevant structural biology problem until recently, is the determination of three dimensional chromosome structure inside the cell's nucleus. Long range chromosomal interactions are believed to be ultimately related to fundamental issues on global and local gene regulation phenomena. A recently devised experimental method for global *chromosome conformation capture* is known as Hi-C. Nuclear DNA is subject to formaldehyde treatment to enhance covalent interactions *glueing* chromosome segments that are three dimensionally adjacent. Then a battery of restriction enzymes is used to cut DNA into pieces. Such pieces are sequenced and the identity of the spatially adjacent regions are then discovered. The data is noisy and often incomplete. For these reasons, a team lead by Yun Li developed a hidden Markov random field method to analyze Hi-C data to detect long range chromosomal interactions [91]. This method combines ideas from MRFs, Bayesian networks and Hidden Markov models. In a nutshell, they assumed a mixture of negative binomials as an Ising prior [22] and supplemented it with Bayesian inference to calculate the joint probabilities *via* a Metropolis-Hastings pseudo-likelihood approach.

Application Box II: Prediction of Low Energy Protein Side Chain Configurations

General problem statement: The prediction of energetically favorable aminoacid chain configurations constrained on the three-dimensional structure of a protein principal chain is a relevant problem in structural biology. Accurate side configuration predictions are key to develop approaches to *de novo* protein folding, to model protein homology and to study protein-protein docking. Yanover and Fromer [83] used a Markov Random Field with pairwise energy interactions supplemented with a belief propagation algorithm to bypass the mean field approximation.

Theoretical/Methodological approach: The authors developed their approach by modeling energy levels (as obtained by simulation and calorimetric techniques) as the relevant variables in a pairwise Markov Random Field. Since local side chain configurations have inhomogeneous contributions to the global energy landscape, a mean field approach will not be accurate. In order to circumvent the other extreme of modeling all detailed molecular interactions, the authors used belief propagation algorithm (BPA), a class of message passing method that performs global optimization (in this case energy minimization) by iterative local calculations between neighboring sites.

Improvements/advantages: We can consider the use of the BPA on top of the MRF, as a compromise between mean field approach (not useful to solve the actual structural biology problem) and full-detail molecular interaction modeling (computationally intractable due to the large combinatorial search space involved).

Limitations: Protein side chain prediction may in many cases be affected by subtle angular variations in the rotamer side chains. The authors have discussed that, to improve the accuracy of their predictions in such cases, it may be useful to resort to continuous-valued (Gaussian) MRFs with their associated BPAs as an avenue for further improvement within the current theoretical framework.

The spatial configuration of proteins within protein assemblies such as membranes it is also relevant to understand the functions

of molecular machines in the cell. By applying a combination of deep recurring neural networks and CRFs, it was possible to predict transmembrane topology and three dimensional coupling in the important family of G-protein coupled receptors (GPCRs). These receptors are able to detect molecules outside the cell and activate cellular responses and are of paramount relevance in immune responses and intercellular signaling [92].

As we have mentioned molecular regulatory networks are models that may conceptually map random fields almost straight forward. They have a graph-theoretical structure already and their interactions are often so complex that modeling them as stochastic dependencies is somehow natural [93]. Depending on the nature of the regulatory interactions to be modeled, different approaches can be followed. Gitter and coworkers, for instance, used latent tree models combining an MRF with a set of hidden (or latent) variables, factorizing the joint probability on a Markov tree [94]. In this work, the action of transcription factor (TFs) was mapped to a set of latent variables and the MRF was used to establish the relationships of conditional independence of groups of neighboring genes, *via* their gene expression patterns obtained from experimental data. Zhong and colleagues [95] used a related approach to infer regulatory networks *via* a *directed* random field, giving rise to a tree structure known as a directed acyclic graph (DAG). In their work, all variables follow a pairwise Markov field with conditional dependencies following parametric Gaussian or multinomial distributions. Although they resorted to a DAG modeling due to its ability to work with *mixed* data (usually undepowered for common MRF approaches), the limitations of these studies to account for regulatory loops has to be considered.

Application Box III: Inference of Tissue-specific Transcriptional Regulatory Networks

General problem statement: Transcriptional regulatory programs determine how gene expression is regulated, thus determining cellular phenotypes and response to external stimuli. Such gene regulatory programs involve a complex network of interactions among gene regulatory elements, RNA polymerase enzymes, protein complexes such as mediator and cohesion machineries and sequence specific transcription factors. Ma and coworkers [96] used a Markov Random Field approach to construct tissue-specific transcriptional regulatory networks integrating gene expression and regulatory sites data from RNA-seq and DNAase-Seq experiments.

Theoretical/Methodological approach: The authors developed an MRF approach with unary (node functions) and binary (edge functions, i.e., pairwise interactions) potentials for transcriptional interaction within a cell line and across cell lines, respectively. With these two potential functions a joint probability distribution is written. To solve the problem, the JPD is mapped to a pseudo-energy optimization (PEO) test *via* logarithmic. transformation. The PEO is in turn transformed into a network maximum flow problem and solved by a loopy BPA.

Improvements/advantages: An original contribution of this work is the use of belief propagation algorithms to solve for a quadratic pseudo-energy functions (with only unary and pairwise potentials) representation and then using iterated conditional modes. This may open an interesting research path for other MRF applications.

Limitations: One possible shortcoming of this approach is the use of linear correlation measures (Pearson coefficients) and linear classifiers (Singular Value Decomposition) for a problem with strong non-linearities (complex biochemical kinetics associated with gene expression). The MRF structure will indeed allow for more general statistical dependency relationships, making the analysis even more robust.

Undirected graphical models in the form of usual MRFs, have been used to construct, tissue-specific transcriptional regulatory networks [96] in 110 cell lines and 13 different tissues, from an integrative analysis of RNASeq and DNAase-Seq data. The authors used a method to minimize the pseudo-energy function by converting the problem to a maximum flow in networks and solving the latter *via* a loopy belief propagation algorithm [97].

To improve on the modeling capabilities of MRFs to describe gene regulatory networks (GRNs) it is becoming customary to include several data sources as a means to partially disambiguate the statistical dependency structures. Banf and Rhee implemented a data integration strategy to their MRF modeling of GRNs in an algorithm called GRACE which exploits the energy function based on unary and binary terms that we previously described in the context of MRF modeling in biological imaging. Low confidence pairwise interactions were removed by mapping the problem to a classification task on imbalanced sets, and following the tenets of Ridge penalized regression [98].

A somehow related method was devised by Grimes, Potter and Datta, who integrate differential network analysis to their study of gene expression data [99]. Their study was based on the idea of using KEGG pathways to construct MRFs as a means to functionally improve differential expression profiling [100, 101]. A similar MRF method was used to improve transcriptome analysis in model (mouse) systems for biomedical research [102]. Data integration can be also used to incorporate biological function information (from metabolic and signaling pathways) to the modeling of statistical Genome Wide Association Studies (GWAS) *via* MRFs [103]. The MRF was then solved by a combination of parametric (inverse gamma) distributed priors and MAP techniques to find the posterior probabilities. This is relevant since the important results of GWAS research in biomedicine (statistical in nature and often poorly informative in the biological sense) can be contextualized *via* pathway interactions as devised *via* this MRF approach.

Though not properly a molecular interaction network study, Long, et al, developed a method combining graph convolutional networks with conditional random fields, to predict human microbe-drug associations [104]. Since there has been a growing emphasis on the ways in which the human microbiome may affect drug responses in the context of precision medicine [105], accurate methods to predict such associations are highly desirable for the design of tailor-made therapeutic interventions.

Since random fields are able to capture not only spatio-temporal and regulatory associations, but are also proper to represent semantic or *grammatical* relationships, they have been thoroughly used in text analysis in biology, being the subjacent texts genomic sequences or pieces of biomedical literature. The group led by Fariselli used hidden CRFs for the problem of biosequence labeling in the prediction of the topology of prokaryotic outer-membrane proteins. Their study was based on a grammatically restrained approach, using dynamic programming much in the tradition of the so-called Boltzmann machines in AI [106]. Poisson random fields over sequence spaces were studied by Zhang and coworkers to detect local genomic signals in large sequencing studies [107].

Moving on to data and literature mining methods based on MRFs, we can mention *passage relevance models* used for the integration of syntactic and semantic elements to analyze biomedical concepts and topics *via* a PGM. The semantic components such as topics, terms and document classes are represented as potential functions of an MRF [108]. Biomedical literature mining strategies using MRFs were also developed to study automated recognition of bacteria named entities [109] to curate experimental databases on microbial interactions. Related methods were previously used to identify gene and protein mentions in the literature using CRFs [110].

4.3 Applications of MRFs in Ecology and Other Areas of Biology

Other applications of random fields in biology include demography and selection to study weakly deleterious genetic variants in complex demographic environments [111] and for species clustering [112], in population genetics. MRFs have also been applied to understand species distribution patterns and endemism and to unveil [113] interactions between co-occurring species in processes governing community assembly [114]; as well as for spatially explicit community occupancy [115] in ecology.

Another group of disciplines in which MRFs have flourished is comprised of Data Science, Computer Science and Modern statistics. The next section will be devoted to presenting and discussing some developments of random fields in that setting.

5 MARKOV RANDOM FIELDS IN DATA SCIENCE AND MACHINE LEARNING

The term *Data Science* refers to a multidisciplinary field devoted to extracting knowledge and insight from structured and unstructured data. It shares commonalities and differences with its parent fields: statistics, computer and information sciences and engineering. However, much of the emphasis is on the extraction of *useful* knowledge from data, putting accuracy and usability above formal mathematical structure if needed. Naturally, Markov random fields as a theoretically powerful methodology that allows for the incorporation of *educated intuition* and has an intrinsic algorithmic nature has called the attention of data scientists. We will present here, but a handful of the many uses and implementations of MRFs in data science and computational intelligence settings. As we will see, these studies share a lot of commonalities with the applications in statistical physics and computational biology while, at the same time, incorporating elements that may cross-fertilize to the modeling schemes in the natural sciences.

5.1 Applications of MRFs in Computer Vision and Image Classification

As we already mentioned in the context of applications of random field to biomedical imaging, segmentation and pattern identification to enhance the resolution of spatial and/or spatio-temporal maps is a common use of MRFs. From the many applications in the field of computerized image processing, we will discuss some that present peculiarities or distinctive features that may be of more general interest. For instance, to face the challenge of capturing three dimensional structure from two-dimensional images, the so-called *depth perception*, Kozik used an MRF-based methodology [116] in which the energy function was modeled *via* a polynomial regression model and a depth estimation algorithm with correlated uncertainties (a sort of twofold autoregressive model). By using these entries Kozik then solved an MAP problem to obtain the maximum likelihood solution to the MRF.

In the context of AI to enhance low-resolution images (the super-resolution problem), Stephenson and Chen devised an adaptive MRF method [117] based on passing-message optimization by a loopy propagation algorithm. Also in the context of AI approaches to image processing Li and Wand developed a combination of MRFs as generative models and deep CNNs to discriminate two-dimensional images to try to solve the so-called *image synthesis problem*, a relevant problem in computer vision with applications both to photo-editing and neuroscience [118]. A problem related to image synthesis is image classification, in which certain features of images are discerned and used to cluster images by similitudes in these feature spaces. Applications in image recognition in security, forensics and scientific microscopy and imaging among others abound. To improve the accuracy of image classification algorithms, Wen and coworkers developed a CRF method in which machine-learned feature functions took the place of the unary and binary terms in the potential energy [119], as in previous cases Gaussian priors and loopy belief propagation algorithms were used to solve the random field.

5.2 Applications of MRFs in Statistics and Geostatistics

Geostatistics and geographical information systems are also quite amenable to be modeled within the MRF paradigm due to their natural spatio-temporal dependency structures. In the context of prediction of environmental risks and the effects of limited sampling, Bohorquez and colleagues developed an approach based on multivariate functional random fields for the spatial prediction of functional features at unsampled locations by resorting to covariates [120]. As in the case of random field

hydrodynamics (mentioned in the physics section), an empirical approach based on continuous field estimators was chosen. Continuous spatio-temporal correlation structures *via* so-called Kriging methods extending the ideas of discrete random fields are commonly used in environmental analysis and risk assessment [121, 122].

Geological modeling is another field at the intersection of geostatistics and geophysics which has adopted the MRF formalism to deal with their problems. A segmentation approach was used for stochastic geological modeling with the use of hidden MRFs [123]. Using a methodological approximation similar to the one used in computer vision and biomedical imaging, latent variable MRFs are used to perform three-dimensional segmentation. The model is supplemented with finite Gaussian mixture models for the parameter calculations and a Gibbs sampling inference framework, following a similar approach to the one developed by the group of Li [124], based on the methods of Rue and Held [125] and by Solberg et al [126] and further developed by Toftaker and Tjelmeland [127]. More refined geostatistical methods have been based on a clever combination of several developments of Markov random field theory. Along these lines, the work by Reuschen, Xu and Nowak [128] is noteworthy, since they used Bayesian inversion (based on Markov conditional independence) to develop a random field approach to hierarchical geostatistical models and used Gibbs sampling MCMC to solve them.

The combined use of ideas from Markov and Gibbs random fields in statistical learning and other approaches in modern statistics has indeed become a fruitful line of research with important theoretical developments and a multitude of applications [24, 34, 129]. The use of MRFs and CRFs as tools for statistical learning has been used in a multitude of settings in both generative and discriminative models [33]. Aside Ising models and MRFs, perhaps the most widely used applications of the random fields are Gibbs sampling and Markov chain Monte Carlo methods that we already mentioned. Due to the generality and the relatively low computational complexity of these sampling/simulation methods, several methods have been developed based on them.

Gibbs sampling is a form of Markov chain Monte Carlo (MCMC) algorithm. MCMC methods are used to obtain a sequence of *observations* of a random experiment by an approximation from a given (specified) multivariate probability distribution when direct sampling is challenging (computationally or otherwise). The essence of the method is building a Markov chain whose equilibrium distribution is precisely the specified multivariate distribution. Then, a sample of such distribution is just a sequence of states of the Markov chain. The use of the Markov property of an MRF allows to use Gibbs sampling as an MCMC method, when the joint probability distribution is not known (or is very complex) but the conditional distributions are known (or easier). Due to this, by using the pairwise Markov property, Gibbs sampling is particularly fit to sampling the posterior distribution of Bayesian networks (understood as a collection of conditional distributions), a quite relevant problem in both, statistical learning and in large computer simulation problems.

Aside from these basic issues, Gibbs sampling has been extensively enhanced over the years. One important improvement has been the incorporation of adaptive rejection sampling [130, 131], particularly useful for situations in which evaluation of the density distribution function is computationally expensive (e.g., non-conjugated Bayesian models). Adaptive rejection sampling can be even applied to modeling *via* non-linear mixed models [131]. To further minimize the computational burden of Gibbs sampling, Meyer and collaborators [132] developed an algorithm which samples *via* Lagrange interpolation polynomials, instead of exponential distributions. Convergence can be also improved by double-adaptive independent rejection sampling [133] which is based on a scheme of minimizing the correlation among samples. Gibbs sampling approaches also allow for the determination of dense distribution simulated sampling from sparse sampled data [134], even in high dimensional latent fields over large datasets [135].

Gao and Gormley implemented a Gibbs sampling scheme based on CRFs weighted *via* neural scoring factors (implemented as parameters in factor graphs) with applications to Natural Language Processing (NLP) [136]. MCMC has also been used, in the context of Gibbs random fields in data pre-processing, to reduce the computational burden of data intensive signal processing [137, 138]. Gibbs sampling can also be applied in parallel within the context of Gaussian MRFs on large grids or lattice models [139]. Parallel Gibbs sampling methods can also be developed in the context of sampling acceleration for structured graphs [140].

Markov random fields and its associated Gibbs measures can also be used to advance statistical methods in large deviation theory [141] and to develop methods of joint probability decomposition based on product measures [142]. Exact factorizability of joint probability distributions is a most relevant question in modern probability [143–146] with important applications in data analytics [147], applied mathematics [148], computational biology [149] and network science [150], among other fields. MRFs also have been applied to embed filtrations on high dimensional hyperparameter spaces. The main idea is using random fields as hierarchical models *projecting* the relevant hyper-parameter space to a lower dimensional filtration [135]. This general problem is closely related with the *feature selection problem* in computer science and data analytics. We will discuss applications of the MRF formalism in that context in the next subsection.

5.3 Applications of MRFs in Feature Selection and AI

Feature selection (FS) refers to a quite general class of problems in computer science, data analysis and AI. Feature selection aims to find the minimum number of maximal relevant features to characterize a high dimensional data set. One outstanding family of methods of feature selection is *regression methods* in which a set of *regression variables* is used to predict one (or a few) dependent variables *via* functional relationships (commonly

linear combinations with a distribution of weights). A subset of the whole set of regression variables is considered statistically significant, in that context those are the *selected features*. FS is a more general problem than linear, multivariate or even non-linear regression. MRF can be used to generalize regression procedures to more complex situations. One notable method was developed by Stoehr, Marin and Pudio [151] who used hidden Gibbs random fields to implement model selection *via* an information theoretical optimization criterion known as *Block likelihood information*. Cilla and coworkers [152] developed a FS method to be used in sequence classification based on hidden CRFs supplemented with a generalized Lasso group regularization method that instead of the colinearity condition employs L1-norm optimization of the parameters. The authors showed that FS outcomes with this method outperforms standard conditional random field approaches.

Feature selection efficacy of MRFs is closely related to the actual structure of the underlying adjacency matrices. Especially relevant is the issue of *separability*. Although non-trivial separability does not preclude the use of MRFs in large datasets, as long as the positive definite nature of the measures is ensured; there may be computational complexity limitations for practical uses. Recently, Sain and Furrer [153] discussed on some general properties of random fields (in particular for multivariate Gaussian MRFs) that need to be taken into account in the design of computationally efficient modeling strategies with such random fields. By designing FS schemes with MRFs based on the optimization of parameter estimation, for instance *via structured learning* it is possible to improve substantially on the computational complexity of such algorithms [154–158]. The graph structure of MRFs can also be optimized to enhance the FS capabilities of the algorithms [159–163]. More information along these lines can be found in the comprehensive review by Adams and Beling [164] and in the one by Vergara and Estevez [165].

As already mentioned the structure of MRF may result advantageous to solve *segmentation* problems or delimitation of statistical dependencies. These are problems that are extremely relevant in the context of computational linguistics and natural language processing applications. We will discuss these in the following subsection.

5.4 Applications of MRFs in Computational Linguistics and NLP

Automated textual identification and *meaning discernment* are extremely complex (and very useful) tasks in current artificial intelligence research and applications. The ability to detect text *patches* with semantic similarity is one of the founding steps in the ability to process natural language by a computer. By combing a deep learning approach (a convolutional neural network) with MRF models, Liu and collaborators [166] devised an effective algorithm for *semantic segmentation* [167], which they called a Deep Parsing Network (DPN). Within the DPN scheme, a CNN is used to calculate the unary terms of a two-term energy function, while the pairwise terms were approximated with a mean-field model. The mean field contributions were iteratively optimized using a back-propagation algorithm able to generalize to higher order *perturbative contributions*. Although the original application of semantic segmentation has been applied to image segmentation, its applications to NLP are somehow straight forward [168, 169].

A similar method was developed earlier by Mai, Wu and Cui and applied to improve word segmentation disambiguation in the Chinese language [170]. Main and colleagues, however, decided to use a CRF on top of a bidirectional maximum matching algorithm. Parameter estimation for the CRF was performed *via* maximum likelihood estimates. These ideas were further advanced by Qiu, et al [171] who used CRFs for clinical entity recognition in Chinese. Speech tagging from voice recordings was performed using a CRF devised by Khan and collaborators [172]. Even computer assisted *fake news* detection [173] and headline prediction [174] can be achieved using CNNs and MRFs.

5.5 Applications of MRFs in the Analysis of Social Networks

Social network analysis, including online social networks, other forms of interpersonal interaction networks and even some social networks in non-human creatures, have become a relevant field of research in recent times (though the subject has been relevant in the contexts of sociology and animal behavior for decades) [175]. The analysis of social network *via* MRFs is becoming more and more common also. As an example, Jia and collaborators have used MRFs to infer attributes in online social network data [176]. Their model used the social network structure itself to develop a pairwise MRF. From empirical training data, the authors used the individual behaviors to learn a probability that each user has a given attribute. Then used that as an a priori probability, compute the posterior probabilities by a loopy belief propagation algorithm over the MRF, to, finally, optimizing the belief propagation algorithm by a *second neighbor* criteria that sparsifies the adjacency matrix. Further optimization of similar ideas was obtained by using graph convolutional networks, i.e., CNNs over CRFs [177]. Attribute inference in social network data *via* MRFs can also be used to improve cybersecurity algorithms [178], to learn consumer intentions [179], to study the epidemiology of depression [180] among other issues. Social networks as well as some classes of molecular interaction and ecological networks are also relevant to the development and improvement of MRF and CRF learning algorithms. This is so since often a sketch (sometimes a detailed one) of the network dependency structure is known a priori [181, 182]. This is yet another instance in which applications may nurture back the formal theory of random fields.

Application Box IV: Inference of User Attributes in Online Social Networks

General problem statement: The attribute inference problem (AIP), i.e., the discovery of personality traits from data on social networks, is a central question on computational social science. It is indeed an (unsupervised) extension of the personality analysis tests of classical psychology with important applications from sociological modeling to

commercial and political marketing, and even national security issues. Jia and collaborators [176] developed an approach to the AIP from public data on online social networks using an MRF with pairwise interactions.

Theoretical/Methodological approach: Given a training dataset, behaviors are used to learn the probabilities that each user (node) has a considered attribute, these are the prior probabilities. Based on the neighborhood structure of a pairwise Markov random field, posterior probabilities are computed *via* a loopy belief propagation algorithm. The MRF has a quadratic pseudo-energy function with node potentials (unary contributions) for each user and edge potentials (pairwise interactions) for every connected pair of nodes, as defined by node correlations. Edge potentials are defined as discrete-valued *spin-like* states $\lambda_{uv} = 1$ if nodes u and v have the same attribute state and $\lambda_{uv} = -1$ if they do not. This way, *homophily* in the social networks mimics spin-alignment in lattice models of magnetism.

Improvements/advantages: To optimize computational performance in large networks, the authors modified the BPA by using a loop renormalization strategy. Hence, circular node correlations are locally computed for each pair of nodes *prior to move to another edge* and then using a linear optimization approach. Thus, there is no need to allocate memory for all circular correlations (loops).

Limitations: More than a limitation itself, an avenue of predictive improvement may be given by extending their MRF approach to allow multi-categorical (or even continuous) state variables. Doing this will make possible to capture the fact that most behavioral attributes are not simply present/absent, but may occur over a range of possibilities.

5.6 Random Fields and Graph Signal Theory

Graph signal theory, also called graph signal processing (GSP) is a field of signal analytics that deals with signals whose domain (as identified by a graph) is irregular [183–185]. In the context of GSP, the vertices or nodes represent probes in which the signal has been evaluated or sensed and the edges are relationships between these vertices. Data processing of the signals exploits the structure of the associated graph. GSP is often seen as an intermediate step between single channel signal processing and spatio-temporal signal analysis. The nature of the edges is determined by the relationship (spatial, contextual, relational, etc.) between the vertices. Whenever edges are defined *via* a statistical dependence structure, GSP can be mapped to either an MRF or a CRF, thus allowing the use of all the tools of random field theory to perform GSP [186, 187]. The networked nature of the domain of signals embedded in a graph, allows the use of spectral graph theoretical methods for signal processing [188–190]. Conversely, correlations between features on the signals are also useful to identify the structure of the underlying graph [191, 192].

GSP has a number of relevant applications, from spatio-temporal analysis of brain data [193]; to analyze vulnerabilities in power grid data [194]; to topological data analysis [195], chemoinformatics [196] and single cell transcriptomic analysis [197], to mention but a few examples. Statistical learning techniques have also being founded on a combination of MRFs and GSP [198, 199], taking advantage of both the networked structure, the statistical dependence relationships and the temporal correlations of the signals [200–202]. Random field approaches to GSP have also been applied in the context of deep convolutional networks [203, 204], often invoking features of the underlying joint conditional probability distributions such as ergodicity [205] and stationarity [206].

6 CONCLUDING REMARKS

As already known in statistical physics for decades, random fields are a quite powerful and versatile theoretical analytical framework. We have discussed here some fundamental ideas of the theory of Markov-Gibbs random fields, namely the notions of statistical dependency on neighborhoods, of potentials and local interactions, of conditional independence relationships and so on. After that, we discussed a handful of (mostly recent) advances and applications of Markov random fields in different physics subdisciplines, as well as in several areas of biology and the data sciences. The main goal of this presentation was not to be comprehensive but to be illustrative of the many ways in which research and applications of random field may be advancing both, inside and outside traditional statistical physics.

In the theoretical and conceptual advances side, we mentioned how random fields may be embedded in general manifolds, how by incorporating quenched fields (or somehow equivalently, by adding quenching potentials) to the usual Izing random field, a whole new phenomenology can be discovered in RFIMs. How Markov and Bayesian networks may be combined in HRFs and how gauge symmetries and other extended fields may broad the scope of MRFs.

By examining the applications in physics and in other disciplines, we discover (or often re-discover) methodological and computational improvements to the inference, analysis and solutions of problems within the MRF/GRF/CRF settings. In these regards, we can mention the use of CNNs as feature extractors on top of random fields, to refine hypotheses about marginals and (*via* convolution) to improve the accuracy of pairwise potential terms. We re-examined how to extend beyond mean-field approaches, either *via* MAP optimization, *via* higher order perturbations solved by neural networks or maximum likelihood approaches (depending on data availability). How, under certain circumstances (still dictated by physical intuition and data constrains) factorization of the partition function may be attained *via* clique potentials obtained from Gaussian (or other multivariate parametric distributions) or even from empirical distributions.

We also analyzed how simulations in random fields may be supplemented with well known methods–within the statistical physics community–, such as simulated annealing, Markov Chain Monte Carlo and importance sampling, but also from methods of wide use in other fields such as stochastic descent back-propagation, factor graph approaches, Gibbs sampling, pseudo-likelihood methods, latent models or loopy belief

propagation algorithms to name a few. And how, under some circumstances, parameter estimation (fundamental in applications involving non-trivial partition functions) can be reframed as a regression problem and benefit from the use of the Ridge and Lasso optimization techniques, dynamic programming and autoregressive modeling.

We want to highlight that, in spite of being a hundred-plus year developed formalism in statistical physics, the theory of Markov-Gibbs random fields is indeed a flourishing one, with many theoretical advances and applications within and outside physics.

AUTHOR CONTRIBUTIONS

EH performed research and wrote the manuscript.

FUNDING

This work was supported by the Consejo Nacional de Ciencia y Tecnología (SEP-CONACYT-2016-285544 and FRONTERAS-2017-2115), and the National Institute of Genomic Medicine, México. Additional support has been granted by the Laboratorio Nacional de Ciencias de la Complejidad, from the Universidad Nacional Autónoma de México. EH is recipient of the 2016 Marcos Moshinsky Fellowship in the Physical Sciences.

ACKNOWLEDGMENTS

The author is grateful to the lively and brilliant academic community that has been behind the Winter Meeting on Statistical Physics for five decades now.

REFERENCES

1. Ising E. Beitrag zur theorie des ferromagnetismus. *Z Physik* (1925) 31:253–8. doi:10.1007/bf02980577
2. Averintsev MB. Description of Markovian random fields by gibbsian conditional probabilities. *Theor Probab Appl* (1972) 17:20–33. doi:10.1137/1117002
3. Averintsev M. Gibbsian distribution of random fields whose conditional probabilities may vanish. *Problemy Peredachi Informatsii* (1975) 11:86–96.
4. Dobrushin RL, Kryukov V, and Toom AL. *Locally interacting systems and their application in biology*. Springer (1978).
5. Stavskaya ON. Markov fields as invariant states for local processes. Locally Interacting Systems and Their Application in Biology. Springer (1978). 113–121. doi:10.1007/bfb0070088
6. Stavskaya ON. Sufficient conditions for the uniqueness of a probability field and estimates for correlations. *Math Notes Acad Sci USSR* (1975) 18:950–6. doi:10.1007/bf01153051
7. Vasilyev NB. Bernoulli and Markov stationary measures in discrete local interactions. Locally interacting systems and their application in biology. Springer (1978). 99–112. doi:10.1007/bfb0070087
8. Dobruschin PL. The description of a random field by means of conditional probabilities and conditions of its regularity. *Theor Probab Appl* (1968) 13:197–224. doi:10.1137/1113026
9. Lanford OE, and Ruelle D. Observables at infinity and states with short range correlations in statistical mechanics. *Commun Math Phys* (1969) 13:194–215. doi:10.1007/bf01645487
10. Hammersley JM, and Clifford P. *Markov fields on finite graphs and lattices*. Unpublished manuscript (1971).
11. Koller D, and Friedman N. *Probabilistic graphical models: principles and techniques (adaptive computation and machine learning series)*. MIT Press (2009).
12. Grimmett GR. A theorem about random fields. *Bull Lond Math Soc* (1973) 5:81–84. doi:10.1112/blms/5.1.81
13. Besag J. Spatial interaction and the statistical analysis of lattice systems. *J R Stat Soc Ser B (Methodological)* (1974) 36:192–225. doi:10.1111/j.2517-6161.1974.tb00999.x
14. Baxter RJ. *Exactly solved models in statistical mechanics*. Elsevier (2016).
15. Cipra BA. An introduction to the Ising model. *The Am Math Monthly* (1987) 94:937–59. doi:10.1080/00029890.1987.12000742
16. McCoy BM, and Wu TT. *The two-dimensional Ising model*. North Chelmsford, MA: Courier Corporation (2014).
17. Thompson CJ. *Mathematical statistical mechanics*. Princeton University Press (2015).
18. Adler M. *Monte Carlo simulations of the Ising model*. Anchor Academic Publishing (2016).
19. Hopfield JJ. Neural networks and physical systems with emergent collective computational abilities. *Proc Natl Acad Sci* (1982) 79:2554–8. doi:10.1073/pnas.79.8.2554
20. Ackley DH, Hinton GE, and Sejnowski TJ. A learning algorithm for Boltzmann machines*. *Cogn Sci* (1985) 9:147–69. doi:10.1207/s15516709cog0901_7
21. Salakhutdinov R, and Larochelle H. Efficient learning of deep Boltzmann machines. Proceedings of the thirteenth international conference on artificial intelligence and statistics. Sardinia, Italy: DBLP (2010) 693–700.
22. Ross KJ, and Snell L. *Markov random fields and their applications*. American Mathematical Society (1980).
23. Essler FHL, Mussardo G, and Panfil M. Generalized Gibbs ensembles for quantum field theories. *Phys Rev A* (2015) 91:051602. doi:10.1103/physreva.91.051602
24. Murphy K. *Machine learning: a probabilistic perspective*. MIT Press (2012).
25. Williams D. *Probability with martingales*. Cambridge University Press (1991).
26. Canonne CL, Diakonikolas I, Kane DM, and Stewart A. *Testing conditional independence of discrete distributions*. Information Theory and Applications Workshop (ITA) (IEEE) (2018). 1–57.
27. Schultz TD, Mattis DC, and Lieb EH. Two-dimensional Ising model as a soluble problem of many fermions. *Rev Mod Phys* (1964) 36:856. doi:10.1103/revmodphys.36.856
28. Brush SG. History of the lenz-ising model. *Rev Mod Phys* (1967) 39:883. doi:10.1103/revmodphys.39.883
29. Isichenko MB. Percolation, statistical topography, and transport in random media. *Rev Mod Phys* (1992) 64:961. doi:10.1103/revmodphys.64.961
30. Sornette D. Physics and financial economics (1776-2014): puzzles, Ising and agent-based models. *Rep Prog Phys* (2014) 77:062001. doi:10.1088/0034-4885/77/6/062001
31. Adler RJ, and Taylor JE. *Random fields and geometry*. Springer Science & Business Media (2009).
32. Ganchev A. About Markov, Gibbs,... gauge theory... finance. Quantum Theory And Symmetries. Springer (2017) 403–12.
33. Freno A, and Trentin E. *Hybrid random fields*. Springer (2011).
34. Friedman J, Hastie T, and Tibshirani R. *The elements of statistical learning*. New York: Springer series in Statistics (2001).
35. Hernández-Lemus E. On a class of tensor Markov fields. *Entropy* (2020) 22:451. doi:10.3390/e22040451
36. Hernández-Lemus E, Espinal-Enríquez J, and de Anda-Jáuregui G. *Probabilistic multilayer networks*. Ithaca, NY: arXiv:1808.07857 (2018).
37. De Domenico M, Solé-Ribalta A, Cozzo E, Kivelä M, Moreno Y, Porter MA, et al. Mathematical formulation of multilayer networks. *Phys Rev X* (2013) 3:041022. doi:10.1103/physrevx.3.041022
38. Kivelä M, Arenas A, Barthelemy M, Gleeson JP, Moreno Y, and Porter MA. Multilayer networks. *J Complex Networks* (2014) 2:203–71. doi:10.1093/comnet/cnu016

39. Boccaletti S, Bianconi G, Criado R, Del Genio CI, Gómez-Gardeñes J, Romance M, et al. The structure and dynamics of multilayer networks. *Phys Rep* (2014) 544:1–122. doi:10.1016/j.physrep.2014.07.001
40. Aizenman M, and Peled R. A power-law upper bound on the correlations in the 2d random field Ising model. *Commun Math Phys* (2019) 372:865–92. doi:10.1007/s00220-019-03450-3
41. Imry Y, and Ma S-K. Random-field instability of the ordered state of continuous symmetry. *Phys Rev Lett* (1975) 35:1399. doi:10.1103/physrevlett.35.1399
42. Berzin AA, Morosov AI, and Sigov AS. Long-range order induced by random fields in two-dimensional O(n) models, and the imry-ma state. *Phys Solid State* (2020) 62:332–7. doi:10.1134/s1063783420020055
43. Berzin AA, Morosov AI, and Sigov AS. A mechanism of long-range order induced by random fields: effective anisotropy created by defects. *Phys Solid State* (2016) 58:1846–9. doi:10.1134/s1063783416090109
44. Bunde A, Havlin S, Roman HE, Schildt G, and Stanley HE. On the field dependence of random walks in the presence of random fields. *J Stat Phys* (1988) 50:1271–6. doi:10.1007/bf01019166
45. Chatterjee S. On the decay of correlations in the random field Ising model. *Commun Math Phys* (2018) 362:253–67. doi:10.1007/s00220-018-3085-0
46. Aizenman M, and Wehr J. Rounding of first-order phase transitions in systems with quenched disorder. *Phys Rev Lett* (1989) 62:2503. doi:10.1103/physrevlett.62.2503
47. Fytas NG, Martín-Mayor V, Picco M, and Sourlas N. Specific-heat exponent and modified hyperscaling in the 4d random-field Ising model. *J Stat Mech* (2017) 2017:033302. doi:10.1088/1742-5468/aa5dc3
48. Fytas NG, Martín-Mayor V, Picco M, and Sourlas N. Review of recent developments in the random-field Ising model. *J Stat Phys* (2018) 172:665–72. doi:10.1007/s10955-018-1955-7
49. Tarjus G, and Tissier M. Random-field Ising and o (n) models: theoretical description through the functional renormalization grou. *The Eur Phys J B* (2020) 93:1–19. doi:10.1140/epjb/e2020-100489-1
50. Ayala M, Carinci G, and Redig F. Quantitative Boltzmann-gibbs principles via orthogonal polynomial duality. *J Stat Phys* (2018) 171:980–99. doi:10.1007/s10955-018-2060-7
51. Dobrushin RL. Perturbation methods of the theory of gibbsian fields. Lectures on probability theory and statistics. Springer (1996) 1–66. doi:10.1007/bfb0095674
52. Essler FHL, Mussardo G, and Panfil M. On truncated generalized Gibbs ensembles in the Ising field theory. *J Stat Mech* (2017) 2017:013103. doi:10.1088/1742-5468/aa53f4
53. Gudder SP. Gaussian random fields. *Found Phys* (1978) 8:295–302. doi:10.1007/bf00715214
54. Sherman S. Markov random fields and Gibbs random fields. *Isr J Math* (1973) 14:92–103. doi:10.1007/bf02761538
55. Luitz DJ, Laflorencie N, and Alet F. Many-body localization edge in the random-field heisenberg chain. *Phys Rev B* (2015) 91:081103. doi:10.1103/physrevb.91.081103
56. Starodubov SL. *A theorem on properties of sample functions of a random field and generalized random fields*. Moscow, Russia: Izvestiya Vysshikh Uchebnykh Zavedenii. Matematika (2011) 48–56.
57. Acar P, and Sundararaghavan V. A Markov random field approach for modeling spatio-temporal evolution of microstructures. *Model Simul Mater Sci Eng* (2016) 24:075005. doi:10.1088/0965-0393/24/7/075005
58. Koninckx T, and Krakoviack V. Dynamics of fluids in quenched-random potential energy landscapes: a mode-coupling theory approach. *Soft matter* (2017) 13:5283–97. doi:10.1039/c7sm00984d
59. Liu Y, Hu J, Wei H, and Saw A-L. A direct simulation algorithm for a class of beta random fields in modelling material properties. *Comput Methods Appl Mech Eng* (2017) 326:642–55. doi:10.1016/j.cma.2017.08.001
60. Chen J, He J, Ren X, and Li J. Stochastic harmonic function representation of random fields for material properties of structures. *J Eng Mech* (2018) 144:04018049. doi:10.1061/(asce)em.1943-7889.0001469
61. Singh R, and Adhikari R. Fluctuating hydrodynamics and the brownian motion of an active colloid near a wall. *Eur J Comput Mech* (2017) 26:78–97. doi:10.1080/17797179.2017.1294829
62. Yamazaki K. Stochastic hall-magneto-hydrodynamics system in three and two and a half dimensions. *J Stat Phys* (2017) 166:368–97. doi:10.1007/s10955-016-1683-9
63. Ullah H, Uzair M, Ullah M, Khan A, Ahmad A, and Khan W. Density independent hydrodynamics model for crowd coherency detection. *Neurocomputing* (2017) 242:28–39. doi:10.1016/j.neucom.2017.02.023
64. Tadić B, Mijatović S, Janićević S, Spasojević D, and Rodgers GJ. The critical barkhausen avalanches in thin random-field ferromagnets with an open boundary. *Scientific Rep* (2019) 9:1–13. doi:10.1038/s41598-019-42802-w
65. Tsukanov AA, and Gorbatnikov AV. Influence of embedded inhomogeneities on the spectral ratio of the horizontal components of a random field of Rayleigh waves. *Acoust Phys* (2018) 64:70–6. doi:10.1134/s1063771018010189
66. Shadaydeh M, Guanche Y, and Denzler J. *Classification of spatiotemporal marine climate patterns using wavelet coherence and markov random field*. American Geophysical Union (2018). Fall Meeting 2018IN31C–0824.
67. Feng R, Luthi SM, Gisolf D, and Angerer E. Reservoir lithology determination by hidden Markov random fields based on a Gaussian mixture model. *IEEE Trans Geosci Remote Sensing* (2018) 56:6663–73. doi:10.1109/tgrs.2018.2841059
68. Wang H, Wellmann F, Verweij E, von Hebel C, and van der Kruk J. *Identification and simulation of subsurface soil patterns using hidden markov random fields and remote sensing and geophysical emi data sets*. Vienna, Austria: EGUGA (2017) 6530.
69. Ko GG, and Rutenbar RA. A case study of machine learning hardware: real-time source separation using Markov random fields via sampling-based inference. IEEE International Conference on Acoustics, Speech and Signal Processing (ICASSP). (IEEE) (2017) 2477–81.
70. Li J, Jiang P, and Zhu H. *A local region-based level set method with markov random field for side-scan sonar image multi-level segmentation*. IEEE Sensors Journal (2020).
71. Ziatdinov M, Maksov A, and Kalinin SV. Learning surface molecular structures via machine vision. *npj Comput Mater* (2017) 3:1–9. doi:10.1038/s41524-017-0038-7
72. Ciliberto C, Herbster M, Ialongo AD, Pontil M, Rocchetto A, Severini S, et al. Quantum machine learning: a classical perspective. *Proc R Soc A* (2018) 474:20170551. doi:10.1098/rspa.2017.0551
73. Li Y, and Ping W. *Cancer metastasis detection with neural conditional random field*. Ithaca, NY: arXiv:1806.07064 (2018).
74. Zhang Z, Zhao T, Gay H, Zhang W, and Sun B. Arpm-net: a novel cnn-based adversarial method with Markov random field enhancement for prostate and organs at risk segmentation in pelvic ct images. *Med Phys* (2020). doi:10.1002/mp.14580
75. Fu H, Xu Y, Lin S, Kee Wong DW, and Liu J. Deepvessel: retinal vessel segmentation via deep learning and conditional random field. International conference on medical image computing and computer-assisted intervention. Springer (2016) 132–9. doi:10.1007/978-3-319-46723-8_16
76. Orlando JI, Prokofyeva E, and Blaschko MB. A discriminatively trained fully connected conditional random field model for blood vessel segmentation in fundus images. *IEEE Trans Biomed Eng* (2016) 64:16–27. doi:10.1109/TBME.2016.2535311
77. Reta C, Gonzalez J, Diaz R, and Guichard J. *Leukocytes segmentation using markov random fields. Software Tools and Algorithms for Biological Systems*. Springer (2011) 345–53.
78. Hahn A, Bode J, Krüwel T, Kampf T, Buschle LR, Sturm VJF, et al. Gibbs point field model quantifies disorder in microvasculature of u87-glioblastoma. *J Theor Biol* (2020) 494:110230. doi:10.1016/j.jtbi.2020.110230
79. Mahmood F, and Durr NJ. Deep learning and conditional random fields-based depth estimation and topographical reconstruction from conventional endoscopy. *Med image Anal* (2018) 48:230–43. doi:10.1016/j.media.2018.06.005
80. Sari NLK, Prajitno P, Lubis LE, and Soejoko DS. Computer aided diagnosis (cad) for mammography with Markov random field method with simulated annealing optimization. *J Med Phys Biophys* (2017) 4:84–93.
81. Nitzken MJ, El-Baz AS, and Beache GM. Markov-gibbs random field model for improved full-cardiac cycle strain estimation from tagged cmr. *J Cardiovasc Magn Reson* (2012) 14:1–2. doi:10.1186/1532-429x-14-s1-p258
82. Johansen AR, Sønderby CK, Sønderby SK, and Winther O. Deep recurrent conditional random field network for protein secondary prediction. Proceedings of the 8th ACM international conference on bioinformatics,

computational biology, and health informatics, Boston, MA: ACM-BCB '17 (2017) 73–8.
83. Yanover C, and Fromer M. Prediction of low energy protein side chain configurations using Markov random fields. Bayesian Methods in Structural Bioinformatics. Springer (2012) 255–84. doi:10.1007/978-3-642-27225-7_11
84. Xu J, Wang S, and Ma J. *Protein homology detection through alignment of markov random fields: using MRFalign*. Springer (2015).
85. Ma J, Wang S, Wang Z, and Xu J. Mrfalign: protein homology detection through alignment of Markov random fields. *Plos Comput Biol* (2014) 10: e1003500. doi:10.1371/journal.pcbi.1003500
86. Wilburn GW, and Eddy SR. Remote homology search with hidden potts models. *Plos Comput Biol* (2020) 16:e1008085. doi:10.1371/journal.pcbi.1008085
87. Gehrmann T, Loog M, Reinders MJT, and de Ridder D. Conditional random fields for protein function prediction. IAPR International Conference on Pattern Recognition in Bioinformatics. Springer (2013) 184–95. doi:10.1007/978-3-642-39159-0_17
88. Loeliger H-A, Dauwels J, Hu J, Korl S, Ping L, and Kschischang FR. The factor graph approach to model-based signal processing. *Proc IEEE* (2007) 95: 1295–322. doi:10.1109/jproc.2007.896497
89. Ray WC, Wolock SL, Callahan NW, Dong M, Li QQ, Liang C, et al. Addressing the unmet need for visualizing conditional random fields in biological data. *BMC bioinformatics* (2014) 15:202. doi:10.1186/1471-2105-15-202
90. Geman S, and Geman D. *Stochastic relaxation, gibbs distributions, and the bayesian restoration of images*. IEEE Transactions on pattern analysis and machine intelligence (1984) 721–41.
91. Xu Z, Zhang G, Jin F, Chen M, Furey TS, Sullivan PF, et al. A hidden Markov random field-based bayesian method for the detection of long-range chromosomal interactions in hi-c data. *Bioinformatics* (2016) 32:650–6. doi:10.1093/bioinformatics/btv650
92. Wu H, Wang K, Lu L, Xue Y, Lyu Q, and Jiang M. Deep conditional random field approach to transmembrane topology prediction and application to gpcr three-dimensional structure modeling. *Ieee/acm Trans Comput Biol Bioinform* (2016) 14:1106–14. doi:10.1109/TCBB.2016.2602872
93. Kordmahalleh MM, Sefidmazgi MG, Harrison SH, and Homaifar A. Identifying time-delayed gene regulatory networks via an evolvable hierarchical recurrent neural network. *BioData mining* (2017) 10:29. doi:10.1186/s13040-017-0146-4
94. Gitter A, Huang F, Valluvan R, Fraenkel E, and Anandkumar A. *Unsupervised learning of transcriptional regulatory networks via latent tree graphical models*. Ithaca, NY: arXiv:1609.06335 (2016).
95. Zhong W, Dong L, Poston TB, Darville T, Spracklen CN, Wu D, et al. Inferring regulatory networks from mixed observational data using directed acyclic graphs. *Front Genet* (2020) 11:8. doi:10.3389/fgene.2020.00008
96. Ma S, Jiang T, and Jiang R. Constructing tissue-specific transcriptional regulatory networks via a Markov random field. *BMC genomics* (2018) 19: 65–77. doi:10.1186/s12864-018-5277-6
97. Kolmogorov V, and Zabih R. What energy functions can be minimized via graph cuts?. *IEEE Trans Pattern Anal Machine Intell* (2004) 26:147–59. doi:10.1109/tpami.2004.1262177
98. Banf M, and Rhee SY. Enhancing gene regulatory network inference through data integration with Markov random fields. *Scientific Rep* (2017) 7:1–13. doi:10.1038/srep41174
99. Grimes T, Potter SS, and Datta S. Integrating gene regulatory pathways into differential network analysis of gene expression data. *Scientific Rep* (2019) 9: 1–12. doi:10.1038/s41598-019-41918-3
100. Wei Z, and Li H. A Markov random field model for network-based analysis of genomic data. *Bioinformatics* (2007) 23:1537–44. doi:10.1093/bioinformatics/btm129
101. Gomez-Romero L, Lopez-Reyes K, and Hernandez-Lemus E. The large scale structure of human metabolism reveals resilience via extensive signaling crosstalk. *Front Physiol* (2020) 11:1667. doi:10.3389/fphys.2020.588012
102. Lin Z, Li M, Sestan N, and Zhao H. A Markov random field-based approach for joint estimation of differentially expressed genes in mouse transcriptome data. *Stat Appl Genet Mol Biol* (2016) 15:139–50. doi:10.1515/sagmb-2015-0070
103. Chen M, Cho J, and Zhao H. Incorporating biological pathways via a Markov random field model in genome-wide association studies. *Plos Genet* (2011) 7: e1001353. doi:10.1371/journal.pgen.1001353
104. Long Y, Wu M, Kwoh CK, Luo J, and Li X. Predicting human microbe-drug associations via graph convolutional network with conditional random field. *Bioinformatics* (2020) 36:4918–27. doi:10.1093/bioinformatics/btaa598
105. Xu J, Yang P, Xue S, Sharma B, Sanchez-Martin M, Wang F, et al. Translating cancer genomics into precision medicine with artificial intelligence: applications, challenges and future perspectives. *Hum Genet* (2019) 138: 109–24. doi:10.1007/s00439-019-01970-5
106. Fariselli P, Savojardo C, Martelli PL, and Casadio R. Grammatical-restrained hidden conditional random fields for bioinformatics applications. *Algorithms Mol Biol* (2009) 4:13. doi:10.1186/1748-7188-4-13
107. Zhang NR, Yakir B, Xia LC, and Siegmund D. Scan statistics on Poisson random fields with applications in genomics. *Ann Appl Stat* (2016) 10: 726–55. doi:10.1214/15-aoas892
108. Urbain J, Frieder O, and Goharian N. Passage relevance models for genomics search. Proceedings of the 2nd international workshop on Data and text mining in bioinformatics. New York, NY: DTMBIO '08 (2008) 45–52.
109. Wang X, Li Y, He T, Jiang X, and Hu X. Recognition of bacteria named entity using conditional random fields in spark. *BMC Syst Biol* (2018) 12:106. doi:10.1186/s12918-018-0625-3
110. McDonald R, and Pereira F. Identifying gene and protein mentions in text using conditional random fields. *BMC bioinformatics* (2005) 6:S6. doi:10.1186/1471-2105-6-s1-s6
111. Vecchyo OD, Marsden CD, and Lohmueller KE. Prefersim: fast simulation of demography and selection under the Poisson random field model. *Bioinformatics* (2016) 32:3516–8. doi:10.1093/bioinformatics/btw478
112. François O, Ancelet S, and Guillot G. Bayesian clustering using hidden Markov random fields in spatial population genetics. *Genetics* (2006) 174: 805–16. doi:10.1534/genetics.106.059923
113. Clark NJ, Wells K, and Lindberg O. Unravelling changing interspecific interactions across environmental gradients using Markov random fields. *Ecology* (2018) 99:1277–83. doi:10.1002/ecy.2221
114. Salinas NR, and Wheeler WC. Statistical modeling of distribution patterns: a Markov random field implementation and its application on areas of endemism. *Syst Biol* (2020) 69:76–90. doi:10.1093/sysbio/syz033
115. Shen Y, and Van Deelen TR. *Spatially explicit modeling of community occupancy using markov random field models with imperfect observation: mesocarnivores in apostle islands national lakeshore*. Cold Spring Harbor, NY: BioRxiv (2020).
116. Kozik R. Improving depth map quality with Markov random fields. Image Processing and Communications Challenges. Springer (2011) 149–56. doi:10.1007/978-3-642-23154-4_17
117. Stephenson TA, and Chen T. Adaptive Markov random fields for example-based super-resolution of faces. *EURASIP J Adv Signal Process* (2006) 2006: 031062. doi:10.1155/asp/2006/31062
118. Li C, and Wand M. Combining Markov random fields and convolutional neural networks for image synthesis. Proceedings of the IEEE Conference on Computer Vision and Pattern Recognition. Ithaca, NY: arXiv:1601.04589 (2016) 2479–86.
119. Wen M, Han H, Wang L, and Wang W. 2d conditional random fields for image classification. International Conference on Intelligent Information Processing. Springer (2006) 383–90.
120. Bohorquez M, Giraldo R, and Mateu J. Multivariate functional random fields: prediction and optimal sampling. *Stoch Environ Res Risk Assess* (2017) 31: 53–70. doi:10.1007/s00477-016-1266-y
121. Baca-Lopez K, Fresno C, Espinal-Enríquez J, Martinez-Garcia M, Camacho-Lopez MA, Flores-Merino MV, et al. Spatio-temporal representativeness of air quality monitoring stations in Mexico city: implications for public health. *Front Public Health* (2020) 8:849. doi:10.3389/fpubh.2020.536174
122. Baca-Lopez K, Fresno C, Espinal-Enriquez J, Flores-Merino MV, Camacho-Lopez MA, and Hernandez-Lemus E. *Metropolitan age-specific mortality trends at borough and neighbourhood level: the case of Mexico city* (2020).
123. Wang H, Wellmann JF, Li Z, Wang X, and Liang RY. A segmentation approach for stochastic geological modeling using hidden Markov random fields. *Math Geosci* (2017) 49:145–77. doi:10.1007/s11004-016-9663-9

124. Li Z, Wang X, Wang H, and Liang RY. Quantifying stratigraphic uncertainties by stochastic simulation techniques based on Markov random field. *Eng Geology* (2016) 201:106–22. doi:10.1016/j.enggeo.2015.12.017
125. Rue H, and Held L. *Gaussian Markov random fields: theory and applications*. Boca Raton, FL: CRC Press (2005).
126. Solberg AHS, Taxt T, and Jain AK. A Markov random field model for classification of multisource satellite imagery. *IEEE Trans Geosci Remote Sensing* (1996) 34:100–13. doi:10.1109/36.481897
127. Toftaker H, and Tjelmeland H. Construction of binary multi-grid Markov random field prior models from training images. *Math Geosci* (2013) 45: 383–409. doi:10.1007/s11004-013-9456-3
128. Reuschen S, Xu T, and Nowak W. Bayesian inversion of hierarchical geostatistical models using a parallel-tempering sequential Gibbs mcmc. *Adv Water Resour* (2020) 141:103614. doi:10.1016/j.advwatres.2020.103614
129. Sutton C, and McCallum A. An introduction to conditional random fields for relational learning. *Introduction Stat relational Learn* (2006) 2:93–128.
130. Gilks WR, and Wild P. Adaptive rejection sampling for Gibbs sampling. *Appl Stat* (1992) 41:337–48. doi:10.2307/2347565
131. Gilks WR, Best NG, and Tan KKC. Adaptive rejection metropolis sampling within Gibbs sampling. *Appl Stat* (1995) 44:455–72. doi:10.2307/2986138
132. Meyer R, Cai B, and Perron F. Adaptive rejection metropolis sampling using Lagrange interpolation polynomials of degree 2. *Comput Stat Data Anal* (2008) 52:3408–23. doi:10.1016/j.csda.2008.01.005
133. Martino L, Read J, and Luengo D. Independent doubly adaptive rejection metropolis sampling within Gibbs sampling. *IEEE Trans Signal Process* (2015) 63:3123–38. doi:10.1109/tsp.2015.2420537
134. Papanikolaou Y, Foulds JR, Rubin TN, and Tsoumakas G. Dense distributions from sparse samples: improved Gibbs sampling parameter estimators for lda. *J Machine Learn Res* (2017) 18:2058–115.
135. Norton RA, Christen JA, and Fox C. Sampling hyperparameters in hierarchical models: improving on Gibbs for high-dimensional latent fields and large datasets. *Commun Stat - Simulation Comput* (2018) 47: 2639–55. doi:10.1080/03610918.2017.1353618
136. Gao S, and Gormley MR. Training for Gibbs sampling on conditional random fields with neural scoring factors. Proceedings of the 2020 Conference on Empirical Methods in Natural Language Processing. Punta Cana, Dominican Republic: EMNLP (2020) 4999–5011.
137. Boland A, Friel N, and Maire F. Efficient mcmc for Gibbs random fields using pre-computation. *Electron J Statist* (2018) 12:4138–79. doi:10.1214/18-ejs1504
138. Kaplan A, Kaiser MS, Lahiri SN, and Nordman DJ. Simulating Markov random fields with a conclique-based Gibbs sampler. *J Comput Graphical Stat* (2020) 29:286–96. doi:10.1080/10618600.2019.1668800
139. Marcotte D, and Allard D. Gibbs sampling on large lattice with gmrf. *Comput Geosciences* (2018) 111:190–9. doi:10.1016/j.cageo.2017.11.012
140. Ko GG, Chai Y, Rutenbar RA, Brooks D, and Wei GY. Flexgibbs: reconfigurable parallel Gibbs sampling accelerator for structured graphs. IEEE 27th Annual International Symposium on Field-Programmable Custom Computing Machines (FCCM). IEEE (2019) 334.
141. Liu W, and Wu L. Large deviations for empirical measures of mean-field Gibbs measures. *Stochastic Process their Appl* (2020) 130:503–20. doi:10.1016/j.spa.2019.01.008
142. Eldan R, and Gross R. Decomposition of mean-field Gibbs distributions into product measures. *Electron J Probab* (2018) 23. doi:10.1214/18-ejp159
143. Shafer GR, and Shenoy PP. Probability propagation. *Ann Math Artif Intell* (1990) 2:327–51. doi:10.1007/bf01531015
144. Zhang NL, and Poole D. Intercausal independence and heterogeneous factorization. Uncertainty Proceedings. Elsevier (1994) 606–14. doi:10.1016/b978-1-55860-332-5.50082-1
145. Kompass R. A generalized divergence measure for nonnegative matrix factorization. *Neural Comput* (2007) 19:780–91. doi:10.1162/neco.2007.19.3.780
146. Cichocki A, Lee H, Kim Y-D, and Choi S. Non-negative matrix factorization with α-divergence. *Pattern Recognition Lett* (2008) 29:1433–40. doi:10.1016/j.patrec.2008.02.016
147. Ding C, Li T, and Peng W. On the equivalence between non-negative matrix factorization and probabilistic latent semantic indexing. *Comput Stat Data Anal* (2008) 52:3913–27. doi:10.1016/j.csda.2008.01.011
148. Xie Y, and Berkowitz CM. The use of positive matrix factorization with conditional probability functions in air quality studies: an application to hydrocarbon emissions in houston, Texas. *Atmos Environ* (2006) 40:3070–91. doi:10.1016/j.atmosenv.2005.12.065
149. Xu J, Cai L, Liao B, Zhu W, Wang P, Meng Y, et al. Identifying potential mirna-disease associations with probability matrix factorization. *Front Genet* (2019) 10:1234. doi:10.3389/fgene.2019.01234
150. Wang Z, Liang J, and Li R. A fusion probability matrix factorization framework for link prediction. *Knowledge-Based Syst* (2018) 159:72–85. doi:10.1016/j.knosys.2018.06.005
151. Stoehr J, Marin J-M, and Pudlo P. Hidden Gibbs random fields model selection using block likelihood information criterion. *Stat* (2016) 5:158–72. doi:10.1002/sta4.112
152. Cilla R, Patricio MA, Berlanga A, and Molina JM. Model and feature selection in hidden conditional random fields with group regularization. International Conference on Hybrid Artificial Intelligence Systems. Springer (2013) 140–9. doi:10.1007/978-3-642-40846-5_15
153. Sain SR, and Furrer R. Comments on: some recent work on multivariate Gaussian Markov random fields. *Test* (2018) 27:545–8. doi:10.1007/s11749-018-0609-z
154. Zhu J, Lao N, and Xing E. Grafting-light: fast, incremental feature selection and structure learning of Markov random fields. Proceedings of the 16th ACM SIGKDD international conference on Knowledge discovery and data mining (2010), 303–12.
155. Liao L, Choudhury T, Fox D, and Kautz HA. Training conditional random fields using virtual evidence boosting. *Ijcai* (2007) 7:2530–5.
156. Lafferty J, Zhu X, and Liu Y. Kernel conditional random fields: representation and clique selection. Proceedings of the twenty-first international conference on Machine learning. New York, NY: ICML '04 (2004) 64.
157. Zhu J, Wang H, and Mao J. Sentiment classification using genetic algorithm and conditional random fields. IEEE international conference on information management and engineering. IEEE (2010) 193–6.
158. Metzler DA. Automatic feature selection in the Markov random field model for information retrieval. Proceedings of the sixteenth ACM conference on Conference on information and knowledge management. (2007) 253–62.
159. Aliferis CF, Statnikov A, Tsamardinos I, Mani S, and Koutsoukos XD. Local causal and Markov blanket induction for causal discovery and feature selection for classification part i: algorithms and empirical evaluation. *J Machine Learn Res* (2010) 11.
160. Adams S, Beling PA, and Cogill R. Feature selection for hidden Markov models and hidden semi-markov models. *IEEE Access* (2016) 4:1642–57. doi:10.1109/access.2016.2552478
161. Brownlee AEI, Regnier-Coudert O, McCall JAW, Massie S, and Stulajter S. An application of a ga with Markov network surrogate to feature selection. *Int J Syst Sci* (2013) 44:2039–56. doi:10.1080/00207721.2012.684449
162. Yu L, and Liu H. Efficient feature selection via analysis of relevance and redundancy. *J machine Learn Res* (2004) 5:1205–24.
163. Slawski M, zu Castell W, and Tutz G. Feature selection guided by structural information. *Ann Appl Stat* (2010) 4:1056–80. doi:10.1214/09-aoas302
164. Adams S, and Beling PA. A survey of feature selection methods for Gaussian mixture models and hidden Markov models. *Artif Intell Rev* (2019) 52: 1739–79. doi:10.1007/s10462-017-9581-3
165. Vergara JR, and Estévez PA. A review of feature selection methods based on mutual information. *Neural Comput Applic* (2014) 24:175–86. doi:10.1007/s00521-013-1368-0
166. Liu Z, Li X, Luo P, Change Loy C, and Tang X. Deep learning Markov random field for semantic segmentation. *IEEE Trans Pattern Anal Mach Intell* (2017) 40:1814–28. doi:10.1109/TPAMI.2017.2737535
167. Hu R, Rohrbach M, and Darrell T. Segmentation from natural language expressions. European Conference on Computer Vision. Springer (2016) 108–24. doi:10.1007/978-3-319-46448-0_7
168. Guo J, He H, He T, Lausen L, Li M, Lin H, et al. Gluoncv and gluonnlp: deep learning in computer vision and natural language processing. *J Machine Learn Res* (2020) 21:1–7.
169. Zhang H, Zhang H, Wang C, and Xie J. Co-occurrent features in semantic segmentation. Proceedings of the IEEE Conference on Computer Vision and Pattern Recognition (2019), 548–57.

170. Mai F, Wu S, and Cui T. Improved Chinese word segmentation disambiguation model based on conditional random fields. Proceedings of the 4th International Conference on Computer Engineering and Networks. Springer (2015) 599–605. doi:10.1007/978-3-319-11104-9_70
171. Qiu J, Zhou Y, Wang Q, Ruan T, and Gao J. Chinese clinical named entity recognition using residual dilated convolutional neural network with conditional random field. *IEEE Trans.on Nanobioscience* (2019) 18: 306–15. doi:10.1109/tnb.2019.2908678
172. Khan W, Daud A, Nasir JA, Amjad T, Arafat S, Aljohani N, et al. Urdu part of speech tagging using conditional random fields. *Lang Resour Eval* (2019) 53: 331–62. doi:10.1007/s10579-018-9439-6
173. Nguyen DM, Do TH, Calderbank R, and Deligiannis N. Fake news detection using deep Markov random fields. Proceedings of the 2019 Conference of the North American Chapter of the Association for Computational Linguistics: Human Language Technologies. Minneapolis, MN: Long and Short Papers (2019) 1391–400.
174. Colmenares CA, Litvak M, Mantrach A, Silvestri F, and Rodríguez H. *Headline generation as a sequence prediction with conditional random fields*. Singapore City, Singapore: Multilingual Text Analysis: Challenges, Models, and Approaches (2019) 201.
175. Knoke D, and Yang S. *Social network analysis*. Perth, Australia: Sage Publications (2019).
176. Jia J, Wang B, Zhang L, and Gong NZ. Attriinfer: inferring user attributes in online social networks using Markov random fields. Proceedings of the 26th International Conference on World Wide Web (2017) 1561–9.
177. Jin D, Liu Z, Li W, He D, and Zhang W. Graph convolutional networks meet Markov random fields: semi-supervised community detection in attribute networks. *Aaai* (2019) 33:152–9. doi:10.1609/aaai.v33i01.3301152
178. Feng B, Li Q, Ji Y, Guo D, and Meng X. *Stopping the cyberattack in the early stage: assessing the security risks of social network users*. Security and Communication Networks (2019).
179. Zhou Q, Xu Z, and Yen NY. User sentiment analysis based on social network information and its application in consumer reconstruction intention. *Comput Hum Behav* (2019) 100:177–83. doi:10.1016/j.chb.2018.07.006
180. Yoon S, Kleinman M, Mertz J, and Brannick M. Is social network site usage related to depression? A meta-analysis of Facebook-depression relations. *J affective Disord* (2019) 248:65–72. doi:10.1016/j.jad.2019.01.026
181. Ö B, Alexander SM, Baggio J, Barnes ML, Berardo R, Cumming GS, et al. Improving network approaches to the study of complex social–ecological interdependencies. *Nat Sustainability* (2019) 2:551–9. doi:10.1038/s41893-019-0308-0
182. Bhattacharya R, Malinsky D, and Shpitser I. Causal inference under interference and network uncertainty. Uncertainty in Artificial Intelligence (PMLR). Ithaca, NY: arXiv:1907.00221 (2020) 1028–38.
183. Stanković L, Daković M, and Sejdić E. Introduction to graph signal processing. Vertex-Frequency Analysis of Graph Signals. Springer (2019) 3–108.
184. Stankovic L, Mandic DP, Dakovic M, Kisil I, Sejdic E, and Constantinides AG. Understanding the basis of graph signal processing via an intuitive example-driven approach [lecture notes]. *IEEE Signal Process Mag* (2019) 36:133–45. doi:10.1109/msp.2019.2929832
185. Ortega A, Frossard P, Kovacevic J, Moura JMF, and Vandergheynst P. Graph signal processing: overview, challenges, and applications. *Proc IEEE* (2018) 106:808–28. doi:10.1109/jproc.2018.2820126
186. Gadde A, and Ortega A. A probabilistic interpretation of sampling theory of graph signals. IEEE international conference on Acoustics, Speech and Signal Processing (ICASSP). (IEEE) (2015) 3257–61.
187. Chen S, Sandryhaila A, and Kovačević J. Sampling theory for graph signals. IEEE International Conference on Acoustics, Speech and Signal Processing (ICASSP). (IEEE) (2015) 3392–6.
188. Stanković L, and Sejdić E. *Vertex-frequency analysis of graph signals*. Springer (2019).
189. Pavez E, and Ortega A. Generalized laplacian precision matrix estimation for graph signal processing. IEEE International Conference on Acoustics, Speech and Signal Processing (ICASSP). (IEEE) (2016) 6350–4.
190. Sandryhaila A, and Moura JM. Discrete signal processing on graphs: graph fourier transform. IEEE International Conference on Acoustics, Speech and Signal Processing. IEEE (2013) 6167–70.
191. Mateos G, Segarra S, Marques AG, and Ribeiro A. Connecting the dots: identifying network structure via graph signal processing. *IEEE Signal Process Mag* (2019) 36:16–43. doi:10.1109/msp.2018.2890143
192. Ji F, and Tay WP. A hilbert space theory of generalized graph signal processing. *IEEE Trans Signal Process* (2019) 67:6188–203. doi:10.1109/tsp.2019.2952055
193. Itani S, and Thanou D. A graph signal processing framework for the classification of temporal brain data. 28th European Signal Processing Conference (EUSIPCO). (IEEE) (2021) 1180–4.
194. Ramakrishna R, and Scaglione A. Detection of false data injection attack using graph signal processing for the power grid. IEEE Global Conference on Signal and Information Processing (GlobalSIP). (IEEE) (2019) 1–5.
195. Stankovic L, Mandic D, Dakovic M, Brajovic M, Scalzo B, Li S, et al. *Graph signal processing–part iii: machine learning on graphs, from graph topology to applications*. Ithaca, NY: arXiv:2001.00426 (2020).
196. Song X, Chai L, and Zhang J. *Graph signal processing approach to qsar/qspr model learning of compounds*. IEEE Transactions on Pattern Analysis and Machine Intelligence (2020).
197. Burkhardt DB, Stanley JS, Perdigoto AL, Gigante SA, Herold KC, Wolf G, et al. *Quantifying the effect of experimental perturbations in single-cell rna-sequencing data using graph signal processing*. Cold Spring Harbor, NY: bioRxiv (2019) 532846.
198. Colonnese S, Pagliari G, Biagi M, Cusani R, and Scarano G. Compound Markov random field model of signals on graph: an application to graph learning. 7th European Workshop on Visual Information Processing (EUVIP). (IEEE) (2018) 1–5.
199. Torkamani R, and Zayyani H. *Statistical graph signal recovery using variational bayes*. IEEE Transactions on Circuits and Systems II: Express Briefs (2020).
200. Ramezani-Mayiami M, Hajimirsadeghi M, Skretting K, Blum RS, and Poor HV. *Graph topology learning and signal recovery via bayesian inference*. IEEE Data Science Workshop (DSW) (IEEE) (2019) 52–6.
201. Colonnese S, Lorenzo PD, Cattai T, Scarano G, and Fallani FDV. A joint Markov model for communities, connectivity and signals defined over graphs. *IEEE Signal Process Lett* (2020) 27:1160–4. doi:10.1109/lsp.2020.3005053
202. Dong X, Thanou D, Rabbat M, and Frossard P. Learning graphs from data: a signal representation perspective. *IEEE Signal Process Mag* (2019) 36:44–63. doi:10.1109/msp.2018.2887284
203. Cheung M, Shi J, Wright O, Jiang LY, Liu X, and Moura JMF. Graph signal processing and deep learning: convolution, pooling, and topology. *IEEE Signal Process Mag* (2020) 37:139–49. doi:10.1109/msp.2020.3014594
204. Jia J, and Benson AR. *A unifying generative model for graph learning algorithms: label propagation, graph convolutions, and combinations*. Ithaca, NY: arXiv:2101.07730 (2021).
205. Gama F, and Ribeiro A. Ergodicity in stationary graph processes: a weak law of large numbers. *IEEE Trans Signal Process* (2019) 67:2761–74. doi:10.1109/tsp.2019.2908909
206. Segarra S, Wang Y, Uhler C, and Marques AG. Joint inference of networks from stationary graph signals. 51st Asilomar Conference on Signals, Systems, and Computers. (IEEE) (2017) 975–979.

Conflict of Interest: The author declares that the research was conducted in the absence of any commercial or financial relationships that could be construed as a potential conflict of interest.

frontiers in Physics

ORIGINAL RESEARCH
published: 22 April 2021
doi: 10.3389/fphy.2021.635269

On the Time Transition Between Short- and Long-Time Regimes of Colloidal Particles in External Periodic Potentials

Daniela Pérez-Guerrero[1], *José Luis Arauz-Lara*[1], *Erick Sarmiento-Gómez*[2]* and *Guillermo Iván Guerrero-García*[3]*

[1]Instituto de Física, Universidad Autónoma de San Luis Potosí, San Luis Potosí, México, [2]Departamento de Ingeniería Física, División de Ciencias e Ingenierías, Universidad de Guanajuato, León, México, [3]Facultad de Ciencias, Universidad Autónoma de San Luis Potosí, San Luis Potosí, México

OPEN ACCESS

Edited by:
Atahualpa Kraemer, National Autonomous University of Mexico, Mexico

Reviewed by:
Michael Schmiedeberg, Friedrich-Alexander-Universität Erlangen-Nürnberg, Germany
Francisco J. Sevilla, Universidad Nacional Autónoma de México, Mexico

***Correspondence:**
Erick Sarmiento-Gómez
esarmiento@fisica.ugto.mx
Guillermo Iván Guerrero-García
givan@uaslp.mx

Specialty section:
This article was submitted to Soft Matter Physics, a section of the journal Frontiers in Physics

Received: *30 November 2020*
Accepted: *03 February 2021*
Published: *22 April 2021*

Citation:
Pérez-Guerrero D, Arauz-Lara JL, Sarmiento-Gómez E and Guerrero-García GI (2021) On the Time Transition Between Short- and Long-Time Regimes of Colloidal Particles in External Periodic Potentials. Front. Phys. 9:635269. doi: 10.3389/fphy.2021.635269

The dynamics of colloidal particles at infinite dilution, under the influence of periodic external potentials, is studied here *via* experiments and numerical simulations for two representative potentials. From the experimental side, we analyzed the motion of a colloidal tracer in a one-dimensional array of fringes produced by the interference of two coherent laser beams, providing in this way an harmonic potential. The numerical analysis has been performed *via* Brownian dynamics (BD) simulations. The BD simulations correctly reproduced the experimental position- and time-dependent density of probability of the colloidal tracer in the short-times regime. The long-time diffusion coefficient has been obtained from the corresponding numerical mean square displacement (MSD). Similarly, a simulation of a random walker in a one dimensional array of adjacent cages with a probability of escaping from one cage to the next cage is one of the most simple models of a periodic potential, displaying two diffusive regimes separated by a dynamical caging period. The main result of this study is the observation that, in both potentials, it is seen that the critical time t^*, defined as the specific time at which a change of curvature in the MSD is observed, remains approximately constant as a function of the height barrier U_0 of the harmonic potential or the associated escape probability of the random walker. In order to understand this behavior, histograms of the first passage time of the tracer have been calculated for several height barriers U_0 or escape probabilities. These histograms display a maximum at the most likely first passage time t', which is approximately independent of the height barrier U_0, or the associated escape probability, and it is located very close to the critical time t^*. This behavior suggests that the critical time t^*, defining the crossover between short- and long-time regimes, can be identified as the most likely first passage time t' as a first approximation.

Keywords: periodic potential, external field, spherical tracer, long time diffusion, most likely escape time

1 INTRODUCTION

A colloidal particle undergoing Brownian motion presents deviations from pure diffusion when such a particle interacts with an external potential or when it moves in a crowded environment. Some examples of crowded environments that affects colloidal motion include the colloidal motion of proteins or organelles in the interior of a cell [1–3], the motion of a tracer particle in complex fluids [4–9] and colloidal motion near the glass transition [10, 11]. On the other hand, examples of external fields that affect Brownian motion are electric and magnetic fields [12], gravitational forces [13–15] and optical manipulation induced by light [16, 17]. The diffusion of tracers in periodic, quasiperiodic, and random external potentials has been also studied in underdamped and overdamped conditions theoretically, experimentally and *via* numerical simulations [18–21].

On the other hand, the main effect of external potentials, or crowded environments, in colloidal dynamics is to promote the appearance of time regimes in which particles might slow down (subdiffusion) or speed up (superdiffusion) their motion as compared with normal diffusion. Generally speaking, a colloidal particle senses its environment when it moves in Brownian motion. As a result, each time regime is related to a particular length scale. The dynamics of a colloidal tracer provides useful information about the concentration of other colloidal macromolecules, the degree of coupling between the tracer and an applied external field, as well as the competition between the energy associated to the external potential and the thermal energy [4, 10, 17, 22].

One of the most simple cases where the appearance of different time regimes has been reported, due to the interaction of a particle with an inhomogeneous external field, is a one dimensional periodic potential interacting with a 2D colloidal suspension [23–25]. Such a system has many advantages: it can be simulated *via* BD simulations and can be experimentally realized by using the interference of two coherent beams, providing energy barriers of height close to the thermal energy, for laser powers smaller than 1 W [26]. A colloidal particle interacting with a periodic potential presents three time regimes related with different effects: free diffusion with a linear mean square displacement can be observed at short times; a plateau in the mean square displacement associated to "caging," produced by the existence of an energy barrier, can be seen at intermediate times; and a hopping motion of the colloidal tracer between adjacent periodic fringes in a second diffusive regime can be observed at long times [23, 24]. Similarly, a random walker simulation have been used extensively to simulate Brownian motion [27–29]. In this type of simulations, the trajectories are obtained from random numbers just as the BD simulations, but the displacement is chosen more simply, not derived from a force. Thus, the confinement is introduced as a spatial condition of no escaping from a region. The height barrier effect is then introduced as a cage-to-cage hopping probability. This allow us to observe a process similar to that displayed by a Brownian particle in a periodic potential, showing a short- and a long-time diffusive regime as a function of time. Note, however, that in the random walker simulation the particle is free to move within the cage in contrast to the cosine-like potential used in the Brownian dynamics approach.

It is important to note that the three time regimes presented above mainly depend on the periodicity of the external potential and the amplitude of the energy barrier, or the hopping probability, and they can extend over several time decades [23, 24, 30]. For example, the short time regime is related with free diffusion and thus is limited to the time the particle takes to diffuse at the bottom part of the potential; the extension of the plateau region is directly related with the amplitude of the potential, and finally the long time diffusion results of a balance between hopping time, and thus related with the amplitude of the potential, and the periodicity of the potential. Furthermore, this potential had been also studied for mean first passage time calculations, giving theoretical predictions for the ratio between the diffusion coefficients associated with its dynamics [31]. In such a scenario, colloidal dynamics can be described by the ratio between the short- and long-time diffusion coefficients [23]. Other quantities of interest are the time at which the caged motion begins, and the time at which the hopping motion starts. As indicated before, the phenomenology found in this potential can be mapped to several other situations. Thus, for complex fluids, the long-time diffusion coefficient is related to the zero shear viscosity [22], whereas the glass transition is related to the so-called alpha relaxation [32]. Despite numerous theoretical, simulation, and experimental studies that had been performed since last century, a complete characterization of the prediction of the short- and long-times diffusion coefficient, using available theoretical models, as well as the study of the critical caging time and the distribution of hoping times, is still lacking.

In this work, the dynamics of a colloidal particle in periodic potentials is studied by using experiments and simulations, focusing in the short- and long-times dynamics. We are particularly interested in the behavior of the critical time at which the MSD changes its curvature when the caging effect appears, and in the distribution of hoping times between adjacent periodic cells. We also compare our results with available theoretical predictions. Our results give a full characterization of the phenomena in terms of energy barriers and the associated dynamical caging, providing a simple model to understand the colloidal dynamics under different, but equivalent scenarios.

2 MODEL AND METHODS

2.1 Experimental Methods

The experimental system consists of a highly dilute water suspension of 1 μm polystyrene spherical particles (Thermo Scientific) confined between one microscope slide and a cover slip. The sample has been prepared by following the procedure described by Carbajal-Tinoco et al. [33].

The experimental set up for the light potential is based on the interference of two beams in the plane of the sample, which produces a periodical array of bright fringes of a specific width. This experimental setup has been fully described elsewhere [34], here we only discuss the main points. The laser beam used has a

spectral width <200 kHz (Azur Light Systems) and range powers between 40 and 500 mW. A half-wave plate and a fixed polarizer allow us to vary the input power by rotating the half-wave plate. The laser beam passes through a beam splitter, which divides the beam in two with the same laser power. Both beams are directed into a prism mirror that reflects the beams parallel each other. The prism is mounted on a base that can be moved manually to change the distance between the beams. A spherical lens initializes the convergence of both beams in order to produce the interference pattern in the focal plane of the lens. The distance of separation between the beams determines the angle ψ of incidence, which defines the periodicity of the intensity pattern. However, it also changes the effective focal distance of the lens due to spherical aberration. Thus, a focusing lens is mounted on a moving stage to correct such effect. This interferometer is coupled using a dichroic mirror to an inverted microscope (OLYMPUS U-LH100-3) with a 60X objective and numerical aperture 0.6, that allows us to obtain high quality clear field images in order to get the time evolution of the system.

The interference of the coherent beams produce an intensity pattern expressed as [35].

$$I(x) = 2I_0\{1 + \cos[2kx\sin(\psi/2)]\}e^{-2(x/\mathrm{R})^2\cos^2(\psi/2)} \quad (1)$$

where I_0 is the intensity of each beam, $k = 2\pi/\lambda_0$, with $\lambda_0 = 488\ \ nm$ the incident beam wavelength and R the laser beam radius. As it can be seen here, the periodicity of the distribution of light is directly related to the angle ψ. For our experimental conditions, the set-up is able to produce fringes between 1.3 and 6.0 μm by varying the position of the prism mirror. As shown before [34], if the periodicity of the light distribution is larger than the size of the particle, such a distribution produces a periodical potential with the same periodicity, where the bright fringes corresponds to the minima in the potential. For this study, the periodicity of the distribution of light was set to 1 μm. Similarly as in optical tweezers, instead of estimating the external potential using the distribution of light and some model of interaction of light with an spherical particle [36, 37], in this work the external potential was calibrated comparing the experimental values of the MSD with those resulting from the Brownian dynamics simulation.

The time evolution of the system has been recorded by using standard video equipment at 30 frames per second, giving an experimental time resolution of 0.033 s. The tracking of the particles has been performed by using Trackpy [38], which implements and extends the Crocker-Grier algorithm in Python language [39]. Furthermore, by placing neutral density filters on the lens of the recording camera, the intensity profile generated by the interference of the beams can be imaged, and thus the spatial position of the minima has been estimated. This is very helpful for the calculation of the spatial-dependent statistical properties. It is important to note that we analyze the trajectories of particles at the center of the field of view since the spatial distribution of light is not homogeneous at the edges due to the Gaussian envelope. This ensures that the variation of the intensity in the region of interest is less than 10%, where the particles interact with a similar external potential. The area in the region of interest corresponds to 1908.5 μm^2, and a total of 2 h of recording, divided in three videos, were analyzed, giving almost 2,000 trajectories. However, most of them are very short, corresponding to particles that remained within the region of interest only for a few frames. Such trajectories contributed to the short time dynamics, and thus giving a reliable quantification of the mean squared displacement at short times as well as of the density of probability of displacements. However, the long time dynamics lacks of statistics as only a few particles remain during the total duration of the video. The duration of each experiment was defined due to the presence of a small drift in the laser beam, producing a motion of the fringes in one direction. We found that during intervals of 20 min there is a very small variation of the position of the fringes, giving confidence in the position of the fringes. Fringes were also found to vibrate due to external mechanical noise, even tough the experiment was performed on an isolated optical table. Once we get the trajectories of the particles we are able to calculate the total average displacement and the mean square displacement of all trajectories of particles in a time interval. A schematic representation of the protocol we have described is shown in **Figure 1**.

2.2 Theoretical Model and Brownian Dynamics Simulations

In this work, we consider that a tracer particle is under the influence of a periodic cosine potential of the form:

$$U(x, U_0, L) = U_0\left(1 - \cos\left(\frac{2\pi x}{L}\right)\right) \quad (2)$$

where U_0 and L are the amplitude and periodicity of the external potential, respectively.

The Brownian dynamics simulations were performed using the method proposed by Ermak and McCammon without hydrodynamic interactions [40]. As the experimental particle concentration is very low, we consider a single particle in a one-dimensional simulation box with periodic boundary conditions along the $x - axis$. In the $y - axis$, the experimentally developed field is constant, and thus we restrict the simulation to a one dimensional problem. In the Brownian dynamics simulations, the position of the particle at time $t + dt$ is calculated from the previous position at time t by using the equation:

$$x(t + dt) = x(t) + \frac{D_0 F(x(t))dt}{k_B T} + R(dt) \quad (3)$$

where D_0 is the translational diffusion coefficient of the particle at short-times, $F(x) = -\frac{dU(x)}{dx}$ is the force that the particle experiences due to the external periodic potential $U(x)$, and $R(dt)$ is a random displacement, having a normal distribution with zero mean value and variance $2D_0dt$, fulfilling the so-called fluctuation-dissipation theorem. In Brownian dynamics simulations, the magnitude of the time step dt is crucial. If it is too short, the computational time can increase significantly. If it is too large, the stochastic differential equation can display

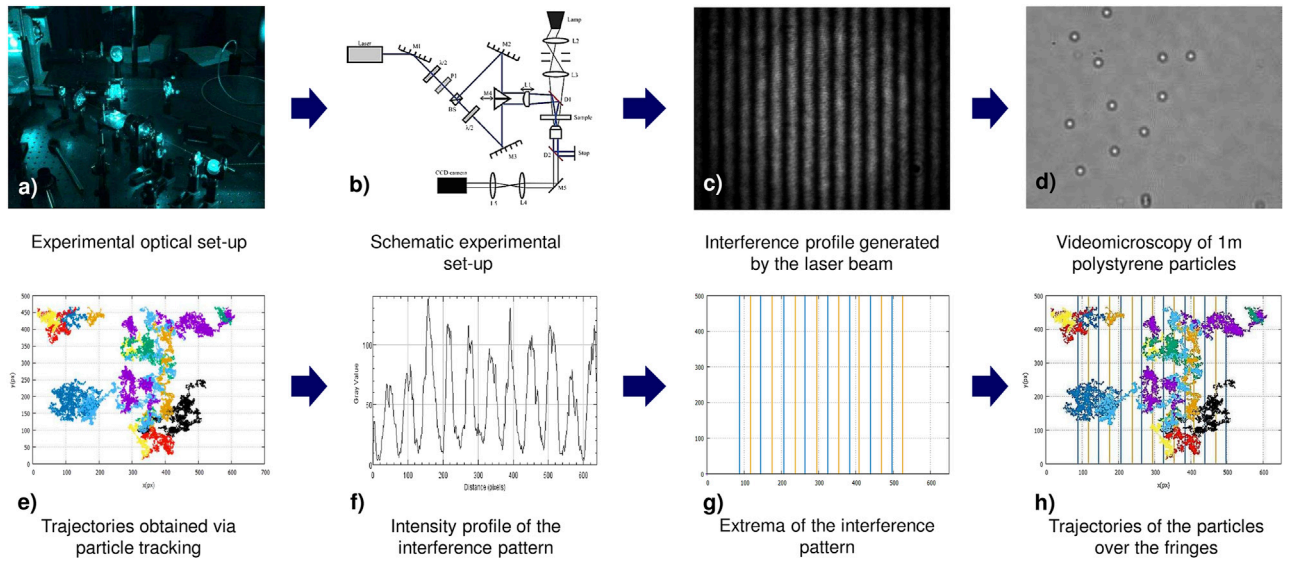

FIGURE 1 | (Color online): Experimental measurement protocol of the dynamic properties of spherical tracers in periodic cosine-like potentials: **(A)** long exposure photograph showing the light path producing the periodic distribution of light; **(B)** schematic representation of the experimental set-up; **(C)** light intensity profile generated experimentally; **(D)** typical bright field images of spherical tracers interacting with the external field; **(E)** trajectories obtained from the experiment using Trackpy; **(F,G)** the maxima and minima of the periodic potentials are estimated from the bright and dark regions displayed in the panel **(C)**; and **(H)** the density of probability is calculated from the information obtained from the trajectories of the particles over the fringes.

incorrect values of the dynamic properties of the system. The use of a single tracer under the influence of an external field allowed us to utilize a time step of 3 μs. Let us note here that the experimental time resolution is an order of magnitude larger. Such time step allowed us to reproduce the analytic mean square displacement of the Brownian harmonic oscillator with an error less than 1 percent for a wide range of spring constants [41]. In a typical Brownian dynamics simulation a maximum $N_{\max} = 1 \times 10^{11}$ times steps have been performed, which is equivalent to a total time of $3 \times 10^5\, s$. Once the positions of the tracer are known as a function of time, and assuming that the statistical properties do not depend on the initial time, the mean square displacement has been calculated as:

$$MSD\left(t_j\right) = \frac{1}{N_{\max} - j} \sum_{i=1}^{N_{\max}-j} \left[x\left(t_i + jdt\right) - x\left(t_i\right)\right]^2 \qquad (4)$$

where $t_i = idt$.

On the other hand, Bellour et. al. [9]. have proposed the following functional form to fit the MSD of tracer particles in worm-like micelle solutions:

$$MSD^{Bellour}\left(t\right) = 2\delta^2\left(1 - \exp\left\{-\left(\frac{D_0 t}{\delta^2}\right)^{\alpha}\right\}\right)^{\frac{1}{\alpha}}\left(1 + \frac{D_M t}{\delta^2}\right) \qquad (5)$$

This equation correctly describes the above mentioned dynamical regimes: short time diffusion within the network of micelles, cage effect at intermediate times, and hopping motion due to breaking of the living polymer giving a second linear regime at long times and thus can be used as a model to estimate some parameters characterizing the MSD of particles in periodical potentials. D_0 is the short time diffusion coefficient, which can be approximated as $D_0 \approx k_B T/6\pi\eta a$ according to the Stokes-Einstein relationship as a first approximation, where $k_B T$ is the thermal energy, η is the solvent viscosity, and a is the particle's radius. Experimentally, the short time diffusion coefficient D_0 is frequently different from $k_B T/6\pi\eta a$ given that D_0 also contains information regarding inter-particle interactions and wall-particle interactions. δ^2 is related to the amplitude of the MSD within the cage and thus, it is usually called the cage size. Notice that in general $2\delta^2$ is not equal to the periodicity L of our oscillatory potential. D_M corresponds to the long time diffusion coefficient, which in our system characterizes the hopping of the tracer between fringes as a function of time in our periodic system. Finally, α is a parameter related to the smoothing of the transition between short times and the caging, and it has a value close to 0.25 in worm-like micelle solutions [5]. The Bellour parametrization was originally proposed by considering that a tracer immersed in a semidilute solution of worm-like micelles was describing three different dynamic regimes in one dimension: 1) at short times the dynamics is Brownian, that is, $MSD(t) = 2D_0 t$, where D_0 is the local diffusion coefficient; 2) at intermediate times, the MSD remains constant for a given time interval, in such a way that $2\delta^2$ is the value of the MSD at the inflexion point; and 3) at long-times the motion becomes diffusive again and the long-time diffusion coefficient corresponds to the macroscopic viscosity of the solution. Thus, the starting point to describe this phenomenology is to hypothesize that the particle is under the influence of a harmonic potential. As a result, the MSD cannot grow indefinitely but reaches a plateau:

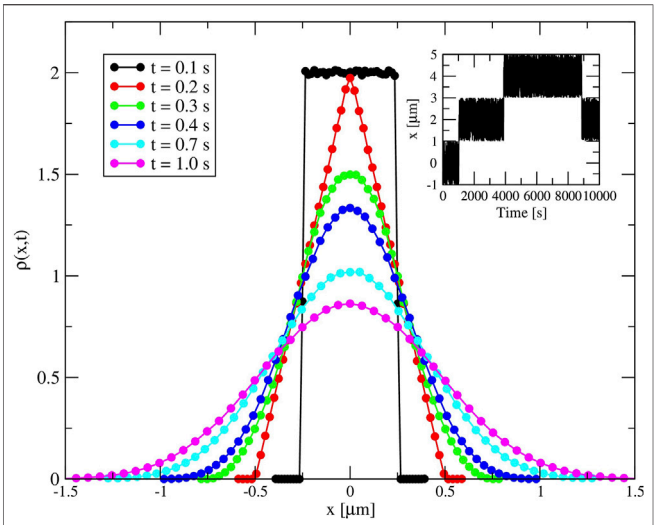

FIGURE 2 | (Color online) $\rho(x,t)$ at different times for the random walker simulation. For $t = 0.1$ s the step distribution is recovered, whereas the probability evolves to a Gaussian after a few steps. Inset: Representative trajectory obtained from the simulation, showing the caging effect and a hopping effect.

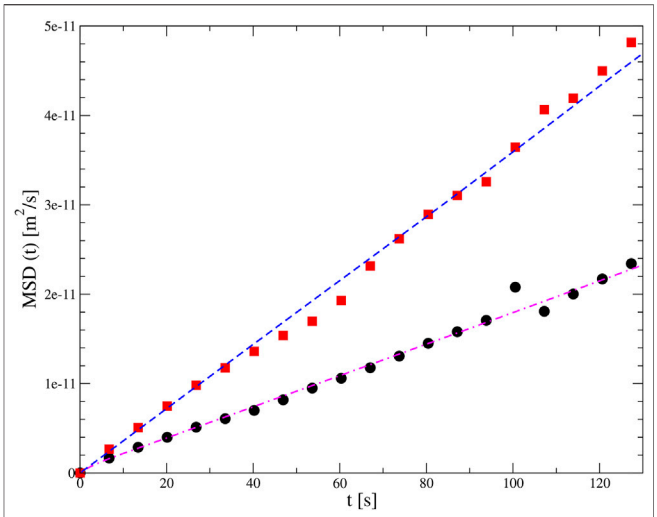

FIGURE 3 | (Color online): Mean square displacement MSD(t) of a spherical tracer as a function of time. The red solid squares and the blue dashed line correspond to the total mean square displacement (associated to the free diffusion in the *y*– and *x* – *axis* directions) associated to experimental and Brownian dynamics results, respectively, in the absence of an external field. The black solid circles and the magenta dot-dashed line correspond to the MSD(t) in the *x* – *axis* associated to experimental and Brownian dynamics results, respectively, in the presence of a periodic cosine-like external field.

$$MSD(t) = \frac{2k_BT}{k_{spring}}\left(1 - \exp\left(-\frac{k_{spring}t}{\gamma}\right)\right) \tag{6}$$

where $D_0 = (k_BT)/\gamma$. By assuming that $k_{spring} = (K_BT)/\delta^2$, it is possible to write

$$MSD(t) = 2\delta^2\left(1 - \exp\left(-\frac{D_0t}{\delta^2}\right)\right) \tag{7}$$

If the exponential is linearized, it is easy to see that at short times $MSD(t) = 2D_0t$, whereas at long times a plateau is reached at $2\delta^2$. One simple form in which the MSD can reach the physical limit $MSD(t) = 2D_Mt$ is by multiplying the analytical MSD associated to a Brownian particle under the influence of a harmonic potential by the term $1 + (D_Mt)/\delta^2$:

$$MSD(t) = 2\delta^2\left(1 - \exp\left(-\frac{D_0t}{\delta^2}\right)\right)\left(1 + \frac{D_Mt}{\delta^2}\right) \tag{8}$$

Even though this last equation is able to reproduce the MSD of a tracer immersed in a semidilute solution of worm-like micelles at short- and long-times, in general fails to describe the onset of the plateau around the inflexion point. Thus, Bellour proposed to add a parameter α in order to adjust the onset of the experimental plateau of the MSD. As one can appreciate here, the same basic arguments employed by Bellour in this heuristic derivation of **Eq. 5** can be used in the case of the systems studied here.

Another methodology to characterize the dynamical behavior of a particle in hindered motion is related with the logarithmic derivative, that corresponds to the temporal behavior of the exponent γ in $MSD \propto t^{\gamma}$. As such, a numerical calculation can be complex due to the experimental noise. We used here a more direct approach by fitting the experimentally obtained MSD to the Bellour model. Afterwards, these fitted parameters have been used in the analytic calculation of the logarithmic derivative of **Eq. 5**.

In order to calculate the long-time diffusion coefficient D_M theoretically, we consider that this quantity corresponds to the effective diffusion coefficient of a hopping Brownian particle that moves a distance L in the presence of a periodic external potential with periodicity L. In such a scenario [42],

$$D_M = D_{eff} = \frac{1}{2}k_{escape}L^2 \tag{9}$$

where $k_{escape} = 1/\tau_{escape}$ is the escape or hopping rate of the Brownian particle. Let us define the mean first passage time (MFPT) τ_{MFPT} as the average time a Brownian particle needs to reach the separatrix manifold for the first time, when was located initially at a position x_0 inside the initial domain of attraction. At large height barriers, the MFPT $\tau_{MFPT}(x_0)$ becomes essentially independent of the starting point, that is, $\tau_{MFPT}(x_0)$ is approximately the same for all starting configurations away from the immediate neighborhood of the separatrix. If the probability of crossing the separatrix to the right or to the left equals one half, the total escape time equals to two times the MFPT, and the escape or hopping rate of the Brownian particle can be written as:

$$k_{escape} = \frac{1}{2\tau_{MFPT}} \tag{10}$$

Thus, **Eq. 9** can be written in terms of the MFPT as:

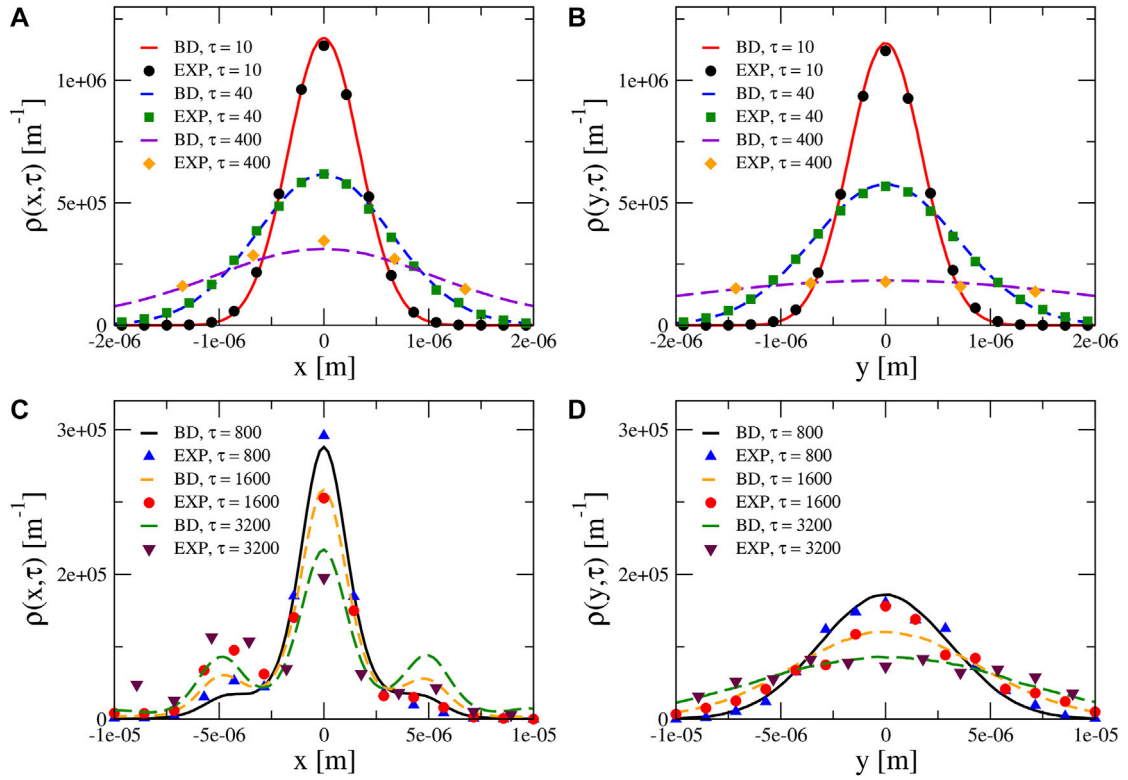

FIGURE 4 | (Color online): Density of probability per unit length of finding a tracer $\rho(x,\tau)$ as a function of the position and the reduced time $\tau = t/\Delta t$, with $\Delta t = (1/30)s$. In panels **(A,C)** there is an applied periodic cosine-like external field in the *x*-axis direction. In panels **(B,D)** there is not an applied external field in the *y*-axis direction. Symbols correspond to experimental measurements. Lines are associated to Brownian dynamics simulations in which $D_0 = 1.8 \times 10^{-13} m^2/s$ and $U_0 = 1.33 k_B T$.

$$D_M = \frac{1}{4\tau_{MFPT}} L^2 \tag{11}$$

On the other hand, the diffusion coefficient of a Brownian particle in the presence of a periodic potential, according to the Kramers approach in the overdamped limit, can be written as [43].

$$D_M^{Kramers} = \frac{w_0 w_b L^2}{2\pi\gamma} \exp\left\{-\frac{E_b}{k_B T}\right\} \tag{12}$$

where $E_b = V(x_{\max}) - V(x_{\min})$, $w_0^2 = V''(x_{\min})$, $w_b^2 = V''(x_{\max})$, and $D_0 = \frac{k_B T}{\gamma}$. If we chose

$$V(x) = U_0\left(1 - \cos\left(\frac{2\pi x}{L}\right)\right) \tag{13}$$

$x_{\min} = 0$, $x_{\max} = \frac{L}{2}$, and $E_b = 2U_0$, **Eq. 12** can be written as:

$$\frac{D_M^{DF}}{D_0} = \frac{2\pi U_0}{k_B T} \exp\left\{\frac{-2U_0}{k_B T}\right\} \tag{14}$$

which is the Dalle-Ferrier et al. [23] (DF) formula for a Brownian particle in a periodic cosine potential. According to Lifson and Jackson [30], the ratio of the long-time diffusion coefficient of a Brownian particle in the presence of a periodic potential $U(x)$ can be written as:

$$\frac{D_M^{LJ}}{D_0} = \frac{1}{\langle \exp\{U(x)/(k_B T)\}\rangle \langle \exp\{-U(x)/(k_B T)\}\rangle} \tag{15}$$

where the brackets $\langle \ldots \rangle$ indicate the average over the unit cell. This result was obtained subsequently by several authors using different routes, mainly based in solving the mean first passage time problem using the one-dimensional Smoluchowski equation.

The corresponding MFPTs can be obtained by equating **Eq. 11** with either **Eq. 12** or **Eq. 15** to yield:

$$\tau_{MFPT}^{DF} = \frac{1}{4\pi} \tau_0 \frac{k_B T}{U_0} \exp\left\{\frac{2U_0}{k_B T}\right\} \tag{16}$$

and

$$\tau_{MFPT}^{LJ} = \frac{1}{2} \tau_0 \langle \exp\{U(x)/(k_B T)\}\rangle \langle \exp\{-U(x)/(k_B T)\}\rangle \tag{17}$$

where

$$\tau_0 = \frac{L^2}{2D_0} \tag{18}$$

is the time that a particle needs to move a distance L in pure Brownian motion, that is, in the absence of any external potential, when the diffusion constant of the particle is D_0. As it is shown below, the Kramers escape time resembles more to the escape times predicted by the Lifson-Jackson prescription and the Brownian dynamics simulations at high values of U_0. On the other hand, notice that in the absence of an external potential

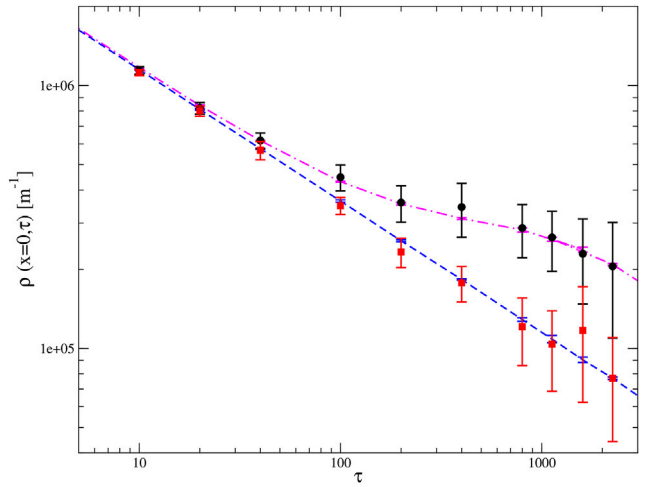

FIGURE 5 | (Color online): Maximum of the density of probability of finding a tracer $\rho(x,\tau)$ at x = 0 as a function of the reduced time $\tau = t/\Delta t$, with Δt = (1/30)*s*. The solid squares and the dashed line correspond to experimental and Brownian dynamics results, respectively, in the absence of an external field. The black solid circles and the magenta dot-dashed line correspond to experimental and Brownian dynamics results, respectively, in the presence of a periodic cosine-like external field.

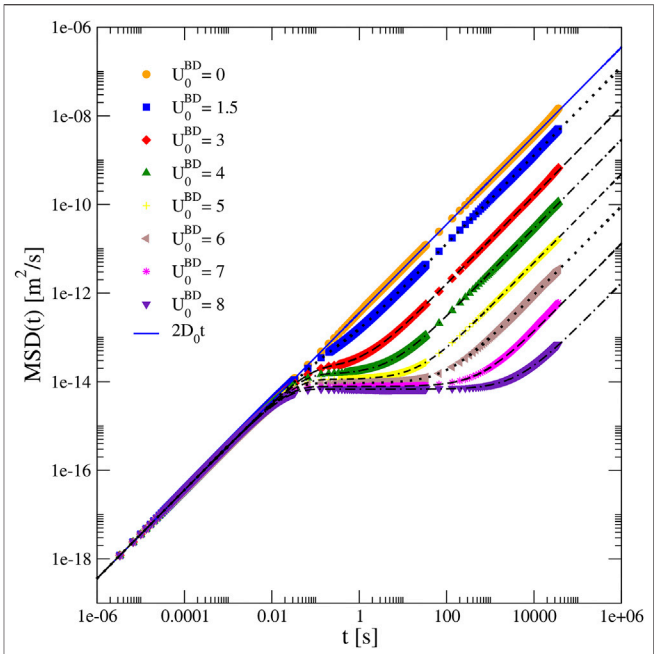

FIGURE 6 | (Color online): Mean square displacement MSD(t) of a spherical tracer as a function of time in the presence of a periodic cosine-like potential of amplitude U_0. Solid symbols correspond to Brownian dynamics simulations in which $L = 1.0 \times 10^{-6}\ m$ and $D_0^{BD} = D_0 = 1.8 \times 10^{-13}\ m^2/s$ for several U_0^{BD} values (in k_BT units). Dotted, dashed, and dot-dashed black lines correspond to Bellour fittings (**Eq. 5**) using the parameters displayed in **Table 1**.

(that is, in pure Brownian motion) the τ_{escape}^{LJ} reduces to τ_0 as expected, whereas the τ_{escape}^{DF} diverges to an infinite time. In addition, note that in the Lifson-Jackson approach the long-time diffusion coefficient D_M requires a numerical integration, whereas the Dalle-Ferrier formula is completely analytical.

2.3 Random Walker

A random walker simulation follows a similar recipe to obtain a trajectory as the Ermak and McCammon algorithm, however the choice of the displacement is generated randomly either following a distribution, or with a defined step size but without specification of the force or diffusion coefficient [27–29]. In our case, such distribution is flat of fixed width δx, instead of the typical Gaussian distribution found experimentally and also simulated in the BD protocol. The time scaling constant is not fixed and can be chosen arbitrarily. In our case it was fixed to a value of $\delta t = 0.1\ s$. The evolution of density of probability $\rho(x,t)$ of finding a tracer at the position x at time t given that a $t = 0$ the particle was located at $x = 0$ produces a Gaussian distribution after a few time steps, thus becoming dynamically equivalent to a BD simulation after such time (see **Figure 2**), as expected. As the distribution if perfectly Gaussian, it is expected also that higher moments are also equivalent. If the width of the distribution δ and the time scaling constant are chosen conveniently, this walker can reproduce the diffusion coefficient, D_0, of the BD simulations at short times. Thus, we can conclude that the implemented random walk simulation follows the most simple selection of displacements between time steps. This naive selection gives an important difference between the BD and the random walk at short times, as the probability function of displacements is not Gaussian in the first few lag times. However, this function evolves to a Gaussian distribution function, and thus not only the second moment but also higher moments are equivalent and indistinguishable from the BD. Thus, at large times both simulations are dynamically equivalent for a free particle.

In order to introduce the cage effect, the particle is located inside a periodic cell of length $L^{\#}$ with potential barriers of vanishing small width at the boundaries. Then the random walker is free to move within the cage, undergoing random steps with displacement probability. The particle can cross the cell boundary to move to an adjacent cage with a transition probability p if a given generated step is out of the cage. The success event gives a transition to the neighboring cage, whereas a failure reflects the step to keep the particle inside the cage. Thus, decreasing the transition probability gives a higher amount of events before a success one, effectively producing confinement within the cell for a given time. Inset in **Figure 2** shows a typical trajectory for a random walker in a cage of size 2 μm and transition probability 0.001, showing the typical confinement and several transitions within the simulation time. A transition probability of zero leads to total confinement, and the walker is unable to escape from the cage. In the opposite, free diffusion is found for a transition probability of 1. Despite that, after few time steps the random walker simulation and the BD simulation are dynamically equivalent for free particles, the case of a caged particle, either in the periodic potential or in a cage with a probability of transition, is different. In this case, a direct computation of the probability density within a unity cell would show that the random walker is almost free within the

TABLE 1 | Bellour fitting parameters D_M^{BD}, δ_{BD}^2, and α^{BD} associated to the Brownian dynamics mean square displacement curves displayed in **Figure 6**, as a function of the maximum height barrier U_0^{BD}. In all Brownian dynamics simulations, $L = 1.0 \times 10^{-6}\, m$ and $D_0^{BD} = D_0 = 1.8 \times 10^{-13}\, m^2/s$.

U_0^{BD} [k_BT]	D_M^{BD} [m^2/s]	δ_{BD}^2 [m^2]	α^{BD}
1.5	6.53×10^{-14}	1.28×10^{-14}	0.80
2.0	3.50×10^{-14}	1.28×10^{-14}	0.92
2.5	1.61×10^{-14}	1.12×10^{-14}	0.84
3.0	8.10×10^{-15}	9.78×10^{-15}	0.93
3.5	3.63×10^{-15}	8.49×10^{-15}	0.93
4.0	1.47×10^{-15}	7.34×10^{-15}	0.96
4.5	6.58×10^{-16}	6.42×10^{-15}	0.98
5.0	2.45×10^{-16}	5.62×10^{-15}	0.92
5.5	9.43×10^{-17}	5.12×10^{-15}	0.95
6.0	4.58×10^{-17}	4.65×10^{-15}	0.99
6.5	1.75×10^{-17}	4.26×10^{-15}	1.00
7.0	6.66×10^{-18}	3.93×10^{-15}	0.95
8.0	8.45×10^{-19}	3.38×10^{-15}	0.97

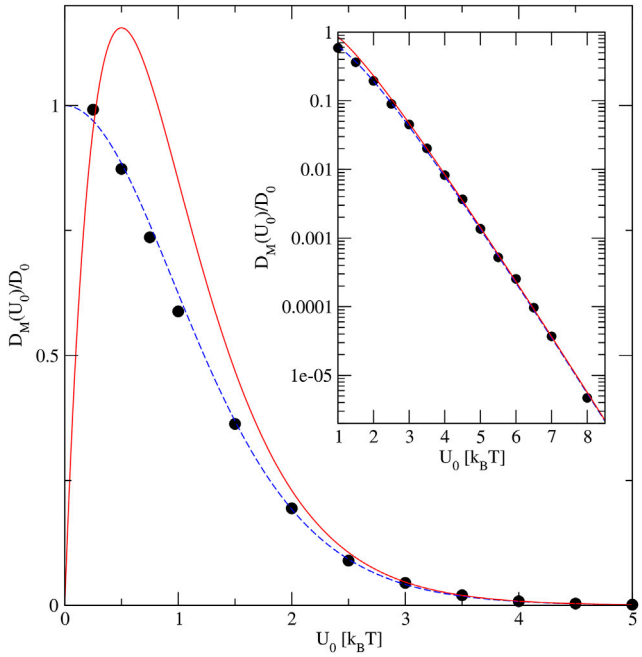

FIGURE 7 | (Color online): Long-time diffusion coefficient $D_M(U_0)$ of a spherical tracer as a function of the maximum height barrier U_0. The black solid circles, the blue dashed-line, and the red solid-line correspond to Brownian dynamics, the Lifson-Jackson prescription (**Eq. 15**), and the Dalle-Ferrier formula (**Eq. 14**), respectively. In all cases, $L = 1.0 \times 10^{-6}\, m$ and $D_0^{BD} = D_0 = 1.8 \times 10^{-13}\, m^2/s$.

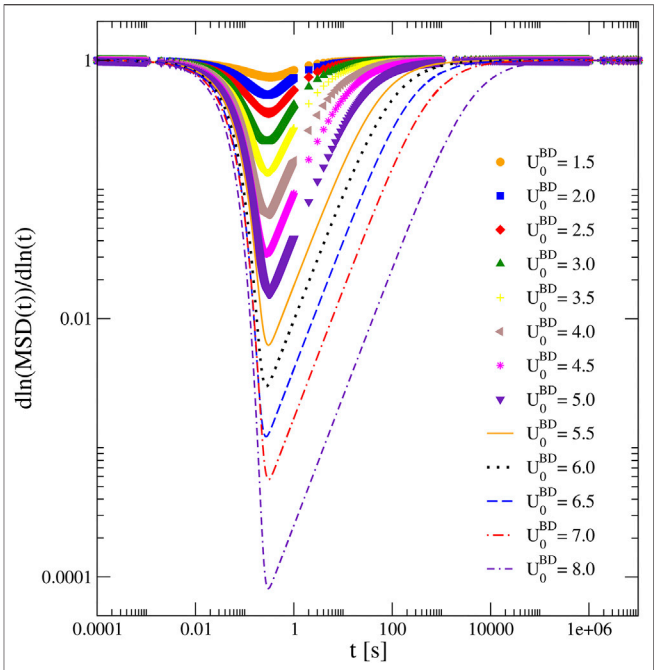

FIGURE 8 | (Color online): Logarithmic derivative of the mean square displacement MSD(t) of a spherical tracer as a function of time in the presence of a periodic cosine-like potential of amplitude U_0. Solid symbols correspond to Brownian dynamics simulations in which $L = 1.0 \times 10^{-6}\, m$ and $D_0^{BD} = D_0 = 1.8 \times 10^{-13}\, m^2/s$ for several U_0^{BD} values (in k_BT units).

cage, giving a probability density almost constant within the cage, whereas the presence of the continuous potential in the BD would produce a more complex scenario. Despite this, and as shown here, choosing properly the parameters of the random walker, the evolution of the MSD is equivalent.

The random walker model is also useful to study the typical mean first passage time problem, that will be used later to analyze our results in terms of the distribution of escape times. However, as in this case the particle either cross the barrier or not, in principle, the random walker undergoes escaping processes, characterized by an escape time τ_E, instead of the mean first passage time. By now it is important to highlight the relation between the escape time problem and the parameters of such stochastic model. Consider first that the potential that can be modeled using the random walker is a flat bottom well with delta barriers as frontiers. When considering the simple case of a flat potential with perfectly absorbing barriers, the mean first passage time, equivalent to escape time only in this case, was found to be $L^{\#2}/(16D_0)$, as expected from this simple model [44]. By including a transition probability p, the escape time can be written as $L^{\#2}/(16D_0p)$, which provides a definition of the long time diffusion coefficient D_M similar to that used in the BD simulation case

$$D_M = \frac{1}{2\tau_E} L^{\#2} \tag{19}$$

where $D_M = 8D_0p$. In such a scenario, the escape time is twice the mean first passage time, which is consistent with a 1/2 probability of jumping to the next cage per event.

3 RESULTS AND DISCUSSION

3.1 Short Time Dynamics

In order obtain the short time diffusion coefficient D_0 of a tracer, and the amplitude of the periodic potential U_0 in our experiment,

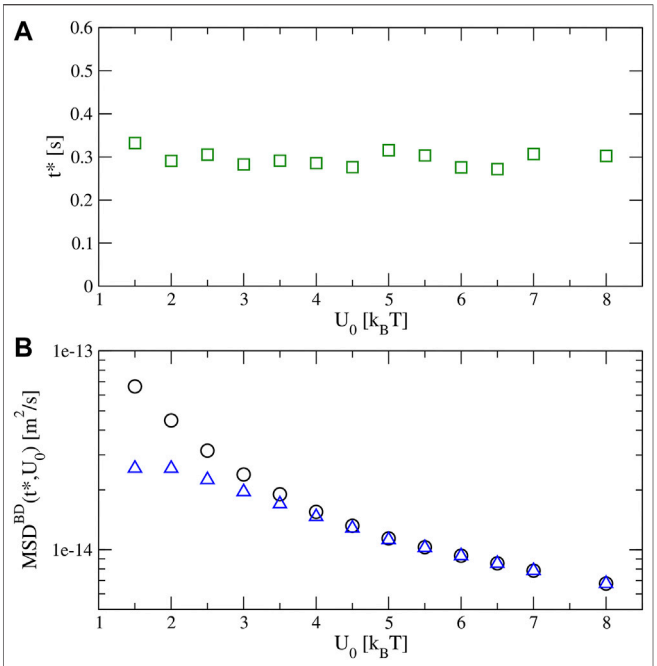

FIGURE 9 | (Color online): **(A)** Critical time t^* at which a change of curvature in the MSD is observed (green squares), and **(B)** mean square displacement at the critical time MSD (t^*) as a function of the maximum height barrier U_0 (black circles). The blue triangles are associated the Bellour fitting parameter $2\delta^{2BD}$ displayed in **Table 1**. These values were obtained from Brownian dynamics simulations in which $L = 1.0 \times 10^{-6}\, m$ and $D_0 = 1.8 \times 10^{-13}\, m^2/s$ in all cases.

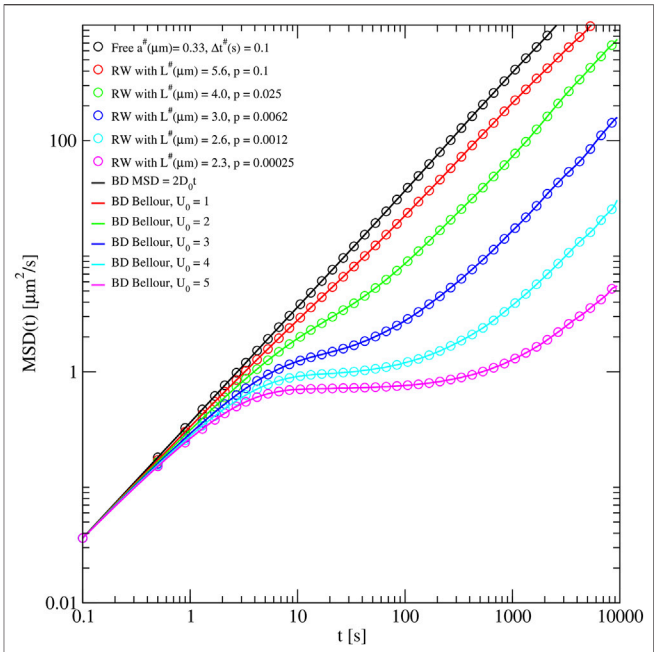

FIGURE 10 | (Color online) Random walker MSD fitting of Brownian dynamics simulations in which the size of the periodic cell is $L = 8$ microns for different energy barriers U_0 (in K_BT units). The fitting parameters used in the random walker are the spatial and time increments $a^{\#}$ and $dt^{\#}$, which determine the short-times diffusion coefficient D_0; and the cage size $L^{\#}$ and the jump probability p, which determine the long-times diffusion coefficient D_M. These values are explicitly indicated in the labels.

we measured the mean square displacements along the *y*– and *x* – *axis* directions as a function of time. Given that along the *y*-axis there is not an applied external field, the tracer experiences free diffusive Brownian motion. Using the total mean square displacement (associated to the free diffusion in the *y*– and *x* – *axis* directions), the short time diffusion coefficient was found to be $D_0 = 1.8 \times 10^{-13}\, m^2/s$, which in turn is used in our Brownian dynamics simulations, allowing us to reproduce the observed experimental behavior as it is shown in **Figure 3**. The reduction of D_0 is about 35% with respect the Stokes-Einstein equation for free diffusion in the bulk, in accordance with previous results for a similar geometry confinement [45]. Some deviations from these value are expected experimentally as the separation between glass plates varies within the sample, but deviations in D_0 are also expected to be small and thus does not greatly affect the comparison between experimental and numerical results. A direct comparison with the experimental mean square displacement measured in the *x*-axis allowed us to fit the maximum height of the periodic potential, resulting in the numerical value of $U_0 = 1.33\, k_BT$. Brownian dynamics simulations of the tracer with the above values of D_0 and U_0 yielded a numerical mean square displacement that correlate very well with experimental measurements in the *x*-axis, as it is shown in **Figure 3**. Some deviations from the perfect linear relation was found in the experimental MSD and associated with the small vibrations reported above. As only a few particles remain withing the field of view for more than 100 s, the long time dynamics is also found to be affected by statistical noise.

A more stringent test for the estimated value of U_0 parameters (fitted *via* the experimental mean square displacement) is to observe if it is able to predict other microscopic time dependent properties such as the density of probability $\rho(x,t)$ of finding a tracer at the position x at time t given that at $t = 0$ the particle was located at $x = 0$. This quantity, obtained from experiments and Brownian dynamics calculations, is shown in **Figure 4**. The behavior of $\rho(x,t)$ in the presence of a periodic external field is shown in panels (a) and (c), whereas $\rho(x,t)$ in the absence of an external field is displayed in panels (b) and (d). In general, good agreement between the experimental and Brownian dynamics data is observed either in presence or in the absence of the periodic external field.

In the absence of an external field, $\rho(x,t)$ displays a Gaussian behavior for all times displayed, as expected. Specifically, the maximum height $\rho(x = 0, t)$ and the width of $\rho(x,t)$ decreases and increases, respectively, as a function of time. In the presence of a periodic external field, a similar behavior to that observed in the absence of an external field is seen only at very short times.

At longer times, the tracer starts to experience the external field and it is seen that: 1) the rate at which the maximum height $\rho(x,t)$ at x = 0 decreases becomes lower compared to the case in which the external field is not applied; and 2) the profile of $\rho(x,t)$ displays multiple damped maxima, which correspond to the spatial localization of the minima of the applied periodic

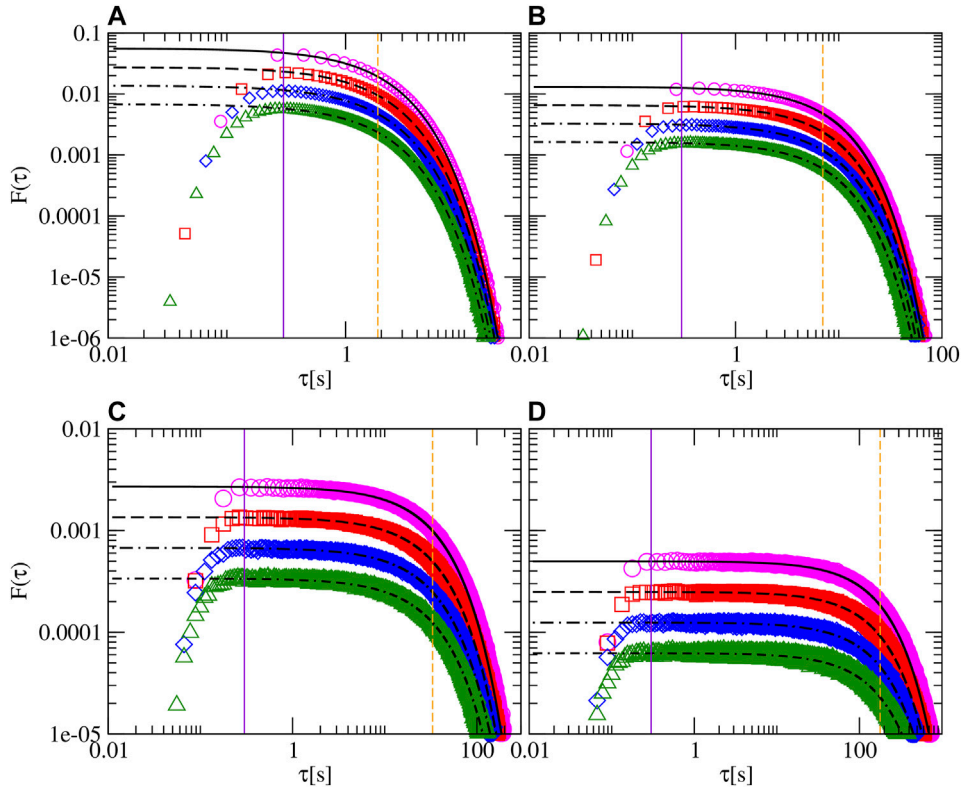

FIGURE 11 | (Color online):Brownian dynamics histograms of the first passage time (FPT) τ for different barrier heights U_0 and Δt bins. The value of U_0 in k_BT units is 1, 2, 3, and 4 for **(A–D)**, respectively. The Δt bin is 0.08, 0.04, 0.02, and 0.01 s for pink circles, red squares, blue diamonds, and green triangles, respectively. Black lines are exponential tail fittings associated to **Eq. 20**. For a given U_0 value, the vertical purple solid line corresponds to the critical time t^*, and the vertical orange dashed line indicates the mean first passage time τ_{MFPT}. The periodicity of the fringe and the short times diffusion coefficient are $L = 1.0 \times 10^{-6}\, m$ and $D_0^{BD} = D_0 = 1.8 \times 10^{-13}\, m^2/s$, respectively, in the Brownian dynamics simulations.

external potential. This effect has been also reported in the literature [23]. A comparison of the rate at which the maximum of the density of probability $\rho(x,t)$ at x = 0 decreases, in the presence and in the absence of the periodic external field, is displayed in **Figure 5** as function of time. Here, an excellent agreement is observed between experimental measurements and Brownian dynamics simulations.

3.2 Mean Square Displacement and Long Time Dynamics

The good agreement observed between experimental and simulation results presented above, motivates a study of long time dynamic properties of the tracer *via* Brownian dynamics simulations for a fixed periodicity L. The MSD of a spherical tracer is displayed in **Figure 6** as a function of time and the amplitude of the periodic potential U_0. Here, we observe that a change of curvature and a plateau appear, which is more noticeable when U_0 increases. As a whole, the behavior of the MSD found here is similar to reported results using simulations and experiments [23, 24]. Moreover, it is observed that the diffusion coefficient at long times, D_M, is significantly lower that the short time diffusion coefficient. D_M and the Bellour parameters δ^2 and α, were estimated by fitting the numerical results obtained from our Brownian dynamics simulations using the Bellour **Eq. 5**. These numerical values are displayed in **Table 1**. In contrast to the case in which tracer particles are dispersed in worm-like micelles solutions, with $\alpha \approx 0.25$, the α parameter here is higher than to 0.9, which gives a sharper transition between the short and the caging times regime. Interestingly, the asymptotic value of one is found in the solution to the Langevin equation for a parabolic potential [16]. The long time diffusion coefficient D_M normalized with the short time diffusion coefficient D_0 is shown in **Figure 7**. In this figure, it is observed that D_M/D_0 decreases rapidly as a function of U_0, as expected from **Figure 6**, reaching a value close to 1×10^{-5} for an energy barrier of $8k_BT$. In order to have a theoretical estimation of D_M at long times, it is possible to use the Lifson-Jackson prescription (**Eq. 15**) or the Dalle-Ferrier et al. formula (**Eq. 14**) if the periodic potential is known. In this study, the periodic cosine potential given by **Eq. 2** is fully defined in terms of the parameters U_0 and L. In **Figure 7**, it is observed that the Lifson-Jackson prescription provides an excellent estimation of the long time diffusion coefficient D_M for all values of the maximum height of the periodic potential U_0 displayed. Contrastingly, the Dalle-Ferrier et al. approach shows a

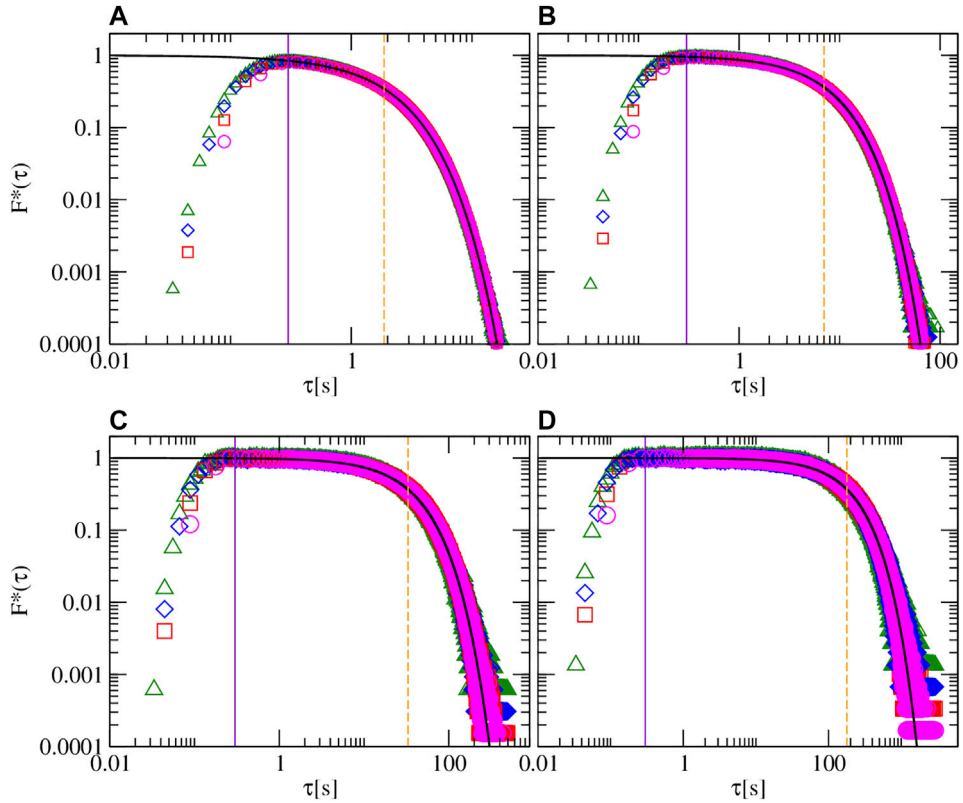

FIGURE 12 | (Color online): Normalized histograms of the first passage times for different barrier heights U_0 and Δt bins. Black lines are exponential tail fittings associated to **Eq. 21**. Locants have the same meaning as that used in **Figure 11**.

reasonable agreement, with the Brownian dynamics data, only for large values of U_0. In this regime, the Dalle-Ferrier et al. data tends to those yielded by the Lifson-Jackson prescription (see the inset of **Figure 7**).

In **Figure 6** it appears that the time t^* at which the first change of concavity of the MSD occurs is the same for all values of U_0 considered here. In order to locate this time more precisely, we calculate the logarithmic derivative of the MSD which is plotted in **Figure 8** for different amplitudes of the periodic potential U_0. At very short and long times, the logarithmic derivative of the MSD tends to one, again showing a purely diffusive behavior. At intermediate values, the logarithmic derivative of the MSD shows a minimum at a time which we identify as t^*, i.e., at which a change of curvature of the MSD curve is observed. The magnitude of the logarithmic derivative at t^* decreases as the energy barrier increases. **Figure 9A** shows the value of t^*as a function of U_0. Here it is observed that t^* oscillates around the numerical value of 0.3 s. This suggests that the magnitude of t^* is independent of the magnitude of U_0 for a fixed periodicity L. In the same figure, the value of the MSD at t^* is shown, indicating a monotonic decrease by increasing U_0.

On the other hand, another interesting feature regarding the Bellour fitting is that the parameter $2\delta^{2BD}$ converge asymptotically to the MSD at the time t^* for large U_0 values, as shown in **Figure 9B**. This gives a new interpretation of $2\delta^2$ in this type of periodical potentials.

The above mentioned effect related with the decrease of the $2\delta^{2BD}$ parameter increasing U_0, can be used to properly select the parameters for the random walker simulation. As a result, it is possible to compare the behavior of the random walker in the most simple periodic potential of periodic flat cages, to that displayed by a Brownian particle under the influence of a periodical potential as 2. If the cage-size and the transition probability p are chosen appropriately, this walker can also reproduce the same trend of the D_M/D_0 ratio as found in the BD simulation. As a consequence of the different potentials (a periodic cosine-like one vs. a flat cage with a delta barrier), the magnitude of the cage size decreases as p increases. Thus, the transition probability p is a monotonic decreasing function of the energy barrier. Interestingly, the MSD of the random walker is able to reproduce very accurately the MSD obtained from the BD simulations as shown in **Figure 10**, showing the same independence of t^* for different transition probabilities (that are associated to different height barriers U_0). This suggests that the behavior of the particles in the two periodic potentials studied here would be the same in other periodic potentials.

3.3 Histograms of First Passage Time

In order to gain further insight about the independence of t^* at different U_0 amplitudes of the periodic potential for a fixed periodicity L, in **Figure 11** the histograms of the first passage

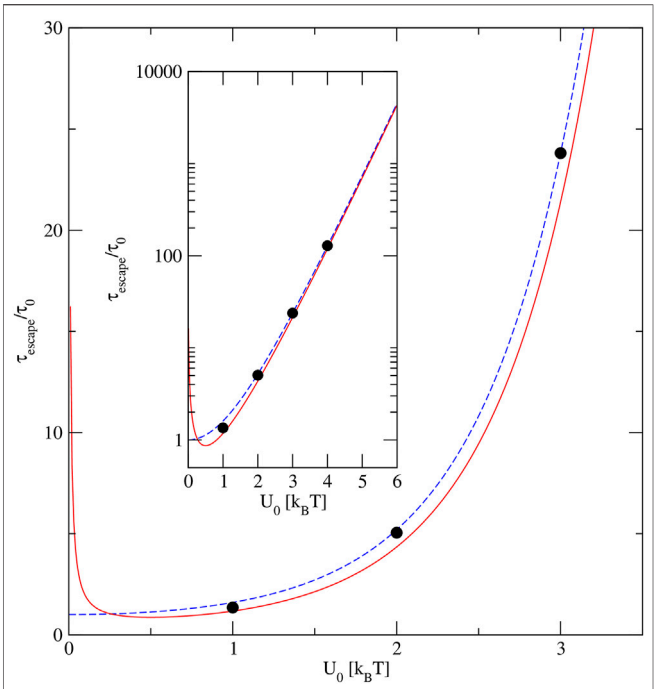

FIGURE 13 | (Color online): Escape time $\tau_{escape} = 2\tau_{MFPT}$ as a function of the barrier height U_0. The black solid circles, the blue dashed-line and the red solid line have been obtained from Brownian dynamics, the Lifson-Jackson prescription (**Eq. 17**), and the Dalle-Ferrier formula (**Eq. 16**), respectively. In all cases, $\tau_0 = \frac{L^2}{2D_0}$, $L = 1.0 \times 10^{-6}\, m$ and $D_0^{BD} = D_0 = 1.8 \times 10^{-13}\, m^2/s$.

time (FPT) τ of the tracer for several values of U_0 and different bin values are displayed. In all analyzed cases, it is observed that short FTPs are very rare events, giving also a measure of the time required for the particles to reach the barrier by Brownian motion. When the magnitude of the FTP increases, its frequency of occurrence increases too. This augment of the frequency of occurrence of the escape time is observed until a critical value t' is reached. At the critical FPT t' the histogram displays a maximum. The time t' is then the most likely FPT of the tracer. For larger FPTs, the associated frequency of occurrence decreases exponentially. Thus, the tail of each FPT histogram (for FPTs larger than t') is fitted to a simple exponential of the form:

$$F(\tau) = A \exp(-K\tau) \tag{20}$$

where F is the frequency of events in the escape time histogram, A is the asymptotic value of F when $\tau = 0$, and K is the decay constant of the escape times. These three quantities depend on the selected values of the bin of the histogram, D_0, U_0, and L. In each panel of **Figure 11**, D_0, U_0, and L are kept constant, and different histograms are displayed as a function of the value of the bin used.

On the other hand, all histograms displayed in **Figure 11** are normalized dividing the value of F by the corresponding value of A, that is:

$$F^*(\tau) = F(\tau)/A \tag{21}$$

These normalized histograms are shown in **Figure 12**. Here, we observe that all normalized MFPT histograms collapse onto the same curve for different bin values. Moreover, it is observed that the most likely FPT t' (that is, the FTP at which a maximum is observed in each histogram) displays approximately a constant value independently of the height of the periodic potential U_0. In addition, the magnitude of t' is very close to the magnitude of t^*. As a result, the change of curvature observed in the MSD at t^* can be physically related to the characteristic time at which the MFPT starts to display its more likely value. Contrastingly, the mean first passage time (MFPT) τ_{MFPT} strongly depends on the value of the height barrier U_0 as it is shown in **Figure 13**. The escape time $\tau_{escape} = 2\tau_{MFPT}$ obtained from the Brownian dynamics simulations are displayed in **Figure 13** as a function of the height barrier U_0. The theoretical values predicted by **Eqs 16**, **17** corresponding to the Dale-Ferrier and the Lifson-Jackson approaches, respectively, are also shown. The Dale-Ferrier formula break downs at low height barriers U_0, whereas the Lifson-Jackson Eq. predicts the expected limit $\tau_{escape} = \tau_0$, where $\tau_0 = \frac{L^2}{2D_0}$. In both theoretical approaches, the escape time τ_{escape} increases exponentially as a function of the height barrier U_0 and both descriptions converge to the same value at height barriers. For all displayed values, the escape time τ_{escape} produced by the Lifson-Jackson equation displays an excellent agreement with the data obtained from the Brownian dynamics simulations. On the other hand, it is interesting to note that the histograms of the FTP displayed in **Figure 12** resemble the distribution of first passage times in complex geometries [46–49], or in energy landscapes [50–53], and are actually closely related. Here, we focus the discussion on the relationship between the histograms of escape times and a more simple statistical quantity such as the MSD.

As pointed out above, important features of the motion of a colloidal particle in a periodic potential are also presented in the simple model of a random walker. Another interesting quantity is the escape time whose histograms for the random walker simulation were also calculated and shown in **Figure 14**. The normalization of the histograms were performed following the same protocol used in the BD simulations. Here, it can be observed a behavior analogous to that observed by BD simulations: the frequency of short escape times increases as the escape time increases. This augment of the frequency of occurrence of the escape time is observed until a critical value t' is reached. At the critical escape time t' the histogram displays a maximum. The time t' is then the most likely escape time of the tracer. For larger escape times, the associated frequency of occurrence decreases exponentially.

Let us define now $t^{\#}$ as the mean time required by the walker to reach the boundary of the cell, given that it started at any point of the cell of length $L^{\#}$. This time is displayed by vertical colored-dashed lines in **Figure 14** for several transition probabilities, which can be associated to the U_0 barrier heights used in the BD simulations. In this figure, it is observed that the time $t^{\#}$ is located very close to the more likely escape time t', which is equal to 15, 17, 17, and 25 s for U_0 equal to 1, 2, 3, and 4 k_BT, respectively. Thus, it is possible to interpret the more likely escape time as the mean time $t^{\#}$ required by the walker to reach one of the boundary of the

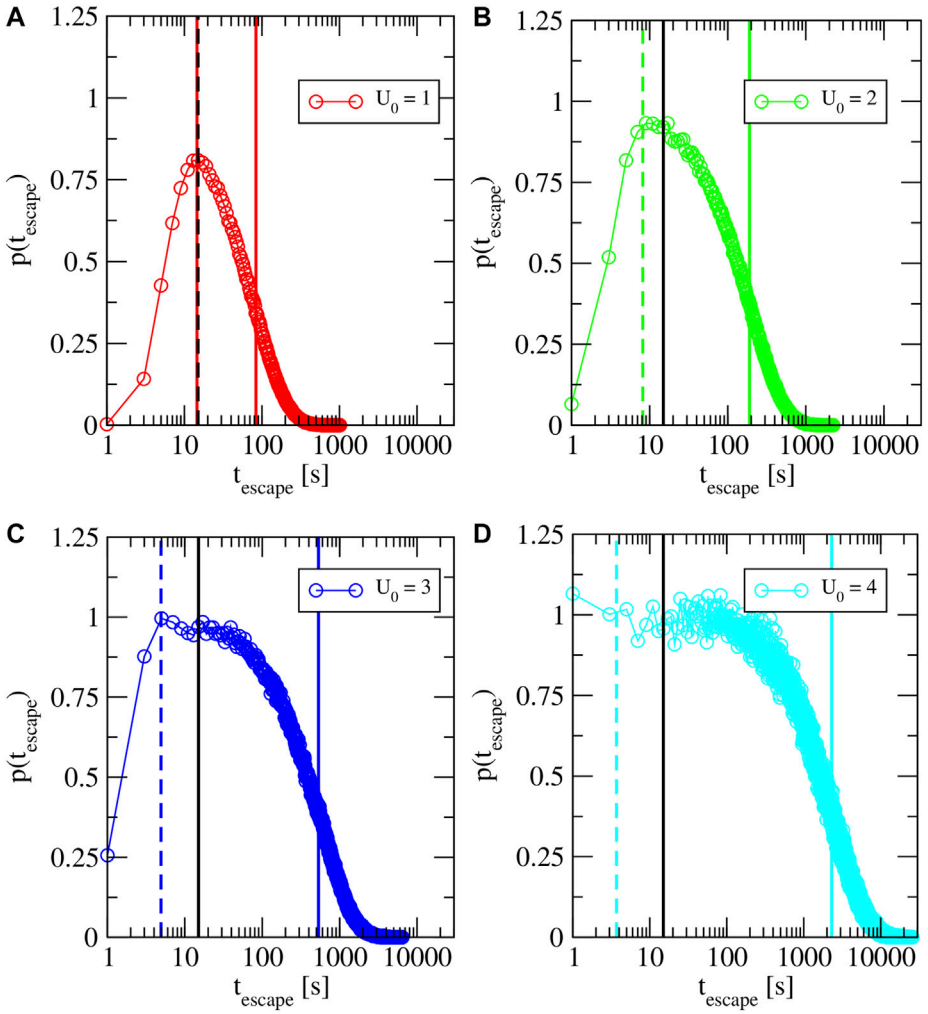

FIGURE 14 | (Color online) Normalized histograms of the escape times obtained from the random walker simulations. The data are labeled according to the target Brownian dynamics simulations displayed in **Figure 10**. Vertical blue, green, and red dashed lines represent the mean time $t^{\#}$ required by the random walker to reach one boundary of a periodic cell of size $L^{\#}$, given that the random walk started at any point inside the periodic cell. Vertical blue, green, and red continuous solid lines are associated to the mean value of the escape time in the random walker model. The vertical black continuous solid line indicates the average critical time t^{*} obtained from the Brownian dynamics data.

cells given that started at any point of a cell of length $L^{\#}$. As this time depends mainly on $L^{\#}$ and not on p, and $L^{\#}$ is of the same order of magnitude for the different U_0 values, all $t^{\#}$ times are located close among them. Moreover, it is observed that all $t^{\#}$ times are close to the average time t^{*} of the BD simulations. Then, it is possible to propose that the characteristic times t' and $t^{\#}$ can be approximated by t^{*}, which can be easily measured from MSD curves. Notice that the mean value of the escape time, displayed as a vertical colored-solid line, strongly depends on the U_0 value. The above mentioned results can be summarized following the next arguments and considering the ensemble of particles located in the periodic potential and undergoing Brownian motion: at long escape times, longer than $t^{\#}$ the escape process can be considered stationary: considering a time window of constant width, at each time window a fraction of the remaining particles are escaping from the potential, giving an exponential decay of the histograms of escape times. Such fraction decreases as U_0 increases. The absence of escape events at very short times, and the further increase is related with an increase in the number of particles reaching the barrier for the first time. This first regime is mostly independent on the energy barrier and dominated by the periodicity of the potential. The independence of the most likely time t' on the energy barrier U_0 is related to the onset of the stationary regime at long times. Thus, the time at which the MSD reaches the plateau and starts to develop the second diffusive regime, characterized by the parameter t^{*}, can be used to differentiate the short- and long-time regimes that the spherical tracer experiences under the influence of a periodic external field, in terms of the behavior of the escape time histograms.

4 CONCLUSION

In this work, we have studied some dynamic properties of a Brownian tracer in two periodic potentials at short- and long-times. For the experimentally obtained harmonic potential, at short-times, the proposed protocol allowed us to estimate the short time diffusion coefficient D_0 and the maximum height of the potential U_0, by performing a numerical fitting of the MSD of the tracer obtained *via* experiments and Brownian dynamics simulations. The precision of these parameters was further tested by calculating another microscopic time dependent property, namely, the linear density of probability per unit length of finding the tracer at a position x at a time t. At long-times, Brownian dynamics simulations were performed to study some dynamic properties of the tracer such as the MSD. The numerical MSDs obtained *via* Brownian dynamics were also fitted to the Bellour equation. Using the parameters found, a simpler random walker simulation was also performed in order to test our results in one of the most simple forms of a periodic potential.

At the level of the MSD, it was observed that a plateau and a change of curvature appear and become more conspicuous when the U_0 increases. The long time diffusion coefficient of the tracer D_M, obtained from the Brownian dynamics simulations, decreased rapidly as a function of U_0 for a fixed periodicity L. In order to estimate D_M from first principles, we used the Lifson-Jackson prescription and the analytic Dalle-Ferrier et al. formula. An excellent agreement between the long time D_M of the tracer obtained *via* the Lifson-Jackson prescription and the corresponding Brownian dynamics simulations is observed. On the other hand, the Dalle-Ferrier et al. formula produces long time D_M coefficients that converge asymptotically, at large U_0 values, to those predicted by our simulations and the Lifson-Jackson approach. By selecting properly the random walker simulation parameters, the same trend of the long time diffusion coefficient is obtained.

In order to locate clearly the time t^* at which a plateau and the first change of curvature appear at large values of U_0, the logarithmic derivative of the MSD was calculated for different values of U_0. It is found that the magnitude of t^* remains approximately constant and independent of U_0 for a fixed periodicity L of the periodic potential, finding the same results for the case of the periodic potential associated to the random walker by increasing the probability of hopping p. The most likely escape time t' of the tracer displays an analogous behavior regarding U_0 or p, and the magnitude of t' is very similar to the magnitude of t^*. Thus, the change of curvature observed in the MSD at t^* can be physically related to the characteristic time at which the escape time starts to display its more likely value. Moreover, the critical time t^* obtained from a single MSD curve can be used as a first approximation of the most likely escape time t', obtained from computationally expensive escape time histograms.

The two periodic potentials studied here *via* experiments, Brownian dynamics, and random walker simulations constitute very simple models useful to characterize or describe more complex systems such as dense polyelectrolyte solutions, jammed spheres, and even crowded biological structures as those found inside living cells. In this sense, if our simple models are able to provide the long time diffusion coefficient D_M of a tracer in a dense and crowded experimental environment, then the associated maximum height and periodicity of the cosine potential can be used as effective parameters describing the characteristic energy barrier that the tracer needs to overcome in order to jump, or escape, from one effective confining cell to another one. The application of this approach to characterize the long time dynamics of a tracer in dense tubular micellar solutions is in progress and will be published elsewhere.

DATA AVAILABILITY STATEMENT

The raw data supporting the conclusions of this article will be made available by the authors, without undue reservation.

AUTHOR CONTRIBUTIONS

ES-G and JA-L designed the experiments. ES-G and DP-G implemented the experimental set-up. DP-G performed the experiments. GG-G and DP-G implemented the BD simulations. ES-G designed and implemented the random walker simulation. GG-G, DP-G, JA-L and ES-G analyzed the data. GG-G, DP-G, JA-L and ES-G wrote the manuscript.

FUNDING

GG-G acknowledges the Marcos Moshinsky Fellowship, the SEP-CONACYT CB-2016 grant 286105, the PRODEP grant UASLP-PTC-652 511-6/2020-8585, the CONACYT grants 261210 and FC-2015-2-1155, and the Laboratorio Nacional de Ingeniería de la Materia Fuera de Equilibrio-279887-2017 for the financial funding. ES-G acknowledges CONACYT Mexico through grant A1-S-9098. Authors thanks Prof. Stefan Egelhaaf for useful discussions.

ACKNOWLEDGMENTS

The authors thankfully acknowledge computer resources, technical advice and support provided by the Laboratorio Nacional de Supercómputo del Sureste de México (LNS), a member of the CONACYT national laboratories, with project No. 202001024N; as well as the Centro Nacional of Supercómputo (CNS) for the computing time provided at THUBAT KAAL II. GG-G. expresses his gratitude for the assistance from the computer technicians at the IF-UASLP.

REFERENCES

1. Golding I, and Cox EC. Physical nature of bacterial cytoplasm. *PRL* (2006) 96: 098102. doi:10.1103/physrevlett.96.098102
2. Tolić-Nørrelykke IM, Munteanu EL, Thon G, Oddershede L, and Berg-Sørensen K. Anomalous diffusion in living yeast cells. *Phys Rev Lett* (2004) 93:078102. doi:10.1103/PhysRevLett.93.078102
3. Weiss M, Elsner M, Kartberg F, and Nilsson T. Anomalous subdiffusion is a measure for cytoplasmic crowding in living cells. *Biophys J* (2004) 87:3518–24. doi:10.1529/biophysj.104.044263
4. Xia Q, Xiao H, Pan Y, and Wang L. Microrheology, advances in methods and insights. *Adv Coll Int Sci* (2018) 257:71–85. doi:10.1016/j.cis.2018.04.008
5. Sarmiento-Gomez E, Lopez-Diaz D, and Castillo R. Microrheology and characteristic lengths in wormlike micelles made of a zwitterionic surfactant and sds in brine. *J Phys Chem B* (2010) 114:12193–202. doi:10.1021/jp104996h
6. Mason TG, and Weitz DA. Optical measurements of frequency-dependent linear viscoelastic moduli of complex fluids. *Phys Rev Lett* (1995) 74:1250–3. doi:10.1103/physrevlett.74.1250
7. Schnurr B, Gittes F, MacKintosh FC, and Schmidt CF. Determining microscopic viscoelasticity in flexible and semiflexible polymer networks from thermal fluctuations. *Macromolecules* (1997) 30:7781–92. doi:10.1021/ma970555n
8. Amblard F, Maggs AC, Yurke B, Pargellis A, and Leibler S. Subdiffusion and anomalous local viscoelasticity in actin networks. *Phys Rev Lett* (1999) 77:4470. doi:10.1103/PhysRevLett.77.4470
9. Bellour M, Skouri M, Munch JP, and Hébraud P. Brownian motion of particles embedded in a solution of giant micelles. *Eur Phys J E* (2002) 8:431–6. doi:10.1140/epje/i2002-10026-0
10. Hunter GL, and Weeks ER. The physics of the colloidal glass transition. *Rep Prog Phys* (2012) 75:066501. doi:10.1088/0034-4885/75/6/066501
11. Weeks ER. Introduction to the colloidal glass transition. *ACS Macro Lett* (2017) 6:27–34. doi:10.1021/acsmacrolett.6b00826
12. Löwen H. Colloidal dispersions in external fields: recent developments. *J Phys Condens Matter* (2008) 20:404201. doi:10.1088/0953-8984/20/40/404201
13. Zhu J, Li M, Rogers R, Meyer W, Ottewill RH, Russel WB, et al. Crystallization of hard-sphere colloids in microgravity. *Nature* (1997) 387:883–5. doi:10.1038/43141
14. Sprenger HJ, Marquardt P, and Tadros TF. The scope of microgravity experiments in colloid science: major conclusions from the workshop. *Adv Coll Int Sci* (1993) 46:343–7. doi:10.1016/0001-8686(93)80048-g
15. Bailey AE, Poon WCK, Christianson RJ, Schofield AB, Gasser U, Prasad V, et al. Spinodal decomposition in a model colloid-polymer mixture in microgravity. *Phys Rev Lett* (2007) 99:205701. doi:10.1103/physrevlett.99.205701
16. Pesce G, Volpe G, Maragó OM, Jones PH, Gigan S, Sasso A, et al. Step-by-step guide to the realization of advanced optical tweezers. *J Opt Soc Am B* (2015) 32: B84–98. doi:10.1364/josab.32.000b84
17. Evers F, Hanes RDL, Zunke C, Capellmann RF, Bewerunge J, Dalle-Ferrier C, et al. Colloids in light fields: particle dynamics in random and periodic energy landscapes. *Eur Phys J Spec Top* (2013) 222:2995–3009. doi:10.1140/epjst/e2013-02071-2
18. Romero AH, and Sancho JM. Brownian motion in short range random potentials. *Phys Rev E* (1998) 58:2833–7. doi:10.1103/physreve.58.2833
19. Sancho JM, Lacasta AM, Lindenberg K, Sokolov IM, and Romero AH. Diffusion on a solid surface: anomalous is normal. *Phys Rev Lett* (2004) 92: 250601. doi:10.1103/physrevlett.92.250601
20. Schmiedeberg M, Roth J, and Stark H. Brownian particles in random and quasicrystalline potentials: how they approach the equilibrium. *Eur Phys J E Soft Matter* (2007) 24:367–77. doi:10.1140/epje/i2007-10247-7
21. Hanes RDL, Schmiedeberg M, and Egelhaaf SU. Brownian particles on rough substrates: relation between intermediate subdiffusion and asymptotic long-time diffusion. *Phys Rev Lett* (2013) 88:062133. doi:10.1103/physreve.88.062133
22. Furst EM, and Squires TM. *Microrheology*. New York, NY: Oxford University Press (2017).
23. Dalle-Ferrier C, Krüger M, Hanes RDL, Walta S, Jenkins MC, and Egelhaaf SU. Dynamics of dilute colloidal suspensions in modulated potentials. *Soft Matter* (2011) 7:2064–75. doi:10.1039/c0sm01051k
24. Velarde SH, and Castaneda-Priego R. Diffusion in two-dimensional colloidal systems on periodic substrates. *Phys Rev E* (2009) 79:041407. doi:10.1103/PhysRevE.79.041407
25. Wei QH, Bechinger C, Rudhardt D, and Leiderer P. Experimental study of laser-induced melting in two-dimensional colloids. *Phys Rev Lett* (1998) 81: 2606. doi:10.1103/physrevlett.81.2606
26. Capellmann RF, Bewerunge J, Platten F, and Egelhaaf SU. Note: using a Kösters prism to create a fringe pattern. *Rev Scientific Instr* (2017) 88:056102. doi:10.1063/1.4982587
27. Metzler R, Jeon JH, Cherstvy AG, and Barkai E. Anomalous diffusion models and their properties: non-stationarity, non-ergodicity, and ageing at the centenary of single particle tracking. *Phys Chem Chem Phys* (2014) 16: 24128–64. doi:10.1039/c4cp03465a
28. Metzler R, and Klafter J. The random walk's guide to anomalous diffusion: a fractional dynamics approach. *Phys Rep* (2000) 339:1–77. doi:10.1016/s0370-1573(00)00070-3
29. Muñoz-Gil G, Garcia-March MA, Manzo C, Celi A, and Lewenstein M. Diffusion through a network of compartments separated by partially-transmitting boundaries. *Front Phys* (2019) 7:31. doi:10.3389/fphy.2019.00031
30. Lifson S, and Jackson JL. On the self-diffusion of ions in a polyelectrolyte solution. *J Chem Phys* (1962) 36:2410–4. doi:10.1063/1.1732899
31. Hänggi P, Talkner P, and Borkovec M. Reaction-rate theory: fifty years after kramers. *Rev Mod Phys* (1990) 62:251–341. doi:10.1103/revmodphys.62.251
32. Megen WV, and Underwood SM. The glass transition in colloidal hard spheres. *J Phys Condens Matter* (1994) 6:A181–186. doi:10.1088/0953-8984/6/23a/026
33. Carvajal-Tinoco MD, de León GC, and Arauz-Lara JL. Brownian motion in quasibidimensional colloidal suspensions. *Phys Rev E* (1997) 56:6962–9. doi:10.1103/PhysRevE.56.6962
34. Sarmiento-Gómez E, Rivera-Morán JA, and Arauz-Lara JL. Energy landscape of colloidal dumbbells in a periodic distribution of light. *Soft Matter* (2019) 15: 3573–9. doi:10.1039/c9sm00472f
35. Jenkins MC, and Egelhaaf SU. Colloidal suspensions in modulated light fields. *J Phys Condens Matter* (2008) 20:404220. doi:10.1088/0953-8984/20/40/404220
36. Ashkin A. Forces of a single-beam gradient laser trap on a dielectric sphere in the ray optics regime. *Biophys J* (1992) 61:569–82. doi:10.1016/s0006-3495(92)81860-x
37. Harada Y, and Asakura T. Radiation forces on a dielectric sphere in the Rayleigh scattering regime. *Opt Commun* (1996) 124:529–41. doi:10.1016/0030-4018(95)00753-9
38. Allan DB, Caswell TA, and Keim NC. trackpy: Trackpy v0.3.2 (Version v0.3.2). Zenodo (2019). doi:10.5281/zenodo.60550
39. Crocker JC, and Grier DG. Methods of digital video microscopy for colloidal studies. *J Colloid Interf Sci* (1996) 179:298–310. doi:10.1006/jcis.1996.0217
40. Ermak DL. A computer simulation of charged particles in solution. i. technique and equilibrium properties. *J Chem Phys* (1975) 62:4189–96. doi:10.1063/1.430300
41. Pérez-Guerrero D. *Statistical transitions of colloidal particles into two-dimensional periodic external potentials (in Spanish)*. [Bachelor's thesis]. San Luis (México): Facultad de Ciencias de la Universidad Autónoma de San Luis Potosí (2018).
42. Ferrando R, Spadacini R, and Tommei GE. Kramers problem in periodic potentials: jump rate and jump lengths. *Phys Rev E* (1993) 48:2437–51. doi:10.1103/physreve.48.2437
43. Pavliotis GA, and Vogiannou A. Diffusive transport in periodic potentials: underdamped dynamics. *Fluct Noise Lett* (2008) 08:L155–L173. doi:10.1142/s0219477508004453
44. McLeish TCB. *Thermal barrier hopping in biological Physics*. Boca Raton, Florida: CRC Press (2006). p. 123–35.
45. Sarmiento-Gómez E, Villanueva-Valencia JR, Herrera-Velarde S, Ruiz-Santoyo JA, Santana-Solano J, Arauz-Lara JL, et al. Short-time dynamics of monomers and dimers in quasi-two-dimensional colloidal mixtures. *Phys Rev E* (2016) 94:012608. doi:10.1103/physreve.94.012608

46. Rupprecht JF, Bénichou O, Grebenkov DS, and Voituriez R. Exit time distribution in spherically symmetric two-dimensional domains. *J Stat Phys* (2014) 158:192–230. doi:10.1007/s10955-014-1116-6
47. Mattos TG, Carlos MM, Metzler R, and Oshanin G. First passages in bounded domains: when is the mean first passage time meaningful?. *Phys Rev E* (2012) 86:031143. doi:10.1103/physreve.86.031143
48. Singer A, Schuss Z, and Holcman D. Narrow escape, part iii: non-smooth domains and riemann surfaces. *J Stat Phys* (2006) 122:491–509. doi:10.1007/s10955-005-8028-4
49. Mejía-Monasterio C, Oshanin G, and Schehr G. First passages for a search by a swarm of independent random searchers. *J Stat Mech Theor Exp* (2011) 2011: P06022. doi:10.1088/1742-5468/2011/06/p06022
50. Chupeau M, Gladrow J, Chepelianskii A, Keyser UF, and Trizac E. Optimizing brownian escape rates by potential shaping. *Proc Natl Acad Sci* (2020) 117: 1383–8. doi:10.1073/pnas.1910677116
51. Coughlan ACH, Torres-Díaz I, Zhang J, and Bevan MA. Non-equilibrium steady-state colloidal assembly dynamics. *J Chem Phys* (2019) 150:204902. doi:10.1063/1.5094554
52. Edwards T, Yang Y, Beltran-Villegas D, and Bevan M. Colloidal crystal grain boundary formation and motion. *Scientific Rep* (2014) 4:6132. doi:10.1038/srep06132
53. Palyulin VV, and Metzler R. How a finite potential barrier decreases the mean first-passage time. *J Stat Mech Theor Exp* (2012) 2012:L03001. doi:10.1088/1742-5468/2012/03/l03001

Conflict of Interest: The authors declare that the research was conducted in the absence of any commercial or financial relationship that could be construed as a potential conflict of interest.

5 APPENDIX

As both the Dalle-Ferrier et al. formula, and the Bellour fitting parameter $2\delta^{2BD}$ converge asymptotically to the Lifson-Jackson prescription, and the MSD at the time t^*, respectively, for large U_0 values, the associated errors are displayed in **Figures 15A,B**. In **Figure 15**, it is observed that the error of the Dalle-Ferrier et al. analytic formula is of the order of ten percent for $U_0 = 3K_BT$. This error can be decreased by increasing the magnitude of U_0. However, the error cannot be reduced less than 2 percent even for maximum heights of the periodic potential as large as $U_0 = 10\ K_BT$. On the other hand, the error in the convergence of the Bellour fitting parameter $2\delta^{2BD}$ regarding the MSD at the time t^* is similar to that displayed by the Dalle-Ferrier et al. formula at $U_0 = 3K_BT$, even though it reduces very quickly becoming as small as 0.01 percent for $U_0 = 3K_BT$.

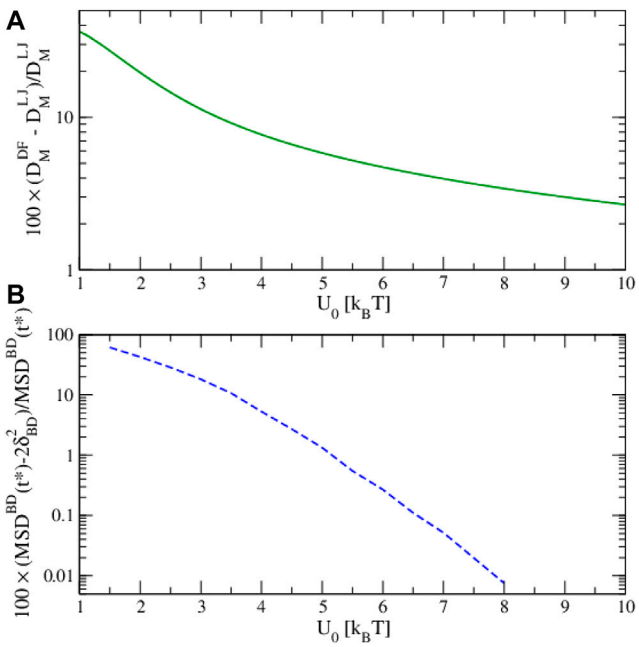

FIGURE 15 | (Color online): **(A)** Error of the long-time diffusion coefficient obtained from the Dalle-Ferrier formula D_M^{DF} regarding the value predicted by the Lifson-Jackson D_M^{LJ} prescription, and **(B)** difference between the fitting Bellour parameter $2\delta^2$ and the mean square displacement at the critical time $MSD\,(t^*)$ as a function of the maximum height barrier U_0. These results were obtained from Brownian dynamics simulations in which $L = 1.0 \times 10^{-6}\,m$ and $D_0 = 1.8 \times 10^{-13}\,m^2/s$ in all cases.

frontiers in Physics

ORIGINAL RESEARCH
published: 11 May 2021
doi: 10.3389/fphy.2021.634547

Quantum Implications of Non-Extensive Statistics

Nana Cabo Bizet[1]*, *César Damián*[2], *Octavio Obregón*[1] and *Roberto Santos-Silva*[3]

[1]Departamento de Física, División de Ciencias e Ingenierías, Universidad de Guanajuato, León, Mexico, [2]Departamento de Ingeniería Mecánica, Universidad de Guanajuato, Salamanca, Mexico, [3]Departamento de Ciencias Naturales y Exactas, CUValles, Universidad de Guadalajara, Jalisco, Mexico

Exploring the analogy between quantum mechanics and statistical mechanics, we formulate an integrated version of the Quantropy functional. With this prescription, we compute the propagator associated to Boltzmann–Gibbs statistics in the semiclassical approximation as $K = F(T)\exp(iS_{cl}/\hbar)$. We determine also propagators associated to different nonadditive statistics; those are the entropies depending only on the probability $S_{\pm}$ and Tsallis entropy S_q. For $S_{\pm}$, we obtain a power series solution for the probability vs. the energy, which can be analytically continued to the complex plane and employed to obtain the propagators. Our work is motivated by the work of Nobre et al. where a modified q-Schrödinger equation is obtained that provides the wave function for the free particle as a q-exponential. The modified q-propagator obtained with our method leads to the same q-wave function for that case. The procedure presented in this work allows to calculate q-wave functions in problems with interactions determining nonlinear quantum implications of nonadditive statistics. In a similar manner, the corresponding generalized wave functions associated to $S_{\pm}$ can also be constructed. The corrections to the original propagator are explicitly determined in the case of a free particle and the harmonic oscillator for which the semiclassical approximation is exact, and also the case of a particle with an infinite potential barrier is discussed.

Keywords: quantropy, nonlinear quantum systems, propagator, nonextensive entropies, path integrals

OPEN ACCESS

Edited by:
Atahualpa Kraemer, National Autonomous University of Mexico, Mexico

Reviewed by:
Angel R. Plastino, National University of Northwestern Buenos Aires, Argentina
Reza Khordad, Yasouj University, Iran
Abdel Tawfik, MTI University, Egypt

***Correspondence:**
Nana Cabo Bizet
nana@fisica.ugto.mx

Specialty section:
This article was submitted to Interdisciplinary Physics, a section of the journal Frontiers in Physics

Received: *28 November 2020*
Accepted: *22 January 2021*
Published: *11 May 2021*

Citation:
Cabo Bizet N, Damián C, Obregón O and Santos-Silva R (2021) Quantum Implications of Non-Extensive Statistics. Front. Phys. 9:634547. doi: 10.3389/fphy.2021.634547

1 INTRODUCTION

Nonextensive entropies depending only on the probabilities have been obtained in [1]. They belong to a family of nonextensive statistical mechanics, relevant for nonequilibrium systems. Renowned examples are Tsallis (S_q) [2, 3] and Sharma-Mital [4]; all of them can be obtained within the framework of Superstatistics [5].

For the entropies depending only on the probability, there are two entropy functionals [1]:

$$S_+ = \sum_l \left(1 - p_l^{p_l}\right), \quad S_- = \sum_l \left(p_l^{-p_l} - 1\right),$$

where the index l runs over the states of the system and p_l denotes the probability of the state l. These expressions can be considered as building blocks for nonextensive entropies without parameters. For example, one can consider $S_1 = (S_+ + S_-)/2$. These entropies are noticeably distinct to Boltzmann–Gibbs (BG) entropy for systems with few degrees of freedom; however, when

the number of degrees of freedom goes to the thermodynamic limit, they match perfectly with BG statistics Cabo [6]. This is when the probability p_l is small, the leading term in S_+ and S_- expansions is the BG entropy. Therefore, in this limit, BG statistics is recovered. They belong to the class of Superstatistics of [5] with an intensive parameter χ^2 distribution found in [1]. These entropies have also been studied in [6–10].

There is a universality of the Superstatistics family [5]. As it has been shown, for several distributions of the temperature, the Boltzmann factor essentially coincides up to the first expansion terms. This has as a consequence that also the entropies associated to these Boltzmann factors have all of them basically the same first corrections to the usual entropy. Furthermore, the three entropies listed here that depend only on the probability are expanded only on the parameter $y = p\ln p$; this is always smaller than 1 giving correction terms to the entropy which at any order are smaller than the previous ones. So, that any function of y proposed as another generalized entropy, depending only on this parameter, when expanded in y will basically coincide with one of the three ones studied here; clearly demanding that the first term in the expansion is $-y$ giving BG entropy. Thus, the entropies S_+, S_-, and their linear combinations can be considered as building blocks to compute any possible modified entropies depending only on the probability.

We are motivated by the concept of Quantropy developed by Baez and Pollard [11] and by nonlinear quantum systems with modified wave functions based on Tsallis statistics in [3, 12, 13]. For example, the work [13] developed a nonlinear quantum mechanics with q-mathematics motivated by Tsallis entropy. In recent years, there have also been other interesting developments in the connections of nonextensive entropies and quantum mechanics [14–25]. Also, the work [26] showed extensions of nonlinear quantum equations arising from an effective one particle treatment of many-body physics, such that the nonlinearity represents the interactions, obtaining wave function solutions that are q-distributions and including the harmonic oscillator potential. There exists as well a connection between nonlinear quantum equations and nonlinear diffusion and Fokker–Planck equations [18, 20] that also is noticed in [26]. Moreover, interesting applications of nonextensive entropies to compute statistical and thermodynamical properties of graphene and 2-dimensional quantum structures [27–30] have been developed. We develop a version of Quantropy in terms of the propagator of a quantum mechanical theory. Our generalized propagators could be connected to the appropriate quantum equations. Baez and Pollard's Quantropy is a functional of the amplitude on the path integral a, with the same functional form as the entropy in terms of the probability $Q = -\int_X a(x)\ln a(x)dx$. Giving the functional

$$\Phi_{\rm BP} = -\int_X a(x)\ln a(x)dx - \alpha\int_X a(x)dx - \lambda\int_X a(x)S(x)dx, \tag{1}$$

where α and λ are Lagrange multipliers and x is a path in the space of all possible paths X. From the search of extrema of this functional, restricted to values of a normalized and an average of the action, Baez and Pollard obtained the relation $a = \exp(iS/\hbar - 1 - \alpha)$ with $\lambda = \frac{1}{i\hbar}$. Then, $a \sim \exp(iS/\hbar)$ with the normalization fixed by the Lagrange multiplier α. This scheme deepens on the relation between Quantum Mechanics and Statistical Physics, which has also been studied in different approaches [31, 32]. For example, in [33], the Fisher Information measure is employed to explore this relation.

In Baez and Pollard's approach, the energy is mapped to the action S and the temperature to $i\hbar$. We consider the same identification but instead we identify E with the classical action S_{cl}. Thus, we consider as the analog of the entropy a functional in terms of the propagator, instead of the amplitude a. This is an extrapolation of the Quantropy [11] to an integration over all classical paths. It is worth to mention that the analog to the microstate in statistical mechanics is a particle path in quantum mechanics. Such that as the partition function in statistical mechanics is the sum over all the microstates, the quantum mechanical analog is the sum over all the paths of the particle (Feynman path integral). The standard expression for the propagator is given semiclassically by $K \sim \exp(iS_{cl}/\hbar)$. We use this fact to define a kind of integrated Quantropy functional now in terms of the propagator for BG statistics, which we extend to the modified statistics S_+, S_-, and S_q.

This article is organized as follows. In **Section 2**, we obtain a series expansion for the probabilities versus βE for the generalized entropies depending only on the probabilities S_+ and S_-. In **Section 3**, we continue these expansions to the complex plane. In **Section 4**, we present a version of Quantropy for BG statistics, S_+ and S_- and S_q. In **Section 5**, we study in particular the case of the free particle propagator, obtained from the extrema of the Quantropy in the cases of S_+ and S_- and S_q for $q < 1$ and $q > 1$. We show that the K_q propagator results exactly in the q-exponential that defines the q-wave function for the free particle [3]. In a similar manner, we argue that the corresponding generalized propagators K_+ and K_- provide us with a procedure to construct Ψ_+ and Ψ_- for the free particle. Our method however gives the possibility to construct K_q, K_+, and K_- also for problems with interactions and by this mean to identify the corresponding wave functions. We also provide a way to perform the normalization inspired in Feynman and Hibbs work [34]. **Section 6** is devoted to the analysis of the harmonic oscillator, and we exemplify with the case corresponding to K_+. Finally, in **Section 7**, we study the K_+ propagator for the particle in an infinite potential barrier. In **Section 8**, we summarize our results and present the conclusion. In a **Supplementary Appendix** we present a numerical study of the propagators.

2 PROBABILITY DISTRIBUTIONS FOR SYSTEMS WITH MAXIMAL S_+ AND S_-

We start by developing a recurrent solution for the probability distribution of the generalized entropy S_+, introduced in [1]. On

the contrary to BG statistics, for a system subjected to S_+ extremization, probability normalization, and energy conservation, there is not a simple inverse function of the probabilities p vs. the values of the energy state E. We overcome this difficulty by finding a series solution to the extremum equation. There are other possible series solutions, but we discuss here one that has a good convergence. At the end of the section, we give also the probability expansion for the entropy S_-, which is obtained by an equivalent Ansatz.

The functional to maximize the S_+ entropy subjected to probability normalization and averaged energy is given by [7, 8]:

$$\Phi_+ = \sum_l \left(1 - p_l^{p_l}\right) - \gamma \sum_l p_l - \beta \sum_l E_l p_l^{p_l+1}. \tag{2}$$

β and γ are Lagrange multipliers and E_l is the energy of the state l, with probability p_l. The average values of energy and the normalization value have been omitted for simplicity. The extrema of **(2)** given by $\frac{\delta\Phi_+}{\delta p_l} = 0$ gives a relation between the energy E and the probabilities p (we have omitted the index l):

$$\beta E = \frac{\left(-\gamma p^{-p} - 1 - \ln p\right)}{\left(1 + p + p\ln p\right)}. \tag{3}$$

Notice that we omit the subindex l from the quantities. Setting the Lagrange multiplier γ to −1, we first expand the previous equation around $p = 0$ that accounts to consider the expansion around $y = p\ln p = 0$. That is, for the exponential of minus **equation (3)**, one gets

$$\begin{aligned} e^{-\beta E} = p - p^2\ln p^2 + 1/2\,p^3\left(\ln p^2 + 2\ln p^3 + \ln p^4\right) \\ +1/6\,p^4\left(-3\ln p^2 - 8\ln p^3 - 9\ln p^4 - 6\ln p^5 - \ln p^6\right) \\ +1/24\,p^5\left(12\ln p^2 + 44\ln p^3 + 70\ln p^4 + 68\ln p^5 + 42\ln p^6 + 12\ln p^7 + \ln p^8\right) + \ldots . \end{aligned} \tag{4}$$

We make the following Ansatz to solve **equation (4)**.

$$p = e^{-\beta E}\left(1 + \sum_{n=1} c_n e^{-n\beta E}\right), \tag{5}$$

where c_n can be functions of βE. Plugging **(5)** in **(4)**, to have the LHS equal to the RHS, the coefficients multiplying the powers of $e^{-n\beta E}$ with $n > 1$ have to vanish. This gives a recurrent expression for the coefficients c_n which for the first four coefficients is solved as

$$\begin{aligned} c_1 &= x^2, \\ c_2 &= 1/2x^2\left(-1 - 2x + 3x^2\right), \\ c_3 &= \frac{1}{6}x^2\left(3 + 4x - 6x^2 - 24x^3 + 16x^4\right), \\ c_4 &= \frac{1}{24}x^2\left(-12 - 16x + 60x^2 + 116x^3 + 30x^4 - 300x^5 + 125x^6\right). \end{aligned} \tag{6}$$

We have denoted βE as x. The coefficients **(6)** give the following approximate solution for the probabilities versus βE:

$$\begin{aligned} p_+ = {} & e^{-x} + e^{-2x}x^2 + \frac{1}{2}e^{-3x}x^2\left(-1 - 2x + 3x^2\right) \\ & + \frac{1}{6}e^{-4x}x^2\left(3 + 4x - 6x^2 - 24x^3 + 16x^4\right) \\ & + \frac{1}{24}e^{-5x}x^2\left(-12 - 16x + 60x^2 + 116x^3 + 30x^4 - 300x^5\right. \\ & \left. + 125x^6\right) + \ldots . \end{aligned} \tag{7}$$

In **Figure 1**, we compare the exact value of p vs. βE with the power series solution **(7)** till 3rd order and with the Boltzmann distribution $e^{-\beta E}$.

Probability Expansion for the Entropy S_-

Consider the other generalized entropy dependent only on the probabilities S_-. For this entropy, the functional to extremize Φ_- reads

$$\Phi_- = \sum_l \left(p_l^{-p_l} - 1\right) - \gamma \sum_l p_l - \beta \sum_l E_l p_l^{1-p_l}. \tag{8}$$

β and γ are Lagrange multipliers, and E_l is the energy of the state l and p_l its probability. Finding the extrema of **(8)** as $\frac{\delta\Phi_-}{\delta p_l} = 0$ and proposing the same Ansatz (5), we obtain a set of equations that can be solved to give the recursive probability solution:

$$\begin{aligned} p_- = {} & e^{-x}\left(1 - e^{-x}x^2 + \frac{1}{2}e^{-2x}x^2\left(-1 - 2x + 3x^2\right)\right. \\ & \left. + \frac{1}{6}e^{-3x}\left(-3x^2 - 4x^3 + 6x^4 + 24x^5 - 16x^6\right)\right)\ldots \end{aligned} \tag{9}$$

3 MODIFIED AMPLITUDE EXPANSIONS

In this section, we use the series solutions for the probabilities in terms of the energy obtained in the previous section, to perform an analytic continuation to the complex plane. Considering a as the amplitude of a path, this is a new complex variable substituting the probability p_l, and A as the action replacing βE_l. This identification will allow to study modified Quantropy functionals, for the definition of Baez and Pollard (equation **(1)**), as well as our definition **(18)**. The usual Quantropy solution will give an exponential $a \sim e^{\frac{iA}{\hbar}}$. In our approach, this would be the propagator $K \sim e^{\frac{iS_{cl}}{\hbar}}$. We want to analyze the new statistics S_+ and S_-. We will find a functional dependence of a vs. A (K vs. S_{cl}) that deviates from the exponential dependence.

The main idea is to complexify first the power expansion solution **(7)** since the amplitude is a complex number, such that we have a solution to the extrema of the modified Quantropy. The functional to extremize reads

$$\Phi_{BP,+} = \int \left(1 - a(x)^{a(x)}\right)dx - \alpha\int a(x)dx - \lambda\int A(x)a(x)^{a(x)+1}dx. \tag{10}$$

Finding the extrema of **(10)** w.r.t. a, i.e., solving $\frac{\delta\Phi_{BP,+}}{\delta a(x)} = 0$, one gets

$$\frac{A}{i\hbar} = \frac{\left(-\gamma a^{-a} - 1 - \ln a\right)}{\left(1 + a + a\ln a\right)} = F\left(a\left(\frac{A}{i\hbar}\right)\right). \tag{11}$$

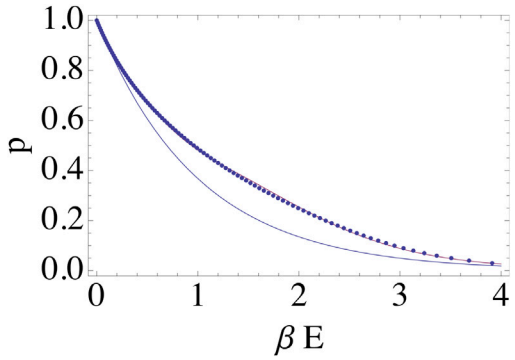

FIGURE 1 | Probability versus βE. The blue line represents the BG statistics distribution. The dots represent the exact dependence in **(3)**, S_+ statistics distribution, while the continuous red curve overlapping with the dotted line represents the power series solution **(7)** till order 3, i.e., up to the e^{-4x} correction.

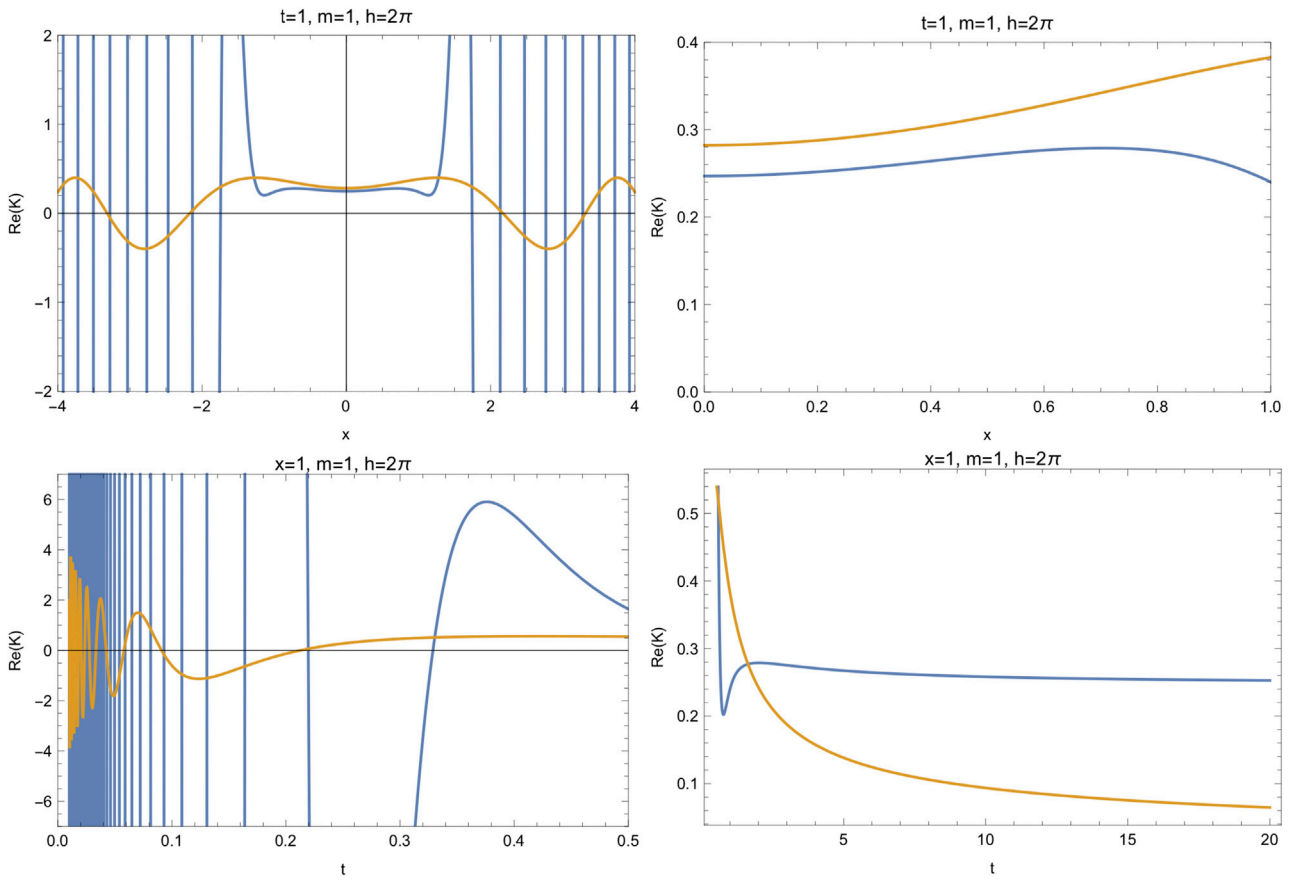

FIGURE 2 | Real parts of the modified propagator (blue line) vs. standard propagator (yellow line), for the free particle for the modified statistics S_+. We set the mass and the Planck constant to unity. The quantum regime is given by $S_{cl} \approx h$. Imposing $S_{cl} \lesssim h$ which translates for fixed $x = 1$ in $t \gtrsim 1/2$, for fixed $t = 1$ translates in $x^2 \lesssim 2$. Notice that in the quantum regime $S_{cl} \approx h$, there are differences between the standard and the modified propagator. In the classical regime, there are many oscillations caused by the series expansion that should sum up when computing more terms. When $S_{cl} \ll h$, then both results coincide. The difference between the results of the modified propagator and the standard free particle is that the modified propagator result could be interpreted as the particle with an effective potential; this would give a spatially bounded wave function.

The range of validity of the propagators expressions depends on the convergence of the imaginary series solution to this equation. The series is obtained by doing the replacement βE by $\frac{A}{i\hbar}$ and p by a in **(3)**. Also, the Lagrange multipliers have to be mapped: β to λ and α to γ. The minus sign gives the right sign after a rotation on the argument of the exponential (similar to a Wick rotation). As the series solution continuation of **(7)**, we obtain the following expression:

$$\begin{aligned} a_+\left(\frac{A}{i\hbar}\right) = e^{iA/\hbar}\Big(1 - \frac{A^2}{\hbar}e^{i(A/\hbar)} \\ -\frac{1}{2}\left(A^2/\hbar^2\right)\left(-1 + 2i(A/\hbar) - 3\left(A^2/\hbar^2\right)\right)e^{i2(A/\hbar)} \\ -\frac{1}{6}\left(A^2/\hbar^2\right)\left(3 - 4i(A/\hbar) + 6\left(A^2/\hbar^2\right) - 24i\left(A^3/\hbar^3\right)\right. \\ \left.+16\left(A^4/\hbar^4\right)\right)e^{3i(A/\hbar)} + \ldots\Big). \end{aligned} \tag{12}$$

Since A has units of action, the argument of the exponentials and the terms on the expansion are adimensional. Substituting this expression on the constraint **equation (11)**, we obtain the real and imaginary parts of $F\left(a\left(\frac{A}{i\hbar}\right)\right)$. In **Figure 2**, the relevant difference of the propagators K_+ obtained employing **(12)** with respect to the standard one can be observed in the region of $S_{cl} \approx \hbar$.

Using the parameter $\lambda = \frac{1}{i\hbar}$ in **(12)**, the expression for the amplitudes becomes

$$\begin{aligned} a_+(A) = e^{-\lambda A}\Big(1 + (\lambda A)^2 e^{-\lambda A} \\ +\frac{1}{2}(\lambda A)^2\left(-1 - 2\lambda A + 3(\lambda A)^2\right)e^{-2\lambda A} \\ +\frac{1}{6}(\lambda A)^2\left(3 + 4\lambda A - 6(\lambda A)^2 - 24(\lambda A)^3\right. \\ \left.+16(\lambda A)^4\right)e^{-3\lambda A} + \ldots\Big). \end{aligned} \tag{13}$$

It is not difficult to observe that all terms of this expansion can be written as derivatives with respect to the parameter λ. If we derive with respect to λ, the usual amplitude we obtain is $\frac{\partial}{\partial\lambda}e^{-\lambda A} = -Ae^{-\lambda A}$. Higher derivates can be written as

$$\left(\frac{\lambda}{n}\right)^m \frac{\partial^m}{\partial\lambda^m}e^{-n\lambda A} = (-1)^m(\lambda A)^m e^{-n\lambda A}, \tag{14}$$

where m and n are positive integers. Thus, we rewrite (3) as

$$\begin{aligned} a_+ = e^{-\lambda A} + \frac{\lambda^2}{4}\frac{\partial^2}{\partial\lambda^2}e^{-2\lambda A} \\ +\frac{1}{2}\left(-\frac{\lambda^2}{3^2}\frac{\partial^2}{\partial\lambda^2} + 2\frac{\lambda^3}{3^3}\frac{\partial^3}{\partial\lambda^3} + 3\frac{\lambda^4}{3^4}\frac{\partial^4}{\partial\lambda^4}\right)e^{-3\lambda A} \\ +\frac{1}{6}\left(3\frac{\lambda^2}{4^2}\frac{\partial^2}{\partial\lambda^2} - 4\frac{\lambda^3}{4^3}\frac{\partial^3}{\partial\lambda^3} - 6\frac{\lambda^4}{4^4}\frac{\partial^4}{\partial\lambda^4} + 24\frac{\lambda^5}{4^5}\frac{\partial^5}{\partial\lambda^5} + 16\frac{\lambda^6}{4^6}\frac{\partial^6}{\partial\lambda^6}\right)e^{-4\lambda A} + \ldots . \end{aligned} \tag{15}$$

One can compute the corrections to any order. Those corrections to the usual amplitude $a_0 = e^{iS/\hbar}$ can be interpreted as higher order interactions of the action at different frequencies[1].

Now, one can apply the same method to determine the distribution arising from the Quantropy with statistics S_-. We also have to perform the extension to the complex plane. The amplitude distribution for the modified Quantropy coming from S_- is given by the following:

$$\begin{aligned} a_- = e^{i(A/\hbar)}\Big(1 + (A/\hbar)^2 e^{i(A/\hbar)} \\ -\frac{1}{2}(A/\hbar)^2\left(-1 + 2i(A/\hbar) - 3(A/\hbar)^2\right)e^{2i(A/\hbar)} \\ +\frac{1}{6}\left(3(A/\hbar)^2 - 4i(A/\hbar)^3 + 6(A/\hbar)^4\right. \\ \left.-24i(A/\hbar)^5 + 16(A/\hbar)^6\right)e^{3i(A/\hbar)} + \ldots\Big). \end{aligned} \tag{16}$$

4 QUANTROPY IN TERMS OF THE PROPAGATOR

In this section, we present as an alternative proposal a kind of integrated version of the Quantropy of [1]. First, we do it for the BG entropy and then for S_+, S_-, and S_q. The change in distribution probabilities which arise from modified entropies in statistics is now reflected in the quantum arena as modifications to the propagators. The propagators between points in space-time $(\mathbf{x}_a, t_a)$ and $(\mathbf{x}_b, t_b)$ in quantum mechanics determine the probability amplitude of particles to travel from certain position to another position in a given time. As modified entropies in statistical physics lead to modified probability distributions, distinct probabilities of propagation over all paths from $(\mathbf{x}_a, t_a)$ and $(\mathbf{x}_b, t_b)$ will arise from a modified Quantropy.

In the work [11], the Quantropy functional associated with BG statistics was formulated, and its maximization leads to the weight on the path integral $a \sim \exp(-\lambda S)$ with $\lambda = 1/i\hbar$. We propose another functional, which in a sense constitutes an integrated version of Quantropy. Its maximization leads to the propagator $K(x) \sim \exp(-\lambda S_{cl}(x))$. The Wentzel–Kramers–Brillouin (WKB) method [35] allows to compute the wave function in a semiclassical approximation. In a sense, this is linked to our approach, in which we maximize a functional which determines the propagator with a semiclassical approximation in terms of the classical action S_{cl}. This is exact for the free particle, the harmonic oscillator as well as for other cases [36, 37]. The procedure is applied to generalized entropy functionals, giving a modified propagator. For the Tsallis statistics, we obtain $K_q(x) \sim \exp_q(-\lambda S_{cl}(x))$. This structure is the same as the one of the wave function for the free particle of the Tsallis statistic $\Psi_q(x) = \exp_q(i(kx - wt))$, which has been proposed as solution of the nonlinear quantum equations of [13]. According to Feynman arguments, one can start with the free particle propagator and determine the corresponding wave function, as discussed in [34]. Thus, our procedure allows to find a propagator which can be identified with the wave function of interest. We should note that the propagator resulting from our procedure will describe not only the

[1]For example, for a massive particle those will be contributions from multiples of the particle mass. For the harmonic oscillator also, there will be contributions with a tower of masses and frequencies.

free particle but to a good approximation any other problem with its corresponding classical action. Our method should give the wave function solution for the problem of interest.

With the same method, we write functionals for S_+ and S_- and obtain probability distributions; we can write the corresponding Quantropies and obtain the propagators K_+ and K_- and correspondingly extrapolate them to the wave functions Ψ_+ and Ψ_-. This would give us the quantum behavior for a given action. The obtained propagators can be related to nonlinear quantum systems studied in the literature [26].

To define our functionals, we use the semiclassical limit to compute the propagator; this is $K(x) = F(a,b)e^{\frac{iS_{cl}(x)}{\hbar}}$, denoting the classical action as $S_{cl}(x)$ and being $F(a,b)$ a constant depending on the time difference $t_b - t_a$. For the free particle and the harmonic oscillator as well as other physical problems [36, 37], this is an exact result.

For the BG statistics, we define the Quantropy functional:

$$\Phi_0 = -\int K(x)\ln K(x)dx - \alpha\int K(x)dx - \lambda\int (S_{cl}(x)K(x))dx. \quad (17)$$

The extrema condition $\frac{\delta\Phi_0}{\delta K(x)} = 0$ gives as solution the propagator dependence $K(x) = e^{-1-\alpha-\lambda S_{cl}(x)}$, with $\lambda = 1/i\hbar$, where the normalization constant α determines $F(a,b)$.

The integrated Quantropy functional for the new S_+ statistic is studied in [1, 6–10] is given by the following:

$$\Phi_+ = \int \left(1 - K(x)^{K(x)}\right)dx - \alpha\int K(x)dx - \lambda\int (S_{cl}(x))K(x)^{K(x)+1}dx. \quad (18)$$

The extrema condition $\frac{\delta\Phi_+}{\delta K(y)} = 0$ with functional derivatives leads to the equation:

$$0 = \int \left(-\delta(x-y)K(x)^{K(x)}\right)(\ln K(x)+1)dx - \alpha\int \delta(x-y)dx - \lambda\int S_{cl}(x)K(x)^{K(x)+1}\delta(x-y)\left(\ln K(x) + \frac{K(x)+1}{K(x)}\right)dx, \quad (19)$$

and by changing the variable notation y to x, this can be written as

$$\lambda S_{cl}(x) = \frac{-1 - \ln K(x) - \alpha K(x)^{-K(x)}}{1 + K(x) + \ln K(x)}. \quad (20)$$

Using our knowledge to solve this type of equation from the statistical physics case, presented in **Section 2**, this gives for the modified propagator the following series solution:

$$K_+(x) = N_+ e^{-\lambda S_{cl}}\Big(1 - e^{-\lambda S_{cl}}(\lambda S_{cl})^2 + e^{-2\lambda S_{cl}}(\lambda S_{cl})^2\left(-1 - 2(\lambda S_{cl}) + 3(\lambda S_{cl})^2\right) - \frac{1}{6}e^{-2S_{cl}\lambda}\times\left(-3S_{cl}^2\lambda^2 - 4S_{cl}^3\lambda^3 + 6S_{cl}^4\lambda^4 + 24S_{cl}^5\lambda^5 - 16S_{cl}^6\lambda^6\right) + \ldots\Big). \quad (21)$$

where N_+ is the normalization constant. This is obtained by taking the normalization $\alpha = -1$. A different normalization would change the coefficients in the expansion (21).

The maximization constraint for the new S_- statistic is given by

$$\Phi_- = \int \left(K(x)^{-K(x)} - 1\right)dx - \alpha\int K(x)dx - \lambda\int (S_{cl})K(x)^{-K(x)+1}dx. \quad (22)$$

The extrema condition $\frac{\delta\Phi_-}{\delta K(x)} = 0$ gives the equation:

$$\lambda S_{cl}(x) = \frac{1 + \ln K(x) + \alpha K(x)^{K(x)}}{1 - K(x) - \ln K(x)}. \quad (23)$$

Using our knowledge of this type of equation from the statistical physics case, we obtain for the modified propagator the series solution:

$$K_-(x) = N_- e^{-\lambda S_{cl}}\Big(1 + e^{(-\lambda S_{cl})}(\lambda S_{cl})^2 - e^{(-\lambda S_{cl})}(\lambda S_{cl})^2(-1 - 2(\lambda S_{cl}) + 3(\lambda S_{cl})^2 + \frac{1}{6}e^{-2S_{cl}\lambda}\left(-3S_{cl}^2\lambda^2 - 4S_{cl}^3\lambda^3 + 6S_{cl}^4\lambda^4 + 24S_{cl}^5\lambda^5 - 16S_{cl}^6\lambda^6\right) + \ldots\Big), \quad (24)$$

N_- is the normalization constant. In the case of Tsallis statistics, the functional is given by the following:

$$\Phi_q = \int \frac{(1 - K(x)^q)}{(q-1)}dx - \alpha\int K(x)dx - \lambda\int (S_{cl})K(x)^q dx, \quad (25)$$

and the solution to $\frac{\delta\Phi_q}{\delta K(x)} = 0$ is

$$K_q(x) = N_q \exp_q(-\lambda S_{cl}(x)), \quad = N_q\left(1 - (1-q)\lambda S_{cl}\right)^{\frac{1}{1-q}}. \quad (26)$$

We have still to discuss the normalization of the different Kernels. This q-propagator is related to the q-wave function for the free particle nonlinear quantum mechanics of [3]. We explore this case which has been studied by other means in the literature [3, 13, 24].

5 FREE PARTICLE PROPAGATORS

In this section, we write a modified propagator up to third order for the free particle in the case of the statistics S_+, S_-, and S_q for $q = 1 - \delta$ and $q = 1 + \delta$ with $\delta > 0$. The values of q less or equal than one are considered in order to compare the different propagators. We determine when the corrections to the usual propagator play an important role which turns to be in the quantum regime characterized by $S_{cl} \approx \hbar$. First, we describe the procedure; then, we describe the normalization; and in the last subsection, we summarize our results.

5.1 Superposition of Kernels

Now, we proceed to describe a generalized Kernel. The generalized complex probability distribution given by expansion (21) can be regarded as a superposition of

Kernels. Furthermore, the superposition will carry to the wave functions. In order to normalize the superposition, we consider that the total Kernel expansion integration is the same as the usual (1 for the free particle), as is explicit in the Quantropy functional (**4**). We show that this coincides with the result for the normalization obtained from propagating the wave function [34]. For the free particle, the unnormalized Kernel is as follows:

$$K_0(x,t;0,0)=\left(\frac{2\hbar\epsilon i\pi}{m}\right)^{(n-1)/2}\left(\frac{1}{n}\right)^{1/2}\exp\left(\frac{imx^2}{2\hbar t}\right),$$

where n is the number of divisions of the time interval and ϵ is an infinitesimal time parameter that satisfies $t=\epsilon n$. This expression arises from computing the path integral to get the following:

$$\begin{aligned}K_0(x,t;0,0)&=\int e^{iS/\hbar}Dx\\&=\int\exp\left(\frac{im}{2\hbar\epsilon}\sum_n(x_n-x_{n-1})^2\right)d^nx\\&=\left(\frac{i\pi}{2A}\right)^{\frac{1}{2}}\left(\frac{2i\pi}{3A}\right)^{\frac{1}{2}}\left(\frac{3i\pi}{4A}\right)^{\frac{1}{2}}\times\ldots\\&\times\left(\frac{(n-1)i\pi}{nA}\right)^{\frac{1}{2}}\exp\left(\frac{iA(x_0-x_n)^2}{n}\right),\end{aligned}\tag{27}$$

with $A=\frac{m}{2\epsilon\hbar}$. This calculation is performed dividing the integral in multiple Gaussian integrals (see [34]). The normalization constant is given by $N=\left(\frac{2\pi i\hbar\epsilon}{m}\right)^{-\frac{n}{2}}$; hence, the normalized propagator reads

$$K_1(x,t;0,0)=\left(\frac{2\hbar ti\pi}{m}\right)^{-1/2}\exp\left(\frac{imx^2}{2\hbar t}\right).\tag{28}$$

We define the unnormalized Kernel for the free particle as

$$k(x,t;1)=\exp\left(\frac{imx^2}{2\hbar t}\right)=e^{-\lambda A},\tag{29}$$

and the first two corrections in K_+ are given by

$$\begin{aligned}k(x,t;2)&=\left(\frac{mx^2}{\hbar t}\right)^2\exp\left(\frac{imx^2}{\hbar t}\right)=(\lambda A)^2\frac{\partial^2}{\partial\lambda^2}e^{-\lambda A},\\k(x,t;3)&=-\left(\frac{m^2x^4}{8\hbar^2t^2}+\frac{m^3x^6}{8i\hbar^3t^3}+3\frac{m^4x^8}{32\hbar^4t^4}\right)\times\exp\left(\frac{3imx^2}{2\hbar t}\right),\\&=\frac{1}{2}\left(-\frac{\lambda^2}{3^2}\frac{\partial^2}{\partial\lambda^2}+2\frac{\lambda^3}{3^3}\frac{\partial^3}{\partial\lambda}+3\frac{\lambda^4}{3^4}\frac{\partial^4}{\partial\lambda^4}\right)e^{-3\lambda A}.\end{aligned}$$

Thus, the generalized Kernel associated with S_+ entropy is given by

$$K_+(x,t)=N_+(k(x,t;1)+k(x,t;2)+k(x,t;3)+\ldots).$$

The normalization constant is determined by the requirement $\int_{-\infty}^{\infty}K_+(x,t)dx=1$, and up to the first corrections is given by $N_+=\frac{1}{1+3/(16\sqrt{2})}=0.883....$ The reason for this normalization is also understood by an argument presented in the following, motivated by Feynmann and Hibbs procedure [34].

Let us also discuss the normalization of the modified propagator with respect to the usual one, as shown in the standard case [34]. We start considering the original unnormalized Kernel for the free particle computed from the path integral:

$$K_{1,0}(x,t;0,0)=2^{\frac{N-1}{2}}\left(\frac{\pi i\hbar t}{mN}\right)^{\frac{N-1}{2}}(N)^{-1/2}\exp\left(\frac{imx^2}{2\hbar t}\right).$$

To determine the normalization constant in the Feynman and Hibbs method, we can apply formulas (2–34) and (4-3) on their book [34] to write the new infinitesimal Kernel between position x_i and x_{i+1}, with $\Delta x_i=x_{i+1}-x_i$, in a time ϵ as follows:

$$\begin{aligned}K_+(i_{i+1},i)&=\frac{1}{A}\exp\left(\frac{i\epsilon}{\hbar}L\left(\frac{\Delta x_i}{\epsilon},\frac{x_{i+1}+x_i}{2},\frac{t_{i+1}+t_i}{2}\right)\right),\\&\left(1+(i\epsilon/\hbar)^2L\left(\frac{\Delta x_i}{\epsilon},\frac{x_{i+1}+x_i}{2},\frac{t_{i+1}+t_i}{2}\right)^2\exp\left(i\epsilon L(v,\overline{x},\overline{t})/\hbar\right)+\ldots\right).\end{aligned}\tag{30}$$

The method consists in writing the wave function at a position x at a time $t+\epsilon$ in terms of the wave function at position $y=x+\eta$ at a time t, explicitly

$$\begin{aligned}\psi(x,t+\epsilon)&=\int_{-\infty}^{\infty}K_+(x,y,\epsilon)\psi(y,t)dy,\\&=\int_{-\infty}^{\infty}\frac{1}{A}\exp\left(\frac{i\epsilon}{\hbar}L\left(\frac{x-y}{\epsilon},\frac{x+y}{2},t\right)\right)\times(1+\ldots)\psi(y,t)dy,\\&=\int_{-\infty}^{\infty}\frac{1}{A}\exp\left(\frac{i\epsilon}{\hbar}L\left(-\frac{\eta}{\epsilon},x+\frac{\eta}{2},t\right)\right)\times(1+\ldots)\psi(x+\eta,t)d\eta,\\&=\int_{-\infty}^{\infty}\frac{1}{A}\exp\left(\frac{im\eta^2}{2\hbar\epsilon}\right)\exp\left(-\frac{i\epsilon V\left(x+\frac{\eta}{2},t\right)}{\hbar}\right)\times(1+\ldots)\psi(x+\eta,t)d\eta.\end{aligned}\tag{31}$$

In the quantum standard theory, the normalization constant can be determined by expanding the LHS of **(31)** $\psi(x,t+\epsilon)=\psi(x,t)+\epsilon\partial_t\psi$ and the RHS $\psi(x+\eta)=\psi(x,t)+\eta\partial_x\psi+\frac{\eta^2}{2}\partial_x^2\psi$ and $\exp(-i\epsilon V/\hbar)=1-\frac{i\epsilon V}{\hbar}+\ldots$; then, we compare the leading term ϵ^0. This implies that

$$\frac{1}{A_0}\int_{-\infty}^{\infty}\exp\left(\frac{im\eta^2}{2\hbar\epsilon}\right)d\eta=1.\tag{32}$$

In a similarly fashion, one gets for the first correction to K_+ written in **(30)**:

$$\frac{1}{A}\int_{-\infty}^{\infty}\exp\left(\frac{im\eta^2}{2\hbar\epsilon}\right)\left(1-\left(\frac{m\eta^2}{2\hbar\epsilon}\right)^2e^{\frac{im\eta^2}{2\hbar\epsilon}}+\ldots\right)d\eta=1.$$

It is worth to mention that the more important contribution to (31) is given for small η's, as well as in our generalized case. It is necessary to check this argument; in order to verify, let us consider the following integrals:

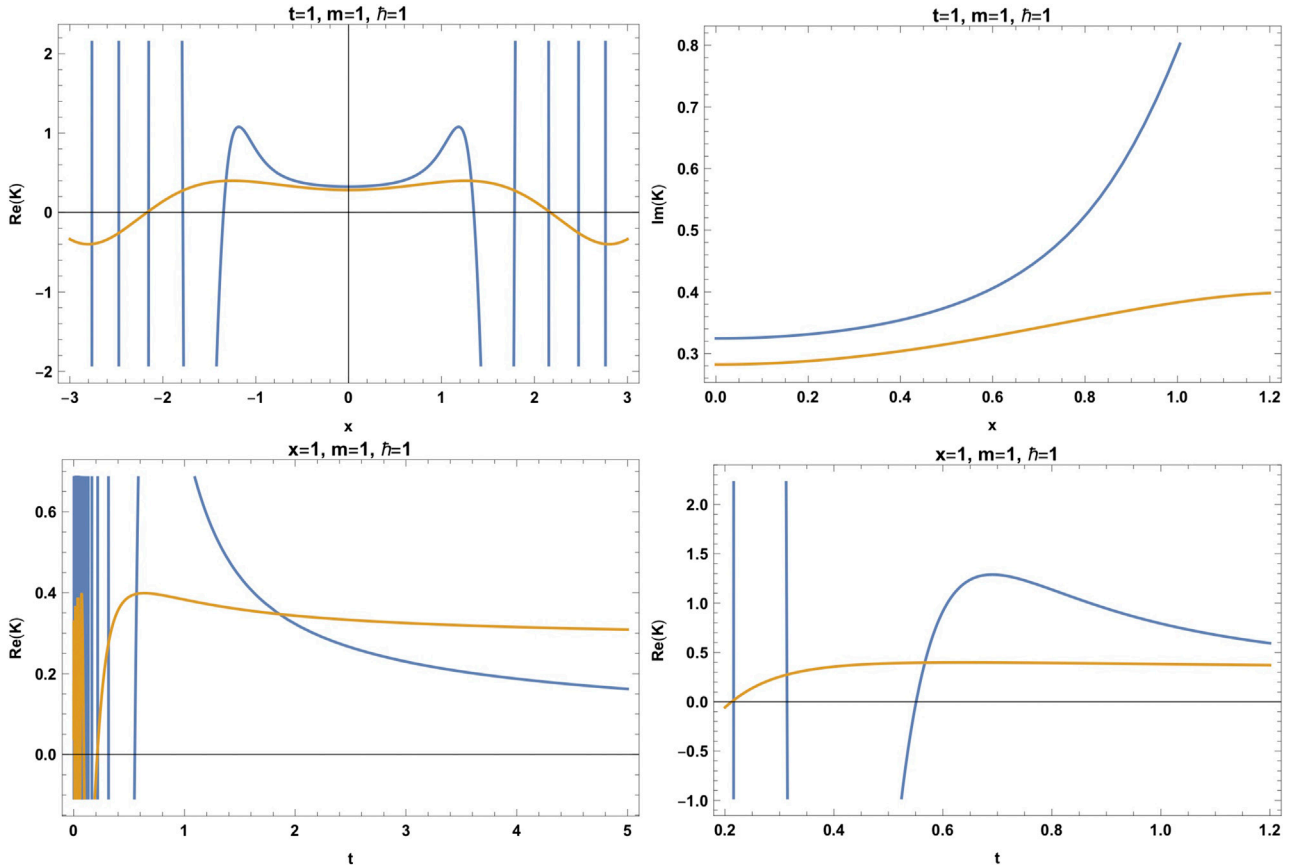

FIGURE 3 | Real parts of the modified propagator (blue line) vs. standard propagator (yellow line), for the free particle for the modified statistics S_-. We set the mass and the Planck constant to unity. Imposing $S_{cl} \lesssim \hbar$ for fixed $x = 1$ translates in $t \gtrsim 1/2$, and for fixed $t = 1$ translates in $x^2 \lesssim 2$.

$$\int e^{iCw^2} dw = \sqrt{i\pi/C}, \quad \int e^{iCw^2} w^4 dw = \frac{3\sqrt{\pi}}{4(-iC)^{5/2}},$$

$$\int e^{iCw^2} w^{2n+1} dw = 0, \quad n \in N.$$

The first correction gives the following relation:

$$A = A_0\left(1 + \frac{3}{16\sqrt{2}} + \dots\right). \tag{33}$$

The previous normalization factor is a general feature to apply to any potential $V(x,t)$, in particular is valid for the cases discussed here. A similar expression holds for the normalization of K_- normalization, and this will be calculated in the next section.

5.2 Analysis of the Propagators

Here, we summarize the propagators obtained with the normalization methods described in previous subsections. The results for K_+ can be extrapolated to K_- and K_q because the method applied to obtain all of the propagators is the same.

Recall the standard propagator of the free particle from the space-time point $(0,0)$ to (x,t) is given by

$$K_1(x,t;0,0) = N_0 \exp\left(\frac{imx^2}{2\hbar t}\right). \tag{34}$$

The constant w.r.t. x is as follows: $N_0 = \sqrt{\frac{m}{2\pi i\hbar t}}$. For the case of S_+ and S_- statistics, the first two contributions to the modified propagators (21) and (24) read:

$$K_\pm = N_\pm \exp\left(\frac{imx^2}{2\hbar t}\right) \times \left(1 \mp \exp\left(\frac{imx^2}{2\hbar t}\right)\left(\frac{imx^2}{2\hbar t}\right)^2 + \dots\right), \tag{35}$$

with $N_+ \sim N_0$. For the Tsallis statics, the associated propagator (26) is given by the expression:

$$K_q(x) = N_q\left(1 + (q-1)\left(\frac{mx^2}{2\hbar it}\right)\right)^{\frac{1}{1-q}}$$
$$= N_q \exp\left(\frac{imx^2}{2\hbar t}\right)\left(1 - (q-1)\left(\frac{m^2x^4}{2\hbar^2 t^2}\right) + \dots.\right). \tag{36}$$

We calculate the normalization constants for $K_\pm$ up to the first correction and exactly K_q to get the following:

$$N_+ = \sqrt{\frac{m}{2\pi i\hbar t}}\,\frac{1}{\left(1 + \frac{3}{16\sqrt{2}} + \dots\right)}, \tag{37}$$

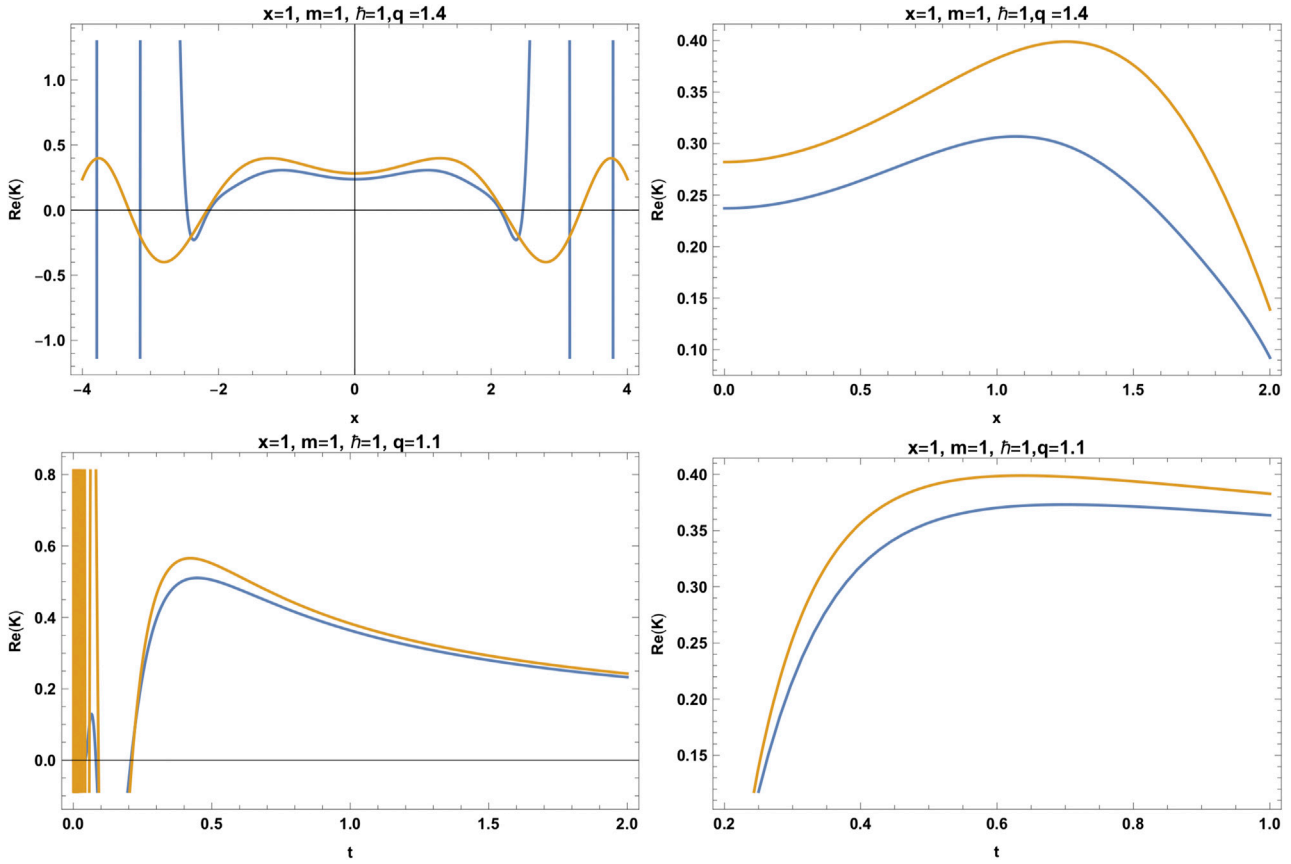

FIGURE 4 | Real parts of the modified propagator (blue line) vs. standard propagator (yellow line), for the free particle for the modified statistics of Tsallis for $q = 1.1$. We set the mass and the Planck constant to unity. Imposing $S_{cl} \lesssim \hbar$, it translates for fixed $x = 1$ in $t \gtrsim 1/2$ and for fixed $t = 1$ translates in $x^2 \lesssim 2$.

$$N_{-} = \sqrt{\frac{m}{2\pi i\hbar t}}\,\frac{1}{\left(1-\frac{3}{16\sqrt{2}}+\ldots\right)}, \tag{38}$$

$$N_q = \sqrt{\frac{m}{2\pi i\hbar t}}\,\frac{\sqrt{(q-1)}\Gamma\left(\frac{1}{(q-1)}\right)}{\Gamma\left(\frac{1}{(q-1)}-\frac{1}{2}\right)}. \tag{39}$$

In the quantum regime $S_{cl} \approx \hbar$, the differences between the propagators K_{+}, K_{-}, K_q, and K_0 are shown in **Figures 2–4**. In **Figure 2** the K_{-} propagator is compared to the usual one. Also, **Figure 3** shows a comparision of the K_{-} propagator with the standard one. The last **Figure 4** shows a comparison between the propagators for the S_q statistics K_q for $q < 1$ and $q > 1$ with the usual one. The region of interest is the quantum regime with $S_{cl} \approx \hbar$. Furthermore, in the classical regime, the oscillations of the standard propagator grow averaging to zero as discussed in [34]. Thus, we are interested in comparing the corrections arising from different statistics in the quantum region of interest and, in the plots, the differences between the standard and the modified propagator can be observed. In the classical regime, there are oscillations that should sum up when computing more terms. When $S_{cl} \ll \hbar$, then both results coincide as shown in **Figure 5**. The modified propagators could be interpreted as describing a particle with an effective potential; this would give a spatially bounded wave function.

6 THE HARMONIC OSCILLATOR

In this section, we apply the formulation of our modified Quantropy of **Section 4** for the case of the harmonic oscillator. We compute the modified propagator constructed by a superposition as it was done previously. The extension of quantum systems employing the modified q-statistics has been made only for the case of the free particle [13] with different arguments. Our proposal allows to search the manifestation of nonextensive statistics in nonlinear quantum systems for generic potentials. We illustrate the procedure calculating only K_{+}, and the other propagators K_{-} and K_q could be similarly calculated.

For the harmonic oscillator with Lagrangian $\mathcal{L} = \frac{m}{2}\dot{x}^2 - \frac{m\omega^2}{2}x^2$, the path integral Kernel reads

$$K(a,b) = \left(\frac{m\omega}{2\pi i\hbar \sin\omega T}\right)^{1/2} \times \exp\left(\frac{im\omega}{2\hbar \sin\omega T}\left((x_a^2 + x_b^2)\cos\omega T - 2x_a x_b\right)\right).$$

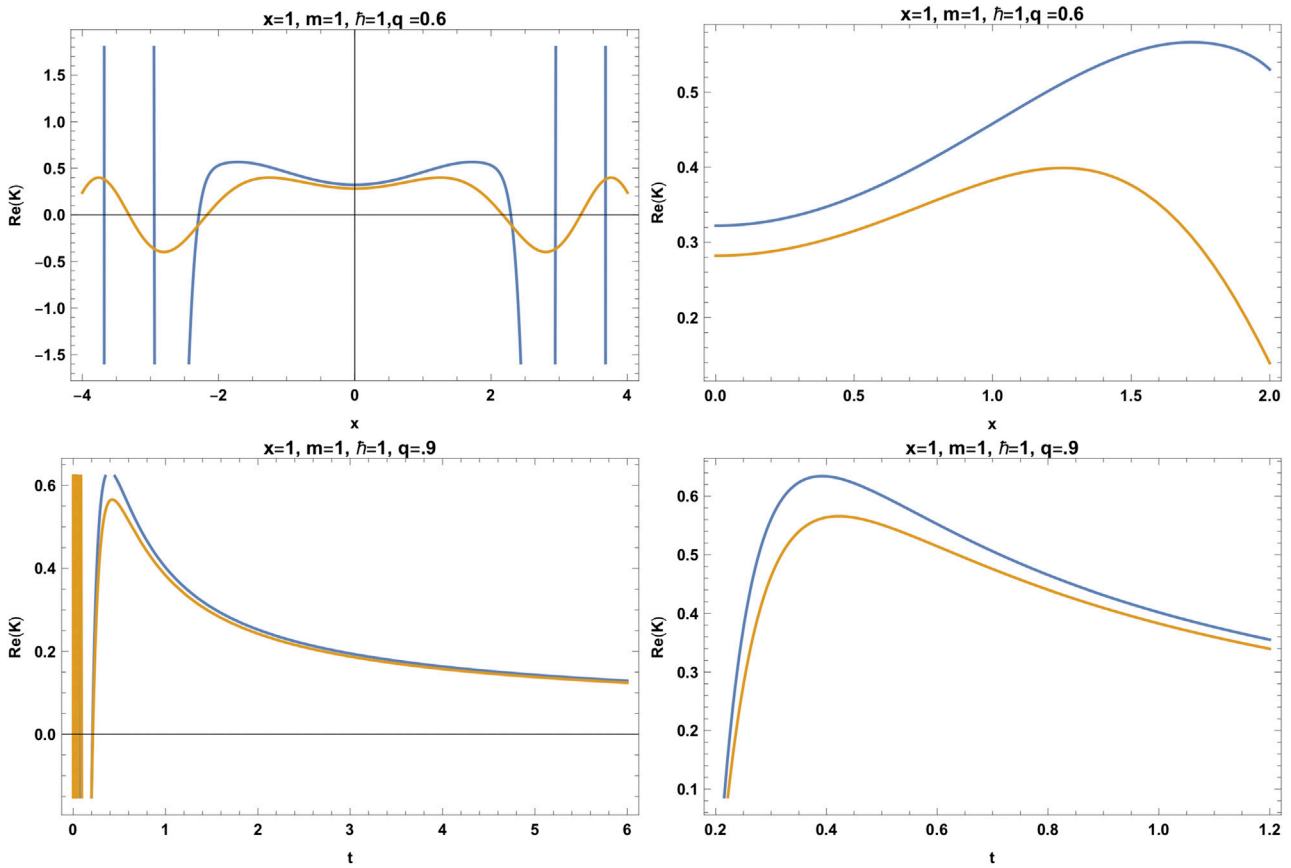

FIGURE 5 | Real parts of the modified propagator (blue line) vs. standard propagator (yellow line), for the free particle for the modified statistics of Tsallis for $q = 0.9$. We set the mass and the Planck constant to unity. Imposing $S_{cl} \lesssim \hbar$, it translates for fixed $x = 1$ in $t \gtrsim 1/2$ and for fixed $t = 1$ translates in $x^2 \lesssim 2$.

Next, following a similar procedure as for the free particle, we compute the generalized Kernel and normalize it. The unnormalized Kernel is given by the following:

$$K(x,t,1) = \exp\Big(-\frac{1}{2}\lambda m\omega\cot(\omega t)x^2\Big). \tag{40}$$

Now, we compute the next terms of the Kernel up to third order, which are as follows:

$$\begin{aligned} K(x,t,2) &= \left(\frac{\lambda}{2}\right)^2 \frac{\partial^2}{\partial\lambda^2}\exp(-2\lambda A) \\ &= \frac{1}{4}\lambda^2 m^2\omega^2 x^4 \exp\Big(-\lambda m\omega\cot(\omega t)x^2\Big), \end{aligned} \tag{41}$$

$$\begin{aligned} K(x,t,3) &= \frac{1}{2}\left(-\frac{\lambda^2}{3^2}\partial_\lambda^2 + 2\frac{\lambda^3}{3^3}\partial_\lambda^3 + 3\frac{\lambda^4}{3^4}\partial_\lambda^4\right)\exp(-3\lambda A) \\ &= \Big(-\frac{1}{8}\lambda^2 m^2\omega^2\cot^2(\omega t)x^4 - \frac{1}{8}\lambda^3 m^3\omega^3\cot^3(\omega t)x^6 \\ &\quad + \frac{3}{32}\lambda^4 m^4\omega^4\cot^4(\omega t)x^8\Big) \times \exp\Big(\frac{-3}{2}\lambda m\omega x^2\cot(\omega t)\Big). \end{aligned} \tag{42}$$

Thus, the total normalized propagator up to third order reads

$$\begin{aligned} K_+(x,t) = \frac{N_+}{\sqrt{2\pi}}\Bigg(&\left(\frac{m\omega\cot(t\omega)}{i\hbar}\right)^{\frac{1}{2}}\exp\left(\frac{-m\omega x^2\cot(t\omega)}{2i\hbar}\right) \\ &+\frac{1}{4}\left(\frac{m\omega\cot(t\omega)}{i\hbar}\right)^{\frac{5}{2}}x^4\exp\left(\frac{-m\omega x^2\cot(t\omega)}{i\hbar}\right) - \frac{1}{8}\Bigg[\left(\frac{m\omega\cot(t\omega)}{i\hbar}\right)^{\frac{5}{2}}x^4 \\ &+\left(\frac{m\omega\cot(t\omega)}{i\hbar}\right)^{\frac{7}{2}}x^6 - \frac{3}{4}\left(\frac{m\omega\cot(t\omega)}{i\hbar}\right)^{\frac{9}{2}}x^8\Bigg]\exp\left(\frac{-3m\omega x^2\cot(t\omega)}{2i\hbar}\right) + \dots\Bigg) \end{aligned} \tag{43}$$

where $N_+ = \frac{1}{\sqrt{\cos(\omega T)}}\frac{1}{\left(1+\frac{3}{16\sqrt{2}}+\frac{1}{96\sqrt{3}}\right)}$. The relative normalization of the modified propagator with respect to the normalization of the usual propagator is a result obtained in **Section 5** [see formulas (**31**–**33**)]. This result is universal, i.e., independent of the action. In **Figure 6**, we compare the propagator for the harmonic oscillator for the standard Quantropy and for the one based on S_+ and S_- statistics. We are interested in the quantum regime given by $S_{cl} \approx \hbar$. There are noticeable effects in that regime. Outside the quantum region, oscillations grow as in the usual case [34]. This behavior occurs in the classical region in which the modified Kernels will also not contribute.

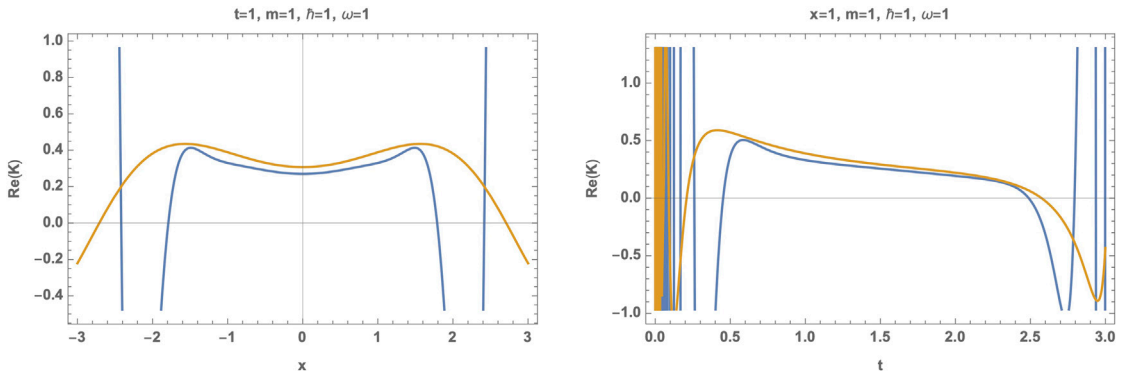

FIGURE 6 | We set the units $m = w = \hbar = 1$. The left image shows the real parts of the normalized propagators for a fixed time $t = 1$, and the region $S_{cl} \lesssim \hbar$ is given by $|x| \lesssim 1.765$. The blue line corresponds to the modified propagator K_+; meanwhile, the yellow one represents the usual propagator $K(x,t,1)$. The right plot is the comparison between the propagators amplitude for $x = 1$ where the blue and the orange are the correction and the usual, respectively, and the quantum region is given by $t \gtrsim 0.464$.

7 POTENTIAL BARRIER

In this section, we apply the formulation of Quantropy developed previously to compute the propagators associated to a particle in an infinite potential barrier given as follows:

$$V(x) = \begin{cases} 0 & x > 0 \\ \infty & x \leq 0 \end{cases}.$$

The standard unnormalized propagator for this problem is given as follows [38]:

$$K(x,t;x_0,0) = \exp\left[\frac{im}{2\pi\hbar t}(x - x_o)^2\right] - \exp\left[\frac{im}{2\pi\hbar t}(-x - x_o)^2\right], \tag{44}$$

where x_0 is the initial position. It is important to specify the initial position since the particle cannot be located at $x \leq 0$; thus, we set $x_0 = \epsilon$, where ϵ is a small positive non zero parameter. This allows to make a comparison with the free particle case. Notice that if we set $x_0 = 0$, the propagator vanishes since the x dependence is quadratic.

Now, we compute the nonlinear propagator associated to the statistics S_+: $K_+(x,t;\epsilon,0)$ up to third order, which is given by expression (24). Since our theory is nonlinear, the superposition principle is not valid, i.e., we cannot consider the difference between the propagators of two free particles, like is done for the usual propagator $K(x,t;x_0,0)$, rather in the semiclassical regime, we consider the logarithm:

$$S_{cl} = \frac{\hbar}{i}\ln(K(x,t;x_0,0)), \tag{45}$$

This allows to substitute S_{cl} into the series expansion (**21**) $K_+(x)$:

$$\begin{aligned} K_+(x,t;\epsilon,0) = &\left[e^{\frac{im(x-\epsilon)^2}{2\pi\hbar t}} - e^{\frac{im(-x-\epsilon)^2}{2\pi\hbar t}}\right] \times \left[1 + \left(e^{\frac{im(x-\epsilon)^2}{2\pi\hbar t}}\right.\right. \\ &\left. - e^{\frac{im(-x-\epsilon)^2}{2\pi\hbar t}}\right)\ln^2\left(e^{\frac{im(x-\epsilon)^2}{2\pi\hbar t}} - e^{\frac{im(-x-\epsilon)^2}{2\pi\hbar t}}\right) \\ &+ \frac{1}{2}\left(e^{\frac{im(x-\epsilon)^2}{2\pi\hbar t}} - e^{\frac{im(-x-\epsilon)^2}{2\pi\hbar t}}\right)^2\left[3\ln^4\left(e^{\frac{im(x-\epsilon)^2}{2\pi\hbar t}} - e^{\frac{im(-x-\epsilon)^2}{2\pi\hbar t}}\right)\right. \\ &+ 2\ln^3\left(e^{\frac{im(x-\epsilon)^2}{2\pi\hbar t}} - e^{\frac{im(-x-\epsilon)^2}{2\pi\hbar t}}\right) - \ln^2\left(e^{\frac{im(x-\epsilon)^2}{2\pi\hbar t}} - e^{\frac{im(-x-\epsilon)^2}{2\pi\hbar t}}\right) \\ &\times\left] + \frac{1}{6}\left(e^{\frac{im(x-\epsilon)^2}{2\pi\hbar t}} - e^{\frac{im(-x-\epsilon)^2}{2\pi\hbar t}}\right)^3\left[16\ln^6\left(e^{\frac{im(x-\epsilon)^2}{2\pi\hbar t}} - e^{\frac{im(-x-\epsilon)^2}{2\pi\hbar t}}\right)\right. \\ &+ 24\ln^5\left(e^{\frac{im(x-\epsilon)^2}{2\pi\hbar t}} - e^{\frac{im(-x-\epsilon)^2}{2\pi\hbar t}}\right) - 6\ln^4\left(e^{\frac{im(x-\epsilon)^2}{2\pi\hbar t}} - e^{\frac{im(-x-\epsilon)^2}{2\pi\hbar t}}\right) \\ &\left.\left. - 4\ln^3\left(e^{\frac{im(x-\epsilon)^2}{2\pi\hbar t}} - e^{\frac{im(-x-\epsilon)^2}{2\pi\hbar t}}\right) + 3\ln^2\left(e^{\frac{im(x-\epsilon)^2}{2\pi\hbar t}} - e^{\frac{im(-x-\epsilon)^2}{2\pi\hbar t}}\right)\right)\right]\right]. \end{aligned} \tag{46}$$

Note that the propagator is ill-defined if ϵ is zero. This propagator oscillates faster than the usual propagator in x, and its amplitude is greater. However, the global behavior of both propagators is quite similar, and the oscillations and the amplitude grow as x increases. For the time dependence in both cases, the propagator tends to zero as t grows (see the set of graphics in **Figure 7**).

In the usual case, the propagator $K(x,t;x_0,0)$ has the following interpretation, the first part corresponds to the classical path of the free particle from $(x_0,0)$ to (x,t), while the second part corresponds to the classical path of a free particle from $(x_0,0)$ bouncing off the wall and going to (x,t). The modified propagator expression suggests a similar interpretation, i.e., the whole propagator can be considered as the sum of both classical paths with the leading terms given by the standard free particle and nonlinear corrections which can be interpreted as an effective potential.

8 FINAL REMARKS

In this work, we explore the novel concept of Quantropy in Quantum Mechanics (Q.M.), which constitutes the analog of the entropy in Statistical Mechanics (S.M.). Mathematically, Quantropy can be regarded as an analytical continuation of

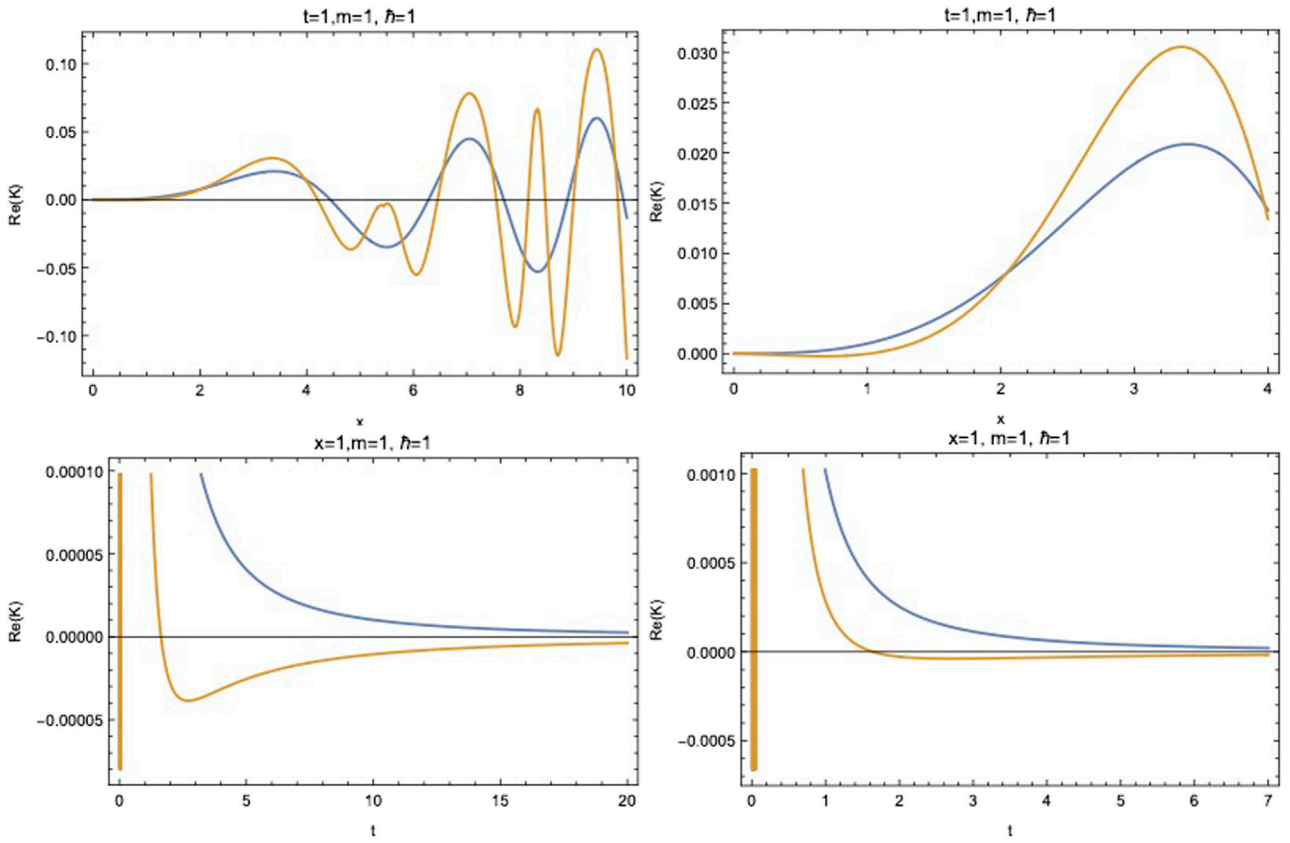

FIGURE 7 | We set the units $m = h = 1$ and $\epsilon = 0.01$; the graphic shows the real parts of the modified propagator (blue line) vs. standard propagator (yellow line).

entropy, performed under the identification of the energy in S.M. to the action in Q.M., and the identification of the temperature to the Planck constant, the map reads: $E \to S$ and $T \to i\hbar$.

We establish a new definition of Quantropy, with the energy mapped to the classical action $E \to S_{cl}$, i.e., we consider that the main entity is the propagator $K(x)$ instead of the amplitude $a(x)$ of the path. Thus, we construct the propagator, a kind of integrated version of the Quantropy $Q_0 = -\int_X K(x)\ln K(x)dx$; in this way, the functional corresponding to the BG under the maximization procedure leads to $K_0 \sim \exp(iS_{cl}/\hbar)$.

We applied this concept to find the quantum mechanical implications of modified entropies S_+, S_-, and S_q, and the associated quantropies lead to generalized propagators, which imply a modified wave functional quantum mechanics (modified Schroedinger equation). Let us point out that the small probabilities limit of modified entropies S_+ and S_- leads to Boltzmann–Gibbs entropy. Similarly in the limit of small path amplitude, one recovers the original Quantropy from the modified functionals. This formalism could be a novel framework to study nonlinear quantum mechanics as those consider in [4, 12, 13]. We also provide an understating of modified propagators associated with Tsallis statistics, leading to wave functions corresponding to q-distributions.

Also, the result for the Tsallis statistics implies a propagator $K_q \sim \exp_q(iS_{cl}/\hbar)$, where $\exp_q(x)$ is the q-exponential; this is relevant since it makes contact with the Tsallis result of modified wave function for the free particle, whose solution is $\psi_q \sim \exp_q(i(kx - \omega t))$. The connection is due to the arguments of [34] in the discussion of the propagator for the free particle $K_0 \sim \exp(iS_{cl}/\hbar)$. They show that the propagator K_0 corresponds to the free particle wave function $\psi_0 \sim \exp(i(kx - \omega t))$. Thus, analogously K_q will lead to ψ_q. As a further work, we need to explore the relations in the case of the modified propagators K_+ and K_-. They will give rise to wave functions whose dependencies will be given by $\Psi_\pm = \exp_\pm(i(kx - \omega t))$, also for the free particle. In this case, we have a recurrent series solution but we do not have exact expressions for these generalized exponentials. As discussed, our proposal provides also generalized propagators K_+, K_-, and K_q for problems with interactions; we illustrated this by considering the K_+ associated with the harmonic oscillator and the infinite potential barrier.

There are hints from previous studies that the modified entropies considered here can be interpreted as linked with modified effective potentials. Therefore, these modifications to the free particle could be related to a usual quantum mechanics with an effective potential [9].

However, these effects could also lead to nonlinear quantum equations explored in the literature with modified wave functions [3, 12, 13, 26]. Furthermore, what we found here based on the concept of Quantropy could be linked to results for quantum systems in terms of usual entropy vs. the density matrix [10]. A system governed by a modified statistics (S_+, S_- or S_q) will lead to modified density-matrix distributions.

Moreover, the modified "propagators" K_+, K_-, and K_q actually are strictly no longer standard propagators because they lack the usual propagation property. This means that is not equivalent to propagate the particle from $(0,0)$ to (t_2,x_2), than to first propagate it from $(0,0)$ to (t_1,x_1) and then from (t_1,x_1) to (t_2,x_2). This occurs because, for example,

$$\int K_+(0,0;x_1,t_1)K_+(x_1,t_1;x_2,t_2)dx_1 \neq K_+(0,0;x_2,t_2).$$

This relates to the fact that in a quantum open systems where these generalized entropies are motivated, the nature of the processes is non-Markovian. Those systems in consideration are modeled with Master Equations (Stochastic) [39]. We consider that this formalism could be a natural framework to study nonlinear quantum mechanics.

We would like to explore further processes where the modified statistics in Quantropy play a central role. This could be done via modified wave functions, which could be interpreted as the usual quantum mechanics with an effective interaction [40] or from nonlinear quantum equations. The modified wave functions will correspond to the modified propagators obtained in this work. In this work, we obtained the modified propagators for the free particle, harmonic oscillator, and the infinite potential barrier associated to the different statistics K_+, K_-, and K_q, discussing the associated quantum behavior. We would also like to explore in future work the quantum mechanical evolution of other physical systems.

DATA AVAILABILITY STATEMENT

The original contributions presented in the study are included in the article/**Supplementary Material**; further inquiries can be directed to the corresponding author.

AUTHOR CONTRIBUTIONS

Here, NB certifies that every author in the present work contributed equally to the research and the writing of the manuscript on the following tasks: conceptualization; formal analysis; funding acquisition; investigation; project administration; resources; software; writing-original draft; and writing-review and editing. All authors contributed to the article and approved the submitted version.

ACKNOWLEDGMENTS

The authors thank Alejandro Cabo, Vishnu Jejjala, Oscar Loaiza-Brito, Miguel Sabido, Marco Ortega, Nelsón Flores-Gallegos, and Pablo López-Vázquez for useful discussions and comments. NB thanks PRODEP NPTC UGTO-515 Project, CIIC 181/2019 UGTO Project, CIIC 290/2020 UGTO Project, CIIC 2021 UGTO and CONACYT Project A1-S-37752. RS-S thanks CONACYT and PRODEP NPTC UDG-PTC-1368 Project and the MCFM PROINPEP-University of Guadalajara for supporting this work. OO thanks CONACYT Project 257919 and CIIC 188/2019 UGTO Project. NB, OO and CD thank the support of the University of Guanajuato.

SUPPLEMENTARY MATERIAL

The Supplementary Material for this article can be found online at: https://www.frontiersin.org/articles/10.3389/fphy.2021.634547/full#supplementary-material

REFERENCES

1. Obregón O. Superstatistics and gravitation. *Entropy* (2010) 12:2067–76. doi:10.3390/e12092067
2. Tsallis C. Possible generalization of Boltzmann-Gibbs statistics. *J Stat Phys* (1988) 52:479–87. doi:10.1007/BF01016429
3. Nobre FD, Rego-Monteiro MA, and Tsallis C. Nonlinear relativistic and quantum equations with a common type of solution. *Phys Rev Lett* (2011) 106:140601. doi:10.1103/PhysRevLett.106.140601
4. Sharma B, and Mital D. New nonadditive measures of inaccuracy. *J Math Sci* (1975) 10:122–33.
5. Beck C, and Cohen E. Physica A: statistical Mechanics and its applications. *Superstatistics* (2003) 322:267–275. doi:10.1016/S0378-4371(03)00019-0
6. Cabo Bizet N, Fuentes J, and Obregón O. Generalised asymptotic equivalence for extensive and non-extensive entropies. *EPL* (2019) 128:60004. doi:10.1209/0295-5075/128/60004
7. Obregón O, and Gil-Villegas A. Generalized information entropies depending only on the probability distribution. *Phys Rev E* (2013) 88:062146. doi:10.1103/PhysRevE.88.062146
8. Obregón O. Generalized information and entanglement entropy, gravitation and holography. *Int J Mod Phys A* (2015) 30:1530039. doi:10.1142/s0217751x15300392
9. Obregón O, Gil A, and Torres J. Computer simulation of effective potentials for generalized Boltzmann-gibbs statistics. *J Mol Liq* (2017) 248:364–9. doi:10.1016/j.molliq.2017.10.027
10. Cabo N, and Obregón O. Exploring the gauge/gravity duality of a generalized von neumann entropy. *Eur Phys J P* (2018) 133:55. doi:10.1140/epjp/i2018-11883-5
11. Baez J, and Pollard B. Quantropy. *Entropy* (2015) 17:772–89. doi:10.3390/e17020772
12. Nobre FD, Rego-Monteiro MA, and Tsallis C. A generalized nonlinear Schrödinger equation: classical field-theoretic approach. *Epl* (2012a) 97:41001. doi:10.1209/0295-5075/97/41001
13. Nobre F, Rego-Monteiro M, and Tsallis C. Nonlinear q-generalizations of quantum equations: homogeneous and nonhomogeneous cases-an overview. *Entropy* (2017) 19:39. doi:10.3390/e19010039
14. Batle J, Plastino AR, Casas M, and Plastino A. Conditionalq-entropies and quantum separability: a numerical exploration. *J Phys A: Math Gen* (2002) 35:10311–24. doi:10.1088/0305-4470/35/48/307
15. Nobre FD, Rego-Monteiro MA, and Tsallis C. A generalized nonlinear Schrödinger equation: classical field-theoretic approach. *Epl* (2012b) 97:41001. doi:10.1209/0295-5075/97/41001
16. Plastino AR, and Tsallis C. Nonlinear Schroedinger equation in the presence of uniform acceleration. *J Math Phys* (2013) 54:041505. doi:10.1063/1.4798999
17. Curilef S, Plastino AR, and Plastino A. Tsallis' maximum entropy ansatz leading to exact analytical time dependent wave packet solutions of a nonlinear

Schrödinger equation. *Physica A: Stat Mech its Appl* (2013) 392:2631–42. doi:10.1016/j.physa.2012.12.041
18. Plastino A, and Rocca MC. From the hypergeometric differential equation to a non-linear Schrödinger one. *Phys Lett A* (2015) 379:2690–3. doi:10.1016/j.physleta.2015.08.015
19. Plastino AR, and Tsallis C. Dissipative effects in nonlinear klein-gordon dynamics. *Epl* (2016) 113:50005. doi:10.1209/0295-5075/113/50005
20. Plastino A, and Rocca MC. Hypergeometric foundations of fokker-planck like equations. *Phys Lett A* (2016) 380:1900–3. doi:10.1016/j.physleta.2016.03.047
21. Pennini F, Ferri G, and Plastino A. q-generalization of quantum phase-space representations. *Physica A: Stat Mech its Appl* (2015) 423:97–107. doi:10.1016/j.physa.2014.12.033
22. Majtey A, Plastino AR, and Plastino A. New features of quantum discord uncovered by q-entropies. *Physica A: Stat Mech its Appl* (2012) 391:2491–9. doi:10.1016/j.physa.2011.11.062
23. Nobre FD, and Plastino AR. A family of nonlinear Schrödinger equations admitting q -plane wave solutions. *Phys Lett A* (2017) 381:2457–62. doi:10.1016/j.physleta.2017.05.054
24. Plastino A, and Rocca MC. Quantum q-field theory: q-Schrödinger and q-Klein-Gordon fields. *EPL* (2017) 118:61004. doi:10.1209/0295-5075/118/61004
25. Plastino A, and Rocca MC. Tsallis' quantum q-fields. *Chin Phys C* (2018) 42:053102. doi:10.1088/1674-1137/42/5/053102
26. Chavanis P. Generalized euler, smoluchowski and Schrödinger equations admitting self-similar solutions with a tsallis invariant profile. *The Eur Phys J Plus* (2019) 134:353. doi:10.1140/epjp/i2019-12706-y
27. Khordad R, and Rastegar Sedehi HR. Magnetic susceptibility of graphene in non-commutative phase-space: extensive and non-extensive entropy. *Eur Phys J Plus* (2019) 134:133. doi:10.1140/epjp/i2019-12558-5
28. Sedehi HRR, and Khordad R. Entropy and specific heat of graphene at low and high temperatures under an external magnetic field. *Solid State Commun* (2020) 313:113911. doi:10.1016/j.ssc.2020.113911
29. Khordad R, Bahramiyan H, and Rastegar Sedehi HR. Effects of strain, magnetic field and temperature on entropy of a two dimensional gaas quantum dot under spin–orbit interaction. *Opt Quan Electronics* (2018) 50:294. doi:10.1007/s11082-018-1557-2
30. Servatkhah M, Khordad R, Firoozi A, Rastegar Sedehi HR, and Mohammadi A. Low temperature behavior of entropy and specific heat of a three dimensional quantum wire: shannon and tsallis entropies. *The Eur Phys J B* (2020) 93:111. doi:10.1140/epjb/e2020-10034-5
31. Abe S, and Okuyama S. Similarity between quantum mechanics and thermodynamics: entropy, temperature, and carnot cycle. *Phys Rev E* (2011) 83:021121. doi:10.1103/PhysRevE.83.021121
32. Yokoi Y, and Abe S. On quantum-mechanical origin of statistical mechanics. *J Phys Conf Ser* (2018) 1113:012012. doi:10.1088/1742-6596/1113/1/012012
33. Flego SP, Plastino A, and Plastino AR. Fisher information, the Hellmann-Feynman theorem, and the Jaynes reciprocity relations. *Ann Phys* (2011) 326:2533–43. doi:10.1016/j.aop.2011.07.009
34. Feynman R, and Hibbs A. *Quantum mechanics and path integrals international series in the earth and planetary sciences*. First Edition. New York, NY: McGraw-Hill College; Edición (1965).
35. Wentzel G. Eine Verallgemeinerung der Quantenbedingungen for die Zwecke der Wellenmechanik. *Z Physik* (1926) 38:518–29. doi:10.1007/bf01397171
36. Stack J. *Semiclassical approximation lecture notes in quantum mechanics*. Champaign, IL: University of Illinois Urbana-Champaign (2013).
37. Heller E. *The semiclassical way to dynamics and spectroscopy*. Princeton, NJ: Princeton University Press (2018).
38. Goodman M. Path integral solution to the infinite square well. *Am J Phys* (1981) 49:843–7. doi:10.1119/1.12720
39. de Vega I, and Alonso D. Dynamics of non-markovian open quantum systems. *Rev Mod Phys* (2017) 89:015001. doi:10.1103/RevModPhys.89.015001
40. Vignat C, Plastino A, Plastino AR, and Sanchez Dehesa J. Quantum potentials with q-Gaussian ground states. *Physica A: Stat Mech its Appl* (2012) 391:1068–73. doi:10.1016/j.physa.2011.09.031

Conflict of Interest: The authors declare that the research was conducted in the absence of any commercial or financial relationships that could be construed as a potential conflict of interest.

frontiers in Physics

ORIGINAL RESEARCH
published: 13 May 2021
doi: 10.3389/fphy.2021.636052

Collective Dynamics in Quasi-One-Dimensional Hard Disk System

Adrián Huerta[1]*, *Taras Bryk*[2,3], *Victor M. Pergamenshchik*[4] and *Andrij Trokhymchuk*[2]

[1] Facultad de Física, Universidad Veracruzana, Xalapa, México, [2] Institute for Condensed Matter Physics, National Academy of Sciences of Ukraine, Lviv, Ukraine, [3] Institute of Applied Mathematics and Fundamental Sciences, Lviv Polytechnic National University, Lviv, Ukraine, [4] Institute of Physics, National Academy of Sciences of Ukraine, Kyiv, Ukraine

We present the results of molecular dynamic studies of collective dynamics in a system of hard disks confined to a narrow quasi-one-dimensional (quasi-1D) channel. The computer simulations have been performed for the specific channel width of 3/2 of disk diameter in which the disk arrangement at close packing resembles zigzag ordering characteristic of a vertically oriented two-dimensional (2D) triangular lattice. In such a quasi-1D system, which is intermediate between 1D and 2D arrays of hard disks, the transverse excitations obey very specific dispersion law typical of the usual optical transverse modes. This is in a sharp contrast both to the 1D case, where transverse excitations are not possible, and to the 2D case, where the regular shear waves with a propagation gap were observed. Other peculiarities of the dispersion of collective excitations as well as some results of disk structuring and thermodynamics of the quasi-1D hard disk system are presented and discussed for a range of hard disk densities typical for fluid and distorted crystal states.

Keywords: hard disks, structure factors, collective dynamics, dispersion of collective excitations, molecular dynamics

OPEN ACCESS

Edited by:
Ramon Castañeda-Priego, University of Guanajuato, Mexico

Reviewed by:
Takeshi Ooshida, Tottori University, Japan
Alessandro Taloni, National Research Council (CNR), Italy
Salvador Herrera-Velarde, Instituto Tecnológico Superior de Xalapa (ITSX), Mexico

***Correspondence:**
Adrián Huerta
adrian.huerta@gmail.com

Specialty section:
This article was submitted to Soft Matter Physics, a section of the journal Frontiers in Physics

Received: *30 November 2020*
Accepted: *08 March 2021*
Published: *13 May 2021*

Citation:
Huerta A, Bryk T, Pergamenshchik VM and Trokhymchuk A (2021) Collective Dynamics in Quasi-One-Dimensional Hard Disk System. Front. Phys. 9:636052. doi: 10.3389/fphy.2021.636052

1. INTRODUCTION

Hard spheres and hard disks are widely accepted as the first choice approximation to model a variety of soft condensed matter objects [1]. In spite of being a rather simple representation of the substance, hard core-based model systems still are capable to recover a number of basic properties and effects related to the structure, thermodynamics (e.g., phase transitions), and dynamics of real systems. Recently, the interest has been revived in the properties of hard sphere fluid confined to a narrow channel of the width that does not exceed two hard core diameters. In such system, commonly referred to as quasi-one dimensional (quasi-1D) system [2], the hard-core particles cannot pass the nearest neighbors and their motion is restricted by the neighbors. Of a particular interest is the so-called single-file quasi-1D system with the width that does not exceed $(1+\sqrt{3}/2)$ of disk diameter [3] as then a disk cannot touch more than one neighbor from each side. This is a substantial simplification that allows one to make a contact with the exact Tonks solution for the purely 1D hard rod system [4]. The reasons for the interest to this system are both basic and applied. The fundamental interest stems from the existence of the analytical transfer matrix approach for the isobaric partition function [5–9] and the exact canonical partition function of this system, which is recently derived in [10]. At present, the theoretical research in this area has been mostly concerned with the efforts (i) to get an insight into the mechanism that governs transformation of

the properties of hard core systems as their dimensionality approaches 2 and 3 [5, 11], and (ii) to consider these systems as glass formers, see [7–9, 12–14] and review [15]. The practical interest stems from the possibility to use such a simple model to capture properties of more complex systems, e.g., to explain diffusion in zeolite and carbon channels [16–18], microfluidic devices [19], in the technology of bio-integrated nanodevices [3] etc. by treating the finite length axis of the quasi-1D system as the pore width.

Confined many-particle systems are very versatile and complex, and computer simulations are a perfect and in the most cases only available tool to study their structure and dynamics. It has been widely applied to study the structure and single-particle dynamics in quasi-1D systems with various model smooth/continuous particle–particle and particle–wall interaction potentials. But even the quasi-1D systems partially involving hard core particles and the quasi-1D systems of pure hard core particles (that are the main subject of present study) can be so different in their physics that comparison of apparently similar effects in such systems often has no much physical sense. For instance, in a quasi-1D system of hard core particles suspended in a viscoelastic liquid solvent their effective interactions are mainly of a hydrodynamic nature and the role of confining walls is not so much in restricting particles' motion as in setting the boundary condition on the liquid solvent's flow. At the same time, in a quasi-1D system of pure hard core particles all interactions are of an entropic nature. Another example concerns a zigzag particle arrangement that very often is the object of fundamental interest for different quasi-1D systems. However, because of the difference in interaction potentials, the general idea of the zigzag geometry is often the only thing in common. For instance, a zigzag structure can occur both in quasi-1D system with extremely short-range interaction such as a hard core repulsion (e.g., see [9]) and in quasi-1D system with long-range interaction such as a screened electrostatic repulsion in dusty plasma (e.g., see review [20]). The difference between these two interactions is known to be fundamental even in a purely 1D geometry in which the phase transition exists only for a long-range particle–particle repulsion [21]. At the same time, the computer simulations studies of dynamic properties of the quasi-1D systems that contain only hard core particles, i.e., the quasi-1D hard core systems, have been primarily performed in the context of glassy dynamics. They were mostly focused on the problems specific for the single particle dynamics such as disk hopping time between different quasi-equilibrium states and defects' dynamics [7, 9, 12], and time dependence of the particle displacement [9, 13]. The glassy behavior of hard disk fluid confined to a narrow hard wall channel was also studied theoretically in [7–9] by analyzing the transverse and longitudinal equilibrium static pair correlation functions by the transfer matrix approach [5].

Our recent computer simulations studies [22, 23] have addressed the collective time correlation functions in the bulk 2D and 3D hard core systems. What in the following is referred to as collective dynamics means correlations in the cooperative motion of a many-particle system. Such an approach to understanding the dynamical processes is general for studies of propagating waves (sound, shear, and heat ones) and relaxation processes (thermal relaxation, structural relaxation, stress relaxation, etc.). The corresponding collective dynamic variables are defined via fluctuations of the conserved quantities: number of particles, longitudinal and transverse components of total momentum, and energy. All these collective dynamic variables are known from the hydrodynamic approach and can be used for theoretical description of the long-wavelength processes. For the theoretical description of collective dynamics beyond the hydrodynamic regime, the set of collective variables is extended by the orthogonal ones (orthogonal to hydrodynamic variables), which represent the longitudinal and transverse components of stress tensor, energy current, etc. More precisely, computer simulations [22, 23] were used to find how collective dynamics of bulk hard spheres and bulk hard disks behaves on different spatial scales. Rather unexpectedly the short-wavelength shear waves were found in both cases from the well-defined peaks of the transverse current spectral functions. Although nature of shear waves in hard-core systems appears to be essentially the same as in simple fluids [24], i.e., they emerge as the short-wavelength excitations due to coupling of the transverse current and transverse component of stress tensor, the hard-core fluids are known for the absence of viscoelastic effects. Interestingly, while there are no short-wavelength shear waves in a 2D hard disk fluid at low particle densities, these were observed in the range of higher densities by showing certain particular features just before the freezing transition.

The present paper is devoted to a quasi-1D hard disk system. An essential difference between the methods to study collective dynamics in hard-core systems and those for models based on analytic/continuous two-body potentials stems from the absence of a local energy minima in the former case. Even in the case of solids composed of hard spheres or hard disks, the particles do not oscillate around the minimum of potential well, but are moving ballistically in the cage formed by the nearest neighbors. This difference gives rise to an interesting specific aspect of the collective dynamics in a hard core system, namely, an existence of strong correlations between the emergence of short-wavelength shear waves and the caging phenomenon [25, 26], which was noticed in the case of 2D hard disk system [22]. As caging inevitably emerges in a hard disk system under quasi-1D confinement, it is quite natural to expect the existence of short-wavelength shear waves in this case as well. Then it is not clear how the collective modes behave when additional confinement is imposed, how the reflections from channel boundaries affect the longitudinal and transverse excitations originated from particle–particle collisions, how the single-particle ballistic motions sum up to form a collective oscillation modes. The case of transverse excitations is of particular interest since latter are not present in the 1D prototype of the quasi-1D hard disk system. All these issues remain unexplored. Therefore, our aim is to perform molecular dynamics simulations of a quasi-1D system of hard disks, calculate its static structural properties, and make a link with the collective dynamics of the system. The rest of the paper is organized as follows. In the next section, we present the information on molecular dynamics simulations; section 3 contains results of the static and dynamic

properties of the studied systems. In the last section, we discuss our findings.

2. MODELING AND SIMULATION DETAILS

The quasi-1D system is modeled by placing N hard disks of diameter σ into elongated rectangular box formed by two walls (lines) of length $L_x \equiv L$ that are separated by a distance $L_y \equiv H = \sigma + h$ with $h < \sigma$ such that disks cannot pass each other. The disk-disk two-body interaction is given by

$$u(r_{ij}) = \begin{cases} \infty, & r_{ij} < \sigma \\ 0, & r_{ij} \geq \sigma \end{cases}, \tag{1}$$

where $r_{ij} = |\mathbf{r}_j - \mathbf{r}_i|$ is the distance between disk centers. Additionally, both confining walls are impenetrable,

$$u_w(r_i) = \begin{cases} 0, & \sigma/2 < y_i < h + \sigma/2 \\ \infty, & \text{otherwise} \end{cases}, \tag{2}$$

thereby forming the hard-wall channel (or pore) of the width $H = \sigma + h$ and of the length L. The ends of the channel are open and the periodic boundary conditions in x-direction are employed.

Taking into account that width $H = \sigma$ corresponds to 1D case, the range of channel widths $\sigma < H < 2\sigma$ could be considered as a bridge between 1D and higher dimensions. Among continuous variety of the quasi-1D system width in this range $\sigma < H < 2\sigma$ there are two, $H/\sigma = 1.5$ and $H/\sigma = 1 + \sqrt{3}/2$, when disk ordering at close packing is commensurate with 2D triangular lattice like milestones on the way from 1D to 2D. To illustrate, **Figure 1** presents two triangular hard disk arrays that correspond to the most common horizontal (**Figure 1A**) and vertical (**Figure 1B**) orientations of 2D triangular lattice that differ by an angle of 30 degrees. The quasi-1D systems that correspond to $H/\sigma = 1.5$ and $H/\sigma = 1 + \sqrt{3}/2$ are shown by hollow disks that at close packing form two very distinct crystalline zigzags. The main distinction concerns a number of nearest neighbors interacting with each disk, i.e., two for $H/\sigma = 1.5$ and four in the case of $H/\sigma = 1 + \sqrt{3}/2$. The narrower quasi-1D systems is more close to the 1D system, while wider quasi-1D system is more close to the 2D system. In the present study, we are considering the narrower quasi-1D system with width fixed at $H/\sigma = 1.5$.

The main body of simulations, in particular, those that concern the collective dynamics, were performed by using a collection of $N = 200$ hard disks at the fixed channel width H with $h/\sigma = 0.5$ and the varied length, $L/\sigma = 400, 350, 300, 250, 220, 198, 190,$ and 180. Thus, eight quasi-1D hard disk systems that are characterized by different disk linear density,

$$l = \frac{N\sigma}{L}, \tag{3}$$

were simulated. For convenience of comparison and discussion, particular values of the linear density l, that corresponds to each channel length L, are shown in **Table 1** together with corresponding values of the disk number density $\rho = N\sigma^2/(HL)$ and packing fraction $\eta = N\pi\sigma^2/(4HL)$, since the latter are often used in the literature on quasi-1D systems. The simulation runs with larger systems up to $N = 2,000$ were performed as well and are properly indicated in the text. Throughout the paper, the disk hard core diameter σ is used as unit of length, while time is in units of $(\beta m\sigma^2)^{1/2}$. In simulations we used $\beta = \sigma = m = 1$, where $\beta = 1/kT$ and m is the mass of a disk.

Initially chosen N disks were located randomly inside the channel of the shortest length L, i.e., the highest density considered. Then initial disk configurations for lower densities were obtained by increasing the channel length L. To handle the collisions of hard disks with each other and with the channel hard walls, we employ the event driven molecular dynamics (MD) algorithm [27, 28]. According to this technique, the temperature is kept constant by scaling appropriately the magnitude of velocities of each hard disk such that kinetic energy of the system agrees with the equipartition theorem. The directions of the velocities of disk particles at the beginning of each run were chosen randomly. Before calculating the averages for static quantities, we ran MD simulations with assigned velocities, as described before, to equilibrate the system.

Collective dynamics was studied via calculation of the density-density, energy-energy, and longitudinal (L) and transverse (T) current–current time correlation functions. In order to get equally time-sampled positions of hard disks, i.e., the disk trajectories, the positions of hard disks between the collisional events were interpolated. Proceeding in this way, for the systems of $N = 200$, 400, and 1,000 hard disks, we recorded the trajectories and velocities along trajectory for each hard disk, totally having dumped 100, 000 configurations for the systems of $N = 200$ particles, but 40,000 configurations for the systems of $N = 400$ particles, and only 20,000 configurations for the systems of $N = 1,000$ particles with the fixed reduced time interval of 0.01.

The following Fourier components were sampled for each configuration. The Fourier component of the particle density

$$n(k,t) = \frac{1}{\sqrt{N}} \sum_{i=1}^{N} e^{ikx_i(t)}, \tag{4}$$

of the longitudinal component of current density

$$J^L(k,t) = \frac{1}{\sqrt{N}} \sum_{i=1}^{N} v_{x,i}(t) e^{ikx_i(t)}, \tag{5}$$

and the transverse component of current density

$$J^T(k,t) = \frac{1}{\sqrt{N}} \sum_{i=1}^{N} v_{y,i}(t) e^{ikx_i(t)}, \tag{6}$$

as well as of the energy density

$$e(k,t) = \frac{1}{\sqrt{N}} \sum_{i=1}^{N} \varepsilon_i^{kin}(t) e^{ikx_i(t)}. \tag{7}$$

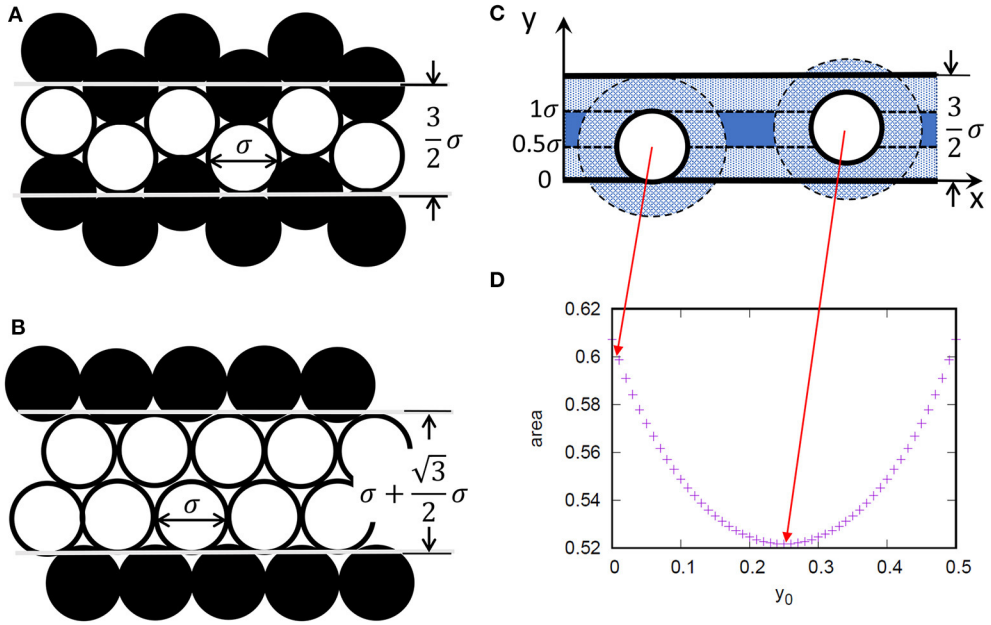

FIGURE 1 | Disk zigzag ordering in a vertically **(A)** and horizontally **(B)** oriented 2D triangular lattice at disk close packing. In the present study, we are employing the quasi-1D hard disk system of width $H = \sigma + h$ with $h/\sigma = 0.5$ that at disk close packing resembles zigzag ordering shown in part **(A)**. The driving force of such a zigzag ordering is entropy, which in the case of hard disk system confined by hard walls is uniquely determined by excluded volume, as it is illustrated in **(C,D)**. In the case of 1D or 2D hard disk systems, excluded volume (the patterned area of width $\sigma/2$ around the disks and near the walls) depends on the distance between disks, i.e., on the disk density only. For the quasi-1D system hard disk, the distance between disks and wall enters the play. In part **(D)**, we illustrate how area (in some relative units), accessible to the centers of other disks (the area of channel filled in blue) depends on the transverse position $y_0 = y_i - h$ of the center of one individual disk. One can see that such an area increases when disk moves to the channel walls and is minimal for its position at the middle of channel.

TABLE 1 | Density parameters (packing fraction η, number density ρ and linear density l) of the quasi-1D hard disk system with channel width $H/\sigma = 1.5$ and varied channel length L for the case of $N = 200$ disks.

L/σ	180	190	198	220	250	300	350	400
η	0.5818	0.5512	0.5289	0.4760	0.4189	0.3491	0.2992	0.2618
ρ	0.7407	0.7018	0.6734	0.6061	0.5333	0.4444	0.3810	0.3333
l	1.1111	1.0526	1.0101	0.9091	0.8	0.6666	0.5714	0.5

Here x_i is the position of disk i along the channel, $v_{x,i}(t), v_{y,i}(t)$ are the components of the ith disk velocity along the channel and perpendicular to the channel, respectively, while ε_i^{kin} is the kinetic energy of ith disk at time t. The wave vector $\mathbf{k}$ is defined along the channel $x-$axis, compatible with the periodicity of simulation box, as $k \equiv k_x = 2\pi m/L_x$ with $m = 1, 2, 3, \ldots$. Note that, due to a non-zero channel width H, the positions and velocities of particles in quasi-1D systems have two components, along (x) and perpendicular (y) to the channel. However, we are using only wave vectors sampled along the channel. The reason is that transverse collective excitations in atomistic systems can propagate if at least two particles take part in the transverse collective motion, i.e., the wave number is below π/σ. In the case of a narrow channel of width $H = 1.5\sigma$ the smallest wavenumber, $k_y = 2\pi/H$, is too large.

Having the Fourier components of energy and particle densities, it is straightforward to calculate the Fourier components of the heat density [24]

$$h(k,t) = e(k,t) - \frac{f_{ne}(k)}{f_{nn}(k)} n(k,t)\,. \tag{8}$$

Here $f_{ne}(k)$ and $f_{nn}(k) \equiv S(k)$ are the static energy–density and density–density correlators, respectively, while $S(k)$ is the static structure factor. The fluctuations of heat density permit calculations of wavenumber-dependent specific heat at constant volume $C_v(k)$, which in the long-wavelength limit tends to its macroscopic value. Another important quantity that can be obtained from observed heat density dynamics is the Landau–Placzek–like ratio, which gives information on the share of contributions from relaxing and propagating processes to specific heat C_v [24, 29].

The above-defined time-dependent Fourier components of corresponding densities, equations 4 - 8, describe fluctuations of conserved quantities in monoatomic fluids and form the set of hydrodynamic variables of macroscopic collective dynamics.

Having dynamic variables (4–8), we calculated the time-dependent density–density correlation function,

$$F_{nn}(k,t) = \langle n(-k,t)n(k,t=0)\rangle\,, \tag{9}$$

time dependent longitudinal and transverse current–current correlation functions,

$$F_{JJ}^{L/T}(k,t) = \langle J^{L/T}(-k,t)J^{L/T}(k,t=0)\rangle\,, \tag{10}$$

and time dependent heat density autocorrelation function,

$$F_{hh}(k,t) = \langle h(-k,t)h(k,t=0)\rangle\,. \tag{11}$$

In what follows, the correlation functions (9–11) were used for numerical time-Fourier transformation in order to obtain the density–density dynamic structure factors $S(k,\omega)$, longitudinal/transverse current spectral functions, $C^{L/T}(k,\omega)$ and the heat-density dynamic structure factor $S_{hh}(k,\omega)$.

3. RESULTS

The system of hard disks in a narrow hard wall channel is anisotropic [5]. The anisotropy is expected due to the system setup $L >> H$, which results in two different pressure components, i.e., the longitudinal, $P_L = F_L/H$, and transverse, $P_T = F_T/L$. Here, F_L and F_T are the force per unit cross-section exerted along the channel length L, and the force on a segment of the horizontal wall of length $L/(N\sigma) = 1/l$, respectively. These forces are both of entropic origin and rather sensitive to be evaluated from computer simulations. Fortunately, these forces can be found from the analytical canonical partition function of a quasi-1D hard disk system reported in [10].

Figure 2 presents the dependencies $P_L(l)$ and $P_T(l)$, as well as $F_L(l)$ and $F_T(l)$ for three channel widths, $H = \sigma + h$, with h fixed at: (a) $h/\sigma = 0.141$, close to the 1D case; (b) $h/\sigma = 0.5$, which is far from both lower 1D and higher single-file limits; and (c) $h/\sigma = 0.866$, which is very close to the terminate width $h/\sigma = \sqrt{3}/2 \sim 0.866025$ of a single-file system. At low linear density, the transverse force F_T is density independent, implying that the vertical disks' motion is ballistic, the vertical free path is maximum, i.e., $H - \sigma$, the disks bounce between channel walls and do not collide with other disks. As for the same low linear density $l \lesssim 0.8$, the transverse force is lower for a wider channel, the frequency of disk bouncing between the horizontal walls has to be lower for wider channels as well.

We see that, for low densities, the transverse pressure P_T is higher than the one along the channel. This is because in that case P_L is determined by a large disk separation along the channel, whereas P_T is determined by a short range of transverse motion bounded from above by $H - \sigma$. As linear density increases toward $l \geq 1$, disks start to mount one upon another, the vertical free paths decrease and transverse pressure and force both rapidly increase. For $h/\sigma = 0.866$, **Figure 2C**, this results in P_T to be always higher than P_L. However, for more narrow channels with $h/\sigma = 0.141$ and $h/\sigma = 0.5$, **Figures 2A,B**, before this happens, at certain value of linear density, which is different for each channel width H, the gaps between disks and walls in transverse direction and the gaps between neighbor disks along the channel become equal, and the pressures on the vertical and horizontal boundaries coincide.

The density distribution profiles, $n_y(y)$, in the transverse $y-$direction, obtained both from the analytical partition function [10] and from MD simulations for quasi-1D hard disk system of the width $H/\sigma = 1.5$, are shown in **Figure 3**. While linear density is low, $l \lesssim 0.8$, the system is roughly homogeneous across the channel as the density profiles $n_y(y)$ are nearly constant and equal to the correspondent linear density l. In contrast, as linear density increases, $l > 1$, the disk distribution across the channel shows the tendency of increase in the regions close to the channel walls and decrease in the middle region of the channel. For the highest studied linear density, $l = 1.111$, the density profile $n_y(y)$ exhibits an almost $\delta-$like shape in the close proximity of the channel walls and practically vanishes elsewhere.

The longitudinal static structure factor, $S(k)$, is calculated from MD simulations in a standard way as instantaneous-time density–density correlator,

$$S(k) \equiv f_{nn}(k) = \langle n(-k,0)n(k,0)\rangle. \tag{12}$$

In **Figure 4**, we show the changes in the first peak of $S(k)$ with decrease of linear density l. Regarding the collective dynamics, one of the most important features is location $K_{\max}$ of the main peak of $S(k)$, since the value of $k = K_{\max}$ has the meaning of a pseudo-Brillouin zone boundary in the considered quasi-1D hard disk fluid at a particular density. In this region of wavenumbers, de Gennes's slowing down of the density fluctuations takes place, which is ultimately reflected in the long tails of the density–density time correlation functions. One can see that for linear densities $l > 1$ the structure factor $S(k)$ is typical for distorted crystals, with the main peak shaped as the sheared-out delta function. For linear densities $l < 1$, one observes typical fluid-like structure factor. In disordered systems where a structural transition takes place, one can find different slopes of the main peak of $S(k)$ on both sides of the transition [30]. In **Figure 5**, we show the main peak position $K_{\max}$ of longitudinal static structure factor $S(k)$ as a function of the linear size L of system that is proportional to the inverse $1/l$ of linear density. The location of the main peak is changing from $K_{\max} \approx 7$ for the case of $L/\sigma = 180$ (the highest linear density $l = 1.111$) down to the value $K_{\max} \approx 4.5$ for $L/\sigma = 400$ (the lowest considered linear density $l = 0.5$). Indeed, one can see that there is a kink in the behavior of the maxima positions, which occurs in the region of linear densities $0.8 < l < 1.01$. According to **Figure 2B**, this range of linear densities corresponds in our system to the thermodynamic state, where the transverse pressure P_T is lower than the longitudinal pressure P_L. It worth to note that in a quasi-1D system with channel width $H/\sigma = 1.866$ the latter newer happens, i.e., always $P_T > P_L$ (see **Figure 2C**), while there is range of linear densities, $0.93 \lesssim l \lesssim 1.01$, where transverse force F_T is slightly smaller than longitudinal force F_L. This density range corresponds to packing fraction range from $\eta = 0.35$ to 0.45 (see Figure 10 of [9]), where the time dependence of the mean-square displacement starts to develop a power-law

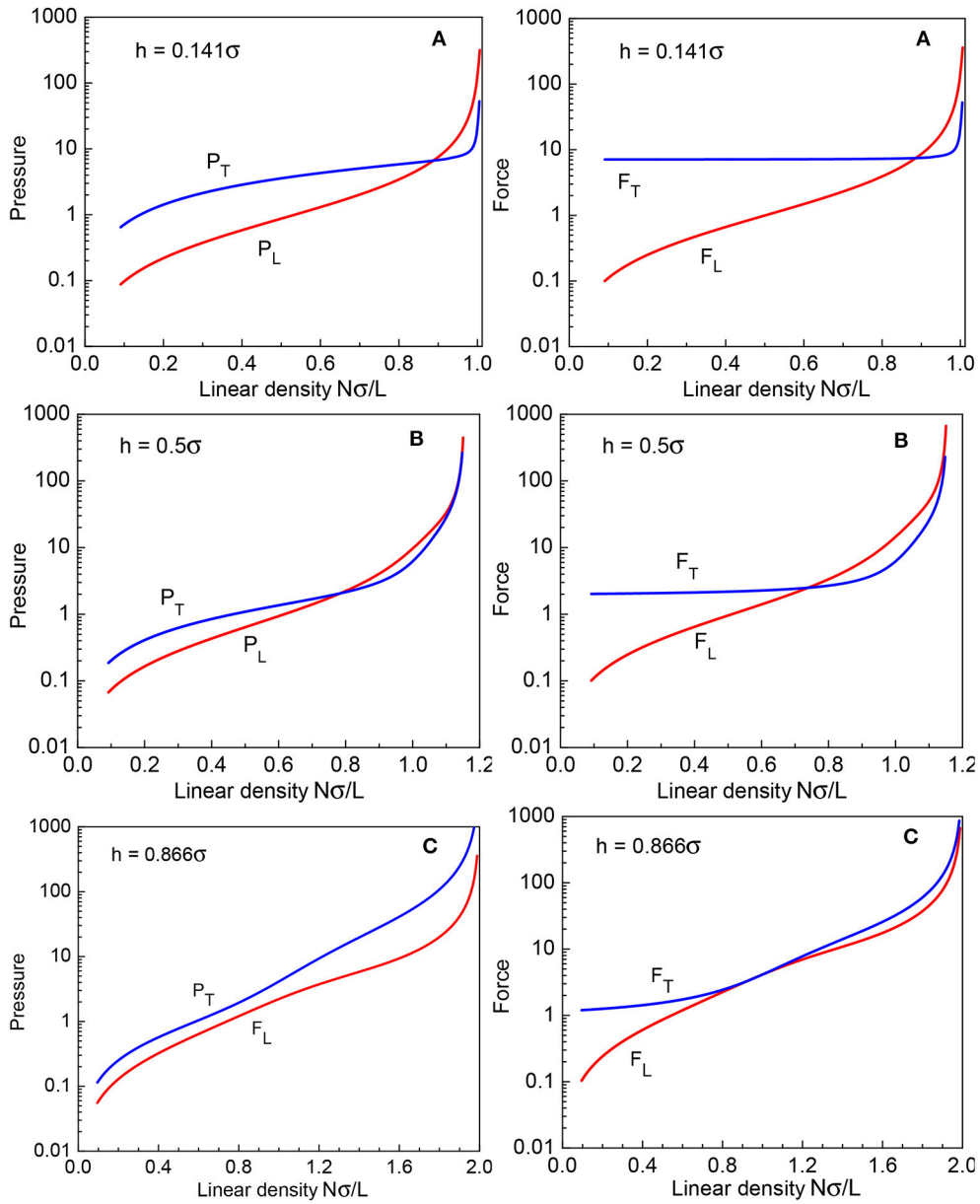

FIGURE 2 | Density dependence of the longitudinal (L) and transverse (T) pressures and forces in quasi-1D hard disk system of different channel width $H/\sigma = 1.141$ **(A)**, 1.5 **(B)**, and 1.866 **(C)** calculated using the analytical canonical partition function [10].

time dependence due to the slow diffusion of defects in the zigzag arrangement of disks, suggested in [12] as a mechanism for the α relaxation.

The single-particle dynamics can be studied by means of the velocity autocorrelation functions

$$\psi(t) = \frac{\langle \mathbf{v}(t) \cdot \mathbf{v}(t=0) \rangle}{\langle \mathbf{v}(0) \cdot \mathbf{v}(0) \rangle}. \tag{13}$$

The velocity autocorrelation functions were already obtained by means of molecular dynamics simulations for the bulk 3D hard sphere [31] and 2D hard disk [22] fluids. In both cases, the authors found that there exists the packing fraction value ($\eta = 0.45$ for 3D case and $\eta = 0.65$ for 2D hard disks) above which the velocity autocorrelation function at short times develops a negative minimum signaling of a nascent caging. In our case, an anisotropic quasi-1D hard disk system shows essentially different behavior for the directions along and across the channel. In **Figure 6**, we show the velocity autocorrelation function $\psi(t)$, its xx- and yy-components, and how they depend on the disk density. The xx-component, $\psi_{xx}(t)$, in the quasi-1D hard disk system behaves in a way very similar to that for bulk 2D hard disk system [22]. It has long-time tails for small linear densities $l \lesssim 0.667$ and changes to a shallow negative minimum at the largest

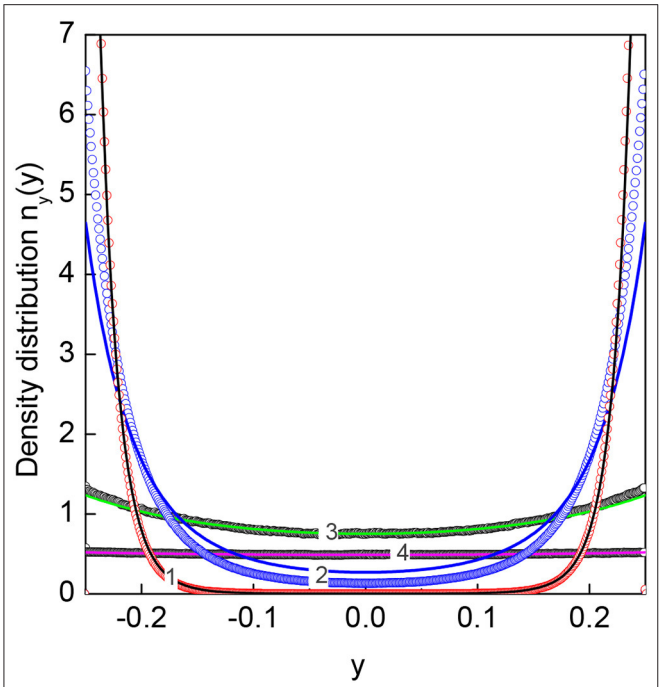

FIGURE 3 | Transverse density profile, $n_y(y)$, of the quasi-1D hard disk system with channel width $H/\sigma = 1.5$ and different disk linear density l: 1—1.111; 2—1.053; 3—0.909; 4—0.5. The symbols correspond to MD simulation data, while solid lines result from the analytical canonical partition function [10].

studied linear density $l = 1.111$ (packing fraction $\eta = 0.582$) due to collisions with the nearest neighbors.

The effect of reflections from the channel hard walls is well seen in the transverse component, $\psi_{yy}(t)$, of the velocity autocorrelation function. It took us by surprise that the characteristic oscillation of $\psi_{yy}(t)$ due to the wall reflections changed its shape, and especially so for the intermediate density $l = 1.01$. Toward shorter times, it became more shallow, transforming for the most dense system, $l = 1.111$, into a very high-frequency heavily damped oscillation. This effect is much better seen in the Fourier-spectrum $\tilde{Z}_{yy}(\omega)$ of the function $\psi_{yy}(t)$ shown in **Figure 7**. The characteristic oscillation due to hard wall reflection is changed starting from $l = 1.01$ to shift toward higher frequencies with increasing oscillation damping. This means that at high densities the zigzag structuring of hard disks prevents their reflections from both channel walls. Instead under zigzag ordering hard disks are reflected from the single nearest wall and from two nearest zigzag neighbors.

The *xx*- and *yy*-components of the velocity autocorrelation function in a quasi-1D system were discussed so far only for the case of hard core particles suspended in a viscoelastic liquid solvent [32]. Similar to our **Figure 6B**, the authors observed a negative minimum and a negative long time tail of the asymptotic form $\sim -t^{-3/2}$ for the component parallel to the channel axis. They also concluded that both findings take place only for sticky boundary condition and does not occur if the solvent can slip over the walls. Our finding of a negative minimum of the velocity autocorrelation function in **Figure 6B** at the highest studied linear density $l = 1.111$ is of a completely different nature as our system consists solely of hard disks, which fly ballistically between hitting hard obstacles. We did try to estimate the exponentials for a negative long-time tail of $\psi_{xx}(t)$. However, even in our case of saved 100,000 configurations with $N = 200$ particles, the noise in the tails was very strong, which did not allow us to reliably estimate the exponents. This shows that the lattice Boltzmann simulations [32] are more appropriate tool for this purpose than the Newtonian MD simulations.

Collective dynamics is usually studied via analysis of the time correlation functions, which store the entire information about collective excitations in the system and their coupling. So far, the collective dynamics has been well-understood on the macroscopic scales in bulk systems, but practically no information is available in the literature on collective excitations in confined low-dimensional systems consisting purely of hard-core particles. The time correlations in the latter case can be essentially different from that in the bulk systems. A simple example of this difference is seen in the transverse dynamics of considered quasi-1D hard disks system, which at the smallest wavenumber accessible in our simulations always shows damped oscillations due to reflection from the channel hard walls. In contrast, in bulk 3d hard-sphere and 2D hard-disk systems, where macroscopic hydrodynamics is valid, no transverse excitations exist at small wavenumbers accessible in simulations. It is seen in **Figure 8** that the change of collective transverse current autocorrelation functions with disk density is practically the same as for the single-particle *yy*-velocity correlations. This makes it evidence that the leading contribution to the transverse current–current time correlation functions comes from the particle reflections from the channel hard walls.

The longitudinal current time correlation functions allow one to estimate the speed of sound for the smallest wavenumbers accessible in simulations. In **Figure 9**, we show the obtained dependence of the speed of sound on the channel length L that is proportional to inverse $1/l$ of linear density (see **Table 1**). As expected, the speed of sound shows a monotonic decrease with increasing channel length, i.e., with decreasing density.

Dispersion of the longitudinal and transverse excitations in the studied quasi-1D hard disk system were obtained from the peak positions of the longitudinal and transverse current spectral functions $C^{L/T}(k,\omega)$ that are the time-Fourier transforms of the MD-derived longitudinal/transverse current–current time correlation functions $F_{JJ}^{L/T}(k,t)$. By employing well-established methodology [24], the latter were analyzed for their peak locations, which for different wave numbers k define the dispersion, $\omega_{L/T}(k)$, of longitudinal and transverse excitations. Typical shapes of the spectral function $C^{L/T}(k,\omega)$ are shown in **Figure 10** for the system of $N = 200$ particles and linear density $l = 1.01$. As the shapes of the spectral functions are noisy, to locate their peak positions and maxima, we made use of the standard Bezier fit for noisy data. The simulations with larger numbers of particles allowed us to access smaller wavenumbers while the dispersion relations within the error bars remained the same.

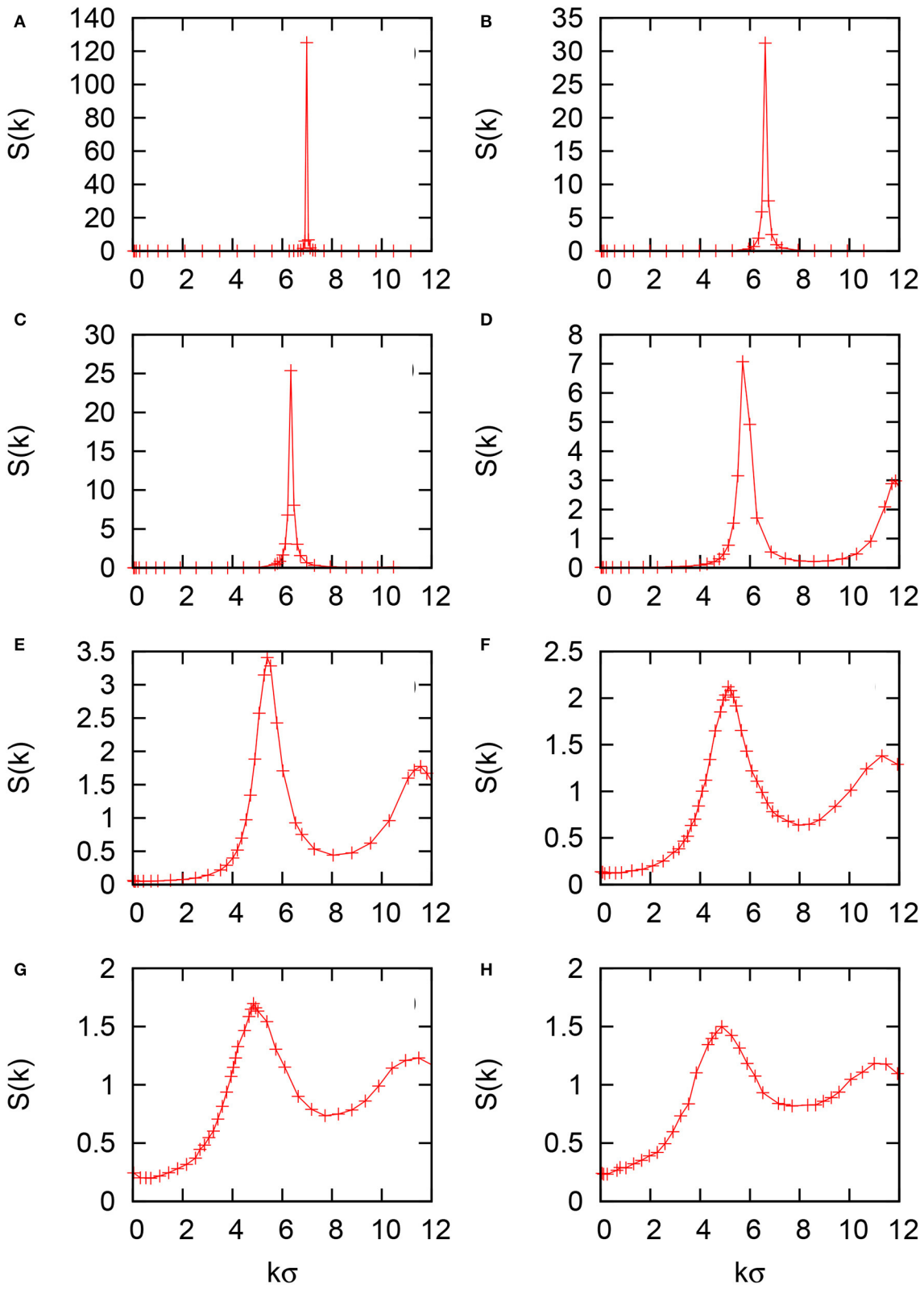

FIGURE 4 | Static structure factor, $S(k)$ of the quasi-1D hard disk system with channel width $H/\sigma = 1.5$ calculated according to the definition equation 12 by using MD-generated 100,000 configurations of $N = 200$ disks. The sequence of panels **(A–H)** corresponds the linear density decreasing from $l = 1.111$ **(A)** to 0.5 **(H)** according to **Table 1**.

Figure 11 show the dispersions $\omega_{L/T}(k)$ of longitudinal and transverse excitations in the quasi-1D hard disk system. The parts of **Figures 11A,B** present data for the linear densities $l < 1$. At first glance in this case the dispersion $\omega_L(k)$ of longitudinal excitations in quasi-1D hard disk system is very similar to that already observed for a 2D hard disk system [22]. When linear

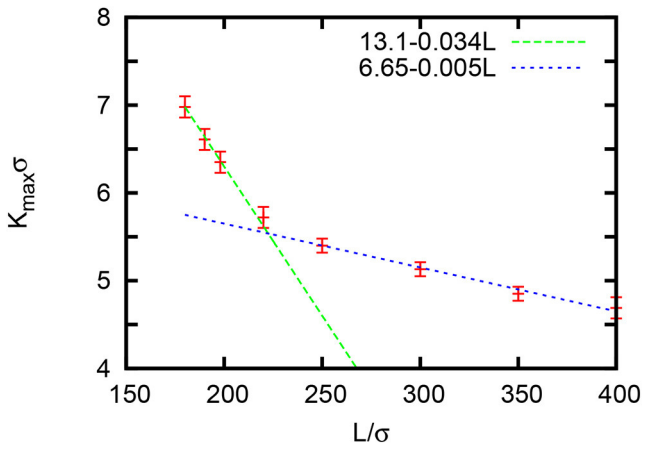

FIGURE 5 | Dependence of the main peak position, K_{max}, of the static structure factor $S(k)$ of quasi-1D hard disk systems with the channel width $H/\sigma = 1.5$ on the channel length L that is proportional to inverse $1/l$ of linear density.

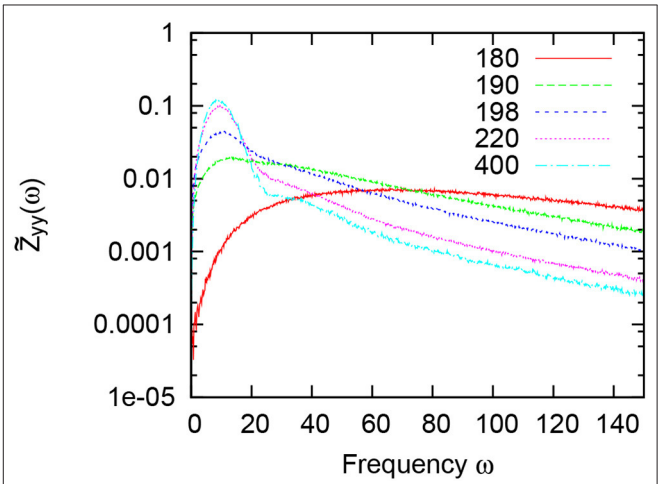

FIGURE 7 | Fourier-spectrum, $\tilde{Z}_{yy}(\omega)$, of the transverse velocity autocorrelation function, $\psi_{yy}(t)$, shown in **Figure 6C**, at different linear densities $l = 1.111(L = 180), 1.053(190), 1.01(198), 0.909(220)$, and $0.5(400)$.

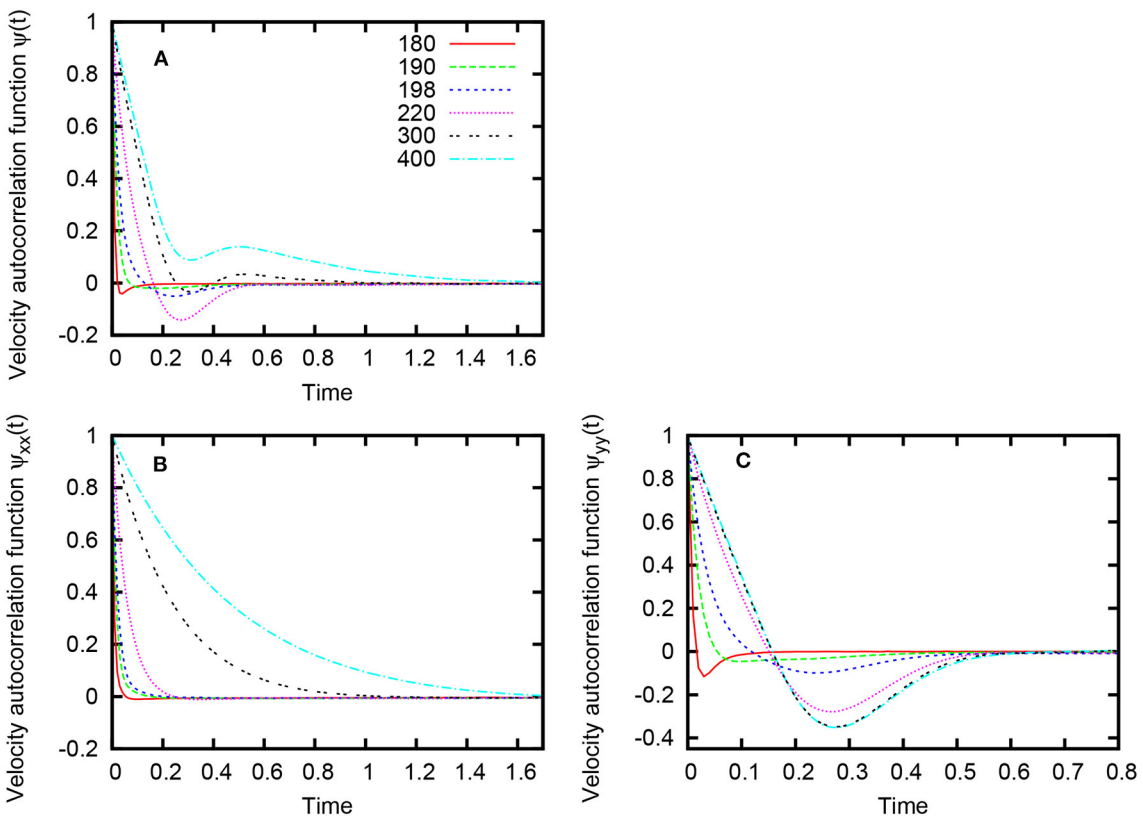

FIGURE 6 | Velocity autocorrelation function, $\psi(t)$ **(A)** and its longitudinal (the *xx* direction along the channel) **(B)** and transverse (the *yy* direction across the channel) **(C)** components for quasi-1D hard disk system with channel width $H/\sigma = 1.5$ at different linear densities $l = 1.111(L = 180), 1.053(190), 1.01(198), 0.909(220), 0.667(300)$, and $0.5(400)$.

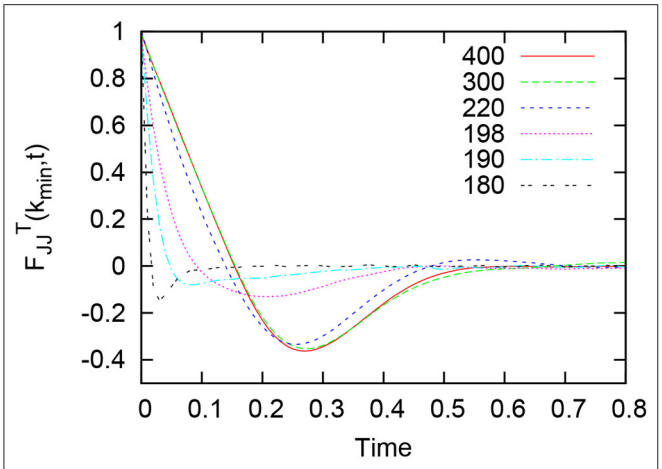

FIGURE 8 | Collective time correlation function of transverse momentum in quasi-1D hard disk system with channel width $H/\sigma = 1.5$ evaluated at the smallest wavenumbers k_{min} accessible in simulations, and for different linear densities $l = 1.111(L = 180), 1.053(190), 1.01(198), 0.909(220), 0.667(300)$, and 0.5(400). The standard hydrodynamic shape of transverse current time correlation function in fluids is the single-exponential one.

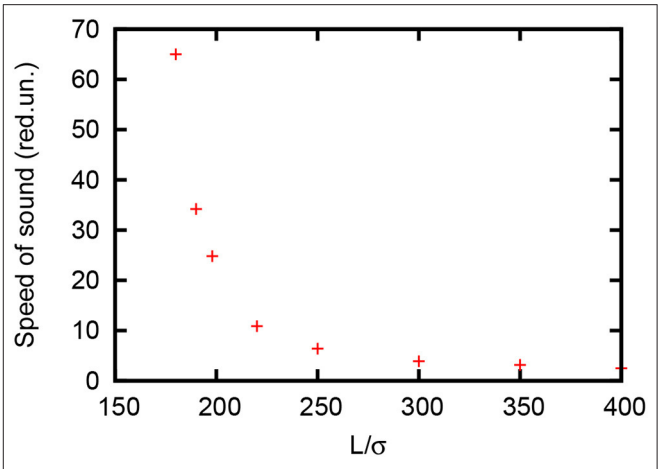

FIGURE 9 | Dependence of the speed of sound c_s in the quasi-1D hard disk system with channel width $H/\sigma = 1.5$ on the channel length L that is proportional to inverse $1/l$ of the linear density.

density is low, $l = 0.5$, the dispersion $\omega_L(k)$ only slightly deviates from being monotonic. But as soon as linear density increases, $l = 0.909$, it shows well-defined minimum around wavenumber values $k \sim 6$ associated with position of the main peak K_{max} of longitudinal structure factor $S(k)$ discussed in **Figures 4**, **5**. The deviation from hydrodynamic dispersion law in the long-wavelength limit for both considered densities persists to be "negative." The "negative" dispersion concerns the negative deviation of the dispersion curve $\omega_L(k)$ at the boundary of hydrodynamic regime from the linear hydrodynamic dispersion law of acoustic modes in considered quasi1-D hard disk system. These effects are similar to those observed in 2D hard disk system with density increase [22]. In contrast, the dispersion $\omega_T(k)$ of transverse excitations is essentially different from those in the case of 2D hard disk system [22]. Namely, for both linear densities $l < 1$ we are observing rather flat shape of the curve $\omega_T(k)$ at reduced frequency ~ 10 with a tendency toward higher frequency values with increase of linear density. In 2D hard disk system, the transverse excitations are of acoustic nature. Moreover, the transverse excitations are absent at low densities and there was observed a long-wavelength propagation gap when they start to appear at higher densities. It is therefore quite natural to attribute the flat transverse mode in a quasi-1D hard disk system to disks' reflections from the channel hard walls. This issue is discussed in more details below.

Parts (c) and (d) of **Figure 11** show similar data for the dispersions $\omega_{L/T}(k)$ of longitudinal and transverse excitations but for the range of linear densities $l > 1$. As for the dispersions of longitudinal excitations, $\omega_L(k)$, we see the tendencies already observed in **Figures 11A,B** under increase of linear density, i.e., the magnitudes of $\omega^L(k)$ maxima are increasing while minima become deeper, reaching zero-frequency values at density $\rho = 1.111$ and being shifted toward larger wavenumber values k. The later again is consistent with the shift for the position K_{max} of the first peak of the longitudinal structure factor $S(k)$ in **Figures 4**, **5**; the "negative" dispersion in long-wavelengths region is preserved as well. Such behavior of $\omega_L(k)$ resembles one for the ordered solids and in [33] is interpreted as a consequence of the emergence a zigzag ordering in a squeezed quasi-1D system. The dispersion of transverse excitations in **Figures 11C,D** does not show notable changes too when the linear density was changing to $l = 1.01$. However, it does show dramatic changes at the highest considered linear density $l = 1.111$. Namely, (i) there is a sharp increase of frequency ω_T up to ~ 70; (ii) the dispersion curve $\omega_T(k)$ itself exhibits bubble-like shape by splitting on low- and high-frequency branches in the range of k-values that coincide with location of the maximum of dispersion $\omega_L(k)$ that implies possibility of longitudinal-transverse excitation coupling on atomic scale in a squeezed almost zigzag ordered quasi-1D hard disk system.

The MD simulations allow one to study the fluctuations of heat density in the system and their effect on collective dynamics. We would like to remind that an adiabatic propagation of sound in fluids causes small deviations of the local temperature and instantaneous temperature gradients, which give rise to relaxation processes of the local temperature via thermal diffusivity. These relaxation process is directly connected with entropy fluctuations and is responsible for the central peak of dynamic structure factors $S(k,\omega)$. In **Figure 12**, we show dynamic structure factors $S(k,\omega)$ as well as heat-density dynamic factors $S_{hh}(k,\omega)$ for three, the lowest wavenumbers in the quasi-1D hard disk system at the highest linear density $l = 1.111$. In both types of spectral functions, the side peaks are caused by longitudinal acoustic excitations, while the central peak for liquid state is caused by entropy fluctuations. In our case of the confined, almost zigzag structure at linear density $l = 1.111$ (channel length $L/\sigma = 180$ and width $H/\sigma = 1.5$), the central peaks of $S(k,\omega)$ and

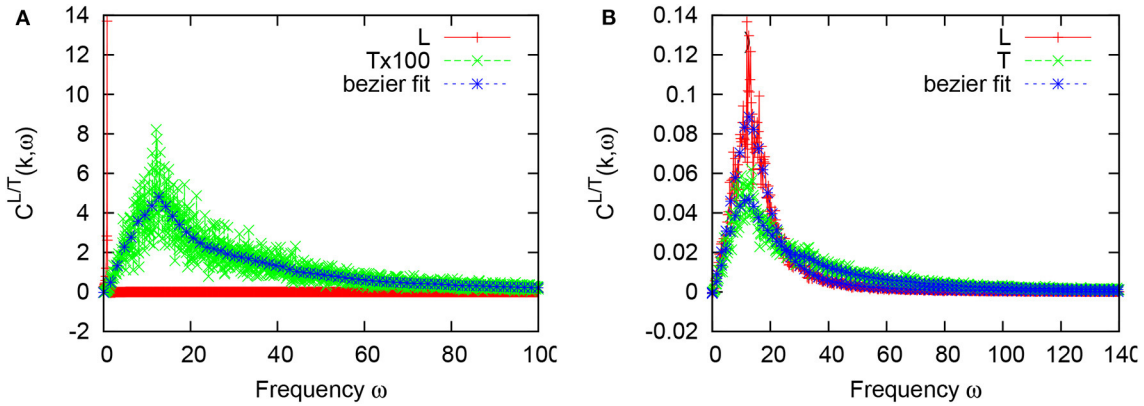

FIGURE 10 | Typical longitudinal (L) and transverse (T) current spectral functions, $C^{L/T}(k,\omega)$, in the long-wavelength region at $k_{\min} = 2\pi/L$ **(A)** and for wave number $k = 17k_{\min}$ **(B)** for the system of $N = 200$ disks and linear density $l = 1.01$. In **(A)**, the transverse spectral function was multiplied by a factor 100 for eye convenience. Blue line-connected asterisks show the Bezier fit applied for estimation of peak position of the noisy spectral functions.

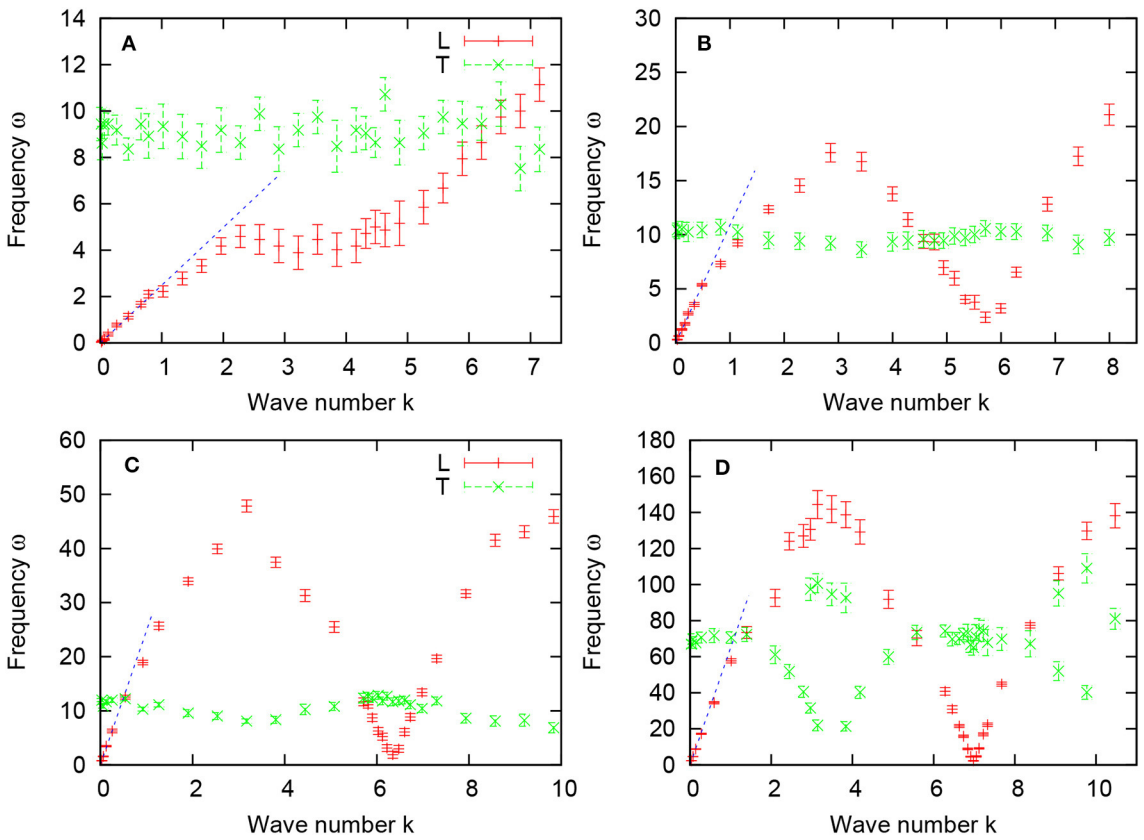

FIGURE 11 | Dispersions of longitudinal (L) and transverse (T) excitations, $\omega_L(k)$ and $\omega_T(k)$, in quasi-1D hard disk system with channel width $H/\sigma = 1.5$ at disk linear density $l = 0.5$ **(A)**, 0.909 **(B)**, 1.01 **(C)**, and 1.111 **(D)**. The dashed straight lines in the small-k region correspond to hydrodynamic dispersion law $\omega = c_s k$ with the corresponding speed of sound c_s shown in **Figure 9**. The raw data for parts **(C,D)** were taken from our preceding paper [33].

$S_{hh}(k,\omega)$ give evidence of the same temperature (sometimes called entropy) relaxation processes typical for fluid state. We calculated $S_{hh}(k,\omega)$ for lower densities too, and observed practically the same shape of $S_{hh}(k,\omega)$ but with a larger smearing of the central and side peaks in comparison with the higher densities.

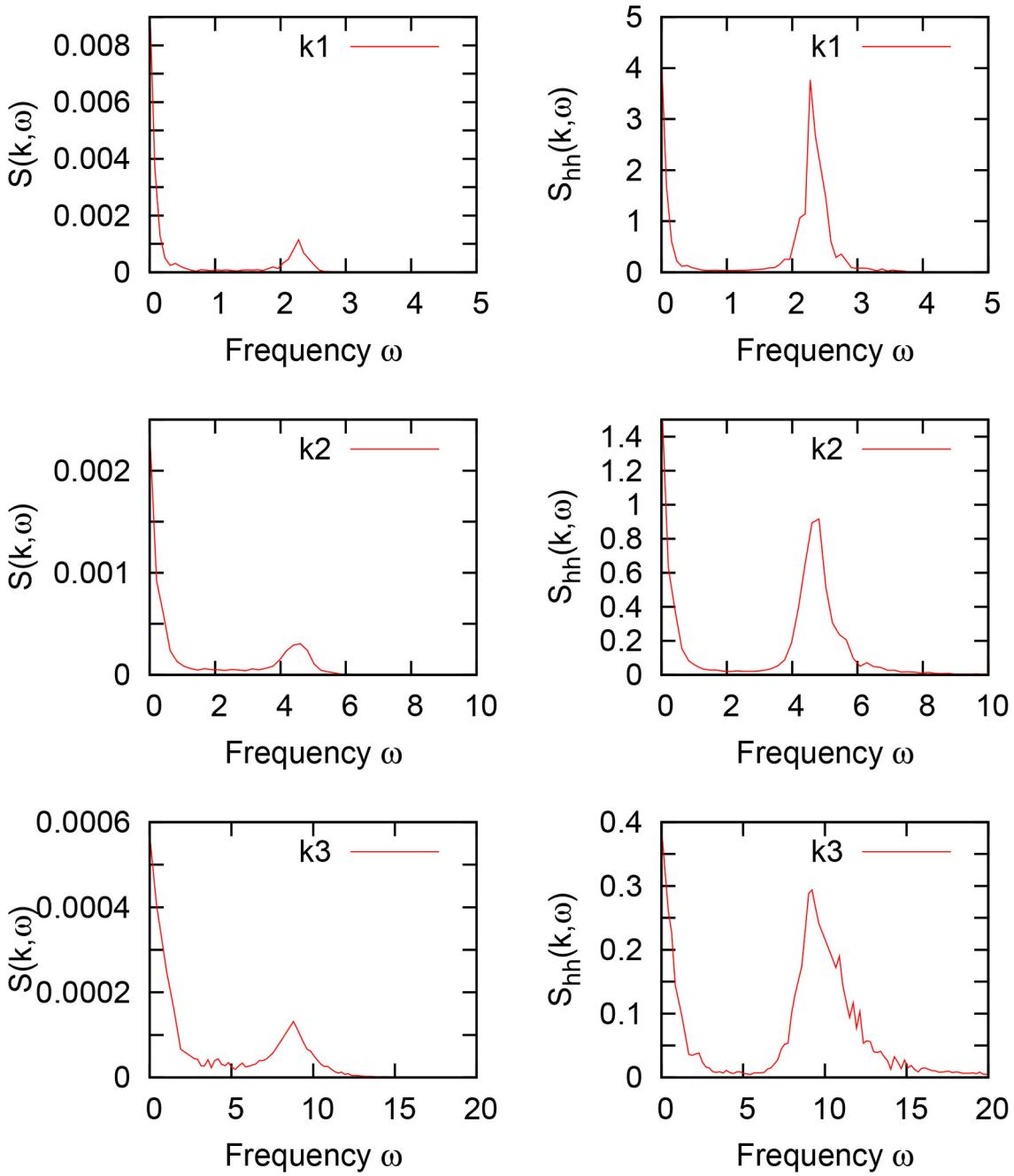

FIGURE 12 | Dynamic structure factor, $S(k,\omega)$, and heat-density dynamic factors, $S_{hh}(k,\omega)$, of the quasi-1D hard disk system with the channel width $H/\sigma = 1.5$ derived from MD simulations at the highest considered linear density $l = 1.111$ for three the smallest wavenumbers $k_1 < k_2 < k_3$.

4. DISCUSSION

In dense, nearly solid-like states of a quasi-1D hard disk system, we observed a rapid increase of the transverse frequency $\omega_T(k)$ in the long-wavelength region $k \sim 0$ from $\omega_T \sim 12$ for linear density $l = 1.01$ in **Figure 11C** to the frequency $\omega_T \sim 70$ for linear density $l = 1.111$ in **Figure 11D**. The shallow minimum in $\omega_T(k)$ profile, observed for linear density $l = 1.01$ at wavenumbers $k \sim K_{max}/2$, also deepens and becomes well-developed. Eventually, however, frequency $\omega_T(k)$ at $k \sim K_{max}/2$ splits into a high- and low-frequency branches at linear density $l = 1.111$ as shown in **Figure 11D**. The observed change in the dispersion $\omega_T(k)$ of transverse excitations as the system changes from rarefied to dense can be explained by formation of the zigzag structure. The transverse low frequency mode, which is due to bouncing between the two hard walls, transforms into the

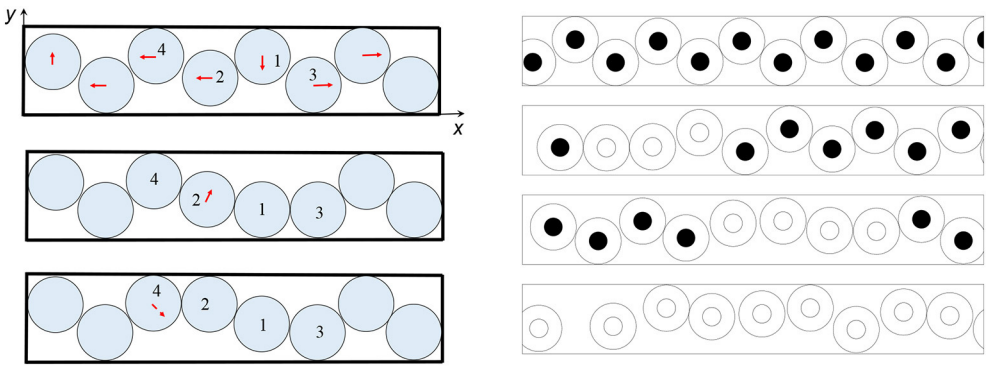

FIGURE 13 | Left: Disks' rearrangement in a pore that creates a window for two disks to exchange their vertical positions. Upper panel: disk in the pore at the average distance along the pore, which is below the disk diameter σ and disks cannot exchange their vertical positions. To let disk 1 go down, disks on the left and right of it get more dense. Mid panel: Disk 1 gets down through the window of size σ between disks 2 and 3. Now disk 2 may get up between disks 4 and 1. Lower panel: The exchange of the vertical positions of disks 1 and 2 is accomplished. Now disk 4 potentially can move down. **Right**: Representative snapshots of disk configurations taken from MD simulations of the quasi1-D hard disk system of the channel width $H/\sigma = 1.5$ to illustrate the schematics of disks' rearrangement. Shown are four the highest considered linear densities from the top to the bottom: $l = 1.111, 1.053, 1.01, 0.909$ that are discussed in **Figure 14**. The filled circles indicate disks that are caged and cannot exchange their vertical positions.

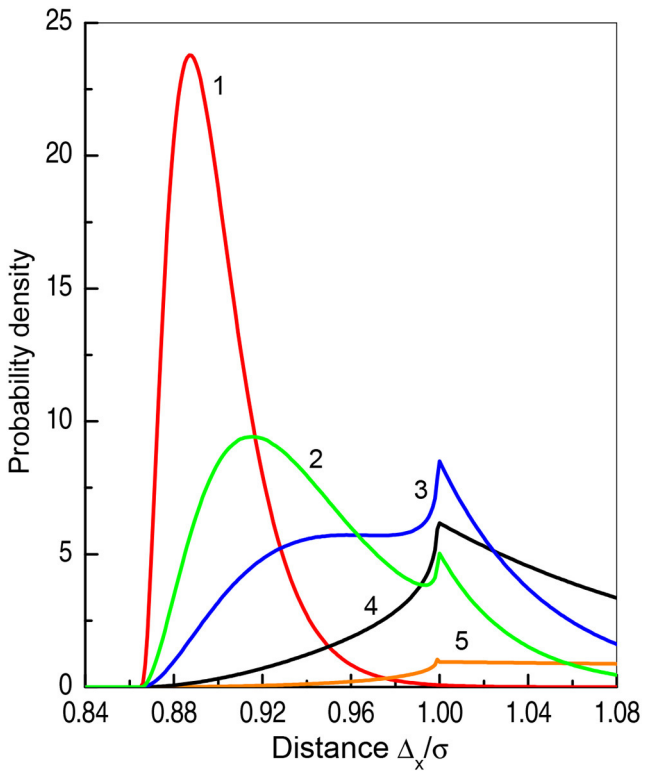

FIGURE 14 | Distribution of actual horizontal distances, Δ_x, between the nearest neighbor disks in quasi-1D hard disk system with channel width $H/\sigma = 1.5$ at disk linear densities $l = 1.111(1), 1.053(2), 1.01(3), 0.909(4)$, and 0.5 (5) derived from MD simulations.

high frequency transverse oscillations between one wall and the nearest neighbors in the zigzag structure. This is also supported by the behavior of the transverse component of the velocity autocorrelation function $\psi_{yy}(t)$ in **Figure 6C**. Inspired by this intriguing behavior, one of us developed an analytical theory [10] of this system, which suggests that it is related to developing window-like defects in the zigzag disks' arrangement [33]. The idea of defects of this kind (defect is a local less packing) has been introduced [12] and employed [7–9, 12–14] to describe glassy dynamics in terms of caged and uncaged states in the disk arrangements in a quasi-1D hard disk system of the channel width $H/\sigma = 1.866$. In [33], such defects were associated with the maximum contact separation of two disks along the channel, which is equal to the disk diameter σ; in [10], their distribution was found analytically as a function of the linear density. As for the densities $l > 1$, the horizontal contact distance between disks and the actual horizontal distance between nearest neighbor disks are very close, this distribution can be well representative of the actual disks separations Δ_x, which is supported by the computer simulation data.

At dense/close packing, the disks form perfect zigzag. As confinement weakens, the tendency to the entropy increase results in an emergence of progressively larger number of window-like defects through which pairs of next neighbor disks uncage and exchange their vertical positions (**Figure 13**). This theoretical prediction of [10] has been confirmed from MD simulations data for the distribution of the actual distances Δ_x between next neighbor disks (**Figure 14**) and is in line with the earlier result [8]. For high linear density, $l = 1.111$, these are distributed around $\Delta_x/\sigma \sim 0.89$ close to the minimum possible contact distance along the pore, $\sqrt{3}/2 \approx 0.87\sigma$. However at slightly lower linear density, $l = 1.053$, in addition to the widening of maximum at $\Delta_x/\sigma \sim 0.92$ we see the appearance of a sharp subpeak at $\Delta_x/\sigma = 1$. In contrast to the wide maximum drifting toward larger Δ_x, the subpeak always remains at $\Delta_x/\sigma = 1$, although its shape is changing: it becomes more and more pronounced and finally exceeds the main peak, signaling approaching a fluid-like state. It points to the exclusive role that next neighbor disk center-to-center distance $\Delta_x = \sigma$

plays. Namely, creation of windows of the width of disk diameter σ ($\sigma-$windows) in the zigzag array, neither wider nor narrower, is the most effective way to gain entropy by uncaging two disks and making them extend their wondering to the whole channel width. The described mechanism of disk's caging/uncaging by their neighbors in quasi-1D hard disk system is fundamentally different to that in quasi-1D system with a long range screened electrostatic repulsion in the dusty plasma [20] where particles stay at finite distances and the zigzag can even transform into a straight line.

In a pure 1D hard disk system, the vertical motion is absent. In a densely packed quasi-1D hard disk system of the width $H/\sigma = 1.5$, it is also prevented by the full caging, but it eventually appears as the confinement weakens. As for sufficiently low density, the vertical disks' motion from one wall to another is possible, here one expects some contribution to the dispersion relation from the nearly ballistic transverse oscillation between the walls. As it comes from the maximum vertical path $H - \sigma$, this contribution $\omega_{\mathrm{T}1}(k)$ to the frequency $\omega_{\mathrm{T}}(k)$ at low density must be lowest possible. At high density, however, the $\sigma-$windows are rare and disks can bounce at most between one wall and the mid plane hence the lowest transverse frequency $\omega_{\mathrm{T}2}$ for higher densities is expected to be roughly twice that for low density, $\omega_{\mathrm{T}2} \sim 2\omega_{\mathrm{T}1}$. The frequency $\omega_{\mathrm{T}2}$ is related to the maximal distance Δ_x at window nuclei, which require local compression and must result in high frequency longitudinal and transverse jitters. One can thus expect that the lowest transverse frequency $\omega_{\mathrm{T}2}$ and the highest longitudinal and transverse frequencies appear near same wavenumbers k. In addition, the group velocity at this wavenumber range has to be zero as windows are not transferred by the waves. The dispersion of the longitudinal and transverse excitations in quasi-1D hard disk system obtained from MD simulations are in line with this picture (**Figures 11C,D**). For linear density $l = 1.01$, the peak at $\Delta_x = \sigma$ (**Figure 14**) indicates that $\sigma-$windows in the zigzag structure are well-developed, the disk order is of a short range, and frequency $\omega_{\mathrm{T}1}$ can be identified with the practically $k-$independent transverse frequency $\omega_{\mathrm{T}}(K_{\max}/2) \sim 10$ in **Figure 11C**. At the same time, for linear density $l = 1.111$, when there are almost no $\sigma-$windows (**Figure 14**), the transverse spectrum splits into the lowest, $\omega_{\mathrm{T}2} \sim 20 \approx 2\omega_{\mathrm{T}1}$, and the highest frequency, $\omega_{\mathrm{T}} \sim 100$, at the wavenumbers k where longitudinal frequency is maximum (see **Figure 11D**). At wavenumbers $k \sim K_{\max}/2$, the curves $\omega_{\mathrm{T}1}(k)$ and $\omega_{\mathrm{T}2}(k)$ are plateaus, which indicate zero group velocities. The continuous longitudinal and transverse modes for linear density $l = 1.111$ are related to the short free path oscillation of mutually caged disks near the walls. Thus, the main properties of $\omega_{\mathrm{T}}(k)$, which are directly related to the vertical motion, are in line with the idea of the role of $\sigma-$windows in the zigzag arrangement.

The interpretation of computer simulation data in terms of the vertical disk motion presented above is also consistent with and well-illustrated by the theoretical dependence of the total transverse force $F_T(l)$ in **Figure 2B**. Indeed, as discussed above, for low linear density l, the transverse force F_T is constant implying the vertical motion to be ballistic because the free path and free time are maximum. In contrast, for high linear density l, the transverse force F_T sharply grows with l, the disks' arrangement is close to a dense zigzag, they cannot cross the middle line of the channel so that the free path and time at best are halves of their maximum values. Finally, this picture is obviously in line with the disk density distribution across the channel in **Figure 3**.

In conclusion, we would like to point out the novel and unexpected development, which stems from the above studies of the collective excitations. It is about a possible Kosterlitz-Thouless scenario in quasi-1D hard disk system [33]. In 2D systems, melting proceeds via the Kosterlitz-Thouless scenario [34]: a crystal develops defects, and their number is growing continuously from zero at zero temperature until the state becomes a liquid. The number of window-like defects in a zigzag arrangement behaves exactly in this way [7, 9, 10, 12]: it is zero only at dense packing and smoothly increases as density goes down. But in the Kosterlitz-Thouless scenario, it is essential that the spatial correlations decrease as a power law at high densities and exponentially at lower densities. At the same time, it is known that if the partition function of a system possesses a transfer matrix property, which has been widely accepted to be the case for a quasi-1D hard disk system, then the correlations can only decay exponentially. Our search for a different correlation behavior is motivated as follows. First, our already published [33, 35] and tentative molecular dynamic results on the system described here indicate that a power law decay is possible. Second, it is shown in Appendix in [10] that the transfer matrix property may be not so universal for quasi-1D systems, which leaves a room for alternative theory. The work is in progress.

DATA AVAILABILITY STATEMENT

The raw data supporting the conclusions of this article will be made available by the authors, without undue reservation.

AUTHOR CONTRIBUTIONS

AH and AT designed the model and the computational framework. AH performed the event driven MD simulations to generate particle trajectories. AT performed the event driven MD simulations of particle distributions. TB used MD-generated trajectories and performed the numerical calculations of collective dynamics properties. VP has contributed the interpretation of the transverse excitation modes in terms of the windowlike defects and the connection between the transverse disk motion and the total forces and pressures on the channel's boundaries. AT supervised the project and wrote the manuscript with support from VP, TB, and AH. All authors discussed the results and contributed to the final manuscript.

FUNDING

TB and AT were supported by NRFU Project 2020.02/0115. VP's work was supported by VC 202 from NAS of Ukraine and NRFU Project 2020.01/0144.

REFERENCES

1. Löwen H. Fun with hard spheres. In: Mecke KR, Stoyan D, editors. *Statistical Physics and Spatial Statistics*. Berlin: Springer (2000). p. 297–331.
2. Barker J. Statistical mechanics of almost one-dimensional systems. *Austr J Phys*. (1962) 15:127–34. doi: 10.1071/PH620127
3. Taloni A, Flomenbom O, Castaneda-Priego R, Marchesoni F. Single file dynamics in soft materials. *Soft Matter*. (2017) 13:1096–106. doi: 10.1039/C6SM02570F
4. Tonks L. The complete equation of state of one, two and three-dimensional gases of hard elastic spheres. *Phys Rev*. (1936) 50:955–63. doi: 10.1103/PhysRev.50.955
5. Kofke D, Post A. Hard particles in narrow pores. Transfer-matrix solution and the periodic narrow box. *J Chem Phys*. (1993) 98:4853–61. doi: 10.1063/1.464967
6. Varga S, Balló G, Gurin P. Structural properties of hard disks in a narrow tube. *J Stat Mech Theory Exp*. (2011) 153:P11006. doi: 10.1088/1742-5468/2011/11/P11006
7. Godfrey MJ, Moore MA. Static and dynamical properties of a hard-disk fluid confined to a narrow channel. *Phys Rev E*. (2014) 89:032111. doi: 10.1103/PhysRevE.89.032111
8. Godfrey MJ, Moore MA. Understanding the ideal glass transition: lessons from an equilibrium study of hard disks in a channel. *Phys Rev E*. (2015) 91:022120. doi: 10.1103/PhysRevE.91.022120
9. Robinson JF, Godfrey ML, Moore MA. Glasslike behavior of a hard-disk fluid confined to a narrow channel. *Phys Rev E*. (2016) 93:032101. doi: 10.1103/PhysRevE.93.032101
10. Pergamenshchik VM. Analytical canonical partition function of a quasi-one-dimensional system of hard disks. *J Chem Phys*. (2020) 153:034502. doi: 10.1063/5.0025645
11. Forster C, Mukamel D, Posch HA. Hard disks in narrow channels. *Phys Rev E*. (2004) 69:022125. doi: 10.1103/PhysRevE.69.066124
12. Bowles RK, Saika-Voivod I. Landscapes, dynamic heterogeneity, and kinetic facilitation in a simple off-lattice model. *Phys Rev E*. (2006) 73:011503. doi: 10.1103/PhysRevE.73.011503
13. Hicks CL, Wheatley MJ, Godfrey MJ, Moore MA. Gardner transition in physical dimensions. *Phys Rev Lett*. (2018) 120:225501. doi: 10.1103/PhysRevLett.120.225501
14. Zhang Y, Godfrey MJ, Moore MA. Marginally jammed states of hard disks in a one-dimensional channel. *Phys Rev E*. (2020) 102:042614. doi: 10.1103/PhysRevE.102.042614
15. Charbonneau P, Kurchan J, Parisi G, Urbani P, Zamponi F. Glass and jamming transitions: from exact results to finite-dimensional descriptions. *Annu Rev Cond Matter Phys*. (2017) 8:265–88. doi: 10.1146/annurev-conmatphys-031016-025334
16. Fois E, Gamba A, Tabacchi G, Quartieric S, Vezzalini G. On the collective properties of water molecules in one-dimensional zeolitic channels. *Phys Chem Chem Phys*. (2001) 3:4158–63. doi: 10.1039/b102231h
17. Kofinger J, Hummer G, Dellago C. Single-file water in nanopores. *Phys Chem Chem Phys*. (2011) 13:15403–17. doi: 10.1039/c1cp21086f
18. Waghe A, Rasaiah JC, Hummer G. Entropy of single-file water in (6,6) carbon nanotubes. *J Chem Phys*. (2020) 137:044709. doi: 10.1063/1.4737842
19. Mark D, Haeberle S, Roth G, von Stetten F, Zengerle R. Microfluidic lab-on-a-chip platforms: requirements, characteristics and applications. *Chem Soc Rev*. (2010) 39:1153–82. doi: 10.1039/b820557b
20. Coste C, Delfau JB, Saint Jean M. Longitudinal and transverse single diffusion in quasi-1D systems. *Biophys Rev Lett*. (2014) 9:333–48. doi: 10.1142/S1793048014400025
21. Dyson FJ. Existence of a phase-transition in a one-dimensional Ising ferromagnet. *Commun Math Phys*. (1969) 12:91–107. doi: 10.1007/BF01645907
22. Huerta A, Bryk T, Trokhymchuk A. Collective excitations in 2D hard-disc fluid. *J Colloid Interface Sci*. (2015) 449:357–63. doi: 10.1016/j.jcis.2014.12.036
23. Bryk T, Huerta A, Hordiichuk V, Trokhymchuk AD. Non-hydrodynamic transverse collective excitations in hard-sphere fluids. *J Chem Phys*. (2017) 147:064509. doi: 10.1063/1.4997640
24. Bryk T, Ruocco G, Scopigno T. Landau-Placzek ratio for heat density dynamics and its application to heat capacity of liquids. *J Chem Phys*. (2013) 138:034502. doi: 10.1063/1.4774406
25. Truskett TM, Torquato S, Sastry S, Debenedetti PG, Stillinger FH. Structural precursor to freezing in the hard-disk and hard-sphere systemsl. *Phys Rev E*. (1998) 58:3083–8. doi: 10.1103/PhysRevE.58.3083
26. Huerta A, Henderson D, Trokhymchuk A. Freezing of two-dimensional hard disks. *Phys Rev E*. (2006) 74:061106. doi: 10.1103/PhysRevE.74.061106
27. Alder BJ, Wainwright TE. Studies in molecular dynamics: general method. *J Chem Phys*. (1959) 31:459–66. doi: 10.1063/1.1730376
28. Donev A, Torquato S, Stillinger FH. Neighbor list collision-driven molecular dynamics simulation for nonspherical hard particles. I. Algorithmic details. *J Computational Phys*. (2005) 202:737–64. doi: 10.1016/j.jcp.2004.08.014
29. Bryk T, Scopigno T, Ruocco G. Heat capacity of liquids: a hydrodynamic approach. *Cond Matt Phys*. (2015) 18:13606. doi: 10.5488/CMP.18.13606
30. Gorelli FA, De Panfilis S, Bryk T, Ulivi L, Garbarino G, Parisiades P, et al. Simple-to-complex transformation in liquid rubidium. *J Phys Chem Lett*. (2018) 9:2909–13. doi: 10.1021/acs.jpclett.8b01094
31. Williams SR, Bryant G, Snook IK, van Megen W. Velocity autocorrelation functions of hard-sphere fluids: long-time tails upon undercooling. *Phys Rev Lett*. (2006) 96:087801. doi: 10.1103/PhysRevLett.96.087801
32. Hagen MHJ, Pagonabarraga I, Lowe CP, Frenkel D. Algebraic decay of velocity fluctuations in a confined fluid. *Phys Rev Lett*. (1997) 78:3785–8. doi: 10.1103/PhysRevLett.78.3785
33. Huerta A, Bryk T, Pergamenshchik VM, Trokhymchuk A. Kosterlitz-Thouless-type caging-uncaging transition in a quasi-one-dimensional hard disk system. *Phys Rev Res*. (2020) 2:033351. doi: 10.1103/PhysRevResearch.2.033351
34. Kosterlitz JM, Thouless DJ. Ordering, metastability and phase transitions in two-dimensional systems. *J Phys C Solid State Phys*. (1973) 6:1181–203. doi: 10.1088/0022-3719/6/7/010
35. Huerta A, Bryk T, Trokhymchuk A. Transverse excitations and zigzag transition in quasi-1D hard-disk system. *arXiv preprint arXiv:190405970v1*. (2019).

Conflict of Interest: The authors declare that the research was conducted in the absence of any commercial or financial relationships that could be construed as a potential conflict of interest.

frontiers in Physics

ORIGINAL RESEARCH
published: 20 May 2021
doi: 10.3389/fphy.2021.636288

Dynamics of Nanoparticle Self-Assembly by Liquid Crystal Sorting in Two Dimensions

*F. Gael Segura-Fernández, Erick F. Serrato-García, J. Emmanuel Flores-Calderón and Orlando Guzmán**

Departamento de Física, Universidad Autónoma Metropolitana Unidad Iztapalapa, Mexico City, Mexico

We study nonlinear dynamical equations for coupled conserved and non-conserved fields describing nanoparticle concentration and liquid crystal order parameter, respectively, and solve them numerically over bidimensional domains. These equations model the rapid segregation of nanoparticles away from nematic domains, which has been observed experimentally in a suspension of gold nanoparticles in 5CB below the isotropic-nematic transition temperature. We contrast the different behaviors obtained when the LC order parameter is treated as a scalar or a tensor, as well as the different rates of evolution observed with each of these. We find, after an instantaneous quench lowering the temperature below the transition one, an initial linear regime where the ordering of the nematic phase proceeds exponentially with time. Only after a lag period the nanoparticle material couples effectively to the LC order parameter and segregates to regions that are less orientationally ordered (extended domain walls for a scalar order parameter, but point disclinations for a tensor one). The lag period is followed by the onset of nonlinear dynamics and saturation of the order parameter. The choice of a scalar or tensor LC order parameter does not change this sequence but results in a clear overshooting of the nonlinear saturation level for the tensor order parameter case. These results are found to be insensitive to weak anchoring due to coupling of gradients of the conserved and non-conserved variables, for the nanoparticle concentrations and anchoring parameters studied. Our modeling approach can be extended in a straightforward manner to cases where the cooling rate is finite and to other systems where a locally conserved concentration is coupled to a orientation field, such as active Langmuir monolayers, and possibly to other examples of nonlinear dynamics in ecological or excitable media problems.

Keywords: dynamic equations, model C, liquid crystal, nanoparticles, mixture, self-assembly, phase separation sorting, conserved and nonconserved fields

OPEN ACCESS

Edited by:
Enrique Hernandez-Lemus, Instituto Nacional de Medicina Genómica (INMEGEN), Mexico

Reviewed by:
Martin Kröger, ETH Zürich, Switzerland
Alejandro Gil-Villegas, University of Guanajuato, Mexico

****Correspondence:***
Orlando Guzmán
oguzman@izt.uam.mx

Specialty section:
This article was submitted to Soft Matter Physics, a section of the journal Frontiers in Physics

Received: *02 December 2020*
Accepted: *13 April 2021*
Published: *20 May 2021*

Citation:
Segura-Fernández FG, Serrato-García EF, Flores-Calderón JE and Guzmán O (2021) Dynamics of Nanoparticle Self-Assembly by Liquid Crystal Sorting in Two Dimensions. Front. Phys. 9:636288. doi: 10.3389/fphy.2021.636288

1. INTRODUCTION

Nonlinear dynamical systems generate intense research because they encompass a large class of phenomena displaying pattern formation, wave-like solutions and even oscillatory patterns of activity [1, 2]. When nonlinear dynamical systems take into account spatial dependencies, they often are modeled in a continuum fashion with partial differential equations. Among the diversity of such systems, the Newell-Whitehead equation (1) finds application diverse fields such as

population growth and epidemics in ecology [3], pattern formation in cloud fields [4], mechanical and chemical engineering [5], and the dynamics of phase transitions [6]:

$$\frac{\partial \phi}{\partial t} - \Gamma \frac{\partial^2 \phi}{\partial x^2} + bu - \epsilon f[u] = 0, \tag{1}$$

where $f[u]$ is a known functional of the unknown u, Γ is a diffusion rate, b is a convection force and ϵ is the magnitude of the nonlinear response.

An example of the application of the Newell-Whitehead equation to soft matter systems occurs for the case of liquid crystals and their isotropic-nematic transition, where the appropriate choice of the functional $f[u]$ leads to the well-known Allen-Cahn [7] or Model A equations [8]. Liquid crystals are a particularly convenient, table-top choice of materials to study the behavior of nonlinear dynamical systems: they are chemically stable at room temperature, highly susceptible to external influences (of thermal, electrical, or magnetic character), and have wide technological application [9].

When nanoparticles are suspended homogeneously in the isotropic phase of a mesogenic fluid, they can undergo rapid self-assembly of micron-sized nanoparticle structures if there is a transition to the nematic phase [10–12]. The hollow structures that can be obtained from such process have a range of sizes and morphologies (such as spheres, cylinders, and foams) that make them attractive for different areas of application [13–15], such as optoelectronics, encapsulation and controlled release, sensing, or catalytic frameworks, among others.

In order to understand this behavior, the Newell-Whitehead equation (corresponding to Model A [8]) must be consistently coupled to a conservation law for the concentration of nanoparticles. We have formerly introduced a thermodynamic model that accounts for the formation of the simplest NP aggregate morphology observed in experiments (micro-shells) as a first-order transition [16], where the excluded volume of the nanoparticles competes with the latent heat of the isotropic-nematic transition to give rise to shells with walls of a definite width for a given temperature quench and initial volume fraction of nanoparticles in the mixture. However, in the self-assembly methodology reported by [12], the final morphology is controlled by the cooling rate and initial concentration of nanoparticles. This indicates that a dynamic model of the system, as opposed to a purely thermodynamic description, is required to analyze it.

A first model addressing this requirement was presented in [12], which combined a Lebwhol-Lasher Monte Carlo simulation of the isotropic-nematic transition which was coupled in a linear fashion to a Cahn-Hilliard equation for the nanoparticle sorting. However, this coupling was one-directional: the nematization order parameter S acted as an external field driving the nanoparticle concentration, but there was no coupling back to the Lebwhol-Lasher simulation.

In this work, we reconsider that previous approach in the context of the dynamic equations of Model C for the time evolution of coupled conserved and non-conserved fields [8]. In our present approach, the nematic order parameter and the nanoparticle concentration follow dynamic equations that are mutually coupled, and therefore we reconsider the nature of the coupling free-energy term. We contrast the different behavior obtained when the liquid crystal is described solely by its (scalar) nematization order parameter S and when it is described with a more detailed alignment tensor $\mathbf{Q}$. To begin with, the former situation does not allow for anchoring of the liquid crystal director, while the second one can. We characterize and contrast the types of structures obtained with the scalar and tensorial models, as well as the different rates of evolution observed with each of these. Further, we investigate the initial segregation process, driven by linear dynamics, and the later non-linear dynamics with numerical simulations.

We report new results quantifying the role of the nanoparticle mobility and the anchoring of the liquid crystal (with respect to nanoparticle concentration gradients present at the edges of the NP aggregates) regarding the impact that the NPs have on the LC dynamics and viceversa. Our results indicate that the tensorial model is characterized by a slower rate of evolution of the alignment tensor field but a faster evolution of the NP concentration field, in comparison to the results of the scalar model. Both display non-linear saturation of their initially exponential dynamics, although the tensorial model shows a clear overshooting with respect to its final saturation behavior.

With our new model, we are able to account for the mutual coupling between the nanoparticles and the mesogenic fluid. It also opens the way for including more realistic models for the NP free energy, beyond the quadratic term that corresponds to a truncation of the NP free energy at the level of its second-virial coefficient. In particular, including the effect of the NP excluded volume as well as the presence of attractive interactions is feasible through known models for the free energy of hard spheres and perturbation theories for Lennard-Jones, square-well and other types of attractive potentials. We also discuss how our results relate to other settings where Newell-Whitehead equations could be coupled to conserved fields, in cases like excitable media, population growth, and epidemics.

2. METHODS

Our analysis relies on the formulation of Model C, by [8], for the dynamical equations of a conserved field coupled with a non-conserved field. For our purposes, the conserved field corresponds to the nanoparticle concentration, $C(\mathbf{x}', t')$. We denote space and time coordinates by $\mathbf{x}'$ and t', respectively, reserving unprimed symbols for non-dimensional coordinates to be introduced below in order to simplify the notation. The non-conserved field corresponds to the order parameter for the liquid crystal. We consider, first, the case where this parameter is taken simply as the scalar nematization,

$$S(\mathbf{x}', t') = \langle P_2(\cos\theta) \rangle, \tag{2}$$

where θ is the angle between the molecular axis of a mesogen and the nematic director, $P_2(x)$ is the second Legendre polynomial, and the angular brackets denote here a coarse-graining average over molecular orientations at the given coordinates. We

also consider the case where the order parameter is the alignment tensor,

$$\mathbf{Q}(\mathbf{x}', t') = \langle \mathbf{uu} - \mathbf{I}/d \rangle, \tag{3}$$

with $\mathbf{u}$ a unit vector in the direction of molecular orientation, $\mathbf{I}$ the identity tensor, and $d = 2, 3$ the dimensionality of $\mathbf{u}$; the angular brackets also denote here a coarse-graining average over molecular orientations at point $\mathbf{x}'$ and time t'.

Within the methodology of Hohenberg and Halperin [8], the dynamic equations are related to the functional derivatives of the system's free energy functional with respect to each of the dynamical fields, but they have different forms depending on the presence or absence of a conservation law for each dynamical variable. We show how to obtain such dynamical equation below.

For the case where the LC order parameter is taken just as the nematization S, we take as the system's free energy functional the following expression:

$$\mathcal{F}[S, C] = \int d\mathbf{x}' \left(\frac{K}{2} \left(\nabla' S \right)^2 + \frac{r}{2} S^2 - wS^3 + uS^4 + \frac{\Omega}{2} C^2 + \frac{\alpha}{2} CS^2 \right). \tag{4}$$

In the previous equation, ∇' denotes differentiation with respect to the spatial coordinates x_i', $r = a(T - T^*)$ is a control parameter that depends on the temperature T, the limit of thermal stability T^* and a positive constant a, while K is an elastic constant, w and u are Landau-de Gennes expansion coefficients [9], Ω is a virial expansion coefficient for the NPs free energy and α is coupling parameter for the conserved and non-conserved fields. They are phenomenological constants with material-specific values. The first four terms in (4) correspond to a Landau-de Gennes expansion, the fifth term is a low-concentration approximation to the free energy of the nanoparticles (to the level of the second virial coefficient), with the last term providing the coupling between the fields.

The Landau-de Gennes expansion coefficients a, T^*, w and u can be determined from microscopic information by simulation [17, 18] or by experimental information about the values of several quantities at the isotropic-nematic transition in the pure liquid crystal: the magnitude of the discontinuity of the nematization S, the temperature shift between the transition temperature, the limit of meta-stability T^*, the phase-transition latent heat and the correlation length [19]. Elastic constants such as K can be calculated from microscopic information about the direct correlation function for the mesogens in a liquid crystal [20, 21], or by analysis of long-wavelength director fluctuations using molecular simulations [22, 23]. For the coupling between the conserved and non-conserved fields, we have chosen a term that is linear in C but is quadratic in S. This choice is similar to that used by Elder and coworkers for the study of binary mixtures [24] and results in a shift in the isotropic-nematic transition temperature, as can be recognized by defining a control parameter $\bar{r}(T, C) = a(T - T^*) + \frac{\alpha}{2} C$. Thus, the first effect of the coupling term is a shift in the isotropic-nematic transition temperature by an amount proportional to $\frac{\alpha}{2a} C$, when compared with that for the pure nematic with $C = 0$. From experimental information as well as molecular simulation modeling, we set $\alpha > 0$ and therefore obtain a reduction in the transition temperature when nanoparticles are present. A second effect of the coupling term $\alpha CS^2/2$, when α is positive, is that the absolute minimum of its contribution to the free energy is zero and can be achieved when non-zero values of C occur at places where $S = 0$. In other, words, segregation of nanoparticles to locally isotropic regions is favored thermodynamically by this term.

For the case where the LC order parameter is the alignment tensor $\mathbf{Q}$, the system's free energy functional is, analogously, taken as:

$$\mathcal{F}[\mathbf{Q}, C] = \int d\mathbf{x}' \left(\frac{K}{2} \left(\nabla' \mathbf{Q} \right)^2 + \frac{r}{2} \operatorname{tr}\mathbf{Q}^2 - w \operatorname{tr}\mathbf{Q}^3 + u \operatorname{tr}\mathbf{Q}^4 + \frac{\Omega}{2} C^2 + \frac{\alpha}{2} C \operatorname{tr}\mathbf{Q}^2 \right). \tag{5}$$

Again, the parameters in this expression are phenomenological and available from experiments [25, 26] and we consider $\alpha > 0$ for the coupling between the fields C and $\mathbf{Q}$, since the isotropic-nematic transition temperature is observed to decrease as the concentration of nanoparticles is increased. When considering molecular orientation of mesogens confined to a plane, hence $d = 2$, the tensor order parameter can be parameterized as

$$\mathbf{Q} = S(\mathbf{nn} - \mathbf{I}/2) \tag{6}$$

and the trace of odd powers of $\mathbf{Q}$ is identically zero. In such situations, substitution of the previous parametrization into (5) shows that the remaining terms $\frac{r}{2}\operatorname{tr}\mathbf{Q^2}$, $u\operatorname{tr}\mathbf{Q^4}$, and $\frac{\alpha}{2} C \operatorname{tr}\mathbf{Q^2}$ contribute to the free energy with $\frac{r}{4} S^2$, $\frac{u}{8} S^4$, $\frac{\alpha}{4} CS^2$, respectively. These differ from the corresponding terms in (4) only by a rescaling of the coefficients r, u, and α. Therefore, the coupling term also favors segregation of nanoparticles into locally isotropic regions.

In this work we present our results for the cases of systems described by the models in Equations (4) and (5) over bidimensional domains. To describe the dynamics after the isotropic-nematic phase transition, we assume in Model C that at time $t' = 0$ the system suffers a sudden quench bringing the temperature below the transition value. We also assume that isothermal conditions throughout the whole sample remain aftwerwards: this allows us to work solely with the dynamical equations of Model C for the conserved and non-conserved fields. For the case where S is the sole order parameter of the LC, these equations are

$$\begin{aligned} \frac{\partial S}{\partial t'} &= -\Gamma \frac{\delta \mathcal{F}}{\delta S}, \\ \frac{\partial C}{\partial t'} &= -\nabla' \cdot \left(-\Gamma_C \nabla' \frac{\delta \mathcal{F}}{\delta C} \right), \end{aligned} \tag{7}$$

where Γ and Γ_C are phenomenological mobilities that here we consider constant. Substitution of the free energy functional

defined in (4) into (7), followed by a change of variables to non-dimensional ones defined by

$$\begin{aligned} s &= \sqrt{\frac{u}{|r|}}S, \\ c &= \frac{\alpha}{|r|}C, \\ \mathbf{x} &= \sqrt{\frac{|r|}{K}}\mathbf{x}', \\ t &= \Gamma|r|t', \end{aligned} \tag{8}$$

yields the following dynamical equations:

$$\begin{aligned} \frac{\partial s}{\partial t} &= \nabla^2 s - (\mathrm{sgn}(r) + c)s - s^3, \\ \frac{\partial c}{\partial t} &= R\nabla^2\left(c + gs^2\right), \end{aligned} \tag{9}$$

where $\mathrm{sgn}(x)$ is the sign function, while R and g are non-dimensional parameters:

$$R = \frac{\Gamma_C \Omega}{\Gamma K}, \tag{10}$$

$$g = \frac{\alpha^2}{2u\Omega}. \tag{11}$$

We point out that, because our assumption of isothermal conditions, we can treat parameter $r = a(T - T^*)$ as constant and so our scaled dynamical equations become independent of r up to its sign; also, the actual nematization S is related to the non-dimensional variable s through a temperature-dependent transformation.

In summary, we notice that (9) contain a Newell-Whitehead equation for the non-conserved field and a diffusion equation for the conserved one that are mutually coupled. The coupling in the former equation amounts to a local shift (by c) in the control parameter $\mathrm{sgn}(r)$, while that in the latter amounts to an additional term driving NP diffusion away from high-nematization regions.

For the case where $\mathbf{Q}$ is the LC order parameter, it is necessary to project $\delta\mathcal{F}/\delta\mathbf{Q}$ onto the set of traceless symmetric tensors, which results in the following expressions:

$$\begin{aligned} \frac{\partial \mathbf{Q}}{\partial t'} &= -\Gamma\left(\frac{\delta\mathcal{F}}{\delta\mathbf{Q}} - \frac{1}{d}\mathrm{tr}\left[\frac{\delta\mathcal{F}}{\delta\mathbf{Q}}\right]\mathbf{I}\right), \\ \frac{\partial C}{\partial t'} &= -\nabla'\cdot\left(-\Gamma_C\nabla'\frac{\delta\mathcal{F}}{\delta C}\right). \end{aligned} \tag{12}$$

If one introduces a reduced alignment tensor as

$$\mathbf{q} = \sqrt{\frac{u}{|r|}}\mathbf{Q}, \tag{13}$$

the dynamical equations in this case reduce to

$$\begin{aligned} \frac{\partial q_{11}}{\partial t} &= \nabla^2 q_{11} - (\mathrm{sgn}(r) + c)q_{11} - q_{11}\left(q_{11}^2 + q_{12}^2\right), \\ \frac{\partial q_{12}}{\partial t} &= \nabla^2 q_{12} - (\mathrm{sgn}(r) + c)q_{12} - q_{12}\left(q_{11}^2 + q_{12}^2\right), \\ \frac{\partial c}{\partial t} &= R\nabla^2\left(c + g\left(q_{11}^2 + q_{12}^2\right)\right), \end{aligned} \tag{14}$$

where the unprimed Laplacian operator denotes differentiation with respect to the non-dimensional spatial coordinates $\mathbf{x}$. Again, (14) correspond to two coupled Newell-Whitehead equations, for the components of the $\mathbf{q}$ tensor and one diffusion equation for the NP concentration: the concentration shifts the coefficients of the linear terms for the non-conserved variables, while their mutual coupling is nonlinear, and the coupling of the non-conserved variables to the conserved field drives diffusion of NPs away from the nematically ordered regions.

While the scalar order parameter model expressed by (9) does not allow us to consider anchoring of the liquid crystal orientation with respect to the NP aggregate interfaces (that is, the requirement that the nematic director $\mathbf{n}$ orients in a particular direction with respect to an interface normal [9]), the tensorial model given by (14) can be augmented to account for anchoring by including a new term to the free energy density in (5) [27, 28]:

$$f_{\mathrm{anch}} = \Lambda\left(\frac{\partial C}{\partial x_i'}\right)\left(\frac{\partial Q_{ij}}{\partial x_j'}\right), \tag{15}$$

where Λ is an anchoring parameter. By coupling the gradients of the concentration C and gradients of the elements of the $\mathbf{Q}$ tensor, for $\Lambda > 0$ lower free energy configurations are obtained when the director is parallel to concentration gradients, hence hometropic at the interface of NP aggregates; if $\Lambda < 0$, then the preferred orientation of the director becomes perpendicular to concentration gradients and the anchoring becomes planar [28]. The corresponding dynamical equations obtained from Model C are:

$$\begin{aligned} \frac{\partial q_{11}}{\partial t} &= \nabla^2 q_{11} - (\mathrm{sgn}(r) + c)q_{11} - q_{11}\left(q_{11}^2 + q_{12}^2\right) \\ &\quad + \frac{\lambda}{2}\left(\frac{\partial^2 c}{\partial x_1^2} - \frac{\partial^2 c}{\partial x_2^2}\right), \\ \frac{\partial q_{12}}{\partial t} &= \nabla^2 q_{12} - (\mathrm{sgn}(r) + c)q_{12} - q_{12}\left(q_{11}^2 + q_{12}^2\right) + \lambda\frac{\partial^2 c}{\partial x_1 \partial x_2}, \\ \frac{\partial c}{\partial t} &= R\nabla^2\left(c + g\left(q_{11}^2 + q_{12}^2\right) - \lambda\left(\left(\frac{\partial^2 q_{11}}{\partial x_1^2} - \frac{\partial^2 q_{11}}{\partial x_2^2}\right)\right.\right. \\ &\quad \left.\left. + 2\frac{\partial^2 q_{12}}{\partial x_1 \partial x_2}\right)\right), \end{aligned} \tag{16}$$

where $\lambda = \frac{\alpha\Lambda}{\Omega u|r|^{1/2}}$.

For the tensorial model, the nematization s and the orientation θ of the director $\mathbf{n} = (\cos\theta, \sin\theta)$ can be obtained from $\mathbf{q}$ using the parametrization

$$\mathbf{q} = s(\mathbf{nn} - \mathbf{I}/2) = \frac{s}{2}\begin{pmatrix} \cos(2\theta) & \sin(2\theta) \\ \sin(2\theta) & -\cos(2\theta) \end{pmatrix}. \tag{17}$$

Comparison between the parametrization of $\mathbf{Q}$ given in (6) and (17), together with the scaling in (13) shows that $s = \sqrt{u/|r|}S$, just as for the scalar model. From the dynamical Equations (9), or (14), (16) and (17), one can show that homogeneous and stationary states can be achieved if the initial NP concentration is uniform $c(\mathbf{x}, 0) = c_0$ and the order parameter is either zero

$s(\mathbf{x},0) = 0$ or given by $s(\mathbf{x},0) = \sqrt{1-c_0}$ if $r < 0$. This work is concerned with the former case since, experimentally, nanoparticles are initially suspended homogeneously in the isotropic phase of 5CB [12].

We solved numerically the dynamical equations, for the models with scalar and tensor LC order parameters (with and without anchoring in the latter case), with a finite difference method over a square grid of $N = 128$ equidistant points in each direction, with periodic boundary conditions. The spacing $\Delta x_i = 1$ and the time step $\Delta t = 0.01$ were chosen together so that the forward Euler method would be stable [1]. In order to imitate the experimental conditions described by [12], we used as initial condition an isotropic state $s(\mathbf{x},0) = 0$ with uniform nanoparticle concentration $c(\mathbf{x},0) = 0.01$. We then added random perturbations to the dynamical variables drawn from a uniform distribution on the interval $[-10^{-3}, 10^{-3}]$. We ran 20 realizations of the dynamics for these randomized initial conditions for each simulated system.

Besides direct visualization of the evolution of the conserved and non-conserved fields, we analyzed the dynamics of the

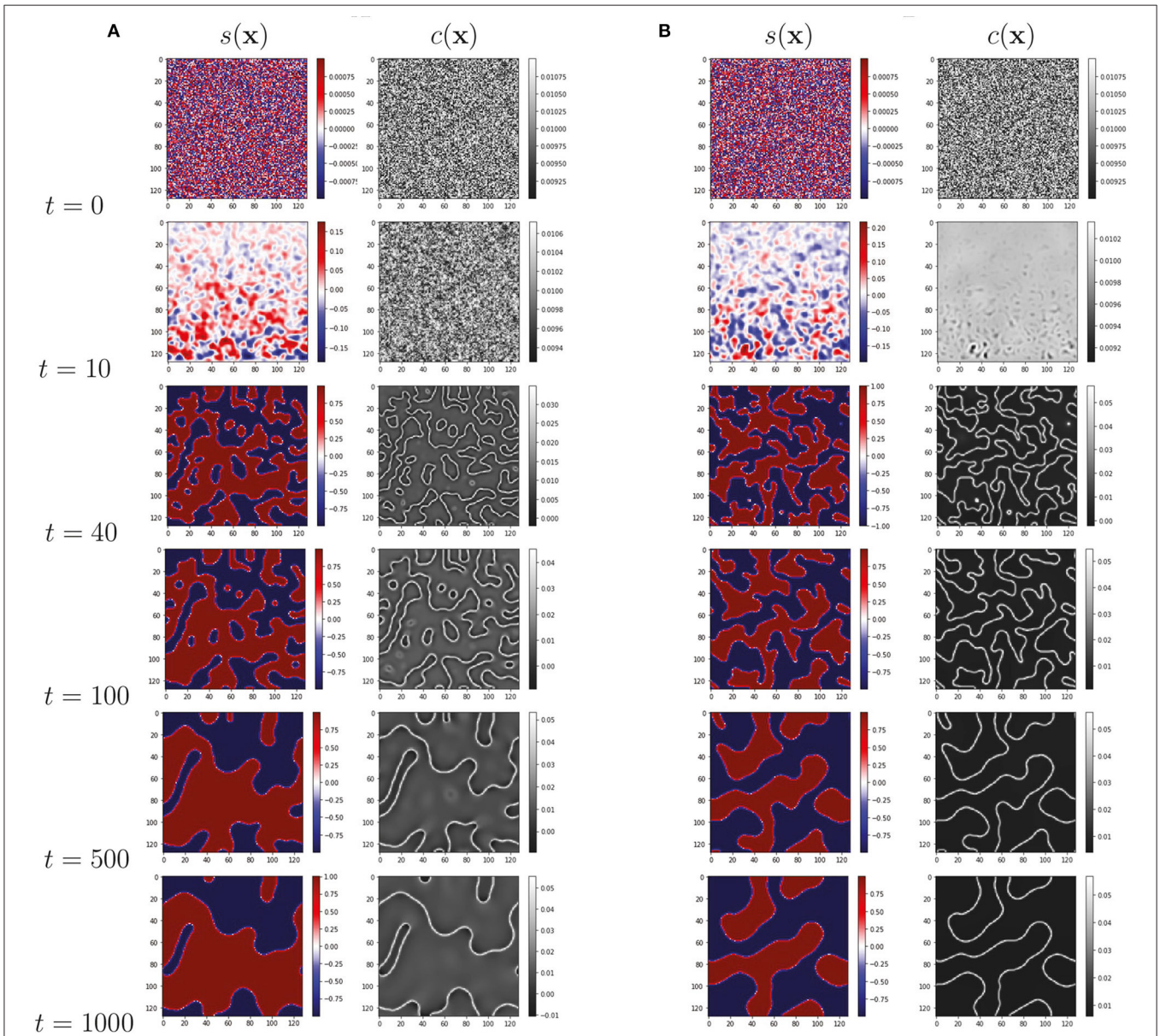

FIGURE 1 | Time evolution of nematization $s(\mathbf{x})$ and NP concentration $c(\mathbf{x})$, from the scalar model (9): **(A)** for NP mobility $R = 0.1$ and **(B)** $R = 10$. NP material segregates to the domain walls where the nematization is diminished with respect to the interior of the nematic domains. This segregation is more pronounced for the more mobile case **(B)**. Parameters $g = 0.005$, $r = -1$, $c_0 = 0.01$ were fixed through both runs. In an homogeneous and steady nematic state $s = \sqrt{1-c_0} = \pm 0.995$ but, once the NPs segregate, we expect that at long times $s = \pm 1$ deep inside the nematic regions.

system in Fourier space by calculating the power spectra

$$P_s(\mathbf{k},t) = s(\mathbf{k},t)s^*(\mathbf{k},t),$$
$$P_c(\mathbf{k},t) = c(\mathbf{k},t)c^*(\mathbf{k},t), \tag{18}$$

where $f(\mathbf{k},t)$ denotes the Fourier transform with respect to space of $f(\mathbf{x},t)$ and f^* is the complex conjugate of f. We also computed the correlation functions

$$C_s(\mathbf{x},t) = \langle s(\mathbf{x}-\mathbf{y},t)s^*(\mathbf{y},t)\rangle_{\mathbf{y}} - \langle s(\mathbf{y},t)\rangle^2_{\mathbf{y}},$$
$$C_c(\mathbf{x},t) = \langle c(\mathbf{x}-\mathbf{y},t)c^*(\mathbf{y},t)\rangle_{\mathbf{y}} - \langle c(\mathbf{y},t)\rangle^2_{\mathbf{y}}, \tag{19}$$

where the angular brackets denote here an average over the whole domain for the spatial coordinates $\mathbf{y}$ followed by a further average

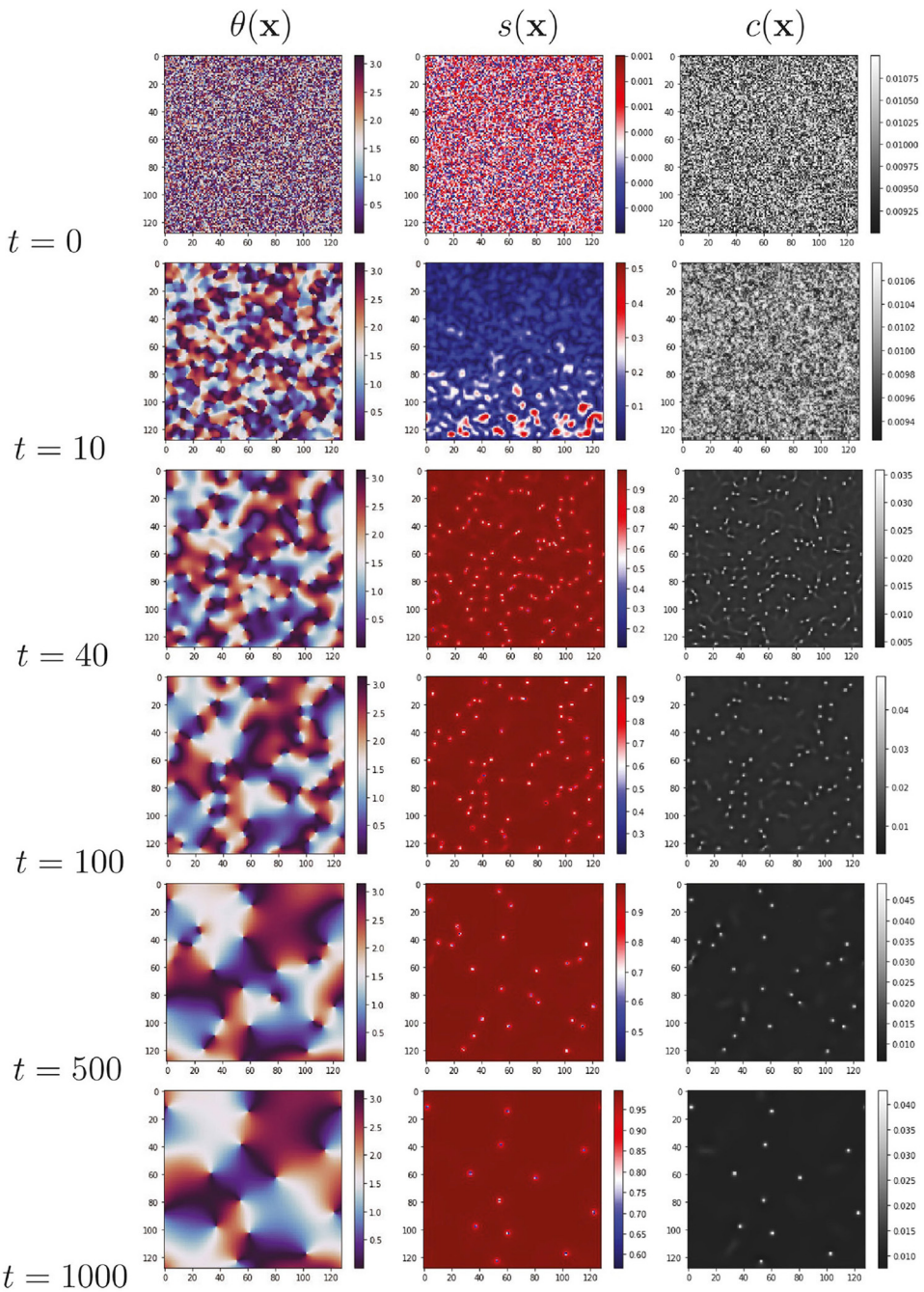

FIGURE 2 | Time evolution of director orientation $\theta(\mathbf{x})$, nematization $s(\mathbf{x})$ and NP concentration $c(\mathbf{x})$ from the tensor dynamical Equations (14), for NP mobility parameter $R = 0.1$. As for the scalar dynamical equations, NP material aggregates at the low nematization regions, which correspond here to point disclinations. As the disclinations annihilate, NP material is released back into the nematic domains where it diffuses away. Parameters $g = 0.005$, $r = -1$, $c_0 = 0.01$ were fixed through the run, so that the equilibrium values of $s = \sqrt{1-c_0} = \pm 0.995$ in the nematic phase.

over multiple independent realizations. In this respect, the power spectra and correlation functions were averaged over the 20 independent realizations corresponding to the same number of randomized initial conditions for a given system.

We computed the correlations length ξ_a, for $a = s, c$, from the correlation functions as

$$\xi_a = \left(\frac{\partial \log C_a}{\partial x}\bigg|_{x=0} \right)^{-1}, \tag{20}$$

obtained by quadratic fitting of the logarithm of the correlation functions C_s and C_c with respect to the radial coordinate $x = |\mathbf{x}|$. Complementary to this method, we also measured a correlation length $L_a = 2\pi/k_a$ from the wave number k_a at which the power spectra $P_a(k, t)$ reaches half of its maximum (which corresponds to the size of the circular patterns shown in **Figure 3**). While both estimates yield proportional values, we found that the second one tracks the increase in the correlation length more robustly. Hence, only the time evolution of the correlation lengths L_s and L_c is presented in the results.

3. RESULTS

Our first results for the time evolution of the nanoparticle-mesogen mixture are shown in **Figure 1** for the model with scalar order parameter. Our numerical simulations show that the nanoparticle concentration grows in time precisely at those regions where the order parameter is close to zero. These regions are domain walls between areas with nematization s of opposite signs. As the domains grow and the domain walls shrink and disappear, the NP concentration "stored" in the domain walls is released back into the domains interior, diffusing back to other nearby walls.

Figure 1A displays the time evolution when the relative mobility parameter $R = 0.1$ corresponds to slow NP diffusion compared to LC relaxation, one can observe that c is higher at the domain walls but still noticeable at the domain interiors. On the other hand, **Figure 1B** shows the time evolution for $R = 10$, corresponding to fast NP diffusion compared to LC relaxation. In this latter case, c is much smaller at the domains' interior and most of the NP material gets confined to the domain walls.

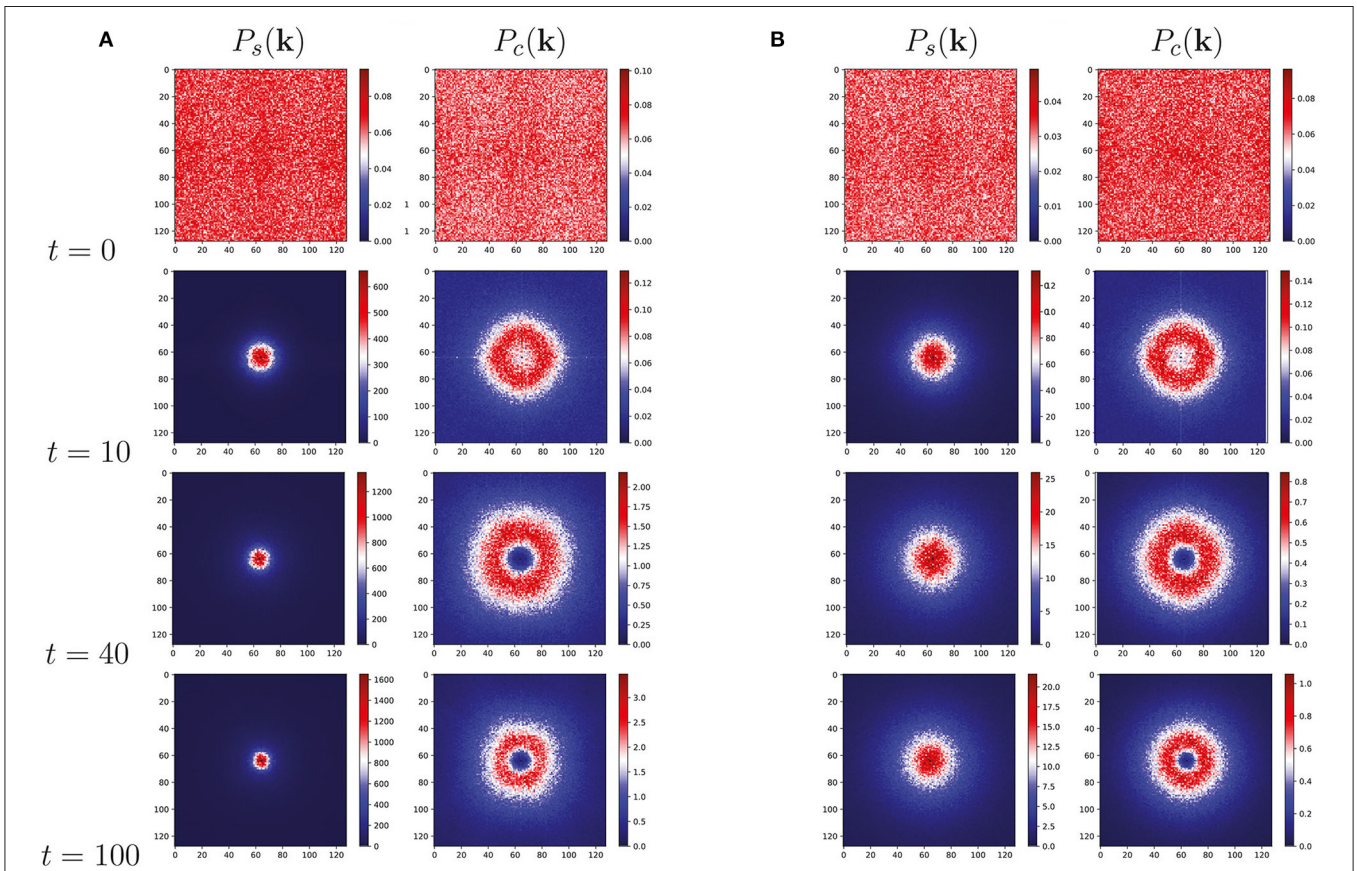

FIGURE 3 | Time evolution of the power spectra of the nematization $P_s(\mathbf{k})$ and the concentration $P_c(\mathbf{k})$ from **(A)** the scalar Equations (9) and **(B)** the tensor Equations (14). As the time increases, the power is concentrated at ever smaller wave numbers $k = |\mathbf{k}|$, indicating that the characteristic length in the system increases with time. Also, the conserved-field power spectra $P_c(\mathbf{k})$ show clear maxima at intermediate wavenumbers, with noticeable smaller values at the origin. Parameters $R = 0.1, g = 0.005, r = -1, c_0 = 0.01$ were fixed through the runs.

Our results for the model with tensor order parameter and no anchoring ($\lambda = 0$) are shown in **Figure 2** and **Supplementary Figure 1**. Again, the numerical simulations show that the NP concentration segregates toward topological defects where the tensor order parameter **q** is close to zero. Now, however, these topological defects are points where the director orientation θ changes abruptly. In this case, the NP "stored" at the defects are released back into the nematic phase when the point disclinations of opposite charge annihilate. The same qualitative behavior was obtained from numerical simulations with negative and positive values of the anchoring coefficient ($\lambda = -0.4, -0.1$, 0.1, and 0.4), corresponding to weak planar and homeotropic anchoring, respectively [28] (see **Supplementary Figure 2**). In this model the nanoparticle aggregates remain on the order of a few order parameter coherence lengths, and thus we observed no formation of NP aggregates large enough to trigger repulsion among them due to anchoring. However, non-zero values of λ do alter the shape of the NP aggregates: those with $-1/2$ topological charge acquire a clearly triangular shape, while those with +1/2 charge become slightly elongated (see **Supplementary Figure 2**).

In order to quantify the characteristic length scales associated with the NP self-assembly at the topological defects in the nematic, we analyzed the power spectra for the conserved and non-conserved fields in our models, $P_s(\mathbf{k}, t)$ and $P_c(\mathbf{k}, t)$. Typical behavior of these power spectra is shown in **Figure 3**, for the cases with scalar and tensor order parameter with $\lambda = 0$ (no anchoring), keeping the same values of R and g in both of them. For both models and for both s and c, we observe that, overall, the power becomes concentrated at ever smaller values of the wave number $k = |\mathbf{k}|$ as time increases. This corresponds, as expected from **Figures 1**, **2**, to an increase in the characteristic length scales for the order parameter and NP concentration fields. Nevertheless, from **Figure 3** we can observe that such length scale increase is faster for s than for c when the LC order parameter is taken as scalar, but slows down noticeably for s when the LC order parameter is taken as a tensor (see **Figure 3B**). The

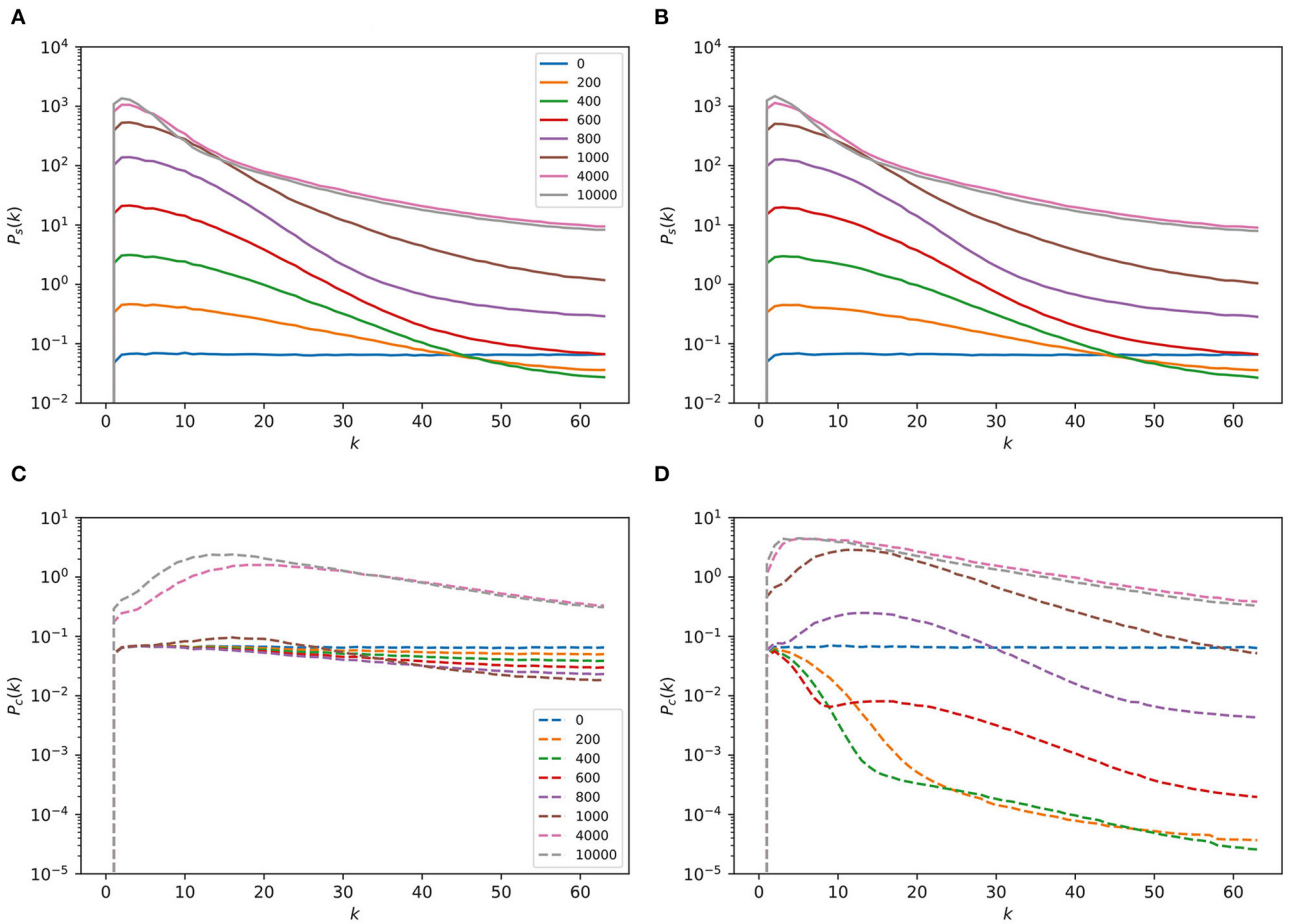

FIGURE 4 | Time evolution of the angular average of the power spectra of the nematization $P_s(k)$ and the concentration $P_c(k)$, as functions of the wave number k, from the scalar Equations (9) for conditions of low and high NP mobility R: **(A)** $P_s(k, t)$ for $R = 0.1$, **(B)** $P_s(k, t)$ for $R = 10$, **(C)** $P_c(k, t)$ for $R = 0.1$, **(D)** $P_c(k, t)$ for $R = 10$. Each curve corresponds to the time indicated in the inset legends. While the nematization power spectrum increases quickly and steadily, the concentration power spectrum $P_c(k)$ for low NP mobility goes through a quiescent stage before undergoing sudden increase, and even initially decreases at high wave numbers for high NP mobility. Parameters $g = 0.005$, $r = -1$, $c_0 = 0.01$ were fixed through the runs.

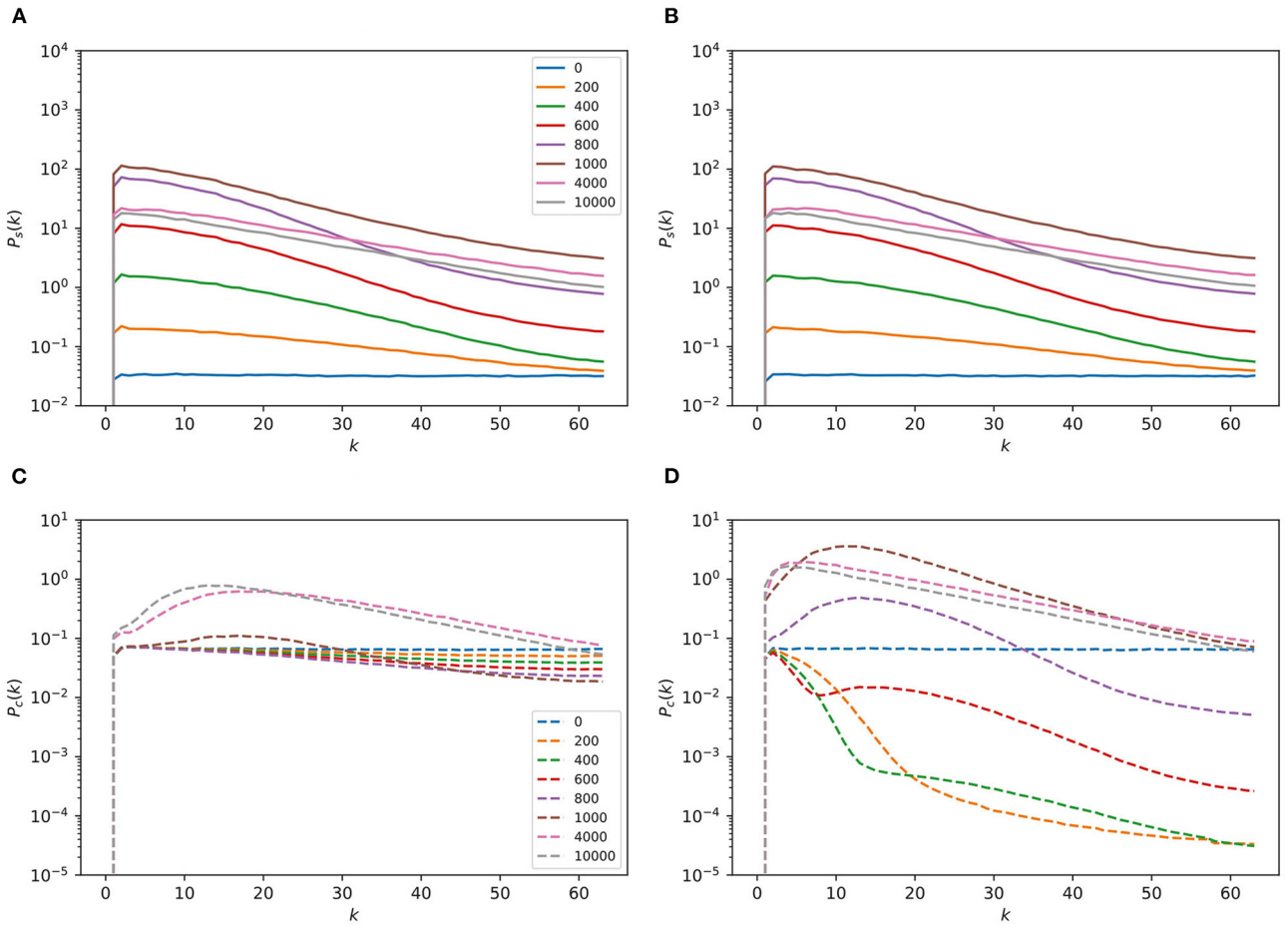

FIGURE 5 | Time evolution of the angular average of the power spectra of the nematization $P_s(k)$ and the concentration $P_c(k)$, as functions of the wave number k, from the tensor Equations (14) for conditions of low and high NP mobility R: **(A)** $P_s(k,t)$ for $R = 0.1$, **(B)** $P_s(k,t)$ for $R = 10$, **(C)** $P_c(k,t)$ for $R = 0.1$, **(D)** $P_c(k,t)$ for $R = 10$. Each curve corresponds to the time indicated in the inset legends. Now, the nematization power spectrum increases quickly but non-monotonically with time. Nevertheless, the concentration power spectrum $P_c(k)$ for low NP mobility still goes through a quiescent stage before undergoing sudden increase, and (initially) decreases at high wave numbers for high NP mobility. Parameters $g = 0.005$, $r = -1$, $c_0 = 0.01$ were fixed through the runs.

numerical solutions with $\lambda \neq 0$ display the same type of behavior and are not shown. Therefore, from this point we focus on the solutions for $\lambda = 0$, although we discuss quantitatively the effect of anchoring on the dynamics later in this section.

To study further the different behaviors observed in the Fourier space, we computed the angular average of the power spectra and plotted the resulting functions $P_s(k,t)$ and $P_c(k,t)$ against the wave number k at different times. For the model with scalar order parameter under conditions of low NP mobility ($R = 0.1$), we show the power spectra for s in **Figure 4A** and that of c in **Figure 4C**. **Figures 4B,D** show the corresponding power spectra, respectively, for conditions of high NP mobility ($R = 10$). For both values of R, the power spectrum $P_s(k,t)$ for the nematization increases very quickly at low values of k, until this increment slows down and saturates (see **Figures 4A,B**). On the other hand, the power spectrum $P_c(k,t)$ for the NP concentration is initially quiescent when the mobility R is small; only after some lag it increases with time and acquires a maximum at intermediate values of k (see **Figure 4C**): this corresponds to the bright rings visible in **Figure 3**. When the mobility R is high, however, the quiescent period is replaced with a process where the power spectrum decreases sharply at high wave numbers, and only later increases and develops a maximum at intermediate values of k (see **Figure 4D**).

The corresponding situation for the model with tensor order parameter is shown in **Figure 5**. Again, for conditions of low NP mobility ($R = 0.1$), we show the power spectra for s in **Figure 5A** and that of c in **Figure 5C**. On the other hand, **Figures 5B,D** show the corresponding power spectra of s and c, respectively, for conditions of high NP mobility ($R = 10$). The power spectrum $P_s(k,t)$ for the nematization still increases rapidly at low values of k, but now the total increment is much reduced when compared with the result from the scalar equations. Eventually, growth is followed by a decrease with increasing time (see **Figures 5A,C**). On the other hand, the behavior of the power spectrum $P_c(k,t)$

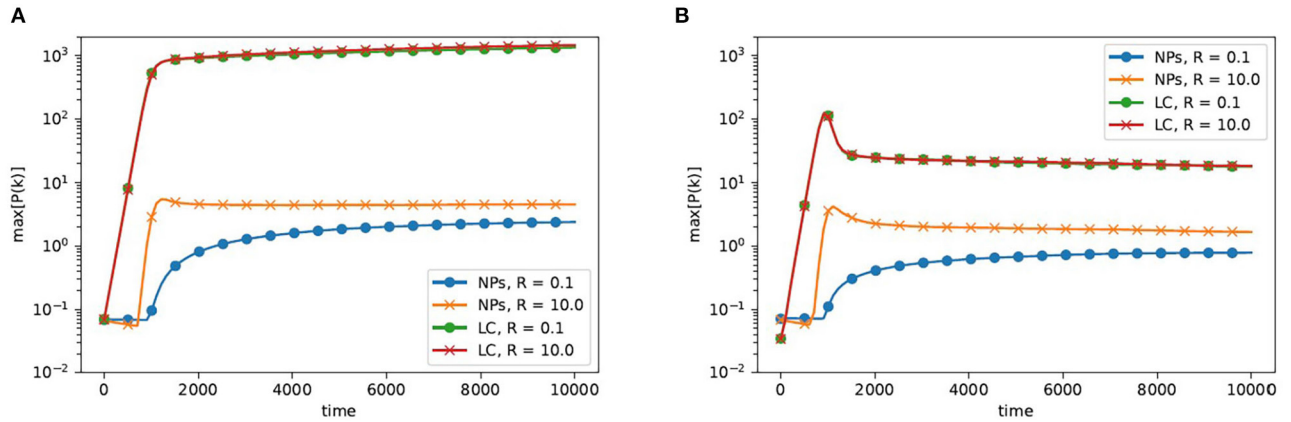

FIGURE 6 | The maxima of the power spectra of the nematization and the concentration, as functions of time, for systems with anchoring parameter $\lambda = 0$ and with low and high NP mobility, from **(A)** the scalar dynamical Equations (9) and from **(B)** the tensor Equations (14). In both **(A,B)** circles correspond to low NP mobility $R = 0.1$ while crosses correspond to fast NP mobility $R = 10$. Initially, the nematization maxima grow exponentially and then saturate, but they show an overshoot with respect to the saturation value in the tensor case **(B)**. On the other hand, the exponential growth of the concentration maxima lags behind the growth of the nematization maxima, but it is also followed by saturation. The lag period is shorter for the case of high NP mobility. Parameters $g = 0.005$, $r = -1$, $c_0 = 0.01$ were fixed through the runs.

for the NP concentration remains qualitatively similar to that in the first model (see **Figures 4B,D**).

An alternative view of the time evolution of the power spectra was obtained by plotting the maximum values of P_s and P_c, as functions of time in a semi-logarithmic scale, as shown in **Figure 6**. First, for the model coupling the NP concentration only to nematization (see **Figure 6A**), we observe a regime where the maximum of the nematization power spectrum grows exponentially with time, followed by saturation. We observe practically the same behavior for low and high values of the NP mobility parameter, $R = 0.1$ and 10 (respectively). Also for the case of scalar order parameter, we observe a lag interval where the maximum of P_c decreases by a small amount before growing rapidly toward some saturation value. Second, for the model coupling c and the tensor order parameter, we again observe exponential growth of the maximum of P_s, regardless of the value of R. Only, in this case, the exponential-growth regime does not reach values as high as in the first model, and it is followed by an overshoot before a decrease to a saturation value. For the second model, the maximum of P_c still shows the lag interval and decrease followed by growth to a saturation value. Here, the high mobility value $R = 10$ leads to a clear overshoot in the maximum of P_c, while the low mobility value does not.

At this point, we present again results for the cases with positive and negative anchoring parameter λ. **Figure 7** compares the time evolution of the maxima of the power spectra for nematization and concentration for conditions of homeotropic anchoring ($\lambda > 0$), planar anchoring ($\lambda < 0$), and absence of anchoring ($\lambda = 0$). We found that for the range of λ considered, corresponding to weak anchoring [28], the dynamics of the LC order parameter and the NP concentration display a minor dependence with the value of the anchoring parameter λ. We interpret this as a consequence that, since the initial concentration of NP was taken as very small, the local concentration remains small even at the NP aggregates, as well as the gradient of c. Thus, the influence of the anchoring that couples the gradients of concentration to those of the order parameter tensor is limited. With this in mind, we focus on the representative case with $\lambda = 0$ in the rest of the results section.

We interpret the initial regimes of exponential growth in the power spectrum of the nematization as the interval where the dynamics can be described by the linear part of the dynamical equations, and the saturation regime as the set-in of the nonlinear saturation state where the nonlinear terms in the dynamics prevent exponential divergence of the nematization field. Also, we interpret the lag in the growth of the concentration power spectrum as arising from the conserved-field dynamics: since the dynamics of c is diffusive, at the linear stability analysis level we do not expect it to give rise to unstable modes at any wave number, only the non-conserved field may produce unstable modes and so in the initial regime (controlled by the linear dynamics) the only exponentially-rising power spectrum is the one for s.

The information contained in the power spectra can be translated back into direct space in the form of the auto-correlation functions for s and c. **Figure 8** shows the time evolution of these correlation functions obtained from the scalar dynamical equations, for $R = 0.1$ and $R = 10$ (the tensor case correlation functions are qualitatively similar and shown in the **Supplementary Figure 3**). These functions decay over a short range, and such correlation range increases with time (as expected). Still, the auto correlation of the NP concentration remains flat over the initial lag period before growing quickly.

Figure 9 shows the time dependence of the correlation lengths. For both the scalar and tensor order parameter models, the nematization correlation length is typically larger than the concentration correlation length. While the nematization correlation length in the scalar order parameter model grows

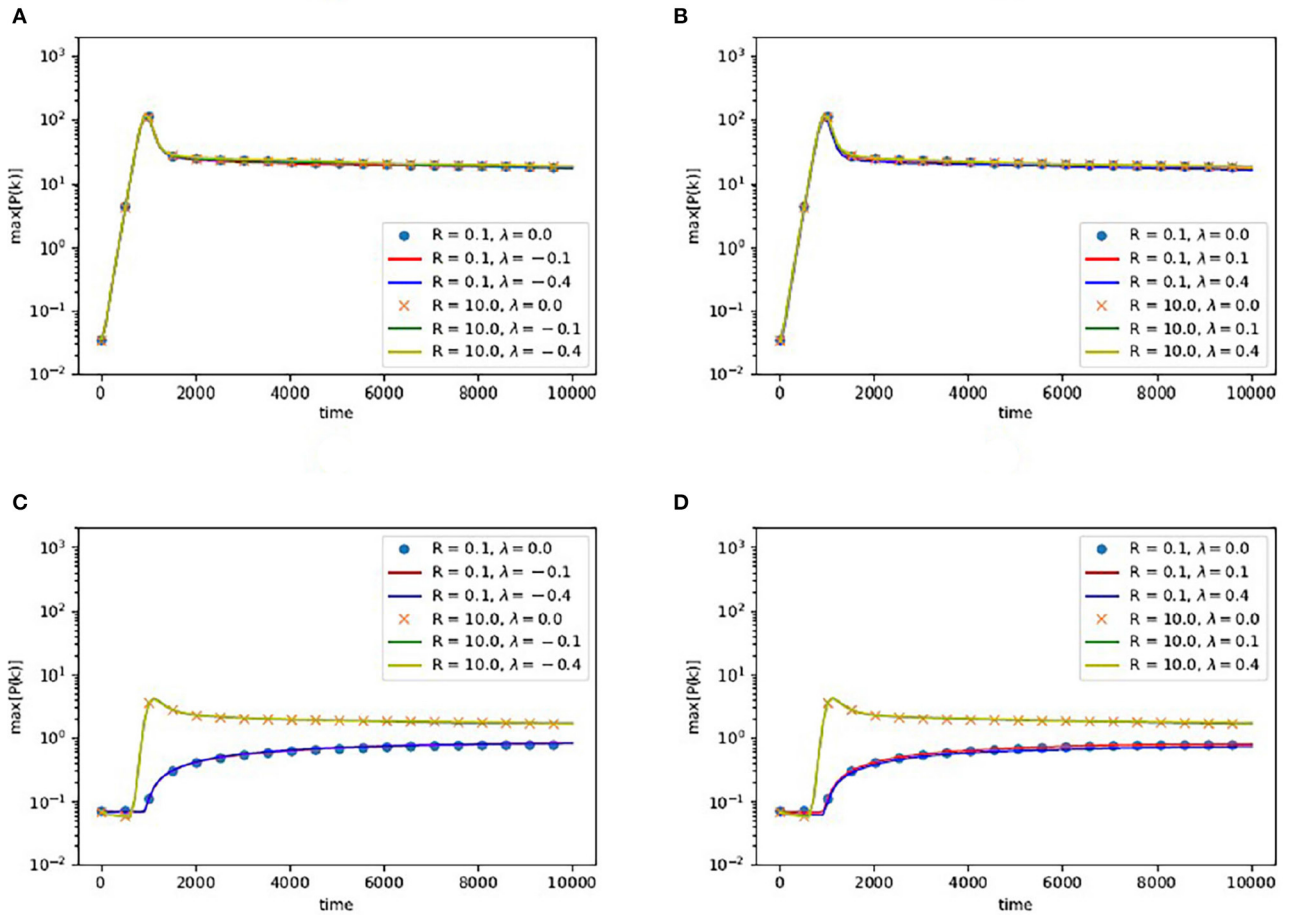

FIGURE 7 | The time evolution of the maxima of power spectra, from the tensor equations incorporating anchoring (14) with NP mobility R=0.1 and $R = 10$, of: **(A)** the nematization when $-0.4 \leq \lambda \leq 0$ (planar anchoring), **(B)** the nematization when $0 \leq \lambda \leq 0.4$ (homeotropic anchoring), **(C)** the NP concentration when $-0.4 \leq \lambda \leq 0$ (planar anchoring), and **(D)** the NP concentration when $0 \leq \lambda \leq 0.4$ (homeotropic anchoring). To facilitate comparisons, circles and crosses indicate data for $\lambda = 0$. For the weak anchoring conditions and low initial NP concentration $c_0 = 0.01$ considered here, the dynamics of the nematization shows only a small dependence with the value of the anchoring parameter. Parameters $g = 0.005$ and $r = -1$ were fixed through the runs.

monotonically with increasing time, in all other cases the correlation lengths show a peak over a time interval that matches the initial linear regime, followed by systematic increase afterwards. The lack of a peak in $L_s(t)$ seems to us to be related to the absence of overshoot in the power spectrum $P_s(k, t)$ for the scalar order parameter model when $R = 0.1$, since the corresponding curve for $R = 10$ (not shown) does show a peak while its corresponding power spectrum does present an overshoot.

4. DISCUSSION

Our results indicate that, for situations where the nanoparticle concentration is so low that approximation of their free energy up to the level of the second virial coefficient is adequate, the ordering of the nematic phase at temperatures below its phase transition proceeds exponentially with time, with little response of the NP material. Such exponential dependence is characteristic of the linear regime where the order parameter is small. Only after a lag the NPs couple effectively to the ordering in the liquid crystal, segregating to the regions where the nematic order parameter is close to zero. These initial stages are followed by the onset of nonlinear dynamics that leads to nonlinear saturation of the order parameter. Whether the LC order parameter is taken as a scalar or tensor does not change this sequence, but affects the kind of topological defects that capture the NP material (domain walls for the scalar case, point disclinations for the tensor one) as well as a clear overshoot of the exponential dynamics with respect to the nonlinear saturation level for the tensor case. We found insensitivity of the solution to the tensorial dynamical equations to the anchoring parameter λ for conditions of weak homotropic or planar anchoring. Since this parameter couples the gradient of the tensor order parameter with gradients in concentration, we interpret this insensitivity as arising from the low value of the conserved initial density: even

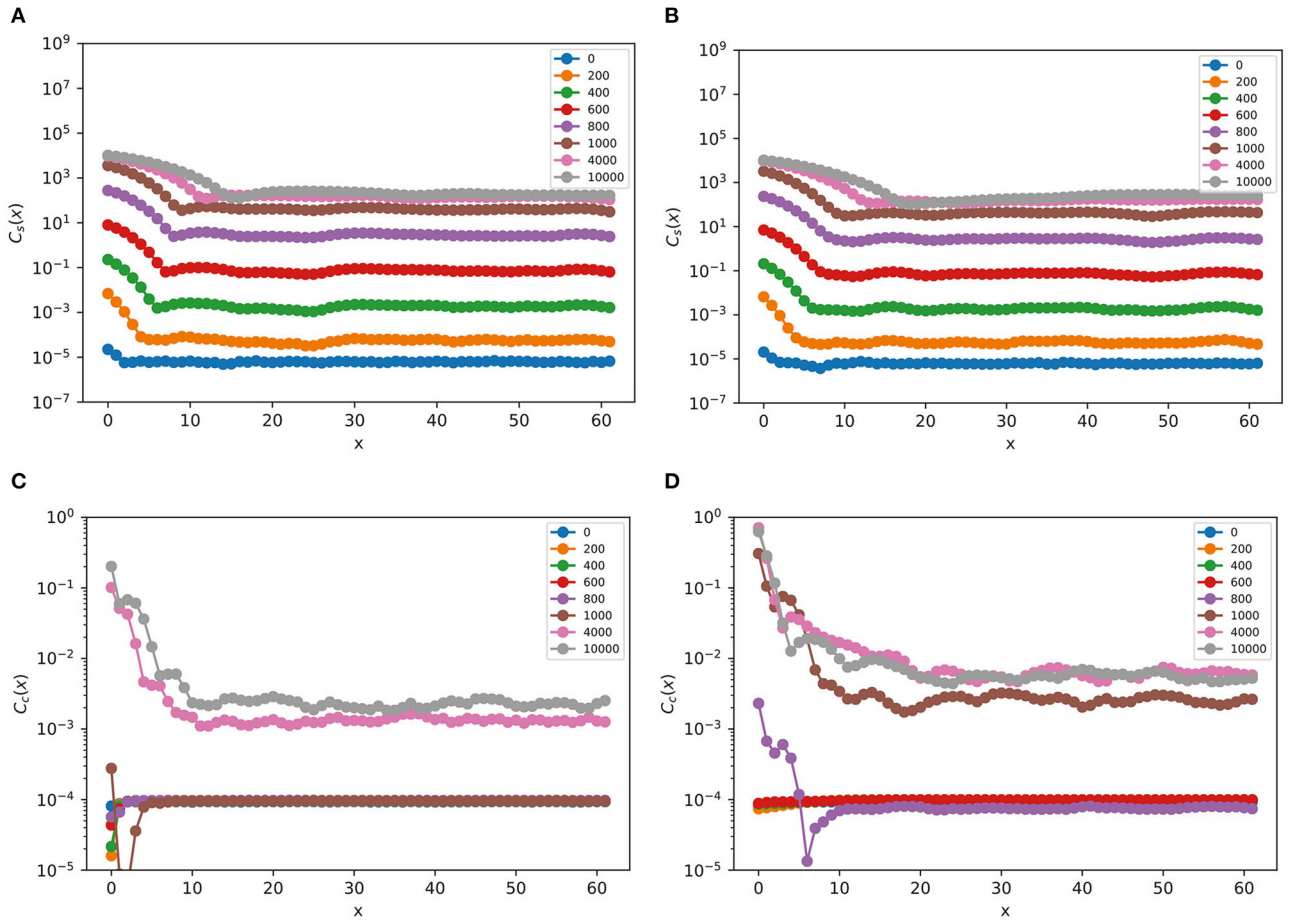

FIGURE 8 | Time evolution of the correlation functions for the nematization and NP concentration from the scalar dynamical Equations (9), as functions of distance x, for low and high NP mobility conditions: **(A)** $C_s(x)$ for $R = 0.1$, **(B)** $C_s(x)$ for $R = 10$, **(C)** $C_c(x)$ for $R = 0.1$, and **(D)** $C_c(x)$ for $R = 10$. The color legends indicate the time t for each correlation function. Initially, the correlation for the nematization increases exponentially with increasing time, while that for the NP concentration remains small. Only after a lag period it rises abruptly. Parameters $g = 0.005$, $r = -1$, $c_0 = 0.01$ were fixed through the runs.

at those regions where NP aggregate the local concentration and gradients remain small and so limit the influence of anchoring on the dynamics.

Compared with the model used by [12], our approach fully couples the dynamical equations for the LC order parameter with the NP concentration. Still, we find that for values of the coupling parameter g and initial NP concentration c_0 as small as considered here (similar to those in experiments), the evolution of the LC component remains largely unaffected even when varying the relative mobility parameter R by two orders of magnitude. Numerical exploration of the dynamics at higher NP higher concentrations is certainly possible and useful for further investigation of the effects of anchoring, but this would require improving the NP free energy expression beyond the second virial coefficient level, as discussed below. For situations where the NP aggregates become sufficiently large and concentrated, they should start to behave as colloidal inclusions in the nematic phase, triggering processes where weak anchoring, as well as orientational elasticity, drive further interaction and structure formation at the colloidal length scale [29–31]. Another issue that should be addressed when considering higher NP concentration is the emergence of additional interactions driven by depletion interactions, as recently revealed by computer simulations [32]. It is also possible to explore the behavior for larger values of the coupling parameter g; preliminary results from molecular simulations indicate that the coupling parameter increases rapidly with pressure.

It is important to mention that the quadratic coupling term used in this work leads to different behavior from the linear one assumed by [12]: a linear coupling would result in preferential segregation of the NP field to regions where s is negative, instead of regions that are locally isotropic. Also, our choice for the free energy of the NPs leads to simple diffusive behavior, instead of the nonlinear dynamics of the Cahn-Hilliard equation,

$$\frac{\partial z}{\partial t} = \nabla^2 \left(z^3 - z - \nabla^2 z \right), \tag{21}$$

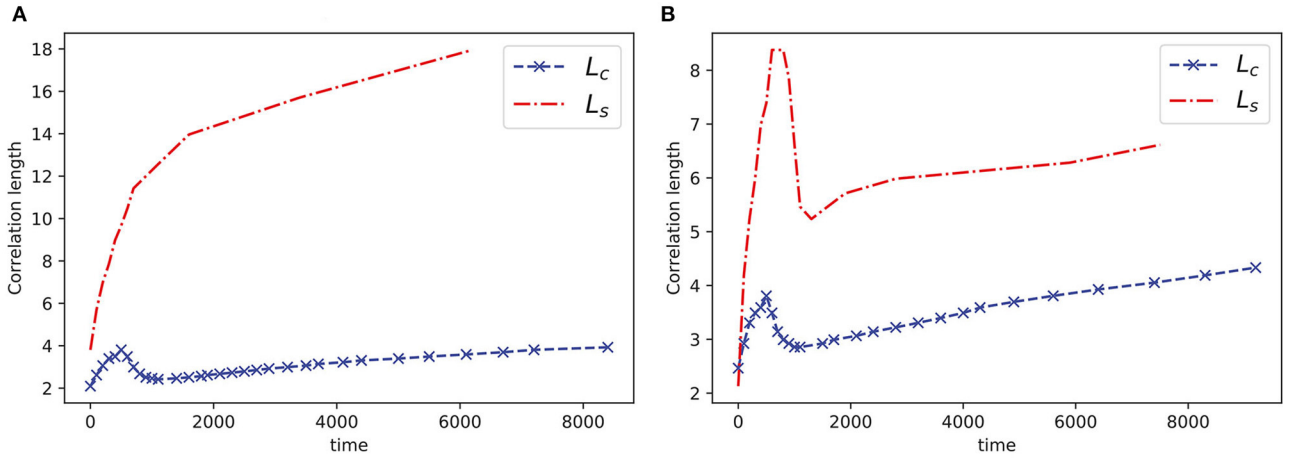

FIGURE 9 | Correlation lengths L_s (top row) and L_c (bottom row) as functions of time for **(A)** the scalar order parameter model and **(B)** the tensor order parameter model. The nematization correlation length is generally larger than the NP concentration correlation length. The peaks in these curves span the initial linear regime. The curve for the nematization correlation length from the scalar dynamical equations does not display a peak. Parameters $R = 0.1$, $g = 0.005$, $r = -1$, $c_0 = 0.01$ were fixed through the runs.

where $z = c - c_c$ is the deviation of the NP concentration from its critical density c_c. In this work, we assume that parameter Ω is positive and, therefore, that the NPs interact repulsively. In the absence of attractive interactions, no critical point is expected and so we used the Model C dynamics as stated. A Cahn-Hilliard treatment would allow us to generalize our model to include the effect of attractive interactions, but another possible route is to replace the expression for the NP free energy with known expressions for a Lennard-Jones [33] or a Square-Well fluid [34] and then use Model C to obtain the nonlinear dynamical equations. We are currently exploring this second avenue.

As mentioned earlier, our non-dimensionalization procedure for the dynamical equations assumes that parameter $r = a(T - T^*)$ is constant, and our numerical simulations correspond to evolution after a temperature quench below the isotropic-nematic transition. In order to simulate finite cooling rates, it would be sufficient to reframe the equations to incorporate a time dependence in parameter r. This would be useful to test directly the hypothesis of Riahinasab et al. that cooling rate and local shifts in the transition temperature due to higher concentration of nanoparticles dictate the morphology of NP assemblies during segregation from the nematic phase, and we plan to perform and report such calculations presently.

The modeling approach followed in this work can be extended to three-dimensional cases, where the tensor order parameter contains five degrees of freedom, but the numerical work becomes more demanding. In particular, our finite difference approach would probably need to be replaced with a more efficient scheme, such as finite element or Galerkin methods. Inclusion of stochastic noise terms into the dynamical equations is also a possibility, although it has been shown by Bray that it is an irrelevant perturbation in a Renormalization Group sense [6, 35]: transitions between the minima in the free energy are possible in the presence of thermal fluctuations (but are seldom observed in simulations over small domains) and the roughness of the interfacial structure is larger as the noise strength increases [35]. Another direction where our modeling approach can be applied is the study of active matter [35], in particular the case of active Langmuir monolayers [36] where a local concentration c of chiral molecules is coupled to a local orientation field $\mathbf{n}$. By extending the description of the orientation to that of a tensor order parameter, defect dynamics beyond the director description could be captured. Finally, we point out opportunities for examining other nonlinear dynamical systems where one or more Newell-Whitehead equations become coupled to a conserved variable. As an instance, even if a quadratic term is absent in the dynamical equations for liquid crystals in two dimensions due to the traceless condition of its tensor order parameter, other systems may admit such a term. The spatially-dependent Nagumo equation contains such nonlinear dependence [3]:

$$\frac{\partial M}{\partial t} = D\nabla^2 M + C_1 M(C_2 - M)(M - C_3), \tag{22}$$

where M represents the local population of a species undergoing motion and birth, death and mutual cooperation or competition, while D, C_1, C_2, C_3 are parameters that account for such processes. In some epidemiological studies [37], a population of a short-lived species (for instance, mosquitoes) interacts with another species (such as large mammals or birds) with a very long lifespan compared to that of the first one. In such cases, as a consequence of a large separation of time scales, it may be interesting to consider the long-lived population as approximately conserved. We are currently surveying other instances of excitable nonlinear media where coupling to locally conserved fields is warranted as a promising research direction.

DATA AVAILABILITY STATEMENT

The datasets presented in this study can be found in online repositories. The names of the repository/repositories and accession number(s) can be found at: https://doi.org/10.6084/m9.figshare.13309568.v3.

AUTHOR CONTRIBUTIONS

OG was responsible for the conception and design of the work. FS-F created and maintained the computer codes. FS-F and ES-G performed the simulations enabling data collection. FS-F, ES-G, JF-C, and OG performed the interpretation of the results. FS-F and OG drafted the article, while ES-G and JF-C critically revised it. Final approval of the version to be published was done by FS-F, ES-G, JF-C, and OG. All authors contributed to the article and approved the submitted version.

FUNDING

OG, FS-F, and JF-C acknowledge funding from Conacyt (Mexico) Proyecto CB-2016-01 286326. ES-G acknowledges a graduate studies scholarship from Conacyt (Mexico). OG acknowledges Universidad Autónoma Metropolitana for funding publication fees.

ACKNOWLEDGMENTS

OG thanks Juan Manuel Noriega Hernández for useful comments regarding unstable modes from a linear stability analysis of the dynamical equations for *s* and *c*.

SUPPLEMENTARY MATERIAL

The Supplementary Material for this article can be found online at: https://www.frontiersin.org/articles/10.3389/fphy.2021.636288/full#supplementary-material

REFERENCES

1. Cross M, Greenside H. *Pattern Formation and Dynamics in Nonequilibrium Systems*. Cambridge, MA: Cambridge University Press (2009).
2. Hoyle R. *Pattern Formation: An Introduction to Methods*. Cambridge, MA: Cambridge University Press (2010).
3. Kenkre VMN, Giuggioli L. *Theory of the Spread of Epidemics and Movement Ecology of Animals*. Cambridge, MA: Cambridge University Press (2021). doi: 10.1017/9781108882279
4. Monroy DL, Naumis GG. Description of mesoscale pattern formation in shallow convective cloud fields by using time-dependent Ginzburg-Landau and Swift-Hohenberg stochastic equations. *Phys Rev E*. (2021) 103:032312. doi: 10.1103/PhysRevE.103.032312
5. Hariharan G. An efficient legendre wavelet-based approximation method for a few Newell-Whitehead and Allen-Cahn equations. *J Membr Biol*. (2014) 247:371–80. doi: 10.1007/s00232-014-9638-z
6. Bray AJ. Theory of phase-ordering kinetics. *Adv Phys*. (1994) 3:357–459.
7. Allen SM, Cahn JW. Coherent and incoherent equilibria in iron-rich iron-aluminum alloys. *Acta Metall*. (1975) 23:1017–26. doi: 10.1016/0001-6160(75)90106-6
8. Hohenberg PC, Halperin BI. Theory of dynamic critical phenomena. *Rev Mod Phys*. (1977) 49:435–79. doi: 10.1103/RevModPhys.49.435
9. de Gennes PG, Prost J. *The Physics of Liquid Crystals*. 2nd Edn. Oxford: Clarendon Press (1993).
10. Rodarte AL, Pandolfi RJ, Ghosh S, Hirst LS. Quantum dot/liquid crystal composite materials: self-assembly driven by liquid crystal phase transition templating. *J Mater Chem C*. (2013) 1:5527–32. doi: 10.1039/c3tc31043d
11. Rodarte AL, Cao BH, Panesar H, Pandolfi RJ, Quint M, Edwards L, et al. Self-assembled nanoparticle micro-shells templated by liquid crystal sorting. *Soft Matter*. (2015) 11:1701–7. doi: 10.1039/C4SM02326A
12. Riahinasab ST, Keshavarz A, Melton CN, Elbaradei A, Warren GI, Selinger RLB, et al. Nanoparticle-based hollow microstructures formed by two-stage nematic nucleation and phase separation. *Nat Commun*. (2019) 10:1–10. doi: 10.1038/s41467-019-08702-3
13. Lou XWD, Archer LA, Yang Z. Hollow micro-/nanostructures: synthesis and applications. *Adv Mater*. (2008) 20:3987–4019. doi: 10.1002/adma.200800854
14. Rodarte AL, Nuno ZS, Cao BH, Pandolfi RJ, Quint M, Ghosh S, et al. Tuning quantum–dot organization in liquid crystals for robust photonic applications. *ChemPhysChem*. (2014) 15:1413–21. doi: 10.1002/cphc.201301007
15. Prieto G, Tüysüz H, Duyckaerts N, Knossalla J, Wang GH, Schüth F. Hollow nano- and microstructures as catalysts. *Chem Rev*. (2016) 116:14056–119. doi: 10.1021/acs.chemrev.6b00374
16. Atzin N, Guzmán O, Gutiérrez O, Hirst LS, Ghosh S. Free-energy model for nanoparticle self-assembly by liquid crystal sorting. *Phys Rev E*. (2018) 97:1–7. doi: 10.1103/PhysRevE.97.062704
17. Kröger M, Ilg P. Derivation of Frank-Ericksen elastic coefficients for polydomain nematics from mean-field molecular theory for anisotropic particles. *J Chem Phys*. (2007) 127:034903. doi: 10.1063/1.2743961
18. Luo AM, Sagis LMC, Ilg P. The Landau free energy of hard ellipses obtained from microscopic simulations. *J Chem Phys*. (2014) 140:124901. doi: 10.1063/1.4868988
19. Anderson VJ, Terentjev EM, Meeker SP, Crain J, Poon WCK. Cellular solid behaviour of liquid crystal colloids 1. Phase separation and morphology. *Eur Phys J E*. (2001) 4:11–20. doi: 10.1007/PL00013680
20. Phuong NH, Germano G, Schmid F. Elastic constants from direct correlation functions in nematic liquid crystals: a computer simulation study. *J Chem Phys*. (2001) 115:7127–234. doi: 10.1063/1.1404388
21. Poniewierski A, Stecki J. Statistical theory of the Frank elastic constants. *Phys Rev A*. (1982) 25:2368–70.
22. Allen MP, Warren MA, Wilson MR, Sauron A, Smith W. Molecular dynamics calculation of elastic constants in Gay–Berne nematic liquid crystals. *J Chem Phys*. (1996) 105:2850–8.
23. Joshi AA, Whitmer JK, Guzmán O, Abbott NL, de Pablo JJ. Measuring liquid crystal elastic constants with free energy perturbations. *Soft Matter*. (2014) 10:882–93. doi: 10.1039/C3SM51919H
24. Elder KR, Morin B, Grant M, Desai RC. Late-time theory for the effects of a conserved field on the kinetics of an order-disorder transition. *Phys Rev B*. (1991) 44:6673–88.
25. Andrienko D. Introduction to liquid crystals. *J Mol Liquids*. (2018) 267:520–41. doi: 10.1016/j.molliq.2018.01.175
26. Coles HJ. Laser and electric field induced birefringence studies on the cyanobiphenyl homologues. *Mol Cryst Liq Cryst*. (1978) 49:67–74. doi: 10.1080/00268947808070330
27. Das SK, Rey AD. Texture formation under phase ordering and phase separation in polymer-liquid crystal mixtures. *J Chem Phys*. (2004) 121:9733. doi: 10.1063/1.1804494
28. Matsuyama A. Morphology of spinodal decompositions in liquid-crystal-colloid mixtures. *J Chem Phys*. (2008) 128:224907. doi: 10.1063/1.2936831
29. Poulin P, Stark H, Lubensky TC, Weitz DA. Novel colloidal interactions in anisotropic fluids. *Science*. (1997) 275:1770–3.

30. Stark H. Physics of colloidal dispersions in nematic liquid crystals. *Phys Rep*. (2001) 351:387–474. doi: 10.1126/science.275.5307.1770
31. Lapointe CP, Mason TG, Smalyukh II. Shape-controlled colloidal interactions in nematic liquid crystals. *Science*. (2009) 326:1083–6. doi: 10.1126/science.1176587
32. Müller D, Kampmann TA, Kierfeld J. Chaining of hard disks in nematic needles: particle-based simulation of colloidal interactions in liquid crystals. *Sci Rep*. (2020) 10:12718. doi: 10.1038/s41598-020-69544-4
33. Stephan S, Staubach J, Hasse H. Review and comparison of equations of state for the Lennard-Jones fluid. *Fluid Phase Equilib*. (2020) 523:112772. doi: 10.1016/j.fluid.2020.112772
34. del Río F, Guzmán O, Martínez FO. Global square-well free-energy model via singular value decomposition. *Mol Phys*. (2018) 116:2070–82. doi: 10.1080/00268976.2018.1461943
35. Desai RC, Kapral R. *Dynamics of Self-Organized and Self-Assembled Structures*. Cambridge, MA: Cambridge University Press (2009). doi: 10.1017/CBO9780511609725
36. Shibata T, Mikhailov AS. Nonequilibrium self-organization phenomena in active Langmuir monolayers. *Chaos*. (2006) 16:037108. doi: 10.1063/1.2213580
37. Strausbaugh LJ, Marfin AA, Gubler DJ. West Nile encephalitis: an emerging disease in the United States. *Clin Infect Dis*. (2001) 33:1713–9. doi: 10.1086/322700

Conflict of Interest: The authors declare that the research was conducted in the absence of any commercial or financial relationships that could be construed as a potential conflict of interest.

frontiers in Physics

ORIGINAL RESEARCH
published: 01 June 2021
doi: 10.3389/fphy.2021.636070

Experimental Resonances in Viscoelastic Microfluidics

Pamela Vazquez-Vergara[1,2], *Ulises Torres-Herrera*[1], *Gabriel A. Caballero-Robledo*[3], *Luis F. Olguin*[2]* *and Eugenia Corvera Poiré*[1]*

[1] *Departamento de Física y Química Teórica, Facultad de Química, Universidad Nacional Autónoma de México, Ciudad de México, Mexico,* [2] *Laboratorio de Biofisicoquímica, Facultad de Química, Universidad Nacional Autónoma de México, Ciudad de México, Mexico,* [3] *Centro de Investigación y de Estudios Avanzados del IPN (Cinvestav), Apodaca, Mexico*

Pulsatile flows of viscoelastic fluids are very important for lab-on-a-chip devices, because most biofluids have viscoelastic character and respond distinctively to different periodic forcing. They are also very important for organ-on-a-chip devices, where the natural mechanical conditions of cells are emulated. The resonance frequency of a fluid refers to a particular pulsatile periodicity of the pressure gradient that maximizes the amplitude of flow velocity. For viscoelastic fluids, this one has been measured experimentally only at macroscales, since fine tuning of rheological properties and system size is needed to observe it at microscales. We study the dynamics of a pulsatile (zero-mean flow) fluid slug formed by a viscoelastic fluid bounded by two air-fluid interfaces, in a microchannel of polymethyl methacrylate. We drive the fluid slug by a single-mode periodic pressure drop, imposed by a piezoactuator. We use three biocompatible polymer solutions of polyethylene oxide as model viscoelastic fluids, and find resonances. We propose a model accounting for surface tension and fluid viscoelasticity that has an excellent agreement with our experimental findings. It also provides an alternative way of measuring relaxation times. We validate the method with parameters reported in the literature for two of the solutions, and estimate the relaxation time for the third one.

Keywords: fluid slug, pulsatile flow, dynamic permeability, microfluidics (experiment), viscoelasticity, interfaces, contact angle, relaxation time

OPEN ACCESS

Edited by:
Enrique Hernandez-Lemus, Instituto Nacional de Medicina Genómica (INMEGEN), Mexico

Reviewed by:
Yannis Dimakopoulos, University of Patras, Greece
Jun Zhang, Griffith University, Australia
Gaetano D'Avino, University of Naples Federico II, Italy

***Correspondence:**
Luis F. Olguin
olguin.lf@comunidad.unam.mx
Eugenia Corvera Poiré
eugenia.corvera@gmail.com

Specialty section:
This article was submitted to Soft Matter Physics, a section of the journal Frontiers in Physics

Received: *30 November 2020*
Accepted: *27 April 2021*
Published: *01 June 2021*

Citation:
Vazquez-Vergara P, Torres-Herrera U, Caballero-Robledo GA, Olguin LF and Corvera Poiré E (2021) Experimental Resonances in Viscoelastic Microfluidics. Front. Phys. 9:636070. doi: 10.3389/fphy.2021.636070

1. INTRODUCTION

The study of oscillatory fluid flow at microscales has become relevant due to the increasing number of applications that use this type of motion. For example: chemical synthesis inside microfluidic channels [1], liquid-liquid extraction [2], mixing by oscillatory cross flow [3–7], cooling of microelectronic circuits by micro oscillating heat pipes [8], inertial focusing of particles of a few microns [9, 10], DNA elongation studies [11] and studies of oscillatory movement of liquid plugs displaced by air in microchannels as model pulmonary flows [12, 13].

Pulsatile flows of viscoelastic fluids are very important for most organ-on-a-chip devices, where the natural mechanical conditions of cells are emulated [14–17], since most natural processes occur at certain characteristic frequencies. The characterization of viscoelastic fluids under non-steady pressure forcing is also important for lab-on-a-chip clinical analysis of biofluids such as blood, mucus, or synovial fluid. The dynamics of polymeric viscoelastic solutions under pulsatile forcing in microchannels is an area of recent development [18]. Flow of these solutions is strongly influenced by chemical properties of the polymer, its molecular weight and ramifications, concentration, the nature of the solvent, temperature and pressure [19].

The fluid response to an oscillatory pressure gradient has often been described by the dynamic permeability, a theoretical linear response function that has been obtained for numerous confined fluids: Newtonian, Maxwellian and general linear viscoelastic fluids, in a wide range of confining geometries [20–27]. It has also been obtained theoretically for Newtonian and viscoelastic fluids confined in elastomeric materials at microscales [28, 29] and for compressible binary fluids [30]. A distinctive feature of the dynamic permeability, when elastic elements are present in the system, is that it presents resonances, which refer to particular pulsatile periodicities of the pressure gradient that maximize the amplitude of fluid velocity. Experimental observation of resonances consists of an increase of flow velocity amplitude at a specific frequency range of the driving pressure gradient, that maximizes the momentum transfer to the fluid. For single fluids, resonances have only been reported experimentally at macroscales [31, 32], since fine tuning of rheological properties and system size is needed to observe them at microscales, in a desired frequency range.

Recently, a model to study the dynamics of a pulsatile (zero-mean flow) fluid slug, consisting of a Newtonian fluid and two air-fluid interfaces, driven by a periodic pressure gradient in a rectangular microchannel, has been proposed [33]. In that model, a stress tensor for a Newtonian fluid, together with Laplace condition for the pressure jump at both sides of the curved air-fluid interfaces, has been considered. Analytical solution of the model showed, for relatively low frequencies, a monotonic increase with frequency of the magnitude of the dynamic permeability as well as the emergence of a resonant behavior, due to the presence of surface tension. Microfluidic experiments were designed and implemented to observe both the low-frequency dynamics and the resonance. The model was then validated against the experimental results and used as a proposed strategy to measure surface tension in dynamic situations.

There are different ways to impose oscillatory frequencies to a fluid inside a microchannel. By using syringe pumps, low frequencies of oscillation (below 10 Hz) are achieved [1]; in contrast, the use of high-speed valves and gas-pressurized fluids [3], mechanical motors [34], heating [35] or mechanical displacement of an air bubble [36] can increase the forcing frequency range to 10–1,000 Hz. Alternative possibilities to impose pulsatile forcing in this frequency interval are the use of a moving train of droplets [37] and the coupling of a loudspeaker diaphragm to a microfluidic chamber [4]. Finally, coupling the displacement of a piezoelectric to a fluid encompasses a wide range of forcing frequencies of the methods described previously [38].

There are several sophisticated theoretical models to study the rheological behavior of PEO solutions, in different ranges of concentration and molecular weights. Of particular importance are the Phan-Thien-Tanner (PTT) model [39, 40] and the Cross model [19]. They have been adequate to study several experimental conditions and driving forces where a complex rheological response, involving elongational and shear thinning effects, has been experimentally observed and theoretically reproduced. However, there is also experimental evidence that a Maxwellian model predicts correctly and accurately the behavior of small ejected, low molecular weight PEO ($1x10^6 g/mol$) droplet jets [41]. Moreover, within microchannels of constant sectional area, several works suggest that for spatially-uniform pressure gradients elongational and shear thinning effects, like the ones considered by the PTT and Cross models, are irrelevant [40, 42, 43]. Furthermore, despite the fact that viscoelastic fluids generally involve several relaxation times, many studies of fluids with complex rheological behavior often report a single dominant Maxwellian-like relaxation time, fitted from their experimental data, since the Maxwell model is used as an archetype in the field.

In this work, we perform experimental and theoretical studies of the dynamics of a pulsatile (zero-mean flow) microfluidic slug, formed by a viscoelastic fluid bounded by two air-fluid interfaces in a rectangular microchannel, and find resonances in the dynamic permeability. We have driven the fluid slug by a single-mode periodic pressure drop, imposed by a piezoactuator in the range from 0.5 to 200 Hz, managing to keep the amplitude of the dynamic pressure drop practically constant at all frequencies. We have determined the displacement of the viscoelastic slug by visualization of the oscillatory movement of air-fluid interfaces. We have used three biocompatible polymer solutions of polyethylene oxide (PEO), as model viscoelastic fluids, because the rheological behavior of PEO has been widely assessed [19, 44, 45]. We propose a linear model accounting for surface tension and fluid viscoelasticity, that has a good qualitative agreement with all of our experimental findings and a quantitative agreement for low pressure drops, where the linear theory is expected to describe the system. Such agreement provides an alternative way of measuring relaxation times. We validate the method against parameters reported in the literature for PEO of two different molecular weights: $1x10^6 g/mol$ (PEO1) and $5x10^6 g/mol$ (PEO5); and estimate the relaxation time for PEO of $8x10^6 g/mol$ (PEO8). This is of great relevance because relaxation times are sometimes difficult to measure for low polymer concentration in conventional rheometers [45–48].

The paper is organized as follows: section 2 describes the experimental procedure and the data analysis; section 3 describes the experimental results including resonances of the dynamic permeability; section 4 introduces a theoretical model for pulsatile viscoelastic slugs; section 5 compares experimental results for the dynamic permeability with predictions obtained from the theoretical model, it also introduces a proposal to measure relaxation times; section 6 summarizes the most important conclusions and perspectives.

2. MATERIALS AND METHODS

2.1. Fluids

We use polyethylene oxide (Sigma-Aldrich) of three different average molecular weights: Mw = $1x10^6$ g/mol (PEO1); Mw = $5x10^6$ g/mol (PEO5) and Mw = $8x10^6$ g/mol (PEO8) to prepare solutions in deionized water at a fixed concentration of 0.1% (mass/volume). The dynamic viscosities, η, of the PEO solutions are: 1.72 mPa.s for PEO1 [41]; 4 mPa.s for PEO5 (approximated from a PEO4 solution at 0.1% (m/v) [19]), and 10 mPa·s for PEO8 [measured with an ARES (RSF III) Rheometer]. The three

polymer solutions have the same surface tension, $\sigma = 62$ mN·m^{-1} [49].

2.2. Microfluidic Device

We machined a straight microchannel (37.48 ± 0.11 mm long, 1.00 ± 0.04 mm wide and 0.31 ± 0.05 mm deep) on a 2 mm-thick polymethyl methacrylate (PMMA) plate using a CNC machine (CNC3018). The channel was sealed with a second PMMA plate with four inlets (**Figure 1**) exposing both parts to volatilized chloroform for 4 min and pressing them by a pair of slides and clamps. The bonding was completed by sonication of the device in ethanol at 50 °C for 15 min [50, 51].

2.3. Experimental Setup

A piezoelectric actuator equipped with flexural hinges as an amplifier device (APF705, Thorlabs) was attached on one of its sides to an elastic membrane that covered a rigid polyethylene cylinder (15 mm long, 4.7 mm diameter). The opposite side of the cylinder has a seal with a tubing (0.51 mm ID, 1.19 mm OD and 1 cm long; Microbore PTFE Tubing, Cole-Parmer) inserted in the middle. The other end of the tubing was introduced into the first microdevice inlet. The movement of the actuator displaces the air in the cylinder and transduces an oscillatory movement to a slug of PEO solution (1.0 cm in length; 3.1 μL) situated in the middle of the microchannel (**Figure 1**). The oscillation frequency and amplitude of the piezoelectric motion was controlled by a multifunction data input/output device (USB-6351, National Instruments) and magnified by a Trek PZD350A High-Voltage amplifier (75–150 V). The pressure drop was measured by a differential pressure sensor (Honeywell 142PC01G) attached by PTFE tubing to the second and third inlets of the microfluidic channel. The fourth inlet was open to the atmosphere. The displacement of the liquid slug was visualized with the aid of an inverted microscope (DM IL LED, Leica) and the movement of the interface closest to the atmosphere outlet (IF2 in **Figure 1**) was recorded with a high-speed camera (Phantom Miro M110, Vision Research). Depending on the driving frequency, videos from 30 fps up to 3,000 fps were acquired after a 10 s

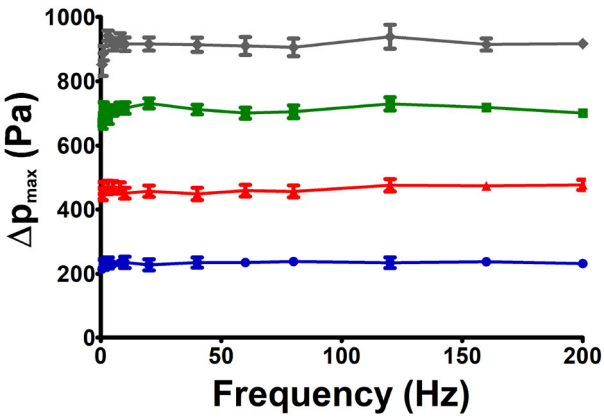

FIGURE 2 | Four different pressure drops were studied for each PEO solution in the range from 0.5 to 200 Hz. The experimental amplitude of pressure drop was held almost constant at 225, 450, 700, or 900 Pa by adjusting the voltage input to the piezoelectric actuator. Data shown corresponds to a PEO8 0.1% solution.

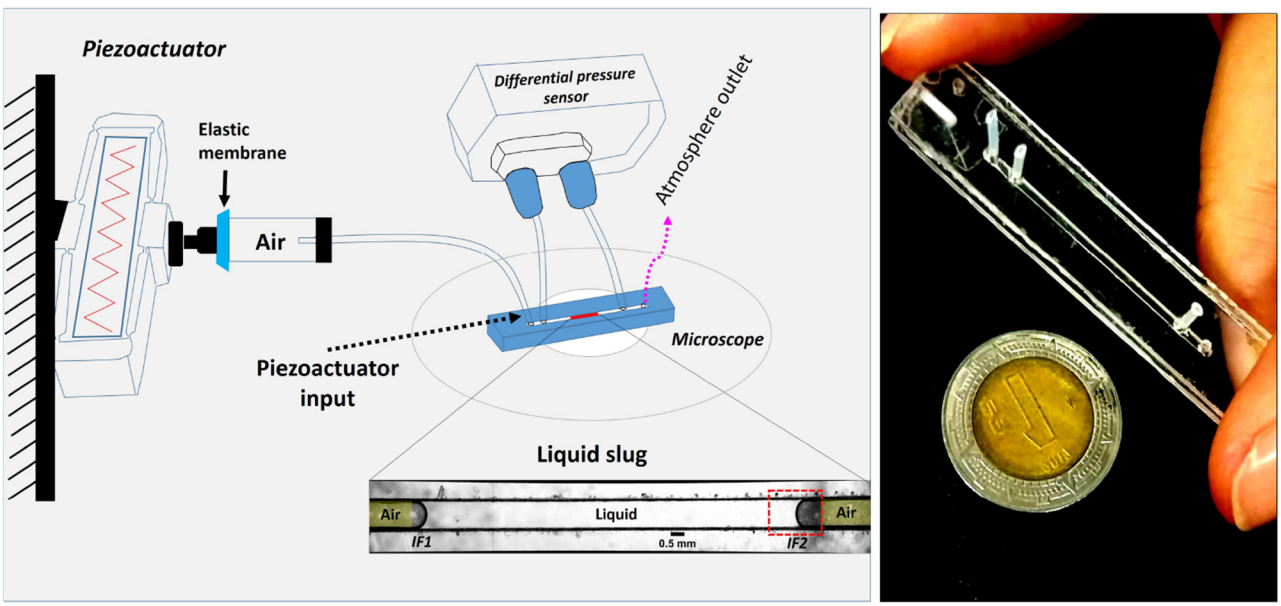

FIGURE 1 | Experimental setup. The displacement of a liquid slug within the microchannel is driven by the periodical movement of the piezoelectric actuator compressing the air trapped between the elastic membrane and the left side of the fluid slug *IF1*. The position of one of the air-liquid interfaces, *IF2*, is visualized and recorded by means of an inverted microscope and a high-speed camera.

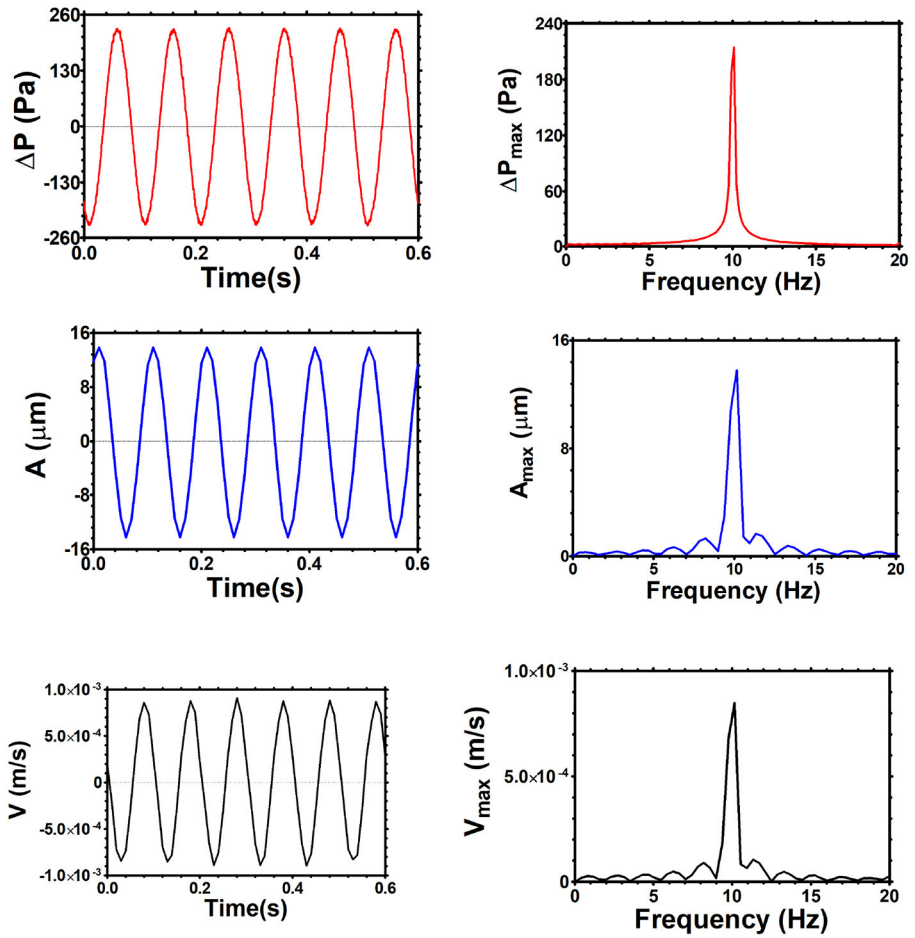

FIGURE 3 | Left: pressure drop, interface displacement, and interface velocity as a function of time for the same experiment. **Right**: Fourier spectrum analysis of the corresponding quantities, showing that all of them have a dominant mode for their dynamics at 10 Hz. Data are for PEO5 0.1%, $\Delta p = 225\ Pa$.

stabilization period of cycling movement to ensure recording after transient states. The size of the fluid slug was verified after each measurement to confirm that no evaporation had occurred.

2.4. Data Analysis

The piezoactuator movement was adjusted by regulating the input voltage to keep the same reference pressure drop for all the range of frequencies studied. For each PEO solution, oscillatory pressure drops of four different amplitudes were used: 225, 450, 700, and 900 Pa, each in the frequency range from 0.5 to 200 Hz (**Figure 2**). The sinusoidal shape of pressure drop allowed us to fit a sinusoidal wave to obtain the amplitude of each signal.

The videos of the interface movement were analyzed using MATLAB utilities, that track the position of all interface points through time, then velocity was obtained by numerically differentiating position data.

To prove that the frequency imposed by the piezoactuator was consistent with the interface movement, Fourier transform of the pressure drop, interface displacement and interface velocity were performed. A dominant peak for the spectrum of all these signals was observed at the same frequency of oscillation of the piezoelectric transducer, indicating that the fluid slug follows the dynamics imposed by the piezoactuator (**Figure 3**).

The dynamic contact angle of the interface was determined from video image analysis of the advancing and receding time lapses. The interface profile at every time, was fitted to a fourth-degree polynomial function. The fit reproduces very well the interface profile and was extrapolated to compute the contact angle at the wall. **Figure 4** top illustrates the change in contact angle at five instants of an oscillation cycle. **Figure 4** bottom shows the dynamic contact angle oscillation in time.

3. RESULTS

The air-fluid interfaces of the polymeric solutions display a characteristic curvature that flattens and bends in every oscillation cycle. This is illustrated in **Figure 4** middle. In **Figure 5**, we show the air-fluid interface of PEO5 0.1% through an entire oscillation cycle at four different frequencies. A maximum amplitude of the displacement, A_{max}, for this experiment occurs at 40 Hz. Peak-to-peak amplitude of the

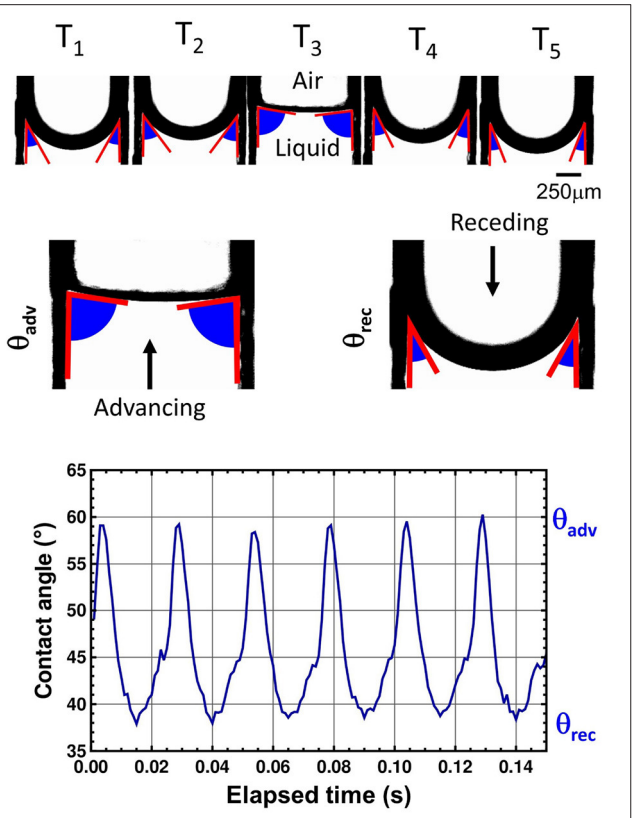

FIGURE 4 | Top: Interface profile at 5 time instants ($T1 - T5$) during an oscillation cycle. **Middle**: The maximum contact angle is associated with the advancing stage of the cycle, while the minimum contact angle is associated with the receding stage of it. **Bottom**: Dynamic angle as a function of time obtained from the interface at the right of the fluid slug *IF2*. Data are for PEO8 oscillating at 40 Hz, driven by a $\Delta p_{max} = 900\ Pa$.

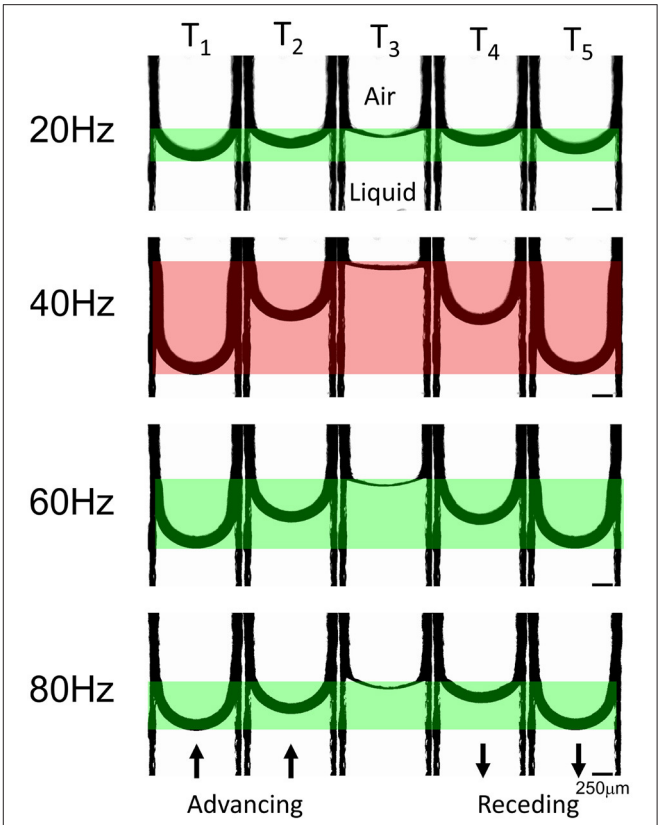

FIGURE 5 | Interface profiles at 5 time instants ($T1 - T5$) during an oscillation cycle for four different frequencies, illustrating that the maximum amplitude of the displacement is a non-monotonic function of frequency. T1 represents the minimum position and T3 the maximum position of the cycle. Data are for PEO5 oscillating in the range [20–80] Hz, driven by a $\Delta p_{max} = 700\ Pa$.

displacement is highlighted in red so the frequency dependent behavior can be assessed visually. It is clear that the neighboring smaller or larger frequencies display a smaller displacement.

By changing the frequency but keeping constant the amplitude of pressure drop driving the movement, a clear non-monotonic behavior of the amplitude of the interface displacement is observed for different driving frequencies, even for the PEO of lowest molecular weight. Top panels in **Figure 6** show that the highest displacement for each fluid increases in magnitude as the imposed pressure rises, which is an expected result for an increasing driving force. The maximum interface movement is observed for PEO1, the fluid with the smallest molecular weight and viscosity. The interface velocity, at the center of the microchannel, as a function of the oscillating frequency shows an asymmetric bell-shape curve for each imposed pressure (**Figure 6** middle panels). As expected, the maximum velocity amplitude rises as the pressure increases for all PEO solutions. The peak of each curve is the resonance frequency, meaning that at this frequency the amplitude of flow velocity is maximum in the frequency range studied. A non-trivial effect is observed in which the resonance frequency decreases with an increasing pressure drop. This is part of the non-linear behavior of the system response. Since we are driving the system with a one-mode pressure drop, we expect that, at least in the linear regime, the amplitude of the interface velocity would be given by the maximum amplitude of the interface displacement multiplied by its frequency. For this reason, the resonances observed in velocity have higher frequencies than those obtained for the amplitude of interface position.

We also analyzed the dynamic permeability of each polymer solution as a function of frequency and amplitude of pressure drop (**Figure 6** bottom panels). We present an operational definition of the amplitude of the local dynamic permeability at the center of the channel, as the ratio between the maximum amplitude of the velocity at the center of the channel, divided by the pressure gradient—given by the quotient of pressure drop, Δp, and slug length, L,—that is,

$$K = \frac{v_{max}}{\Delta p / L}\ . \tag{1}$$

Derivation of Equation (1) will be given in section 4 Model for small pressure drop values; however, we will use this operational definition for all pressure drops studied, since it

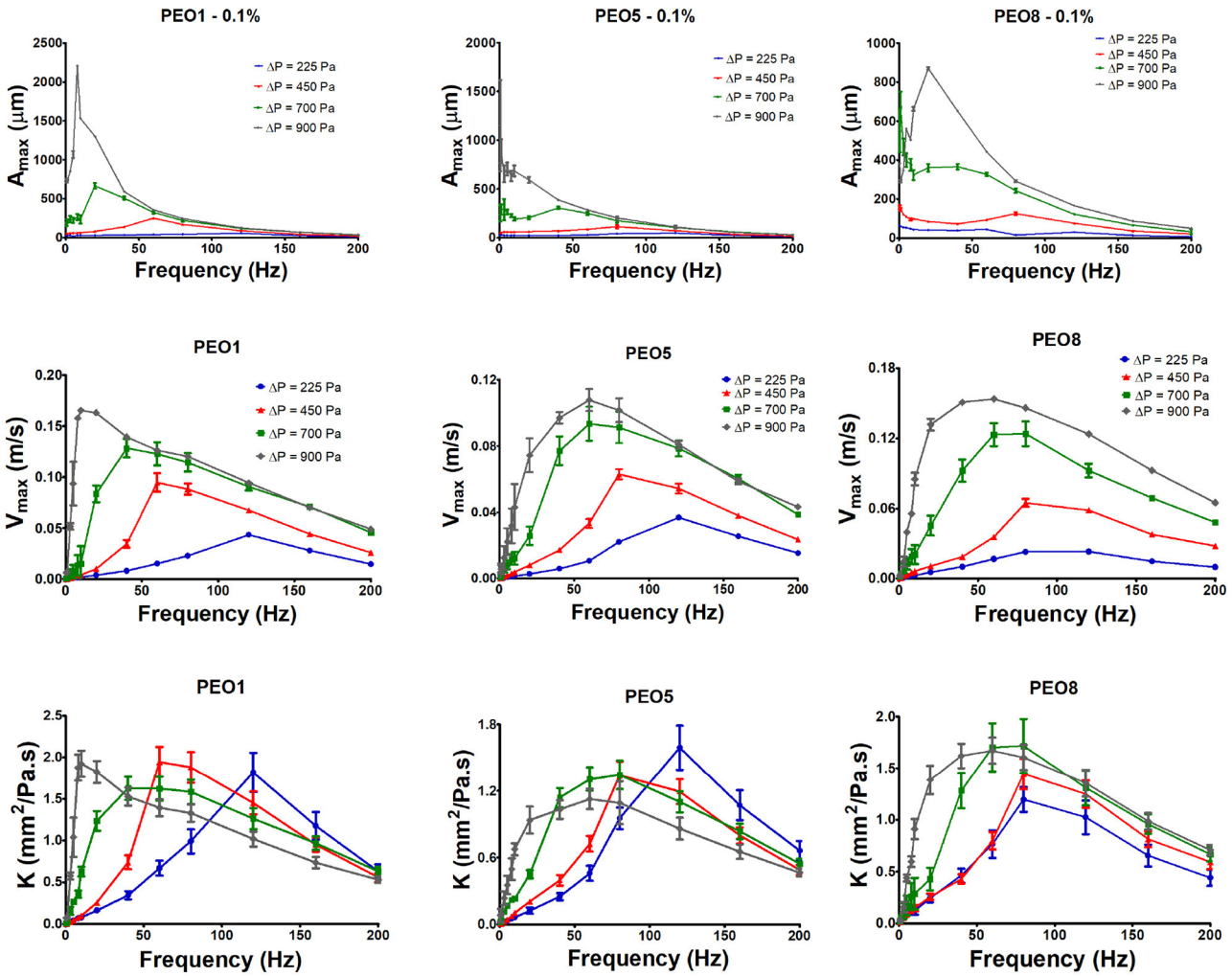

FIGURE 6 | Maximum amplitude of displacement, maximum amplitude of velocity and modulus of dynamic permeability, as a function of driving frequency for the three PEO polymeric solutions and 4 different maximum amplitudes of the driving pressure drop.

is a convenient way to cancel out the small differences in pressure drop amplitude for the different frequencies tested (see **Figure 2**). In this sense, K can be interpreted as a velocity rescaled by a pressure gradient. Accordingly, in the bottom panels of **Figure 6**, we observe that the resonance frequencies of the local permeability are roughly the same as those obtained for velocity data. Also, as pressure drop increases, the resonance frequency of the permeability decreases. This effect is more pronounced for low molecular weights. For the dynamic permeability value at resonance, there is no clear trend when the amplitude of the pressure drop changes. For details and graphs describing this behavior, see **Supplementary Material**.

Regarding the dynamics of the contact angle, we found that advancing angles are larger than receding ones. As an example, **Figure 7** shows the dynamic angles obtained when the amplitude of pressure drop is 225 Pa. It has been reported in the literature that, when velocity increases, the advancing angle augments and the receding angle decreases, so a larger difference between them should be observed [52–55]. The difference of advancing and receding angles, $\Delta\theta = \theta_{adv} - \theta_{rec}$ (sometimes called contact angle hysteresis [52]), is shown as a function of frequency in **Figure 8**. For a single-mode oscillatory flow, the fluid velocity increases with frequency up to the resonance and then decreases. We can observe that the same trend exists for $\Delta\theta$ as a function of frequency. The fact that the dynamic contact angle difference is affected by the interface velocity, has previously been reported for capillary numbers close to the ones of our experiments ($Ca = 10^{-5}$ to 10^{-3}) [53, 55]. This phenomenon is attributed to surface roughness and chemical heterogeneity [56, 57], but there is an influence of the fluid rheological properties, like shear thinning or elasticity [53]. In our slug, an important component of elasticity is given by the presence of two interfaces.

4. MODEL

In order to explain theoretically our experimental results, we build up a model containing two basic features: the viscoelastic character of the fluid and the elastic character of interfaces. The

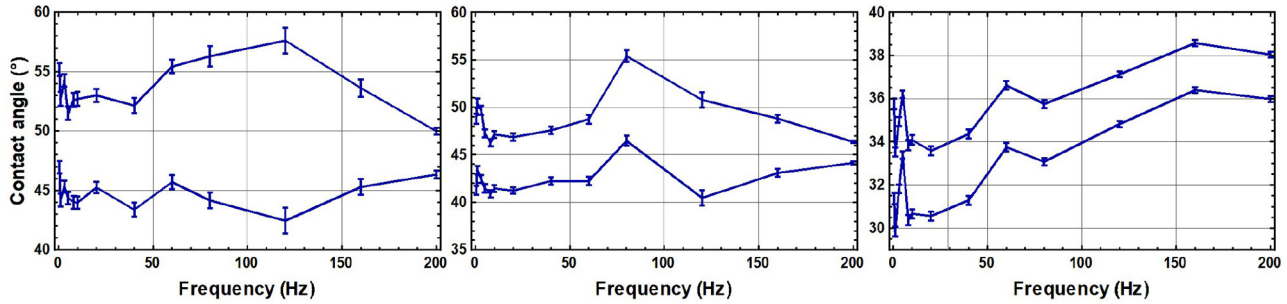

FIGURE 7 | Contact angle as a function of frequency. For each plot, the upper line corresponds to the advancing angle and the lower line corresponds to the receding angle. **Left**: PEO1. **Center**: PEO5. **Right**: PEO8. The difference between advancing and receding angle diminish as the molecular weight is higher.

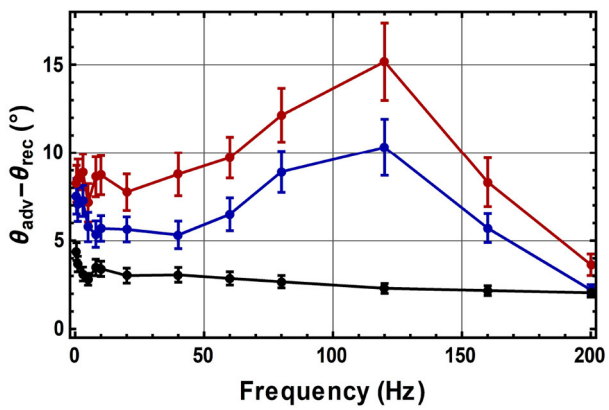

FIGURE 8 | Contact angle hysteresis as a function of frequency for the three PEO solutions with different molecular weights for $\Delta p = 225$ Pa (red line: PEO1; blue line: PEO5; black line: PEO8).

interplay between these two elasticities will lead to a complex behavior, the simpler the rheology of the viscoelastic fluid, the easier the understanding of the physical interaction. Because of this, we present a model for the uniaxial dynamics of a viscoelastic slug, taking into account the presence of interfaces and the viscoelastic character of a single-relaxation-time fluid, that could be extended to models containing more characteristic times. We build up a model for the dynamics of viscoelastic slugs over a model presented for the dynamics of a Newtonian slug [33].

A study of a pulsatile fluid slug consisting of a Newtonian fluid and two air-fluid interfaces driven by a periodic pressure gradient, has been recently proposed and validated [33]. In that model, a stress tensor for a Newtonian fluid of the form $\tau = -\eta\nabla v$, together with Laplace condition for the pressure jump at both sides of the air-fluid curved interfaces, $\Delta p = \Delta p_{driving} + \sigma\kappa_1 + \sigma\kappa_2$, has been considered. In these expressions, η is the fluid viscosity, v is the axial fluid velocity, σ is the surface tension of the air-fluid interfaces, κ_1 and κ_2 are the left and right hand side curvatures, respectively, and $\Delta p_{driving}$ is the pressure drop external to the fluid slug (on the air side). The dynamics for such Newtonian slugs is described by an integro-differential equation in space and time, which, in frequency domain, can be written as a simple equation, differential in space and algebraic in frequency, that reads:

$$-i\omega\rho\hat{v} = -\frac{\Delta\hat{p}_{driving}}{L} + \left[\eta + i\frac{2\sigma}{\omega L}\right]\nabla^2\hat{v}, \tag{2}$$

where ω denotes angular frequency, ρ is the fluid density, L is the length of the fluid slug, and $\hat{v}$ and $\hat{p}$ denote Fourier transforms of velocity and pressure, respectively. This equation incorporates momentum conservation, the stress tensor for a Newtonian fluid, Laplace equation for the pressure jump at the interfaces, an approximation of interface curvatures as concavities, and continuity of velocities at both interfaces. This model has given a correct description of the experimental dynamics of a water slug and of a 70% glycerol solution in water slug, when interfacial curvatures are considered to be a response to a dynamic external pressure gradient $\Delta p_{driving}/L$. Details of the derivation of Equation (2) can be seen in [33].

A *Newtonian slug stress tensor*, that integrates stresses of the Newtonian fluid and the interfaces, of the form

$$\hat{\tau}^N_{slug} = -\left[\eta + i\frac{2\sigma}{\omega L}\right]\nabla\hat{v}, \tag{3}$$

substituted in the linearized momentum conservation equation for uniaxial flow in the x direction,

$$-i\omega\rho\hat{v} = -\frac{\Delta\hat{p}_{driving}}{L} - \left[\nabla\cdot\hat{\tau}_{slug}\right]_x\ , \tag{4}$$

gives exactly Equation (2) for the dynamics of a Newtonian slug. A stress tensor of the form (3) for a material consisting of a volume of fluid and two air-fluid interfaces, has not been introduced in the literature, to the best of our knowledge, since classical treatments describe both fluid phases and apply boundary conditions at air-fluid interfaces, rather than describing the system fluid-interfaces as a composite material. Vazquez-Vergara et al. [33] together with discussion in the previous paragraph, show that introduction of a *slug stress tensor*, as the one in Equation (3), is a consistent approach to describe the zero-mean flow, linear pulsatile dynamics of Newtonian slugs.

Viscoelastic fluids might involve, in general, several relaxation times. The coupling of such times with the characteristic time given by the presence of interfaces, is expected to lead to a complex dynamics of viscoelastic slugs. To understand such coupling, we start by introducing the simplest model of a viscoelastic slug, consisting of a volume of linear Maxwellian fluid, that has a single relaxation time, and two air-fluid interfaces, with surface tension σ.[1] We propose the following expression for the *viscoelastic slug stress tensor:*

$$\hat{\tau}_{slug}^{\mathrm{VE}} = -\frac{\left[\eta + i\frac{2\sigma}{\omega L}\right]}{1 - i\omega t_r}\nabla\hat{v}. \tag{5}$$

where the parameter t_r is the Maxwell relaxation time. Equation (5) reduces to the constitutive equation of a Newtonian slug (Equation 3) in the limit $t_r \to 0$, and reduces to the Maxwell model in the absence of interfaces [58], that is, in the limit $\sigma \to 0$. Along with the previous consistency proofs, experimental validity of the model given by Equation (5) must be demonstrated.

When the stress tensor (Equation 5) is substituted in the momentum conservation equation (Equation 4), we can obtain an equation for the dynamics of a viscoelastic slug,

$$\left[\eta + i\frac{2\sigma}{\omega L}\right]\nabla^2\hat{v} - i\omega\rho(1 - i\omega t_r)\hat{v} = (1 - i\omega t_r)\frac{\Delta\hat{p}_{driving}}{L} \ . \tag{6}$$

Solution of Equation (6) subject to no-slip boundary conditions, for flow in a rectangular microchannel whose plates are separated by a distance $2l$, gives a linear relation between velocity and pressure drop in frequency domain, that is,

$$\hat{v}(z,\omega) = -K(z,\omega)\frac{\Delta\hat{p}_{air}}{L} \ , \tag{7}$$

where z is the coordinate perpendicular to the plates. The complex local dynamic permeability, $K(z,\omega)$, is given by

$$K(z,\omega) = -\frac{1}{i\omega\rho}\left[1 - \frac{\cos(Az)}{\cos(Al)}\right] \ \text{with} \ A^2 = i\omega\rho\left[\frac{1 - i\omega t_r}{\eta + i\frac{2\sigma}{\omega L}}\right]. \tag{8}$$

This linear relation is expected to coincide with experimental results, for low values of the pressure drop, where $K(z,\omega)$ is independent of the amplitude of the pulsatile forcing.

It is worth noticing that Equations (7) and (8), which are the solution for the dynamics of a Maxwellian slug given by our model, are consistent with the pulsatile solution of the linear Maxwell model for a single fluid in a rectangular cell in the limit of zero surface tension given in [26] (equivalent to the solution in [23, 24, 59] in the cylindrical case).

Expressions (7) and (8) are valid for general periodic time-dependent pressure drops, consisting of an arbitrary number of sinusoidal modes. In particular, for a one-mode driving pressure drop of frequency ω_0, it can be shown that, in time domain, the amplitude of the velocity at the center of the cell, v_{max}, is related to the amplitude of the pressure drop, Δp_{max}, as

$$v_{max} = \left|K(z=0,\omega_0)\right|\frac{\Delta p_{max}}{L} \ , \tag{9}$$

which is in agreement with the operational definition of K, used to compute the permeability from experimental data in Equation (1).

Our model has been deliberately developed for zero-mean pulsatile flows, due to the oscillatory nature of our experimental driving force. It therefore cannot be used to model fronts in imbibition-like systems, where the pressure drop has always the same sign and the interface curvature is due to wetting. In our case, curvature effects due to wetting cancel out since they have opposite signs on the left and right side interfaces [33], and the dynamics of the slug will be governed by the instantaneous interfacial curvatures caused by pulsatile forcing.

5. COMPARISON WITH EXPERIMENTAL RESULTS

We compare the experimental results for K at low-amplitude pressure drops (225 Pa) from **Figure 6** with $K(0,\omega_0)$ derived from the linear model developed in the previous section. For the figures, we simply use K to denote the local dynamic permeability at the center of the microchannel. **Figure 9** shows experimental and theoretical predictions of K as a function of the driving frequency for three PEOs. A log-log scale has been used to highlight the tendency of low frequency data.

Figure 9 left shows, with green dots, the permeability K obtained from experimental data for PEO1. With a red continuous line, it shows the theoretical permeability, as predicted by our model for a Maxwellian slug, obtained from Equation (8) with $z = 0$ and a relaxation time, $t_r = 1.78$ *ms*, reported as Maxwellian in the literature [41]. As reference, we have also plotted, in a blue continuous line, the theoretical permeability for a Newtonian slug. As **Figure 9** left shows, the agreement between experimental data and theoretical prediction for a slug of a viscoelastic fluid obeying Equation (8) is excellent, both, at low frequencies and around resonance; **Figure 9** middle shows equivalent curves for PEO5. Since the relaxation time, at the concentration used in our experiments, is not reported in the literature, we took one reported for PEO4, as surrogate [19]. The agreement between the green dots, obtained from experimental data, and the red line predicted by our model, is very good, both, at small frequencies and around resonance, despite the fact that the relaxation time used was obtained from a fit to a Cross model [19, 60].

Before discussing **Figure 9** right for PEO8, for which there is no relaxation time reported in the literature, at the desired concentration, we will discuss the theoretical behavior of the resonance frequency, in terms of characteristic frequencies of the system.

We can define three characteristic frequencies of the system that depend on viscosity, η, surface tension, σ, relaxation time,

[1] This model can be generalized to other models containing more characteristic times, in a more or less straightforward manner. For example, for a linearized Oldroyd-B model, containing two relaxation times t_r and t_2, the viscoelastic stress tensor proposed for the fluid slug would be $\hat{\tau}_{slug}^{\mathrm{OB}} = -\frac{\left[\eta + i\frac{2\sigma}{\omega L}\right](1 - i\omega t_2)}{(1 - i\omega t_r)}\nabla\hat{v}$.

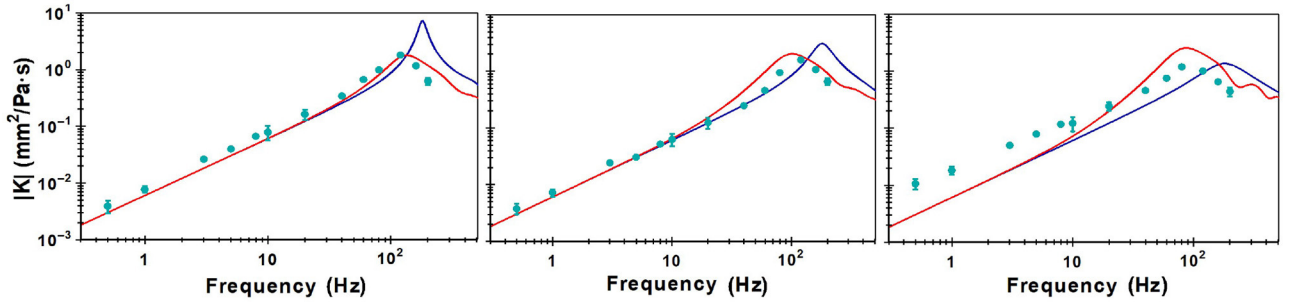

FIGURE 9 | Comparison of theoretical (red and blue lines) and experimental results (green dots) for dynamic permeability for PEO solutions at 225 Pa of: **(left)** PEO1 solution; **(middle)** PEO5 solution; **(right)** PEO8 solution.

t_r, and system's geometry, l (half the microchannel thickness), as

$$\omega_\eta = \frac{\eta}{\rho l^2}\,, \quad \omega_\sigma = \frac{2\sigma}{\eta L} \quad \text{and} \quad \omega_{relax} = \frac{1}{t_r}\,. \tag{10}$$

In terms of these frequencies, the argument of the cosine term, Al, in Equation (8), can be written as

$$A^2 l^2 = i\frac{\omega}{\omega_\eta}\left[\frac{1 - i(\omega/\omega_{relax})}{1 + i(\omega_\sigma/\omega)}\right]. \tag{11}$$

We find two different regimes for the resonance frequency. For $\omega_{relax} \ll \omega_\eta$, the resonance frequency, ω_{res}, is given by

$$\omega_{res} = \frac{\pi}{2}\left(\omega_\eta\,\omega_\sigma\right)^{1/2}\,, \tag{12}$$

while for $\omega_{relax} \gg \omega_\eta$, it is given by

$$\omega_{res} = \frac{\pi^{2/3}}{2^{1/3}}\left(\omega_\eta\,\omega_\sigma\,\omega_{relax}\right)^{1/3}\,. \tag{13}$$

The resonance frequency, with the proper scaling to make the second of these regimes collapse, is given in **Figure 10**.

We have found numerically the maximum of the local dynamic permeability in Equation (8) using characteristic values of ω_η and ω_σ for each of the three PEO solutions employed in the experiments. We have plotted the resonance frequency as a function of the independent variable $\omega_{relax}/\omega_\eta$. The red curve corresponds to PEO1, the blue curve to PEO5 and the gray curve to PEO8. Red and blue dots over the curves (for PEO1 and for PEO5, respectively) represent pairs $(t_r^{lit}, \omega_{res}(t_r^{lit}))$, in the corresponding rescaled units of the graph, where $\omega_{res}(t_r^{lit})$ is the theoretical resonance obtained using a relaxation time from the literature.

Our resonance curves in **Figure 10** could serve "as a rheometer" to validate or estimate viscoelastic relaxation times. Such a procedure is schematized with horizontal dashed lines in **Figure 10**, which relate a reasonable resonance frequency range—obtained by visual inspection of **Figure 9**—, with a range of possible relaxation times, obtained from the vertical dashed lines, through the theoretical curve in **Figure 10**. To validate our method, we have estimated that the resonance

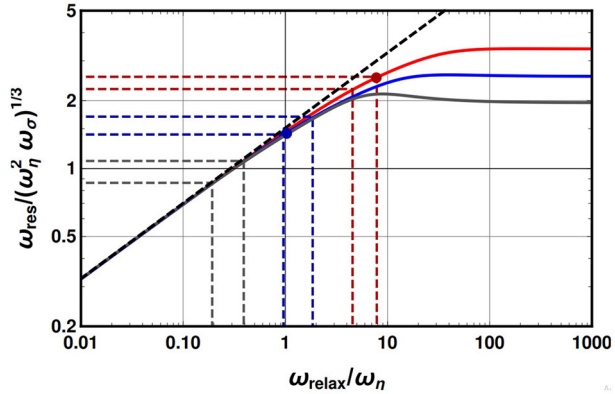

FIGURE 10 | Illustration for the way of estimating the value of relaxation time (through ω_{relax}) by visual estimation of the resonance frequency, and its corresponding error bars. The theoretical model predicts a relation between resonance frequency and relaxation frequency that can be exploited to validate or estimate relaxation times. We have used PEO1 solution (red dashed lines), and PEO5 solution (blue dashed lines) to validate the method. Then we have used the method to estimate the relaxation of the PEO8 solution, from its experimental resonance (gray dashed lines). Red and blue intervals, marked with dashed lines, are in agreement with theoretical data of resonance frequency and relaxation times (placed as a circle red dot) for PEO1 and (placed as a circle blue dot) for PEO5. Black dashed line represents an approximated relation for ω_{res} in Equation (13). Continuous lines are exact results for resonance, obtained by numerical means.

frequency for PEO1, is in the range [120:136] Hz, and in the range [100:120] Hz for PEO5. As **Table 1** shows, the range of relaxation times estimated by the theory—from measurement of the experimental resonance frequency—are in agreement with the values for the relaxation time reported in the literature. We consider that, as a proof of concept, this validates our method for estimating relaxation times of single-relaxation-time viscoelastic fluids. Accordingly, we estimate from **Figure 9** that, for PEO8, the resonance frequency is in the range [80:100] Hz, and estimate that the relaxation time would be in the range [6.8:14.8] *ms*. Even though this range is wide, when considering a value in the middle of this range, we obtain the red curve in **Figure 9** for the dynamic permeability,which, despite being less accurate

TABLE 1 | Comparison between reported values in the literature of viscoelastic relaxation time and the range estimated by the theoretical model via the experimental resonance.

System	Reported t_r (ms)	Estimated t_r via fitting to model (ms)
PEO1	1.78[a]	1.76–3.04
PEO5	5.8[b]	3.21–6.21
PEO8	–	6.76–13.76

(a) Taken from [41]. (b) Taken from [19].

than the ones for the lower molecular weight polymers, still gives a reasonable agreement for both, the tendency of the experimental permeability at low frequencies, and the region around resonance. It is important to note that the relaxation times obtained with our method follow the trend that, the larger the molecular weight of PEO, the larger the relaxation time. This is in qualitative agreement with global trends observed in literature for a vast range of concentrations and molecular weights in PEO aqueous solutions [19, 41, 61]. Our method promises to be valuable for low molecular weight polymers, for which relaxation times are difficult to obtain experimentally by conventional means. For high molecular weight polymers, more sophisticated models, including shear thinning, might result necessary to describe the dynamics and to obtain rheological parameters from it, as it happens for high concentrations of low molecular weight polymer solutions [19, 45]. It is worth mentioning that the size of the fluid slug can be experimentally adjusted to fall in the range where the approximated black dashed line in **Figure 10** is valid, that is, whenever it agrees with the exact value of resonance frequency, given by the continuous lines; at such regime, there is a simple analytical relation between resonance frequency and relaxation time, and the indirect determination of relaxation times could be carried out easily using Equation (13). In contrast, the plateau observed for each continuous line on the right side of **Figure 10**, corresponds to the regime where the resonance frequency is given by Equation (12), when the relaxation time is not relevant. The curves differ from each other due to their viscous frequency, ω_η.

Our theory is also able to predict the contact angle, given an initial shape of the interface. Several models for front dynamics in the literature establish a difference between a static contact angle at equilibrium situations, and the angle observed due to an imbibition-like front dynamics, where the pressure gradient has always the same sign, this is typically called a dynamic contact angle. In addition to such descriptions, recent studies have dealt with a different time-varying dynamic contact angle, which is affected not only by imbibition phenomena but also by oscillatory driving forces [62]. This is the case of our dynamic contact angle. We explain in a nutshell how do we compute dynamic contact angles from our theoretical model: our differential equation gives the slug velocity $v(z,t)$ as a function of pressure drop. Since interface shape, $u(z,t)$, and velocity are related through $\partial u/\partial t = v$, once the velocity $v(z,t)$ is known, we can integrate this equation to obtain $u(z,t) = \int v(z,t)dt + u_0(z)$, where $u_0(z)$ is an integration constant which gives the interface profile at rest (or, equivalently, at very high frequencies). Once the interfacial profile is known in time, the arctangent of its slope close to the wall gives the dynamic contact angle.

It is worth mentioning that our experiments measure an angle along the channel width, not along the channel height, which is the dimension modeled in Equation (6). So, it is necessary to find out a relation between the angles measured in both planes. We follow Tabeling results [63] on steady flow where the relation between the slope of flow velocity at the channel walls in both planes obeys a linear relation of the form

$$\left.\frac{\partial v}{\partial y}\right|_{y=W/2} = m\left.\frac{\partial v}{\partial z}\right|_{z=l} \tag{14}$$

where m is a factor that only depends on the aspect ratio $W/2l$ (see **Figure 11** left). Since for a single-mode oscillatory flow, interface shapes and velocity are linearly related through the driving frequency, that is, ω_0, as $v(y,z,t) = \omega_0 u(y,z,t)$, an equivalent relation can be proposed for interfacial profiles, u, as

$$\left.\frac{\partial u}{\partial y}\right|_{y=W/2} = m\left.\frac{\partial u}{\partial z}\right|_{z=l} \tag{15}$$

This geometrical relation between the slope at both confining dimensions is illustrated in **Figure 11** left. The dynamics of both angles is illustrated in **Figure 11** right.

With the correction explained above, the experimentally obtained contact angles are compared to the ones predicted by our model. This is shown in **Figure 12**. We find that the contact angle predicted by the theory is larger than the one obtained from experiments; however, our theory correctly predicts the phase difference between the angle and the pressure gradient.

A model for single Maxwellian fluids accounting for channel width and height, has found that the effect of the second confining dimension is relevant only at high frequencies [64]. We therefore consider that if such analysis were extended to Maxwellian slugs, it would not affect the conclusions regarding resonances and dynamic permeabilities presented in this work.

6. CONCLUSIONS AND PERSPECTIVES

We have made a thorough experimental study of the dynamic behavior of pulsatile fluid slugs made by three biocompatible viscoelastic fluids [65]. We have studied their responses in a wide frequency range, from [0.5:200] Hz, at four different amplitudes of the pressure drop, which have been maintained practically constant in all the frequency range. We have chosen the dynamic permeability as a parameter to characterize the fluid dynamics since, in the regime where flow and pressure drop are linearly related, it can be analytically demonstrated that it is a response function of the system to a pulsatile pressure drop. At higher pressure drops, it is a convenient way to represent a rescaled velocity, which cancels, to linear order, the small differences in pressure drop amplitude applied at different frequencies. We have found that the permeability of the three viscoelastic slugs present resonances, that is, a special frequency range of the

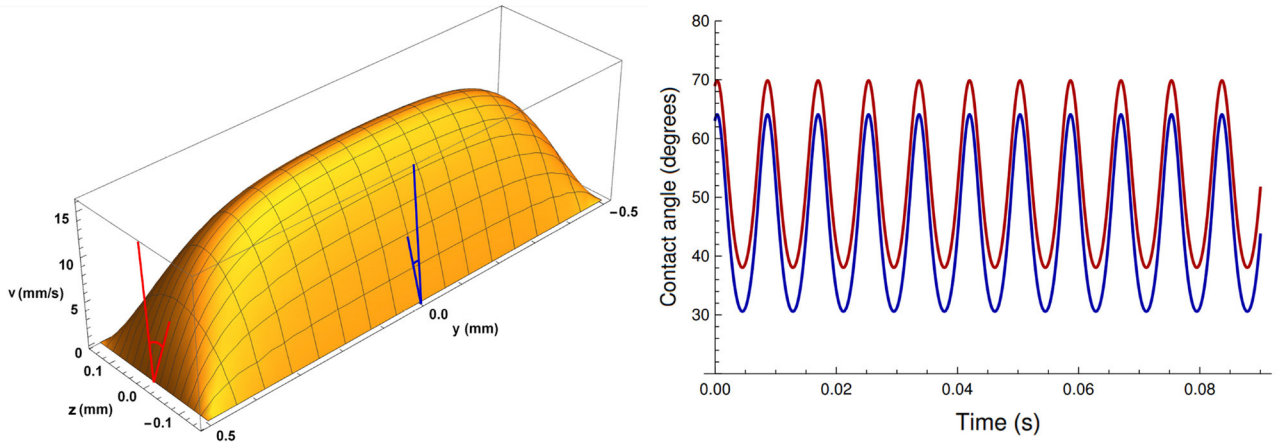

FIGURE 11 | Left: Illustration of an instantaneous velocity profile in a cross section of a rectangular microchannel, computed theoretically following [63]. **Right**: Illustration of the time behavior of the angle (given by the arctan of the slope) along the channel width (red), and along the channel height (blue), for a channel whose width is three times its height.

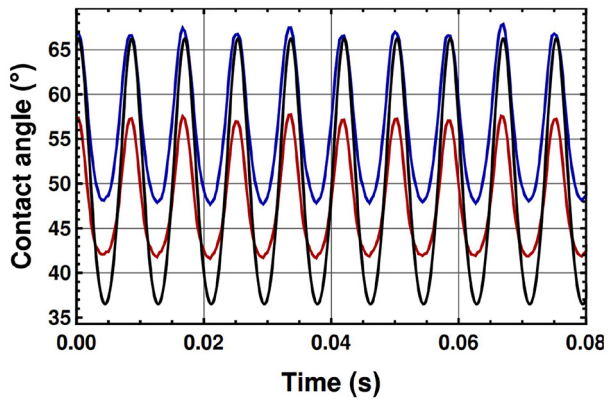

FIGURE 12 | Comparison between predicted and measured contact angles for a slug of PEO1 solution pulsated at frequency of 120 Hz, and a pressure drop amplitude of 225 Pa. Blue and red lines correspond to the contact angle, obtained from experimental measurements, at the left and right walls of the microchannel, respectively; black line corresponds to the theoretical prediction. Agreement between theoretical and experimental results is noticeable, particularly because their oscillation is in phase.

oscillatory pressure gradient that maximizes the amplitude of flow velocity.

We have also developed a continuum-mechanics linear model of viscoelastic slugs, containing both, the elasticity of the fluid and the elasticity given by air-fluid interfaces, through surface tension. The slug model gives excellent agreement with our experimental results at low-amplitude pressure drops. Such an agreement was a necessary condition for model validation. The dynamic permeability at all frequencies coincides very well for PEO1 and PEO5 solutions, both, at small frequencies and at resonance. Coincidence of experimental and theoretical resonances provides an alternative strategy for measuring relaxation times. We validated this strategy with relaxation times reported in the literature for PEO1 and PEO5 solutions, and estimated the relaxation time for PEO8. With such estimation, the dynamic permeability for PEO8 gives the correct slope as a function of frequency (in log-log scale), at small frequencies, and gives a very good agreement around resonance. It is worth mentioning that viscoelastic fluids, in general, have several relaxation times. If one uses a single-relaxation-time model, this one should correspond approximately to the larger characteristic time experimentally observed. Our model for viscoelastic slugs could be extended, in a more or less straightforward manner, to models with several relaxation times. The problem for validation in that case, would be the lack of experimental information in the literature of the several relaxation times reported for a specific molecular weight and a specific concentration of a polymer solution obeying a specific model.

Finally, we have compared the dynamics of the contact angle, and found that theory and experiments predict similar amplitudes and exactly the same phase shift with respect to the oscillatory pressure drop. In our experiments, the interface motion is negligible close to the wall, when compared to the motion of the interface at the center of the channel. For this reason, we have not included slip in our model and the contact line displacement is not a concern for our relatively small-amplitude pressure drops.

This is the first time that experimental resonances of the dynamic permeability of viscoelastic fluids, confined at microscales, are reported in the literature. Our results are relevant for flow and shear rate control, with potential applications to many systems, like organ-on-a-chip devices where the natural mechanical conditions of cells are emulated [14–17]; and biofluids, which are typically viscoelastic, are present. Our results could also be useful to study how cells would respond to different imposed, non-physiological, external stresses [66–71].

DATA AVAILABILITY STATEMENT

The raw data supporting the conclusions of this article will be made available by the authors, without undue reservation.

AUTHOR CONTRIBUTIONS

PV-V performed the experiments. UT-H and ECP developed the analytical model and performed analytical calculations. PV-V and UT-H carried out data curation. GC-R designed the preliminary experimental settings and performed the preliminary experiments. PV-V and LO designed the final experimental setting. LO directed the experiments. PV-V, LO, and ECP wrote the original draft. GC-R, LO, and ECP did the funding acquisition. LO and ECP supervised the investigation. ECP conceptualized the project and coordinated the work. All authors gave final approval for publication.

FUNDING

PV-V acknowledges CONACyT (Mexico) for 2-year postdoctoral funding through Project 219584. UT-H acknowledges financial support from CONACyT (Mexico) through Fellowship No. 589015. GC-R acknowledges financial support from CINVESTAV (Mexico) for open access expenses. LO acknowledges financial support from Faculty of Chemistry, UNAM, through PAIP Project 5000-9023. ECP acknowledges financial support from Faculty of Chemistry, UNAM, through PAIP Project 5000-9011. ECP acknowledges financial support from CONACyT (Mexico), through project 219584. The authors acknowledge financial support from DGAPA, UNAM, through PAPIIT Projects IT203318 and IN113421.

ACKNOWLEDGMENTS

The authors thank Pablo E. Guevara-Pantoja and Patricia Cerda Hurtado for technical assistance and Aimee Torres Rojas for analysis of preliminary data. The authors thank Julien Lombard for useful discussions.

SUPPLEMENTARY MATERIAL

The Supplementary Material for this article can be found online at: https://www.frontiersin.org/articles/10.3389/fphy.2021.636070/full#supplementary-material

REFERENCES

1. Abolhasani M, Jensen KF. Oscillatory multiphase flow strategy for chemistry and biology. *Lab Chip*. (2016) 16:2775–84. doi: 10.1039/C6LC00728G
2. Lestari G, Salari A, Abolhasani M, Kumacheva E. A microfluidic study of liquid-liquid extraction mediated by carbon dioxide. *Lab Chip*. (2016) 16:2710–8. doi: 10.1039/C6LC00597G
3. Tabeling P, Chabert M, Dodge A, Jullien C, Okkels F. Chaotic mixing in cross-channel micromixers. *Philos Trans R Soc Lond Ser A Math*. (2004) 362:987–1000. doi: 10.1098/rsta.2003.1358
4. Vishwanathan G, Juarez G. Generation and application of sub-kilohertz oscillatory flows in microchannels. *Microfluid Nanofluid*. (2020) 24:1–10. doi: 10.1007/s10404-020-02373-z
5. Xie Y, Chindam C, Nama N, Yang S, Lu M, Zhao Y, et al. Exploring bubble oscillation and mass transfer enhancement in acoustic-assisted liquid-liquid extraction with a microfluidic device. *Sci Rep*. (2015) 5:12572. doi: 10.1038/srep12572
6. Glasgow I, Lieber S, Aubry N. Parameters influencing pulsed flow mixing in microchannels. *Anal Chem*. (2004) 76:4825–32. doi: 10.1021/ac049813m
7. Glasgow I, Aubry N. Enhancement of microfluidic mixing using time pulsing. *Lab Chip*. (2003) 3:114–20. doi: 10.1039/B302569A
8. Qu J, Wu H, Cheng P, Wang Q, Sun Q. Recent advances in MEMS-based micro heat pipes. *Int J Heat Mass Transf*. (2017) 110:294–313. doi: 10.1016/j.ijheatmasstransfer.2017.03.034
9. Mutlu BR, Edd JF, Toner M. Oscillatory inertial focusing in infinite microchannels. *Proc Natl Acad Sci USA*. (2018) 115:7682–7. doi: 10.1073/pnas.1721420115
10. Alizadehgiashi M, Khabibullin A, Li Y, Prince E, Abolhasani M, Kumacheva E. Shear-induced alignment of anisotropic nanoparticles in a single-droplet oscillatory microfluidic platform. *Langmuir*. (2018) 34:322–30. doi: 10.1021/acs.langmuir.7b03648
11. Jo K, Chen YL, De Pablo JJ, Schwartz DC. Elongation and migration of single DNA molecules in microchannels using oscillatory shear flows. *Lab Chip*. (2009) 9:2348–55. doi: 10.1039/b902292a
12. Signe Mamba S, Magniez JC, Zoueshtiagh F, Baudoin M. Dynamics of a liquid plug in a capillary tube under cyclic forcing: memory effects and airway reopening. *J Fluid Mech*. (2018) 838:165–91. doi: 10.1017/jfm.2017.828
13. Signe Mamba S, Zoueshtiagh F, Baudoin M. Pressure-driven dynamics of liquid plugs in rectangular microchannels: influence of the transition between quasi-static and dynamic film deposition regimes. *Int J Multiph Flow*. (2019) 113:343–57. doi: 10.1016/j.ijmultiphaseflow.2018.10.019
14. Huh D. A human breathing lung-on-a-chip. *Ann ATS*. (2015) 12:S42–4. doi: 10.1513/AnnalsATS.201410-442MG
15. Atencia J, Beebe DJ. Controlled microfluidic interfaces. *Nature*. (2005) 437:648–55. doi: 10.1038/nature04163
16. Reyes DR, Iossifidis D, Auroux PA, Manz A. Micro total analysis systems. 1. Introduction, theory, and technology. *Anal Chem*. (2002) 74:2623–36. doi: 10.1021/ac0202435
17. Stone HA, Stroock AD, Ajdari A. Engineering flows in small devices: microfluidics toward a lab-on-a-chip. *Annu Rev Fluid Mech*. (2004) 36:381–411. doi: 10.1146/annurev.fluid.36.050802.122124
18. Vishwanathan G, Juarez G. Steady streaming flows in viscoelastic liquids. *J Nonnewton Fluid Mech*. (2019) 271:104143. doi: 10.1016/j.jnnfm.2019.07.007
19. Ebagninin KW, Benchabane A, Bekkour K. Rheological characterization of poly(ethylene oxide) solutions of different molecular weights. *J Colloid Interface Sci*. (2009) 336:360–67. doi: 10.1016/j.jcis.2009.03.014
20. Zhou MY, Sheng P. First-principles calculations of dynamic permeability in porous media. *Phys Rev B*. (1989) 39:12027. doi: 10.1103/PhysRevB.39.12027
21. Castro M, Bravo-Gutiérrez ME, Hernández-Machado A, Corvera Poiré E. Dynamic characterization of permeabilities and flows in microchannels. *Phys Rev Lett*. (2008) 101:224501. doi: 10.1103/PhysRevLett.101.224501
22. López de Haro M, del Rio JA, Whitaker S. Flow of Maxwell fluids in porous media. *Transp Porous Media*. (1996) 25:167–92. doi: 10.1007/BF00135854
23. del Rio JA, López de Haro M, Whitaker S. Enhancement in the dynamic response of a viscoelastic fluid flowing in a tube. *Phys Rev E*. (1998) 58:6323. doi: 10.1103/PhysRevE.58.6323

24. Collepardo-Guevara R, Corvera Poiré E. Controlling viscoelastic flow by tuning frequency during occlusions. *Phys Rev E*. (2007) 76:026301. doi: 10.1103/PhysRevE.76.026301
25. Corvera Poiré E, Hernández-Machado A. (2010). Frequency-induced stratification in viscoelastic microfluidics. *Langmuir*. (2010) 26:15084. doi: 10.1021/la1024422
26. Bravo-Gutiérrez ME, Castro M, Hernández-Machado A, Corvera Poiré E. Controlling viscoelastic flow in microchannels with slip. *Langmuir*. (2011) 27:2075. doi: 10.1021/la103520a
27. Tsiklauri D, Beresnev I. Enhancement in the dynamic response of a viscoelastic fluid flowing through a longitudinally vibrating tube. *Phys Rev E*. (2001) 63:046304. doi: 10.1103/PhysRevE.63.046304
28. Torres Rojas AM, Pagonabarrraga I, Corvera Poiré E. Resonances of Newtonian fluids in elastomeric microtubes. *Phys Fluids*. (2917) 29:122003 doi: 10.1063/1.5001061
29. Torres Rojas AM, Corvera Poiré E. Cooperation and competition of viscoelastic fluids and elastomeric microtubes subject to pulsatile forcing. *Phys Rev Fluids*. (2020) 5:063303. doi: 10.1103/PhysRevFluids.5.063303
30. Lombard J, Pagonabarraga I, Corvera Poiré E. Dynamic permeability of a compressible binary fluid mixture. *Phys Rev Fluids*. (2020) 5:064201. doi: 10.1103/PhysRevFluids.5.064201
31. Castrejón-Pita JR, del Río JA, Castrejón-Pita AA, Huelsz G. Experimental observation of dramatic differences in the dynamic response of Newtonian and Maxwellian fluids. *Phys Rev E*. (2003) 68:046301. doi: 10.1103/PhysRevE.68.046301
32. Torralba M, Castrejón-Pita JR, Castrejón-Pita AA, Huelsz G, Del Río JA, Ortin J. Measurements of the bulk and interfacial velocity profiles in oscillating Newtonian and Maxwellian fluids. *Phys Rev E*. (2005) 72:016308. doi: 10.1103/PhysRevE.72.016308
33. Vazquez-Vergara P, Torres-Herrera U, Olguin LF, Corvera Poiré E. Singular behavior of microfluidic pulsatile flow due to dynamic curving of air-fluid interfaces. *Phys Rev Fluids*. (2021) 6:024003. doi: 10.1103/PhysRevFluids.6.024003
34. Srinivasan V, Kumar S, Asfer M, Khandekar S. Oscillation of an isolated liquid plug inside a dry capillary. *Heat Mass Transf Stoffuebertragung*. (2017) 53:3353–62. doi: 10.1007/s00231-017-2064-x
35. Wang B, Xu JL, Zhang W, Li YX. A new bubble-driven pulse pressure actuator for micromixing enhancement. *Sens Actuat A Phys*. (2011) 169:194–205. doi: 10.1016/j.sna.2011.05.017
36. Khoshmanesh K, Almansouri A, Albloushi H, Yi P, Soffe R, Kalantar-zadeh K. A multi-functional bubble-based microfluidic system. *Sci Rep*. (2015) 5:9942. doi: 10.1038/srep09942
37. Basilio PA, Torres Rojas AM, Corvera Poire E, Olguín LF. Stream of droplets as an actuator for oscillatory flows in microfluidics. *Microfluid Nanofluid*. (2019) 23:64. doi: 10.1007/s10404-019-2237-7
38. Vázquez-Vergara P, Torres Rojas AM, Guevara-Pantoja PE, Corvera Poiré E, Caballero-Robledo GA. Microfluidic flow spectrometer. *J Micromech Microeng*. (2017) 27:077001. doi: 10.1088/1361-6439/aa71c2
39. Moschopoulos P, Dimakopoulos Y, Tsamopoulos J. Electro-osmotic flow of electrolyte solutions of PEO in microfluidic channels. *J Colloid Interface Sci*. (2020) 563:381–93. doi: 10.1016/j.jcis.2019.12.052
40. Pérez-Salas KY, Sánchez S, Ascanio G, Aguayo JP. Analytical approximation to the flow of a sPTT fluid through a planar hyperbolic contraction. *J Nonnewton Fluid Mech*. (2019) 272:104160. doi: 10.1016/j.jnnfm.2019.104160
41. Mathues W, Formenti S, McIlroy C, Harlen OG, Clasen C. CaBER vs ROJER-Different time scales for the thinning of a weakly elastic jet. *J Rheol*. (2018) 62:1135–53. doi: 10.1122/1.5021834
42. Zatloukal M. Differential viscoelastic constitutive equations for polymer melts in steady shear and elongational flows. *J Nonnewton Fluid Mech*. (2003) 113:209–27. doi: 10.1016/S0377-0257(03)00112-5
43. Gupta S, Wang WS, Vanapalli SA. Microfluidic viscometers for shear rheology of complex fluids and biofluids. *Biomicrofluidics*. (2016) 10:043402. doi: 10.1063/1.4955123
44. Zilz J, Schäfer C, Wagner C, Poole RJ, Alves MA, Lindner A. Serpentine channels: micro-rheometers for fluid relaxation times. *Lab Chip*. (2014) 14:351–8. doi: 10.1039/C3LC50809A
45. Casanellas L, Alves MA, Poole RJ, Lerouge S, Lindner A. The stabilizing effect of shear thinning on the onset of purely elastic instabilities in serpentine microflows. *Soft Matter*. (2016) 12:6167–75. doi: 10.1039/C6SM00326E
46. Del Giudice F, Haward SJ, Shen AQ. Relaxation time of dilute polymer solutions: a microfluidic approach. *J Rheol*. (2017) 61:327–37. doi: 10.1122/1.4975933
47. Vadillo DC, Mathues W, Clasen C. Microsecond relaxation processes in shear and extensional flows of weakly elastic polymer solutions. *Rheol Acta*. (2012) 51:755–69. doi: 10.1007/s00397-012-0640-z
48. Rodd LE, Scott TP, Cooper-White JJ, McKinley GH. Capillary break-up rheometry of low-viscosity elastic fluids. *Appl Rheol*. (2005) 15:12–27. doi: 10.1515/arh-2005-0001
49. Cao BH, Kim MW. Molecular weight dependence of the surface tension of aqueous poly (ethylene oxide) solutions. *Faraday Discuss*. (1994) 98:245–52. doi: 10.1039/fd9949800245
50. Ogilvie IRG, Sieben VJ, Floquet CFA, Zmijan R, Mowlem MC, Morgan H. Reduction of surface roughness for optical quality microfluidic devices in PMMA and COC. *J Micromech Microeng*. (2010) 20:065016. doi: 10.1088/0960-1317/20/6/065016
51. Zhang Z, Wang X, Luo Y, He S, Wang L. Thermal assisted ultrasonic bonding method for poly(methyl methacrylate)(PMMA) microfluidic devices. *Talanta*. (2010) 81:1331–8. doi: 10.1016/j.talanta.2010.02.031
52. Lei D, Lin M, Li Y, Jiang W. A two-angle model of dynamic wetting in microscale capillaries under low capillary numbers with experiments. *J Colloid Interface Sci*. (2018) 520:91–100. doi: 10.1016/j.jcis.2018.02.074
53. Kim JH, Rothstein JP. Dynamic contact angle measurements of viscoelastic fluids. *J Nonnewton Fluid Mech*. (2015) 225:54–61. doi: 10.1016/j.jnnfm.2015.09.007
54. Johnson RE, Dettre RH, Brandreth DA. Dynamic contact angles and contact angle hysteresis. *J Colloid Interface Sci*. (1977) 62:205–12. doi: 10.1016/0021-9797(77)90114-X
55. Hoffman RL. A study of the advancing interface. I. Interface shape in liquid-gas systems. *J Colloid Interface Sci*. (1975) 50:228–41. doi: 10.1016/0021-9797(75)90225-8
56. Dettre RH, Johnson RE Jr. Contact angle hysteresis. IV. Contact angle measurements on heterogeneous surfaces. *J Phys Chem*. (1965) 69:1507–15. doi: 10.1021/j100889a012
57. Gao L, McCarthy TJ. Contact angle hysteresis explained. *Langmuir*. (2006) 22:6234–7. doi: 10.1021/la060254j
58. Morrison FA. *Understanding Rheology*. New York, NY: Oxford University Press (2001).
59. Broer LJF. On the hydrodynamics of visco-elastic fluids. *Appl Sci Res A*. (1956) 6:226–36. doi: 10.1007/BF03185038
60. Cross MM. Rheology of non-Newtonian fluids: a new flow equation for pseudoplastic systems. *J Colloid Sci*. (1965) 20:417–37. doi: 10.1016/0095-8522(65)90022-X
61. Dinic J, Zhang Y, Jimenez LN, Sharma V. Extensional relaxation times of dilute, aqueous polymer solutions. *ACS Macro Lett*. (2015) 4:804–8. doi: 10.1021/acsmacrolett.5b00393
62. Flores Gerónimo J, Hernández-Machado A, Corvera Poiré E. Enhanced imbibition from the cooperation between wetting and inertia via pulsatile forcing. *Phys Fluids*. (2019) 31:032107. doi: 10.1063/1.5086028
63. Tabeling P. *Introduction to Microfluidics*. New York, NY: Oxford University Press (2005).
64. Torres-Herrera U. Dynamic permeability of fluids in rectangular and square microchannels: shift and coupling of viscoelastic bidimensional resonances. *Phys Fluids*. (2021) 33:012016. doi: 10.1063/5.0038099
65. Barthel MJ, Schacher FH, Schubert US. Poly (ethylene oxide)(PEO)-based ABC triblock terpolymers-synthetic complexity vs. application benefits. *Polymer Chem*. (2014) 5:2647–62. doi: 10.1039/C3PY01666H
66. Dai G, Kaazempur-Mofrad MR, Natarajan S, Zhang Y, Vaughn S, Blackman BR, et al. Distinct endothelial phenotypes evoked by arterial waveforms derived from atherosclerosis-susceptible and -resistant regions of human vasculature. *Proc Natl Acad Sci USA*. (2004) 101:14871–6. doi: 10.1073/pnas.0406073101
67. Weibel DB, Whitesides GM. Applications of microfluidics in chemical biology. *Curr Opin Chem Biol*. (2006) 10:584–91. doi: 10.1016/j.cbpa.2006.10.016

68. Meldrum DR, Holl MR. Microscale bioanalytical systems. *Science*. (2002) 297:1197–8. doi: 10.1126/science.297.5584.1197
69. Sato M, Ohashi T. Biorheological views of endothelial cell responses to mechanical stimuli. *Biorheology*. (2005) 42:421–41.
70. McCue S, Noria S, Langille BL. Shear-induced reorganization of endothelial cell cytoskeleton and adhesion complexes. *Trends Cardiovasc Med*. (2004) 14:143–51. doi: 10.1016/j.tcm.2004.02.003
71. Yoshino D, Funamoto K, Sato K, Sato M, Lim CT. Hydrostatic pressure promotes endothelial tube formation through aquaporin 1 and Ras-ERK signaling. *Commun Biol*. (2020) 3:1–11. doi: 10.1038/s42003-020-0881-9

Conflict of Interest: The authors declare that the research was conducted in the absence of any commercial or financial relationships that could be construed as a potential conflict of interest.

frontiers in Physics

ORIGINAL RESEARCH
published: 17 June 2021
doi: 10.3389/fphy.2021.642364

Semiflexible Polymer Enclosed in a 3D Compact Domain

Pavel Castro-Villarreal[1]* *and J. E. Ramírez*[2]*

[1]Facultad de Ciencias en Física y Matemáticas, Universidad Autónoma de Chiapas, Tuxtla Gutiérrez, Mexico, [2]Centro de Agroecología, Instituto de Ciencias, Benemérita Universidad Autónoma de Puebla, Puebla, Mexico

The conformational states of a semiflexible polymer enclosed in a volume $V := \ell^3$ are studied as stochastic realizations of paths using the stochastic curvature approach developed in [Rev. E 100, 012503 (2019)], in the regime whenever $3\ell/\ell_p > 1$, where ℓ_p is the persistence length. The cases of a semiflexible polymer enclosed in a cube and sphere are considered. In these cases, we explore the Spakowitz–Wang–type polymer shape transition, where the critical persistence length distinguishes between an oscillating and a monotonic phase at the level of the mean-square end-to-end distance. This shape transition provides evidence of a universal signature of the behavior of a semiflexible polymer confined in a compact domain.

Keywords: semiflexible polymer, stochastic curvature, shape transition, critical persistence length, mean-square end-to-end distance, worm-like chain

OPEN ACCESS

Edited by:
Atahualpa Kraemer, National Autonomous University of Mexico, Mexico

Reviewed by:
Pramod Kumar Mishra, Kumaun University, India
Wolfhard Janke, Universität Leipzig, Germany
Enrique Hernandez-Lemus, Instituto Nacional de Medicina Genómica (INMEGEN), Mexico

***Correspondence:**
Pavel Castro-Villarreal
pcastrov@unach.mx
J. E. Ramírez
jerc.fis@gmail.com

Specialty section:
This article was submitted to Interdisciplinary Physics, a section of the journal Frontiers in Physics

Received: *15 December 2020*
Accepted: *19 May 2021*
Published: *17 June 2021*

Citation:
Castro-Villarreal P and Ramírez JE (2021) Semiflexible Polymer Enclosed in a 3D Compact Domain. Front. Phys. 9:642364. doi: 10.3389/fphy.2021.642364

1 INTRODUCTION

Semiflexible polymers is a term coined to understand a variety of physical systems that involve linear molecules. The most popular polymers are industrial plastics, like polyethylene or polystyrene, with various applications in daily life [1, 2]. Another prominent example is the DNA compacted in the nucleus of cells or viral DNA/RNA packed in capsids [3, 4]. These last examples are of particular interest since they are confined semiflexible polymers. Indeed, biopolymers' functionality is ruled by their conformation, which in turn is considerably modified in the geometrically confined or crowded environment inside the cell [5–7].

A common well-known theoretical framework used to describe the fundamental properties of a semiflexible polymer is the well-known worm-like chain model (WLC), which pictures a polymer as a thin wire with a flexibility given by its bending rigidity constant α [8]. The central quantity in this model is the persistence length defined by $2\alpha/(k_BT(d-1))$ [9, 10], with d being the space dimension; however, here we simply use $\ell_p := \alpha/(k_BT)$[1], which is the characteristic length along the chain over which the directional correlation between segments disappears. k_BT is the thermal energy, with k_B and T being the Boltzmann constant and the bath temperature, respectively [11].

In the absence of thermal fluctuations, when $\alpha \gg k_BT$, the conformations of the polymer are well understood through different curve configurations determined by variational principles [12, 13]. For the WLC model, the bending energy functional is given by

$$H[\mathbf{R}] = \frac{\alpha}{2}\int ds\kappa^2(s), \tag{1}$$

[1]For the sake of notation, the dimension of the space in the persistence length definition is hidden. In those cases where an explicit dependence on the dimension is needed, it should be adequately scaled by the factor $2/(d-1)$.

where $\mathbf{R}(s)$ is a polymer configuration and $\kappa(s)$ is the curvature of the chain, with s being the arc-length parameter. Additional terms can be added to the Hamiltonian to account for other effects, including multibody interactions, external fields, and constraints on the chain dimensions [14, 15]. When the thermal fluctuations are relevant, that is, $\alpha \simeq k_B T$, then it is usual to introduce a statistical mechanics description. Since $H[\mathbf{R}]$ represents the bending energy for a curve configuration $\mathbf{R}$, the most natural approach is to define the canonical probability density

$$\mathcal{P}(\boldsymbol{R})\mathcal{D}\boldsymbol{R} := \frac{1}{\mathcal{Z}_c}\exp\left(-\frac{\ell_p}{2}\int ds\kappa^2(s)\right)\mathcal{D}\boldsymbol{R}, \tag{2}$$

where $\mathcal{Z}_c$ is the canonical partition function and $\mathcal{D}\boldsymbol{R}$ is an appropriate functional measure. In this description, the theory turns out to be a one-dimensional statistical field theory. Nonetheless, the theory is not easy to tackle since $\kappa(s)$ acquires nonlinear terms in $\mathbf{R}$. To avoid this difficulty, a different perspective was introduced by Saito's et al. [8], where the following probability density function was studied:

$$\mathcal{P}(\boldsymbol{T})\mathcal{D}\boldsymbol{T} := \frac{1}{\mathcal{Z}_s}\exp\left(-\frac{\ell_p}{2}\int ds\kappa^2(s)\right)\mathcal{D}\boldsymbol{T}, \tag{3}$$

instead of **Eq. 2**. Here $\mathcal{Z}_s$ is the Saito's partition function and $\mathcal{D}\mathbf{T}$ is an appropriate functional measure for the tangent direction of a given polymer configuration $\mathbf{R}$. The Saito's partition function can be solved since one has $\kappa^2(s) = (d\mathbf{T}(s)/ds)^2$; thus, one can relate $\mathcal{Z}_s$ with the Feynman's partition function for a quantum particle in the spherical surface described by $\mathbf{T}^2 = 1$. For the cases when the semiflexible polymer is in an open Euclidean space, the Saito's approach works very well. For instance, it reproduces the standard results of Kratky–Porod [16], among other results [8, 14]. However, for the cases when the semiflexible polymer is confined to a bounded region of the space, the Saito's approach is difficult to use, with some exceptional cases like the situation for semiflexible polymers confined to a spherical shell [24].

For semiflexible polymers in plane space, an alternative theoretical approach to the above formalisms was introduced in [17]. This consists of postulating that each conformational realization of any polymer in the plane is described by a stochastic path satisfying the stochastic Frenet equations, defined by $\frac{d}{ds}\mathbf{R}(s) = \mathbf{T}(s)$ and $\frac{d}{ds}\mathbf{T}(s) = \kappa(s)\mathbf{N}(s)$, where $\mathbf{R}(s)$ is the configuration of the polymer, $\mathbf{T}(s)$ is the tangent vector to the curve describing the chain at s, $\mathbf{N}(s) := \epsilon\mathbf{T}(s)$ is the normal stochastic unit vector, with ϵ a rotation by an angle of $\pi/2$, and $\kappa(s)$ is the stochastic curvature that satisfies the following probability density function:

$$\mathcal{P}(\kappa)\mathcal{D}\kappa := \frac{1}{\mathcal{Z}_{s-c}}\exp\left(-\frac{\ell_p}{2}\int ds\kappa^2(s)\right)\mathcal{D}\kappa, \tag{4}$$

where $\mathcal{Z}_{s-c}$ is the partition function in the stochastic curvature formalism and $\mathcal{D}\kappa$ is an appropriate measure for the curvature. This, in particular, implies a white noise-like structure, that is, $\langle\kappa(s)\rangle = 0$ and $\langle\kappa(s)\kappa(s')\rangle = \delta(s-s')/\ell_p$ [17]. This theoretical framework successfully explains, by first principles, the Kratky–Porod results for free chains confined to an open 2D-plane. Moreover, it correctly describes the mean-square end-to-end distance for semiflexible polymers confined to a square box, a key descriptor of the statistical behavior of a polymer chain.

In the present work, we carry out an extension of the stochastic curvature approach for semiflexible polymers in the three-dimensional space $\mathbb{R}^3$. In particular, we analyze the conformational states of a semiflexible polymer enclosed in a bounded region in three-dimensional space. This polymer is in a thermal bath with a uniform temperature. The shapes adopted by the polymer are studied through the mean-square end-to-end distance as a function of the polymer total length as well as its persistence length. In particular, we analyze the cases of a polymer confined to a cube of side a and a sphere of radius R.

The plan of this article is as follows. In **Section 2**, we introduce the stochastic Frenet equations for the semiflexible polymers in three-dimensional spaces, and by using a standard procedure, we derive the corresponding Fokker–Planck equation. In particular, the Kratky–Porod result for polymers in a 3D open space is obtained. **Section 3** contains the derivation of the mean-square end-to-end distance for semiflexible polymers confined to a compact domain. In **Section 4**, we present the analysis of the mean square end-to-end distance for the cases when the compact domain corresponds with a cube of side a and a sphere of radius R. Finally, **Section 5** contains our concluding remarks.

2 PRELIMINARY NOTATION AND SEMIFLEXIBLE POLYMERS IN 3D

Let us consider a polymer in a three-dimensional Euclidean space $\mathbb{R}^3$ as a space curve γ, $\mathbf{R}: I \subset \mathbb{R} \to \mathbb{R}^3$, parametrized by an arc-length, s. For each point $s \in I$, a Frenet–Serret trihedron can be defined in terms of the vector basis $\{\mathbf{T}(s), \mathbf{N}(s), \mathbf{B}(s)\}$, where $\mathbf{T}(s) = d\mathbf{R}/ds$ is the tangent vector, whereas $\mathbf{N}(s)$ and $\mathbf{B}(s)$ are the normal and bi-normal vectors, respectively. It is well known that each regular curve γ satisfies the Frenet–Serret structure equations, namely, $d\mathbf{T}/ds = \kappa(s)\mathbf{N}$, $d\mathbf{N}/ds = -\kappa(s)\mathbf{T} - \tau(s)\mathbf{B}$ and $d\mathbf{B}/ds = \tau(s)\mathbf{N}$, where $\kappa(s)$ and $\tau(s)$ are the curvature and the torsion of the space curve, respectively. In addition, the fundamental theorem of space curves estates that given continuous functions $\kappa(s)$ and $\tau(s)$, one can determine the shape curve uniquely, up to a Euclidean rigid motion [18].

2.1 Stochastic Curvature Approach in 3D

In order to study the conformational states of a semiflexible polymer, we adapt the stochastic curvature approach introduced in [17] to the case of semiflexible polymers in 3D Euclidean space. For the 2D Euclidean space, the formalism starts by postulating that each conformational realization of any polymer is described by a stochastic path satisfying the stochastic Frenet equations. In the 3D case, it is enough to consider the following stochastic equations:

$$\frac{d}{ds}\mathbf{R}(s) = \mathbf{T}(s), \tag{5a}$$

$$\frac{d}{ds}\mathbf{T}(s) = \mathbb{P}_{\mathbf{T}}\boldsymbol{\kappa}(s), \tag{5b}$$

where $\mathbf{R}(s)$, $\mathbf{T}(s)$, and $\boldsymbol{\kappa}(s)$ are now random variables. Here, $\boldsymbol{\kappa}(s)$ is named as stochastic vectorial curvature. Also, a normal projection operator $\mathbb{P}_{\mathbf{T}} = 1 - \mathbf{T} \otimes \mathbf{T}$ has been introduced such that $\mathbf{T}(s) \cdot \frac{d}{ds}\mathbf{T}(s) = 0$. According to these equations, it can be shown that $|\mathbf{T}(s)|$ is a constant that can be fixed to unit, where $|\ |$ is the standard 3D Euclidean norm. The remaining geometrical notions also turn into random variables as follows. The stochastic curvature is defined by $\kappa(s) := |\boldsymbol{\kappa}(s)|$. The stochastic normal and bi-normal vectors are defined by $\mathbf{N}(s) := \boldsymbol{\kappa}(s)/\kappa(s)$ and $\mathbf{B}(s) := \mathbf{T}(s) \times \boldsymbol{\kappa}(s)/\kappa(s)$, respectively, where $\kappa(s)$ is the stochastic curvature. In addition, the stochastic torsion is defined with the equation $\tau(s) := \mathbf{N}(s) \cdot \frac{d}{ds}\mathbf{B}(s)$.

In addition to the stochastic **Eq. 5a** and **Eq. 5b**, the random variable $\boldsymbol{\kappa}(s)$ is distributed according to the probability density function

$$\mathcal{P}(\boldsymbol{\kappa})\mathcal{D}\boldsymbol{\kappa} := \frac{1}{\mathcal{Z}_{\mathrm{s-c}}} \exp\left(-\beta H[\boldsymbol{\kappa}]\right)\mathcal{D}\boldsymbol{\kappa}, \tag{6}$$

where $H[\boldsymbol{\kappa}] = \frac{\alpha}{2}\int \boldsymbol{\kappa}^2 ds$ is the bending energy and α is the bending rigidity modulus. This energy functional corresponds to the continuous form of the WLC model [8]. Also, in **Eq. 6**, $\mathcal{Z}_{\mathrm{s-c}}$ is an appropriate normalization constant, $\mathcal{D}\boldsymbol{\kappa} := \prod_{i=1}^{3}\mathcal{D}\kappa_i$ is a functional measure, and $\beta = 1/k_B T$ is the inverse of the thermal energy. The Gaussian structure of the probability density implies the zero mean $\langle \kappa_i(s)\rangle = 0$ and the following 3*D* fluctuation theorem:

$$\langle \kappa_i(s)\kappa_j(s')\rangle = \frac{1}{\ell_p}\delta_{ij}\delta(s-s'), \tag{7}$$

where $\kappa_i(s)$ is the i–th component of the stochastic vectorial curvature $\boldsymbol{\kappa}(s)$.

2.2 From Frenet–Serret Stochastic Equations to Hermans–Ullman Equation in 3D

In this section, we present the Fokker–Planck formalism corresponding to the stochastic **Eq. 5a** and **Eq. 5b**. This description allows us to determine an equation for the probability density function associated to the position and direction of the endings of the polymer $P(\mathbf{R}, \mathbf{T}|\mathbf{R}', \mathbf{T}'; s) = \langle \delta(\mathbf{R} - \mathbf{R}(s))\delta(\mathbf{T} - \mathbf{T}(s))\rangle$, where $\mathbf{R}$ and $\mathbf{R}'$ are the ending positions of the polymer, and $\mathbf{T}$ and $\mathbf{T}'$ are the corresponding directions, respectively. The parameter s is the polymer length.

Now, the stochastic Frenet–Serret **Eq. 5a** and **Eq. 5b** can be identified with a multidimensional stochastic differential equation in the Stratonovich perspective; thus, applying the standard procedure [19], we find the following Fokker–Planck type equation:

$$\frac{\partial P}{\partial s} + \nabla \cdot (\mathbf{T}\, P) = \frac{1}{2\ell_p}\Delta_g P, \tag{8}$$

where $\mathbf{T}$ is identified with the unit normal vector on S^2, thus satisfying the condition $\mathbf{T}^2 = 1$. The operator Δ_g is the Laplace–Beltrami of the sphere S^2. Similarly, as the situation for semiflexible polymers confine to a plane space [17], this equation is exactly the same as the one obtained by Hermans and Ullman in 1952 [20], where the heuristic parameter they included can now be identified exactly with $1/(2\ell_p)$. In addition, we can make a contact with the Saito's approach [8] by considering the marginal probability density function:

$$\mathcal{Z}_{\mathrm{s}}(\mathbf{T}, \mathbf{T}', s) \propto \int d^3\mathbf{R} d^3\mathbf{R}' P(\mathbf{R}, \mathbf{T}|\mathbf{R}', \mathbf{T}', s). \tag{9}$$

Using the Hermans–Ullman equation, we can show that $\mathcal{Z}_{\mathrm{c}}$ satisfies a diffusion equation on a spherical surface with diffusion coefficient equal to $1/(2\ell_p)$ [8], that is,

$$\frac{\partial \mathcal{Z}_{\mathrm{c}}}{\partial s} = \frac{1}{2\ell_p}\Delta_{S^2}\mathcal{Z}_{\mathrm{s}}. \tag{10}$$

An immediate consequence of the above equation is the exponential decay of the correlation function between the two ending directions $C(L) := \langle \mathbf{T}(L) \cdot \mathbf{T}(0)\rangle = \exp(-L/\ell_p)$, where L is the polymer length. Indeed, this expectation value satisfies the following equation: $\frac{d}{ds}C(s) = \frac{1}{2\ell_p}\frac{1}{4\pi}\int_{S^2} d\Omega\, (\mathbf{T}(s) \cdot \mathbf{T}(s'))\Delta_{S^2}\mathbb{Z}$, where $d\Omega$ is the solid angle and 4π is a normalization constant. Now, we can integrate twice by parts the r.h.s of last equation and since S^2 is a compact manifold the boundary terms vanish. Also, using $\Delta_{S^2}\mathbf{T} = -\frac{2}{R^2}\mathbf{T}$, it is found that the correlation function satisfies the ordinary differential equation $\frac{d}{ds}C(s) = -\frac{2}{R^2}C(s)$. Now, we solve this equation using the initial condition $C(s' = 0) = 1$ and the length of the polymer set up by $s = L$.

2.3 Modified Telegrapher Equation

As in the situation of the two-dimensional case [17], we carry out a multipolar decomposition for HU equation in 3D. This consists of expanding the probability density function $P(\mathbf{R}, \mathbf{T}|\mathbf{R}', \mathbf{T}'; s)$ in a linear combination of the Cartesian tensor basis elements 1, T_i, $T_iT_j - \frac{1}{3}\delta_{ij}$, $T_iT_jT_k - \frac{1}{5}\delta_{(ij}T_{k)}$, $\cdots$, where the symbols (ijk) means symmetrization of the indices i, j, and k, that is, $\delta_{(ij}T_{k)} = \delta_{ij}T_k + \delta_{jk}T_i + \delta_{ki}T_j$ whose expansion coefficients are hydrodynamic-like tensor fields. These tensors are $\rho(\mathbf{R}, s)$, meaning by the manner how the ending positions are distributed in the space; $\mathbb{P}(\mathbf{R}, s)$, meaning as the local average of the polymer direction; $\mathbb{Q}_{ij}(\mathbf{R}, s)$, pointing the way how the directions are correlated along the points of the space, etc. These tensors are the moments associated to the Cartesian tensor basis, for example, $\mathbb{P}_i = \int \frac{d\Omega}{4\pi}T_i P(\mathbf{R}, \mathbf{T}, s)$. These fields satisfy the following hierarchy equations:

$$\frac{\partial \rho(\mathbf{R}, s)}{\partial s} = -\partial_i \mathbb{P}^i(\mathbf{R}, s), \tag{11}$$

$$\frac{\partial \mathbb{P}_i(\mathbf{R}, s)}{\partial s} = -\frac{1}{\ell_p}\,\mathbb{P}_i(\mathbf{R}, s) - \frac{1}{3}\,\partial_i \rho(\mathbf{R}, s) - \partial^j \mathbb{Q}_{ij}(\mathbf{R}, s), \tag{12}$$

$$\frac{\partial \mathbb{Q}_{ij}(\mathbf{R}, s)}{\partial s} = -\frac{3}{\ell_p}\mathbb{Q}_{ij}(\mathbf{R}, s) - \frac{1}{5}\mathbb{T}_{ij}(\mathbf{R}, s) - \partial^k \mathbb{R}_{ijk}(\mathbf{R}, s), \tag{13}$$

where $\mathbb{T}^{ij} = \partial^i \mathbb{P}^j + \partial^j \mathbb{P}^i - \frac{2\delta^{ij}}{3}\partial_k \mathbb{P}^k$.

Now, by combining **Eq. 11** and **Eq. 12**, we can obtain a modified telegrapher equation:

$$\frac{\partial^2\rho(\mathbf{R},s)}{\partial s^2}+\frac{1}{\ell_p}\frac{\partial\rho(\mathbf{R},s)}{\partial s}=\frac{1}{3}\nabla^2\rho(\mathbf{R},s)+\partial_i\partial_j\mathbb{Q}^{ij}(\mathbf{R},s), \tag{14}$$

where ∇^2 is the 3D Laplacian. In a mean-field point of view, one can consider the preceding equation as an equation for the probability density function $\rho(\mathbf{R},s)$ under the presence of a mean-field $\mathbb{Q}_{ij}(\mathbf{R},s)$. In particular, $\mathbb{Q}_{ij}(\mathbf{R},s)$ does not play any role for the mean-square end-to-end distance for a semiflexible polymer in the open Euclidean 3D space. Indeed, let us define the end-to-end distance as $\delta\mathbf{R}:=\mathbf{R}-\mathbf{R}'$; thus, the mean-square end-to-end distance is given by

$$\langle\delta\mathbf{R}^2\rangle_{\mathcal{D}}\equiv\int_{\mathcal{D}\times\mathcal{D}}\rho(\mathbf{R}|\mathbf{R}',s)\delta\mathbf{R}^2d^3\mathbf{R}d^3\mathbf{R}'. \tag{15}$$

Now, we implement the same procedure used in [17] to calculate the mean-square end-to-end distance in the open three-dimensional space $\mathcal{D}=\mathbb{R}^3$, where it is used as the modify telegrapher of **Eq. 14** and the traceless property of $\mathbb{Q}_{ij}(\mathbf{R},s)$. We can reproduce the standard Kratky–Porod [16] result for a semiflexible polymer in the three-dimensional space [16, 20].

$$\langle\delta\mathbf{R}^2\rangle_{\mathbb{R}^3}=2\ell_pL-2\ell_p^2\left(1-\exp\left(-\frac{L}{\ell_p}\right)\right) \tag{16}$$

with the typical well-known asymptotic limits: diffusive regime $\langle\delta\mathbf{R}^2\rangle\simeq 2\ell_pL$ for $L\gg\ell_p$, and ballistic regime $\langle\delta\mathbf{R}^2\rangle\simeq L^2$ for $L\ll\ell_p$.

3 SEMIFLEXIBLE POLYMER IN A COMPACT DOMAIN

In this section, we apply the hierarchy equations developed in the previous section in order to determine the conformational states of a semiflexible polymer confined to a compact volume domain of size V. From the hierarchy **Eq. 12** and **Eq. 13**, the tensors $\mathbb{P}_i(\mathbf{R},s)$ and $\mathbb{Q}_{ij}(\mathbf{R},s)$ damp out as e^{-L/ℓ_p} and e^{-3L/ℓ_p}, respectively. Furthermore, if we consider that the semiflexible polymer is enclosed in a compact volume $V:=\ell^3$, with a typical length ℓ; thus, as long as we consider cases when $3\ell/\ell_p$ is far from one, we may assume that $\mathbb{Q}_{ij}(\mathbf{R},s)$ is uniformly distributed. This condition corresponds to truncate the hierarchy equations at the second level; that is, the only equations that survive in this approximation are **Eq. 11** and **Eq. 12**.

In the latter situation, the distribution $\rho(\mathbf{R},s)$ of the endings of the semiflexible polymer is described through the following telegrapher's equation:

$$\frac{\partial^2\rho(\mathbf{R},s)}{\partial s^2}+\frac{1}{\ell_p}\frac{\partial\rho(\mathbf{R},s)}{\partial s}=\frac{1}{3}\nabla^2\rho(\mathbf{R},s) \tag{17}$$

that satisfies the initial conditions

$$\lim_{s\to 0}\rho(\mathbf{R}|\mathbf{R}',s)=\delta^{(3)}(\mathbf{R}-\mathbf{R}'), \tag{18}$$

$$\lim_{s\to 0}\frac{\partial\rho(\mathbf{R}|\mathbf{R}',s)}{\partial s}=0. \tag{19}$$

The condition **Eq. 18** means that the polymers' ends coincide when the polymer length is zero, whereas **Eq. 19** means that the polymer length does not change spontaneously. In addition, since the polymer is enclosed in the compact domain $\mathcal{D}$ of volume $V(\mathcal{D})$, we also impose a Neumann boundary condition

$$\nabla\rho(\mathbf{R}|\mathbf{R}',s)\big|_{\mathbf{R},\mathbf{R}'\in\partial D}=0,\quad\forall s, \tag{20}$$

where ∂D is a surface bounding the domain $\mathcal{D}$. This boundary condition means that the polymer does not cross the boundary neither wrap the domain. The procedure to obtain a solution of the above telegrapher's **Eq. 17** is identical to the one developed in [17]. We just have to take into account the right factors and the dimensionality considerations. In this sense, the probability density function is given by

$$\rho(\mathbf{R}|\mathbf{R}';s)=\frac{1}{V(\mathcal{D})}\sum_{\mathbf{k}\in I}G\left(\frac{s}{2\ell_p},\frac{4\ell_p^2}{3}\lambda_{\mathbf{k}}\right)\psi_{\mathbf{k}}^{\dagger}(\mathbf{R})\psi_{\mathbf{k}}(\mathbf{R}'), \tag{21}$$

where we recall from [17].

$$G(v,w)=e^{-v}\left[\cosh\left(v\sqrt{1-w}\right)+\frac{\sinh\left(v\sqrt{1-w}\right)}{\sqrt{1-w}}\right] \tag{22}$$

and $\{\psi_{\mathbf{k}}\}$ and $\{\lambda_{\mathbf{k}}\}$ are a complete set of orthonormal eigenfunctions and a set of corresponding eigenvalues of the Laplace operator $-\nabla^2$ in $\mathbb{R}^3$. Notice that each $\psi_{\mathbf{k}}(\mathbf{R})$ must satisfy the Neumann boundary equation $\nabla\psi_{\mathbf{k}}|_{\mathbf{R}\in\partial\mathcal{D}}=0$. In addition, it is known [21, 22] that for Neumann boundary Laplacian eigenvalue problem, there is a zero eigenvalue $\lambda_0=0$ corresponding to a positive eigenfunction given by $\psi_0=1/\sqrt{V}$.

Now, using **Eq. 21**, the mean-square end-to-end distance $\langle\delta\mathbf{R}^2\rangle_{\mathcal{D}}$ can be computed in the standard fashion by

$$\langle(\delta\mathbf{R})^2\rangle_{\mathcal{D}}=\sum_{\mathbf{k}\in I}a_kG\left(\frac{s}{2\ell_p},\frac{4\ell_p^2}{3}\lambda_{\mathbf{k}}\right), \tag{23}$$

where the coefficients of a_k are obtained from

$$a_k=\frac{1}{V(\mathcal{D})}\int_{\mathcal{D}\times\mathcal{D}}(\mathbf{R}-\mathbf{R}')^2\psi_{\mathbf{k}}^{\dagger}(\mathbf{R})\psi_{\mathbf{k}}(\mathbf{R}')d^3\mathbf{R}d^3\mathbf{R}'. \tag{24}$$

We can have a further simplification after squaring the end-to-end distance inside the last integral. It is not difficult to see that the square terms $\mathbf{R}^2$ and $\mathbf{R}'^2$ in $(\mathbf{R}-\mathbf{R}')^2$ only the zero mode contribute; thus, we have

$$\langle(\delta\mathbf{R})^2\rangle_{\mathcal{D}}=2\sigma^2(\mathbf{R})-\frac{2}{V(\mathcal{D})}\sum_{\mathbf{k}\neq 0}\mathbf{r}_{\mathbf{k}}^{*}\cdot\mathbf{r}_{\mathbf{k}}\,G\left(\frac{s}{2\ell_p},\frac{4\ell_p^2}{3}\lambda_{\mathbf{k}}\right), \tag{25}$$

where $\sigma^2(\mathbf{R}):=\langle\mathbf{R}^2\rangle_g-\langle\mathbf{R}\rangle_g^2$ is called the mean-square end position, $\langle\cdots\rangle_g:=\frac{1}{V(\mathcal{D})}\int_{\mathcal{D}}d^3\mathbf{R}\cdots$ is termed as the geometric average, and the factor $\mathbf{r}_{\mathbf{k}}:=\int_{\mathcal{D}}\mathbf{R}\psi_{\mathbf{k}}(\mathbf{R})d^3\mathbf{R}$ for $\mathbf{k}\neq 0$. The factor $\mathbf{r}_{\mathbf{k}}$ can be written in a simpler form for Neumann boundary conditions, since $\psi_{\mathbf{k}}=-\frac{1}{\lambda_{\mathbf{k}}}\nabla^2\psi_{\mathbf{k}}$, and by integrating out by parts, this factor is expressed in terms of a boundary integral

$$\mathbf{r}_{\mathbf{k}}=\frac{1}{\lambda_{\mathbf{k}}}\oint_{\partial\mathcal{D}}dS\,\mathbf{n}\psi_{\mathbf{k}}(\mathbf{R}_S), \tag{26}$$

where $\mathbf{R}_S\in\partial\mathcal{D}$ and dS is the area element of $\partial\mathcal{D}$. Since the function $G(v,w)$ decays exponentially as the polymer length gets larger values,

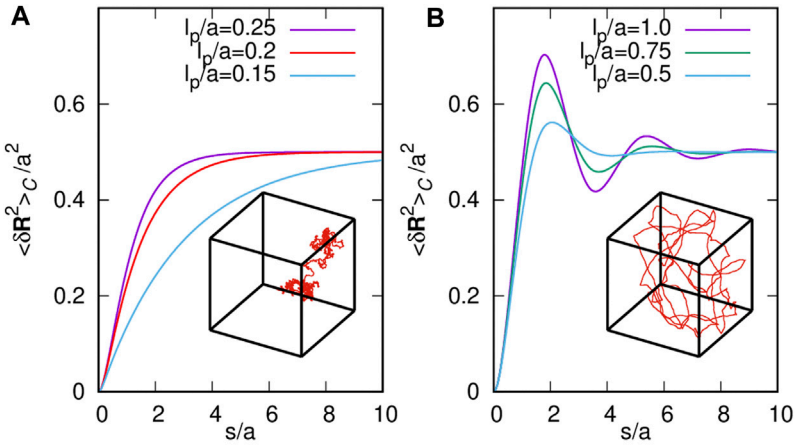

FIGURE 1 | Monotonous and oscillating behaviors of the mean-square end-to-end distance (**Eq. 30**) of polymers with ℓ_p below **(A)** and above **(B)** the critical persistence length $\ell_p^* = \sqrt{3}/(2\pi)a$ in cubic confinement. Inside the plotting area, we sketch the conformational states of each class of polymers.

we can convince ourselves that twice the mean-square end position corresponds to a saturation value for the mean-square end-to-end distance. An additional property of $\mathbf{r}_\mathbf{k}$ is the identity

$$\frac{1}{V(\mathcal{D})}\sum_{\mathbf{k}\neq 0}\mathbf{r}_k^*\mathbf{r}_\mathbf{k} = \sigma^2(\mathbf{R}). \tag{27}$$

This identity can be proved using the completeness relation of the eigenfunctions, that is, $\sum_\mathbf{k}\psi_\mathbf{k}^*(\mathbf{R})\psi_\mathbf{k}(\mathbf{R}') = \delta^{(3)}(\mathbf{R}'-\mathbf{R})$. This identity allows us to prove that in general $\langle(\delta\mathbf{R})^2\rangle_\mathcal{D}$ starts at zero.

4 RESULTS

4.1 Semiflexible Polymer Enclosed by a Cube Surface

In this section, we provide results for the mean-square end-to-end distance for a semiflexible polymer enclosed inside of a cube domain. All the problems are reduced to solve the Neumann eigenvalue problem $-\nabla^2\psi = \lambda\psi$ with Neumann boundary condition, when the compact domain $\mathcal{C} := \{(x,y,z)\in\mathbb{R}^3 : 0\le x\le a, 0\le y\le a, 0\le z\le a\}$ is a cube of side a in the positive octant. This problem is widely studied in different mathematical physics problems [21, 23]. The eigenfunctions in this case can be given by

$$\psi_\mathbf{k}(\mathbf{R}) = \frac{N_{nmp}}{a^{3/2}}\cos\left(\frac{\pi n}{a}x\right)\cos\left(\frac{\pi m}{a}y\right)\cos\left(\frac{\pi p}{a}z\right), \tag{28}$$

where x, y, and z are the standard Cartesian coordinates, and $\mathbf{R} = (x,y,z)$ is the usual vector position. The eigenfunctions are enumerated by the collective index nmp, with $n,m,p = 0,1,2,\cdots$. N_{nmp} is a normalization constant with respect to the volume of the cube $V(\mathcal{D}) = a^3$, whose values are given by $N_{000} = 1$; $N_{n00} = N_{0n0} = N_{00n} = \sqrt{2}$, for $n\neq 0$; $N_{np0} = N_{n0p} = N_{0np} = 2$, for $n,p\neq 0$; and $N_{npm} = 2\sqrt{2}$, for $n,m,p\neq 0$. The eigenvalues of the Laplacian are given by $\lambda_\mathbf{k} = \mathbf{k}^2$, where $\mathbf{k} = \left(\frac{\pi n}{a},\frac{\pi m}{a},\frac{\pi p}{a}\right)$. Now, we proceed to calculate $\mathbf{r}_\mathbf{k}$ using its definition, that is, $\mathbf{r}_\mathbf{k} = \int_\mathcal{C}\mathbf{R}\psi_\mathbf{k}(\mathbf{R})d^3\mathbf{R}$. The three components are given by

$$\begin{aligned}(\mathbf{r}_\mathbf{k})_x &= -\sqrt{2}\,\frac{a^{5/2}}{n^2\pi^2}(1-(-1)^n)\delta_{m0}\delta_{p0},\\ (\mathbf{r}_\mathbf{k})_y &= -\sqrt{2}\,\frac{a^{5/2}}{m^2\pi^2}(1-(-1)^m)\delta_{n0}\delta_{p0},\\ (\mathbf{r}_\mathbf{k})_z &= -\sqrt{2}\,\frac{a^{5/2}}{p^2\pi^2}(1-(-1)^p)\delta_{n0}\delta_{m0},\end{aligned} \tag{29}$$

In the following, we use the general expression in **Eq. 25** for the mean-square end-to-end distance. The mean-square end position can be easily calculated as $\sigma^2(\mathbf{R}) = \frac{a^2}{4}$. Since the Kronecker delta in $\mathbf{r}_\mathbf{k}$, each contribution of $(\mathbf{r}_\mathbf{k})_i$ is the same, thus taking into account the correct counting factor, the mean-square end-to-end distance is

$$\langle\delta\mathbf{R}^2\rangle_\mathcal{C} = \frac{a^2}{2} - 24a^2\sum_{k=1}^{\infty}\frac{\left(1-(-1)^k\right)}{k^4\pi^4}G\left(\frac{s}{2\ell_p},\frac{4}{3}\left(\frac{\ell_p}{a}\right)^2\pi^2k^2\right). \tag{30}$$

Following the same line of argument performed in [17], it is observed that $24\sum_{k=1}^{\infty}\frac{(1-(-1)^k)}{k^4\pi^4} = \frac{1}{2}$ consistently with **Eq. 27**; thus, up to a numerical error of 10^{-2}, we claim that

$$\begin{aligned}\frac{\langle\delta\mathbf{R}^2\rangle_\mathcal{C}}{a^2} \simeq \frac{1}{2} - \frac{1}{2}\exp\left(-\frac{L}{2\ell_p}\right)\Bigg\{&\cosh\left[\frac{L}{2\ell_p}\left(1-\frac{4\pi^2}{3}\frac{\ell_p^2}{a^2}\right)^{\frac{1}{2}}\right]\\ &+\left(1-\frac{4\pi^2}{3}\frac{\ell_p^2}{a^2}\right)^{-\frac{1}{2}}\sinh\left[\frac{L}{2\ell_p}\left(1-\frac{4\pi^2}{3}\frac{\ell_p^2}{a^2}\right)^{\frac{1}{2}}\right]\Bigg\}\end{aligned} \tag{31}$$

Let us remark that for any fixed value of a, the r.h.s of **Eq. 31**, as a function of L, shows the existence of a critical persistence length, $\ell_p^* = \sqrt{3}a/(2\pi)$ such that for all values of $\ell_p > \ell_p^*$, it exhibits an oscillating behavior, whereas for $\ell_p < \ell_p^*$, it is monotonically increasing. In **Figure 1**, we show the behavior of the mean-square end-to-end distance versus the length of the polymer for several

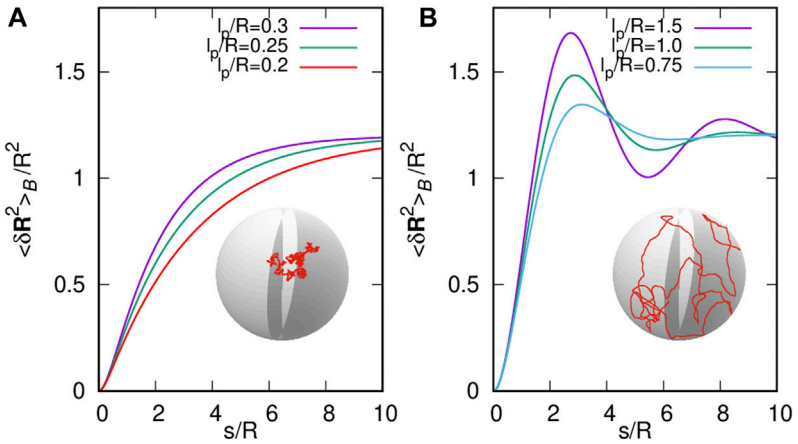

FIGURE 2 | Monotonous and oscillating behaviors of the mean-square end-to-end distance (**Eq. 37**) of polymers with ℓ_p below **(A)** and above **(B)** the critical persistence length $\ell_p^* = \sqrt{3}R/(2\alpha_1)$ in spherical confinement. Inside the plotting area, we sketch the conformational states of each class of polymers.

values of the persistence length below and above ℓ_p^*. Moreover, we also show sketches of conformational states corresponding to the monotonous and oscillating behaviors of the mean-square end-to-end distance. In addition, the same mathematical structure as the mean-square end-to-end distance found by Spakowitz and Wang [24] is noticeable for semiflexible polymers wrapping a spherical shell, and recently for semiflexible polymers confined to a square box [17].

4.2 Semiflexible Polymer Enclosed by a Spherical Surface

In this section, we provide results for the mean-square end-to-end distance for a semiflexible polymer enclosed inside of a spherical domain. All the problems are reduced to solve the Neumann eigenvalue problem $-\nabla^2\psi = \lambda\psi$ with Neumann boundary condition when the compact domain $\mathcal{B} := \{\mathbf{r} \in \mathbb{R}^3 : \mathbf{r}^2 \le R^2\}$ is a center ball of radius R. This problem is widely studied in different mathematical physics problems [21, 23]. The eigenfunctions in this case can be given in terms of spherical Bessel functions $j_\ell(x)$ and spherical harmonic functions $Y_{\ell m}(\theta,\varphi)$:

$$\psi_{\ell mk}(r,\theta,\varphi) = N_{\ell k}\, j_\ell\!\left(\alpha_{\ell k}\frac{r}{R}\right) Y_{\ell m}(\theta,\varphi), \tag{32}$$

where r, θ, and φ are the standard spherical coordinates. The factor $N_{\ell k}$ is a normalization constant with respect to the volume of the ball $\mathcal{B}$, given by

$$N_{\ell k} = \frac{\sqrt{2}}{R^{3/2}}\,\frac{\alpha_{\ell k}}{j_\ell(\alpha_{\ell k})\left(\alpha_{\ell k}^2 - \ell(\ell+1)\right)^{1/2}}. \tag{33}$$

The coefficients $\alpha_{\ell k}$ are the roots of $\partial j_\ell(x)/\partial x$, which, by using the identity $\ell j_{\ell-1}(x) - (\ell+1)j_{\ell+1} = (2\ell+1)\partial j_\ell(x)/\partial x$, satisfy the equation $\ell j_{\ell-1}(\alpha_{\ell k}) = (\ell+1)j_{\ell+1}(\alpha_{\ell k})$. The eigenfunctions are enumerated by the collective index ℓmk, with $\ell = 0, 1, 2, \cdots$ counting the order of spherical Bessel functions, $m = -\ell, -\ell+1, \cdots, \ell$, and $k = 1, 2, 3, \cdots$ counting zeros. The eigenvalues of the Laplacian are given by $\lambda_{\ell mk} = \alpha_{\ell k}^2/R^2$, which are independent of the numbers m. Now, we proceed to calculate $\mathbf{r}_{\ell mk}$ by using **Eq. 26**. It is enough to calculate $\oint_{S^2} dS\,\mathbf{n}\, Y_{\ell m}(\theta,\varphi)$, since $\mathbf{n} \propto Y_{1m}$; thus, $\oint_{S^2} dS\,\mathbf{n}\, Y_{1,\pm1}(\theta,\varphi) = -\sqrt{\frac{2\pi}{3}}R^2(\pm1, i, 0)$ and $\oint_{S^2} dS\,\mathbf{n}\, Y_{1,0}(\theta,\varphi) = 2\sqrt{\frac{\pi}{3}}R^2(0,0,1)$. Now, we call $\alpha_{1k} := \alpha_k$; then, using **Eq. 33** one has

$$\mathbf{r}_{1,\pm1,k} = -2\sqrt{\frac{\pi}{3}}\,\frac{R^{5/2}}{\alpha_k\left(\alpha_k^2 - 2\right)^{1/2}}(\pm1, i, 0), \tag{34}$$

$$\mathbf{r}_{1,0,k} = 2\sqrt{\frac{2\pi}{3}}\,\frac{R^{1/2}}{\alpha_k\left(\alpha_k^2 - 2\right)^{1/2}}(0,0,1), \tag{35}$$

where roots $\{\alpha_k\}$ satisfy the equation $j_0(\alpha_k) = 2j_2(\alpha_k)$. Using explicit functions of the spherical Bessel functions, the root condition is $F(\alpha_k) = 0$, where

$$F(x) = \left(\frac{x^2}{2} - 1\right)\sin x + x\cos x. \tag{36}$$

In the following, we use the general expression (**Eq. 25**) for the mean-square end-to-end distance. We calculate the mean-square end position, $\sigma^2(\mathbf{R}) = \frac{3}{5}R^2$, and use the factors $\mathbf{r}_{\ell mk}$; thus, the mean square end-to-end distance is

$$\langle \delta\mathbf{R}^2\rangle_{\mathcal{B}} = \frac{6}{5}R^2 - 12R^2\sum_{k=1}^{\infty}\frac{1}{\alpha_k^2\left(\alpha_k^2-2\right)}G\!\left(\frac{s}{2\ell_p}, \frac{4}{3}\left(\frac{\ell_p}{R}\right)^2\alpha_k^2\right). \tag{37}$$

Following the same line of argument performed in [17], we observe numerically that $12\sum_{k=1}^{N}\frac{1}{\alpha_k^2(\alpha_k^2-2)} \to 6/5$ as N increases; this is consistent with **Eq. 27**. Thus, up to a numerical error 10^{-2}, we claim that

$$\frac{\langle \delta\mathbf{R}^2\rangle_{\mathcal{B}}}{R^2} \simeq \frac{6}{5} - \frac{6}{5}\exp\!\left(-\frac{L}{2\ell_p}\right)\left\{\cosh\left[\frac{L}{2\ell_p}\left(1 - \frac{4\alpha_1^2}{3}\frac{\ell_p^2}{R^2}\right)^{\frac{1}{2}}\right] + \left(1 - \frac{4\alpha_1^2}{3}\frac{\ell_p^2}{R^2}\right)^{-\frac{1}{2}}\sinh\left[\frac{L}{2\ell_p}\left(1 - \frac{4\alpha_1^2}{3}\frac{\ell_p^2}{R^2}\right)^{\frac{1}{2}}\right]\right\} \tag{38}$$

Let us remark that for any fixed value of R, the r.h.s of **Eq. 38**, as a function of L, shows the existence of a critical persistence length, $\ell_p^* = \sqrt{3}R/(2\alpha_1)$, with $\alpha_1 \simeq 2.08158$ according to **Eq. 36** such that for all values of $\ell_p > \ell_p^*$, it exhibits an oscillating behavior, whereas for $\ell_p < \ell_p^*$, it is monotonically increasing. In **Figure 2**, we show the behavior of the mean-square end-to-end distance versus the length of the polymer for several values of the persistence length below and above ℓ_p^*. Moreover, we also show sketches of conformational states corresponding to the monotonous and oscillating behaviors of the mean-square end-to-end distance. In addition, it is noticeably that the same mathematical structure as the mean-square end-to-end distance found by Spakowitz and Wang [24] for semiflexible polymers wrapping a spherical shell, and recently for semiflexible polymers, confined to a square box [17].

5 CONCLUDING REMARKS

In this work, we carry out an extension of the stochastic curvature formalism introduced in [17] to analyze the conformational states of a semiflexible polymer in a thermal bath for the cases when the polymer is in the open space $\mathbb{R}^3$ and when it is in a bounded domain $\mathcal{D} \subset \mathbb{R}^3$. The basic idea of formalism in the 3D case is followed by two postulates, that is, each conformational state corresponds to the realization of a path described by the stochastic Frenet–Serret **Eq. 5a** and **Eq. 5b**, to introduce a stochastic curvature vector $\boldsymbol{k}(s)$, and a second postulate that gives the manner how $\boldsymbol{\kappa}(s)$ is distributed according to the thermal fluctuations.

In the case of a polymer in an open space $\mathbb{R}^3$, the standard Kratky–Porod formula for polymers is reproduced in three dimensions [16], while when the polymer is confined to a space bounded region $\mathcal{D} \subset \mathbb{R}^3$, the conformational states show the existence of a critical persistence length ℓ_p^* such that for all values of $\ell_p > \ell_p^*$, the mean square distance from end to end exhibits an oscillating behavior, while for $\ell_p < \ell_p^*$, it exhibits a monotonic behavior in both cases of a cubic region and a spherical region. Furthermore, for each value of ℓ_p, the function converges to twice the mean-square end position $\sigma^2(\mathbf{R})$, that is, twice the variance of $\mathbf{R}^2$ with respect to the volume of the domain. The critical persistence length, therefore, distinguishes two conformational behaviors of the semiflexible polymer in the bound domain. On the one hand, polymers with persistence length below the critical value have a conformation similar to a Brownian random path. On the other hand, polymers with persistence length above the critical value adopt smooth conformations. In addition, it is highlighted that the mean-square end-to-end distance exhibits the same mathematical form for the discussed cases along with the manuscript (**Eq. 31** and **Eq. 38**) and with the results reported for a polymer enclosed to a square box and rolling up a spherical surface [17, 24]. Nevertheless, the value difference of saturation and the critical persistence length reflect the particular geometric nature of the compact domain, including the dimensionality of the space. Note the particular mathematical expression in our work is due to the probability density function of the polymer's ends, which is governed by a modified telegrapher equation. As a consequence of this resemblance, it can be concluded that the shape transition from oscillating to monotonous conformational states provides furthermore evidence of a universal signature for a semiflexible polymer enclosed in compact space.

DATA AVAILABILITY STATEMENT

The original contributions presented in the study are included in the article/Supplementary Material, and further inquiries can be directed to the corresponding authors.

AUTHOR CONTRIBUTIONS

Both authors contributed to the formulation of the method and the writing of the manuscript. JR contributed to the numerical analysis that provides the figures, while PC-V contributed to the mathematical calculations.

ACKNOWLEDGMENTS

PC-V and JR acknowledge financial support by Consejo de Ciencia y Tecnología del Estado de Puebla (CONCYTEP).

REFERENCES

1. Ronca S, "Polyethylene," *In* Brydson's Plastics Materials (8th ed.) (M Gilbert, ed.), pp. 247–78. Butterworth-Heinemann, 8th ed. ed., 2017. doi:10.1016/b978-0-323-35824-8.00010-4
2. Wünsch J. *Polystyrene: Synthesis, Production and Applications*. RAPRA Technology Limited, Rapra Technology Limited (2000).
3. Cifra P, and Bleha T. Shape Transition of Semi-flexible Macromolecules Confined in Channel and Cavity. *Eur Phys J E* (2010) 32(3):273–9. doi:10.1140/epje/i2010-10626-y
4. Locker CR, and Harvey SC. A Model for Viral Genome Packing. *Multiscale Model Simul* (2006) 5(4):1264–79. doi:10.1137/060650684
5. Köster S, Kierfeld J, and Pfohl T. Characterization of Single Semiflexible Filaments under Geometric Constraints. *Eur Phys J E* (2008) 25(4):439–49. doi:10.1140/epje/i2007-10312-3
6. Reisner W, Morton KJ, Riehn R, Wang YM, Yu Z, Rosen M, et al. Statics and Dynamics of Single Dna Molecules Confined in Nanochannels. *Phys Rev Lett* (2005) 94:196101. doi:10.1103/physrevlett.94.196101
7. Benková Z, Rišpanová L, and Cifra P. Structural Behavior of a Semiflexible Polymer Chain in an Array of Nanoposts. *Polymers* (2017) 9(8):313. doi:10.3390/polym9080313
8. Saitô N, Takahashi K, and Yunoki Y. *The Statistical Mechanical Theory of Stiff Chains* (1967).
9. Kleinert H, and Chervyakov A. Perturbation Theory for Path Integrals of Stiff Polymers. *J Phys A: Math Gen* (2006) 39:8231–55. doi:10.1088/0305-4470/39/26/001

10. Benetatos P, and Frey E. Linear Response of a Grafted Semiflexible Polymer to a Uniform Force Field. *Phys Rev E Stat Nonlin Soft Matter Phys* (2004) 70: 051806. doi:10.1103/PhysRevE.70.051806
11. Adsorption of polymers and polyelectrolytes. In Solid-Liquid Interfaces. In: J Lyklema, editor. *Vol. 2 of Fundamentals of Interface and Colloid Science*. Academic Press (1995). p. 5–1. – 5–100.
12. Guven J, and Vázquez-Montejo P. Confinement of Semiflexible Polymers. *Phys Rev E Stat Nonlin Soft Matter Phys* (2012) 85(2):026603–16. doi:10.1103/PhysRevE.85.026603
13. Guven J, María Valencia D, and Vázquez-Montejo P. Environmental Bias and Elastic Curves on Surfaces. *J Phys A: Math Theor* (2014) 47(35). doi:10.1088/1751-8113/47/35/355201
14. Spakowitz AJ, and Wang ZG. End-to-end Distance Vector Distribution with Fixed End Orientations for the Wormlike Chain Model. *Phys Rev E Stat Nonlin Soft Matter Phys* (2005) 72:041802. doi:10.1103/PhysRevE.72.041802
15. Chen JZY. Theory of Wormlike Polymer Chains in Confinement. *Prog Polym Sci* (2016) 54-55:3–46. doi:10.1016/j.progpolymsci.2015.09.002
16. Kratky O, and Porod G. Röntgenuntersuchung Gelöster Fadenmoleküle. *Recl Trav Chim Pays-bas* (1949) 68(12):1106–22. doi:10.1002/recl.19490681203
17. Castro-Villarreal P, and Ramírez JE. Stochastic Curvature of Enclosed Semiflexible Polymers. *Phys Rev E* (2019) 100:012503. doi:10.1103/PhysRevE.100.012503
18. Montiel S, and Ros A. *Curves and Surfaces, Vol. 69*. American Mathematical Soc. (2009).
19. Gardiner CW. Handbook of Stochastic Methods for Physics. *Chem Nat Sci* (1986) 25.
20. Hermans JJ, and Ullman R. The Statistics of Stiff Chains, with Applications to Light Scattering. *Physica* (1952) 18(11):951–71. doi:10.1016/s0031-8914(52)80231-9
21. Feshbach H. *Methods of Theoretical Physics*. New York: McGraw-Hill (1953).
22. Chavel I. *Eigenvalues in Riemannian Geometry, Vol. 115*. Academic Press (1984).
23. Grebenkov DS, and Nguyen B-T. Geometrical Structure of Laplacian Eigenfunctions. *SIAM Rev* (2013) 55(4):601–67. doi:10.1137/120880173
24. Spakowitz AJ, and Wang Z-G. Semiflexible Polymer Confined to a Spherical Surface. *Phys Rev Lett* (2003) 91:166102. doi:10.1103/physrevlett.91.166102

Conflict of Interest: The authors declare that the research was conducted in the absence of any commercial or financial relationships that could be construed as a potential conflict of interest.

Advantages of publishing in Frontiers

OPEN ACCESS
Articles are free to read for greatest visibility and readership

FAST PUBLICATION
Around 90 days from submission to decision

HIGH QUALITY PEER-REVIEW
Rigorous, collaborative, and constructive peer-review

TRANSPARENT PEER-REVIEW
Editors and reviewers acknowledged by name on published articles

Frontiers
Avenue du Tribunal-Fédéral 34
1005 Lausanne | Switzerland

Visit us: www.frontiersin.org
Contact us: frontiersin.org/about/contact

REPRODUCIBILITY OF RESEARCH
Support open data and methods to enhance research reproducibility

DIGITAL PUBLISHING
Articles designed for optimal readership across devices

FOLLOW US
@frontiersin

IMPACT METRICS
Advanced article metrics track visibility across digital media

EXTENSIVE PROMOTION
Marketing and promotion of impactful research

LOOP RESEARCH NETWORK
Our network increases your article's readership